Journal of Engineering and Technology for Industrial Applications

ISSN 2447-0228

June 2025

Volume 11/ No 53

Editor-in-Chief: J. C. Leite

www.itegam-jetia.org

ITEGAM - JETIA ISSN 2447-0228 Online
Journal of Engineering and Technology for Industrial Applications (JETIA)

O **ITEGAM-JETIA: Journal of Engineering and Technology for Industrial Applications** is a publication of the Galileo Institute of Technology and Education of the Amazon (ITEGAM), located in the city of Manaus since 2008. JETIA publishes original scientific articles covering all aspects of engineering. Our goal is the dissemination of research original, useful and relevant presenting new knowledge on theoretical or practical aspects of methodologies and methods used in engineering or leading to improvements in professional practice. All the conclusions presented in the articles It should be state-of-the-art and supported by current rigorous analysis and balanced assessment. Public magazine scientific and technological research articles, review articles and case studies.
JETIA will address topics from the following areas of knowledge: Mechanical Engineering, Civil Engineering, Materials and Mineralogy, Geosciences, Environment, Information and Decision Systems, Processes and Energy, Electrical and Automation, Mechatronics, Biotechnology and other Engineering related areas.

Publication Information:
ITEGAM-JETIA (ISSN 2447-0228), (online) is published by Galileo Institute of Technology and Education of the Amazon on a every two months (February, April, June, August, October and December).

Contact information:

Web page: www.itegam-jetia.org
Email: editor@itegam-jetia.org
Galileo Institute of Technology and Education of the Amazon (ITEGAM).

Joaquim Nabuco Avenue, No. 1950. Center. Manaus, Amazonas. Brazil.
Zip Code: 69020-031. Phone: (92) 3584-6145.

Previous Notice
All statements, methods, instructions and ideas are the sole responsibility of the authors and do not necessarily represent the view of ITEGAM -JETIA. The publisher is not responsible for any damage and / or damage to the use of the contents of this journal. The concepts and opinions expressed in the articles are the sole responsibility of the authors.

Directory

ITEGAM - JETIA ISSN 2447-0228 Online
Journal of Engineering and Technology for Industrial Applications (JETIA)

ITEGAM-JETIA. v.11, n.53. June of 2025. Manaus - Amazonas, Brazil. ISSN 2447-0228 (ONLINE)
https://www.itegam-jetia.org

SUMMARY

EVALUATION OF THE MECHANICAL PROPERTIES OF CONCRETE MIXED WITH WATER-SOLUBLE POLYMER **6**
Dele Roger Simeon, Aliu Adebayo Soyingbe, Rabiu Aminu

REVOLUTIONIZING MASS PRODUCTION: A DUAL POWER PORTABLE PHOTOGRAPHIC SILKSCREEN PATTERN EQUIPMENT **17**
Halima A. Sahim-Sali, Joshua R. Apolinario, Spencer Vape Araneta Gregorio, Anna Rose Relativo Amalan, Kevin Maningo, Ernesto Bantug

ASSESSMENT OF THE POTENTIAL FOR ENERGY RECOVERY IN A SUGAR CANE MILL **21**
Jorge Guevara Rodríguez, Juan Pedro Henández Touset, Lirianet Fuentes Ramírez

OPERATIONAL FACTORS INFLUENCING QUALITY CONTROL IN ORE MILLING: A SYSTEMATIC REVIEW **25**
Eliana de Jesus Lopes, Guilherme Graciano dos Santos, Adriano Ricardo Almeida Alexandre

IMPROVING INVERTER EFFICIENCY FOR ELECTRIC VEHICLES: EXPERIMENTAL VALIDATION OF THE NEURAL NETWORK-BASED SHE TECHNIQUE USING RT-LAB **34**
Seyf Eddine Bechekir, Mokhtaria Jbilou, Mostefa Brahami, Fatima Zohra Boudjella, Imen Souhila Bousmaha, Mimouna Oukli, Said Nemmich

INTEGRATING VGG RE-TRAINED FEATURE EXTRACTION WITH MACHINE LEARNING FOR KNEE OSTEOARTHRITIS SEVERITY LEVELS DETECTION USING X-RAY IMAGES **41**
Simeon Yuda Prasetyo, Ghinaa Zain Nabiilah

MACHINE LEARNING TECHNIQUES FOR IDENTIFYING TEXTUAL PROPAGANDA ON SOCIAL MEDIA: DEVELOPMENT OF A DETECTING DIGITAL MANIPULATION SYSTEM **48**
Belkacem Mostefai, Tarek Boutefara, Abid Chahinez, Marwa Aberkane

PRACTICAL IMPLEMENTATION OF A SMART HOME MODEL USING ARDUINO AND SENSORS **55**
Soufiane Hachani, Okba Benelmir

DESIGN AND DEVELOPMENT OF NOVEL COOLING ARRANGEMENT FOR PV CELL **62**
Keval Chandrakant Nikam, Amit Umbrajkar, Sandesh Solepatil, Vandana Patil, Chetan Pawar, Vedant Jirafe, Piyush Bhosale

NUMERICAL ANALYSIS OF HYGROTHERMAL EFFECTS ON LOW-VELOCITY IMPACT CONTACT FORCE IN S-GLASS/POLYESTER COMPOSITE PLATES **70**
Rabouh Mustapha, Kamel Zouggar, Khelifa Guerraiche

DELINEATION OF GROUNDWATER POTENTIAL ZONES USING INTEGRATED VERTICAL ELECTRICAL SOUNDING AND GEOSPATIAL TECHNIQUES IN THE BASEMENT COMPLEX OF IJESHA ISU EKITI, SOUTHWESTERN NIGERIA **76**
Taofeek O. Ewumi, Funmilola O. Ogunlana, Akintunde Akinola Oyedele

ANALYSIS OF LORA SIGNAL PROPAGATION IN URBAN ENVIRONMENT **81**
David Alan de Oliveira Ferreira

HEALTH CLASSIFICATION OF PUMPS USING TRANSFORMER-BASED DEEP LEARNING **87**
Arunachalam Shivaa T V, Jayaprasanth Devakumar, Arunshankar Jayabalan

ITEGAM - JETIA
ISSN 2447-0228 Online
Journal of Engineering and Technology for Industrial Applications (JETIA)

ENERGY IMPACT OF LIGHTING SYSTEM REPLACEMENT IN A PUBLIC EDUCATION INSTITUTION **95**
Willan Almeida Fernando Alberto Benger, Cristian Roberto Ruschetti, Matias Meira, Silvano Renato Rossi, Juan Pablo Pendones

ANALYTICAL AND NUMERICAL MODELING OF THE TRANSIENT BEHAVIOR OF AN EARTH CONNECTION DURING THE INJECTION OF AN ELECTROMAGNETIC WAVE **103**
Mohammed Chebout, Azizi Hakim, Daoud Sekki, Mohammed Charif Kihal, Marouane Kihal

AI-DRIVEN FIRE DETECTION AND SUPPRESSION SYSTEM WITH REAL-TIME REMOTE MONITORING **110**
Metahri Dhiyaeddine, Dekar Amina, SettingsKadi Halima Bouchra

USING BAYESIAN NETWORKS AND FUZZY LOGIC TO PREDICT WAREHOUSE PLANNING DISRUPTION RISKS **117**
Kerouich Abdelilah, Azmani Abdellah, Azmani Monir

PATCHDETECT: BREAST CANCER DETECTION COMBINING UNET-RESNET-50 AND PATCH EMBEDDING LSTM **127**
Hadj Ahmed Bouarara, kadda Benyahia

SUSTAINABLE SOLUTIONS FOR URBAN INFRASTRUCTURE: THE ENVIRONMENTAL AND ECONOMIC BENEFITS OF USING RECYCLED CONSTRUCTION AND DEMOLITION WASTE IN PERMEABLE PAVEMENTS **135**
Eliomar Gotardi Pessoa

ANALYSIS OF THE PERFORMANCE OF HELICAL PILES UNDER VARIOUS LOAD AND GEOMETRY CONDITIONS **140**
Eliomar Gotardi Pessoa

DEVELOPMENT OF HYBRID EXEMPLAR BASED DLSRGAN MODEL FOR RESTORATION OF THE DISTORTED SIGNALS **146**
Tammineni Shanmukha Prasanthi, Swaraiya Madhuri Rayavarapu, Gottapu Sasibhushana Rao, Rajkumar Goswami

DESIGN AND IMPLEMENTATION OF A SCALABLE LORA-BASED IOT IRRIGATION SYSTEM WITH DUAL CONTROL MECHANISMS **150**
Salahedin Rehan, Esra Alhame, Esra Hassan

TYPE-2 FUZZY CONTROL OF DFIG FOR WIND ENERGY CONVERSION SYSTEMS **159**
Mohamed Abdeldjabbar Kouadria, Selman Kouadria, Mohamed Amine Bouzid

APPLICATION OF MACHINE LEARNING FOR REAL-TIME PHISHING ATTACK DETECTION **167**
Akshay Shankar Agrawal, Sanketi Raut, Andrina Dsouza, Jimit Mehta, Prajwal Naik

PLANNING OF DISTRIBUTED GENERATION SOURCES WIND AND PV IN IEEE 33-BUS SYSTEM **175**
Krar Shakir Alibrahimi, Seyed Mohamed Hassan Hossaini

BIMODAL TECHNIQUE FOR ENHANCEMENT OF PICTURE QUALITY OF MEDICAL IMAGES **182**
Akeem Abimbola Raji, Oluwaseun Ibrahim Adebisi, Adewale Olubunmi Akinola, Benson Ayoade Ogundare

OPTIMIZED PID TUNING IN LONGITUDINAL CONTROL OF ELECTRIC AUTONOMOUS VEHICLES: A COMPARATIVE STUDY OF JELLYFISH SEARCH AND GENETIC ALGORITHM **191**
Asmaa Guendouz, Mustapha Hatti, Abdelhalim Tlemçani

ITEGAM - JETIA
ISSN 2447-0228 Online
Journal of Engineering and Technology for Industrial Applications (JETIA)

AI-POWERED SIMULTANEOUS MULTI-VEHICLE SPEED ESTIMATION FOR INTELLIGENT TRAFFIC MONITORING IN DEVELOPING REGIONS USING YOLOV7 AND DEEPSORT **198**
Ahmed Merrad, Walid Daoud, Aissa Dalouli, Boubakeur Latrech, Abdelkader Nabil Nouri

PERFORMANCE ANALYSIS OF A 90MM MULTI LAUNCHER MISSILE SYSTEM INTEGRATED WITH RADAR FOR VITAL OBJECT AIR DEFENSE AGAINST HIGH SPEED AND STEALTH AERIAL THREATS **206**
Nur Rachman Supadmana Muda

WATERPROOFING APPLICATIONS IN MASONRY STRUCTURES: A CASE STUDY IN RESIDENTIAL BUILDINGS IN THE NORTH OF MANAUS, BRAZIL **213**
Wmilison Sousa da Silva, Edinaldo José de Sousa Cunha

DESIGN OF PARTICLE SWARM OPTIMIZATION-BASED PID CONTROLLER FOR HIGH-PERFORMANCE PMSM SPEED CONTROL **221**
Mohammed Obaid Mustafa, Ghufran Saad Mohammed

Journal of Engineering and Technology for Industrial Applications

ITEGAM-JETIA

Manaus, v.11 n.53, p. 6-16. May./ June., 2025.
DOI: https://doi.org/10.5935/jetia. v11i53.961

ISSN ONLINE: 2447-0228

RESEARCH ARTICLE OPEN ACCESS

EVALUATION OF THE MECHANICAL PROPERTIES OF CONCRETE MIXED WITH WATER-SOLUBLE POLYMER

Dele Roger Simeon[1], Aliu Adebayo Soyingbe[2], and Rabiu Aminu[3]

[1,2,3] Department of Building, University of Lagos, Lagos, Nigeria.

[1]http://orcid.org/0000-0002-3927-7547, [2]http://orcid.org/0000-0002-7992-6556, [3]http://orcid.org/0009-0005-2527-2111

Email: simeondele2@gmail.com, dsimeon@unilag.edu.ng, asoyingbe@unilag.edu.ng, rabiuaminu67@gmail.com

ARTICLE INFO

Article History
Received: November 21, 2023
Revised: January 20, 2025
Accepted: May 15, 2025
Published: May 31, 2025

Keywords:
Admixture,
Bonding,
Mass concrete,
Polyvinyl Alcohol,
Water-soluble polymer.

ABSTRACT

Polyvinyl alcohol (PVA) is a water-soluble polymer whose impact on concrete properties requires further investigation. Thus, this study established the appropriate dose and applicability of PVA to produce the foremost improvement in the mechanical characteristics of concrete. The study produced 40 concrete cubes and 12 cylinders of concrete specimens at 0%, 0.5%, 1%, 1.5%, and 2% doses of PVA. A number of tests were carried out on the specimens to ascertain their performances. The results showed that a 0.5% addition of PVA to the concrete mixture yields an optimal compressive strength of 24.98N/mm^2 after 28 days, while the tensile strength increased as the percentage of PVA increased. Besides, the bond strength of the PVA-modified concrete decreased as the proportion of PVA in the concrete mixture increased. The study concludes that a 0.5% addition of PVA to concrete is the ideal dose for enhanced compressive strength. Also, the study concludes that, while the tensile strength of concrete increases with increasing PVA doses, the bond strength of concrete and rebars decreases as the percentage of PVA increases. This implies that PVA is unsuitable for reinforced concrete structural works. The study therefore recommends that PVA should be applied for non-structural reinforced concrete works.

I. INTRODUCTION

Concrete is one of the most often utilized building materials and is regarded as a composite material made of cement, water, and aggregates [1], [2]. The properties of hardened concrete include its strength, durability, and dimensional stability. [3] substantiate that these properties of concrete may be enhanced through the introduction of different chemical admixtures, such as plasticizers, superplasticizers, and polymers. [4] posit that a category of admixtures called polymers are commonly employed in products like cement binders and notable examples include recognized additions of latexes, organosilicon compounds, polyvinyl acetate, polyvinyl alcohol (PVA), and other polymer cement compositions.

PVA has been demonstrated to increase concrete's mechanical properties and durability by boosting its compressive strength, tensile, and flexural strength [5]. Previous studies have shown that PVA has the ability to considerably improve the characteristics of concrete, making it an important addition to the manufacturing process [5, 6, 7]. In this regard, [8] found that adding PVA as a bonding admixture to concrete can boost its compressive strength. The authors note that a 0.3% addition of PVA by the unit weight of cement was the ideal mix ratio for maximizing compressive strength enhancement. Similarly, [9] found that PVA can improve the compressive strength of concrete by up to 26% at a dosage of 1% PVA by weight of cement. Besides, [10] opine that the addition of PVA fibre to concrete greatly enhanced its tensile strength while only somewhat improving its compressive strength. While noting that the higher the amount of fibre inclusion, the greater the potential of pore connections in the matrix, resulting in a drop in the tensile strength of concrete. Meanwhile, [11] conducted studies on self-curing concrete of M30 grade by using PVA.

It was discovered that 2% PVA gives lower compressive strength and split tensile strength in comparison to water-cured specimens without self-curing agents. Consequently, it has been revealed that the addition of PVA at large doses over 1.5% of cement does not provide the predicted results in strength and cannot be employed realistically. [12] investigated the use of recycled concrete aggregate with PVA, and the results revealed the

maximum inclusion (2%) resulted in a 52% improvement in strength over the reference concrete with 0% incorporation. While PVA has been extensively applied to building and infrastructural projects on the global stage, there are fewer studies on the African continent on the application of PVA in concrete on these monumental projects. The Egyptian study by [13] examined the behavior of Reinforced Concrete Columns with PVA Under Fire. In addition, the Egyptian study by [14] evaluated the enhancement of tensile strength of high strength Concrete using PVA Fibre. Yet, in the context of Nigeria, very limited studies are currently available on the technical know-how and competence regarding the proper application of PVA in the Nigerian concrete industry.

This has created a gap in the need for literature on the applications of PVA as an admixture for concrete works in Nigeria. Also, the majority of literature on PVA used concrete manufactured with cement and aggregates in the country where these studies were undertaken [14-17]. Hence, studies on PVA utilizing Nigerian concrete materials are required since the characteristics of various materials vary depending on their geographical origin**.**

Considering the foregoing, this study establishes the appropriate dose and applicability of PVA to produce the foremost improvement in the mechanical characteristics of concrete. The objectives of this study are to evaluate the impacts of PVA addition to concrete mixtures, identify the mechanical characteristics of the resulting concrete, and find the appropriate PVA dose for concrete manufacturing. The study is significant because it increases concrete workability, lowers permeability, reduces cracking and improves cement-aggregate adhesion, resulting in a more resilient and flexible concrete structure.

II. THEORETICAL REFERENCE

II.1 DEFINITION AND MECHANICAL CHARACTERISTICS OF CONCRETE

Concrete is defined as a highly complex heterogeneous material whose response to stress is determined not only by the response of the individual components but also by the interaction between those components. The components of concrete are binder (cement), aggregates (fine and coarse), and water. According to [2], concrete is one of the most widely utilized products in the building and construction sector. Oftentimes, admixtures are added to the concrete mixture immediately before or during mixing to enhance concrete properties for diverse desired effects. On such admixture is PVA, which according to [4], has been classified as a polymeric additive that enhances the mechanical properties of concrete.

The mechanical qualities of concrete, such as its tensile, flexural, and compressive strengths, define a structure's ability to support loads and maintain its overall structural integrity. Accordingly, a prerequisite for how the concrete may be loaded is that it is able to create the appropriate mechanical strength [18]. The addition of polymers to concrete can drastically alter its mechanical properties [14], [19]. It has high adherence to the concrete substrate, high tensile and flexural strength, and low shrinkage and permeability [20]. PVA is typically added to the concrete mix during the mixing process, along with the other dry ingredients [21].

II.2 BIBLIOMETRIC EVALUATION OF PVA CONCRETE

The Scopus and VOSviewer programme was used to perform a bibliometric evaluation, with the terms "PVA" and "Concrete" on dimensionAI and "PVA" or "Polyvinyl Alcohol" and "Concrete" on Scopus to search for relevant publications. The review's aim was to assess the present status of research on the use of PVA in concrete manufacture. The findings of this research are visually shown in Figures 1 through 6. Based on co-author and citation patterns, the Scopus and VOSviewer programme were used to trace the links between the papers discovered.

According to the findings of the investigation, the most often referenced publications on the subject originated in China, the United States and Canada, India and Malaysia, Australia, Japan and South Korea, the United Kingdom and Germany. While each of these countries represented a separate continent, it was discovered that there were few publications from Africa.

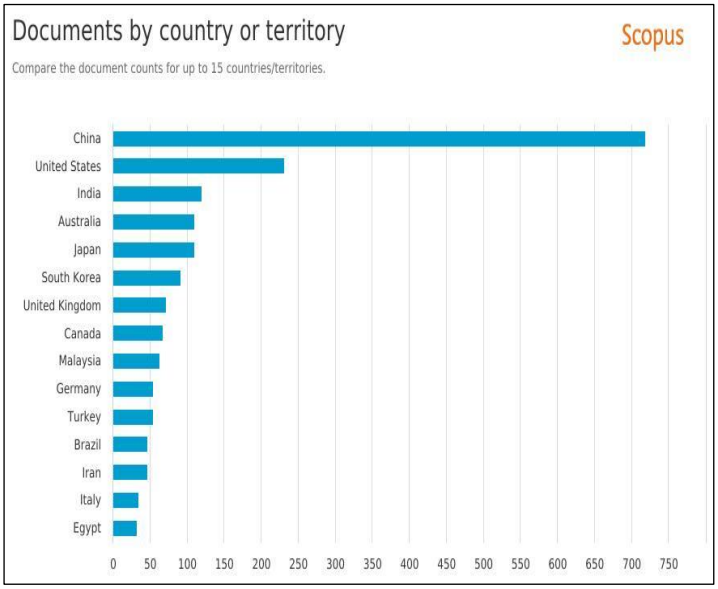

Figure 1: Scopus Analysis.
Source: Authors, (2025).

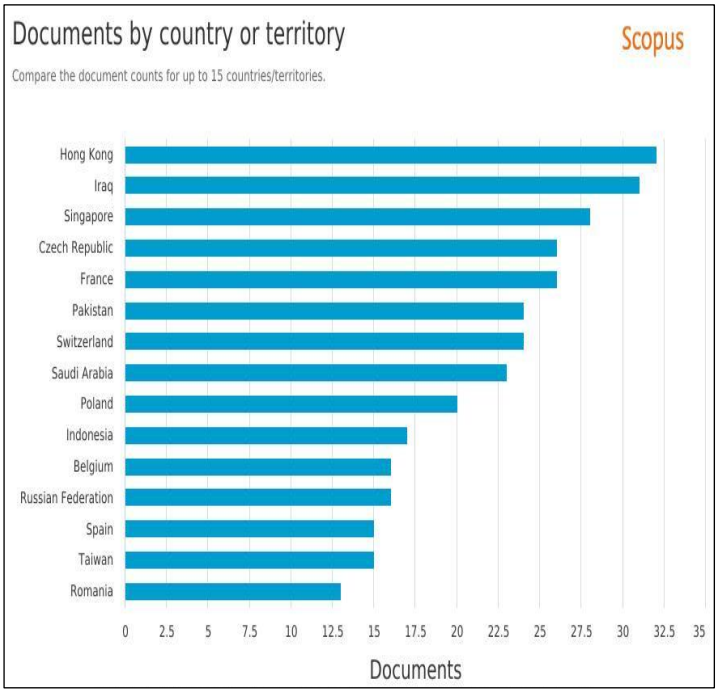

Figure 2: Scopus Analysis
Source: Authors, (2025).

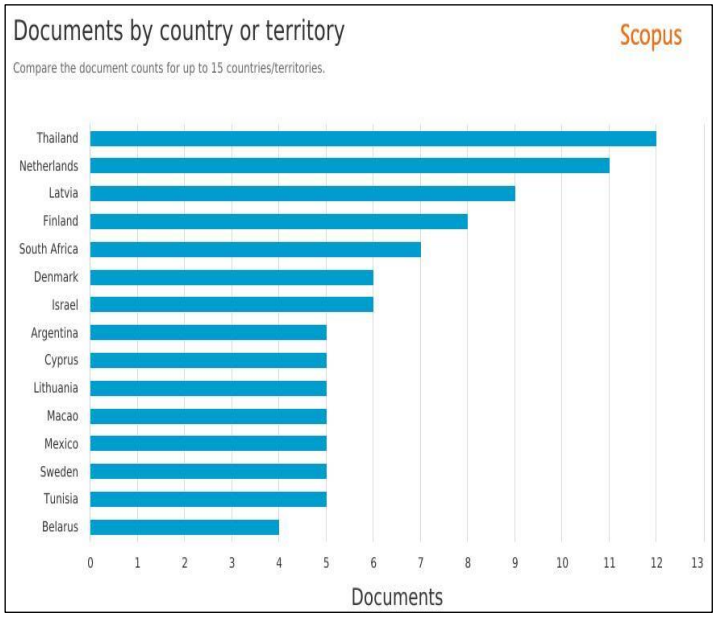

Figure 3**:** Scopus Analysis.
Source: Authors, (2025).

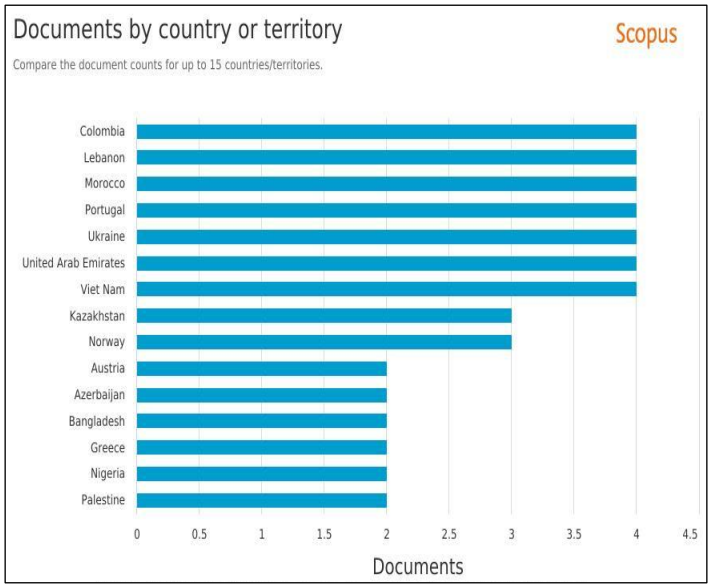

Figure 4: Scopus Analysis.
Source: Authors, (2025).

According to the Scopus data, Nigeria has just two articles out of a total of 4240 papers matching the keywords. According to the findings of the bibliometric evaluation, there is a substantial amount of research being undertaken on the subject of employing PVA in concrete manufacturing, with the bulk of the studies coming from Asia, North America, and Europe. Yet, it was discovered that there is minimal study in this sector in Africa. This might imply a knowledge and awareness gap in the region about the potential benefits of PVA in concrete manufacturing.

This absence of research in Africa might have serious consequences for the continent's construction industry. As a result, investigations on PVA employing African concrete materials are required. Despite the potential benefits of PVA, few researches have been conducted on the technical knowledge and experience required for the right usage and use of PVA in concrete production. As a result, further study is required to improve experimental procedures, strengthen a systematic approach, and enhance specialized understanding.

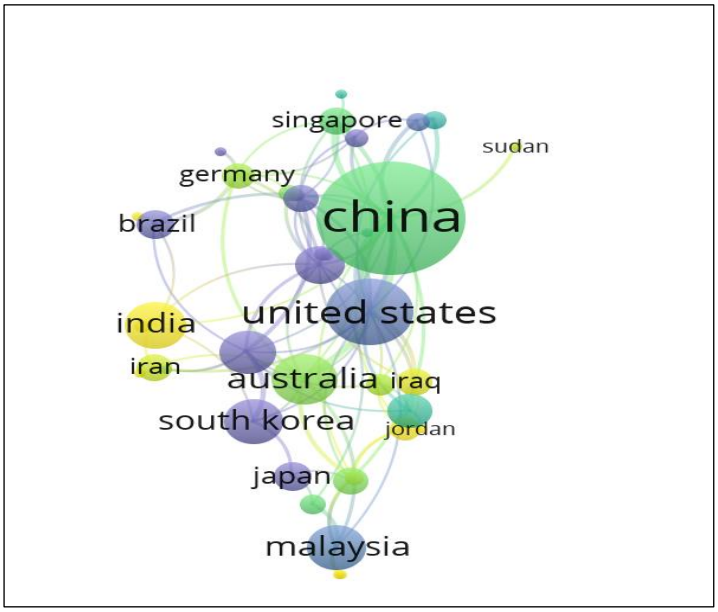

Figure 5: VOSviewer graphical representation of authors of PVA works of literature by country of origin.
Source: Authors, (2025).

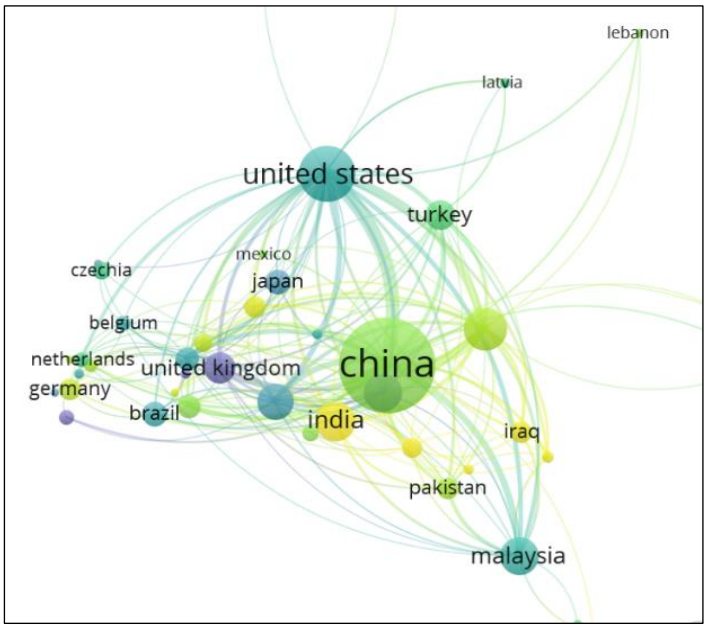

Figure 6: VOSviewer graphical representation of citations of PVA works of literature by country of origin
Source: Authors, (2025).

II.3 EFFECTS OF PVA ON THE MECHANICAL PROPERTIES OF CONCRETE

11.3.1 COMPRESSIVE STRENGTH OF PVA ENHANCED CONCRETE

According to [22], compressive strength is the capacity of concrete to support compressive loads. It is often determined by applying a load on cylindrical concrete specimens until failure [23]. The type and quantity of cement, the water-to-cement ratio, the aggregate size and type, and the curing conditions all have an impact on the compressive strength of concrete [24]. Besides, temperature has an impact on the compressive strength of concrete as well. Concrete has a stronger compressive strength at low temperatures than it does at normal temperatures [25].

The impact of PVA on the compressive strength of concrete has been the subject of several investigations. PVA may be added to concrete as a boding additive to increase its compressive strength. [26] assessed the addition of polyvinyl acetate to increase the strength of porous concrete for a mix ratio of 1:2:4 with a 0.4% water-to-cement ratio. Concrete was produced with 0%, 0.25%, 0.5%, 0.75%, and 1% addition of PVA in order to compare the strength. The results indicate that concrete produced using 0.75 addition of polyvinyl acetate gave the maximum strength at 28 days with 11.46 N/mm^2 with the control sample producing 8.36 N/mm^2 at 28 days.

In the same vein, [27] carried out a similar experiment using a concrete ratio of 1:2:4 at 0.4% water cement ratio with a 0%, 0.25%, 0.5%, 0.75%, and 1% addition of PVA. The results revealed that the compressive strength of concrete increases, with an increasing percentage of PVA proportion. The 1% addition of PVA produced the highest compressive strength of 13.78 N/mm^2 at 28 days. [28] discovered that a 0.3% addition of PVA fibre to a concrete mixture gave the optimum results after 28 days. According to [29], the addition of fibre typically results in a 16% increase in compressive strength at 28 days with an optimal fibre volume fraction of 0.25%.

Meanwhile, [30] averred that a 0.4% of addition of PVA to concrete is the optimal amount required to enhance the properties of concrete. This present study notes that the ideal proportions of PVA in concrete might differ depending on the environment, the properties of the material, and the testing setup. Diverse environmental and contextual factors may be taken into account by different authors and research, resulting in variances in the suggested PVA dose for concrete to achieve maximum performance in different locations and situations. This study therefore attempts to establish a universal mixing and testing protocol to maximum dosage that will enhance the compressive strength and improve concrete performance.

11.3.2 TENSILE STRENGTH OF PVA ENHANCED CONCRETE

One essential characteristic of concrete that is critical to evaluating its mechanical performance is its tensile strength [31]. It is the fundamental characteristic used to analyse concrete fracture processes and estimate the structure's resistance to cracking [32]. The capacity of concrete to bear tension is known as tensile strength, and it is commonly assessed using a split tensile test, which involves applying a weight to a cylindrical specimen [31]. The splitting technique is mostly used to assess the tensile strength of concrete since direct tensile tests need an eccentric specimen installation and because the specimen's geometric axis and physical centre of gravity may vary [25].

Similar to compressive strength, tensile strength in concrete is often lower and influenced by the same elements [33]. With an increase in the maximum temperature, several of the parameters influencing the tensile strength dramatically decrease [34]. According to research by [35] on the impact of PVA on the mechanical properties of geopolymer concrete based on fly ash, a volume fraction of 0.8% was suggested in order to obtain good toughness and tensile qualities while preserving the compressive performance of the concrete. [12] investigated the use of recycled concrete aggregate with PVA, and the results show that the maximum inclusion of 2% PVA resulted in a 52% improvement in the tensile strength of the concrete produced over the reference concrete with 0% incorporation.

11.3.3 BOND STRENGTH OF PVA-ENHANCED CONCRETE

It has been discovered that PVA has a greater impact at younger ages when cement hydration has not yet fully contributed to the binding [36]. According to [30], bond resistance may be decreased by using PVA fibre in levels higher than 0.6% with the study's specimen exhibiting a 0.8% concentration of PVA fibre demonstrating the situation. As the amount of PVA fibre in fresh concrete increases, its workability decreases. Meanwhile, [37] affirmed that the quantity of PVA used impacts the bond strength of concrete. Insisting that the bond strength of concrete increases as the percentage of addition of PVA increases.

III. MATERIALS AND METHODS

III.1 MATERIALS

The materials used in the study were ordinary Portland cement (OPC), fine aggregate (Sharp sand), coarse aggregate (Granite), PVA, and water.

III.1.1 Ordinary Portland Cement

The cement used in the experimental study was "Elephant Supaset" Cement which is a Portland Limestone Cement, conforming to the Nigerian Industrial Standards NIS 444-1: 2003 & EN 197-1:2011 specifications for Cement. The cement is produced by Lafarge Africa Plc. This cement is of grade 42.5. It is available in specially designed 50 kg bags. It is displayed in Figure 7.

Figure 7: Elephant Supaset cement packaging
Source: Authors, (2025).

III.1.2 FINE AGGREGATE

The fine aggregate used in the experimental study was river sand obtained through a local supplier from the Ogun River Basin. The sand was screened to remove any impurities and particles using sieve no. 230 and conforms to the requirements of BS EN 12620 for sand and test sieve with a mesh size of 63 microns (um). The sharp sand used contains no substances that are liable to lead to unsoundness or react in a harmful way with the concrete produced. It is displayed in Figure 8.

Figure 8: Sieving of fine aggregate (sand).
Source: Authors, (2025).

III.1.3 COARSE AGGREGATE

The coarse aggregate used in the experimental study was crushed Granite obtained from local quarry sites in Ogun state, Nigeria. Although the coarse aggregates come in different sizes, aggregate sizes ranging from 12-19mm were used for the study. It is shown in Figure 9.

Figure 9: Coarse aggregate (Granite)
Source: Authors, (2025).

III.1.4 PVA POWDER

The polyvinyl alcohol (PVA) powder used in the experimental study was procured from a local chemical market at Ojota, Lagos state. PVA is the compound of Polyethylene Glycol. It is a water-soluble synthetic polymer. It is represented in Figure 3.4. PVA is an odourless and tasteless, translucent, white colour in Crystal form with a density ranging from 1.17-1.3g/cm^3. The properties of the PVA powder used are further displayed in Table 10.

Figure 10: PVA Additive
Source: Authors, (2025).

Table 1: Properties of PVA powder.

PVA Properties	Colour	State	Density (g/cm^3)	Tensile strength	Chemical Symbol
	White	Solid (granules)	1.17-1.3	1500Mpa	$(C_4H_6O_2)x$

Source: Authors, (2025).

III.1.5 WATER

The water used in the experimental study was clean and potable. It was removed unsoiled and devoid of harmful levels of oils, acids, alkalis, salts, sugar, organic material, and other things that might harm concrete. Water is a necessary component in the making of concrete and is important for the hydration of cement.

III.2 METHODS

The preparation of samples and tests was carried out at the Department of Building and Civil and Engineering department at the University of Lagos Concrete Laboratory.

III.2.1 MIX DESIGN

The mix design for the experimental study was based on the BS 1881 standard for making and curing concrete test specimens in the laboratory. The mix proportions for the control mix and the PVA-modified mixes are presented in Tables 2 and 3. Table 2 shows the mix proportion used to prepare the specimens for compressive and pull-out tests. The mix was obtained by multiplying the volume of the concrete specimen by the density of the concrete. Waste and shrinkage were factors in the calculation. The total number of cubes per mix reference is 8. That is 4 cubes for compressive test strength and 4 cubes per mix reference for the pull-out test. Resulting in a total of 20 cubes for each compressive and pull-out test respectively.

Table 3 shows the mix proportions for the cylindrical specimen. The total number of cylindrical specimens per mix reference is 4. That is, 4 cylindrical specimens per mix reference resulting in a total of 12 cylindrical specimens for the split tensile test.

Table 2: Mix proportion for cubical specimens.

Mix Ref	Cement (kg)	Fine Aggregate (kg)	Coarse Aggregate (kg)	Water (kg)	PVA (kg)	w/c Ratio
CP0	12.22	24.44	48.88	8	0	0.66
CP.5	12.22	24.44	48.88	8	0.061	0.66
CP1	12.22	24.44	48.88	8	0.12	0.66
CP1.5	12.22	24.44	48.88	8	0.18	0.66
CP2	12.22	24.44	48.88	8	0.24	0.66

Source: Authors, (2025).

Table 3: Mix proportion for cylindrical specimens.

Mix Ref	Cement (kg)	Fine Aggregate(kg)	Coarse Aggregate(kg)	Water (kg)	PVA (kg)	w/c Ratio
T0	10.178	20.356	40.712	6.62	0	0.65
T1	10.178	20.356	40.712	6.62	0.10	0.65
T2	10.178	20.356	40.712	6.62	0.20	0.65

Source: Authors, (2025).

III.2.2 MIXING AND PRODUCTION OF SPECIMENS

Prior to mixing, the cubical and cylindrical moulds were thoroughly cleaned and oiled to allow for simple de-moulding once the concrete had set before curing commences. The materials were also batched by weight prior to mixing. The concrete mixes were prepared by first adding the PVA to water in the specified proportions and mixing for 2 minutes. The powder is gently added to the cold water to avoid the formation of lumps as it becomes sticky and has the tendency to form lumps. This is necessary to prevent it from entraining the air. The coarse aggregate, fine aggregate, and cement were then added to the mix in the concrete mixer drum. Water was then added gradually while mixing until a homogenous concrete mixture was obtained. For the specimens used for the compressive strength test, the concrete was then placed into 150mm x 150mm x 150mm cube moulds and adequately compacted with the aid of a compacting rod. This same procedure was also used when preparing the 150mm diameter cylindrical specimens for the split tensile test. As regards the specimens for the pull-out tests, 12mm diameter reinforcement cut into 450mm height was inserted into the cubic mould before the concrete was placed. It is shown in Figure 11.

Figure 11: Cleaning of moulds to receive mixed concrete.
Source: Authors, (2025).

III.2.3 WORKABILITY TEST

The slump test was carried out on the different batches of concrete produced to obtain a workable concrete using a 300mm high slump cone and tamping rod. The test was carried out in line with B.S. 1881: Part 102: 1983. It is depicted in Figure 12.

Figure 12: Workability of concrete.
Source: Authors, (2025).

III.2.4 DE-MOULDED SPECIMEN AND CURING

A total of 20 numbers of concrete cubic specimens of 150x150x150 mm were produced for the compressive test. Similarly, another 20 cubic specimens with 12mm rebars inserted when the concrete was placed were produced to carry out the pull-out test to check for the bond strength of the concrete and reinforcement. A total of 12 numbers of cylindrical specimens of 150 mm diameter and height of 300 mm were produced to aid out the split tensile test. All the specimens produced were de-moulded, placed into the curing tank, and cured for 7 and 28 days respectively. It is displayed in Figure 13.

Figure 13: Specimens and curing.
Source: Authors, (2025).

IV. RESULTS AND DISCUSSIONS

IV.1 WORKABILITY

Workability is the ease with which concrete mixes can be compacted. The Slump test is a common method for determining the workability of a wet concrete mix. The slump test was performed conforming to B.S. 1881: Part 102: 1983. The slump test is the most effective method for verifying the workability of concrete both in the lab and on the job site. The slump test is a handy control test that provides the workability result. In this experiment, the effects of PVA powder on concrete workability were investigated. The slump values of each of the specimens are given in Tables 4 and 5, which show the slump values and water-to-cement (w/c) ratios for different concrete mixtures.

As shown in Table 4, it can be observed that workability of the cubical sample decreased from 50mm to 21mm as the PVA content increased from 0% to 1%, while workability is increased from 21mm to 124mm as the PVA content increases from 1% to 2%. The workability of the cylindrical specimen rose from 15mm to 80mm as the PVA concentration increased from 0% to 2%, as shown in Table 5. This demonstrates that the concrete's ability to be worked has risen as a result of employing higher PVA addition rates. The results of [38], who discovered that adding more water makes the mixture more workable, lend credence to this assertion.

The rise in slump value indicates that the PVA addition has enhanced the concrete's workability by making it more fluid and manageable. The fact that PVA, a polymer that dissolves in water and functions as a dispersion, helps to separate the particles in concrete mixes and lowers viscosity, may help to explain this. The fact that the water-to-cement (w/c) ratio remained constant throughout all combinations is significant since it shows that an increase in water content was not the cause of the rise in slump value. This is important because concrete's strength and durability might be compromised by adding additional water to it.

Table 4: Slump test for the cubical mix.

Percentage PVA Dosage	Slump (mm)	w/c Ratio	Slump	Consistency grade
CP 0	50	0.65	True	Stiff
CP 0.5	25	0.65	True	Stiff
CP 1	21	0.65	True	Stiff
CP 1.5	66	0.65	True	Plastic
CP 2	124	0.65	Shear	Plastic

Source: Authors, (2025).

Table 5: Slump test for the cylindrical mix design.

Percentage PVA Dosage	Slump (mm)	w/c Ratio	Slump	Consistency grade
T0	15	0.65	True	Stiff
T1	35	0.65	True	Stiff
T2	80	0.65	Shear	Plastic

Source: Authors, (2025).

IV.2 COMPRESSIVE STRENGTH TEST

The concrete specimens' compressive strength was tested in line with the BS EN 12390-3:2019 standard. The concrete specimens were tested by putting them in a compression testing machine and applying a compressive force till failure. The compressive strength of the concrete was then estimated by dividing the greatest load applied to the specimen by its cross-sectional area. The compressive strength was determined at 7 and 28 days after casting and the results are presented in Figure 14.

It is obvious that the addition of PVA had an influence on the strength of the concrete at both the 7-day and 28-day marks based on the compressive strength findings of the experiment to explore the effect of PVA on concrete. The CP0.5 mix exhibited the maximum compressive strength after 7 and 28 days, with compressive strength values of 18.00 N/mm^2 and 24.98 N/mm^2. As compared to the control (CP0) mixes, which had compressive strength values of 16.25 N/mm^2 and 20.65 N/mm^2, this was a substantial improvement. At the 7-day point, the compressive strengths of the CP1 and CP1.5 mixtures were 13.52 N/mm^2 and 12.59 N/mm^2, respectively. At the 7-day point, the CP2 mix's compressive strength was the lowest, at just 8.42 N/mm^2. Additionally, at the 28-day point, the compressive strength values of the CP1, CP1.5, and CP2 mixtures were 19.45 N/mm^2, 17.58 N/mm^2, and 11.13 N/mm^2 respectively.

It can be inferred that the maximum compressive strength of concrete occurs at 0.5% addition of PVA to the concrete mix. This therefore suggests that the optimum compressive strength of concrete is attained at 0.5 PVA addition to concrete. This finding is consistent with those of [39-41]. Nevertheless, as demonstrated in the CP1, CP1.5, and CP2 mixes, the impact of PVA powder on compressive strength tends to decrease at greater concentrations. As indicated in CIP- (Concrete in Practice) and the American Society for Testing and Materials (ASTM C31/39), an average value of 15N/mm^2 may be utilised for Non-Critical Structural Works. Values more than 15N/mm^2 are ideal for Critical Structural Works, whereas values less than this benchmark are suitable for Non-Critical and Non-Structural Works. As illustrated in Figure

14, up to 1.5% addition of PVA with cement is suitable for critical structural works. However, as seen in Figure 16, PVA is unsuitable for reinforced concrete structural works, because its addition to reinforced concrete mixes does not bond effectively.

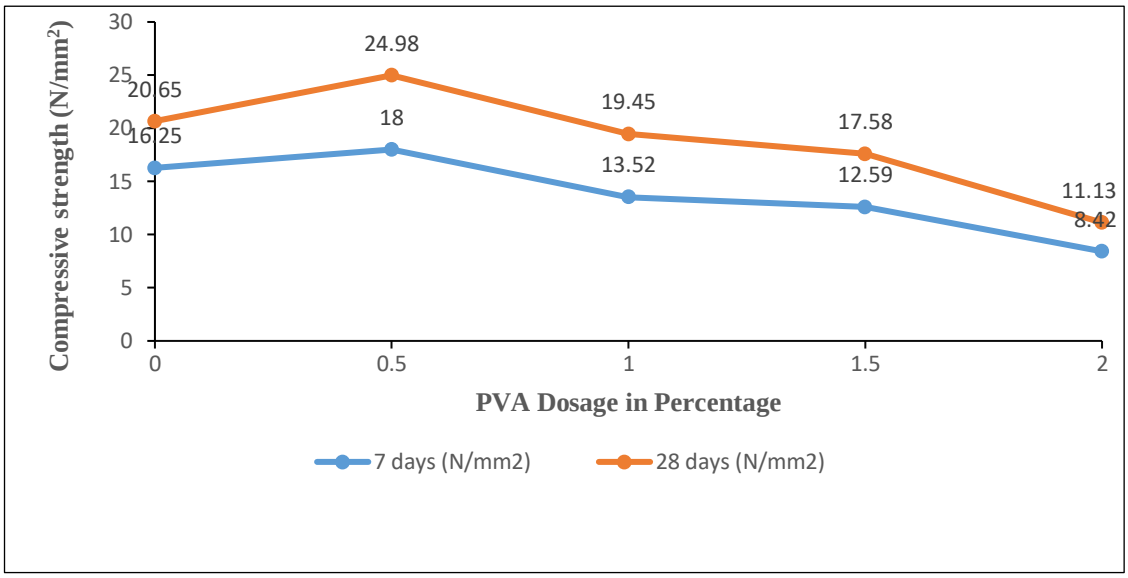

Figure 14: Compressive strength values at 7 and 28 days.
Source: Authors, (2025).

IV.3 TENSILE STRENGTH TEST

The concrete sample's tensile strength was evaluated using the BS EN 12390-6 standard. The concrete specimens were tested by putting them in a split tensile testing machine and applying a tensile force till failure. Three cylinders each were cast for each percentage ranging from 0% to 2% at 7 and 28 curing days. The tensile strength of the concrete was estimated by dividing the greatest load applied to the specimen by its cross-sectional area. Tensile strength was measured seven and twenty-eight days after cure. The tensile test results are presented in Figure 15.

From Figure 15, it can be observed that the tensile strength test results increase with increased percentage replacement of cement with PVA. As demonstrated by the rise in strength from T0 to T1 and T2, the tensile strength of the concrete rose as the proportion of PVA increased. At 7 days, the tensile strength of the control mix (T0) was 1.31 N/mm^2, but the strength of the mix containing the least quantity of polyvinyl alcohol powder (T1) was 1.40 N/mm^2, suggesting a 7% increase. The tensile strength of the mix with the highest concentration of polyvinyl alcohol powder (T2) was 1.57 N/mm^2, representing a 20% increase over the control mix. The tensile strength of the control mix (T0) increased to 1.61 N/mm^2 after 28 days, whereas the strength of the mix with the lowest amount of PVA (T1) increased to 2.17 N/mm^2, a 35% increase. The tensile strength of the mix with the greatest proportion of PVA (T2) was 2.22 N/mm^2, an increase of roughly 38% above the control mix. This implies that as the concentration of PVA in the concrete grows, so does its tensile strength. These results conform to the findings of [42].

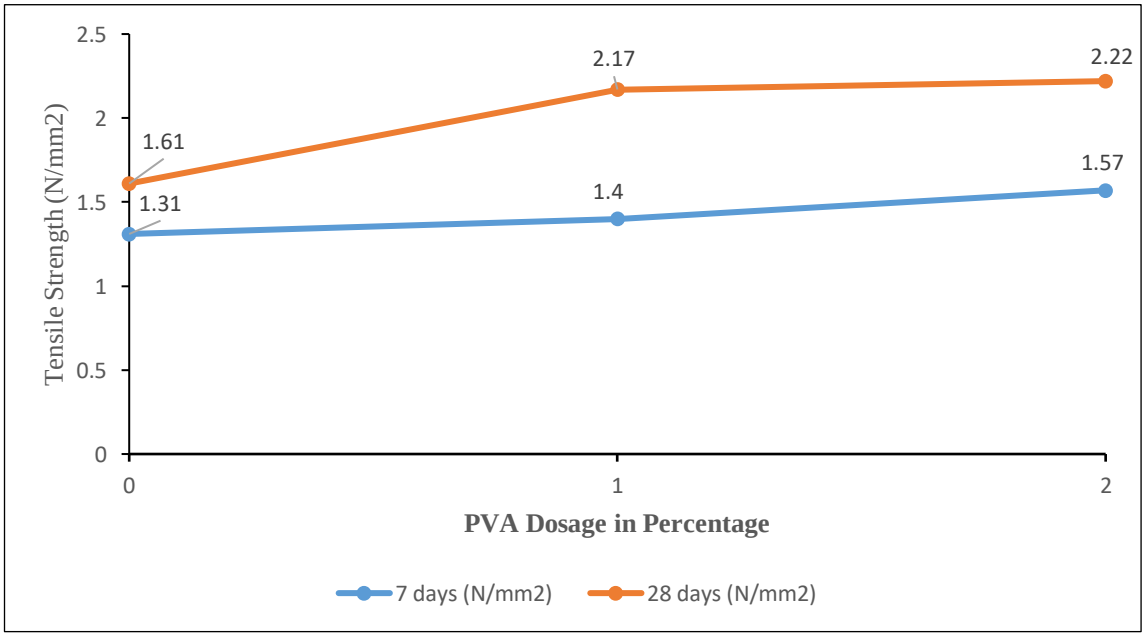

Figure 15: Tensile test results after 7 and 28 days.
Source: Authors, (2025).

IV.4 PULL-OUT (BOND) TEST

A pull-out test is a method for determining the strength of the connection between a concrete surface and a reinforcing bar or anchor. This test was typically carried out by fully inserting a steel rod into the concrete at 75mm from the bottom of the mould and then drawing it out at a steady rate of displacement while measuring the force needed. The specimen's bonding strength was tested at 7 and 28 days after casting. The pull-out test results are presented in Figure 16.

The control mix, CP0, had the strongest bond strength at 7 and 28 days, with pull-out strengths of 13.24 KN and 31.14 KN, respectively. Indicating that PVA does not bond well with reinforced concrete as the bonding strength is decreased as the amount of PVA powder in the mixture rises. For instance, the pull-out values of 12.75 KN at 7 days and 16.77 KN at 28 days, showing a 3.7% and 46% decline, respectively, respectively, the CP0.5 mix demonstrated weaker bond strength than the CP0 mix. The result remained at higher polyvinyl alcohol powder concentrations, with CP1, CP1.5, and CP2 combinations all displaying weaker bonds after 7 and 28 days. The CP2 mix had the weakest binding, with pull-out strengths of 1.47 KN at 7 and 28 days, an 85.13% decrease. This result corroborates the findings of [36] that PVA has a greater impact at younger ages when cement hydration has not yet been fully set. According to the results, adding PVA to concrete can weaken the bond that holds reinforcing bars to the concrete. With higher PVA percentages, the bonding strength was more noticeably reduced.

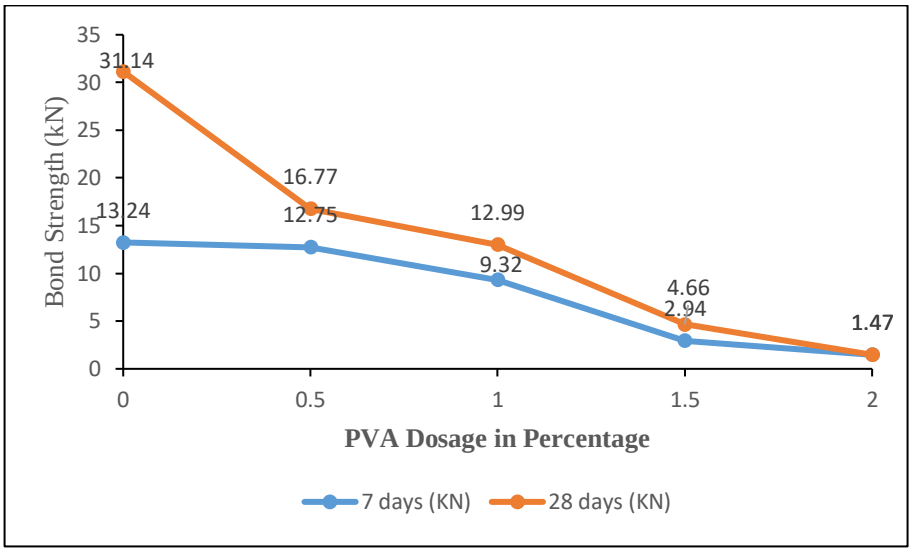

Figure 16: Pull out strength results after 7 and 28 days.
Source: Authors, (2025).

V. CONCLUSIONS

The following conclusions are drawn from the study's findings: The addition of PVA to the concrete mix has a significant influence on the workability of the concrete. The slump values of the concrete mixes increased as the amount of PVA was increased with constant water-to-cement (w/c) ratios. This implies that PVA acts as a dispersion, helping in particle separation in the concrete mix and decreasing viscosity, hence improving workability.

The maximum compressive strength of concrete occurs at 0.5% PVA application to the concrete mix. This implies that the optimal compressive strength of concrete is obtained with 0.5 PVA dosage. Also, the tensile strength of concrete increases with increasing PVA doses. Besides, the bonding strength between the concrete and the reinforcing bar is decreased when PVA is added to it.

The findings revealed that the bonding strength of concrete reduces by 46% with a 0.5% PVA admixture and keeps declining as the PVA dose increases. This implies that regardless of PVA dosage in a concrete mixture, there is a significant decline in bonding strength in concrete and reinforcement. The study therefore recommends that PVA should be applied for non-structural concrete works such as mass or plain concrete. This may be accomplished through the application of 0.5% doses of PVA in plain concrete mixes by Builders and Engineers to enhance the compressive strengths of the concretes produced.

VI. AUTHOR'S CONTRIBUTION

Conceptualization: Dele Roger Simeon, Aliu Adebayo Soyingbe and Rabiu Aminu.
Methodology: Dele Roger Simeon, Aliu Adebayo Soyingbe and Rabiu Aminu.
Investigation: Dele Roger Simeon, Aliu Adebayo Soyingbe and Rabiu Aminu.
Discussion of results: Dele Roger Simeon, Aliu Adebayo Soyingbe and Rabiu Aminu.
Writing – Original Draft: Dele Roger Simeon, Aliu Adebayo Soyingbe and Rabiu Aminu.
Writing – Review and Editing: Dele Roger Simeon, Aliu Adebayo Soyingbe and Rabiu Aminu.
Supervision: Dele Roger Simeon, Aliu Adebayo Soyingbe and Rabiu Aminu.
Approval of the final text: Dele Roger Simeon, Aliu Adebayo Soyingbe and Rabiu Aminu.

VIII. REFERENCES

[1] Oladiran, O. J., Simeon, D. R., & Olatunde, O. A. (2020).Investigating the Performance of Palm KernelShells and Periwinkle Shells as Coarse Aggregates in Concrete. Lautech Journal of Civil andEnvironmental Studies, 4(1), 123-133 https://doi.org/10.36108/laujoces/0202/40(0131)

[2] Chakraborty, S., & Thakur, N. (2021). Strength assessment ofconcrete using rice husk ash, recycled concrete aggregate and polyvinyl alcohol fiber. *IOP Conference Series: Earth and Environmental Science*, *889*(1). https://doi.org/10.1088/1755-1315/889/1/012020

[3] Mohammed, T. U., Ahmed, T., Apurbo, S. M., Mallick, T. A., Shahriar, F., Munim, A., & Awal, M. A. (2017). Influence of Chemical Admixtures on Fresh and Hardened Properties of Prolonged Mixed Concrete. *Advances in Materials Science and Engineering*, *2017*. https://doi.org/10.1155/2017/9187627

[4] Sabitov, Y., Dyussembinov, D., & Bazarbayev, D. (2021). Effect of modifiers and mineral additives from industrial waste on the quality of aerated concrete products. *Technobius*, *1*(4), 0010. https://doi.org/10.54355/tbus/1.4.2021.0010

[5] Manfaluthy, M. L., & Ekaputri, J. J. (2017). The Application of PVA Fiber to Improve the Mechanical Properties of Geopolymer Concrete. *MATEC Web of Conferences*, *138*. https://doi.org/10.1051/matecconf/201713801020

[6] Du, E., Yan, Y., & Guo, J. (2017). Mechanical property test of polyvinyl alcohol (PVA) fiber reinforced concrete. *Chemical Engineering Transactions*, *62*, 727–732. https://doi.org/10.3303/CET1762122

[7] Jalal, A., Hakim, L., & Shafiq, N. (2021). Mechanical and post-cracking characteristics of fiber reinforced concrete containing copper-coated steel and PVA fibers in 100% cement and fly ash concrete. *Applied Sciences (Switzerland)*, *11*(3), 1–14. https://doi.org/10.3390/app11031048

[8] Ansari, A., Amanullah, Madne, N., Sufiyan, M. Z., & Siddiqua, A. (2019). A Review Paper on Experimental Investigation of Crumb Rubber Concrete. *Journal of Emerging Technologies and Innovative Research*, *6*(5), 1006–1009.

[9] Tan, Y., Xu, Z., Liu, Z., & Jiang, J. (2022). Effect of Silica Fume and Polyvinyl Alcohol Fiber on Mechanical Properties and Frost Resistance of Concrete. *Buildings*, *12*(1). https://doi.org/10.3390/buildings12010047

[10] Cibilakshmi, G., & Jegan, J. (2020). A DOE approach to optimize the strength properties of concrete incorporated with different ratios of PVA fibre and nano-Fe2O3. *Advanced Composites Letters*, *29*, 1–16. https://doi.org/10.1177/2633366X20913882

[11] Akram, V., & Balachandiran, P. (2018). *Experimental Study of Self Curing Concrete By Using Poly*. *9*(3), 102–105.

[12] Mukesh, T. S., Kulanthaivel, P., Gowthaman, G., & Hariharan, J. (2022). Study on Physical and Mechanical Properties of Porous Concrete using Recycled Concrete Aggregate. *Materials Research Proceedings*, *23*, 304–310. https://doi.org/10.21741/9781644901953-35

[13] Ghazaly, H. El, A, A. A. E., Said, M., & M, M. A. (2019). *Behavior of Reinforced Concrete Columns with (PVA) Under Fire : 3*, *54-64*.

[14] Abdelrahman, A., Elshahat, A., Refaey, A., Ali, O., Salah, I., & Said, K. (2021). *Enhancement of Tensile Strength of High Strength Concrete using Polyvinyl Alcohol Fibre (PVA)*. 652–655.

[15] Annam, R. (2015). *Study of Mechanical Properties of PVA Fiber- Reinforced Concrete With Raman Spectroscopic Analysis*. 30. http://digitalcommons.wku.edu/theses/1460

[16] Roopakala, A. C. G., Shivaraju, B. G. D., & Usha, C. S. (2021). *Experimental study on properties of self-curing concrete incorporated with PEG and PVA*. *8*(4), 821–828.

[17] Norsariza, W., Husin, W., Yusof, N. M., & Nasir, N. H. (2022). Workability and Strength between Poly vinyl Alcohol (PVA) and Silica Fume (SF) with Portland Composite Cement (PCC) in Cement Mixture. *Asian Journal of Fundamental and Applied Sciences*, *3*(3), 17–24. https://doi.org/10.55057/ajfas.2022.3.3.3

[18] Solahuddin, B. A., & Yahaya, F. M. (2021). A Review Paper on The Effect of Waste Paper on Mechanical Properties of Concrete. *IOP Conference Series: Materials Science and Engineering*, *1092*(1), 012067. https://doi.org/10.1088/1757-899x/1092/1/012067

[19] Muwashee, R. S. (2018). Mechanical properties of polyvinylacetate (pva) concrete improved with silica fume. *International Journal of Civil Engineering and Technology*, *9*(10), 763–770.

[20] Sadrmomtazi, A., & Khoshkbijari, R. K. (2019). Determination and Prediction of Bonding Strength of Polymer Modified Concrete (PMC) as the Repair Overlay on the Conventional Concrete Substrate. *KSCE Journal of Civil Engineering*, *23*(3), 1141–1149. https://doi.org/10.1007/s12205-019-0113-3

[21] Abbas, W. A., Gorgis, I. N., & Hussein, M. J. (2019). Performance of Cement Mortar Composites Reinforced with Polyvinyl Alcohol Fibers. *IOP Conference Series: Materials Science and Engineering*, *518*(2). https://doi.org/10.1088/1757-899X/518/2/022045

[22] Yehia, S., Abdelfatah, A., & Mansour, D. (2020). Effect of aggregate type and specimen configuration on concrete compressive strength. *Crystals*, *10*(7), 1–26.

[23] Osman, M. H. B., Kai, O. S., Adnan, S. H., Salim, S., Rahman, M., Jaafar, A., Jeni, M. L. A., & Yahya, N. F. (2021). Mechanical properties of concrete containing expanded polystyrene (EPS) and palm oil fuel ash (POFA). *AIP Conference Proceedings*, *2347*(July). https://doi.org/10.1063/5.0052774

[24] Hamada, H., Alattar, A., Tayeh, B., Yahaya, F., & Almeshal, I. (2022). Influence of different curing methods on the compressive strength of ultra-high-performance concrete: A comprehensive review. *Case Studies in Construction Materials*, *17*(August), e01390. https://doi.org/10.1016/j.cscm.2022.e01390

[25] Huo, Y., Sun, H., Lu, D., Chen, Z., & Yang, Y. (2022). Mechanical properties of concrete at low and ultra - low temperatures - a review. *Journal of Infrastructure Preservation and Resilience*. https://doi.org/10.1186/s43065-022-00063-4

[26] Meshram, M. H. V. (2018). Enhancing the Strength of Porous Concrete by using the Polyvinyl Acetate. *International Journal for Research in Applied Science and Engineering Technology*, *6*(5), 1612–1615. https://doi.org/10.22214/ijraset.2018.5261

[27] Warghane, S. R. (2018). Use of Polyvinyl Alcohol in Pervious Concrete to Increasing the Strength. *International Journal for Research in Applied Science and Engineering Technology*, *6*(5), 1336–1340. https://doi.org/10.22214/ijraset.2018.5219

[28] Devi, M., Kannan, L., kumar, M. G., & achalam, T. S. V. (2017). Flexural Behavior of Polyvinyl Alcohol Fiber Reinforced Concrete. *International Journal of Civil Engineering*, *4*(6), 26–30. https://doi.org/10.14445/23488352/ijce-v4i6p104

[29] Noushini, Amin, Samali, B., & Vessalas, K. (2013). Flexural toughness and ductility characteristics of polyvinyl-alcohol fibre reinforced concrete (PVA-FRC). *Proceedings of the 8th International Conference on Fracture Mechanics of Concrete and Concrete Structures, FraMCoS 2013*, 1110–1121.

[30] Zerfu, K., & Ekaputri, J. J. (2021). Bond strength in PVA fibre reinforced fly ash-based geopolymer concrete. *Magazine of Civil Engineering*, *101*(1). https://doi.org/10.34910/MCE.101.5

[31] Gul, A., Alam, B., Iqbal, M. J., Ahmed, W., Shahzada, K., Javed, M. H., & Khan, E. A. (2021). Impact of Length and Percent Dosage of Recycled Steel Fibers on the Mechanical Properties of Concrete. *Civil Engineering Journal*, *7*(10), 1650–1666. https://doi.org/10.28991/cej-2021-03091750

[32] Słowik, M., & Akram, A. (2022). Length effect at testing splitting tensile strength of concrete. *Materials*, *15*(1). https://doi.org/10.3390/ma15010250

[33] Shodolapo, O. F., & Franky, I. K. (2020). Tensile/Compressive/Flexural Strength Relationships for Concrete using Kgale Aggregates with Botchem as Binder. *International Journal of Scientific & Engineering Research*, *11*(5), 1056–1063. http://www.ijser.org

[34] Dabbaghi, F., Dehestani, M., & Yousefpour, H. (2022). Residual mechanical properties of concrete containing lightweight expanded clay aggregate (LECA) after exposure to elevated temperatures. *Structural Concrete*, *23*(4), 2162-2184.

[35] Zhang, P., Han, X., Zheng, Y., Wan, J., & Hui, D. (2021). Effect of PVA fiber on mechanical properties of fly ash-based geopolymer concrete. *Reviews on Advanced Materials Science*, *60*(1), 418–437. https://doi.org/10.1515/rams-2021-0039

[36] Kristiawan, S., Santosa, B., Purwanto, E., & Caesar, R. A. (2018). Slant shear strength of fibre reinforced polyvinyl acetate (PVA) modified mortar. *MATEC Web of Conferences*, *195*, 1–9. https://doi.org/10.1051/matecconf/201819501016

[37] Tibbetts, C. M., Riding, K. A., & Ferraro, C. C. (2021). A critical review of the testing and benefits of permeability-reducing admixtures for use in concrete. *Cement*, *6*(August), 100016. https://doi.org/10.1016/j.cement.2021.100016

[38] Echeta, C. B., Ikponmwosa, E. E., & Fadipe, A. O. (2013). Effect of partial replacement of granite with washed gravel on the characteristic strength and workability of concrete. *ARPN Journal of Engineering and Applied Sciences*, *8*(11), 954-959.

[39] Zhang, P., Han, X., Zheng, Y., Wan, J., & Hui, D. (2021). Effect of PVA fiber on mechanical properties of fly ash-based geopolymer concrete. *Reviews on Advanced Materials Science*, *60*(1), 418–437. https://doi.org/10.1515/rams-20210039

[40] Vafaei, D., Hassanli, R., Ma, X., Duan, J., & Zhuge, Y. (2021). Sorptivity and mechanical properties of fiber-reinforced concrete made with seawater and dredged sea-sand. *Construction and Building Materials*, *270*, 121436.

[41] Nematzadeh, M., Dashti, J., & Ganjavi, B. (2018). Optimizing compressive behavior of concrete containing fine recycled refractory brick aggregate together with calcium aluminate cement and polyvinyl alcohol fibers exposed to acidic environment. *Construction and Building Materials*, *164*, 837-849.

[42] Yeganeh, A. E. (2015). Structural behaviour of reinforced high performance concrete frames subjected to monotonic lateral loading. *Ryerson University MASc thesis*, 108.

Journal of Engineering and Technology for Industrial Applications

ITEGAM-JETIA

Manaus, v.11 n.53, p. 17-20. May/June., 2025.
DOI: https://doi.org/10.5935/jetia. v11i53.1028

ISSN ONLINE: 2447-0228

RESEARCH ARTICLE OPEN ACCESS

REVOLUTIONIZING MASS PRODUCTION: A DUAL POWER PORTABLE PHOTOGRAPHIC SILKSCREEN PATTERN EQUIPMENT

Halima A. Sahim-Sali[1], Joshua R. Apolinario[2], Spencer vape A. Gregorio[3], Anna rose R. Amalan[4], Kevin C. Maningo[5] and Ernesto F. Bantug[6]

[1,2,3,4,5,6] Zamboanga Peninsula State Polytechnic University– R.T Lim boulevard, Zamboanga City, Philippines.

[1]http://orcid.org/0009-0006-2091-2770, [2]http://orcid.org/0009-0005-7173-6407, [3]http://orcid.org/0009-0004-5367-7303, [4]http://orcid.org/0009-0009-5515-3964, [5]http://orcid.org/0009-0008-0285-1083, [6]http://orcid.org/0009-0009-6216-2666

Email: salisahim.halima@gmail.com, pongjosh.0909@gmail.com, vapegregorio11@c.com, amalanannarose@gmail.com

ARTICLE INFO

Article History
Received: January 04, 2024
Revised: January 20, 2025
Accepted: May 15, 2025
Published: May 31, 2025

Keywords:
Portable Photographic Silkscreen-Pattern Equipment
Dual Power Source,
Renewable Energy,
Operational Adaptability.

ABSTRACT

This research endeavors to introduce and evaluate the efficacy of a newly designed Portable Photographic Silkscreen Pattern Equipment integrated with a dual power source. Engaging a cohort of 88 participants across various departments, alongside input from eight experts in Drafting Technology at Zamboanga City State Polytechnic College, a survey questionnaire facilitated data collection via a convenience sampling approach. The study unequivocally establishes the "highly acceptable" nature of the equipment in terms of design, functionality, and portability. Noteworthy attributes include its facilitation of pattern transfer to silkscreen for efficient mass production and its adaptable use of renewable energy, rendering it operational in diverse environments, including remote areas and educational institutions. The equipment's superior portability, robust construction, and systematic wiring organization enhance its practicality. Experimentally, processing silkscreen pattern emulsion exhibits a minor time disparity between alternating current (AC) and solar battery power, with a mere one-minute difference (4 minutes on AC, 3 minutes on solar power). This study heralds a promising innovation in pattern transfer technology, poised to revolutionize mass production while championing sustainability and operational adaptability.

I. INTRODUCTION

In the pursuit of innovative solutions for modern production challenges, this study undertook the ambitious task of conceptualizing, designing, and crafting a portable photographic silkscreen pattern equipment fortified with a dual power source. The research set its sights on addressing the pressing need for an efficient and versatile tool to facilitate the transfer of patterns or designs onto silkscreens, enabling mass production with ease.

Engaging a cohort of 88 respondents hailing from diverse departments, comprising twenty individuals per department, alongside the insightful input from eight esteemed instructors and professors specialized in Drafting Technology at the Zamboanga City State Polytechnic College, this study navigated through the realms of design, functionality, and portability of the Portable Photographic Silkscreen Pattern Equipment with Dual Power Source. Employing a survey questionnaire and embracing a convenience sampling methodology, the research adeptly collected comprehensive data. The findings unequivocally resonate a unanimous verdict – the design, functionality, and portability of this cutting-edge equipment stand endorsed as "highly acceptable" by the discerning participants.

Notably, this groundbreaking equipment not only streamlines the process of transferring patterns onto silkscreens for mass production but also boasts the ingenious integration of renewable energy sources. This dual power feature renders it adaptable to diverse environments, including remote areas or educational institutions. Its remarkable portability, sturdy construction, and systematic wiring organization further enhance its practicality and convenience. Furthermore, the experimental phase of this project unearthed intriguing performance metrics, showcasing the equipment's efficiency. Processing the emulsion of silkscreen patterns exhibited a time disparity of merely one minute

between the alternating current (AC) and solar battery power sources - a mere 4-minute operation on AC and 3 minutes on solar power.

The compelling results of this study herald a promising paradigm shift in the realm of pattern transfer technologies, showcasing the viability and efficacy of a portable, dual-powered solution poised to revolutionize mass production processes while championing sustainability and operational adaptability.

This set also establishes the research question, the objectives of the work and hypothesis, if necessary, the importance and limitations of the study. Establishes the method used at work. It is written in the present tense.

II. THEORETICAL REFERENCE

Screen printing is a traditional print technique that has been used for many years. In the screen-printing process, a type of stencil design is created on fine mesh or polyester fabric, with several layers of ink pushed through this stencil layout onto the surface of the print material. All the different ink colors are applied using a different screen stencil to create the final printed effect. Areas of the print material which need to be left clear are covered with an impermeable substance to prevent ink contamination [1].

The technique of silk-screen printing, also known as screen processing or screen printing, involves brushing ink onto a fine-mesh screen that holds the image to be printed, then forcing the image through the screen's openings. It's utilized for printing on glass, skis, surfing boards, credit cards, billboard posters, wallpaper patterns, writing on bottles and clothes, and printed circuit board pictures in the electronics sector. Irritating dermatitis can be brought on by potential irritants including inks and cleaning products. Organic solvents may have harmful side effects, including neurotoxicity. The true allergens listed in silk-screen printers include triglycidyl isocyanurate, epoxy resin, diaminodiphenyl-methane, and acrylate components of UV-curing chemicals, which are the most common allergies [2].

The study's goal is to investigate the various T-shirt printing techniques. Kushtia Zone is the one I have chosen to get my data from. Kushtia, a historic city, has long been known for its fabric printing industry. One of the occupations of the people of Kushtia is t-shirt printing. In Bangladesh, t-shirts are printed using a variety of techniques, including screen printing, heat transfer, and dye sublimation. In Bangladesh, however, screen printing is the most often used method. It is less expensive and simple to use. Even though screen printing is the best method in Bangladesh, there are obstacles in the way of its advancement. The printing process is laborious, and the final goods produced are of poor quality. Additionally, the "Portable T-shirt Printing Machine" has been created to reduce the issues that local printers have while screen printing. The 80 cm long, 50 cm wide, and 15 cm high portable t-shirt printing machine is lightweight and portable, allowing for printing anywhere there is or is not electricity. The steel frame that is adjustable may be used to accommodate screens of any size, from 45 cm by 45 cm to 16 cm by 16 m or even smaller. The research methodology utilized in the qualitative, or descriptive, approach. 110 people make up the study's sample population, or 33% of the target population. Interviews, observations, and questionnaires were employed as the data collection methods. The study's primary conclusions were that developing a machine can speed up the conventional screen printing procedure. Additionally, there is a direct correlation between the speed and skill of the t-shirt printing process and the money made [3].

The dimensionless efficiency of incandescent lights, which typically ranges from 2% to 13%, may be calculated as a function of filament temperature using Planck's radiation formula. Similarly, the efficacy of incandescent light bulbs is approximated as a function of temperature using the known spectrum luminous efficiency of the human eye, with values ranging from 8–24 L W−1 for bulbs with a power of 10–1000 W. The efficiency and efficacy results allow for the estimate of the filament temperature for any lamp with known efficacy, and they compare favorably with published data [4].

More efficient solar cells are just one use of advanced solar energy harvesting technology. There are possibilities for research and development in the related hardware used to store this sporadic resource on the grid and provide electricity from solar cells to households and businesses. Lewis examines the current state of these fields as well as solar thermal and solar fuels energy harvesting techniques [5].

III. MATERIALS AND METHODS

This study used experimental approach and quantitative research design to empirically analyze the data. Specifically, it made used of the descriptive statistics on the arithmetic mean was used to measure the value that represented their level acceptance in terms of the portability, functionality, and design of the portable photographic silkscreen pattern equipment with dual power source. There were eighty-eight (88) respondents selected from amongst the four (4) departments of the college namely the Techer Education Department, Institute of Technology Education, Department of Technology Education, and Department of Arts and Sciences were carefully analyzed using statistical tools.

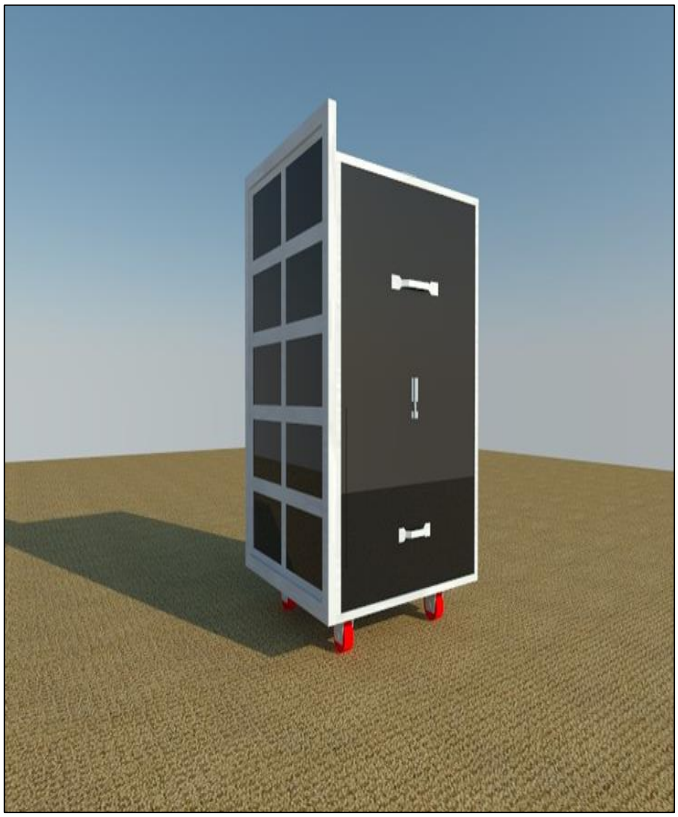

Figure 1: Shows the Perspective View of the Portable Photographic Silkscreen Pattern Equipment with Dual Power. Source: Authors, (2025).

Table 1: Rating scale, mean range descriptive rating for the perceptions statements designed to determine the level of the acceptability of the portable photographic silkscreen pattern equipment with dual power source in term of, design, portability, and functionality.

Table 1: shows that in this study anything between 1.00 to 1.74 was interpreted as “strongly disagree”, a mean score that fell between 1.75 to 2.49 was interpreted as “disagree” and mean score from 2.50 to 3.25 was interpreted as “agree: lastly, those that fell from 3.26 to 4.00 meant “strongly agree”.

Mean range	Descriptive rating
3.26 - 4.00	Strongly Agree
2.50 - 3.25	Agree
1.75 - 2.49	Disgree
1.00 - 1.74	Storngly Disasgree

Source: Authors, (2025).

IV. RESULTS AND DISCUSSIONS

Table 2: Drafting technology students evaluation result on the level of design acceptability on photographic printing silkscreen pattern equipment.

Statements	Departments			
	TED	DTE	ITE	DAS
Portability				
1. A Portable Photographic Silk screen Pattern Equipment is well constructed as plan	3.8	3.8	3.8	3.75
2. The project is installed with casters for ease in mobility.	4.0	3.7	3.8	3.9
3. The materials used in the project is made of good quality.	3.8	3.7	3.75	3.7
4. The equipment is suitable for making pattern in printing process.	3.8	3.7	3.85	3.75
5. The electrical layout is well installed and organized.	4.0	3.6	3.85	3.75
6. The color of the equipment is pleasing and appropriate for classroom and industry use.	4.0	3.6	3.75	3.75
Mean:	3.90	3.68	3.80	3.14
Overall mean:	3.63			
Interpretation:	Strongly Agree			

Legend: (1.0 – 1.80 Strongly Disagree, 1.81 – 2.50 Disagree, 2.51 – 3.25 Agree, and 3.26 – 4.0 Strongly Agree)
Source: Authors, (2025).

Table 2 (Drafting Technology Students Evaluation in terms of Design). There were six (6) statement to be rated in terms of design. Students from four (4) departments strongly agreed to the design of A Portable Photographic Silkscreen Pattern Equipment with Dual Power Source. To be specific, Teacher Education Department, Students rated a weight mean of 3.9, while students from Department of Technology Education rated a weight mean of 3.68, and also the Institute of Technical Education rated a weight mean of 3.8, lastly the Department of Arts and Science give a rate mean of 3.14 which gave an overall mean of 3.63 which signified strongly agreed interpretation among the students from the four (4) Department who evaluated this project.

Table 3: Drafting technology students evaluation result on the level of acceptability on photographic silkscreen pattern equipment in terms of functionality.

Statements	Departments			
	TED	DTE	ITE	DAS
Functionality				
1. The equipment can operate manually.	4.0	3.65	3.95	3.7
2. The Portable Photographic Silkscreen pattern equipment with Dual power source produce quality print out.	4.0	3.7	3.75	3.7
3. The equipment can be operated through direct current by using solar energy that stored to a solar gel battery.	4.0	3.7	3.8	3.8
4. The wiring diagram is properly installed.	3.95	3.55	3.7	3.8
5. The electrical layout is well organized.	3.95	3.55	3.8	3.65
6. The Portable photographic silkscreen pattern equipment with dual power source is using a reflector to increase the heat of the incandescent bulb.	4.0	3.55	3.8	3.65
7. The Portable photographic silkscreen pattern equipment with dual power source has an inverter installed to regenerate power from battery to produce a maximum power.	4.0	3.7	3.85	3.65
Mean:	3.99	3.63	3.81	3.71
Overall mean:	3.78			
Interpretation:	Strongly Agree			

Legend: (1.0 – 1.80 Strongly Disagree, 1.81 – 2.50 Disagree, 2.51 – 3.25 Agree, and 3.26 – 4.0 Strongly Agree).
Source: Authors, (2025).

Table 3 (Drafting Technology Students Evaluation in terms of functionality). There were seven (7) statement to be rated in terms of functionality. Students from four (4) selected departments strongly agreed to the functionality of the Portable Photographic Silkscreen Pattern Equipment with Dual Power Source. To be specific, Teacher Education Department students rated a weight mean of 3.99, while students from Department of Technology Education rated a weight mean of 3.63, and also the Institute of Technical Education rated a weight mean of 3.81, lastly the Department of Arts and Science give a rate mean of 3.71 which gave an overall mean of 3.78 which signified strongly agreed on functionality of photographic silkscreen pattern equipment among the students from the four (4) Department who evaluated this project. The development of the photographic silkscreen pattern equipment functionality carefully considered the following: locally made, materials availability, cost-efficiency, and replicability. This is in accordance with the findings of S.A Onasanya in 2003, states *“that possible to produce effective and qualitative instructional media in Nigeria and that locally produced hardware could also be produced at a relatively competitive rate with the imported ones”* [6].

Table 4: Drafting technology students evaluation result on the level of acceptability on photographic printing silkscreen pattern equipment in terms of portability.

Statements	Departments			
	TED	DTE	ITE	DAS
Portability				
1. A Portable Photographic Silk screen Pattern Equipment with Dual power source is made of light materials.	4.0	4.0	4.0	3.75
2. The equipment is easier to carry by using the stroller handle and two placement holders at left and right side of the equipment for easy handling.	4.0	4.0	4.0	3.75
3. The drawer compartment are used for convenient replacement of materials and also it can be used as ventilation purposes.	4.0	4.0	3.0	3.75
4. A Portable Photographic silkscreen pattern equipment with Dual power has four rollers installed for pushing purposes.	4.0	4.0	4.0	3.75
5. The size of the equipment is well constructed according to materials specification.	4.0	4.0	4.0	3.75
Mean:	4	4	3.8	3.75
Overall mean:	3.89			
Interpretation:	Strongly Agree			

Legend: (1.0 – 1.80 Strongly Disagree, 1.81 – 2.50 Disagree, 2.51 – 3.25 Agree, and 3.26 – 4.0 Strongly Agree).
Source: Authors, (2025).

Table 4 (Drafting technology students are evaluated for Portability). In terms of design, there were seven (7) statements to be evaluated. The design of the Portable Photographic Silkscreen Pattern Equipment with Dual Power Source was enthusiastically supported by students from four (4) chosen departments. To be more precise, the Department of Teacher Education students gave this project a weight mean of 4.0, the Department of Technology Education students gave it a weight mean of 4.0, the Institute of Technical Education students gave it a weight mean of 3.80, and the Department of Arts and Science students gave it a weight mean of 3.75.

This resulted in an overall mean of 3.89, which indicated that the students from the four (4) Departments who evaluated this project had a strongly agreed on the portability of the on photographic printing silkscreen pattern equipment. It is important for an equipment made to be portable so that it can easily be moved from one place to another aside from that it can meet the industry demands in mass production of a product design in doing that, increased in the income follows. This is in conformity with the study of Selase et all in 2017 states that: *"the speed of the traditional screen-printing process can be increased when a machine is developed. Also, the fastness and efficiency of the t-shirt printing process have a direct relation with the income earned"* [7].

V. CONCLUSIONS

Teachers and students can both utilize the portable photographic silkscreen pattern equipment with a dual power supply for demonstrations inside or outside of the classroom as educational tools to produce high-quality results. They can be used for demonstration in printing T-shirt and other silk materials; it can also transfer the design clearly and produce quality output. The installed wheels may also help for ease in mobility and lastly, the device has a dual power source to avoid the effect of power interruptions.

The components of the equipment assembled in this project are constructed according to each function. The electrical wirings of the equipment are safely installed and work properly. A Portable Photographic Silkscreen Pattern Equipment with Dual Power Source Materials is Available in Any Enterprise. The portable photographic silkscreen pattern equipment with dual power source can operate from direct current (AC) power and solar energy because it has a solar gel battery that serves as energy storage and comes from the solar panel. The top surface of the equipment can be used as a table for the printing shirt process. The respondents of this study agreed with its portability, design, and functionalities.

Due of its portability and low cost, the project can be commercialized. Battery controller is required for the solar panel and solar gel battery. The project provides as study material for upcoming researchers. Experts advised that the battery and inverter should be compatible to prevent unnecessary costs. If the professionals are consulted, you may also utilize LED, fluorescent, and halogen bulbs. The building's layout may be made better. Experts strongly advise using solid wire. Speaker wire can be stretched by a minimum of two meters. For additional enhancements, the project's color can be changed. The apparatus can also be made more portable.

VI. AUTHOR'S CONTRIBUTION

Conceptualization: Halima A. Sahim-Sali, Joshua R. Apolinario and Anna rose A. Amalan.
Methodology: Halima A. Sahim-Sali and Ernesto F. Bantug.
Investigation: Spencer vape A. Gregorio and Kevin C. Maningo.
Discussion of results: Halima A. Sahim-Sali, Joshua R. Apolinario and Spencer vape A. Gregorio.
Writing – Original Draft: Halima A. Sahim-Sali.
Writing – Review and Editing: Halima A. Sahim-Sali and Kevin C. Maningo
Resources: Anna rose A. Amalan.
Supervision: Halima A. Sahim-Sali and Joshua R. Apolinario.
Approval of the final text: Halima A. Sahim-Sali, Kevin C. Maningo and Ernesto F.Bantug.

VII. REFERENCES

[1] Borney display solution, "Digital Printing vs Screen Printing – Advantages & Disadvantages," *Borney Disp. Solut.*, pp. 1–2, 2019.

[2] A. Goossens, "Silk-Screen Workers," pp. 2–7, 2019.

[3] L. Jahangir, "Different Methods of T Shirt Printing: A Comparative Analysis," *Can. J. Res. Soc.*, vol. 8, no. 1, 2018.

[4] D. C. Agrawal, H. S. Leff, and V. J. Menon, "Efficiency and efficacy of incandescent lamps," *Am. J. Phys.*, vol. 64, no. 5, pp. 649–654, 1996, doi: 10.1119/1.18260.

[5] N. S. Lewis, "Research opportunities to advance solar energy utilization," *Science (80-.).*, vol. 351, no. 6271, pp. 1–8, 2016, doi: 10.1126/science.aad1920.

[6] S. . Onasanya, "Silkscreen Printing Technology: Implications for Locally Produced Instructional Media," *Jos Educ. Forum*, vol. 2, no. 0, pp. 203–209, 2003.

[7] G. R. Selase, "Portable T-Shirt Printing Machine," vol. 57, pp. 36–51, 2017.

Journal of Engineering and Technology for Industrial Applications

ITEGAM-JETIA

Manaus, v.11 n.53, p. 21-24. May/June., 2025.
DOI: https://doi.org/10.5935/jetia. v11i53.1141

ISSN ONLINE: 2447-0228

RESEARCH ARTICLE OPEN ACCESS

ASSESSMENT OF THE POTENTIAL FOR ENERGY RECOVERY IN A SUGAR CANE MILL

Jorge Guevara Rodríguez[1], Juan Pedro Hernández Touset [2], Lirianet Fuentes Ramírez[3]

[1] Heriberto Duquesne Sugar Agro-industrial Company, Remedios Cuba
[2,3] Department of Chemical Engineering, Faculty of Chemistry and Pharmacy, Universidad Central "Marta Abreu" de Las Villas, Santa Clara. Cuba

[1]http://orcid.org/0009-0009-7436-5233, [2]http://orcid.org/0000-0002-0032-8685, [3]http://orcid.org/0009-0001-2318-5920

Email: jorgeguevararodriguez0@gmail.com, juanpedro@uclv.edu.cu, lframirez@uclv.cu

ARTICLE INFO

Article History
Received: June 0, 2024
Revised: January 20, 2025
Accepted: May 15, 2025
Published: May 31, 2025

Keywords:
Sugar mill
thermal energy
heat
integration
recovery

ABSTRACT

One of the problems identified in the sugar industry is the poor management of science and innovation. This paper aims to identify potential energy and water savings and opportunities to improve thermal efficiency in a sugar cane mill using energy analysis and heat integration methods. Methods of energy analysis and pinch analysis are applied using Aspen Energy Analyzer. The establishment of 10 energy performance indicators, which are not currently reported for this industry, will help to define an energy baseline and systematically measure efficiency in the industry. The current hot and cold supply requirements are not met for a minimum allowable temperature difference of 10°C. The design of the heat exchanger network allows 52.23% of the maximum recoverable energy to be recovered. There is a high excess of the current hot supply duty over the minimum hot duty, behaviour associated with the data extraction system. This study will allow us to continue the research with new heat exchangers and full inter-plant integration.

I. INTRODUCTION

The main internal problems identified that correspond to the industry are: (1) poor valuation of by-products and derivatives, (2) high obsolescence and poor technical condition of agro-industrial machinery, especially in the energy base, (3) insufficient management and lack of management models that ensure economic efficiency, quality and safety, non-compliance with technologies established in technical directives, (4) insufficient use of automation and computerisation, and (5) insufficient management of science and innovation, insufficient preparation and motivation of personnel.

The current energy base of the sugar factory has technological deficiencies in steam generation with high biomass and water consumption, which causes instability of the operating parameters of the primary equipment and at the same time increases steam consumption and molasses quality parameters.

There are also objective barriers that limit the use of SEC for energy performance assessment, such as training in energy management and the perception of the economic benefits of identifying energy savings potential in industries. The relevance of the research is given by its contribution to the definition of current SEC, energy targets and energy recovery potential, which are rarely expressed.

The study aims to identify the potential energy and water savings and opportunities to improve thermal efficiency in a sugar cane mill by applying energy use analysis and heat integration methods.

II. THEORETICAL REFERENCE

II.1 SPECIFIC ENERGY CONSUMPTION AND ENERGY RECOVERY

Specific energy consumption (SEC) is often used as an energy performance indicator to evaluate or measure energy efficiency performance, both in the literature and in international standards. Although several research studies have adopted SEC as an indicator of progress towards improved energy efficiency, publications on critical assessments of the use of SEC are scarce. In general, SEC is calculated by dividing the amount of energy used by the amount of products. However, both products and energy sources are often chosen arbitrarily, depending on the

purpose of using SEC. For example, SEC can be calculated for the total amount of products or for individual products from the product mix. Similarly, SEC can be calculated for the total primary energy used or for specific energy sources, e.g. how much electricity and heat were used separately to produce a unit of product [1].

The integrated production of first and second generation ethanol from sugarcane is expected to increase the sustainability of the sugarcane production plant, improving its economic and environmental impact as well as the energy efficiency of the whole process. Sugarcane is used to produce sugar, ethanol and electricity. In addition, sugarcane biomass power plants have some advantages over conventional power plants, which are currently based on hydroelectric power generation: faster construction, lower operational risks and costs, and easier environmental licensing.

Electricity is expected to become as important a product in the sugarcane sector as ethanol and sugar [2]. Many graphical and mathematical techniques have been developed for the efficient design of new and retrofitted energy systems. Process Integration (PI) has been used extensively to increase the energy efficiency of processing systems.

The technique, also known as Pinch Analysis (PA), was first introduced to analyse energy flows in process heat exchanger networks based on the second law of thermodynamics [3]. PI focuses on the unity of the process, rather than optimising each process separately, and in turn maximises the resource use efficiency of the industry [4].

Retrofitting a sugar mill's cogeneration unit for the purpose of surplus electricity production may not always be feasible due to, among other things, the seasonality of sugar cane production and the higher costs associated with modern equipment. Given the lower cost of producing electricity from bagasse than from other energy sources, there should be a clear motivation to produce electricity from sugarcane for export to the national grid [5].

A study applied pinch technology to a sugar production process to calculate minimum energy targets [6], where the juice from each evaporation stage is considered as hot streams, but these streams reduce their temperature by vacuum action and not by cooling, therefore the minimum cooling requirement is high. These are soft streams and should not be used for PA. Heat exchanger networks (HENs) have been widely used for energy recovery in process industries.

However, the flexibility problem has usually been ignored in the design of HENs, so they lack sufficient ability to cope with process variations. On the other hand, the synthesis of inter-plant HENs has received increasing attention in recent years due to its potential for overall site energy savings [7]. Intermediates play an important role in indirect inter-plant heat integration. Each of them has a unique performance in heat recovery, but they are rarely used together, which simplifies the problem but limits the extent of heat recovery [8].

III. MATERIALS AND METHODS

Energy management in the paper manufacturing process is based on the Cuban standard ISO 50001: 2019 and a methodology for energy use [9]. Energy Performance Indicators (EnPIs) are determined by applying energy analysis and heat integration. The pinch analysis methodology is used to determine network targets, minimum temperature difference and maximum energy recovery (MER) [10].

Data processing was carried out using Aspen Energy Analyser [11]. The main activities carried out in the energy audit were: (1) analysis of current energy use and consumption, (2) current and minimum energy obligations. The study also includes (3) the identification of energy resource savings to improve energy recovery for the subsequent estimation of economic feasibility.

IV. RESULTS AND DISCUSSIONS

The sugar mill has a crushing capacity of 2,700 t/d. The steam supply consists of a water tube boiler with a superheated steam generation capacity of 60 t/h at 1.34 MPa and 318 ^{o}C, which consumes bagasse. The superheated steam at 1.34 MPa is consumed by 2 backpressure turbogenerators of 1.5 MW and 2.5 MW. The exhaust steam at 0.218 MPa is consumed by the first-effect evaporator in a four-effect evaporator system. Juice heaters consume vapours from the first and second effect evaporators. An alcohol distillery near the sugar mill consumes the molasses, juices and steam from the first-effect evaporator.

Contaminated condensate is recovered for technological use in the evaporators, heaters and tanks. For the energy diagnosis, the current consumption (at least three months) of raw materials, energy resources (electricity, water) and production is recorded and analysed. Mass and energy balances are provided, as well as juice flow, steam consumption, thermal power and evaporator vapour flows, which are essential heat and mass flows for estimating energy performance indicators (EnPIs) or SEC, also for applying the pinch analysis method.

Table 1 shows the results of the steam, heat and water balances in the sugar cane mill, expressed in terms of energy performance indicators.

Tabla 1: Energy performance indicators

Parameters	Value
Specific steam consumption, t steam / t cane	0.48
Specific steam consumption, t steam / t bagasse	2.23
Low pressure steam consumption% cane	35.74
Specific steam consumption in turbogenerators, t / MWh	13.95
Specific bagasse consumption,t / MWh	6.23
Electricity generation, kWh / t cane	34.66
Specific thermal energy consumption,MJ / t cane	1,490
Water make-up, %	26.1
Heat Losses, %	21.0
Thermal efficiency, %	79.0
Steam duty, t/h	54
Thermal power, MW	46.6

Source: Authors, (2025).

Figure 1 shows the process flow sheet and the data for the streams presented in Table 2. The streams considered in the analysis are: Steam to heater (H1); Steam to heater 2 (H2); Steam to heater 3 (H3); Vapour to heater 4 (H4); Vapour from 4th effect (H5); Vapour from pan 1 (H6); Raw juice to heater 1 (C1); Raw juice to heater 2 (C2); Raw juice to heater 3 (C3); Clear juice to evaporator (C4); Thin juice from 1st effect (C5); Condensate from 1st effect (C6); Steam (S); Cooling water (CW).

The process equipment is: heaters (1-4), evaporators (I - IV), pan I (PI). Other parameters are specific heat capacity (cp); heat capacity flow rate (CP); inlet temperature (Ti); outlet temperature (To); film heat transfer coefficient (h) and heat load (ΔH). Vapour properties are calculated for 0.2 MPa.

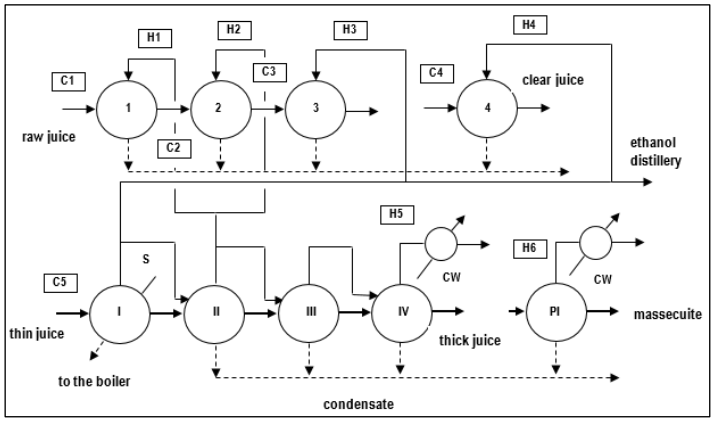

Figure 1: Process flow sheet.
Source: Authors, (2025)

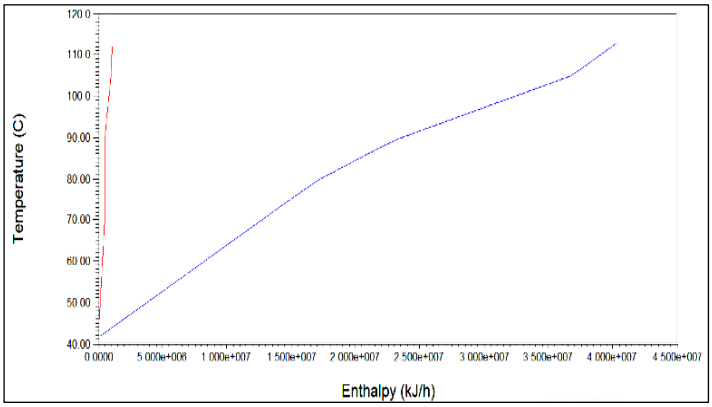

Figure 2: Composite curve diagram.
Source: Authors, (2025).

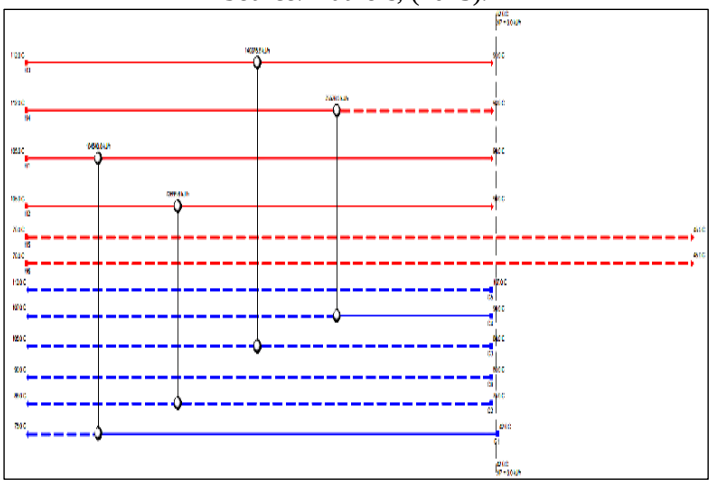

Figure 3: HEN Design.
Source: Authors, (2025).

The global minimum temperature difference (ΔTmin) in this case is set at 10 °C, as this is the minimum temperature difference between the process streams. There is a pinch point at 47 ºC, with a hot and cold pinch at 5 ºC and 42 ºC. The minimum hot and cold loads are 39,240,000 kJ/h and 143,800 kJ/h respectively. The composite curves in Figure 2 show the minimum hot and cold duties. There is an energy potential (MER) of 905,941 kJ/h that can be recovered.

Table 2: Stream data.

Stream	Ti (ºC)	To (ºC)	m (kg/h)		cp (kJ/ kgºC	CP=m·cp (kJ/hºC)
H1	105	90	6,54		1.88	12,302.72
H2	105	90	2,58		1.88	4,846.64
H3	112	90	3,39		1.88	6,380.72
H4	112	90	3,35		1.88	6,298
H5	70	45	3,93		1.88	7,382.76
H6	70	45	7,00		1.88	13,160
C1	42	75	116,86		3.84	448,746.24
C2	75	88	116,86		3.84	448,746.24
C3	88	105	116,86		3.84	448,746.24
C4	90	107	115,32		3.84	442,855.68
C5	107	113	115,32		3.84	442,855.68
C6	80	90	40,21		4.19	168,479.9

Source: Authors, (2025).

Figure 3 shows the position of the heat exchangers in the feasible combinations. According to the flow splitting algorithms, above the pinch the number of hot flows (Nh) must be less than or equal to the number of cold flows (Nc) and it is verified that all combinations above the pinch are feasible (CPh ≤ CPc). Table 3 shows the heat exchanger data as a result of the HEN design.

Table 3: Heat Exchangers data.

HeatExchanger	Cold Stream	Ti (°C)	To (°C)	Hot Stream	Ti (°C)	To (°C)	Load (kj/h)	Area (m^2)	Tmin Cold (°C)	Tmin Hot (°C)
E-100	C1	42	42.41	H1	105	90	184.541	0.52	62.58	48
E-101	C2	42.41	42.57	H2	105	90	72.699.6	0.20	62.42	47.59
E-102	C3	42.47	42.78	H3	112	90	140,376	0.37	69.21	47.53
E-103	C4	90	90.17	H4	112	100	75,576	0.77	21.82	10

Source: Authors, (2025).

As can be seen in Table 3, the cold streams do not reach the outlet temperatures due to the limitations of the method that considers sensible heat. This assumption results in high temperature differences at the hot and cold ends, smaller heat transfer areas and lower heat recovery, but avoids violations of the second law of thermodynamics. The modified design of the heat recovery network allows 52.23% of the maximum energy recovery to be recovered. The current hot utility of 167,760,000 kJ/h, shown in Table 1, is far from the minimum hot utility.
A fuel net calorific value of 43,157 kJ/kg, 150 days of operation per year (crushing season), 20 hours per day and a fuel (FO) price of $512.9/t are assumed. The four heat exchangers provide annual savings of 39.6 tonnes and $20,310 /year in fuel costs.

V. CONCLUSIONS

The establishment of 10 energy performance indicators, which are not currently reported for this industry, will help to define an energy baseline and systematically measure efficiency in the industry. The current hot and cold supply requirements are not met for a minimum allowable temperature difference of 10°C. The design of the heat exchanger network allows 52.23% of the maximum recoverable energy to be recovered. There is a high excess of the current hot supply duty over the minimum hot duty, behaviour associated with the data extraction system. This study

will allow us to continue the research with new heat exchangers and full inter-plant integration.

VI. AUTHOR'S CONTRIBUTION

Conceptualization: Jorge Guevara Rodríguez**,** Juan Pedro Hernández Touset.
Methodology: Juan Pedro Hernández Touset.
Investigation: Jorge Guevara Rodríguez, Juan Pedro Hernández Touset, Lirianet Fuentes Ramírez.
Discussion of results: Jorge Guevara Rodríguez, Juan Pedro Hernández.
Writing – Original Draft: Juan Pedro Hernández Touset.
Writing – Review and Editing: Jorge Guevara Rodríguez, Juan Pedro Hernández Touset.
Supervision: Jorge Guevara Rodríguez.
Approval of the final text: Jorge Guevara Rodríguez, Juan Pedro Hernández Touset, Lirianet Fuentes Ramírez.

VII. REFERENCES

[1] Lawrence, A., Thollander P., Andrei M., Karlsson, M., "Specific Energy Consumption/Use (SEC) in Energy Management for Improving Energy Efficiency in Industry: Meaning, Usage and Differences", Energies, vol.12, no. 2, 247, pp. 1-22, January 2019, https://doi.org/10.3390/en12020247

[2] Dias, M., Junqueira, T., Cavalett, O., Pavanello, L., Cunha, M., Jesus, C., Filho, R., Bonomi, A., "Biorefineries for the production of first and second generation ethanol and electricity from sugarcane", Applied Energy, vol. 109, pp. 72-78, September 2013, https://doi.org/10.1016/j.apenergy.2013.03.081

[3] Al-Mayyahi M., Albadran F.A., Fares M.N., "Retrofitting Design of Heat Exchanger Using Supplytarget Diagram", Chemical Engineering Transactions, vol. 75, pp. 625-630, 2019, https://doi.org/10.3303/CET1975105

[4] Jain S., Bandyopadhyay S., Varbanov P.S., Klemeš J.J., "Pinch Analysis Approach for Segregated Targeting Networks with Forbidden Matches", Chemical Engineering Transactions, vol. 94, pp. 103-108, 2022 https://doi.org/10.3303/CET2294017

[5] Birru, E., Erlich, C., Martin, A., "Energy performance comparisons and enhancements in the sugar cane industry. Biomass Conversion and Biorefinery", vol. 9, pp. 267–282, 2019, https://doi.org/10.1007/s13399-018-0349-z

[6] Pratap., N., Kesari, J., Pinch Analysis and Heat Integration in a Sugar Industry using Hint Software, SSRG International Journal of Mechanical Engineering, vol. 6, no. 8, pp. 6-15, 2019, https://doi.org/10.14445/23488360/IJME-V6I8P102

[7] Tao R., Liu L., Gu S., Zhuang Y., Zhang L., Du J., "Flexible Synthesis of Inter-Plant Heat Exchanger Networks Considering the operation of Intermediate Circles", Chemical Engineering Transactions, vol. 81, pp. 13-18, 2020 https://doi.org/10.3303/CET2081003

[8] Linlin Liu, Changhao Wu, Yu Zhuang, Lei Zhang, and Jian Du, "Interplant Heat Integration Method Involving Multiple Intermediate Fluid Circles and Agents: Single-Period and Multiperiod Designs", Ind. Eng. Chem. Res., vol. 59, no. 10, pp. 4698–4711, 2020, https://doi.org/10.1021/acs.iecr.9b06561

[9] Hernández, J.P., de Armas, A.C., Espinosa, R., Pérez, O., Guerra, L., "Energy analysis procedure for the conversion of sugar cane industries into biorefineries, Revista Universidad y Sociedad, vol. 13 no.5, pp. 277-288, Septiembre 2021, https://rus.ucf.edu.cu/index.php/rus/article/view/2234/2208

[10] Klemeš, J. J. (Ed), Handbook of Process Integration (PI): Minimisation of Energy and Water Use, Waste and Emissions, Woodhead Publishing Limited, Cambridge, 2013

[11] Aspentech, Aspen Energy Analyzer V 10. Aspen Technology Inc., 2017, https://www.aspentech.com/en/products/engineering/aspen-energy-analyzer

Journal of Engineering and Technology for Industrial Applications

ISSN ONLINE: 2447-0228

ITEGAM-JETIA

Manaus, v.11 n.53, p. 25-33. May/June., 2025.

DOI: https://doi.org/10.5935/jetia. v11i53.1160

RESEARCH ARTICLE OPEN ACCESS

OPERATIONAL FACTORS INFLUENCING QUALITY CONTROL IN ORE MILLING: A SYSTEMATIC REVIEW

Eliana de Jesus Lopes[1], Guilherme Graciano dos Santos[2] and Adriano Ricardo Almeida Alexandre[3]

[1] Centro Universitário INTA
[2] Manserv Engineering
[3] Municipal Department of Urban and Public Services

[1]https://orcid.org/0000-0003-0496-1661, [2]http://orcid.org/0009-0008-7985-416X, [3]http://orcid.org/0000-0003-2396-2854

Email: prof.eng.eliana@gmail.com, guilhermes930@gmail.com, adricaral@gmail.com

ARTICLE INFO

Article History
Received: June 18, 2024
Revised: January 20, 2025
Accepted: May 15, 2025
Published: May 31, 2025

Keywords:
Quality control,
Ball mill,
Comminution,
Cement production process,
Ore industry.

ABSTRACT

Quality control in ball mill operations in the ore industry is crucial for ensuring the final product's quality and the equipment's efficient operation. Despite its relevance, there is a scarcity of studies on this topic. This bibliographic study, based on the PRISMA protocol, involved scientometric and qualitative bibliographic analysis. The analysis revealed that the topic is rarely addressed in the literature, resulting in a limited portfolio. The identified studies explore advanced techniques such as algorithms and mathematical modeling to optimize the grinding process and improve product quality. Research also discusses advanced control systems to ensure compliance in mill operations, leading to reduced variability in material granulometry, energy savings, and increased production. Furthermore, contributions include implementing virtual sensors to monitor cement fineness in real-time, optimizing operations, and enhancing the final product's quality. However, there is a notable lack of research focused on the particle separator, a crucial component in the grinding process. These findings provide valuable insights for the effective management and operation of ball mills in the mining industry and underscore the need for future research to address these gaps.

I. INTRODUCTION

In recent years, the world has been facing sanitary, political, and economic crises that impact businesses across all sectors, prompting companies to develop strategic plans to remain competitive [1]. In this context, industries have been affected at various levels, primarily due to the COVID-19 pandemic, the Russia-Ukraine war, and the Israel-Palestine conflict, which have disrupted the production and distribution of products and materials[2], [3].

The mineral processing industry has unique characteristics, balancing financial returns with concerns for environmental preservation and impact reduction [4]. In Brazil, the mineral processing industry has shown symbolic and consistent growth each year, with a 62% increase in revenue in 2021 compared to the previous year and an 11% increase in cement demand [5].

Among the mineral processing industries, cement manufacturing has paralleled the growth of the real estate market, driven by the rise in civil and public construction projects, making it one of the primary materials in these products [6]. Cement industries are present in all regions of Brazil, covering activities from extraction and processing of the ore to the production, packaging, and distribution of cement [7], [8].

In cement manufacturing, the comminution process is considered one of the most important in the mineral industry, as it is responsible for reducing the size of ore particles [9]. Various factors can influence this type of operation, from the raw material to be processed to the sizing parameters directly related to the process [10].

In the comminution process, one of the most critical pieces of equipment is the ball mill, which performs the final fragmentation work. Therefore, precise operational control is necessary to ensure the quality of the final product [10].

Given the importance of this equipment in the segment's outcomes, the research question arises: What is the state of the literature on ball mill operations in the context of quality control?

The objective of this research is to understand the landscape of the literature regarding operational factors influencing quality control in ore milling operations, with a particular focus on ball mills, such an important piece of equipment in cement production.

II. THEORETICAL REFERENCE

II.1 QUALITY CONTROL IN THE ORE INDUSTRY

Quality control in the industry is a set of practices and processes implemented to ensure that products and services meet established quality requirements and standards [11], [12]. Quality control in the mining industry is extremely important to ensure that extracted minerals meet established quality requirements and standards [13]. This industry deals with the exploration and processing of minerals, which are used in a wide range of sectors such as metallurgy, civil construction, the chemical industry, among others.

Thus, the quality control process begins with the extraction of minerals, during which samples are collected at different points in the mine for analysis [14]. These samples undergo laboratory tests to determine the chemical composition, physical characteristics, and properties of the minerals [15]. This information is essential for evaluating the quality of the minerals and identifying their viability for use.

Laboratory tests are also used to determine the presence and concentration of impurities in the minerals [16]. These impurities can include undesirable chemical elements, environmental contaminants, or minerals of low commercial value [17]. The identification and quantification of these impurities are important to ensure that the minerals meet the quality requirements established by customers and environmental regulations [4].

In addition to laboratory tests, techniques such as real-time analysis and automation are used to monitor and control the mineral production process [18]. Sensors and devices are installed at facilities to collect real-time data on parameters such as moisture, particle size distribution, and mineral concentration [19], [20]. This data is analyzed to identify deviations and variations, allowing for immediate adjustments to keep the mineral quality within established standards [21].

Another crucial aspect of quality control in the mining industry is the implementation of quality management systems that adhere to international standards, such as ISO 9001 [22]. These systems assist in standardizing processes, documenting activities, and continuously improving operations [23]. Adopting these standards helps companies demonstrate compliance with quality requirements and build trust with customers and stakeholders. Continuous employee training and the promotion of a quality culture within the organization are also fundamental [24]. Well-trained teams that are aware of the importance of quality control can identify potential problems and implement effective solutions, contributing to the consistency and excellence of the final products [23]. In this way, quality control becomes an integrated element at all levels of production, from extraction to the delivery of the final product to the customer.

II.2 CEMENT MANUFACTURING PROCESS

To better understand the grinding operation, it is essential to comprehend the cement production process. This operation involves several stages, starting with the extraction of raw materials and crushing, preparation of raw meal, the clinker phase where the raw materials are burned, the cement grinding operation, and finally, the packaging. Figure 1 provides a detailed illustration of this process.

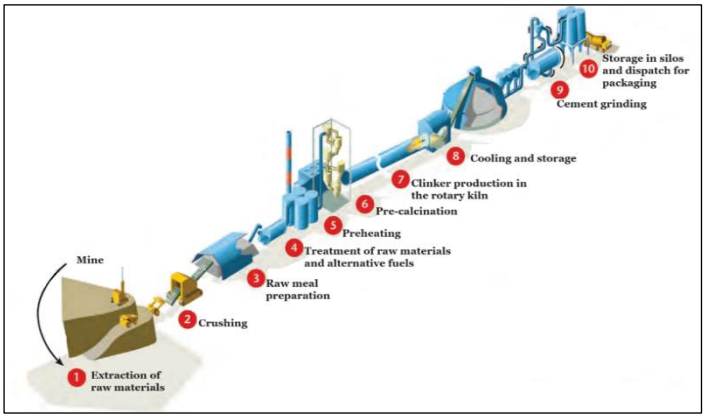

Figure 1: Cement manufacturing process.
Source: [25].

Thus, the process begins with the extraction of the primary component in cement production, which is extracted from carbonate deposits through quarry blasting, where limestone is removed, transported, and classified according to the physical and chemical composition present in the raw material [26]. The extracted material has large and disproportionate dimensions, making loading and transport difficult, especially when the production unit is not in the same location or near the mining site. Therefore, a crushing process is carried out, which fragments the limestone, making it easier to handle [27].

Subsequently, the raw meal preparation stage involves mixing the limestone with other "corrective" components such as bauxite, iron ore, clay, and sand to achieve better chemical stability. Various methods can be used to determine the correct dosage of the mixture, including the percentage of clay or corrective limestone [25]. The multiple chemical analyses conducted to meet the strict control of cement production may indicate the need to add residues from the production processes of other industries, such as pozzolan or blast furnace slag, to replace the raw meal material or the fuels used for clinker burning in the kiln [14], [16].

In this context, during the preheating phase, the raw meal is transported and inserted into vertical heat cyclones, where it meets the hot gases from the kiln in the opposite direction. This preheats the raw meal, initiating the first chemical reactions necessary for clinker formation. Subsequently, the precalcination process occurs in a chamber located at the bottom of the preheating cyclones, just above the kiln, known as the precalciner. After being precalcined, the raw meal moves to the next phase, entering the rotary kiln, where it is heated by fuel in a burner that can reach temperatures of 1,450°C. The precalcined meal slides through the kiln, which is slightly inclined and rotates about three to five times per minute [4], [25].

With this, the cooling stage occurs immediately when the material exits the kiln at a high temperature and is directed to a cooler (chamber) that blows cold air from electric air blowers [27]. This results in heat exchange and the generation of hot air that is reused in the process, providing better thermal efficiency for the kiln. This completes the clinker production process, and this material is then used as the primary raw material in cement production. It must be mixed with gypsum, which functions to control the setting time, with an average addition of between 3% to 4%. However, in addition to gypsum, it may be necessary to add other materials to control the quality and cost of the product [28].

In such a way, the grinding of these materials is traditionally carried out by ball mills, though some industries use horizontal roller mills [29]. In this process, grinding occurs through the

interaction of grinding bodies with the particles to be ground, driven by the rotational movement of the mill. The control parameters initially consider the reliability of raw material dosing and the rotational speed of the particle separator, as higher rotation speeds result in finer material. This is a key quality parameter for cement, as it directly relates to the concrete's strength [30]. Consequently, the ground product is stored in cement silos, ready for bulk distribution in trucks or bagged on pallets.

As discussed, the cement production process is complex, involving a series of technical parameters and critical activities with a high degree of risk, thus requiring a qualified workforce. Additionally, much of this process is automated and controlled via computer at a central operations panel, significantly reducing the risk of accidents for field operators. This is a major advantage for the plant, highlighting the importance of constant maintenance of these systems [18].

II.3 COMMINUTION PRINCIPLES AND MECHANISMS

In the mineral processing industry, comminution is the process of ore fragmentation, whether by explosives or other methods. Thus, the crushing stage is primarily used after the extraction of materials in mining areas due to the size of the minerals and the specifications and adjustments needed for transport or direct commercialization [31].

Considering that electrical energy consumption is directly linked to comminution, it is the operation responsible for the largest share of energy usage [9]. In a competitive market, the high production costs associated with increased energy consumption directly impact the final product price for customers. This remains a significant challenge for equipment manufacturers, who strive to enable energy efficiency without compromising the operational effectiveness of the equipment [32].

In the technological realm, mineral processing circuits consider that the energy required for fragmentation depends on material characteristics such as size, density, and composition [16]. Each ore presents unique characteristics, necessitating individualized study to determine the most suitable equipment. Precise adjustments of operational parameters are crucial to ensure the ball mill operates efficiently and produces a high-quality final product [19]. Therefore, it is essential that the operation and monitoring of operational parameters are conducted by trained and experienced professionals.

The relationship between energy consumption and the degree of granulometry of the product generated by the grinding process is direct [33]. Monitoring fragmentation through the particle separation process is essential to determine the comminution efficiency level and prevent unnecessary processing of raw materials.

Determining a more economical and efficient process has been a significant challenge for scientists and the mineral processing industry. Despite being the subject of long-standing research, no relevant alternatives have been generated for industrial implementation [13]. In this context, it is evident that there are no comminution equipment options efficient enough to reduce the cost of these operations. Consequently, industries often use inefficient comminution mechanisms and primitive methods. These mechanisms typically include compression, abrasion, impact, and shearing [31].

Automation enhances industrial processes' effectiveness through constant parameter control [34]. The advancement of computational tools allows for frequent diagnostics of operations and simulations that relate mathematical models to previous stages of the process. This capability enables the establishment and comparison of scenarios, facilitating the projection of future industrial installations [9].

Comminution equipment operates based on the principle of applying mechanical energy, which results in the fragmentation of materials. The shape and size characteristics of the particles represent the operational mode [31]. The primary interaction mechanisms of the equipment are compression, impact, attrition, and abrasion, as illustrated in Figure 2.

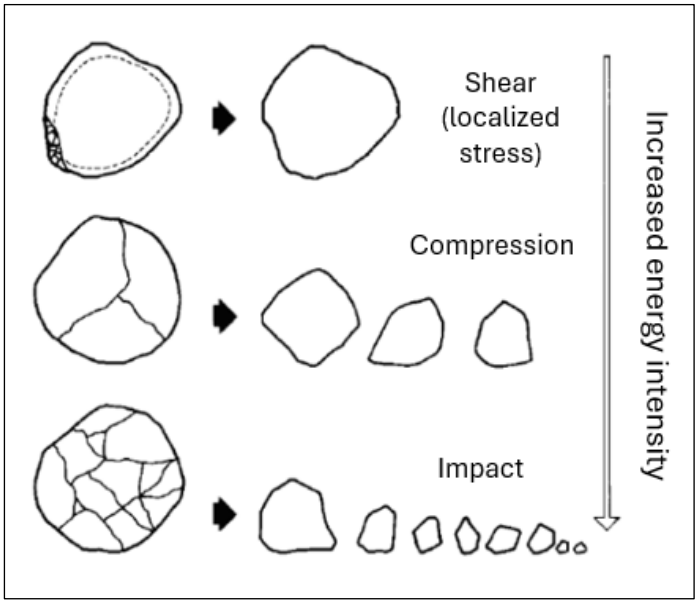

Figure 2: Fracture Mechanisms.
Source: [35].

In the compression mechanism, force is applied slowly and successively to the rock, allowing fractures to appear and subsequently break. This type of mechanism typically generates coarser and fewer fine fragments [35]. The impact mechanism utilizes rapid force applied to the particles with greater intensity than the material's strength. In this mechanism, the particles absorb more energy than necessary for fragmentation, generally producing finer material [36].

Shear comminution, while generating high energy consumption, produces a significant amount of superfine material. This mechanism is predominant in milling operations and ball mills, occurring when ore fragments move against each other, causing wear through friction [37]. Abrasion involves movement similar to friction fragmentation, differing by the particles moving in opposite directions, resulting in the production of fine material [31].

Efficient ball mill operation requires monitoring the grinding medium flow to ensure effective collisions. This avoids impact with the mill's inner lining or other grinding bodies, which results in energy loss during the process [29], [35]. Consequently, numerical simulations are necessary to address this deficiency.

II.4 CHARACTERISTICS AND MECHANISMS OF THE BALL MILL

Considered a commonly used equipment in the mineral processing industry, ball mills have a rotating cylindrical structure lined with steel or rubber plates [35]. Inside, they contain a charge of free grinding media that interact with each other due to the mill's rotational movement, facilitating particle comminution [30]. Figure 3 shows the equipment known as a ball mill.

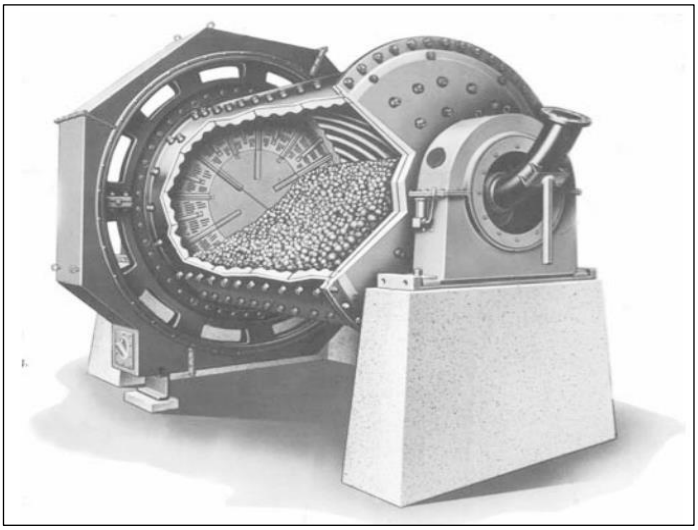

Figure 3: Ball Mill.
Source: [38].

This type of equipment is used in grinding operations involving coarser materials, as the balls have a larger contact surface, facilitating the production of fines. It should be noted that mills with a length/diameter ratio of 1.5 to 1m or smaller are not considered ball mills [39]. When they have a length greater than 3 to 5m, they are usually divided into compartments, with different ball diameters in each compartment, requiring precise sizing to define this division [40].

In the mill operation, the grinding charge can assume three movement regimes: cascading, cataracting, and centrifugation [41]. Figure 4 shows the reported types.

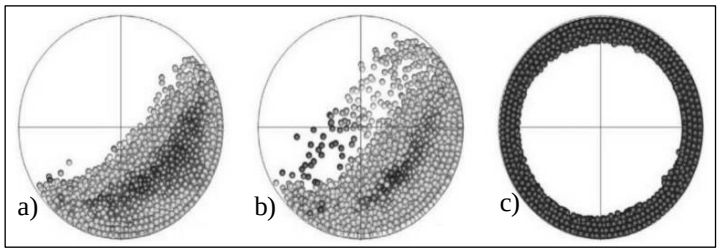

Figure 4: Operating Regimes.
a) Cascading; b) Cataracting and c) Centrifugation.
Source: [41].

The cascading regime (or cascade) is characterized by the rotational movement of the mill lifting the balls to a certain height, where they slide over each other in a cascading form due to the force of attraction [30]. This type of regime does not provide high energy generation from the impact between the bodies, and the material is broken by abrasion, making it ideal for producing a final product due to the capacity for fine production.

In the cataracting regime (or cataract), the grinding load is carried to higher elevations and detaches, falling onto the particles to be ground, causing fragmentation by impact. This is ideal for handling coarser material [42]. It is important to note that operations in this regime must be well-monitored and planned to ensure that the falling bodies land on the material to be ground and not on the mill lining. If the latter occurs, it would lead to faster wear of the lining, consequently reducing performance in terms of production [43]. Besides the mechanical operating parameters, the raw material greatly influences the yield, with factors such as moisture, porosity, initial dimensions, and shapes impacting the mill's operational efficiency [29].

Finally, the centrifugation regime occurs when the mill's rotational movement is high, causing the grinding media to be held against the walls, following the circular motion [42]. The critical speed is defined as the point where centrifugal force and gravitational force act on the particles in equilibrium, resulting in centrifugation [44].

The grinding media are indispensable components in an operating mill, responsible for performing the comminution work through interaction mechanisms. They are typically spherical, made of cast iron or steel, and come in various sizes, depending on the ore particles [45].

Determining the size of the grinding media can present a problem in some situations, considering two scenarios. In the first scenario, increasing the size of the load favors impact interaction between the particles, resulting in the breakage of larger particles [31]. The second scenario considers smaller media, increasing the contact surface area and enhancing friction interaction, thus increasing the grinding capacity. Therefore, it is recommended to define a mix of sizes among the media in the same chamber, considering the feed granulometry and the final product requirements [35].

The degree of filling is referenced according to the percentage of the mill's occupancy, which, in practice, does not exceed 50% of the mill's internal volume. This factor directly affects the grinding performance due to the motor's power, potentially damaging the equipment if the load exceeds the capacity [31].

The primary factor for the efficiency of the grinding operation is the mill's rotational speed. Literature and manufacturer manuals present varying values, making them questionable due to discrepancies when compared [30].

The mill's internal lining is crucial for operation, requiring perfect condition for optimal performance. High operational speed is a factor that can quickly wear down the lining. In the 1920s, it was common to use around 80% of the critical speed, but studies have shown that operating at about 57% of the critical speed reduces energy consumption without significantly affecting the mill's production [7].

The rotational speed determines the flow regime of the load inside the mill. Low speeds reduce the rotation number, causing the load to roll over itself, producing a cascading motion [10]. Conversely, high rotation speeds cause the load to follow parabolic trajectories, a movement known as cataracting.

The dynamic separator used in grinding operations classifies the particle size of the ground material, directing it to the end of the process or back to the beginning for reprocessing until it reaches the specified fineness [37]. The internal structure consists of a cage made of vertical bars and blades. In this type of operation, three simultaneous forces interact: the weight of the particles, the drag force of the air current, and the centrifugal force. Besides the physical aspect, there are three types of separators: first-generation, second-generation, and third-generation, all serving the same function [30].

Efficiency is achieved through the mass balance between two sub streams: the final product and the reject. When the rotational speed of the separator is high, there is an increase in both production and fines, leading to more material being rejected. Consequently, the finished product tends to decrease [46]. This occurs due to the overload factor of the mill. With the increase in the separator's rotation, the operation tends to reduce the feed to avoid overload. In other words, the production volume tends to fall with fine parameter requirements. In most scenarios, the separator

retains about 20% of the material, with the remaining 80% being the finished product [30].

III. MATERIALS AND METHODS

This research can be classified as a Literature Review [47], which was based on the following steps of the Preferred Reporting Items for Systematic Reviews and Meta-Analyses (PRISMA) Protocol: (i) selection of Bibliographic Portfolio (BP) on quality in ball mill operations (ii) bibliometric analysis of the selected portfolio; (iii) systemic analysis of BP articles; and (iv) research question and opportunities highlighted based on the knowledge built during the process (Figure 5).

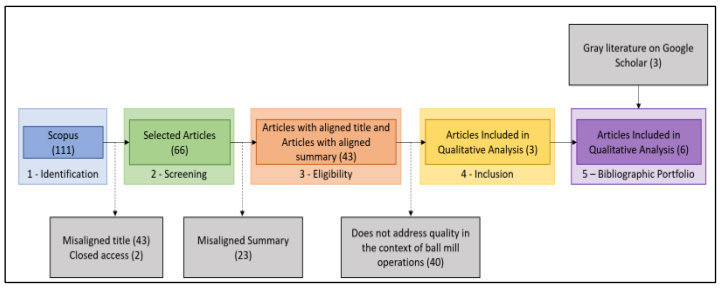

Figure 5: Article selection process based on PRISMA.
Source: Authors, (2025).

The academic database used was Scopus, employing the combination of the terms "ball mills," "quality," and "operations," with the following search string: (TITLE-ABS-KEY ("ball mills") AND TITLE-ABS-KEY (operation*) AND TITLE-ABS-KEY (quality)).

Inclusion criteria were defined as follows: only journal articles, only articles aligned with the topic, and only empirical articles. Exclusion criteria included: duplicate articles, articles not aligned with the topic, articles that do not address the impacts on quality due to operational factors in ball mill operations, and articles that do not meet the other inclusion criteria.

After the selection process, the portfolio contained only 3 aligned articles. To complement the research, the same search was conducted on Google Scholar, seeking documents aligned with this study. Only 3 aligned documents were found, resulting in a Bibliographic Portfolio of just 6 scientific documents aligned with the research, as shown in Table 1.

Table 1: Bibliographic Portfolio on Quality in Ball Mill Operations.

Authors	Source	Capes 2017-2020	Percentil
[43]	Mining Informational and Analytical Bulletin	-	49
[40]	Holos	A1	-
[48]	IEEE Transactions on Industrial Informatics	A1	98
[49]	Panduan Konseling Behavioral dengan	-	-
[50]	Powder Technology	A1	88
[29]	Federal Institute of Espírito Santo	-	-

Source: Authors, (2025).

For the bibliometric analysis, the software tools used were Mendeley, R-Studio with Bibliometrix, and VOSviewer for word clouds. The qualitative analysis was conducted based on the complete reading of the texts, highlighting their main contributions.

IV. RESULTS AND DISCUSSIONS

IV.1 SCIENTOMETRIC ANALYSIS

Quality control in ball mill operations in the mining industry is a topic that has been inadequately addressed in the literature and has shown irregular trends over the years, with significant variations. There is a noticeable gap between 2005 and 2013, during which there were no publications focused on quality control in milling operations using ball mills. After 2015, there is a higher frequency of publications involving the topic, but these are sporadic and include only specific studies. This irregularity suggests a need for greater attention and investment in research in this area to promote a more consistent and comprehensive understanding of the operational factors that influence quality in the use of ball mills.

When examining the co-occurrence of keywords, it is observed that out of 45 keywords, only 39 form a connected set. Figure 6 illustrates the co-occurrence network of keywords, showing the relationships and interactions between different terms. The red and green clusters are visually distinct, with "particle size" positioned centrally, highlighting its role in bridging the equipment-related and operation-related aspects of research. These keyword clusters help identify the core areas of research and highlight the interconnected nature of equipment characteristics and operational factors in quality control processes within ball mill operations in the mining industry.

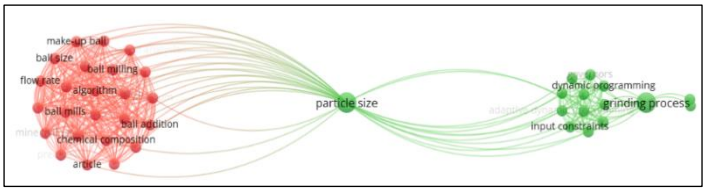

Figure 6: Keyword Clusters on Quality Control in Ball Mill Operations in the Ore Industry.
Source: Authors, (2025).

The analysis of keyword clusters in the context of quality control in ball mill operations within the mining industry reveals two main groups that are interconnected through the keyword "particle size": Ball Mill Equipment and Activities (Cluster 1 – red; Keywords: ball mills, grinding, milling, energy consumption, efficiency, operational parameters, etc.); and Operational Factors (Cluster 2 – green; Keywords: quality control, process optimization, monitoring, performance, product quality, etc.).

The Cluster 1 focuses on the ball mill equipment and the various activities involved in its operation. It is notable for having a larger number of interconnected keywords, suggesting that the characteristics and functionality of the equipment are of significant relevance in related studies. The higher density of keywords in this cluster indicates a strong emphasis on understanding and optimizing the physical and mechanical aspects of ball mills.

The Cluster 2 is concentrated on the right side of the figure and pertains to the operational factors affecting ball mill performance. It encompasses research on quality control measures, monitoring systems, and optimization techniques aimed at enhancing the efficiency and output quality of the milling process. The keywords in this cluster emphasize the importance of process management and operational adjustments in achieving optimal performance.

The keyword "particle size" serves as a crucial link between the two clusters. It is central to the discussion on quality control in ball mill operations, as it relates to both the characteristics of the

equipment and the operational factors. Particle size is a key parameter in assessing the efficiency of the milling process and the quality of the final product.

One can observe a low interaction among authors and a restricted collaboration network in the research on the topic. Only two groups are connected in the same study. In this Bibliographic Portfolio, the significant number of citations attributed to the articles by [48] and [40] stands out. This observation suggests that these works have been widely recognized and referenced in the literature on the subject in question.

The relevance of these articles may lie in their contribution to advancing knowledge in the field, possibly presenting innovative approaches, robust methodologies, or impactful results. Furthermore, their influence may reflect their acceptance by the academic community and their ability to provide valuable insights that have significant implications for research and practice in the studied area.

Regarding the sources, only 3 are indexed in Scopus/Web of Science, with percentiles, and three of them are classified by Capes in the 2017-2020 quadrennium with an A1 rating.

The scientometric analysis reveals that the topic of quality control in milling operations using ball mills is still underexplored in the scientific literature. The earliest publication dates to 2005, authored by only one author. There is a significant gap until the publication by Gedraite et al. in 2014 [40]. Since then, there has been an average of one publication every two years.

This irregular behavior and the presence of gaps between publications indicate the need for greater focus and investment in research in this area, aiming to develop a deeper and more comprehensive understanding of the operational factors that impact quality in ore milling using ball mills.

IV.2 QUALITY CONTROL IN BALL MILL OPERATIONS

Quality control in ball mill operations, especially in the mining industry, is essential to ensure the quality of the final product, improve equipment operationalization, and prevent waste, environmental impacts, among other factors [20].

Upon analyzing the BP, it is noticeable that this topic, although very relevant and essential for the operations of this type of equipment, lacks associated studies. However, there is a technical deepening aimed at optimizing the equipment through the use of algorithms and mathematical modeling [48].

According to [43], the study addresses the efficiency of the milling process itself but emphasizes that as a consequence, this should increase the quality of the materials obtained. Thus, the research aims to combine two methodologies that simulate possible scenarios of the milling process in two fields of operation, and ultimately apply the combination of these methods directly to the process, with the aim of expanding the operating capacity.

The first method addresses the movement of the medium in a ball mill, for which the discrete element method (DEM) is used. However, processes in the mining industry are linked to particle movement in a fluid flow, for which the process can be modeled by computational fluid dynamics (CFD). Thus, the direction of the study is to explore the possibility of combining and applying the two DEM-CFD methods.

From Chimwani, Mulenga, and Hildebrandt's perspective [50] the distribution of ball sizes is crucial for controlling product quality and ensuring maximum production. Thus, the study's objective is to find the ball mixture that ensures compliance with this requirement. In this context, the authors developed an algorithm capable of simulating grinding circuits focused on ball wear, and this model was validated, providing relevant results for the issue. Therefore, this work has significant characteristics as it addresses the problem and approaches the topic with technical relevance, well-explained by the authors.

Following the same research line, [48], also developed a study based on algorithms and simulations, which concerns the efficiency of the ore grinding process. According to the authors, this efficiency depends on the circulating load and the particle size of the product, making these two operational points crucial for quality control in the operation. Simulations were conducted, obtaining significant results.

Considering the approach of the three studies mentioned earlier, these belong to the empirical reports extracted from Scopus, having relevance due to the recognition of the database. Thus, we observe an important point regarding the methodology model, as both studies use mathematical modeling to conduct simulations. Such observation is essential due to the positive outcome presented by the journals, contributing safely and accurately to the operation.

The three reports retrieved from Google Scholar focus on the installation of systems and hardware in computers, aiming to monitor the grinding process and improve operational practices that contribute to the operation itself, consequently presenting elevated aspects regarding quality control.

The study conducted by [49], aims to control the speed and rotation in the grinding process using a ball mill. To optimize this process, a frequency inverter controlled by Compact Field point hardware and LabVIEW software was employed. The system was studied, and a speed control application for the grinding process was developed within the programming environment. This application allows for the combination of different speeds according to the mill's load. Subsequently, tests were conducted in a laboratory setting, where the operation was managed by considering a series of factors to ensure reliable results. The results of the laboratory simulations showed that the optimization objective was satisfactorily achieved, as expected by the authors.

According to [40] developed an advanced control system that incorporates a multivariable controller coupled with a regulatory control system. The implementation of this system in a ball mill allows the operation to achieve compliance conditions, ensuring maximum efficiency and improving the final product's milling finish. As a result, the system demonstrated significant benefits, including reduced variability in the material's particle size distribution after grinding, decreased energy consumption, and increased production output.

Finally, [29] believes that providing online information about cement fineness is a significant opportunity for the cement grinding process using ball mills. This approach can optimize operations, reduce energy consumption, and enhance the quality of the final product. The study presents three types of supervised regression models for predicting cement fineness: Multilayer Perceptron Neural Network (MLP), Support Vector Machine (SVM), and Radial Basis Function Neural Network (RBFNN).

Tests were conducted on a laboratorial scale to obtain fineness data for the material entering and exiting the mill. Subsequently, a virtual sensor based on the MLP model was designed and implemented. The system was tested in a real-world setup, and despite the complexity of deploying this system, data preprocessing enabled advantageous results, providing greater accuracy in monitoring cement fineness.

Regarding the operational factors addressed in the studies, applications involving software, system automation, and mathematical modeling focused on quality control in grinding operations were evident. However, the entire Bibliographic

Portfolio lacked research directed towards the particle separator, an essential component in the grinding process responsible for classifying the size of comminuted material particles. The integrity and operation of this equipment are crucial for maintaining quality parameters in the process.

V. CONCLUSIONS

This study revealed that quality control in ball mill grinding operations is still an underexplored topic in the scientific literature, despite its industrial importance, especially in mining. Through a systematic analysis of the existing literature, it was possible to map the conducted studies, identify significant gaps, and better understand the methods and approaches used so far.

The bibliographic analysis of the portfolio revealed that the existing studies predominantly focus on strategies for controlling the fineness of the mill's output material, highlighting the importance of this parameter in ensuring the quality of the final product. These studies also emphasize benefits in terms of costs and operational efficiency. The bibliometric analysis revealed a scarcity of authors and a limited collaboration network, suggesting that the participation of larger groups could enrich and enhance ideas in this complex area. However, there is a growth trend driven by new technologies and market demands.

The studies indexed in Scopus stand out for their process simulations aimed at resource optimization and operational cost reduction, while the studies identified in the Google Scholar database focus on practical applications in a laboratorial scale. There is little intersection between these types of studies, indicating the need for greater integration between theoretical and practical approaches.

The analyzed studies do not sufficiently address the use of the particle separator, a crucial component for quality control and the proper functioning of the ball mill. Additionally, the control of the mix of ball sizes, which is essential for optimizing the grinding process, deserves more in-depth study.

This study is pioneering in bringing theoretical elements that support scientific work in the mining industry, which extensively uses ball mills. It significantly contributes to the literature by identifying new directions for future research, highlighting opportunities for both empirical and theoretical studies.

For future work, it is recommended to conduct empirical research that directly involves command centers, exploring practical applications in the industrial environment. Comparative studies between laboratory experiments and applications on real equipment would enrich discussions on the topic. Furthermore, future studies could focus on the use of particle separators and deepen the study of the ball mix to ensure quality control in the mineral grinding process using ball mills.

In this interim, it is concluded that although the topic is crucial for the industry, the literature on quality control in ball mills is limited and dispersed. This study not only fulfills the objective of mapping the current state of research but also establishes a robust starting point for future investigations, encouraging the continuity and deepening of research in this vital area.

VI. AUTHOR'S CONTRIBUTION

Conceptualization: Eliana de Jesus Lopes, Guilherme Graciano dos Santos, Eng. and Adriano Ricardo Almeida Alexandre, Dr.
Methodology: Eliana de Jesus Lopes, Guilherme Graciano dos Santos, Eng. and Adriano Ricardo Almeida Alexandre, Dr.
Investigation: Eliana de Jesus Lopes, Guilherme Graciano dos Santos, Eng. and Adriano Ricardo Almeida Alexandre, Dr.
Discussion of results: Eliana de Jesus Lopes, Guilherme Graciano dos Santos, Eng. and Adriano Ricardo Almeida Alexandre, Dr.
Writing – Original Draft: Eliana de Jesus Lopes, Guilherme Graciano dos Santos, Eng. and Adriano Ricardo Almeida Alexandre, Dr.
Writing – Review and Editing: Eliana de Jesus Lopes, Guilherme Graciano dos Santos, Eng. and Adriano Ricardo Almeida Alexandre, Dr.
Resources: Eliana de Jesus Lopes, Guilherme Graciano dos Santos, Eng. and Adriano Ricardo Almeida Alexandre, Dr.
Supervision: Eliana de Jesus Lopes, Guilherme Graciano dos Santos, Eng. and Adriano Ricardo Almeida Alexandre, Dr.
Approval of the final text: Eliana de Jesus Lopes, Guilherme Graciano dos Santos, Eng. and Adriano Ricardo Almeida Alexandre, Dr.

VII. REFERENCES

[1] Q. Liu, X. Qu, D. Wang, J. Abbas, and R. Mubeen, "Product Market Competition and Firm Performance: Business Survival Through Innovation and Entrepreneurial Orientation Amid COVID-19 Financial Crisis," *Front. Psychol.*, vol. 12, no. 1, pp. 1–12, Mar. 2022, doi: 10.3389/fpsyg.2021.790923.

[2] Z. Cekerevac and M. Bogavac, "Impact of covid-19 and Ukraine-Russia war on the international trade and logistics," *MEST J.*, vol. 11, no. 1, pp. 19–30, Jan. 2023, doi: 10.12709/mest.11.11.01.03.

[3] H. Zhang, "The Impact of COVID-19 on the Manufacturing Industry and Solutions," *Highlights Business, Econ. Manag.*, vol. 13, no. 1, pp. 142–148, May 2023, doi: 10.54097/hbem.v13i.8637.

[4] J. J. Marquina Araujo *et al.*, "Environmental impacts in the commercialization of minerals," in *Proceedings of the 21th LACCEI International Multi-Conference for Engineering, Education and Technology (LACCEI 2023): "Leadership in Education and Innovation in Engineering in the Framework of Global Transformations: Integration and Alliances for Integra*, 2023, pp. 1–12. doi: 10.18687/LACCEI2023.1.1.254.

[5] IBRAM, "Mineração em números 2022," *IBRAM*, 2022. https://ibram.org.br/publicacoes/?txtSearch=&checkbox-section%5B%5D=1236 (accessed Apr. 16, 2024).

[6] M. D. Gala and M. M. Bhoyar, "Equity Research Analysis of Cement Industry," *MET Manag. Rev.*, vol. 08, no. 02, pp. 44–56, 2021, doi: 10.34047/MMR.2020.8206.

[7] A. C. R. da R. Souza, H. C. Gomes, and I. F. G. Guimarães, "A statistical analysis of the relationship of civil construction GDP to cement production in Brazil," *Res. Soc. Dev.*, vol. 11, no. 7, p. e27011729902, May 2022, doi: 10.33448/rsd-v11i7.29902.

[8] D. C. Reis, M. Quattrone, J. F. T. Souza, K. R. G. Punhagui, S. A. Pacca, and V. M. John, "Potential CO 2 reduction and uptake due to industrialization and efficient cement use in Brazil by 2050," *J. Ind. Ecol.*, vol. 25, no. 2, pp. 344–358, Apr. 2021, doi: 10.1111/jiec.13130.

[9] A. R. Hasankhoei, M. Maleki-Moghaddam, A. Haji-Zadeh, M. E. Barzgar, and S. Banisi, "On dry SAG mills end liners: Physical modeling, DEM-based characterization and industrial outcomes of a new design," *Miner. Eng.*, vol. 141, p. 105835, Sep. 2019, doi: 10.1016/j.mineng.2019.105835.

[10] R. de F. Oliveira, "Uma revisão dos princípios de funcionamento e métodos de dimensionamento de moinhos de bolas," Escola de Engenharia da Universidade Federal de Minas Gerais, 2012.

[11] W. I. M. da Silva, D. B. de Alencar, and J. de A. Brito Junior, "Management integration plan in a civil construction company," *ITEGAM- J. Eng. Technol. Ind. Appl.*, vol. 5, no. 20, pp. 1–10, 2019, doi: 10.5935/2447-0228.20190075.

[12] V. V. Reznikova and I. M. Kravets, "Goods quality management and control systems," *Econ. Law*, vol. 1, no. 1, pp. 3–18, May 2022, doi: 10.15407/econlaw.2022.01.003.

[13] N. Pryadko, I. Mladetsky, S. Dziuba, and K. Ternova, "Investigation of the

control characteristics of mineral processing technology indicators," *IOP Conf. Ser. Earth Environ. Sci.*, vol. 970, no. 1, p. 012001, Jan. 2022, doi: 10.1088/1755-1315/970/1/012001.

[14] A. de Faria Junior, G. de Tomi, L. M. Sant'Agostino, and J. F. C. L. Costa, "O impacto do tipo de amostragem no controle de qualidade na lavra," *Rem Rev. Esc. Minas*, vol. 63, no. 2, pp. 385–392, Jun. 2010, doi: 10.1590/S0370-44672010000200025.

[15] H. Lieberwirth, O. Popov, T. Aleksandrova, and N. Nikolaeva, "Scientific substantiation and practical realization of selective comminution process of polymetallic mineral raw materials," *E3S Web Conf.*, vol. 192, no. 1, p. 02003, Sep. 2020, doi: 10.1051/e3sconf/202019202003.

[16] W. Xu *et al*., "Process Mineralogy Characteristics and Flotation Application of a Refractory Collophanite from Guizhou, China," *Minerals*, vol. 11, no. 11, p. 1249, Nov. 2021, doi: 10.3390/min11111249.

[17] W. D. Judge and G. Azimi, "Recent progress in impurity removal during rare earth element processing: A review," *Hydrometallurgy*, vol. 196, no. 1, p. 105435, Sep. 2020, doi: 10.1016/j.hydromet.2020.105435.

[18] A. Massaro, "Advanced Control Systems in Industry 5.0 Enabling Process Mining," *Sensors*, vol. 22, no. 22, p. 8677, Nov. 2022, doi: 10.3390/s22228677.

[19] D. Back, D. Theisen, W. Seo, C. S.-J. Tsai, and D. B. Janes, "Development of Interdigitated Capacitive Sensor for Real-Time Monitoring of Sub-Micron and Nanoscale Particulate Matters in Personal Sampling Device for Mining Environment," *IEEE Sens. J.*, vol. 20, no. 19, pp. 11588–11597, Oct. 2020, doi: 10.1109/JSEN.2020.2995960.

[20] E. Brattich *et al*., "How to Get the Best from Low-Cost Particulate Matter Sensors: Guidelines and Practical Recommendations," *Sensors*, vol. 20, no. 11, p. 3073, May 2020, doi: 10.3390/s20113073.

[21] A. Figiel and I. Ková, "Safety requirements for mining systems controlled in automatic mode," *Acta Montan. Slovaca*, vol. 25, no. 1, pp. 417–436, 2020, doi: 10.46544/AMS.v25i3.13.

[22] N. Singh, A. P. Singh, and A. P. Singh, "Quality management systems and ISO 9000 effectiveness: A review," *Indian J. Pharm. Pharmacol.*, vol. 7, no. 3, pp. 142–146, Oct. 2020, doi: 10.18231/j.ijpp.2020.024.

[23] "Design of Methodological Platform to Support the Integration of Standardized Quality Management Systems Applicable in the Mining Industry," *Acta Montan. Slovaca*, vol. 1, no. 27, pp. 1017–1027, Feb. 2023, doi: 10.46544/AMS.v27i4.15.

[24] E. de J. Lopes, A. B. V. de Souza, J. Í. da S. Pierre, R. A. Rêgo Júnior, and F. A. F. da Ponte, "Application of methods-time measurement as a tool to improve productivity in a beauty salon," *ITEGAM- J. Eng. Technol. Ind. Appl.*, vol. 8, no. 35, pp. 1–10, 2022, doi: 10.5935/jetia.v8i35.817.

[25] G. Visedo and M. Pecchio, *Roadmap Tecnológico do Cimento: potencial de redução das emissões de carbono da indústria do cimento brasileira até 2050*. Rio de Janeiro: SNIC, 2019. [Online]. Available: https://coprocessamento.org.br/wp-content/uploads/2019/11/Roadmap_Tecnologico_Cimento_Brasil_Book-1.pdf

[26] H. Gokcekus, N. Ghaboun, D. U. Ozsahin, and B. Uzun, "Evaluation of Cement Manufacturing Methods Using Multi Criteria Decision Analysis (MCDA)," in *2021 14th International Conference on Developments in eSystems Engineering (DeSE)*, Dec. 2021, pp. 39–43. doi: 10.1109/DeSE54285.2021.9719399.

[27] C. Tregambi *et al*., "Solar-driven production of lime for ordinary Portland cement formulation," *Sol. Energy*, vol. 173, no. 1, pp. 759–768, Oct. 2018, doi: 10.1016/j.solener.2018.08.018.

[28] B. B. Mariani, J. da S. Andrade Neto, N. S. de Amorim Júnior, and D. V. Ribeiro, "Efeito da incorporação de resíduo de TiO2 (MNR) na formação das fases mineralógicas de clínquer Portland," *Ambient. Construído*, vol. 19, no. 1, pp. 57–71, Mar. 2019, doi: 10.1590/s1678-86212019000100293.

[29] R. Pereira, "Estimativa da finura do cimento durante o processo de moagem em moinhos de bolas," Instituto Federal do Espírito Santo, 2020. [Online]. Available:https://repositorio.ifes.edu.br/bitstream/handle/123456789/703/DISSERTAÇÃO_Estimativa_Finura_Cimento_Processo_Moagem.pdf?sequence=1&isAllowed=y

[30] X. Lu, B. Kiumarsi, T. Chai, Y. Jiang, and F. L. Lewis, "Operational Control of Mineral Grinding Processes Using Adaptive Dynamic Programming and Reference Governor," *IEEE Trans. Ind. Informatics*, vol. 15, no. 4, pp. 2210–2221, 2019, doi: 10.1109/TII.2018.2868473.

[31] P. Semsari Parapari, M. Parian, and J. Rosenkranz, "Breakage process of mineral processing comminution machines – An approach to liberation," *Adv. Powder Technol.*, vol. 31, no. 9, pp. 3669–3685, Sep. 2020, doi: 10.1016/j.apt.2020.08.005.

[32] M. Eisenlauer and U. Teipel, "Comminution energy and particulate properties of cutting and hammer-milled beech, oak, and spruce wood," *Powder Technol.*, vol. 394, no. 1, pp. 685–704, Dec. 2021, doi: 10.1016/j.powtec.2021.03.072.

[33] C. Ciobanu, P. Tudor, G.-A. Constantin, and G. Musuroi, "Determination of granulometrical composition of the clinker by grinding in a ball mill to determine the specific consumption of additional energy," *E3S Web Conf.*, vol. 180, no. 1, p. 04007, Jul. 2020, doi: 10.1051/e3sconf/202018004007.

[34] C.-J. J. L. Farrell *et al*., "Two-step penalised logistic regression for multi-omic data with an application to cardiometabolic syndrome," *PLoS One*, vol. 11, no. 1, pp. 1150–1156, 2021, doi: 10.1016/j.jcin.2015.04.006.

[35] C. D. C. RODRIGUES, "Dimensionamento De Moinho De Bolas Utilizando O Método Do Balanço Populacional," *Eng. Minas do Dep. Eng. Minas*, pp. 1–9, 2019, doi: .1037//0033-2909.I26.1.78.

[36] W. Zhou, D. Wang, G. Ma, X. Cao, C. Hu, and W. Wu, "Discrete element modeling of particle breakage considering different fragment replacement modes," *Powder Technol.*, vol. 360, no. 1, pp. 312–323, Jan. 2020, doi: 10.1016/j.powtec.2019.10.002.

[37] T. Kundu, S. Kanta Das, S. Kumar Tripathy, and S. I. Angadi, "Performance evaluation of the VSK separator for treating mineral fines," *Miner. Eng.*, vol. 167, 2021, doi: 10.1016/j.mineng.2021.106883.

[38] Metso, *Manual de Britagem*, 6th ed. Metso Minerals, 2005.

[39] N. A. Toprak, A. H. Benzer, C. E. Karahan, and E. S. Zencirci, "Effects of grinding aid dosage on circuit performance and cement fineness," *Constr. Build. Mater.*, vol. 265, no. 1, p. 120707, Dec. 2020, doi: 10.1016/j.conbuildmat.2020.120707.

[40] R. Gedraite, S. M. da S. Neiro, A. S. Morais, L. Vieira, and L. A. Rodrigues, "Considerações práticas sobre controle avançado de processo aplicado a moinho de bolas," *HOLOS*, vol. 3, pp. 122–132, Jul. 2014, doi: 10.15628/holos.2014.1764.

[41] R. Y. Yang, A. B. Yu, L. McElroy, and J. Bao, "Numerical simulation of particle dynamics in different flow regimes in a rotating drum," *Powder Technol.*, vol. 188, no. 2, pp. 170–177, Dec. 2008, doi: 10.1016/j.powtec.2008.04.081.

[42] O. Ishnazarov, J. Mavlonov, and D. Mardonov, "Control of ball mill operation depending on ball load and ore properties," *E3S Web Conf.*, vol. 461, no. 1, p. 01091, Dec. 2023, doi: 10.1051/e3sconf/202346101091.

[43] A. S. Opalev and A. A. Palivoda, "Modeling of the liquid-solid particle systemin the coupling solution of the task in rocky dem and ansys fluent ," *Min. Informational Anal. Bull.*, no. 12–1, pp. 78–93, 2022, doi: 10.25018/0236_1493_2022_121_0_78.

[44] A. D. Bardovskiy, S. M. Gorbatyuk, A. M. Keropyan, and P. Y. Bibikov, "Assessing Parameters of the Accelerator Disk of a Centrifugal Mill Taking into Account Features of Particle Motion on the Disk Surface," *J. Frict. Wear*, vol. 39, no. 4, pp. 326–329, Jul. 2018, doi: 10.3103/S1068366618040037.

[45] C. Mayer-Laigle, R. K. Rajaonarivony, X. Rouau, and C. Fabre, "Properties of biomass powders resulting from the fine comminution of lignocellulosic feedstocks by three types of ball-mill set-up," *Open Res. Eur.*, vol. 1, 2022, doi: 10.12688/openreseurope.14017.2.

[46] Y. Liu, J. G. Song, W. L. Zhu, D. L. Zhang, H. B. Wen, and R. Huang, "Effect of Ball Milling Technology on Properties of Refractory Waste," *Key Eng. Mater.*, vol. 927, no. 1, pp. 143–148, Jul. 2022, doi: 10.4028/p-49gm95.

[47] E. de J. Lopes, M. Bouzon, and M. de C. Carneiro Neto, *Revisão Sistemática*. Sobral: CBL, 2024. [Online]. Available: https://www.researchgate.net/publication/378007404_Revisao_Sistematica

[48] X. Lu, B. Kiumarsi, T. Chai, Y. Jiang, and F. L. Lewis, "Operational Control of Mineral Grinding Processes Using Adaptive Dynamic Programming and Reference Governor," *IEEE Trans. Ind. Informatics*, vol. 15, no. 4, pp. 2210–2221,

2019, doi: 10.1109/TII.2018.2868473.

[49] D. A. ANABUKI, “Aplicação do controle de um processo de moagem em moinho de bolas através do sistema Labview-Compact Fieldpointinversor de freqüência,” Universidade Federal de Pernambuco, 2005.

[50] N. Chimwani, F. K. Mulenga, and D. Hildebrandt, “Ball size distribution for the maximum production of a narrowly-sized mill product,” *Powder Technol.*, vol. 284, pp. 12–18, Nov. 2015, doi: 10.1016/j.powtec.2015.06.037.

Journal of Engineering and Technology for Industrial Applications

ITEGAM-JETIA

Manaus, v.11 n.53, p. 34-40. May/June., 2025.
DOI: https://doi.org/10.5935/jetia. v11i53.1244

ISSN ONLINE: 2447-0228

RESEARCH ARTICLE OPEN ACCESS

IMPROVING INVERTER EFFICIENCY FOR ELECTRIC VEHICLES: EXPERIMENTAL VALIDATION OF THE NEURAL NETWORK-BASED SHE TECHNIQUE USING RT-LAB

Seyf Eddine Bechekir[1], Mokhtaria Jbilou[2], Mostefa Brahami[3], Fatima Zohra Boudjella[4], Imen Souhila Bousmaha[5], Mimouna Oukli[6] and Said NEMMICH[7]

[1, 2, 3] Intelligent Control and Electrical Power Systems Laboratory, Department of Electrical Engineering, Djillali Liabes University of Sidi Bel-Abbes, Algeria,
[4] Intelligent Control and Electrical Power Systems Laboratory, Department of Electrical Engineering, Djillali Liabes University of Sidi Bel-Abbes, Algeria, University of Belhadj Bouchaib, Ain-Temouchent.
[5] Higher School in Applied Sciences ESSAT of Tlemcen, Tlemcen, Algeria
[6] Applied Materials Laboratory (A.M.L), Faculté de Genie Electrique, University Djillali Liabes of Sidi Bel Abbes, 2200 SidiBel Abbes Algeria
[7] APELEC Laboratory, Djillali Liabes University of Sidi Bel-Abbes, Sidi Bel-Abbes, 22000, Algeria

[1]http://orcid.org/0000-0002-6143-7164, [2]http://orcid.org/0000-0001-9791-3815, [3]http://orcid.org/0000-0002-5246-3715
[4]http://orcid.org/0000-0002-5595-9476, [5]http://orcid.org/0000-0002-3107-8260, [6]http://orcid.org/0000-0002-4871-6919
[7]http://orcid.org/0000-0002-7767-0032,

Email: seyfeddine.electrotechnique@gmail.com, harmel71@yahoo.fr, mbrahami@yahoo.com, fatimazohraboudjella@gmail.com, imenbousmaha@yahoo.fr, ouklimouna22@gmail.com, nemmichsaid@gmail.com,

ARTICLE INFO

Article History
Received: August 8, 2024
Revised: January 20, 2025
Accepted: May 15, 2025
Published: May 31, 2025

Keywords:
Three-Phase Inverter,
Selective Harmonic Elimination,
Electric Vehicle,
Artificial Neural Networks,
Newton-Raphson Method,
RT-LAB,

ABSTRACT

Inverters are essential for converting direct current to alternating current in electric vehicles, relying on pulse width modulation (PWM) for efficiency. This study presents a real-time Selective Harmonic Elimination PWM (SHE-PWM) algorithm using artificial neural networks, validated with the OP5600 RT LAB simulator. Unlike the traditional Newton-Raphson method, this approach employs a neural network trained on a database of pre-calculated switching angles, allowing for the precise elimination of specific harmonics while maintaining control of the signal's fundamental component. Although it offers similar accuracy to Newton-Raphson, the neural method provides significantly faster processing. MATLAB/Simulink simulations and experimental results on the RT-LAB simulator confirm the algorithm's capability to calculate optimal switching angles and produce high-performance PWM waveforms. The study highlights the neural network-based SHE technique's advantages, including its ability to model complex systems, robustness to noisy data, and versatility. This approach improves inverter performance and offers new optimization possibilities for various applications, including electric vehicles. The simulator results validate the alignment of real and simulated control signals.

I. INTRODUCTION

In the field of electricity, power electronics is a vital domain that encompasses various activities such as the electrical grid, transportation (urban, railways, maritime...), renewable energy, and industry. Currently, energy has become one of the crucial aspects of human daily life. Therefore, it has become necessary to enhance the performance of power electronic devices. The latter can contribute to improving the quality of electrical signals [1],[2].

The aim of this work is to develop a new real-time PWM (Pulse Width Modulation) algorithm based on neural network principles, enabling the selective elimination of harmonics and control of the fundamental frequency.

In this context, the inverter powers the propulsion system, which is the heart of the Electric Vehicle (EV). This system

consists of an electric actuator, a transmission device, and wheels. The drive, comprising the entire electric motor and static converters, coupled with electronic control, forms the core of the propulsion system in the EV.

The asynchronous motor can operate over a wide speed range with low torque ripples if coupled with appropriate control. Selective Harmonic Elimination (SHE) PWM is a technique used in electric vehicles. PWM control is frequently adapted to the static converters of electric vehicles. Several control methods have been developed with the goal of generating a sinusoidal voltage at the inverter output with minimal harmonics [3],[4].

According to the literature, there are several PWM control techniques that differ in how they define the switching instants of the switches. These include sampled sine waveform modulation and vector-based PWM control based on phase voltage dispersion, as well as SHE PWM [5],[6].. It is certain that choosing a better control strategy for an inverter feeding a three-phase cage induction machine significantly improves system performance [7],[8].

In the scope of our work, we will focus on the SHE PWM technique. Our objective is to implement neural network-based SHE-PWM control in real-time using RT-Lab, with control of the fundamental frequency and selective harmonic elimination. This application is intended for electric vehicles. The switching angles are calculated based on the principles of neural networks..

II. MATERIALS AND METHODS

II.1 USEFUL INVERTER

Figure 1 shows the classic two-stage inverter. It's composed of three transistor switching arms. Each arm is composed of two cells, each with a diode and a transistor that work in forced switching. [9],[10].

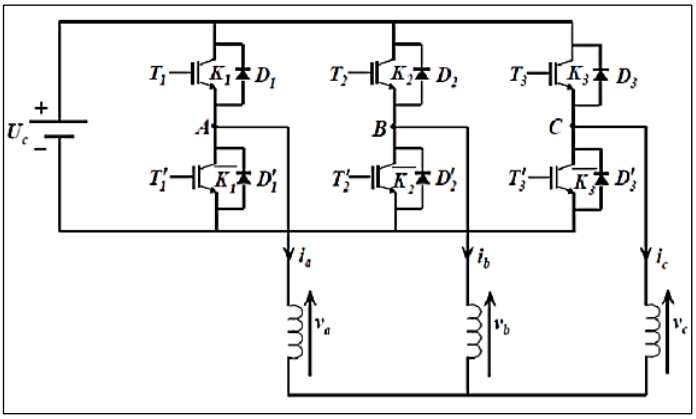

Figure 1: Schematic of the two-stage inverter.
Source : F.Z. Boudjella et al, (2022)

II.2 CONTROL STRATEGY

- Selective harmonic elimination technique SHE

Either the output voltage of the three-phase inverter at two periodic levels and with an amplitude equal to the unit, see Figure 2. [11],[12].

In this case, the output voltage $v(t)$ can be written in Fourier series:

$$v(t) = a_0 + \sum_{n=1}^{\infty}[a_n cos(nwt) + b_n sin(nwt)] \quad (1)$$

According to the properties of the voltage $v(t)$, (half-wave antisymmetric, quarter-wave symmetry), we find after simplification that:

$$a_0 = 0 a_n = 0 b_n = \frac{4}{n\pi}\left[1 + 2\sum_{k=1}^{k}(-1)^k \cos(n\alpha_k)\right] \quad (2)$$

Where, n, is an odd number, which must be different from a multiple of 3 for three-phase assemblies and k, represents the number of switches per quarter wave or the number of cuts per half-wave.

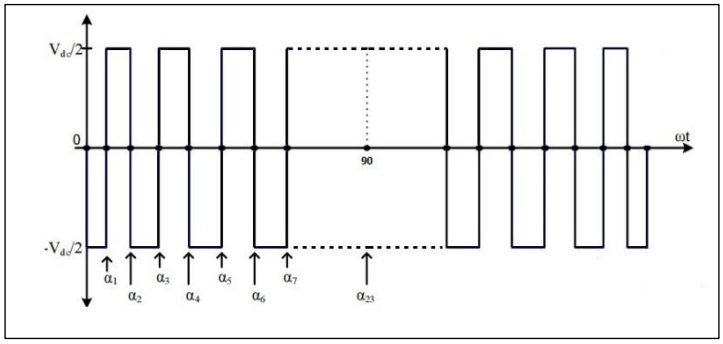

Figure 2: Form of a calculated PWM voltage.
Source: Authors, (2025)

Finally, the tension $v(t)$can be written as:

$$v(t) = \sum_{n=1}^{\infty}[b_n sin(nwt)] \quad (3)$$

The equation (3) has k unknown variables α1, α2, α3, ..., αk, called switching angles.

The values of these angles are calculated in order to assign a determined value to the fundamental a1 and to cancel the amplitudes an of the first (k -1) harmonics.

These equations are non-linear. The Newton-Raphson method will be used to solve this system of non-linear to unknown m equations [13].

The equation (4) is a system of non-linear m equations α1, ..., ..., αk. It is desired to assign a determined value im, called 'modulation index', to the amplitude a1 of the fundamental and to annul the amplitudes bn of the first (*k -1*) harmonics. A system of m non-linear equations to k unknown of the form is thus obtained:

$$b(1) = \frac{4}{\pi}[1 - 2\cos(\alpha 1) + 2\cos(\alpha 2) - \ \ldots - 2\cos(\alpha_{23})] - im$$
$$b(5) = \frac{4}{5\pi}[1 - 2\cos(5\alpha 1) + 2\cos(5\alpha 2) - \ \ldots - 2\cos(5\alpha_{23})]$$
$$b(7) = \frac{4}{7\pi}[1 - 2\cos(7\alpha 1) + 2\cos(7\alpha 2) - \cdots - 2\cos(7\alpha_{23})]$$
$$b(11) = \frac{4}{11\pi}[1 - 2\cos(11\alpha 1) + 2\cos(11\alpha 2) - \cdots - 2\cos(11\alpha_{23})]$$
$$b(13) = \frac{4}{13\pi}[1 - 2\cos(13\alpha 1) + 2\cos(13\alpha 2) - \cdots - 2\cos(13\alpha_{23})]$$
$$b(67) = \frac{4}{67\pi}[1 - 2\cos(67\alpha 1) + 2\cos(67\alpha 2) - \cdots - 2\cos(67\alpha_{23})] \quad (4)$$

After solving the non-linear equations simultaneously, the switching angles can be obtained. For the entire modulation index range (im =0.02~1.15), the angle paths for the proposed switching pattern are shown in Figure 3:

The angles are calculated using a modified Newton-Raphson method, as detailed in our article [5]. This method enables commutation angles to be determined without the need for prior initial values.

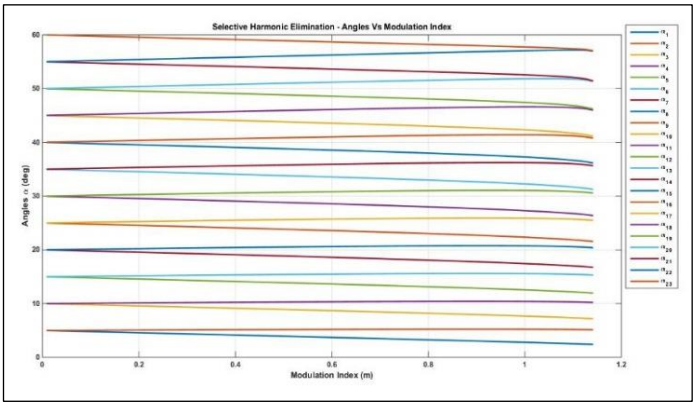

Figure 3: Trajectories of the 23 switching angles as a function of the modulation index for two-stage inverters.
Source : Authors, (2025).

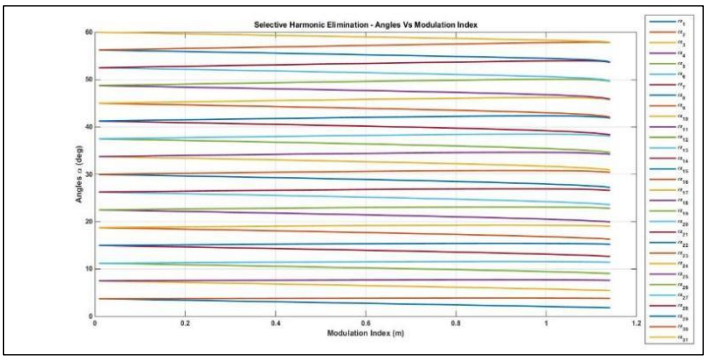

Figure 4: Trajectories of the 31 switching angles as a function of the modulation index for two-stage inverters.
Source: Authors, (2025)

II.3 ANN-BASED SHEPWM GENERATION

An Artificial Neural Network (ANN) stands as a potent instrument grounded in the patterns observed in biological neurons, effectively capturing the complexities of non-linear systems. Comprising interlinked neurons, this network facilitates communication through transmission of signals along weighted connections. These connection weights adapt through a learning process during training. The resultant output, denoted as yj, can be described as follows:

$$y_i = f(w_{ji}x_i) \quad (5)$$

The activation function is denoted as 'f', the input signal is represented as 'xi', and the connection weight is labeled as 'wji'. The expression for the error 'E', which is the sum of squared differences between the expected and obtained values of the output neurons, can be expressed as follows:

$$E = \frac{1}{2}\sum_j (y_{dj} - y_i)^2 \quad (6)$$

The passage in question deals with the use of a desired value "ydj" for output neuron j and the actual output "yj" of this neuron [14-16]. Various artificial neural network (ANN) architectures have been documented in the scientific literature. For this study, a specific type of neural network, known as a feedforward neural network, was used. The training process involves the application of the backpropagation learning algorithm. The activation functions used are sigmoidal for input and hidden layer neurons, and linear for output layer neurons. The architecture of the ANN used in this study is illustrated in Figure 5.

II.4 SYSTEM ARCHITECTURE

To simplify the architecture, we opt for a neural network consisting of an input layer, a hidden layer, and an output layer.

Figure 5: ANN Training.
Source: Authors, (2025)

The training process is shown in Figure 5, it stopped after 20 iterations for 23 angles and 207 iterations for 31 angles when the validation checks were carried out, the training performance is shown in Figure 6, the final regression was 99% as shown in Figure 7.

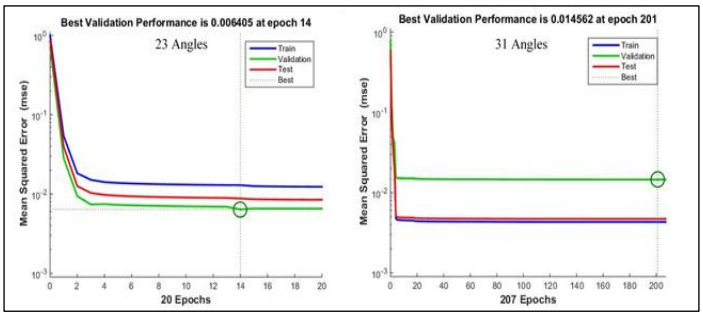

Figure 6: ANN Training performance.
Source: Authors, (2025)

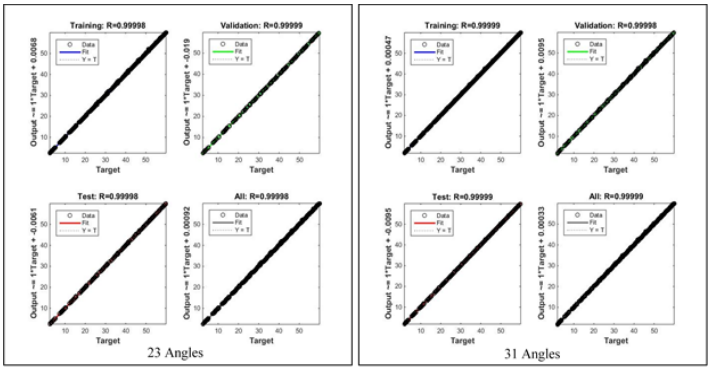

Figure 7: ANN Training regression.
Source: Authors, (2025)

Figure 8 shows the error between exact and approximate angles as a function of the modulation index “im”, covering a range of values from 0.02 to 1.15 for m = 23. In figure 9, the error is plotted as a function of the modulation index “im” for m = 31. This representation completes the analysis by allowing a comparison of errors for different values of m.

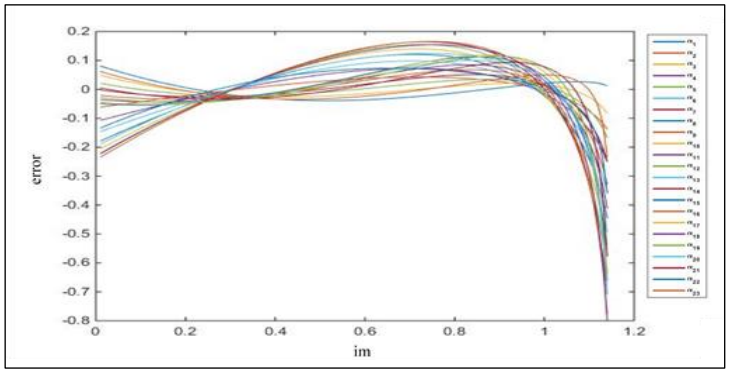

Figure 8: Variation in error between exact and ANNSHE angles over the entire range of im for m = 23.
Source: Authors, (2025)

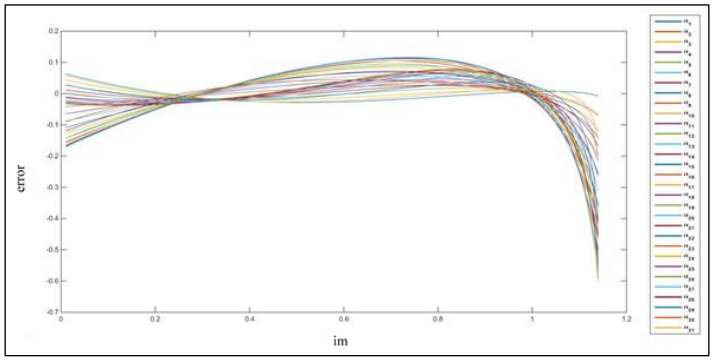

Figure 9: Variation in error between exact and ANNSHE angles over the entire range of im for m = 31.
Source: Authors, (2025)

III. RESULTS AND DISCUSSIONS

The Simulink diagram of the PWM technique is as follows:

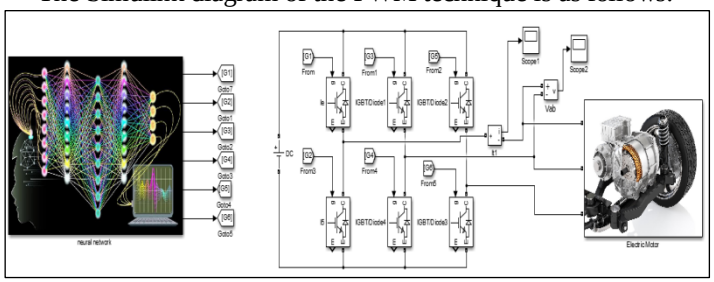

Figure 10: The Simulink diagram of the SHE-PWM technique
Source: Authors, (2025)

The following results are obtained for output voltage and current:

For voltage:

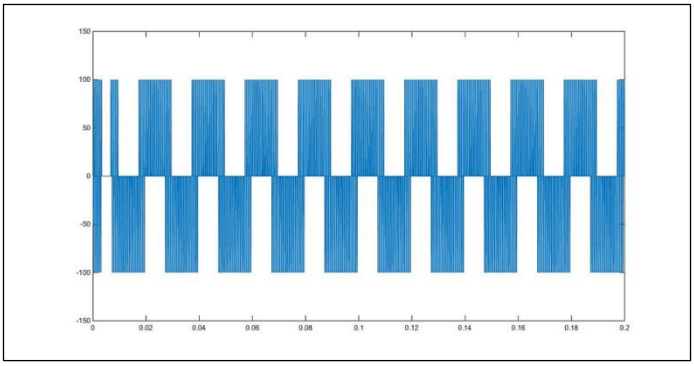

Figure 11: Voltage Waveform (M=0.1).
Source: Authors, (2025)

After analyzing the Total Harmonic Distortion (THD) of voltage and current, we observe the following figures:

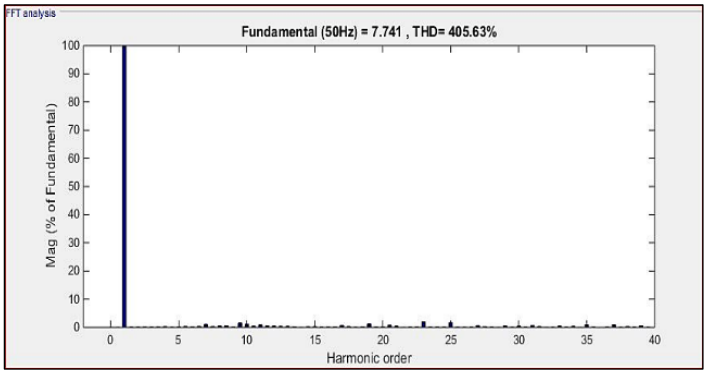

Figure 12: Output Voltage Harmonic Spectrum for m=0.1
Source: Authors, (2025)

For current:

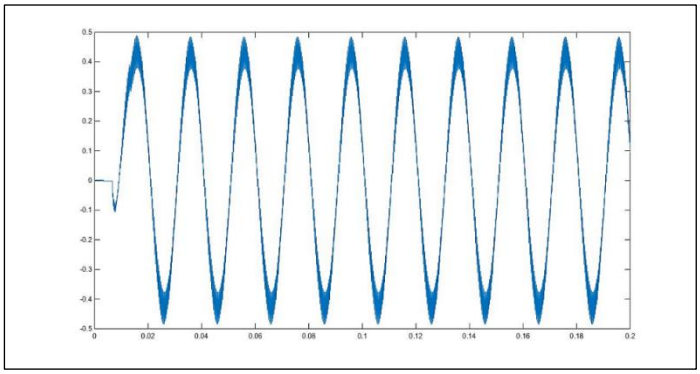

Figure 13 : Output Current Waveform Over Time (m=0.1)
Source: Authors, (2025)

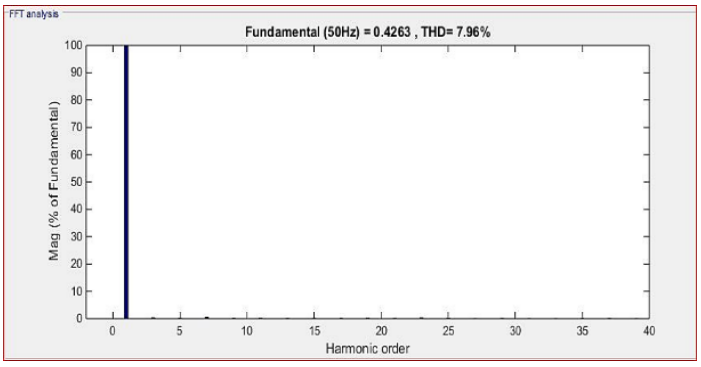

Figure 14: Output Current Harmonic Spectrum for m=0.1
Source: Authors, (2025)

Interpretation

According to the simulation results, it is evident that: as seen in Figure 7, the switching angles approximated by our neural network are very close to the exact angles, with a maximum error less than 0.0016 degrees.

Figure 12 demonstrates that the current waveform in the load closely resembles a sinusoidal shape. From Figure 13, it is evident that the selected current harmonics are eliminated, and the fundamental component is optimal. Therefore, we can conclude that our neural PWM algorithm exhibits high accuracy in computing switching angles and provides efficiency in eliminating desired harmonics.

The neural PWM control allows for:

- Ability to model complex structures and irregular data.
- Consideration of nonlinear relationships (interactions) between variables.
- Reasonable robustness to noisy data.
- Capability to model a wide range of diverse problems.

III.1 PRACTICAL IMPLEMENTATION THROUGH THE RT-LAB SIMULATOR

We introduce the control section into the RT-LAB software on the reference out block to obtain the following results [18]:

A. SHE PWM Control

The diagram of the PWM technique in RT-Lab is as follows:

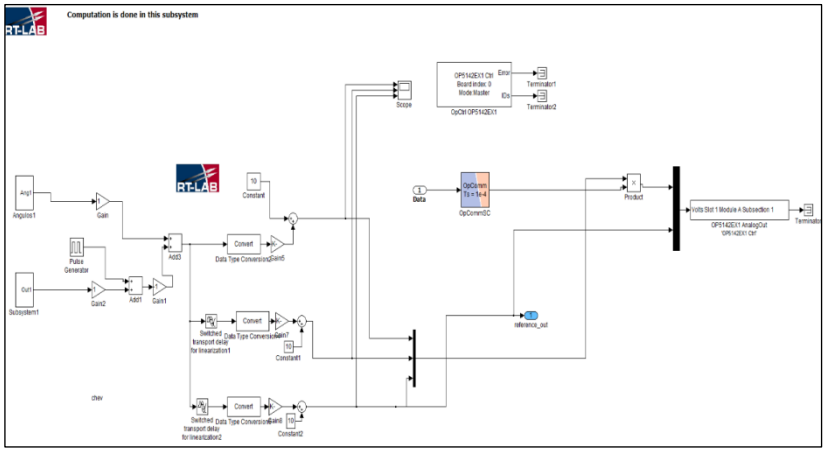

Figure 15: Block Diagram of Pre-calculated PWM Control using RT-Lab.
Source: Authors, (2025)

B. Architecture of the developed inverter

The block diagram of the inverter is shown in Figure 17. The power circuit switches are controlled by an OP5600 RT LAB simulator [19],[20]. The photo of the inverter is shown in Figure 18

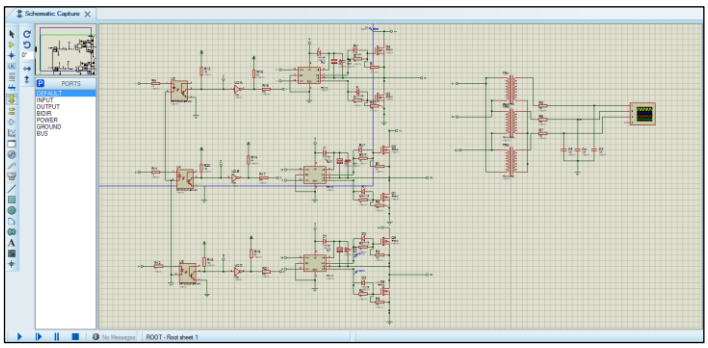

Figure 16: Power circuit of the inverter.
Source: Authors, (2025)

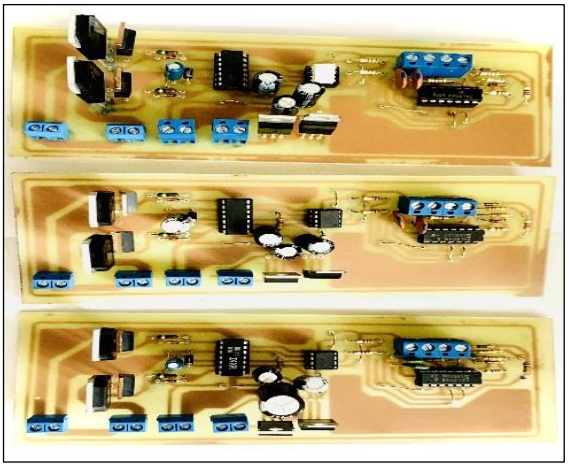

Figure 17: Photo of the inverter.
Source: Authors, (2025)

We present the voltage waveform for 23 angles at various frequencies and modulation indices.

For a modulation index im=0.1 and a frequency f=40:

❖ **Using a neural network**

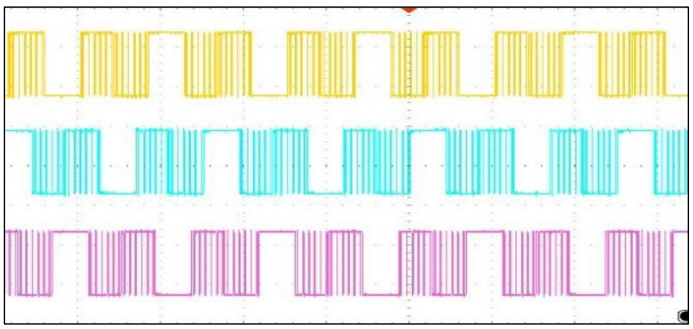

Figure 18: Voltage with Neural Network.
Source: Authors, (2025)

❖ **Using Newton-Raphson**

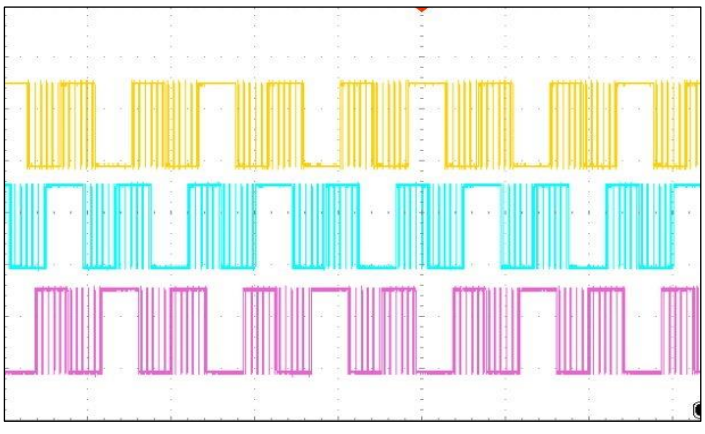

Figure: 19. Voltage with Newton-Raphson.
Source: Authors, (2025)

For a modulation index im=0.2 and a frequency f=20:

❖ **Using a neural network**

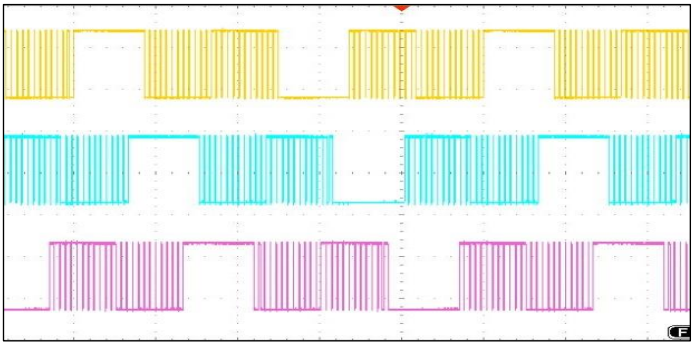

Figure 20 : Voltage with Neural Network.
Source: Authors, (2025)

❖ **Using Newton-Raphson**

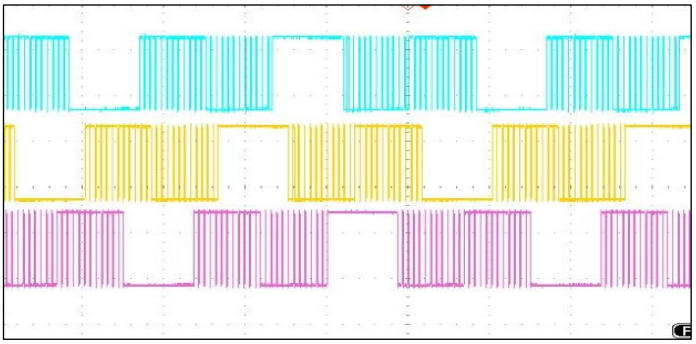

Figure 21 : Voltage with Newton-Raphson.
Source: Authors, (2025)

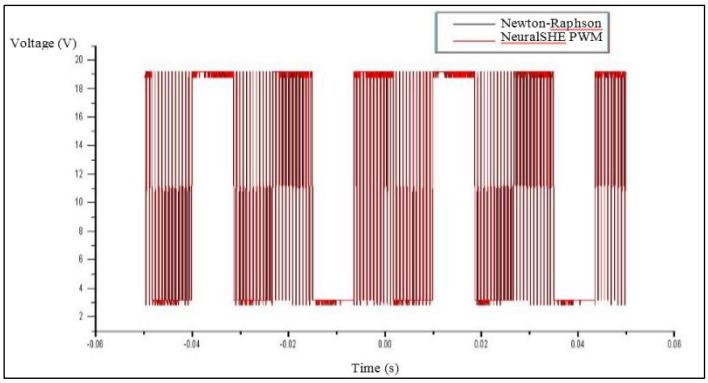

Figure 22: Comparative Study between SHE PWM Control (Newton-Raphson and NeuralSHE PWM).
Source: Authors, (2025)

For a modulation index im=0.1 and a frequency f=40, it is observed that the signals generated by both methods are identical with a small margin of error.

- **Interpretation of results**

The simulation results demonstrate that the signal quality improves as the modulation index increases, and the neural PWM control produces the same signal as the SHE PWM control.

It is noted that:

- The signals obtained using the RT-Lab Simulator for im = 0.2 and m = 23 (Figure 20 and 21) are identical to those obtained using Simulink MATLAB.

- The signals obtained using the RT-Lab Simulator for im = 0.1 and m = 23 (Figure 18 and 19) are identical to those obtained using Simulink MATLAB.

- There is a similarity between the control signals obtained using the RT-Lab Simulator for im = 0.1 (Figure 18 and 19) and im = 0.2 (Figure 20 and 21) compared to those obtained using Simulink MATLAB.

The RT-Lab simulator allows visualization of control signals on the oscilloscope, demonstrating the overlay between real signals and those obtained through simulation.

VI. CONCLUSION

In this work, we studied a selective harmonic elimination PWM control with fundamental control based on neural network theory, aiming to control a three-phase inverter for electric vehicles.

We modeled the three-phase asynchronous machine fed by an inverter, then presented various types of inverters and discussed different control strategies for these inverters. Based on the advantages and disadvantages of pre-calculated PWM control, it appeared to be the most suitable for varying the speed of asynchronous machines.

We solved the nonlinear equation system using MATLAB software with the Newton-Raphson method to calculate the switching angles of the inverter switches. Simulation results in MATLAB Simulink demonstrated the effectiveness of the control in eliminating desired harmonics. The drawback of this technique is the computation time for switching angles.

Artificial neural networks generate real-time switching angles for the switches. Simulations of this technique in MATLAB Simulink show the accuracy of calculating switching angles and efficiency in eliminating desired harmonics. Multiples of three harmonics are automatically eliminated in the case of phase-to-phase voltage.

The RT-Lab simulator was used to experimentally verify the generation of control signals. Simulation results show a similarity between the signals generated by the RT-Lab simulator and those obtained through Simulink MATLAB.

The results obtained from this research can significantly contribute to the advancement of electric vehicle technology and the broader field of power electronics. By optimizing the performance of three-phase inverters through selective harmonic elimination and precise control of the fundamental component, the proposed neural network-based PWM algorithm can lead to more efficient and reliable electric vehicle propulsion systems. This, in turn, can promote the widespread adoption of electric vehicles, reducing greenhouse gas emissions and mitigating the environmental impact of transportation.

Furthermore, the versatility of the neural network-based SHE technique opens up opportunities for its application in various other domains, such as renewable energy systems, industrial motor drives, and power quality improvement. The ability to model complex, non-linear systems and handle noisy data makes this approach attractive for a wide range of real-world scenarios.

VI. REFERENCES

[1] Al Attar, Houssein, Ghanes, Malek, Hamida, Mohamed, et al. Control strategies design and comparison of DC-DC LLC converter in V2X mode for electric vehicle charger application. In : 2021 IEEE Conference on Control Technology and Applications (CCTA). IEEE, 2021. p. 1154-1159.

[2] Al Attar, Houssein, Hamida, Mohamed Assaad, Ghanes, Malek, et al. Review on Modeling and Control Strategies of DC–DC LLC Converters for Bidirectional Electric Vehicle Charger Applications. Energies, 2023, vol. 16, no 9, p. 3946.

[3] Ali Khan, Muhammad Yasir, Liu, Haoming, Yang, Zhihao, et al. A comprehensive review on grid connected photovoltaic inverters, their modulation techniques, and control strategies. Energies, 2020, vol. 13, no 16, p. 4185.

[4] BOUROUGA, Zohra, BATTACH, Amel, et HANINI, Noureddine. Etude et commande d'un onduleur multi niveaux a structure modulaire par la technique d'élimination sélective des harmoniques. 2019.

[5] Bousmaha, Imen Souhila, Bechekir, Seyf Eddine, Abdeslam, Djaffar Ould, et al. SHEPWM in three-phase voltage source inverters by modified Newton–Raphson. International Journal of Power Electronics and Drive Systems (IJPEDS), 2023, vol. 14, no 1.

[6] Boudjella, Fatima Zohra, Boukli Hacène, Fouad, Bouchakour, Abdelhak, et al. Simulation and realisation of a three-phase inverter controlled through sinus triangle and space vector pulse width modulation for photovoltaic systems. International Journal of Ambient Energy, 2022, vol. 43, no 1, p. 2360-2368.

[7] Barnes, John GP. An algorithm for solving non-linear equations based on the secant method. The Computer Journal, 1965, vol. 8, no 1, p. 66-72.

[8] Buccella, Concettina, Cimoroni, Maria Gabriella, et Cecati, Carlo. Mathematical proof of a harmonic elimination procedure for multilevel inverters. Mathematics and Computers in Simulation, 2021, vol. 184, p. 69-81.

[9] BECHEKIR, S., BOUSMAHA, I. S., BRAHAMI, M., et al. Realization of an inverter with PWM command for photovoltaic system. In : 2017 5th International Conference on Electrical Engineering-Boumerdes (ICEE-B). IEEE, 2017. p. 1-6.

[10] Bechekir, S., Brahami, M., Abdeslam, D. Ould, et al. Development of a Low-Cost Ozone Generator Supply-Optimization Using Response Surface Modeling. International Journal of Plasma Environmental Science and Technology, 2019, vol. 13, no 01, p. 7-13.

[11] Chabni, Faycal, Taleb, Rachid, et HelAIMI, M.'Hamed. ANN-based SHEPWM using a harmony search on a new multilevel inverter topology. Turkish Journal of Electrical Engineering and Computer Sciences, 2017, vol. 25, no 6, p. 4867-4879.

[12] Kalkal, Pratik et Teja, AV Ravi. A Novel Selective Harmonic Mitigation PWM Technique With THD Minimization Using Second-Order Sliding Modes. IEEE Transactions on Industrial Electronics, 2024.

[13] Deniz, Erkan, Aydogmus, Omur, et Aydogmus, Zafer. Implementation of ANN-based selective harmonic elimination PWM using hybrid genetic algorithm-based optimization. Measurement, 2016, vol. 85, p. 32-42.

[14] GuellaL, A., Larbès, C., et Hassaine, L. Une nouvelle approche MLI basée sur le principe des réseaux de neurone pour la commande des onduleurs. Journal of Renewable Energies, 2012, vol. 15, no 1, p. 57–66-57–66.

[15] Jing, Tao, Maklakov, Alexander, et Radionov, Andrey. Two selective harmonic control techniques applied in 10kV grid with three-level NPC inverter. In : 2019 IEEE Russian Workshop on Power Engineering and Automation of Metallurgy Industry: Research & Practice (PEAMI). IEEE, 2019. p. 75-79.

[16] Khelifa, Siham, Semmah, Abdelhafid, Bechekir, Seyfeddine, et al. Direct vector control for doubly fed induction generator-based wind turbine using sliding mode controller tested using RT-LAB OP5600. In : 2023 International Conference on Advances in Electronics, Control and Communication Systems (ICAECCS). IEEE, 2023. p. 1-7.

[17] Poorfakhraei, Amirreza, NarimanI, Mehdi, et Emadi, Ali. A review of modulation and control techniques for multilevel inverters in traction applications. IEEE Access, 2021, vol. 9, p. 24187-24204.

[18] Rauf, Abdul Mannan, Abdel-Monem, Mohamed, Geury, Thomas, et al. A Review on Multilevel Converters for Efficient Integration of Battery Systems in Stationary Applications. Energies, 2023, vol. 16, no 10, p. 4133.

[19] Salahi, Ismail, Chabani, Sououdi Boumediene, et al. ETUDE, Modélisation et commande d'un onduleur à trois niveaux à structure NPC. 2021. Thèse de doctorat. Université Ahmed DRAIA-Adrar.

[20] Wang, Chenxu, Zhang, Qi, Chen, Dunzhi, et al. Application of Newton Identities in Solving Selective Harmonic Elimination Problem With Algebraic Algorithms. IEEE Journal of Emerging and Selected Topics in Power Electronics, 2022, vol. 10, no 5, p. 5870-5881.

Journal of Engineering and Technology for Industrial Applications

ITEGAM-JETIA

Manaus, v.11 n.53, p. 41-47. May/June., 2025.
DOI: https://doi.org/10.5935/jetia. v11i53.1252

ISSN ONLINE: 2447-0228

RESEARCH ARTICLE OPEN ACCESS

INTEGRATING VGG RE-TRAINED FEATURE EXTRACTION WITH MACHINE LEARNING FOR KNEE OSTEOARTHRITIS SEVERITY LEVELS DETECTION USING X-RAY IMAGES

Simeon Yuda Prasetyo[1] and Ghinaa Zain Nabiilah[2]

[1,2]Bina Nusantara University, Indonesia.

[1]http://orcid.org/0000-0002-6077-4003, [2]https://orcid.org/0000-0001-7638-7449

Email: simeon.prasetyo@binus.ac.id,ghinaa.nabiilah@binus.ac.id

ARTICLE INFO

Article History
Received: August 16, 2024
Revised: January 20, 2025
Accepted: May 15, 2025
Published: May 31, 2025

Keywords:
Knee osteoarthritis detection,
Machine learning,
VGG Re-trained Feature Extraction,
X-ray imaging

ABSTRACT

Knee osteoarthritis, a degenerative joint disease affecting weight-bearing joints such as the knees and hips, poses substantial diagnostic hurdles due to its complicated pathophysiology and development. Traditional diagnostic methods rely heavily on clinical examinations and imaging techniques like X-rays, which can be subjective and vary with clinician experience. To overcome these problems, new advances in machine learning (ML) and deep learning (DL) offer promising alternatives for improving the accuracy of knee osteoarthritis identification. This study proposes a novel methodology that combines retrained VGG models with various machine learning techniques. The Knee Osteoarthritis Dataset with Severity Grading is preprocessed, and features are extracted using fine-tuned VGG16 and VGG19 models. A number of machine learning models, including Naive Bayes, K-Nearest Neighbors, Decision Tree, Random Forest, Bagging, and AdaBoost, are then trained using these extracted characteristics. These models' performance is assessed using metrics including F1-score, recall, accuracy, and precision. The results reveal that the combination of VGG19 with fine-tuning and Random Forest achieves the best performance, with an impressive accuracy of 62.68%. This approach significantly improves diagnostic accuracy and holds potential for enhancing clinical decision-making and management of knee osteoarthritis, offering a robust tool for early detection and personalized treatment strategies.

I. INTRODUCTION

Weight-bearing joints, including the knees and hips, are susceptible to the complex illness known as osteoarthritis (OA). Significantly contributing factors to its etiology include advanced age, high body mass index (BMI), and joint malalignment [1]. OA is a common type of arthritis that produces severe pain, stiffness, and swelling in the affected joints. Knee osteoarthritis in particular is one of the commonest forms of arthritis [2].

Knee osteoarthritis (KOA) is a slowly progressive disease that involves the degradation of cartilage, remodeling of bone, and inflammation [3]. The knee is the joint in the human body most commonly afflicted by this most prevalent musculoskeletal degenerative disease [4]. Pathologically, KOA is defined by a number of structural alterations in the knee joint, such as the development of osteophytes, inflammation of the synovium, subchondral sclerosis, and erosion of cartilage [5].

The impact of knee osteoarthritis extends beyond physical discomfort, as it is associated with a 35-37% increased risk of reduced time-to-mortality, primarily driven by pain [6]. Furthermore, KOA is linked to an increased risk of all-cause mortality, with disability and deteriorations in quality of life being significant contributors [7]. Early and accurate detection is essential for effective treatment and management of knee osteoarthritis because of the significant impact it has on an individual's health and quality of life. Imaging tools like X-rays and clinical examinations play a major role in traditional diagnostic methods. However, a clinician's experience and subjective judgment may have a role in how X-ray pictures are interpreted. Recent developments in artificial intelligence, notably in machine learning and deep learning, present intriguing answers to these

problems. Modern developments in deep learning (DL) and machine learning (ML) have greatly improved the ability to identify and categorize knee osteoarthritis (OA) from medical imaging, especially X-ray pictures. Numerous research works have exhibited the effectiveness of these computational techniques in enhancing clinical results and diagnostic precision.

Attaining state-of-the-art performance in knee osteoarthritis severity classification from X-ray images has been demonstrated by machine learning techniques, such as logistic regression [8]. These algorithms can handle large datasets and identify patterns that are often indistinguishable to the human eye, providing a robust tool for medical diagnostics. Deep convolutional neural networks (CNNs), a subset of machine learning models, have been particularly effective in detecting patellofemoral osteoarthritis from knee radiographs. Studies have demonstrated that CNN-based models outperform conventional reference models, offering higher accuracy and reliability [9]. Medical image analysis benefits greatly from CNNs' capacity to automatically learn and extract characteristics from unprocessed input.

Furthermore, machine learning methods, especially CNN networks, can enhance the diagnosis of knee osteoarthritis by analyzing real-world X-ray imaging data. These models reduce the workload for doctors by providing automated and precise diagnostic suggestions, thus facilitating more efficient clinical workflows [10]. Enhancing patient outcomes might be greatly increased by using these cutting-edge computational tools into clinical practice. Deep learning techniques also play a crucial role in the early detection of osteoarthritis. By accurately identifying the disease at its initial stages, these methods can help prevent further cartilage damage and bone injury, thereby enabling timely and effective interventions [11]. Early diagnosis is essential for managing OA, as it can significantly slow disease progression and improve the quality of life for patients.

Clinical diagnoses have been improved and necessary medical interventions have been expedited by the use of machine learning in the early diagnosis and prediction of knee osteoarthritis. Machine learning models, including deep neural networks, have been shown to enhance clinical decision-making processes, providing clinicians with valuable insights derived from complex data [12]. This capability underscores the transformative potential of machine learning in healthcare.

According to utilized Deep Siamese CNN combined with ResNet-34 for the detection and classification of knee OA severity. This study employed the dataset from [13] along with a private hospital dataset for validation, achieving a balanced accuracy of 61.0%. Although this method demonstrated good performance, the slight difference in accuracy compared to the proposed method suggests that the choice of classifier and precise tuning can significantly enhance performance [14].

Nurmirinta et al. implemented a two-stage classification approach using Balanced Random Forest and MRI features, resulting in a higher balanced accuracy of 65.9%. This approach benefited from the detailed and high-resolution MRI data, which provide more comprehensive insights into knee joint structures compared to X-ray images [15]. According to adopted a CNN-based automatic detection approach with image processing techniques and MRI images, achieving a balanced accuracy of 61.0%. Into Cueva et al., this result underscores the importance of dataset composition and model architecture in influencing outcomes [16].

The Osteo-NeT system, which uses sequential convolutional neural network-based transfer learning models to identify knee osteoarthritis from X-ray images, is one prominent example. Predictive accuracy has increased with this system, and the pretrained VGG-16 model has proven to be the most effective [17]. Transfer learning allows models to leverage knowledge from previously trained networks, enhancing their performance on new, related tasks and reducing the need for extensive labeled datasets.

The present study aims to explore the potential of VGG re-trained feature extraction in enhancing the detection and classification of knee osteoarthritis using X-ray pictures. This is based on the encouraging findings of previous research, which suggest integrating it with different machine learning techniques. By leveraging the strengths of both deep learning and traditional machine learning techniques, this proposed approach aims to develop a diagnostic tool that could potentially assist clinicians in the early detection and effective management of knee osteoarthritis.

II. METHODOLOGY

II.1 DATASET

The dataset utilized in this study, known as the "Knee Osteoarthritis Dataset with Severity Grading," sourced from [13], [18], is tailored for knee osteoarthritis (OA) detection and severity grading through X-ray images. Comprising 8,260 X-ray images, the dataset provides a comprehensive representation of knee conditions across various severity levels. According to the Kellgren-Lawrence (KL) grading system, these images are categorized into five grades: Grade 0, which denotes a healthy knee image, and Grade 4, which denotes significant osteoarthritis. The following is how the pictures are distributed by grade: Grade 0 comprises 3,253 images, Grade 1 includes 1,495 images, Grade 2 consists of 2,175 images, Grade 3 encompasses 1,086 images, and Grade 4 contains 251 images. Each grade signifies distinct pathological changes in the knee joint, including osteophyte formation, joint space narrowing, and sclerosis, providing valuable insights for diagnostic and prognostic purposes.

This diverse representation allows for the exploration of the entire spectrum of knee OA severity, enabling comprehensive model training and evaluation. Moreover, the dataset is partitioned into three subsets—training, validation, and testing—with respective proportions of 70%, 10%, and 20%. This partitioning strategy ensures the robustness and generalizability of developed machine learning models by facilitating thorough model tuning and validation on unseen data.

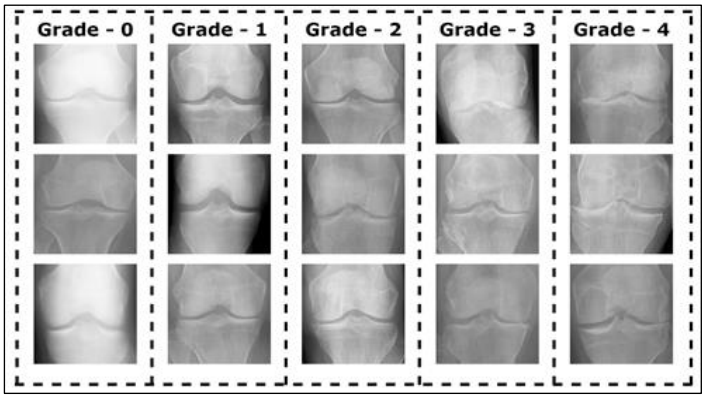

Figure 1: Example of X-ray images illustrating knee OA severity levels.
Source: Authors, (2025).

Figure 1 depicts sample images from the dataset used in this research, showcasing the variations in knee OA severity captured in the X-ray images. Overall, the "Knee Osteoarthritis Dataset with Severity Grading" serves as a valuable resource for advancing

research in knee OA diagnosis and management through computational methods, enabling researchers to develop and evaluate machine learning models for accurate and reliable knee OA detection, ultimately contributing to improved patient care and outcomes in clinical practice.

II.2 PROPOSED METHOD

The proposed methodology adopts a multi-step approach integrating deep learning and traditional machine learning techniques for knee osteoarthritis (OA) detection from X-ray images. Initially, the Knee Osteoarthritis Dataset with Severity Grading undergoes preprocessing, including resizing each X-ray image to 224x224x3 dimensions. This step enhances the images for subsequent feature extraction and model training processes without further partitioning into training, validation, and testing sets. The feature extraction phase, pretrained VGG16 and VGG19 models, initialized with weights trained on ImageNet, are utilized to extract deep features from the X-ray images. These models are fine-tuned on the knee osteoarthritis dataset to adapt to its specific characteristics, enhancing their feature representation capabilities. Subsequently, the classifier heads of the pretrained VGG models are removed, and the extracted features are integrated into the pipeline.

Following the feature extraction, various machine learning models, including Naive Bayes, K-Nearest Neighbors (KNN) with different values of K (1, 3, 5), Decision Tree, Random Forest, Bagging, and AdaBoost, are trained on the extracted features. These models learn patterns and relationships between the features and the corresponding knee OA severity grades, facilitating effective detection.

The performance evaluation of the developed models employs commonly used metrics such as accuracy, precision, recall, and F1-score. The evaluation is conducted solely on the validation set to fine-tune hyperparameters and optimize model performance. Finally, the best-performing models are assessed on the testing set to evaluate their generalization ability and robustness, aiming to develop an effective diagnostic tool for knee osteoarthritis detection using X-ray images, thereby providing valuable insights for clinical practice. The proposed configuration can be seen in Figure 2.

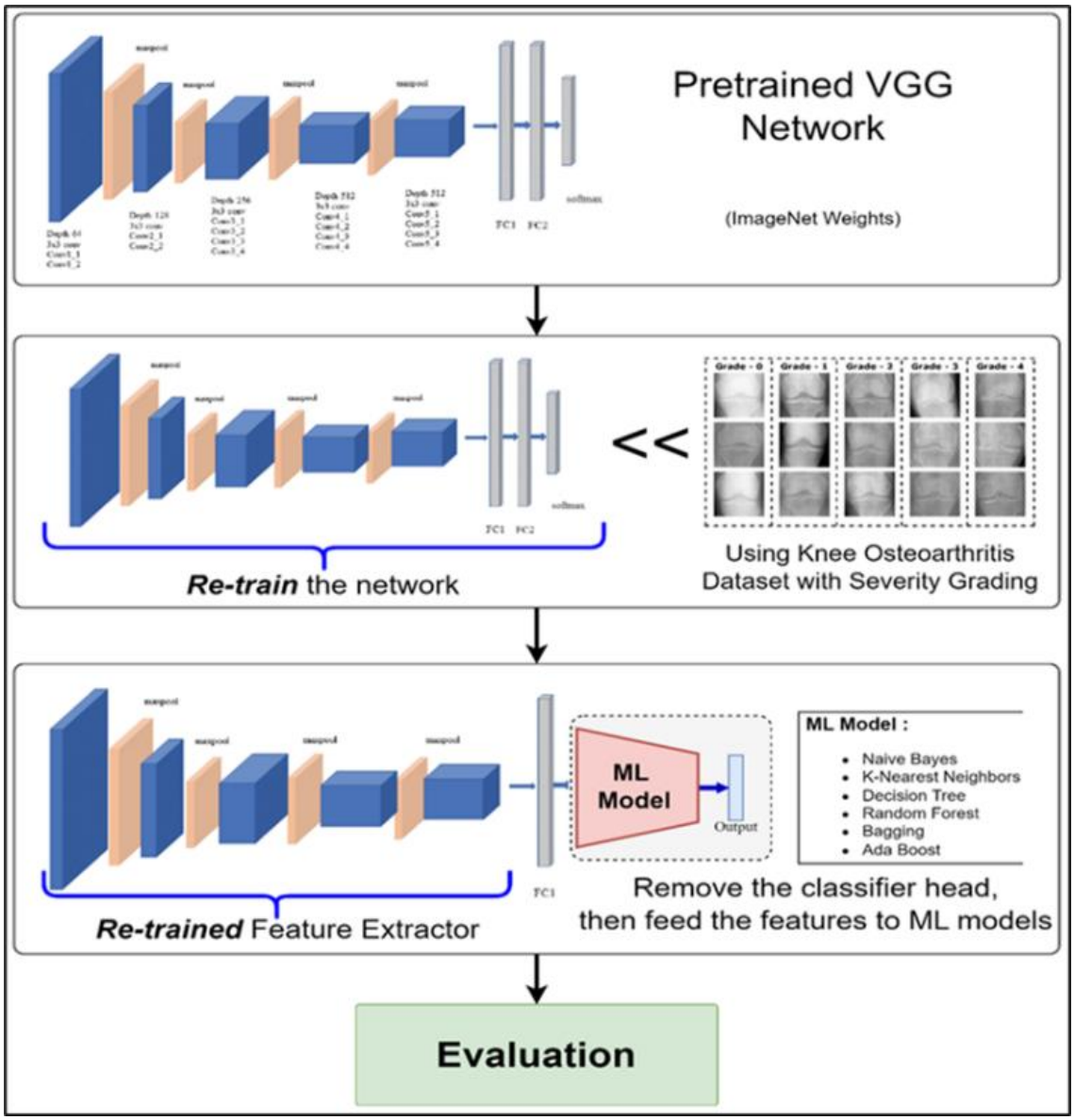

Figure 2: Proposed configuration (Integrating VGG Re-trained Feature Extraction with Machine Learning).
Source: Authors, (2025).

II.3 CONVOLUTIONAL NEURAL NETWORK

Convolutional Neural Networks (CNNs) are pivotal in computer vision, renowned for their proficiency in recognizing visual patterns within image data. Pretrained CNN models, trained extensively on datasets like the ImageNet Large Scale Visual Recognition Challenge (ILSVRC), exhibit exceptional adaptability and precision in identifying diverse objects. Through transfer learning, these models can be repurposed for various tasks, expediting development and deployment. CNNs integrate feature extraction and classification, discerning intricate patterns from images with robust adaptability to variations.

Convolution procedures are used by the Convolutional Neural Network (CNN) to extract features from the input pictures. The convolution operation between a kernel $\boldsymbol{K}$ and a input image $\boldsymbol{I}$ is mathematically defined as:

$$(I * K)(x,y) = \sum_{m}\sum_{n} \boldsymbol{I}(m,n) \cdot \boldsymbol{K}(x-m, y-n) \qquad (1)$$

where $\boldsymbol{I}(m,n)$ represents the pixel value at position (m,n)(m, n)(m,n) in the input image, and $\boldsymbol{K}(x-m, y-n)$ represents the kernel value. Pooling operations, which follow convolution, reduce the spatial dimensions by taking the maximum or average values within a specified window, enhancing the network's ability to capture spatial hierarchies in the data. Foundational layers like Convolution and Pooling progressively extract hierarchical features, enhancing efficacy across tasks, facilitating nuanced analysis of visual data [19], [20].

II.4 VGG

Deeper and more complex networks are being developed in Convolutional Neural Network (CNN)-based model building in an effort to achieve higher detection accuracy, and VGG is an example of this strategy. The winning team in the 2014 ILSVRC challenge, Simonyan and Zisserman, demonstrated a significant breakthrough by using only modest 3x3 convolutional filters and expanding the depth of the convolutional block to include 16–19 convolutional layers.

The VGG16 architecture consists of five maximum pooling layers and thirteen convolutional layers, each of which has an activation function that is a rectified linear unit (RELU). The first two, each with 4096 channels, and the third, with 1,000 channels and a softmax activation function, are the three fully connected layers that comprise the categorization block [21].

The number of convolutional layers utilized in each convolutional block is what distinguishes VGG16 from VGG19. Compared to VGG16, which has thirteen convolutional layers, VGG19 has sixteen. Notably, the input picture is downscaled using 2x2 maximum pooling layers with a stride of 2, and the entire kernel size utilized in the VGG architecture is 3 x 3. Before it reaches the classification block, the downsampled and filtered image that is produced when an RGB image with dimensions of 224x224x3 is used as the standard input for the convolutional networks of VGG16 is 7x7x512.

The backpropagation approach is used to update the model's parameters during the fine-tuning stage in order to minimize the category cross-entropy loss. Frequently employed in multi-class classification issues, the categorical cross-entropy loss, or $\bar{\boldsymbol{L}}$, is defined as follows:

$$L(y,\hat{y}) = -\sum_{i=1}^{N}\sum_{j=1}^{C} y_{ij}\ \log(_{\hat{y}_{ij}}) \qquad (2)$$

where y_{ij} is a binary indication (0 or 1) if class label j is the proper classification for observation i, $\hat{y}_{ij}$ is the anticipated probability that observation i belongs to class j, $\boldsymbol{N}$ is the number of observations, and $\boldsymbol{C}$ is the number of classes. The weight updates during training are computed as follows:

$$W_{t+1} = W_t - \eta \frac{\partial L(W_t)}{\partial W_t} \qquad (3)$$

where $\boldsymbol{W_t}$ indicates the iteration's weights $\boldsymbol{t}$, $\boldsymbol{\eta}$ is the learning rate, and $\frac{\partial L(W_t)}{\partial W_t}$ shows how the loss slopes in relation to the weights.

This architectural design helps to successfully integrate deep learning and conventional machine learning techniques for improved diagnostic accuracy. It also makes it possible for the VGG models to adapt to the subtleties of knee osteoarthritis detection from X-ray images. These two factors work together to optimize the VGG models' performance [22].

II.5 PERFORMANCE EVALUATION

In order to determine how effective a system is, performance evaluation is essential. This is especially true for classification tasks, where measurements such as accuracy, precision, recall, and F1-score are commonly utilized. The system's accuracy in categorizing data is assessed by the ratio of properly predicted cases to the whole dataset, which allows the system to successfully distinguish between positive and negative examples. Precision gauges the system's accuracy in precisely identifying true positive predictions. In contrast, recall measures the system's ability to correctly identify actual positive instances, crucial in scenarios where missing positive instances incurs significant costs.

The F1-score provides a comprehensive evaluation by combining precision and recall, offering a holistic assessment metric, particularly beneficial for addressing datasets with imbalanced class distributions. These metrics provide a comprehensive knowledge of a model's performance across several categorization elements, providing a full evaluation of its efficacy [23].

III. RESULTS AND DISCUSSION

This study's experimental setup made use of the Google Colab Pro platform and the Python programming language, as well as a GPU T4 with 25 GB of RAM for effective processing. Important libraries such as scikit-learn, TensorFlow, and Keras were used; these allowed access to different pre-trained architectures and weights from ImageNet, which helped with the creation and optimization of the deep learning models.

The optimization procedure was continually guided by the cross-entropy loss function throughout the tests. During the first transfer learning phase, the training protocol was designed to consist of 10 epochs with a batch size of 16 and an initial learning rate of 0.0001. To improve the performance of the model, a methodical fine-tuning approach was used, which involved unfreezing layers one at a time with an adjusted learning rate of 0.00001. The use of callbacks improved training process monitoring and control, enhancing experiment reproducibility and transparency.

Table 1: Performance Results of Proposed Models.

Base Model	Configuration	Accuracy (%)	Precision (%)	Recall (%)	F1-Score (%)
VGG16	Base (TL)	45.954	36.591	45.954	36.125
	Base + FT	62.258	58.981	62.258	59.021
	Base + FT + NB	37.923	46.979	37.923	37.723
	Base + FT + KNN-1	53.080	53.090	53.080	52.970
	Base + FT + KNN-3	55.085	53.323	55.085	53.027
	Base + FT + KNN-5	58.394	56.412	58.394	55.903
	Base + FT + DT	50.969	51.289	50.969	51.088
	Base + FT + RF	60.775	56.196	60.775	56.190
	Base + FT + Bagging	59.843	57.793	59.843	58.281
	Base + FT + Ada Boost	51.993	46.203	51.993	47.193
VGG19	Base (TL)	45.229	35.934	45.229	35.571
	Base + FT	60.930	58.059	60.930	54.325
	Base + FT + NB	36.957	46.482	36.957	37.050
	Base + FT + KNN-1	53.200	53.075	53.200	52.858
	Base + FT + KNN-3	56.763	55.564	56.763	54.498
	Base + FT + KNN-5	58.756	57.131	58.756	55.978
	Base + FT + DT	48.853	49.079	48.853	48.950
	Base + FT + RF	**62.681**	**58.414**	**62.681**	**57.549**
	Base + FT + Bagging	58.756	55.505	58.756	56.191
	Base + FT + Ada Boost	52.899	48.045	52.899	47.894

Source: Authors, (2025).

Table 2: Comparison of Methods for Knee Osteoarthritis Detection and Classification.

urce	Method	Dataset	Number of Classes	Accuracy (%)
Our(s)	*Proposed*	Chen [13]	5	62.68
Cueva, 2022 [14]	Deep Siamese CNN + fine-tuned ResNet-34	Chen [13] + Private hospital dataset	5	61.0
Nurmirinta, 2024 [15]	Two-stage classification	multiple sources MRI images	3	65.9
Hemanth, 2023 [16]	Deep Siamese CNN + fine-tuned ResNet	N/A	5	61.0

Source: Authors, (2025).

After the fine-tuning phase, the classifier heads of the pre-trained VGG16 and VGG19 models were removed. The extracted features were then fed into various machine learning models using scikit-learn, including Naive Bayes, K-Nearest Neighbors (KNN) with different values of K (1, 3, 5), Decision Tree, Random Forest, Bagging, and AdaBoost, to enhance the detection capabilities.

The results of these experiments, including evaluations of accuracy, precision, recall, and F1-score for each model configuration, are presented in Table 1. This comprehensive approach aimed to develop an effective diagnostic tool for knee osteoarthritis detection using X-ray images, providing valuable insights for clinical practice.

The most effective model configuration, according to an examination of the performance data, is the VGG19 base model combined with Random Forest (RF) as the machine learning algorithm and fine-tuning (FT). With an astounding accuracy of 62.681%, this setup is the best-performing model out of all the configurations that were examined. Furthermore, this model exhibits balanced metrics for precision, recall, and F1-score, showing strong performance across a variety of evaluation criteria.

This configuration successfully captures the intricate patterns and correlations found in the knee osteoarthritis dataset by utilizing the re-trained features taken from the VGG19 model and the ensemble learning power of Random Forest. This model's high accuracy rate indicates that it can correctly categorize X-ray pictures into distinct severity degrees of osteoarthritis in the knee, which is useful information for clinical diagnosis and therapy choices.

The VGG19-based design is clearly the most successful in this investigation, even though other configurations, such the VGG16 base model with fine-tuning and Random Forest, which reaches an accuracy of 60.775%, also show promising performance. Its exceptional accuracy highlights how crucial model and algorithm selection are to maximizing knee osteoarthritis detection systems' diagnostic accuracy.

Overall, knee osteoarthritis can now be better identified and classified from X-ray images thanks to the suggested methodology of combining VGG re-trained feature extraction with machine learning models, especially the combination of VGG19 with fine-tuning and Random Forest. This model shows robust performance across several evaluation measures and attains the maximum accuracy, which makes it a suitable choice for practical clinical applications. Additionally, Figure 3 illustrates the confusion matrix of the best-performing model based on test data, providing further insights into its performance.

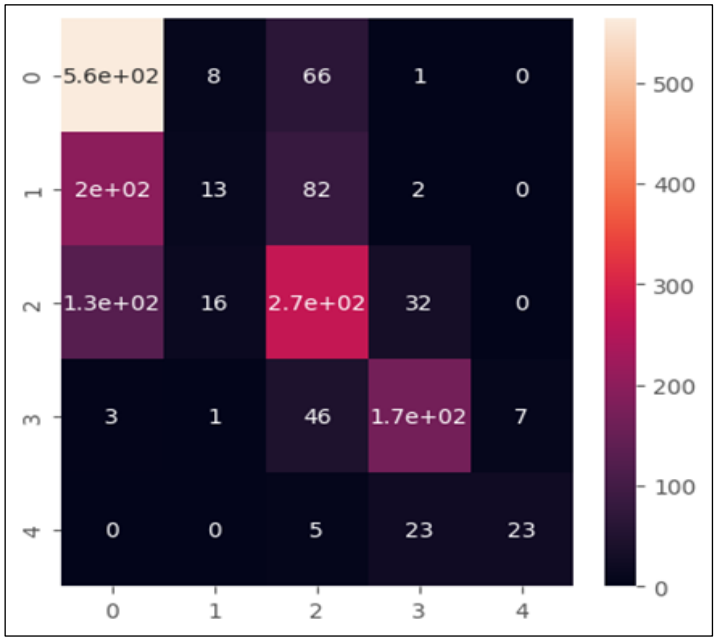

Figure 3: Confusion matrix for VGG19 + FT + RF model.
Source: Authors, (2025).

In this study, the method employed is integrating VGG re-trained feature extraction with machine learning for detecting knee osteoarthritis severity levels using X-ray images. The confusion matrix presented in the results section illustrates the distribution of correct and incorrect predictions made by the proposed model.

To provide a broader context, we compare this model's performance with other recent studies that have utilized different methodologies for the same task. The table 2 summarizes these comparisons in terms of method, dataset, number of classes, and balanced accuracy.

The proposed method, which integrates VGG re-trained feature extraction with machine learning, achieved a balanced accuracy of 62.68%. This performance indicates the model's effectiveness in accurately classifying different severity levels of knee osteoarthritis from X-ray images. The confusion matrix results further illustrate the model's robustness in handling the inherent imbalance in the dataset, reflecting a strong capability to differentiate between the classes.

Comparing this with other studies, Cueva et al. (2022)[14] utilized a Deep Siamese CNN combined with ResNet-34, achieving a balanced accuracy of 61.0%. This minor difference suggests that while the methodologies are similar, the fine-tuning of the VGG model and the choice of Random Forest as the classifier in the proposed method likely contributed to the slightly higher accuracy. Specifically, VGG19's depth and capacity for feature extraction may have allowed it to capture more nuanced patterns in the X-ray images, which, when combined with the robust ensemble learning approach of Random Forest, resulted in better overall performance.

According to[15] employed a two-stage classification approach using Balanced Random Forest and MRI features, which resulted in a higher balanced accuracy of 65.9%. This approach benefited from the detailed and high-resolution data provided by MRI images, which offer more comprehensive insights into knee joint structures compared to X-ray images. While this method shows the advantage of using more detailed imaging modalities, it also indicates that improvements could be made by integrating multiple types of imaging data in future work.

In [16] also used a CNN-based automatic detection approach with MRI images and image processing techniques, achieving a balanced accuracy of 61.0%. Similar to Cueva et al., the slightly lower accuracy compared to the proposed method highlights the potential advantages of using VGG re-trained features with a Random Forest classifier. The Random Forest's ability to handle high-dimensional data and its robustness against overfitting likely contributed to the improved performance.

Overall, the proposed method demonstrates competitive performance and provides a strong foundation for further research and development in this area. The integration of VGG19's powerful feature extraction capabilities with the ensemble learning strength of Random Forest appears to be a particularly effective combination for this application. Future improvements could involve leveraging more detailed imaging modalities or combining multiple types of data to further enhance the accuracy and robustness of knee osteoarthritis detection models.

IV. CONCLUSION

In conclusion, a viable method for improving the identification and categorization of knee osteoarthritis using X-ray pictures is the integration of VGG re-trained feature extraction with different machine learning algorithms. With an astounding accuracy of 62.681%, the VGG19 base model with fine-tuning and Random Forest combination proves to be the most successful of the evaluated combinations. Precision, recall, and F1-score are just a few of the evaluation parameters this model performs well on, highlighting its potential for precise diagnosis in clinical contexts. The findings highlight the importance of fine-tuning pre-trained models and selecting appropriate machine learning algorithms to optimize diagnostic accuracy.

For future work, integrating additional imaging modalities such as MRI could potentially improve diagnostic accuracy. Exploring advanced deep learning architectures and further fine-tuning of the model parameters could also enhance performance. Additionally, expanding the dataset with more diverse samples and including real-world clinical data would help in validating the model's applicability in practical clinical settings. These steps could lead to the development of even more accurate and reliable diagnostic tools for knee osteoarthritis detection.

V. AUTHOR'S CONTRIBUTION

Conceptualization: Simeon Yuda Prasetyo and Ghinaa Zain Nabiilah
Methodology: Simeon Yuda Prasetyo and Ghinaa Zain Nabiilah
Investigation: Simeon Yuda Prasetyo and Ghinaa Zain Nabiilah
Discussion of results: Simeon Yuda Prasetyo and Ghinaa Zain Nabiilah
Writing – Original Draft: Simeon Yuda Prasetyo and Ghinaa Zain Nabiilah
Writing – Review and Editing: Simeon Yuda Prasetyo and Ghinaa Zain Nabiilah
Resources: Simeon Yuda Prasetyo and Ghinaa Zain Nabiilah
Approval of the final text: Simeon Yuda Prasetyo and Ghinaa Zain Nabiilah

VI. REFERENCES

[1] E. Rezuş, A. Burlui, A. Cardoneanu, L. A. Macovei, B. I. Tamba, and C. Rezuş, "From Pathogenesis to Therapy in Knee Osteoarthritis: Bench-to-Bedside," Int J Mol Sci, vol. 22, no. 5, 2021, doi: 10.3390/ijms22052697.

[2] L. Yue and J. Berman, "What Is Osteoarthritis?," JAMA, vol. 327, no. 13, p. 1300, Apr. 2022, doi: 10.1001/jama.2022.1980.

[3] R. Giordano, K. K. Petersen, H. H. Andersen, O. Simonsen, and L. Arendt-Nielsen, "Serum Inflammatory Markers in Patients With Knee Osteoarthritis: A Proteomic Approach," Clin J Pain, vol. 36, no. 4, 2020, [Online]. Available: https://journals.lww.com/clinicalpain/fulltext/2020/04000/serum_inflammatory_markers_in_patients_with_knee.1.aspx

[4] D. Primorac et al., "Comprehensive Review of Knee Osteoarthritis Pharmacological Treatment and the Latest Professional Societies' Guidelines," Pharmaceuticals, vol. 14, no. 3, 2021, doi: 10.3390/ph14030205.

[5] M. H. M. Yunus, A. Nordin, and H. Kamal, "Pathophysiological Perspective of Osteoarthritis," Medicina (B Aires), vol. 56, no. 11, 2020, doi: 10.3390/medicina56110614.

[6] K. M. Leyland et al., "Knee osteoarthritis and time-to all-cause mortality in six community-based cohorts: an international meta-analysis of individual participant-level data," Aging Clin Exp Res, vol. 33, no. 3, pp. 529–545, 2021, doi: 10.1007/s40520-020-01762-2.

[7] J. Clarke, "Knee OA increases risk of all-cause mortality," Nat Rev Rheumatol, vol. 16, no. 3, p. 126, 2020, doi: 10.1038/s41584-020-0381-9.

[8] T. Tariq, Z. Suhail, and Z. Nawaz, "Machine Learning Approaches for the Classification of Knee Osteoarthritis," in 2023 3rd International Conference on Electrical, Computer, Communications and Mechatronics Engineering (ICECCME), 2023, pp. 1–6. doi: 10.1109/ICECCME57830.2023.10252236.

[9] N. Bayramoglu, M. T. Nieminen, and S. Saarakkala, "Machine learning based texture analysis of patella from X-rays for detecting patellofemoral osteoarthritis," Int J Med Inform, vol. 157, p. 104627, 2022, doi: https://doi.org/10.1016/j.ijmedinf.2021.104627.

[10] K. Zeng et al., "[Retracted] Multicentre Study Using Machine Learning Methods in Clinical Diagnosis of Knee Osteoarthritis," J Healthc Eng, vol. 2021, p. 1765404, 2021, doi: 10.1155/2021/1765404.

[11] R. Kanthavel, R. Dhaya, and H. Bangali, "Analysis On Deep Learning Approaches For Timely Detection Of Osteoarthritis," 2021.

[12] H. V. K. Ratna et al., "Machine learning and deep neural network-based learning in osteoarthritis knee," World J Methodol, vol. 13, no. 5, pp. 419–425, Dec. 2023, doi: 10.5662/wjm.v13.i5.419.

[13] P. Chen, "Knee Osteoarthritis Severity Grading Dataset," 2018, Mendeley Data.

[14] J. H. Cueva, D. Castillo, H. Espinós-Morató, D. Durán, P. Díaz, and V. Lakshminarayanan, "Detection and Classification of Knee Osteoarthritis," Diagnostics, vol. 12, no. 10, Oct. 2022, doi: 10.3390/diagnostics12102362.

[15] T. A. T. Nurmirinta, M. J. Turunen, R. K. Korhonen, J. Tohka, M. K. Liukkonen, and M. E. Mononen, "Two-Stage Classification of Future Knee Osteoarthritis Severity After 8 Years Using MRI: Data from the Osteoarthritis Initiative," Ann Biomed Eng, 2024, doi: 10.1007/s10439-024-03578-x.

[16] Hemanth S. R, Tharun K, Charan Raj H. S, Chadan S, and Chadanmagar M, "CNN based automatic detection of knee osteoarthritis severity using mri images and image processing techniques," International Research Journal of Modernization in Engineering Technology and Science, May 2023, doi: 10.56726/irjmets40187.

[17] H. A. Alshamrani, M. Rashid, S. S. Alshamrani, and A. H. D. Alshehri, "Osteo-NeT: An Automated System for Predicting Knee Osteoarthritis from X-ray Images Using Transfer-Learning-Based Neural Networks Approach," Healthcare, vol. 11, no. 9, 2023, doi: 10.3390/healthcare11091206.

[18] "Kaggle." [Online]. Available: https://www.kaggle.com/datasets.

[19] S. Awasthi, E. Kapoor, A. P. Srivastava, and G. Sanyal, "A New Alzheimer's Disease Classification Technique from Brain MRI images," in 2020 International Conference on Computation, Automation and Knowledge Management (ICCAKM), 2020, pp. 515–520. doi: 10.1109/ICCAKM46823.2020.9051485.

[20] S. Muhammed et al., "Improved Classification of Alzheimer's Disease With Convolutional Neural Networks," in 2023 IEEE Signal Processing in Medicine and Biology Symposium (SPMB), 2023, pp. 1–7. doi: 10.1109/SPMB59478.2023.10372725.

[21] K. Simonyan and A. Zisserman, "Very deep convolutional networks for large-scale image recognition," 3rd International Conference on Learning Representations, ICLR 2015 - Conference Track Proceedings, pp. 1–14, 2015.

[22] S. Y. Prasetyo, I. N. Alam, I. D. A. Rachmawati, E. S. Purwanto, and H. Ngarianto, "VGG-Powered Convolutional Neural Networks in Diabetic Retinopathy Classification: A Comparative Investigation," in 2023 3rd International Conference on Smart Cities, Automation & Intelligent Computing Systems (ICON-SONICS), 2023, pp. 26–31. doi: 10.1109/ICON-SONICS59898.2023.10435080.

[23] D. M. W. Powers, "Evaluation: from precision, recall and F-measure to ROC, informedness, markedness and correlation," no. January 2008, 2020, [Online]. Available: http://arxiv.org/abs/2010.16061.

Journal of Engineering and Technology for Industrial Applications

ISSN ONLINE: 2447-0228

ITEGAM-JETIA

Manaus, v.11 n.53, p. 48-54. May/June., 2025.

DOI: https://doi.org/10.5935/jetia. v11i53.1443

RESEARCH ARTICLE OPEN ACCESS

MACHINE LEARNING TECHNIQUES FOR IDENTIFYING TEXTUAL PROPAGANDA ON SOCIAL MEDIA: DEVELOPMENT OF A DETECTING DIGITAL MANIPULATION SYSTEM

Belkacem mostefai[1], Tarek Boutefara[2] , Abid Chahinez[3] and Aberkane Marwa[4]

[1] Faculty of Exact Sciences and Computer Science, Djelfa University, 17000 DZ, Djelfa, Algeria.
[2,3,4] Faculty of Exact Sciences and Computer Sciences, University of Jijel,18000 DZ Jijel, Algeria.

[1]http://orcid.org/ 0000-0002-2118-8407, [2]http://orcid.org/0000-0002-7222-9387, [3] http://orcid.org/0009-0001-5469-5878, [4]http://orcid.org/0009-0001-7771-3098

Email: b.mostefai@univ-djelfa.dz, t_boutefara@univ-jijel.dz, abidshahinez@gmail.com, aberkanmerwa@gmail.com

ARTICLE INFO

Article History
Received: November 30, 2024
Revised: January 20, 2025
Accepted: May 15, 2025
Published: May 31, 2025

Keywords:
Propaganda Detection,
Social media,
Machine Learning Techniques,
Linguistic Analysis,
Digital manipulation,

ABSTRACT

The dissemination of propaganda on social media presents a significant challenge in today's digital age. Utilizing advanced tools and diverse methods, propaganda aims to influence public opinion on a massive scale. Social media platforms serve as prime channels for such messages, leveraging sophisticated strategies to shape public perceptions and attitudes. This research aims to develop an advanced system capable of evaluating whether the content disseminated on these platforms qualifies as propaganda. The hypothesis suggests that it is possible to distinguish propaganda from non-propaganda texts on social media by analyzing specific linguistic features. Employing advanced linguistic analysis and machine learning methods, this detection system achieves approximately 70% accuracy, indicating its promising potential for effectively identifying propaganda. This approach could significantly enhance the transparency and reliability of online information, encouraging a more informed and critical use of social media.

I. INTRODUCTION

Propaganda is a powerful tool for shaping collective perceptions and influencing individual behavior [1]. While it has historically been used in political, cultural, and commercial contexts, its integration with social media has amplified its impact, making it a potent mechanism for widespread influence [2], [3]. With vast user networks, social media platforms enable the rapid and viral spread of propaganda, posing significant threats to democracy, public health, and social cohesion. Initially rooted in political and religious campaigns, propaganda has evolved into sophisticated digital strategies [4]-[6]. The spread of propaganda on social media alters the global perception of events, particularly in conflict situations [7], [8]. The use of these platforms to disseminate unverified and sensationalist content misleads and reinforces unfounded prejudices. This distortion of reality severely hampers international conflicts, exacerbates societal divisions, and undermines trust in institutions, highlighting the urgent need to promote fact-checking and critical thinking in the contemporary media landscape. [9], [10].

Propaganda often employ persuasive techniques such as emotional appeals, misinformation, and targeted messaging to manipulate public opinion [11]. Social media enhances both top-down and peer-to-peer dissemination, utilizing tactics like astroturfing [12], bot-generated content [13], and algorithmic manipulation to amplify certain narratives while suppressing others [14]. Machine learning, also known as machine learning, is a field of artificial intelligence based on mathematical and statistical methods. Its goal is to enable computers to learn from data without requiring explicit programming for each task [15].

Recent advancements in artificial intelligence (AI) and natural language processing (NLP) have enabled innovative methods to detect and counteract propaganda [16], [17]. These technologies analyze text patterns to identify manipulative strategies, such as extreme polarization and emotional persuasion [18]-[20]. Recent research investigates the potential of an

automated system to detect propaganda in real-time, aiming to enhance transparency in digital communication. Our research focused on detecting propaganda in texts on social media, aiming to identify content that sought to manipulate users' opinions and behaviors. A structured approach was employed, leveraging a manually annotated dataset of texts (tweets) sourced from specified social platform (Twitter as one of leading social media platforms), where content was categorized based on its propaganda characteristics and type. To prepare the data, various preprocessing techniques were applied enabling text normalization and the extraction of relevant information. Additionally, TF-IDF (Term Frequency-Inverse Document Frequency [21]) feature extraction was used to identify the most significant terms within propaganda texts. Our methodology proposed an effective process for text preprocessing and feature engineering, transforming a collection of raw documents into a numerical feature matrix. These features were further refined through various machine learning models, which supported the classification of texts as manipulative or authentic. The system's efficacy was evaluated based on precision, recall, and overall accuracy. The obtained results showed acceptable performance of our propaganda detection system, which successfully detected and correctly classified the majority of propaganda in the texts used for evaluation testing.

II. RESEARCH METHODOLOGY

We will hypothesize that it will be possible to distinguish propaganda texts from non-propaganda texts on social media by analyzing the specific linguistic features of these texts. To validate this hypothesis, we will use a supervised approach. The goal will be to build a classifier capable of categorizing propaganda texts into distinct categories, as well as identifying non-propaganda texts on social media. Our methodology follows a pipeline architecture in which a processing pipeline connects several transformation modules. Data pass through these modules sequentially, with the output of each module serving as the input for the next one [22]. In our research study, we have chosen to adopt a pipeline architecture as shown in Figure 1. The Different stages of our system pipeline: (1) Data collection (2) Data Preprocessing (3) Feature extraction (4) Classification (5) Evaluation. In the flowing subsections, we describe each stage of our system in detail.

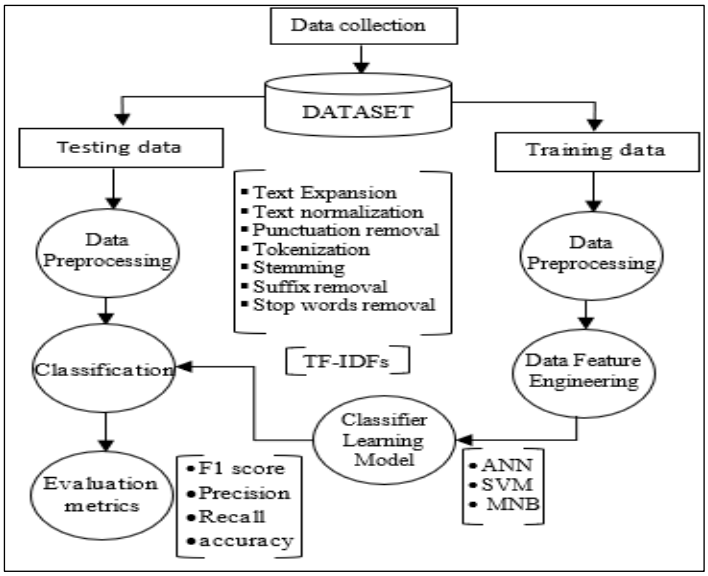

Figure 1: Pipeline Methodology Steps for a Textual Propaganda Classification System.
Authors, (2025).

II.1 DATASET COLLECTION

Given the unavailability of free access to social media databases, we took the initiative to create our own dataset. To achieve this, we adopted a manual approach to collect a substantial number of tweets on a timely and relevant issue that has become a prominent subject of propaganda on social media platforms. By leveraging targeted hashtags and keywords, we gathered a significant volume of tweets. After a thorough selection process, we retained a sample of one thousand tweets to ensure a representative analysis. To detect propaganda, tweets can be classified based on either content analysis or network analysis. In our research, we aimed to ensure that the corpus supports both classification methods to enable greater flexibility when designing the classifier. Accordingly, we gathered the necessary information to capture both the tweet content and the social network elements. Table 1 illustrates the structure of our corpus, which consists of twenty-one columns, each providing detailed information about the tweets. These columns are categorized into five categories of data Analysis: *Content Analysis, Network Analysis (Network Nodes and Network Locations), Technical Data Analysis, and Propaganda Nature Analysis*. As shown in Table1, in addition to the information about the tweets, we add columns to annotate the tweets according to their nature of propaganda, including: fake news, intimidation, concealment, manipulation and name calling. The created dataset support both classification methods, however, this paper focus on performing a classification based on content and leave the network aspect for future work.

Table 1: Column structure of the social media textual propaganda dataset.

Data Category	Column	Type	Description
Content Analysis	text of tweet	String	Full text of the tweet.
	hashtags	String	Hashtags included in the tweet.
	Views count	Integer	Number of views of the tweet.
	Retweets count	Integer	Number of retweets of the tweet.
	Likes count	Integer	Number of likes on the tweet.
	Responses count	Integer	Number of responses to the tweet.
Network Analysis	tweet author	String	Name of the tweet's author.
	profile	String	User's profile information.
	user followers	Integer	Tweet author's follower count
	user following	Integer	Tweet author's following count
	mention	String	Users mentioned in the tweet.
	retweet	String	Original tweet.
Technical Data Analysis	id	String	Unique tweet identifier.
	tweet link	String	URL of the tweet.
	date and hour	Date	Tweet's date and time.
	UserName	String	Tweet author's username
Propaganda Nature Analysis	fake news	Integer	Tweet contains false info?
	intimidation	Integer	Tweet contains intimidation?
	concealment	Integer	Tweet contains concealment?
	manipulation	Integer	Tweet contains manipulation?
	name calling	Integer	Tweet contains defamation?

Source: Authors, (2025).

II.2 DATA PREPROCESSING

There are various techniques for preprocessing textual data [21]. In our study, the goal of preprocessing is to prepare the text in a way that makes it easier to analyze and manipulate, facilitating the recognition and identification of propaganda types. To achieve this, we applied an automated preprocessing procedure to process both the textual data in our dataset. The preprocessing procedure executes the following seven operations in a single sequence:

(1) Expansion of Textual Contractions: To ensure clarity and optimal readability, certain text contractions are expended.
(2) Text normalization: To ensure the database is clear and readable, certain special characters are normalized.
(3) Punctuation removal: Removing commas, periods, and semicolons, as these marks are primarily used in written human communication.
(4) Tokenization: This is the process of dividing text into atomic units or tokens resembling words. This step aims to segment the text into individual words.
(5) Stemming: An automatic natural language processing technique that reduces words to their base or root form to ensure accurate representation of names and entities.
(6) Suffix removal: To ensure consistent, uniform, and precise normalization, specific suffixes such as "ist", "est", "less", "ian", and "en" are removed from proper nouns and specific entities.
(7) Stop words elimination: Stop words are removed because they play a minor role in classification tasks.

II.2 DATA FEATURE ENGINEERING

The pervious preprocessing step produces a unique vocabulary of terms present across the preprocessed documents. Following this, in order to evaluate the significance of each term within a document relative to the entire corpus, data features engineering is applied using Algorithm 1:

Algorithm 1: Feature Extraction from Textual Propaganda Data

```
1: Input: data
2: Start
3: pre-processed data ← pre-processing(data)
   vocabulary ← unique words from pre-processed data
   TF-IDFs ← []
4: For each document do
5:   For each term in vocabulary do
6:     Calculate TF (term frequency) in the current document
7:     Calculate IDF (inverse document frequency) for the term
       TF-IDF ← TF * IDF
       Add TF-IDF to TF-IDFs
8:   End For
9: End For
10: Convert TF-IDFs to a TF-IDF matrix
11: Return TF-IDF matrix
```

The proposed algorithm calculates the TF-IDF (**T**erm **F**requency-**I**nverse **D**ocument **F**requency) scores for each term in every document using the following equation:

$$TF - IDF\ \ (t, w, D) = TF(t, w) \times IDF(t, D)$$

- $T(t, w) = o_t / n_w$, where o_t is the number of occurrences of term $\boldsymbol{t}$ in document $\boldsymbol{w}$, and n_w is the total number of terms in the document.
- $ID(t, D)$: $log(N/n)$, where $\boldsymbol{N}$ is the total number of documents, and $\boldsymbol{n}$ is the number of documents in which term $\boldsymbol{t}$ appears.
- $TF - ID(t, w, D)$ Matrix of $TF - IDF$ scores are calculated for each term in each document. Each row represents a document, and each column represents a term from the vocabulary, with the corresponding $TF - IDF$ value

The resulting matrix is used for various natural language processing tasks such as text classification, information retrieval, or document similarity analysis.

II.3 CLASSIFICATION

To classify social network texts into categories (propaganda vs. non-propaganda, and various types of propaganda), we employ three supervised classification methods, well-known for their simplicity and efficiency: Artificial Neural Network (**ANN**) with Multi-Layer Perceptron [23], Support Vector Machine (**SVM**) [24], and Multinomial Naive Bayes (**MNB**)[25].

Before apply these classifiers, the data are splatted into training and testing sets. Then, we initialize the classifiers models using the training data in order to learn patterns in the TF-IDF scores associated with different document categories. Once trained, we use these models to predict the labels of the test data. Finally, to evaluate the models' performance, we calculate evaluation metrics such as accuracy, precision, recall, and F1-score.

Algorithm 2 describe the ANN classification. ANN classifier uses the TF-IDF matrix to detect patterns through multiple layers of perceptrons. These layers, including an input layer, one or more hidden layers, and an output layer, allow the network to learn complex relationships in the data. Texts are classified as propaganda or non-propaganda based on the patterns learned from the TF-IDF scores during training.

Algorithm 2: Artificial Neural Network (ANN) Classification.

```
Input: TF-IDF matrix, yyy
Begin
3. X←X \leftarrowX← TF-IDF matrix
4. Y←Y \leftarrowY← Class label vector
5. Split XXX and YYY into training and testing sets
6. Convert labels into a 1D array
7. Select and initialize the Multi-Layer Perceptron model
8. Predict the labels of the test data using the trained Multi-Layer
Perceptron model
9. Calculate accuracy, precision, recall, and F1-score between the
predicted labels and the true labels
10. Return the model's performance (accuracy, precision, recall, F1-
score)
End.
```

Algorithm 3 describe the SVM classification, SVM uses the TF-IDF matrix to represent data in a multi-dimensional space, grouping texts of the same category close together. Categories are separated by a clear margin that is as wide and distinct as possible. New texts are classified as propaganda or non-propaganda based on which side of the margin they fall.

Algorithm 1: SVM Classification

Input: TF-IDF matrix, yyy
Begin
3. X←X \leftarrowX← TF-IDF matrix
4. Y←Y \leftarrowY← Class label vector
5. Split XXX and YYY into training and testing sets
6. Convert labels into a 1D array
7. Select and initialize the Support Vector Machine model
8. Predict the labels of the test data using the trained Support Vector Machine model
9. Calculate accuracy, precision, recall, and F1-score between the predicted labels and the true labels
10. Return the model's performance (accuracy, precision, recall, F1-score)
End

Algorithm 4 describe the MNB classification, MNB classifiers use the TF-IDF matrix with Bayes' theorem to estimate the probability of a text belonging to the propaganda or non-propaganda category. Despite assuming feature independence, MNB achieves reliable results with minimal training data, making it an efficient approach for text classification.

Algorithm 4: Naive Bayes Classification

Input: TF-IDF matrix, yyy
2. **Begin**
3. X←X \leftarrowX← TF-IDF matrix
4. Y←Y \leftarrowY← Class label vector
5. Split XXX and YYY into training and testing sets
6. Convert labels into a 1D array
7. Select and initialize the Multinomial Naive Bayes model
8. Predict the labels of the test data using the trained Multinomial Naive Bayes model
9. Calculate accuracy, precision, recall, and F1-score between the predicted labels and the true labels
10. Return the model's performance (accuracy, precision, recall, F1-score)
End

Algorithm 5 is designed to classify new texts. It uses the three supervised classification methods with the TF-IDF matrix to classify texts as propaganda or not, while also considering the probability predicted by the models for more precise and nuanced classification.

III. MATERIALS AND METHODS

In our work, we used Python to implement our propaganda detection system on the X platform. Python stands out as a powerful and elegant programming language, offering easy readability and comprehension. It shares most of its features with many other languages, making it a versatile tool for real-world applications.

Additionally, being open-source, it benefits from a unique standard implementation and a welcoming, extensive developer community [67]. Several Python libraries were utilized to develop the propaganda detection system, supporting tasks from data preprocessing to model evaluation and interface development:

Algorithm 5: Machine Learning for Propaganda Text Classification

Input: text, yyy, threshold
Begin
3. Train the classification model on the TF-IDF matrix and training labels
4. Preprocess the input text
5. Engineer features from the preprocessed text
6. Predict the label of the engineered features using the trained classification model
7. Use the prediction with probability
8. If the probability >>> threshold, then
9. **Propaganda**, probability of the class
10. Else
11. **Not propaganda**
12. End If
End

1. **NumPy**: NumPy is a Python library specializing in array manipulation, including multidimensional arrays and matrices, as well as mathematical functions to operate on them [68]. It was used to convert target data into one-dimensional arrays, ensuring compatibility with the machine learning models in scikit-learn.
2. **NLTK (Natural Language Toolkit)**: NLTK is a suite of Python modules dedicated to natural language processing research and teaching. It provides tools, datasets, and tutorials to facilitate linguistic analysis and algorithm development [69]. It was used for natural language preprocessing tasks such as tokenization, stemming, and stopword removal. This preprocessing helped simplify the analysis of text in the project.
3. **Scikit-learn**: Scikit-learn is an open-source Python library for machine learning that offers tools for classification, regression, clustering, dimensionality reduction, and more [70]. It was employed to evaluate model performance using metrics such as accuracy, precision, F1-score, and recall. It was also used to split datasets and build models, particularly with the MLPClassifier.
4. **Pandas**: Pandas is a Python library designed for data manipulation and analysis, particularly for tabular data like spreadsheets and relational databases [71]. It was used to efficiently and consistently read and handle our dataset, which was stored in a CSV file.
5. **Flask**: Flask is a lightweight web development framework for Python, known for its simplicity and flexibility [72]. It was utilized to develop the user interface for the propaganda detection system, providing a simple and accessible front-end for interaction.
6. **CSV Format**: The CSV (Comma-Separated Values) format is a type of plain text file used to store tabular data, where each row represents a record, and fields are separated by a delimiter, typically a comma [73]. It was used to store the dataset in a tabular format, with semicolon delimiters. This format allowed easy manipulation and seamless import of data into our program.

Each of these tools played a critical role in achieving the project's objectives, contributing to data processing, model building, and user interface design. By combining their functionalities, the propaganda detection system was efficiently implemented. Furthermore, we integrated our Python code into a local web page using Flask for communication. The user interface is built with HTML, CSS, JavaScript, and Bootstrap, providing an interactive and smooth user experience.

IV. RESULTS AND DISCUSSIONS

IV.1 SYSTEM USER INTERFACE OVERVIEW

The propaganda classification system was implemented as web-based platform. Our site includes an intuitive homepage that allows quick access to the next page (see Figure 2). The propaganda detection interface includes an area to enter text, a detection button, a button to display more details, and another button to return to the homepage (see Figure 3).

Figure 1: Screenshot : propaganda detection system homepage.
Source: Authors, (2025).

Figure 2: Screenshot: the propaganda detection interface.
Source: Authors, (2025).

IV.2 EVALUATION RESULTS

To classify the text as propaganda or not, as well as to determine the specific categories of propaganda among the five defined, we used an MLPClassifier model. This model was initialized with two hidden layers of sizes 100 and 50, a relu activation function, and an "adam" solver. We partitioned our data with an 80/20 ratio and set the seed to 42 to ensure the reproducibility of the results. We utilized the predict_proba method from scikit-learn classification models to obtain an array of probabilities for each class.

This method provides the likelihood associated with each class for every text instance, enabling us to evaluate the model's confidence in its predictions for each specific propaganda category. In our approach, and after extensive testing, we defined specific thresholds for each propaganda category to fine-tune the model's sensitivity and determine whether a text qualifies as propaganda.

For instance, the threshold for the Fake News category was set at 0.0333, while Intimidation required a higher threshold of 0.108. Similarly, Concealment had a threshold of 0.004, Manipulation was set at 0.008, and Name Calling at 0.005. These thresholds ensure that texts with classification probabilities below the specified values for each category are not classified as belonging to that propaganda type, enhancing the precision and reliability of our classification system.

We conducted a comprehensive evaluation by comparing the performance of selected classifier algorithms, including the ANN, SVM and MNB classifier. Through this evaluation, we used a variety of performance metrics for each model: F1 score, precision, recall, and accuracy. In the following, we present the classification results through various tables (Table 2, Table 3, Table4 et Table 5) and figures (Figure 4, Figure 5, Figure 6 and Figure 7).

In the comparison tables below, we detail the performance of each classifier for each propaganda category. The obtained results clearly demonstrate the superiority of the ANN model for our specific context. This meticulous evaluation process allowed us to make an informed decision regarding the choice of the propaganda classification model in five distinct categories : fake news, intimidation, dissimulation, manipulation and name calling.

Table 2: Accuracy of classifiers by propaganda category.

Accuracy of :	ANN	SVM	Naive bayes
fake news	0.72	0.71	0.70
intimidation	0.69	0.67	0.66
dissimulation	0.78	0.77	0.77
manipulation	0.72	0.70	0.70
name calling	0.63	0.61	0.61

Source: Authors, (2025).

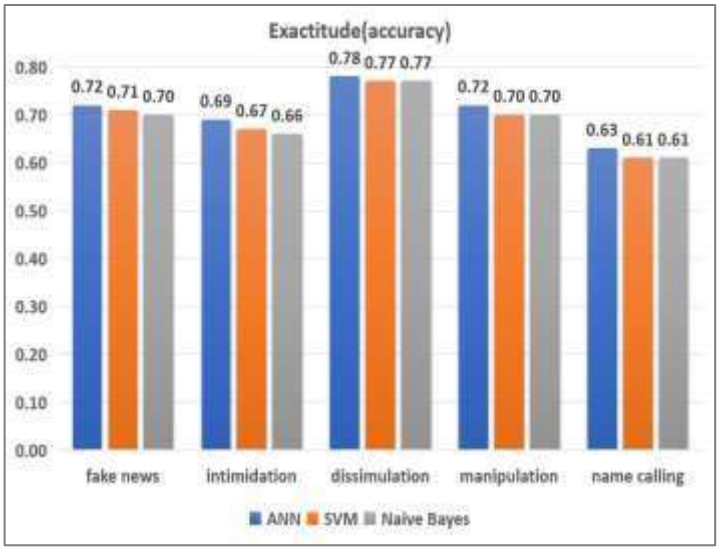

Figure 4: Accuracy comparative representation.
Source: Authors, (2025).

Table 3: Precision of classifiers by propaganda category.

Precision of:	ANN	SVM	Naive bayes
fake news	0.70	0.62	0.67
intimidation	0.63	0.52	0.62
dissimulation	0.67	0.66	0.66
manipulation	0.67	0.65	0.65
name calling	0.61	0.59	0.58

Source: Authors, (2025).

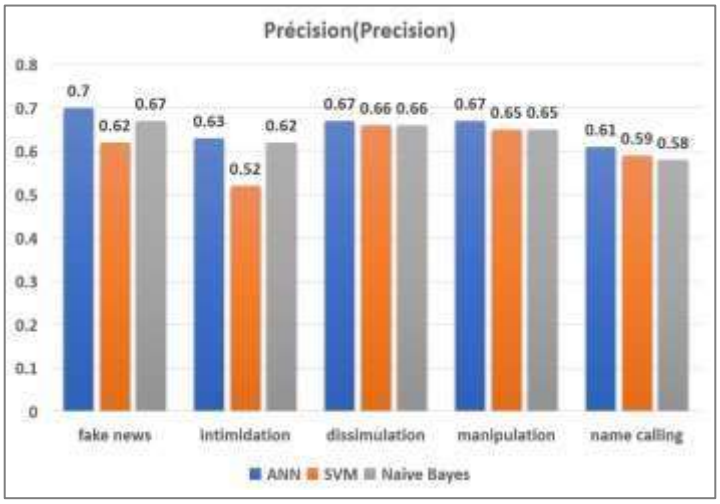

Figure 5: Precision Comparative representation.
Source: Authors, (2025).

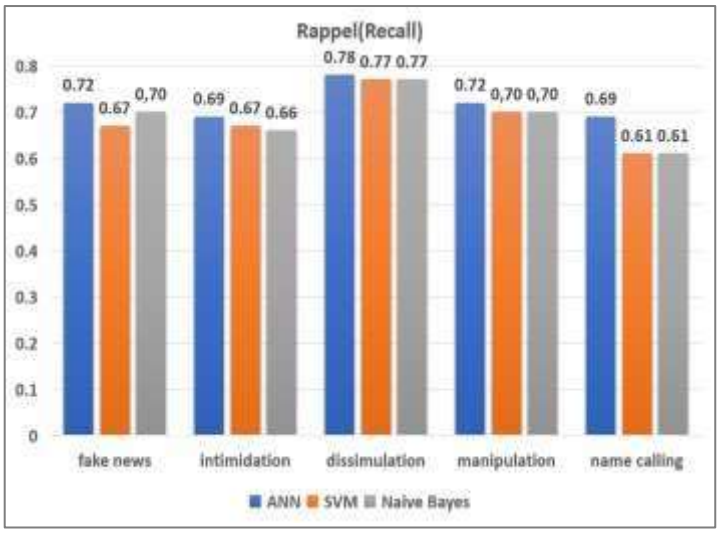

Figure 6: Recall Comparative representation.
Source: Authors, (2025).

Table 4: Recall of classifiers by propaganda *category.*

Rappel :	ANN	SVM	Naive bayes
fake news	0.72	0.67	0.70
intimidation	0.69	0.67	0.66
dissimulation	0.78	0.77	0.77
manipulation	0.72	0.70	0.70
name calling	0.69	0.61	0.61

Source: Authors, (2025).

Table 5: F1 Scores of classifiers *by propaganda category.*

F1-score :	ANN	SVM	Naive bayes
fake news	0.71	0.70	0.68
intimidation	0.66	0.64	0.63
dissimulation	0.71	0.70	0.70
manipulation	0.69	0.67	0.67
name calling	0.61	0.58	0.58

Source: Authors, (2025).

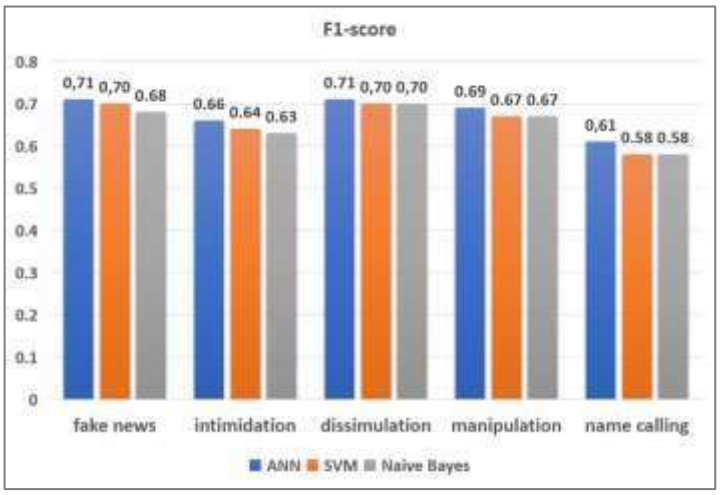

Figure 7: Comparative representation F1-score.
Source: Authors, (2025).

IV.3 DISCUSSION AND RELATED WORK

The results of our study demonstrate that the ANN-based propaganda classification model performs well, achieving an accuracy of around 70%, which indicates a robust capacity for detecting propaganda in text-based content. However, accuracy can still be improved. Our approach effectively identifies nuanced manipulation techniques through the use of tailored thresholds for classification, which gives it an edge in adaptability compared to other models.

When comparing our work to previous studies, several key differences emerge. In [26], authors focuses on detecting COVID-19-related propaganda using an improved ANN and hybrid feature engineering, achieved 77.15% accuracy. However, its reliance on binary classification and focus on specific hashtags restricts its ability to capture the full range of propaganda types. In [27], SVM and MNB classifiers are used to distinguish propagandist from non-propagandist text, achieved an accuracy of 69.2%. While the study employed a hybrid approach to feature engineering, its reliance on news-based datasets and a binary classification model limits its applicability to diverse social media content. In [28], authors introduced a framework combining TF-IDF and sentiment analysis for propaganda detection, achieving 69.2% accuracy. However, its binary classification model and focus solely on textual data limit its ability to capture the complex, multi-dimensional nature of modern propaganda. In [29], to recognize propaganda on Social Networks, authors explore machine learning models like SVM, Random Forest, and advanced deep learning techniques such as RoBERTa, primarily focuses on theoretical aspects and lacks practical implementation, methods, or results.

In contrast to other studies [26-28], our approach categorizes various forms of digital manipulation, employing tailored thresholds and adapting effectively to a wider range of propaganda types. This makes our approach more versatile and capable of identifying nuanced manipulation techniques across diverse social media platforms. Furthermore, while authors in [29] presented a theoretical proposition without actual implementation or results, our study provides a concrete methodology with data collection, preprocessing, feature extraction, and model evaluation, demonstrating the practical application and effectiveness of our system in detecting propaganda.

V. CONCLUSIONS

Propaganda, while often used to communicate ideas and messages, carries significant risks when exposed excessively, especially when it involves manipulative techniques and aggressive rhetoric. These risks include misinformation, manipulation of opinions, and other forms of deception, all of which can compromise objective understanding, erode trust in institutions, and destabilize democratic processes.

The main objective of our study was to develop an accessible tool to help users distinguish between information and propaganda on social media. We proposed a classification system that detects propaganda by analyzing its linguistic characteristics. Through theoretical research and the use of preprocessing techniques like tokenization, stemming, and stop-word elimination, we created a corpus of manually annotated tweets from the social platform X (Twitter) for training our classifier. Our system, which employed supervised classification algorithms, achieved an accuracy of approximately 70%. While further improvements remain necessary, the proposed approach, if integrated into web platforms and social networks, could play a crucial role in identifying and mitigating digital manipulation, thereby fostering greater transparency, accountability, and trust in digital communication.

For future work, a larger datasets and more in-depth testing are essential for enhancing its accuracy. Additionally, integrating network analysis would improve its ability to differentiate between propaganda and non-propaganda content. Future developments should also focus on adapting the system for real-world use, allowing internet users to verify the accuracy of the information they encounter, thus strengthening the ability to classify and address propaganda in social media environments.

VI. AUTHOR'S CONTRIBUTION

Conceptualization: Belkacem mostefai and Tarek Boutefara.
Methodology: Belkacem mostefai and Tarek Boutefara.
Investigation: Abid Chahinez and Aberkane Marwa.
Discussion of results: Belkacem mostefai,Tarek Boutefara, Abid Chahinez and Aberkane Marwa.
Writing – Original Draft: Belkacem mostefai**.**
Writing – Review and Editing: Belkacem mostefai and Tarek Boutefara.
Resources: Tarek Boutefara.
Supervision: Belkacem mostefai and Tarek Boutefara.
Approval of the final text: Belkacem mostefai and Tarek Boutefara

VII REFERENCES

[1] Y. Zhu and K.-w. J. D. J. Fu, "How propaganda works in the digital era: soft news as a gateway," vol. 12, no. 6, pp. 753-772, 2024.

[2] P. Baines, N. Snow, and N. OâÂ Â²Shaughnessy, "The Sage handbook of propaganda," 2019.

[3] D. J. P. A. Q. Walton, "What is propaganda, and what exactly is wrong with it," vol. 11, no. 4, pp. 383-413, 1997.

[4] M. Alhouseini and M. Saaideh, "The Influence of Social Media on Contemporary Global Politics," 2023.

[5] S. Okafor and J. Asogwa, "USE OF SOCIAL MEDIA AS A TOOL FOR POLITICAL PROPAGANDA IN ENUGU METROPOLIS."

[6] J. J. P. Chan and S. Criticism, "Online astroturfing: A problem beyond disinformation," vol. 50, no. 3, pp. 507-528, 2024.

[7] D. Sotiraki, "Media Framing by The Washington Post on TikTok: Shaping

[8] Public Perception of the Ukraine Conflict," ed, 2023.

[9] C. Ghosh, "The Impact of Social Media on Conflict Perception: Case Studies of Russia-Ukraine and Gaza Conflicts."

[10] A. J. J. o. D. Juneström, "An emerging genre of contemporary fact-checking," vol. 77, no. 2, pp. 501-517, 2021.

[11] A. Acht, "Who is benefitting from fact-checking on social media–user or platform? Examining the impact of different fact- checking approaches on social media platforms on user's perception of trust," 2024.

[12] M. P. J. M. i. s. C. E. P. Goswami, "Fake News and Cyber Propaganda: A study of manipulation and abuses on Social Media,"
pp. 535-544, 2018.

[13] B. J. P. d. l. i. García-Orosa, "Disinformation, social media, bots, and astroturfing: the fourth wave of digital democracy," vol. 30, no. 6, 2021.

[14] M. Orabi, D. Mouheb, Z. Al Aghbari, I. J. I. P. Kamel, and Management, "Detection of bots in social media: a systematic review," vol. 57, no. 4, p. 102250, 2020.

[15] E. Spencer, Narrative Control: Media Bias, Censorship, and Elections 2024: The Fight for Truth Amidst Media Narratives and Election Propaganda. Centurion Press, 2024.

[16] L. Rouvière, "Apprentissage supervisé-Machine learning," 2022.

[17] G. D. S. Martino, S. Cresci, A. Barrón-Cedeño, S. Yu, R. Di Pietro, and P. J. a. p. a. Nakov, "A survey on computational propaganda detection," 2020.

[18] B. M. Almotairy, M. Abdullah, and D. Alahmadi, "Detection of Computational Propaganda on Social Networks: A Survey," in Science and Information Conference, 2023, pp. 244-263: Springer.

[19] J. J. I. r. o. s. Serrano-Puche, "Digital disinformation and emotions: exploring the social risks of affective polarization," vol. 31, no. 2, pp. 231-245, 2021.

[20] V.-A. Oliinyk, V. Vysotska, Y. Burov, K. Mykich, and V. Basto-Fernandes, "Propaganda Detection in Text Data Based on NLP and Machine Learning," in MoMLeT+ DS, 2020, pp. 132- 144.

[21] P. N. Ahmad, L. Yuanchao, K. Aurangzeb, M. S. Anwar, Q.
M. u. J. S. O. C. Haq, and Applications, "Semantic web-based propaganda text detection from social media using meta-learning,"
pp. 1-15, 2024.

[22] F. J. U. h. w. l. c. g. t.-i.-t.-f.-i.-d. Karabiber, "Tf-idf—term frequencyinverse document frequency," 2020.

[23] H. Hapke and C. Nelson, Building machine learning pipelines. O'Reilly Media, 2020.

[24] A. Rana, A. S. Rawat, A. Bijalwan, and H. Bahuguna, - "Application of multi layer (perceptron) artificial neural network in the diagnosis system: a systematic review," in 2018 International conference on research in intelligent and computing in engineering (RICE), 2018, pp. 1-6: IEEE.

[25] D. A. Pisner and D. M. Schnyer, "Support vector machine," in Machine learning: Elsevier, 2020, pp. 101-121.

[26] F. Sabry, Naive Bayes Classifier: Fundamentals and Applications. One Billion Knowledgeable, 2023.

[27] A. M. U. D. Khanday, B. Bhushan, R. H. Jhaveri, Q. R. Khan,
R. Raut, and S. T. J. M. I. S. Rabani, "NNPCov19: Artificial Neural Network-Based Propaganda Identification on Social Media in COVID-19 Era," vol. 2022, no. 1, p. 3412992, 2022.

[28] A. M. U. D. Khanday, Q. R. Khan, and S. T. J. B. S. J. Rabani, "Detecting textual propaganda using machine learning techniques," vol. 18, no. 1, pp. 0199-0199, 2021.

[29] A. M. U. D. Khanday, M. A. Wani, S. T. Rabani, Q. R. Khan, and A. A. J. P. o. Abd El-Latif, "HAPI: An efficient Hybrid Feature Engineering-based Approach for Propaganda Identification in social media," vol. 19, no. 7, p. e0302583, 2024.

[30] R. R. Yellu, S. B. Dodda, B. K. Sharma, S. Dhar, and S. J. L.
P. I. Temara, "A Machine Learning Approach to Recognising Propaganda on Social Networks," vol. 44, no. 3, pp. 3184-3190, 2024

Journal of Engineering and Technology for Industrial Applications

ITEGAM-JETIA

Manaus, v.11 n.53, p. 55-61. May/June., 2025.
DOI: https://doi.org/10.5935/jetia. v11i53.1517

ISSN ONLINE: 2447-0228

RESEARCH ARTICLE OPEN ACCESS

PRACTICAL IMPLEMENTATION OF A SMART HOME MODEL USING ARDUINO AND SENSORS

Soufiane Hachani[1], Okba Benelmir[2]

[1] Department of Electrotechnical, Faculty of Technological Sciences, University of Ferhat Abbes, Setif, Algeria.
[2,] Departmant of Electronical, Faculty of Technological Sciences, University of Mohamed Khider, Biskra, Algeria .

[1]http://orcid.org/ 0009-0000-4817-397X, [2]http://orcid.org/0009-0001-2167-6208

Email: hachani.soufiane@univ-setif.dz , o.benelmir@univ-biskra.dz

ARTICLE INFO

Article History
Received: December 31, 2024
Revised: January 20, 2025
Accepted: May 15, 2025
Published: May 31, 2025

Keywords:
Practical Implementation,
Smart Home Model,
Arduino,
Sensors,

ABSTRACT

This paper focuses on the design and implementation of a physical model of a smart home with automated control systems to enhance resource management, energy efficiency, and user comfort. The model, built using wood and cardboard as primary materials, integrates multiple sensors connected to an Arduino microcontroller for autonomous operation. The smart home functions include:Regulating fan speed based on ambient temperature using a temperature sensor. Managing the water tank via a water level sensor to ensure optimal filling. Controlling outdoor lighting based on ambient light intensity detected by a light sensor. Activating a security alarm by touch detection using a touch sensor. Dynamic solar panel orientation based on time to maximize solar energy capture. This work demonstrates a practical and feasible approach to exploring smart home technologies, with a focus on integrating automation and renewable energy into real-world scenarios. The proposed system serves as a scalable and sustainable model for future applications, bridging the gap between theoretical research and practical application.

I. INTRODUCTION

Smart homes have emerged as a transformative solution to meet the growing demand for sustainable, energy-efficient, and user-friendly living environments. By leveraging technologies such as the Internet of Things (IoT), renewable energy, and automation, these systems improve resource management and enhance daily convenience [1],[2]. The increasing accessibility of microcontrollers such as Arduino has greatly contributed to the scalability and practicality of smart home applications [3],[4].

This research focuses on the practical construction of a smart home prototype using a physical model made of wood and cardboard, integrating multiple sensors and systems controlled by an Arduino microcontroller. The proposed system automates basic household functions, in line with contemporary trends in energy efficiency and automation [5],[6].

Key features of the system include : Temperature-based fan speed regulation: A temperature sensor dynamically adjusts fan speed to maintain indoor comfort while conserving energy [7],[8].

Water tank management : A water level sensor ensures optimal refilling to prevent flooding and conserve water resources [9],[10].

Automated outdoor lighting: A light sensor adjusts lighting based on ambient light intensity, reducing unnecessary energy consumption [5],[11].

Security enhancement: A touch sensor triggers a security alarm system in response to unauthorized interactions, addressing growing concerns about home safety [12],[13].

Solar panel orientation : A time-based sun tracking system maximizes solar energy harvest, demonstrating the integration of renewable energy into smart home designs [14],[15].

The integration of these features demonstrates a practical application of smart technologies to create a sustainable and smart home environment. By using IoT and automation technologies, this project not only explores innovative solutions but also provides a practical basis for the development of smart home systems [1-10]. Furthermore, it addresses key challenges such as energy optimization, resource conservation, and safety, contributing to the growing field of smart home research [2-8].

II. GENERAL MODEL OF THE SYSTEM USED

The diagram in (Figure 1) shows the general model that was used in this paper. As a basic point, we created a manual system and an automatic system for each element.

To understand the diagram, you must know the following : A 9-volt battery is used to power the Arduino.

A 12-volt battery to power the alarm, servo motor and external lighting.

A 3-12 Vcc switching block to power the DC motor and fan as needed with a variable voltage.

As for the sensors, they are connected to the Arduino to provide it with the physical quantities related to the environment surrounding the house through which it decides the outputs.

As for using a relay, it is very necessary because the Arduino voltage in the outputs is 5 v, which closes the relay to allow a higher voltage to pass to the element that needs to be operated.

As for the manual and automatic mode, we use a three-way switch that we will discuss later.

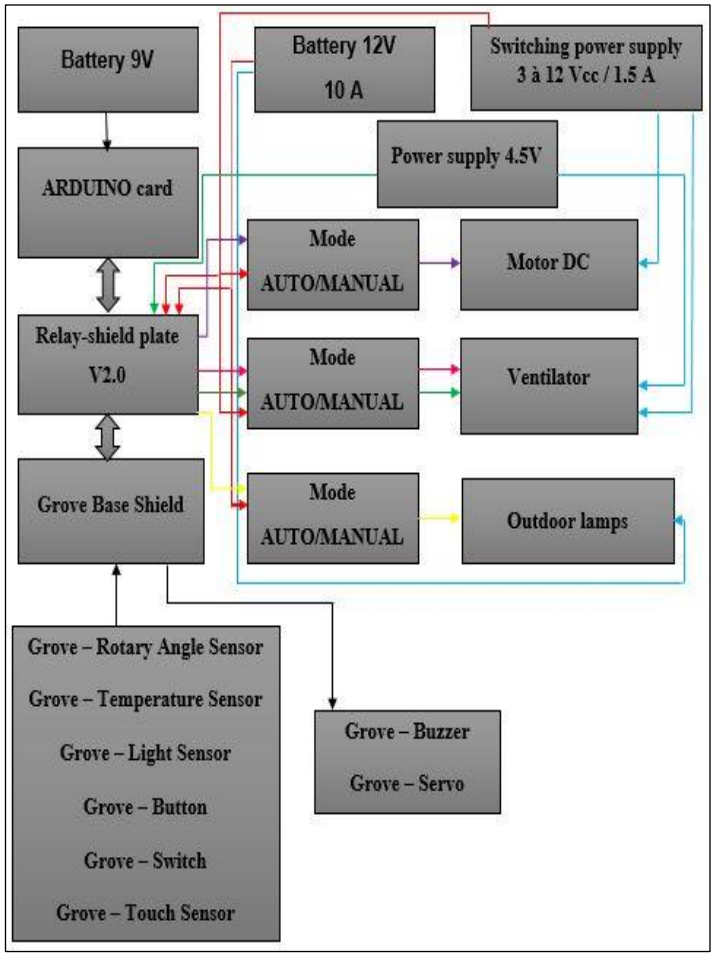

Figure 1: General model of the system used.
Source: Authors (2025)

III. CREATION OF THE MODEL

We created a wooden model (Figure 2) with a base (80 x 80) cm^2, the width of the house is 40 cm, the length is 70 cm and the height is 70 cm. Then we cover the model with white paper.

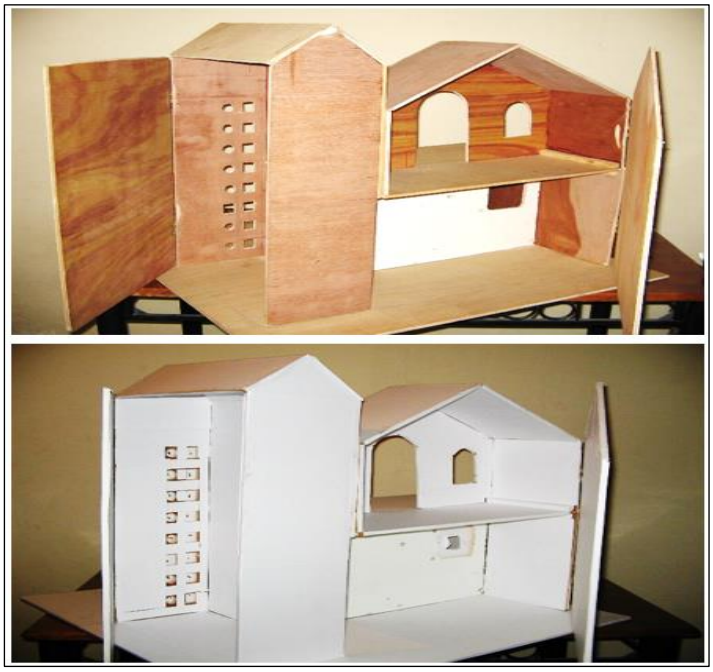

Figure 2: View of the model.
Source: Authors (2025)

IV. WIRING

Generally speaking, all actuators are supplied with a voltage of 12 V and they are wired as follows (Figure 3).

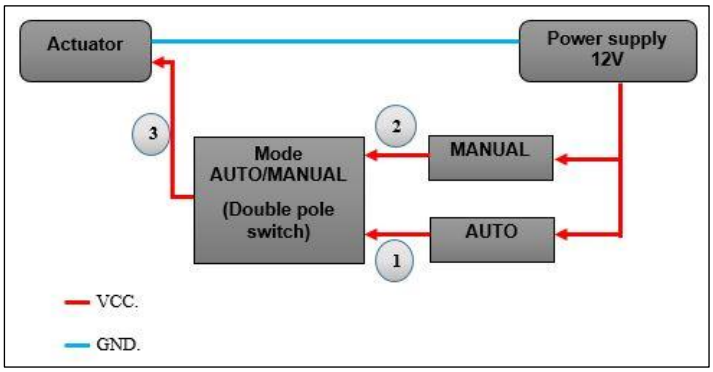

Figure 3: Wiring an actuator in a general way.
Source: Authors (2025)

V. DOUBLE POLE SWITCH

witch that allows you to choose a direction for the current (Figure 4).

Figure 4: Wiring the double pole switch.
Source: Authors (2025).

VI. MODE MANUAL WIRING

This mode is very simple and known (Figure 5).

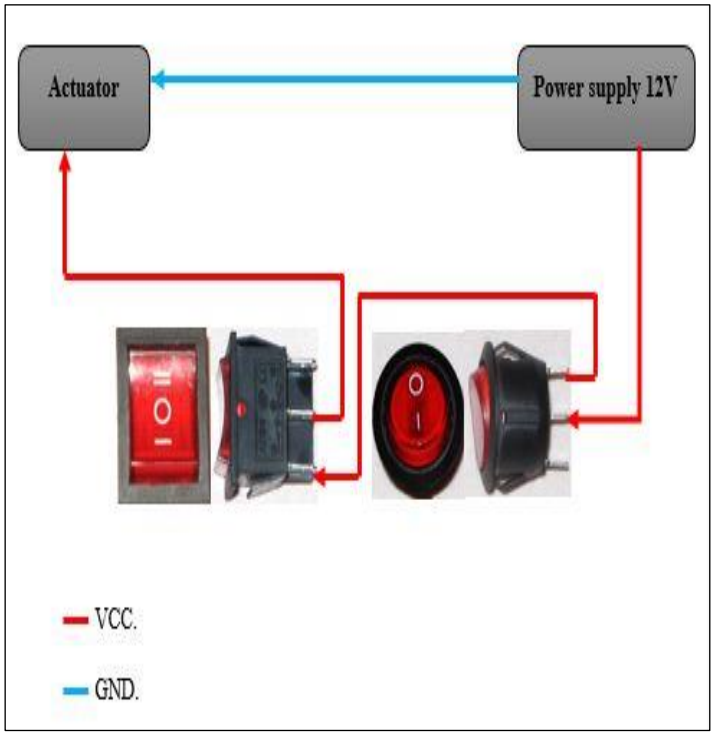

Figure 5: Wiring an actuator to manual mode.
Source: Authors (2025).

VII. FUN WIRING

All actuators are wired as the previous figure except that the fan is wired as follows since (Figure 6) it contains three speeds each one has its voltage.

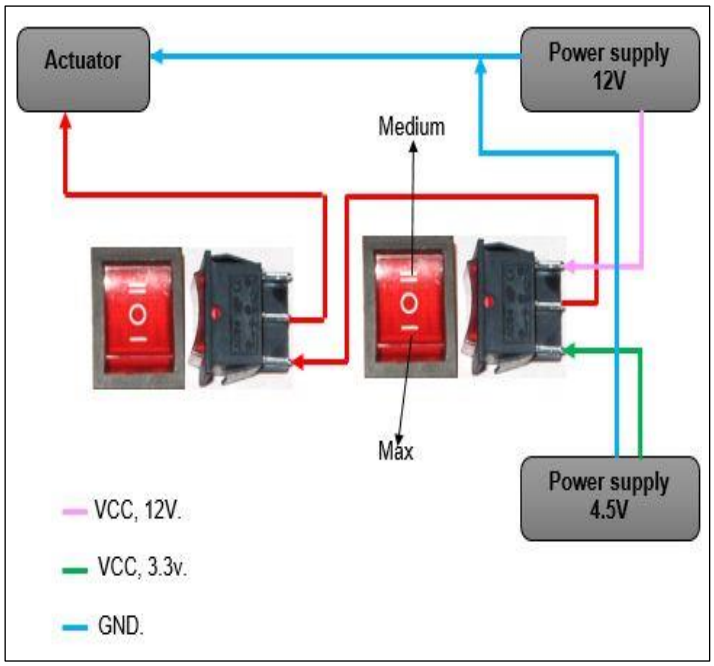

Figure 6 : Manual fun wiring.
Sourace: Authors (2025).

VIII. THE 9V BATTERY

We used a rechargeable 9V battery (Figure 7) to power the ARDUINO board.

Figure 7: 9V rechargeable battery.
Source: Authors (2025).

IX. AUTO MODE

To talk about wiring you have to see the connection of all the shields with the ARDUINO card (Figure 8).

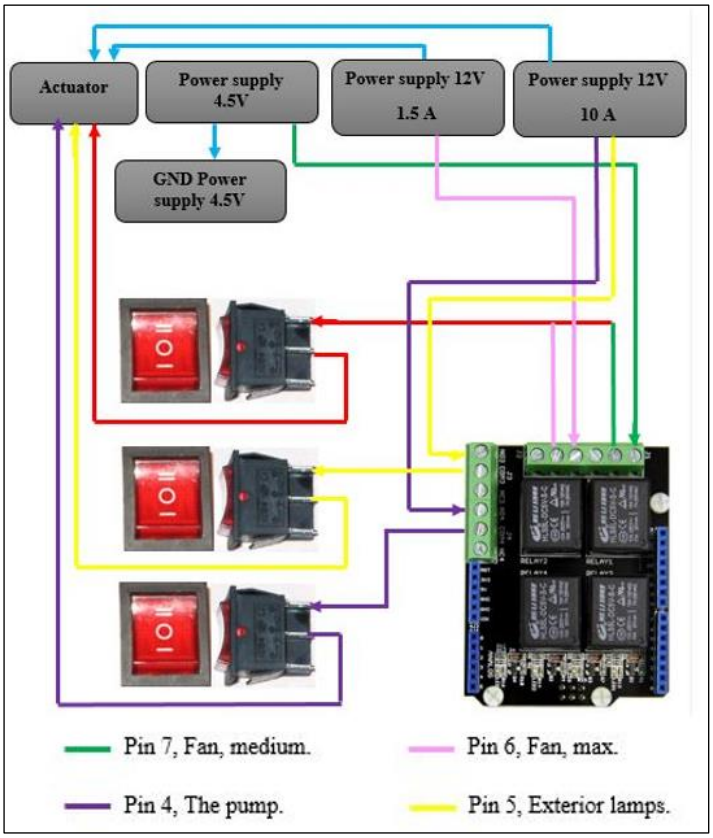

Figure 8: ARDUINO system AUTO-Mode wiring.
Source: Authors (2025).

X. AIR CONTROL

We want to control the fan speed according to the temperature. From 25°C to 40°C, the fan runs at medium speed, and with a temperature above 40°C, the fan runs at maximum speed, and if it is below 25°C, the fan is turned off.

The following two flowcharts (Figure 9a), (Figure 9b) represent the operation of the air control system AUTO and MANUAL respectively.

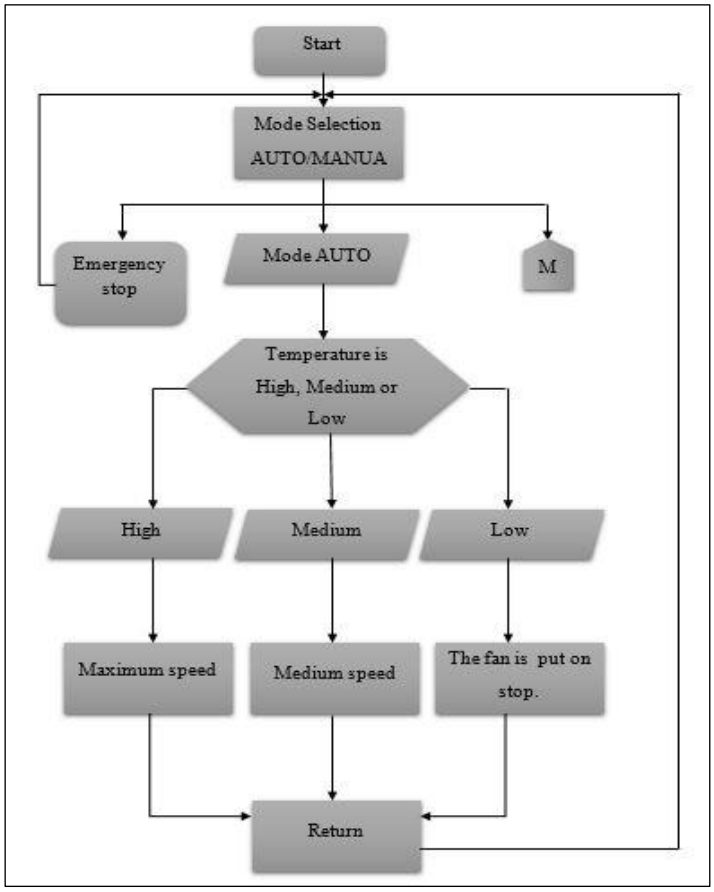

Figure 9.a: Air control "AUTO-Mode"
Source: Authors (2025)

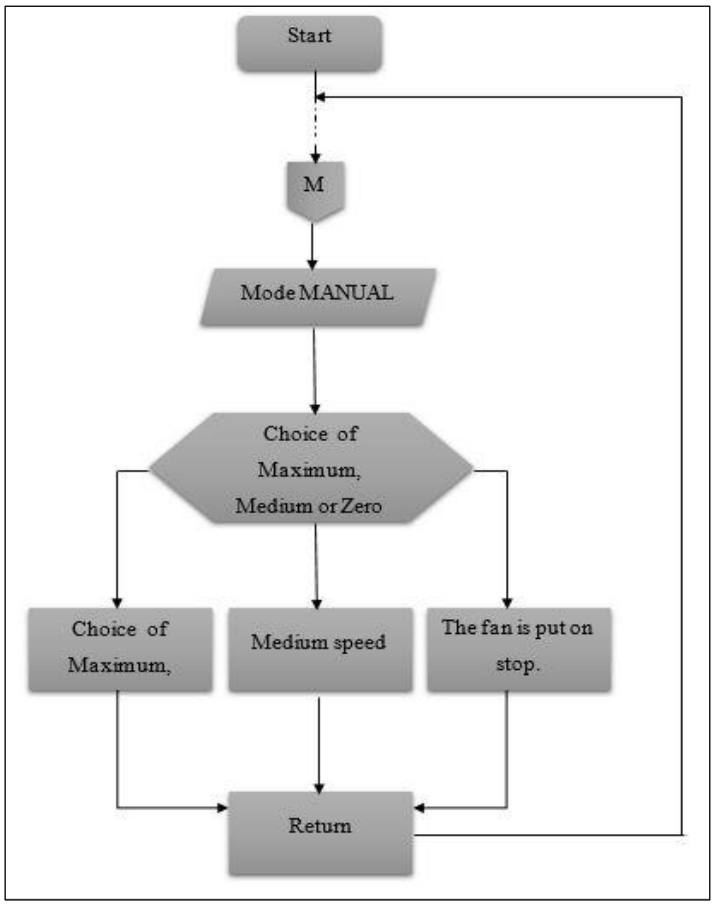

Figure 9.b : Air control « MANUAL-Mode ».
Source: Authors, (2025).

XI. TANK FILLING SYSTEM

We want to control the pump according to the following rules:

If the water level is below the minimum => turn on the pump.

After operation, if the water level reaches the maximum => turn off the pump.

The following two flowcharts (Figure10a) (Figure10b) represent the operation of the AUTO and MANUAL tank filling system respectively.

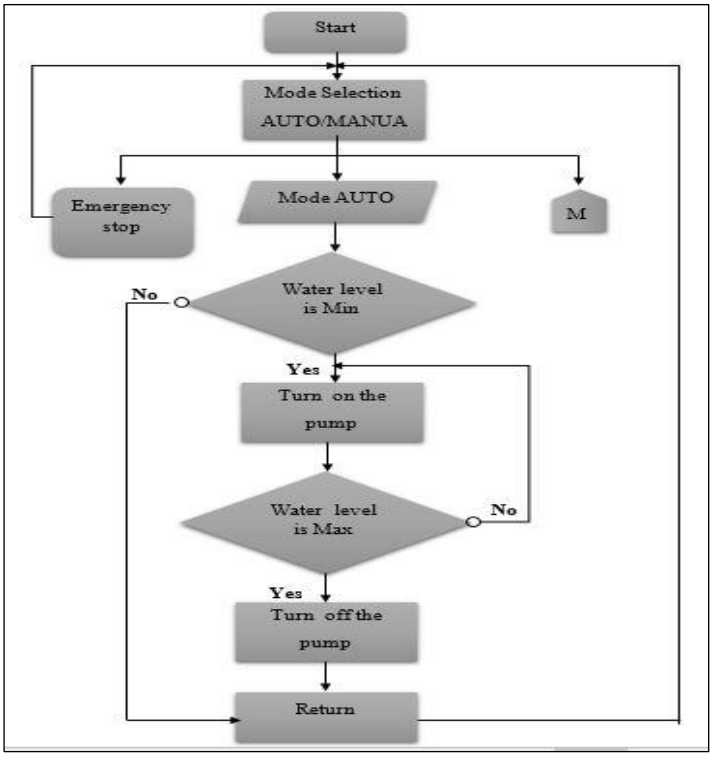

Figure 10.a: Tank filling system "AUTO-Mode"
Source: Authors (2025)

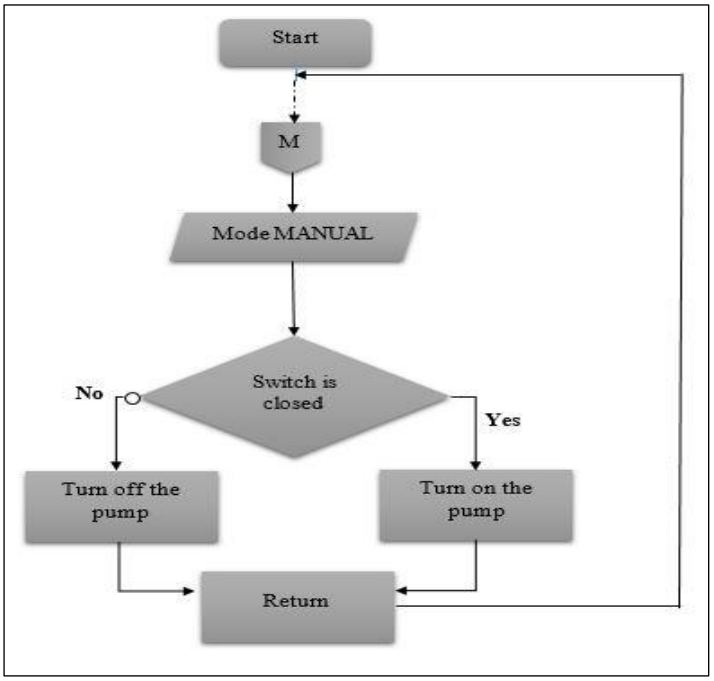

Figure 10.b: Tank filling system "MANUAL-Mode".
Source: Authors (2025).

XII. OUTDOOR LIGHTING

The role of this system and the outdoor lighting of the house; for this we use an LDR light sensor which has the same principle of the temperature sensor but here the sensor affected by the light and gives us a voltage value which depends on the lighting power.

We choose the value 300 (dusk) as a reference for the following rule: If the luminescent < =300 => turn on the lamp.

If not => turn off the lamp.

The following flowcharts represent the operation of this system (Figure 11b), (Figure 11a) MANUAL and AUTO mode respectively.

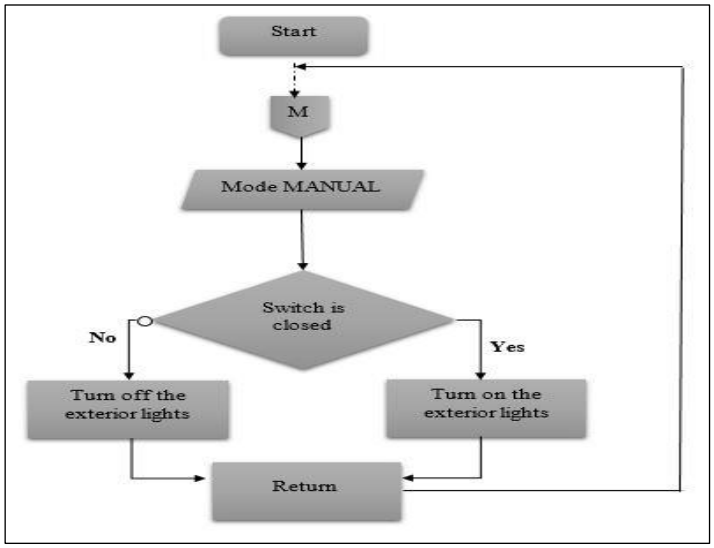

Figure 11.b : Exterior lighting system “MANUAL-Mode”
Source: Authors (2025

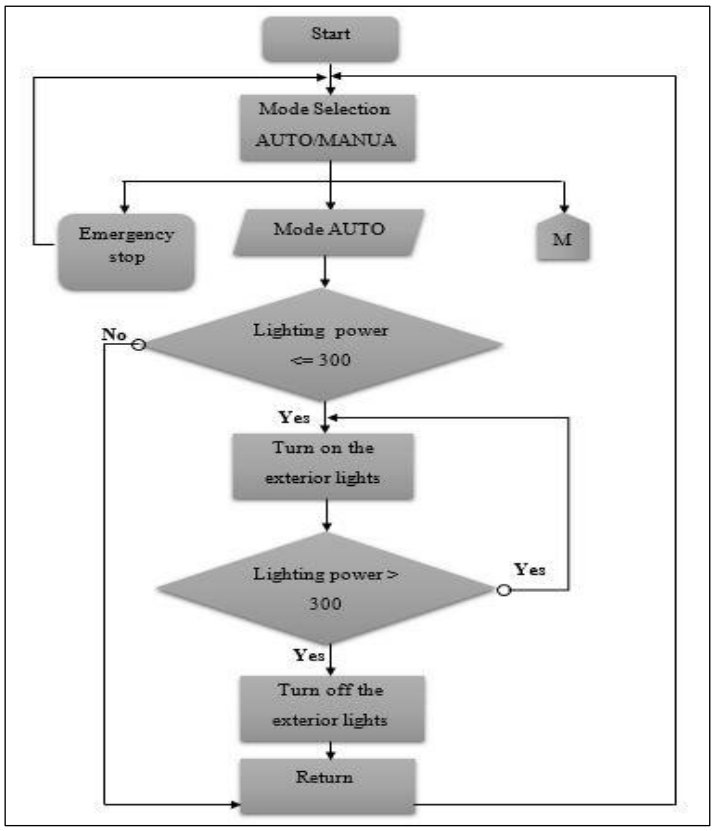

Figure 11.a: Exterior lighting system “AUTO-Mode”
Source: Authors (2025)

XIII. THE ALARM

The purpose of the alarm is security and ringing for the house. The switch connected to pin 11 decides one or the other; we use the same simulation rules.

The following flowchart represents the operation of this system (Figure12).

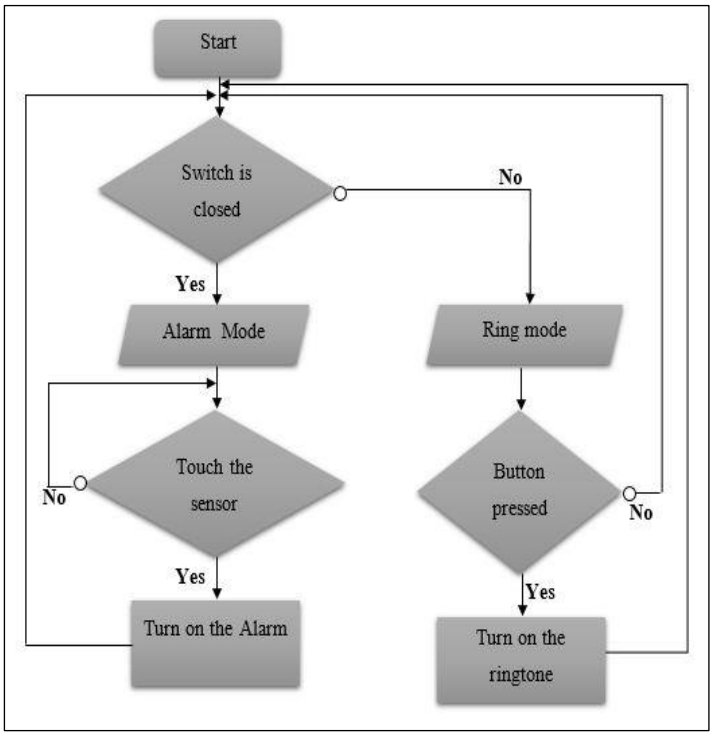

Figure 12: Alarm and bell system.
Source: Authors (2025).

XIV. RESULTS AND DISCUTIONS

We executed the ARDUINO program and we obtained the following results (Figure 13) (Figure 14).

Figure 13: ARDUINO system results
Source: Authors (2025)

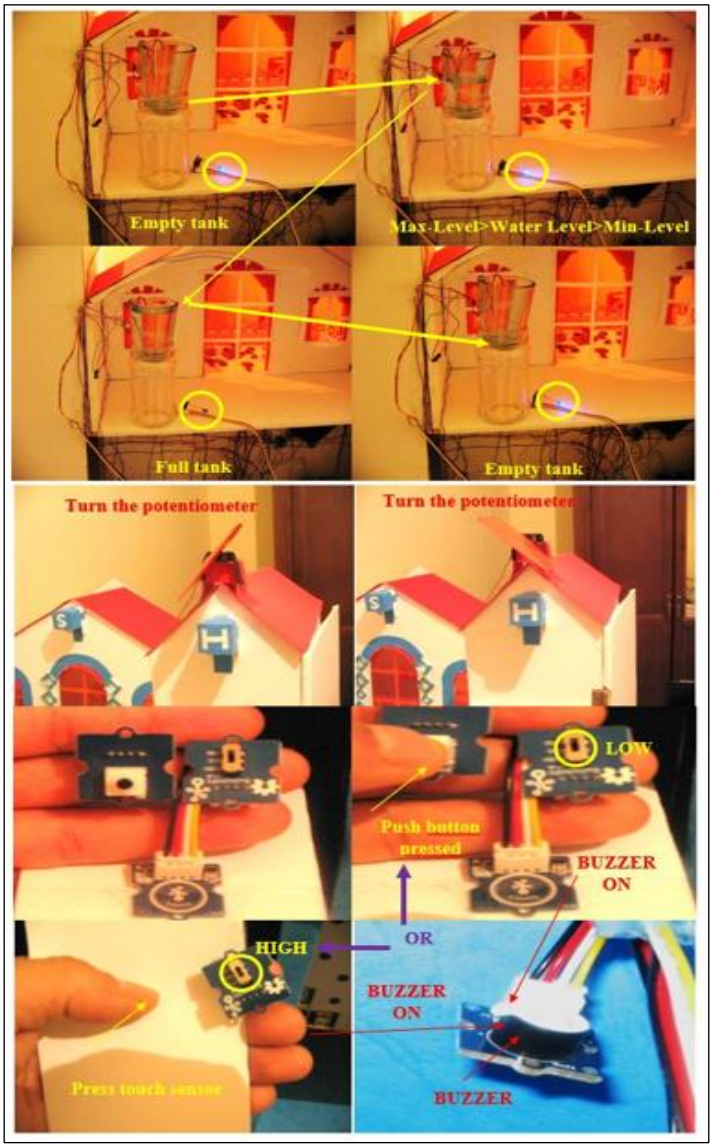

Figure 14: ARDUINO system results (folloing)
Source : Authors (2025)

The results obtained from the smart home prototype demonstrate the successful implementation and functionality of all the designed systems. Each component performed as expected, validating the effectiveness of the proposed approach. The temperature sensor effectively regulated the fan speed, ensuring optimal indoor comfort while conserving energy. Similarly, the water level sensor reliably monitored and maintained the water tank level, automating the refilling process and preventing overflows.

The outdoor lighting system, controlled by the light sensor, responded accurately to changes in ambient light, significantly reducing unnecessary energy consumption. The security alarm, activated by the tactile sensor, operated seamlessly, enhancing the safety features of the smart home prototype. Finally, the solar panel tracking system achieved precise orientation adjustments based on time, optimizing solar energy harvesting and demonstrating the potential for renewable energy integration in smart homes.

These results highlight the robustness and reliability of the Arduino-based design, confirming its suitability for real-world applications. The successful operation of the prototype underscores the effectiveness of sensor-based automation in addressing key aspects of energy efficiency, resource management, and home security. This success also provides a solid foundation for future enhancements.

XV. CONCLUSIONS

The implementation of the smart home prototype has been entirely successful, with all integrated systems functioning as intended. The automation of fan speed, water tank management, outdoor lighting, security alarm, and solar panel tracking has demonstrated the effectiveness and reliability of the proposed model. This success highlights the potential for Arduino-based systems to provide cost-effective and efficient solutions for smart home automation.

Looking ahead, we aim to expand the functionality of this model by incorporating voice control technologies. Future developments will focus on enabling voice-based control of additional home systems, such as air conditioning, television, and indoor lighting. This advancement will further enhance user convenience and the overall adaptability of the smart home system.

By building on the current achievements, this project sets a strong foundation for exploring advanced automation technologies and integrating them seamlessly into smart home applications.

XVI. AUTHOR'S CONTRIBUTION

Conceptualization: Soufiane Hachani and Okba Benelmir.
Methodology: Soufiane Hachani and Okba Benelmir.
Investigation: Soufiane Hachani and Okba Benelmir.
Discussion of results: Soufiane Hachani and Okba Benelmir.
Writing – Original Draft: Soufiane Hachani.
Writing – Review and Editing: Soufiane Hachani and Okba Benelmir.
Resources: Okba Benelmir..
Supervision: Okba Benelmir.
Approval of the final text: Soufiane Hachani and Okba Benelmir.

XVII. DISCLAIMER

The authors declare that they received no financial support or grants from any public, commercial, or non-profit entities for this research. All the views expressed in this work are solely those of the authors.

XVIII. REFERENCES

[1] A. Smith et al., "Smart homes and energy efficiency," *Journal of Sustainable Living*, vol. 12, no. 3, pp. 45-60, 2022. [Online]. Available: https://doi.org/xxxxxxx

[2] B. Williams et al., "IoT-based systems in modern homes," *International Journal of Smart Technologies*, vol. 8, no. 1, pp. 99-115, 2021. [Online]. Available: https://doi.org/xxxxxxx

[3] J. Li and S. Choi, "Arduino-based microcontroller applications," *Journal of Electronics and Automation*, vol. 5, no. 2, pp. 32-48, 2020. [Online]. Available: https://doi.org/xxxxxxx

[4] X. Wang and Y. Zhang, "Microcontroller advancements in smart homes," *Technology and Innovation Journal*, vol. 7, no. 4, pp. 56-74, 2020. [Online]. Available: https://doi.org/xxxxxxx

[5] L. Garcia and R. Martinez, "Automation and energy efficiency in modern homes," *Energy Efficiency Review*, vol. 9, no. 2, pp. 100-115, 2019. [Online]. Available: https://doi.org/xxxxxxx

[6] P. Miller and K. Smith, "The role of automation in energy-saving smart homes," *Journal of Home Automation*, vol. 11, no. 1, pp. 45-60, 2020. [Online]. Available: https://doi.org/xxxxxxx

[7] D. Johnson and J. Lee, "Temperature-based regulation in home automation systems," *Energy Conservation Journal*, vol. 13, no. 1, pp. 72-88, 2021. [Online]. Available: https://doi.org/xxxxxxx

[8] M. Oliver and T. White, "Dynamic energy regulation in smart homes," *Journal of Smart Building Systems*, vol. 10, no. 3, pp. 115-130, 2021. [Online]. Available: https://doi.org/xxxxxxx

[9] S. Kumar and V. Patel, "Water conservation through automated systems in homes," *Water Resources and Technology Journal*, vol. 6, no. 2, pp. 25-38, 2020. [Online]. Available: https://doi.org/xxxxxxx

[10] D. Nguyen and H. Tran, "Smart home systems for resource management," *Renewable Resources Journal*, vol. 12, no. 4, pp. 80-95, 2020. [Online]. Available: https://doi.org/xxxxxxx

[11] A. Davis and P. Taylor, "Efficient lighting systems in smart homes," *Journal of Lighting Technology*, vol. 14, no. 3, pp. 65-80, 2021. [Online]. Available: https://doi.org/xxxxxxx

[12] F. Ahmed and M. Khan, "Security and safety in smart homes," *Journal of Smart Security Systems*, vol. 7, no. 2, pp. 22-35, 2021. [Online]. Available: https://doi.org/xxxxxxx

[13] C. Ramirez and S. Perez, "Enhancing security through smart sensors," *International Journal of Security Technologies*, vol. 10, no. 1, pp. 58-72, 2021. [Online]. Available: https://doi.org/xxxxxxx

[14] L. Chen and F. Huang, "Solar panel orientation systems in smart homes," *Renewable Energy Technology Journal*, vol. 15, no. 3, pp. 105-120, 2022. [Online]. Available: https://doi.org/xxxxxxx

[15] G. Martin and J. Thompson, "Innovations in solar energy for smart homes," *Journal of Renewable Energy Solutions*, vol. 13, no. 4, pp. 150-165, 2021. [Online]. Available: https://doi.org/xxxxxxx

Journal of Engineering and Technology for Industrial Applications

ITEGAM-JETIA

Manaus, v.11 n.53, p. 62-69. May/June., 2025.

DOI: https://doi.org/10.5935/jetia. v11i53.1520

ISSN ONLINE: 2447-0228

RESEARCH ARTICLE OPEN ACCESS

DESIGN AND DEVELOPMENT OF NOVEL COOLING ARRANGEMENT FOR PV CELL

Keval Chandrakant Nikam[1], Amit Umbrajkar[2], Sandesh Solepatil[3], Vandana Patil[4], Chetan Pawar[5],Vedant Jirafe[6], Piyush Bhosale[7], Dhruv Res[8], Ayush More[9], Laxmikant Jathar[10], Sagar Shelare[11]

[1,2,3,4,5] Department of Mechanical Engineering, D Y Patil International Univerisity, Akurdi, Pune,India
[6,7,8,9]Department of Mechanical Engineering,Dr D Y Patil Institute of Engineering,Management and Research,Akurdi,Pune,India
[10]Department of Mechanical Engineering, Army Institute of Technology, Pune, India
[11]Mechanical Engineering Department, Priyadarshini College of Engineering, Hingna Road, Nagpur 440019, Maharashtra, India

[1]https://orcid.org/0000-0003-2628-9781, [2]https://orcid.org/0000-0002-9740-6677 , [3]https://orcid.org/0000-0002-8005-4994
[4]https://orcid.org/0000-0001-8729-4176, [5]https://orcid.org/0000-0002-2612-8171, [6]https://orcid.org/0009-0006-9829-3367
[7]https://orcid.org/0009-0002-3135-2159, [8]https://orcid.org/0009-0004-1209-0143, [9] https://orcid.org/0009-0006-6080-3798
[10]https://orcid.org/0000-0002-5755-9820, [11]https://orcid.org/0000-0002-3368-3587

Email: nikamkeval26@gmail.com, ameethumbrajkaar@gmail.com, sandeshpatil310@gmail.com, patil.vandana40@gmail.com, p.chetan0408@gmail.com, vedantjirafe@gmail.com, piyushbhosale2003@gmail.com , dhruv.res@gmail.com, ayushmore317@gmail.com, lax.jathar73@gmail.com, Sagmech24@gmail.com,

ARTICLE INFO

Article History
Received: January 1, 2025
Revised: January 20, 2025
Accepted: May 15, 2025
Published: May 31, 2025

Keywords:
photovoltaic cell,
polycrystalline,
baffles,
ethylene glycol,
evaporation rate.

ABSTRACT

The demand for sustainable energy has highlighted the importance of photovoltaic (PV) Cells in power generation. However, polycrystalline PV cell efficiency is hindered by temperature sensitivity. This leads to design a novel cooling system using cooling medium. The cooling system with and without baffles are preferred for experimentation. The ethylene glycol is in demand due to its availability and miscible nature in water at all concentration. The concentration of ethylene glycol is varied from 5%, 10%, 15% and 20% to study the evaporation rate of water. The requirement of water for cooling PV is also studied with and without adding ethylene glycol. With the help of ethylene glycol, the efficiency enhancement without compromising rate of evaporation is achieved. The outcome of the present paper indicates that efficiency of polycrystalline PV Cell is increased by 1.725% using novel cooling system with 20% of ethylene glycol concentration.

I. INTRODUCTION

Sunlight is open source of energy. The poly-crystalline photovoltaic cells (PV) are used to collect and convert this energy into electrical energy [1]. The solar energy is just the procurement of the sun's energy. It is noticed that 70 % to 80% solar radiation is wasted for heating of the environment and 5% to 20 % of the sun radiation is only converted to electricity for consumption and rest of is reflected to the environment [2]. The polycrystalline PV Cell have wide applications including Off-grid energy inception, businesses, manufacturing, as well as in domestic usage. The photovoltaic was first seen in plant life and its usage as food source converting the radiance into consumable energy. Later the various materials were studied which absorbs the radiance and converts the energy into electric energy. The mostly preferred materials used in solar panel are Gallium Nitride, Silicon, Cadmium telluride, Copper Indium Gallium Selenide (CIGS), and amorphous silicon. However, silicon is widely used for its remarkable properties in terms of efficiency up to 25% with perovskite-silicon heterojunction [3] and also due to availability [4]. The PV panel comes with different crystal structures of mono-crystalline, poly-crystalline, thin-film or perovskite and its selection depends on the working condition of surroundings [5]. The mono-crystalline silicon grants remarkable properties of imperishability and efficiency. The polycrystalline cells are made by melting silicon crystals together. In Thin-Film cell, the substrate is deposited with thin layer of Silicon. The perovskite consists of hybrid organic and inorganic material which mainly include methylammonium lead halides[6],[7].

The PV construction includes a variety of layers. When the sunlight strikes the surface of first layer the energy transfer take place in form of electrons this movement of electrons from one layer to another is cause of electric generation [8]. The highly sensitive nature of monocrystalline photovoltaic cell towards the temperature's variation as compared with amorphous and polycrystalline photovoltaic cells make it limited use in power generation. Also the fill factor and efficiency decrease with increase in temperature [9]. The limitation of PV cell is that when rise in temperature diminishing the output reduces the efficiency led to improvement of system. One of the major causes among all of them is heating and dust saturation on the panel.

The temperature change occurred on the surface of the PV cell is due to continuous exposure to sunlight and generation of electricity. This overheating phenomenon of PV cell leads to decrease overall efficiency of power generation. The overheating of the panel led to slackening of power output and life of panel. Consistent with review 1°C upsurge in surface temperature cause lessening of 0.5% efficiency [10]. The overheating PV cell is ended by the application of chilling systems and which leads to rise in output, reliability and longevity of the PV cell. This cooling effect could be achieved with various methods some of the techniques are active, passive cooling.

The natural factors affecting the heating of the panel are wind velocity, moisture, sunlight, atmospheric temperature and dust contained nearby. To apply restriction on the heating of panel the variety of cooling techniques are implemented [11]. The active cooling techniques includes coolant (usually fluid), this method of cooling also involve extrinsic mechanisms and systems such as fans. The active cooling techniques increases overall efficiency by consuming some energy in drawing fluid The passive cooling techniques are further sorted into three category's passive cooling with air, water, and conductive cooling. Passive would need supplementary equipment such as heat pipes and sinks to drive natural convection. Therefore, it is found be more implementable as compared to active cooling [12].

Many researcher focuses on use of nanofluids as coolant, however, nanofluids suffer from aggregation issues [13]. The combination of paraffin jelly and perlite segment improves the desired output [14]. In air-based cooling the effective amount of flow rate will assure desired temperature changes, this system assures an average reduction of temperature by 9°C. The temperature difference varies with flow rate of air, the enhancement of efficiency varies between 7 to 12.6 %. Overheating problems of solar panel are reduced by using air-based cooling system [15]. The liquid based cooling system include continuous flow of fluid through the system. A thin film of coolant is passed through system cause increase in efficiency and overall efficiency of solar panel observed to be 13.9% [16]. According to Li Zhu, Robert F Boehm, et.al. experimentation temperature of system liquid immersion cooling maintained temperature up-to 45°C, where 30°C inlet water temperature [17]. The sprinklers sprays on the water P.V. modules increasing the efficiency up to 13.5% in extreme weather environments [18]. Spraying on the solar panel cell reduces heating and improves performance by 1.35 – 3.26%. Application of heat pipe results in increment of efficiency 3.11% as compared to conventional system [19]. Materials used for heat pipes include copper, aluminum, etc. The fins in the systems usually fit at some angle which ranges from 0 to 40 degrees, this ensures more energy output. Electric efficiency achieved by system is 29% and temperature reduction occur is 28.95% [20]. In Evaporative cooling various fluids can be implemented but the most feasible one is silica gel. The reduction in temperature by silica gel came across 16%, and upscaled the panel efficiency by 8.76% [21]. Other methods involve Materials such as copper or aluminum must be stick behind the PV panel so that the heat gets distributed in all thermoelectric generators . The overall solar conversion efficiency was 40% [22]. There exists variety of gap in the field of cooling technology for photovoltaic cell.

The impact of cooling system on photovoltaic cell is studied reports suggested that there is need for better and efficient cooling system that can improve the performance. The first parameter raises concern towards durability and longevity of the cooling system. The next important criteria are use of water as coolant can increase efficiency at the cost of high evaporation rate. There are several studies available on cooling methods with natural or forced convection in the back of the panel. The mixture of water with ethylene glycol forms a coolant.

The use of ethylene glycol with water as coolant is favourable coolant medium due to it availability and thermal exergy efficiency. Several researchers varied different concentration of ethylene glycol in water from 50% to 60% to check the impact on PV cell efficiency [23-26]. The limited literature is available on consumption of water and its evaporation rate during cooling of PV cell. The present study focuses on water with ethylene glycol as coolant. The objective is to minimize evaporation rate by finding optimize concentration of ethylene glycol with water. The proposed setup integrates the usage of baffles on panel back and use of evaporative techniques to cool the reused coolant.

II. MATERIALS AND METHODS

The setup of cooling system is shown in Figure 1. The polycrystalline PV cell panel of capacity 75W was taken for study. It consists of polycrystalline PV panel with cooling system attached back of the panel. The cooling system arrangement consists of 45 baffles as shown in Figure 2. The cooling system is fitted at the panel back. The earthen vessel is customary made to ensure cooling of coolant coming after cooling the PV cell. The present solar panel efficiency = 14.17%. The three cases are considered for testing. The case 1 shown in Figure 3 is dry testing setup without any cooling system to examine the behaviour of panel efficiency with respect to increase in surface temperature of panel. The case 2 shown in Figure 4 consist of cooling of PV Cell with using water as a coolant to examine increase in the efficiency of panel. The case 3 shown in Figure 5 consist of cooling of PV cell with using ethylene glycol as a coolant to examine increase efficiency of the panel. The specification of components used is enlisted in table 1.The design calculation is tabulated in Table 2.

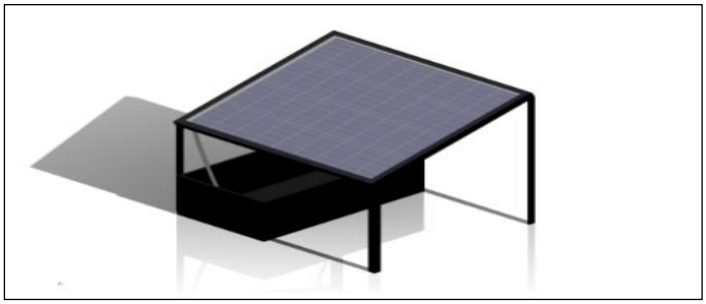

Figure 1: Isometric layout of setup.
Source: Authors, (2025).

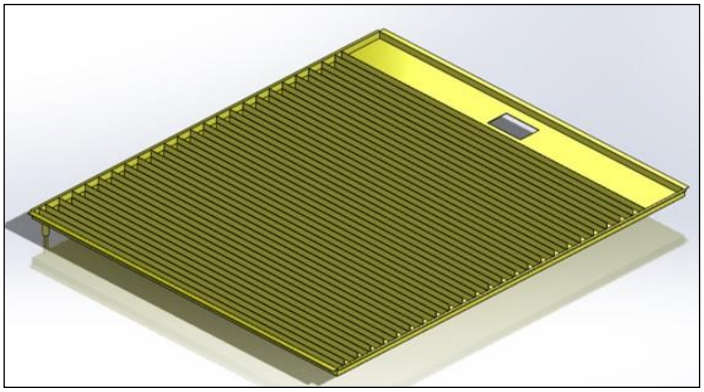

Figure 2: Cooling system with baffles.
Source: Authors, (2025).

Table 1: Specification of Components.

Sr. No.	Components	Specification
1	Polycrystalline PV Panel	75W, Size –780x670x30mm,8Kg Vmax -18.22V, Imax -4.29A
2	Frame	Mild steel
3	Panel Back with baffles	GI Sheet with zinc coating
4	Push connectors	Polybutylene Terephthalate
5	Tubes	Polybutylene Terephthalate
6	Water pump	12V DC solar water pump
7	Coolant Reservoir Tank	Terracotta Water Reservoir Tank
8	Synthetic Primer	Zinc chromate primer
9	Temperature Sensor	DS18B20 resolution up to 12 bits over a range of -55°C to +125°C
10	Arduino Uno	Arduino Uno R3 with ATmega328P microcontroller chip with Ju
11	Coolant	Ethylene Glycol • Solubility: Soluble in water and Miscible in all proportions • Boiling point:197.30C. • Specific Heat capacity: Ethylene glycol 30% by volume /water,700C (3.87) KJ/kg-K • Thermal Conductivity: 0.254 W/m-K at 300C

Source: Authors, (2025).

Table 2: Design Calculations.

Sr. No.	Design Parameters		Ref.
1	Heat gain by Water, q = m C_p dt		[27]
2	EVA silicon specific heat (C_p) =3135 J/Kg K		[27]
3	Flow rate, Q = A x V **For Water,** Water specific heat (C_{pw}) = 4180 J/kg k. ṁ = 6 lps q = 150480 J Diameter of pipe for water will be 61.644 mm	**For Ethylene Glycol:** ṁ = 0.0556 lps Diameter of pipe for Ethylene Glycol will be 8.822 mm	[28]
4	V = 0.91 m/s²		[28]
5	Efficiency $= \frac{\text{Panel Power (in kW)}}{\text{Panel Length x Panel Width (in m)}} \text{x } 100\%$		[29]
6	power output efficiency: Efficiency, $\eta_P = \frac{P_{mean}\ (\text{in kW})}{P_{max}(in\ kW)} \text{x } 100\%$		[29]
7	Performance ratio:		[29]
	Performance Ratio, PR $= \frac{P_{mean}\ (\text{in kW})/P_{max}(in\ kW)}{E_{mean}(in\ kW)} \text{x } 100\%$		
8	Maximum Power: $P_{max} = V_{max} \times I_{max}$ Measured Power: $P_{mean} = V_{mean} \times I_{mean}$		[30]

Source: Authors, (2025).

Figure3: Dry Testing Setup.
Source: Authors, (2025).

Figure 4: Wet Testing Setup with water
Source: Authors, (2025).

Figure 5: Wet Testing Setup with Ethylene Glycol.
Source: Authors, (2025).

III. RESULTS AND DISCUSSIONS

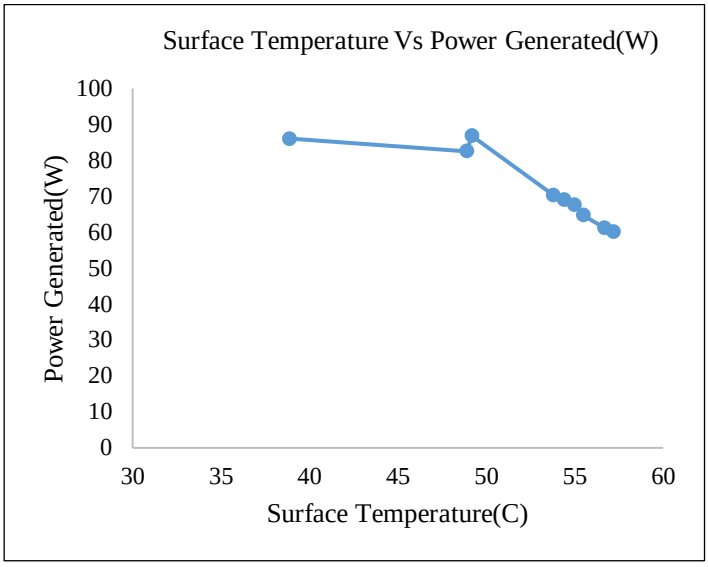

Figure 6: Surface Temperature Vs Power Generated.
Source: Authors, (2025).

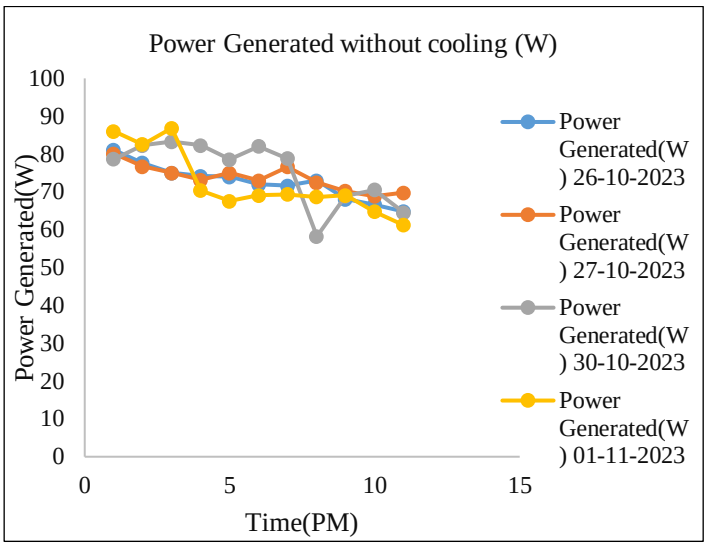

Figure 7: Power Generated without cooling.
Source: Authors, (2025).

The power generation data was recorded from month of October 2023 to May 2024. On 26/10/23, 27/10/23, 30/10/23, 4/4/24 data without cooling arrangement and data with cooling arrangement was recorded on 15/04/24, 17/04/24, 18/04/24, 19/04/24, 20/04/24, 21/04/24, 22/04/24, 23/04/24, 24/04/24, 25/04/24, 26/04/24, 27/04/24, 28/04/24. The Figure 6 indicates that power generation decreases with an increase in surface temperature. At lower surface temperatures (~35°C), power generation remains high (~100 W). As surface temperature rises to 55°C, power generation declines significantly (~60 W). This suggests that the system's efficiency is inversely proportional to surface temperature. Effective cooling mechanisms are crucial to maintaining higher power generation levels.

The Figure7 indicates that power generation without cooling decreases gradually over time during the day across all dates (26-10-2023, 27-10-2023, 30-10-2023, and 01-11-2023). Peak power generation (~90 W) occurs early in the day but declines to ~60 W later in the afternoon due to rising ambient and surface temperatures.

Table 3: (Test Data from 24/04/24, 25/04/24,28/04/24 With Cooling Arrangement).

	24/04/24 (20% Concentratio)		25/04/24 (20% Concentration)		28/04/24 (5% Concentration)	
Time(PM)	Surface Temp.	Power(P=I^2*R)	Surface Temp.	Power(P=I^2*R)	Surface Temp.	Power(P=I^2*R)
8:15 AM	38.46	12.9	-	-	38.86	20.0
8:30 AM	40.56	4.67	39.6	12.67	40.56	29.4
8:45 AM	42.63	9.28	41	15.03	43.2	32.7
9:00 AM	44.69	9.95	38.13	38.20	41.3	33.2
9:15 AM	46.19	33.1	37.75	43.28	39.19	41.2
9:30 AM	48	41.6	37.88	45.95	39.94	47.3
9:45 AM	45.25	38.7	38.63	51.22	41.44	50.0
10:00 AM	48.6	39.4	39.38	53.91	38	54.9
10:15 AM	50.75	40.8	41.69	57.51	38	60.5
10:30 AM	53.54	45.9	40.13	62.24	38.13	63.1
10:45 AM	56.74	44.7	41.25	64.17	39.13	64.8
11:00 AM	58.5	63.1	41.36	67.29	39.13	67.2
11:15 AM	52.5	66.7	41.96	68.92	42.02	69.0
11:30 AM	41	70.8	43.63	70.99	43.2	71.0
11:45 AM	42.25	71.7	45.19	71.65	44.2	70.9
12:00 PM	42.25	72.3	45.19	72.06	44.38	71.2
12:15 PM	42.85	60.0	45.19	71.84	46.1	71.3
12:30 PM	43.88	31.5	44.6	76.81	46.25	70.8
12:45 PM	43.25	58.4	45.04	74.74	47.06	71.9
1:00 PM	43.25	70.9	45.17	77.17	47.25	68.6
1:15 PM	43.69	73.22	45.23	79.98	46.6	69.1
1:30 PM	43.76	75.33	45.23	80.85	45.2	63.4
1:45 PM	44	70.41	45.86	76.86	47.75	64.5
2:00 PM	44.23	77.469	45.53	62.04	45.8	51.8
2:15 PM	44.23	69.92	45.16	59.61	46.13	55.9
2:30 PM	44.69	62.25	44.5	57.61	42.85	16.5
2:45 PM	44.2	66.47	41.32	55.34	42.5	57.5
3:00 PM	43.67	53.55	43.67	53.09	43	46.0
3:15 PM	43.55	49.26	43.55	48.98	43.96	55.6
3:30 PM	43.13	46.67	43.13	46.42	44.25	56.3
3:45 PM	43.13	42.49	43.13	42.20	45	57.3
4:00 PM	42.89	41.94	42.89	41.69	45	54.2
4:15 PM	42.62	40.46	42.62	40.46	45	52.0
4:30 PM	41.9	44.09	41.9	44.01	44	47.2

Source: Authors, (2025).

The Table 3, 4 and 5 gives an ideology that sun radiance heats the panel with energy conversation and lead to the degradation of efficiency. Also, with use of alternative cooling methods the conversion of energy from radiance to useable energy could be converted. Here the application of Ethylene Glycol with water in different percentage had increase the efficiency and power output on a scalable factor. The different percentage of concentration of Ethylene Glycol is used to reduce the evaporation rate of water as seen rate of evaporation is decrease by 25% for 5% Ethylene Glycol with water. Alternatively, the combination of Ethylene Glycol and Water at different concentration are studied 10%, 15% & 20%. From which the 20% concentration of Ethylene Glycol is mention and efficiency is calibrated.

Table 4: (Consumption of Cooling Fluid).

Date	Total water used for test (L)	Concentration of Ethylene glycol (%)	Total Fluid after end of the day (L)	Loss of fluid (L)
21/04	40	5	30	10
22/04	40	10	32	8
23/04	40	15	33.5	6.5
24/04	40	20	35	5
25/04	35	20	30	5
26/04	40	15	33.5	6.5
27/04	40	10	32	8
28/04	40	5	30	10

Source: Authors, (2025).

Table 5: (Consumption of Water and Ethylene Glycol).

Date	Remaining Water (L)	Remaining Ethylene glycol (L)	Consumption of Water (L)	Consumption of Ethylene glycol (L)
21/04	28.5	1.5	9.5	0.5
22/04	28.8	3.2	7.2	0.8
23/04	28.475	5.025	5.525	0.975
24/04	28	7	4	1
25/04	24	6	4	1
26/04	28.475	5.025	5.525	0.975
27/04	28.8	3.2	7.2	0.8
28/04	28.5	1.5	9.5	0.5

Source: Authors, (2025).

5% Concentration: On 21-04-2024 and 28-04-2024, the total fluid loss is 10 L per day, with 30 L remaining at the end of the day. This indicates a consistent rate of fluid loss. Daily water consumption is 9.5 L, and ethylene glycol consumption is 0.5 L. This suggests a higher water-to-glycol consumption ratio compared to other concentrations.

10% Concentration: On 22-04-2024 and 27-04-2024, the fluid loss increases to 8 L per day, leaving 32 L at the end of the day. The slightly higher fluid retention compared to 5% concentration might suggest improved system efficiency. Daily water consumption decreases to 7.2 L, and ethylene glycol consumption rises to 0.8 L. The increased glycol consumption indicates better thermal performance and reduced water evaporation.

15% Concentration: On 23-04-2024 and 26-04-2024, fluid loss reduces to 6.5 L, with 33.5 L remaining at the end of the day. This concentration achieves the lowest fluid loss among all tested values. Water consumption further decreases to 5.525 L per day, with ethylene glycol consumption at 0.975 L. The ratio indicates an optimal balance, resulting in lower fluid loss overall.

20% Concentration: On 24-04-2024 and 25-04-2024, fluid loss is 5 L, with 35 L remaining at the end of the day. The least fluid loss observed at this concentration highlights its effectiveness in minimizing coolant consumption. Water consumption reduces to 4 L, while ethylene glycol consumption increases to 1 L. This concentration achieves the most efficient water usage, with higher glycol

Power generation plots without providing cooling are plotted with the help of experimental data to get insights such as maximum power generated and behavior of power generation with respect to time.

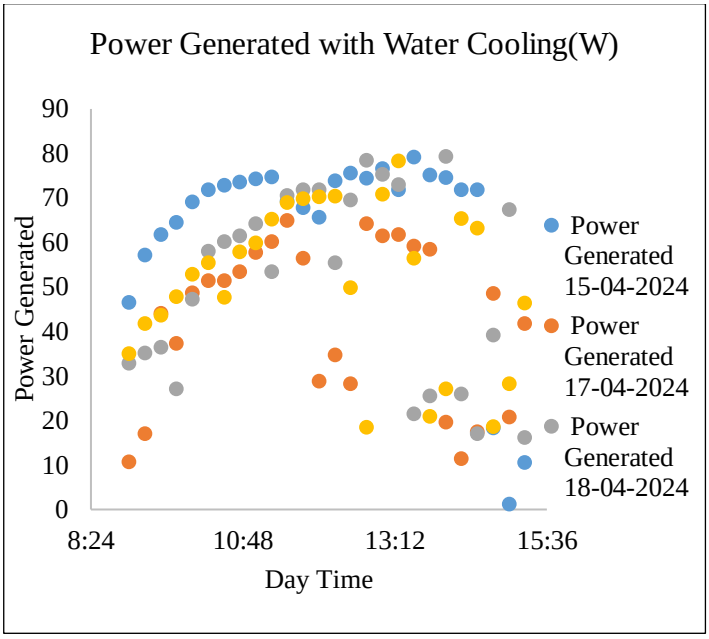

Figure 8: Power Generated with water cooling.
Source: Authors, (2025).

This Figure 8 represents power generation with water cooling across different times of the day on two dates: April 15, 2024, and April 17, 2024. Power generation increases gradually in the morning (starting from around 8:24) and reaches its peak during midday (near 13:12). A decline in power generation is observed as the day progresses into the afternoon (by 15:36). April 15, 2024 (Blue Data Points): The power generated consistently trends higher, with values reaching closer to 80–90 W during peak hours. April 17, 2024 (Orange Data Points): Power generation appears lower overall, with fewer instances exceeding 70 W and scattered data points indicating more variability. Water cooling may influence peak power generation positively, as seen with the higher outputs around midday. The variability in data between the two days could suggest external factors like environmental conditions (e.g., temperature, sunlight availability) affecting the system.

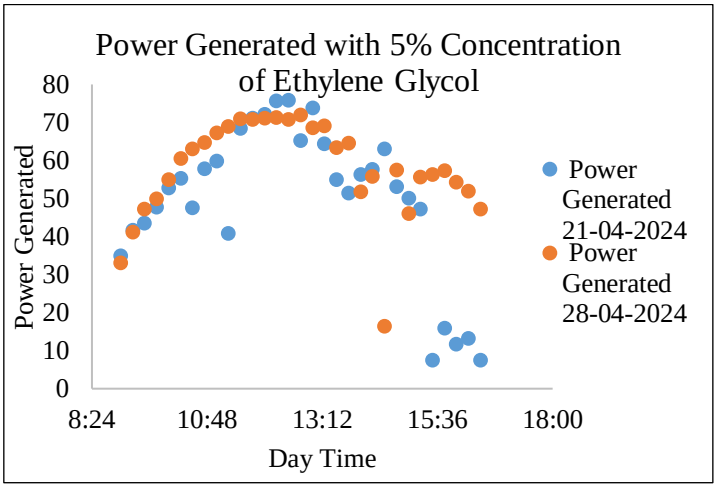

Figure 9: Power Generated with 5% Concentration of Ethylene Glycol
Source: Authors, (2025).

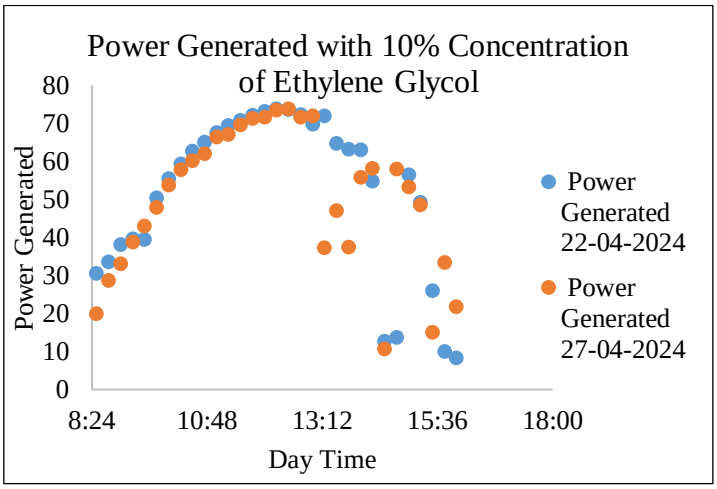

Figure 10: Power Generated with 10% Concentration of Ethylene Glycol
Source: Authors, (2025).

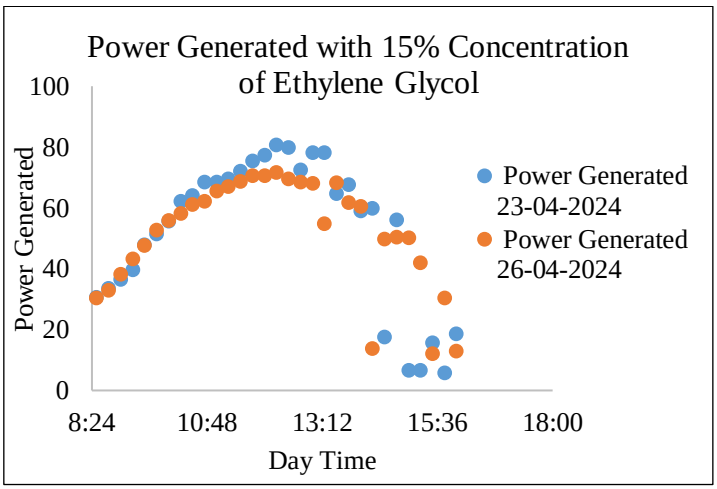

Figure 11: Power Generated with 15% Concentration of Ethylene Glycol
Source: Authors, (2025).

The figures 9,10 and 11 illustrate the power generated at varying concentrations of ethylene glycol (5%, 10%, 15%, and 20%) over two distinct days for each concentration.

5% Concentration: Power generation peaks between 10:48 and 13:12 for both days (21-04-2024 and 28-04-2024), with values reaching approximately 70 W.A sharp decline in power generation is observed after 13:12.Power generation on 28-04-2024 is lower across the day compared to 21-04-2024.

10% Concentration: The peak power generation increases slightly compared to the 5% concentration, reaching approximately 75 W. Similar temporal trends are observed, with a peak around 13:12 and a decline thereafter. Power generated on 27-04-2024 is consistently lower than on 22-04-2024.

15% Concentration: Power generation reaches nearly 90 W, indicating a further increase with higher ethylene glycol concentration. The trend of power peaking around 13:12 is consistent. Power generated on 26-04-2024 is slightly lower than on 23-04-2024.

20% Concentration: The highest power generation is recorded at this concentration, peaking near 100 W. The decline in power generation post-peak is more gradual compared to lower concentrations. Data for 25-04-2024 shows slightly reduced power compared to 24-04-2024.

Increasing the concentration of ethylene glycol from 5% to 20% results in higher peak power generation, demonstrating a positive correlation between concentration and power output. Across all concentrations, power generation follows a consistent diurnal pattern, peaking during midday and declining in the late afternoon. For each concentration, the second day consistently shows reduced power generation compared to the first, potentially due to variations in environmental factors such as temperature, sunlight intensity, or system efficiency.

IV. CONCLUSIONS

Fluid loss decreases as the concentration of ethylene glycol increases, with 20% concentration exhibiting the least loss (5 L/day). The reduced fluid loss suggests that higher glycol concentrations are more effective in reducing evaporation and leaks. Water consumption decreases progressively from 9.5 L/day at 5% concentration to 4 L/day at 20% concentration. Ethylene glycol consumption increases proportionally, with higher concentrations ensuring better thermal performance and fluid retention. The 20% concentration demonstrates the best results in terms of minimal fluid loss and efficient consumption of both water and ethylene glycol. While the 15% concentration also shows promising results, it slightly underperforms compared to 20%.

The study also highlights that the influence of ethylene glycol concentration on power generation efficiency. The 20% concentration yields the highest power output, suggesting it as the most effective concentration within the tested range. However, environmental and operational conditions appear to impact daily performance, necessitating further investigation to optimize the system for consistent power generation. The future research focuses on optimizing cooling designs, evaluating environmental impacts, and exploring advanced technologies to achieve consistent and efficient performance.

VI. AUTHOR'S CONTRIBUTION

Conceptualization: Keval Chandrakant Nikam, Vedant Jiraffe,Piyush Bhosale
Methodology: Dhruv Res, Aayush More.
Investigation: Vedant Jiraffe,Piyush Bhosale, Dhruv Res, Aayush More.

Discussion of results: Keval Chandrakant Nikam,Sandesh Solepatil,Vandana Patil,Chetan Pawar
Writing – Original Draft: Keval Chandrakant Nikam.
Writing – Review and Editing: Amit Umbrajkar,Laxmikant Jathar, Sagar Shelare.
Resources: Vedant Jiraffe.
Supervision: Laxmikant Jathar,Sagar Shelare.
Approval of the final text: Keval Chandrakant Nikam, Amit Umbrajkar, Sandesh Solepatil, Vandana Patil, Chetan Pawar,Vedant Jirafe,Piyush Bhosale,Dhruv Res,Ayush More, Laxmikant Jathar,Sagar Shelare

VII. ACKNOWLEDGMENTS

Authors are thankful to the management of D Y Patil International University, Akurdi, Pune for providing research facility.

VIII. REFERENCES

[1]. Kalogirou, S.A.: Chapter 1 - Introduction to Renewable Energy Powered Desalination. Presented at the (2018). https://doi.org/https://doi.org/10.1016/B978-0-12-815244-7.00001-5.

[2]. Tripanagnostopoulos, Y.: 3.08 - Photovoltaic/Thermal Solar Collectors. Presented at the (2012). https://doi.org/https://doi.org/10.1016/B978-0-08-087872-0.00308-5.

[3]. Nikitina, V., Reichel, C., Erath, D., Kirner, S., Richter, A., Rößler, T., De Rose, A., Kraft, A., Neuhaus, H.: Shingling meets perovskite-silicon heterojunction tandem solar cells. Sol. Energy Mater. Sol. Cells. 263, 112590 (2023). https://doi.org/https://doi.org/10.1016/j.solmat.2023.112590.

[4]. Xu, C., Isabella, O., Vogt, M.R.: Future material demand for global silicon-based PV modules under net-zero emissions target until 2050. Resour. Conserv. Recycl. 210, 107824 (2024). https://doi.org/https://doi.org/10.1016/j.resconrec.2024.107824.

[5]. Preet, S., Smith, S.T.: A comprehensive review on the recycling technology of silicon based photovoltaic solar panels: Challenges and future outlook. J. Clean. Prod. 448, 141661 (2024). https://doi.org/https://doi.org/10.1016/j.jclepro.2024.141661.

[6]. Li, A., Zou, S., Peng, C.-W., Ni, M., Dai, L., Han, W., Lu, Z., Chen, Z., Su, X.: Improving the light trapping ability and flexural strength of ultrathin monocrystalline silicon wafers with submicron pyramid textures. Sol. Energy Mater. Sol. Cells. 271, 112847 (2024). https://doi.org/https://doi.org/10.1016/j.solmat.2024.112847.

[7]. Maalouf, A., Okoroafor, T., Jehl, Z., Babu, V., Resalati, S.: A comprehensive review on life cycle assessment of commercial and emerging thin-film solar cell systems. Renew. Sustain. Energy Rev. 186, 113652 (2023). https://doi.org/https://doi.org/10.1016/j.rser.2023.113652.

[8]. Lu, Y., Hao, Z., Feng, S., Shen, R., Yan, Y., Lin, S.: Direct-Current Generator Based on Dynamic PN Junctions with the Designed Voltage Output. iScience. 22, 58–69 (2019). https://doi.org/https://doi.org/10.1016/j.isci.2019.11.004.

[9]. Ouédraogo, A., Zouma, B., Ouédraogo, E., Guissou, L., Bathiébo, D.J.: Individual efficiencies of a polycrystalline silicon PV cell versus temperature. Results Opt. 4, 100101 (2021). https://doi.org/https://doi.org/10.1016/j.rio.2021.100101.

[10]. Siecker, J., Kusakana, K., Numbi, B.P.: A review of solar photovoltaic systems cooling technologies. Renew. Sustain. Energy Rev. 79, 192–203 (2017). https://doi.org/https://doi.org/10.1016/j.rser.2017.05.053.

[11]. Sohail, A., Rusdi, M.S., Waseem, M., Abdullah, M.Z., Pallonetto, F., Sultan, S.M.: Cutting-edge developments in active and passive photovoltaic cooling for reduced temperature operation. Results Eng. 23, 102662 (2024). https://doi.org/https://doi.org/10.1016/j.rineng.2024.102662.

[12]. Elnaby Kabeel, A., El Hadi Attia, M., Abdelgaie, M., Khelifa, A., Abdel-Aziz, M.M.: Experimental study on energy and exergy assessments of a new PV system with a concave cover for active cooling and self-cleaning. Renew. Energy Focus. 47, 100512 (2023). https://doi.org/https://doi.org/10.1016/j.ref.2023.100512.

[13]. Shu, L., Zhang, J., Fu, B., Xu, J., Tao, P.: Ethylene glycol-based solar-thermal fluids dispersed with reduced graphene oxide. 10282–10288 (2019). https://doi.org/10.1039/c8ra09533g.

[14]. Govindasamy, D., Kumar, A.: Experimental analysis of solar panel efficiency improvement with composite phase change materials. Renew. Energy. 212, 175–184 (2023). https://doi.org/https://doi.org/10.1016/j.renene.2023.05.028.

[15]. Patil, M., Sidramappa, A., Shetty, S.K., Hebbale, A.M.: Experimental study of solar PV/T panel to increase the energy conversion efficiency by air cooling. Mater. Today Proc. 92, 309–313 (2023). https://doi.org/https://doi.org/10.1016/j.matpr.2023.05.007.

[16]. Sainthiya, H., Beniwal, N.S.: Different Types of Cooling Systems Used in Photovoltaic Module Solar System : A Review. 1500–1506 (2017).

[17]. Zhu, L., Boehm, R.F., Wang, Y., Halford, C., Sun, Y.: Water immersion cooling of PV cells in a high concentration system. Sol. Energy Mater. Sol. Cells. 95, 538–545 (2011). https://doi.org/10.1016/j.solmat.2010.08.037.

[18]. Ashok Kumar, L., Indragandhi, V., Teekaraman, Y., Kuppusamy, R., Radhakrishnan, A.: Design and Implementation of Automatic Water Spraying System for Solar Photovoltaic Module. Math. Probl. Eng. 2022, 7129610 (2022). https://doi.org/https://doi.org/10.1155/2022/7129610.

[19]. Nakkaew, S., Chitipalungsri, T., Ahn, H.S., Jerng, D.-W., Asirvatham, L.G., Dalkılıç, A.S., Mahian, O., Wongwises, S.: Application of the heat pipe to enhance the performance of the vapor compression refrigeration system. Case Stud. Therm. Eng. 15, 100531 (2019). https://doi.org/https://doi.org/10.1016/j.csite.2019.100531.

[20]. Torbatinezhad, A., Rahimi, M., Ranjbar, A.A., Gorzin, M.: Performance evaluation of PV cells in HCPV/T system by a jet impingement/mini-channel cooling scheme. Int. J. Heat Mass Transf. 178, 121610 (2021). https://doi.org/https://doi.org/10.1016/j.ijheatmasstransfer.2021.121610.

[21]. Hamed, M.H., Hassan, H., Ookawara, S., Nada, S.A.: PV thermal regulation and water harvesting hybrid system using evaporative cooling of silica gel layer. Process Saf. Environ. Prot. 181, 243–265 (2024). https://doi.org/https://doi.org/10.1016/j.psep.2023.11.009.

[22]. Parthiban, R., Ponnambalam, P.: An Enhancement of the Solar Panel Efficiency : A Comprehensive Review. 10, 1–15 (2022). https://doi.org/10.3389/fenrg.2022.937155.

[23]. Kazemian, A., Hosseinzadeh, M., Sardarabadi, M., Passandideh-Fard, M.: Experimental study of using both ethylene glycol and phase change material as coolant in photovoltaic thermal systems (PVT) from energy, exergy and entropy generation viewpoints. Energy. 162, 210–223 (2018). https://doi.org/10.1016/j.energy.2018.07.069.

[24]. Sandhya, M., Ramasamy, D., Kadirgama, K., Harun, W.S.W., Saidur, R.: Experimental study on properties of hybrid stable & surfactant-free nanofluids GNPs/CNCs (Graphene nanoplatelets/cellulose nanocrystal) in water/ethylene glycol mixture for heat transfer application. J. Mol. Liq. 348, 118019 (2022). https://doi.org/https://doi.org/10.1016/j.molliq.2021.118019.

[25]. Upadhyay, V., Rashmi, Himanshu Khadloya, P., Raja Sekhar, Y., D Sai Anoop Reddy, A., Reddy, B.: Experimental studies on solar flat plate collector with internally grooved tubes using aqueous ethylene glycol. Appl. Sol. Energy. 53, 222–228 (2017). https://doi.org/10.3103/S0003701X17030112.

[26]. Hemmat Esfe, M., Saedodin, S., Mahian, O., Wongwises, S.: Thermal conductivity of Al2O3/water nanofluids. J. Therm. Anal. Calorim. 117, 675–681 (2014). https://doi.org/10.1007/s10973-014-3771-x.

[27]. Ruiz-reina, E., Sidrach-de-cardona, M., Piliougine, M.: Heat Transfer and Working Temperature Field of a Photovoltaic Panel under Realistic Environmental Conditions. COMSOL Conf. 1–26 (2014).

[28]. Ciano, T., Ferrara, M., Babanezhad, M., Khan, A., Marjani, A.: Prediction of velocity profile of water based copper nanofluid in a heated porous tube using CFD and genetic algorithm. Sci. Rep. 11, 10623 (2021). https://doi.org/10.1038/s41598-021-90201-x.

[29]. Jean, J., Brown, P.R., Jaffe, R.L., Buonassisi, T., Bulović, V.: Pathways for

solar photovoltaics. Energy Environ. Sci. 8, 1200–1219 (2015). https://doi.org/10.1039/C4EE04073B.

[30]. Ogbulezie, J.C., Njok, A.O., Panjwani, M.K., Panjwani, S.K.: The impact of high temperature and irradiance source on the efficiency of polycrystalline photovoltaic panel in a controlled environment. 10, 3942–3947 (2020). https://doi.org/10.11591/ijece.v10i4.pp3942-3947.

Journal of Engineering and Technology for Industrial Applications

ITEGAM-JETIA

Manaus, v.11 n.53, p. 70-75. May/June., 2025.
DOI: https://doi.org/10.5935/jetia. v11i53.1532

ISSN ONLINE: 2447-0228

RESEARCH ARTICLE OPEN ACCESS

NUMERICAL ANALYSIS OF HYGROTHERMAL EFFECTS ON LOW-VELOCITY IMPACT CONTACT FORCE IN S-GLASS/POLYESTER COMPOSITE PLATES

Mustapha Rabouh[1], Kamel Zouggar[2] and Khelifa Guerraiche[3]

[1] Laboratory of Development in Mechanics and Materials (LDMM) University of Djelfa , Algeria
[2] Laboratory of Mechanics of Structures and Solids (LMSS)Faculty of Technology, Djillali Liabès University of Sidi Bel-Abbès, Algeria.
[3] Mechanical Engineering Department, Faculty of Technology, University of Batna 2, Batna, Algeria NMISSI Laboratory, Faculty of Science and Technology, Biskra University, Biskra, Algeria.

[1]https://orcid.org/0009-0003-2657-0714, [2]https://orcid.org/0000-0001-8495-3754, [3]https://orcid.org/0000-0002-6759-0602

Email: mustapha.rabouh@univ-djelfa.dz, zouggarkamel.zk@gmail.com, guer.khelifa@yahoo.com

ARTICLE INFO

Article History
Received: January 5, 2025
Revised: January 20, 2025
Accepted: May 15, 2025
Published: May 31, 2025

Keywords:
Aged composite
Impact
Design of Experiments (DOE)
Hygrothermal conditions
Numerical simulation.

ABSTRACT

Bonded fiber-reinforced polymer (FRP) composites, particularly CFRP, are widely utilized in structural applications due to their lightweight and sustainable properties. However, their long-term performance is compromised under environmental conditions that introduce moisture and thermal stresses, leading to hygrothermal effects. This study investigates the influence of hygrothermal environments on the contact force of S-glass fiber-reinforced polyester composite plates subjected to low-velocity impact. The research employs finite element modeling using ABAQUS/Explicit to simulate impact behaviors and validate the results against experimental data for aged and non-aged samples. Additionally, a Design of Experiments (DOE) approach is implemented via MODDE 5 software to analyze key parameters and develop a predictive mathematical model. The findings aim to bridge knowledge gaps in understanding the durability and impact response of composite materials in adverse environments, providing insights for structural health monitoring and design optimization.

I. INTRODUCTION

Bonded fiber-reinforced polymer composites (CFRP) have become increasingly popular in various fields, including mechanical and civil engineering, due to their potential for lightweight, sustainable construction solutions, particularly as structural elements like beams and columns [1]. However, CFRP materials face challenges when exposed to environmental factors that introduce moisture and temperature gradients, impacting their long-term performance [2].

Studies have been conducted to assess the behavior of FRP composites under diverse environmental conditions [3],[4]. Despite these efforts, certain harsh environmental impacts on bond durability such as water immersion, high humidity, and freeze-thaw cycles are not yet fully understood [5]. The durability of CFRP under moisture exposure is primarily governed by the rate of water and ion diffusion, as ions rely on water as a transport medium [6]. This diffusion affects the material interfaces, leading to hygrothermal stresses. Moisture absorption at bonded interfaces and within the constituent materials raises the need for a more detailed understanding of its impact. Modeling these diffusion effects has proven challenging, with limited success in translating findings into simulation analyses [7].

Research has recently begun focusing on how environmental parameters impact shock absorption and safety in CFRP for structural health monitoring [8]. The literature highlights a gap in studies on low-velocity impact responses of composites under controlled hygrothermal environments. Impact modeling typically produces contact stresses (impact forces) that may cause matrix cracking or delamination in composite materials [4]. Prolonged exposure to thermal and moisture stresses can further compromise the longevity of these structures.

This study thus focuses on modeling and analyzing the effects of hygrothermal environments on the contact force of S-glass fiber-reinforced polyester composite plates subjected to low-velocity impact, using the finite element software ABAQUS/Explicit. The analysis is divided into two phases: the

first phase involves creating a numerical model of low-velocity impact and comparing the results with experimental data on aged and non-aged plates under environmental effects [8]. In the second phase, the numerical results are integrated into MODDE 5 software [9] to establish a Design of Experiments (DOE) framework, identifying key influencing parameters and developing a mathematical model to describe the contact force within the domain under study.

II. NUMERICAL MODELLING PROCEDURES

II.1 MATERIAL

In order to verify the validity of the numerical modeling with the experimental findings presented in [8], a composite plate using C3D8R elements is subjected to low-velocity impact by a projectile with a hemispherical tip. To achieve this, a numerical simulation model is developed using the finite element code ABAQUS/Explicit, which is designed to account for all relevant problem variables, along with the integration of an implemented subroutine (VUMAT) (Figure 1). The S-Glass/Polyester plates are modeled with a stacking sequence of (0°3/90°3) and dimensions of 150×100×4.5mm3. Further details regarding the material structure and modeling techniques can be found in references [8],[10].

The material properties and diffusivity constants along the three primary axes are presented in Table 1. The diffusivities for unidirectional composites are defined as follows:

Table 1: Mechanical and hygrothermal properties of S-Glass/Epoxy Plate.

Fibre Vf	3.40000E-01	$^{+}S_1$ (MPa)	1.56060E+03
Thickness (mm)	0.00000E+00	$^{+}S2$ (MPa)	5.49168E+01
E11 (MPa)	3.19141E+04	$^{-}S_1$ (MPa)	-8.32999E+02
E22 (MPa)	6.64106E+03	$^{-}S_2$ (MPa)	-2.69726E+02
E33 (MPa)	6.64106E+03	S_{12} (MPa)	1.12859E+02
G12 (MPa)	2.27120E+03	$^{+}e_1$ (mm/mm)	4.89000E-02
G13 (MPa)	2.27120E+03	$^{+}e_2$ (mm/mm)	8.26928E-03
G23 (MPa)	2.17689E+03	$^{-}e_1$ (mm/mm)	-2.61013E-02
NU12	3.10628E-01	$^{-}e_2$ (mm/mm)	-4.06149E-02
NU13	3.10628E-01	e_{12} (mm/mm)	4.96914E-02
NU23	5.21721E-01	K_1 (W/mm/K)	5.57763E-04
CTE1 (mm/mm/C)	2.48764E-05	K_2 (W/mm/K)	1.66348E-04
CTE2 (mm/mm/C)	2.23585E-04	K_3 (W/mm/K)	1.66348E-04
CTE3 (mm/mm/C)	2.23585E-04	Density (g/mm3)	1.60488E-03
D11=D22=D33 mm2/s,	3.06000 E-12		

Source: Authors, (2025).

$$\begin{cases} D_x = D_{11}: \text{Diffusivity parallel to the fiber direction in a lamina;} \\ D_y = D_{22}: \text{Diffusivity perpendicular to the fiber orientation in a lamina;} \\ D_y = D_{22}: \text{Diffusivity through the thickness of a stacked laminate.} \end{cases}$$

Note. 1:
Three energy levels impact corresponding to three drop heights respectively: $E_1 = 9J \rightarrow H = 0.5m$, $E_2 = 13J \rightarrow H = 0.75m$ and $E_3 = 18J \rightarrow H = 1m$ were simulated. In this papers, just the first level was presented to show the agrees between experiments and the numerical model.

II.2 SIMULATION CONDITIONS ARE [10]

- **Boundaries conditions (BCs):** To assure the same BCs of [8], the plate supports are fixed to bloc translation in z plane and lets the other freedom degrees free. In the impactor we just released the z translation.
- **Loading:** Two methods can be used to load impactor. The first is varying the drop high and introduce gravity as load for the striker. The second is introducing a predefined field expressed by the impact velocity for each drop high value. In this case, the contact is assured between the plate and impactor. The two methods lead to the same results.
- **Time of simulation:** The time of simulation is the contact time duration token from the experimental data, divided by the number of increments to finish the step.
- **The hygrothermal condition** is expressed in term of moisture which is applied to the simulated samples on the top surface and on the four sides while the bottom is insulated. Since moisture equilibrium content is not dependent upon the direction of the fibres, the equilibrium value was the same in different directions.

Note. 2:
All BCs and loadings are represented in respectively in Figure.1

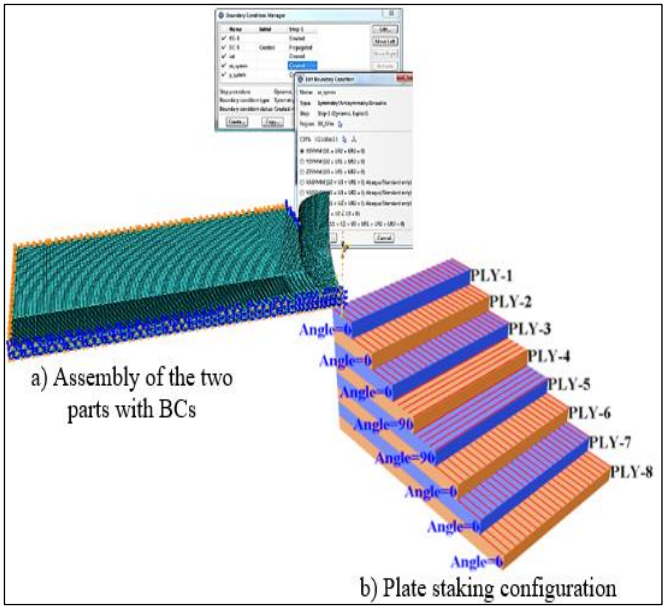

Figure 1: Modelling of the impact test.
Source: Authors, (2025).

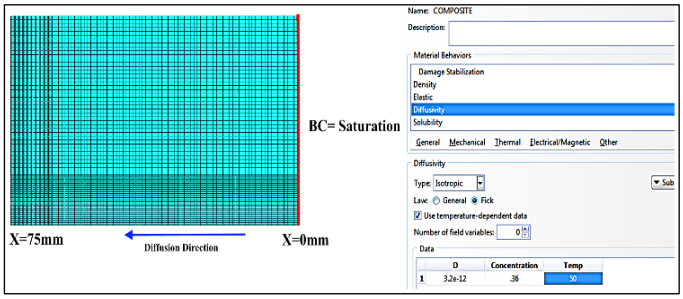

Figure 2: Quarter Model in ABAQUS for Diffusion convergence Analysis.
Source: Authors, (2025).

The ABAQUS model needs to produce accurate results for both relatively short periods of time (120 days) and for much longer periods so another analysis was run to simulate 5000^2 *seconds* using the same model. The 289 days simulated analysis is performed using the real conditions of 50°C with 95% RH and the boundary conditions were applied in the same manner as experiments drived by [8].

II.3 COMPARISON OF THE CONTACT FORCE COMPUTED VERSUS EXPERIMENTED

- Values of the contact force at node through the centre of the plates were graphed in Figure: 3(a), (b) and (c) for the first energy level of 9J (Drop high H=0.5m) in the two cases of aged and non-aged specimens.
- Numerical and experimental results of the contact force were compared to determine the efficiency of the numerical model. It is observed that the contact forces show the same mathematical curves for both plates under hygrothermal conditions and those non-aged seen Figure 3(b). A delay is registered on the contact force in the aged plates; This can be explained by the spongious effects due to the moisture adsorption in the plate.
- The overall measurement results summarized in Table 2, it is noted that the F_{IMP}^{Max} value matches with a light difference to those obtained experimentally.
- The experiments and the simulation indicate that the maximal contact forces F_{IMP}^{Max} decreases with increases of the moisture concentration.
- After analysis of impact phenomena under hygrothermal conditions it can be said that the adsorption can have a benefit effect in decreasing impact forces see Figure 4. In the other hand, after a threshold of concentration, this will be a disadvantage because it will create damages in the composite structure.

The modeling approach provides a significant advantage in numerically reproducing experimental tests without time constraints. For instance, the numerical values of F_{IMP}^{Max} in the table correspond to the case of the drop height.

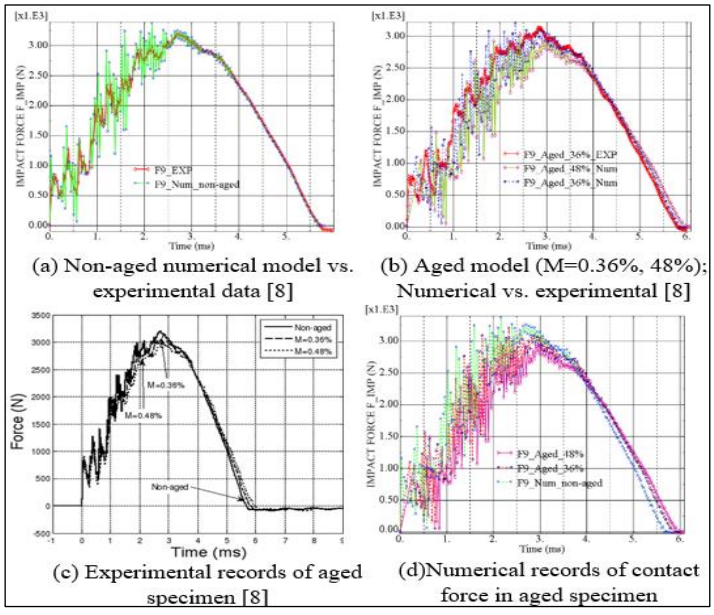

Figure 3: Average Impact Force for 9J energy.
Source: Authors, (2025).

Table 2: Records of the Maximum value of the contact forces.

H(m)	M(%)	F_{EXP}	F_{Num}	Error
0,5	0	3217	3257	1.24
0,75	0	3730	3772.56	1.14
1,0	0	4171	4201	0.7
0,5	0,36	3140	3181.12	1.31
0,75	0,36	3702	3748.43	1.2
1,0	0,36	//	4146.25	//
0,5	0,48	3002	3039.27	1.2
0,75	0,48	3500	3543.46	1.29
1,0	0.48	//	3997.67	//

Source: Authors, (2025).

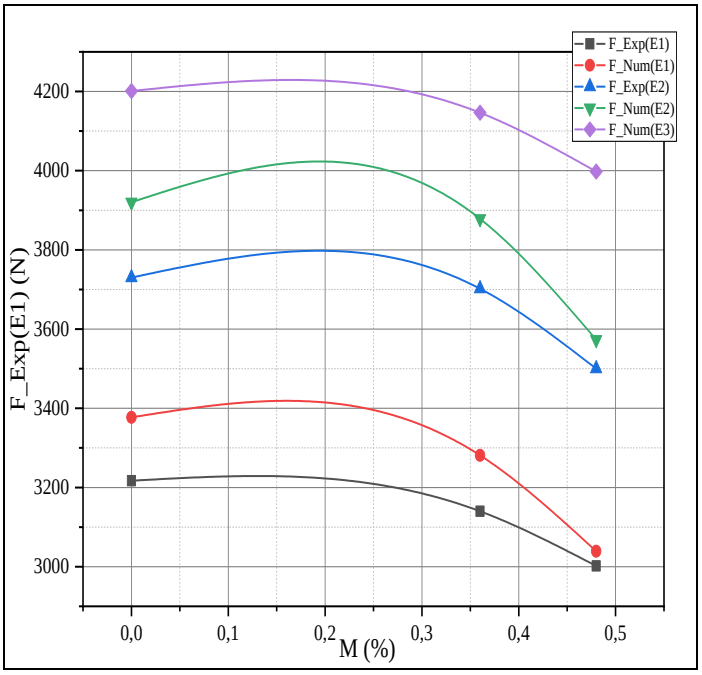

Figure 4: Maximum values of the contact forces as function as the moisture and the energy level.
Source: Authors, (2025).

III. DESIGN OF EXPERIMENTS (DOE) IMPLEMENTATION

Experimental design is how to conduct and plan experiments in order to extract the maximum amount of information from the collected data (The basic idea is to vary all relevant factors simultaneously x_i as drop high 'H' and moisture values 'M' in this case of study, over a set of planned experiments, and then connect the results expressed in terms of the quantity of interest y (numerical contact force) by means of a mathematical model. This model is then used for interpretation, predictions and optimization.

Both factors 'H' and 'M' are represented by a graduated and oriented axis as shown in Figure 5. The Design Space is established to estimate the area of operability or robustness. The range of variation of each factor is defined by a low level noted -1 and a high level noted +1. This arrangement permits the elaboration of the design matrix, see Table 3.

Such a designed plan in which each of the two factors has only two levels is referred to as Factorial plan of 2^2.

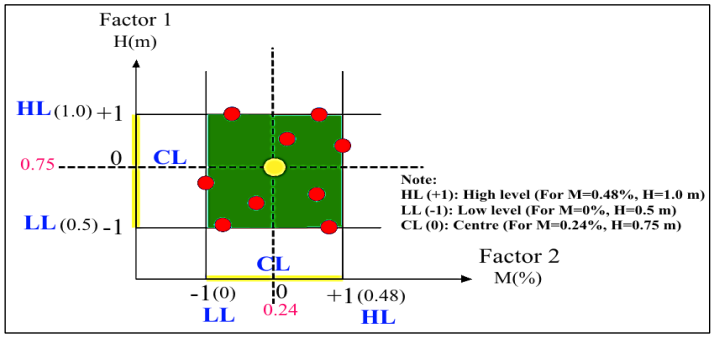

Figure 5: Design space of experiments.
Source: Authors, (2025).

Table 3: Design matrix.

Experience N°	Factor 1: High(m)	Factor 2: Moisture(%)
1	-1	-1
2	1	-1
3	-1	1
4	1	1
5	-1	0
6	1	0
7	0	-1
8	0	1
9	0	0

Source: Authors, (2025).

III. 1 MATHEMATICAL MODEL

To highlight how vary the response, according to each factor and improve their interaction a DOE plan is established using the Modde V5 software [9]. A Central Composite Designs Face Centred (CCF) plan is chosen [9],[11]. A system of 9 equations with 6 unknowns is resolved. Thus, the following equation is obtained:

$$y = a_0 + a_1x_1 + a_2x_2 + a_{12}x_1x_2 + a_{11}x_1^2 + a_{22}x_2^2 + e \quad (1)$$

The determination of the coefficients $a_0, a_1, a_2x_2, a_{11}, a_{12}$ and a_{22} of the model is obtained using Multiple Linear Regression (MLR) in order to minimize the sum of squares of the residuals.

III. 1.1 QUALITY OF PREDICTIVE MODEL

The efficiency of the predictive model fit by examining the following plots and lists:

- The Summary of the fit, R^2, Q^2 represented on Figure 6 describe the quality and validity of the model; According to the obtained results were R^2, Q^2 tend to 1(see the Analysis of Variance Table 4), it is concluded that quality of the model predicting contact force is highly successful. All these parameters affect plots for screening designs.

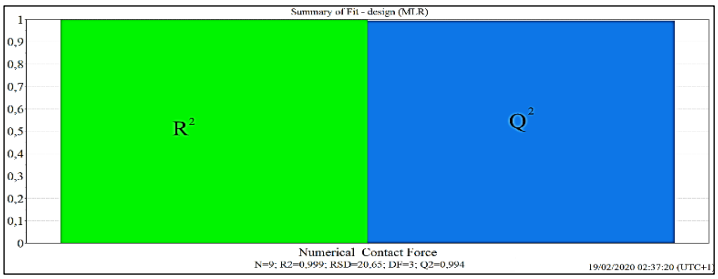

Figure 6: Descriptive quality of the model

- Results shown on Figure 7 gives a good insight on the effect of the factors coefficients of the mathematical model. It is found that the factor of the height of impact is the most influential (477.2) followed by the mass of absorbed moisture (–108.36). Right after, the registered coefficient in terms of the square of the height of impact relapse to the value of (-51.1), followed in decreasing order by the square of the mass of absorbed water (-147.94) and finally by the combined effect of the height of impact and the mass of water absorbed (4.4). All factors' coefficients collected data are reported in Table 5.

- The signs of the coefficients are disregarded because the importance is on the absolute values indicating the weight of the coefficients.

Table 5: Coefficients of the factors and their interactions.

Numerical Contact Constant	Coeff. SC	Std. Err.	P	Conf. int(±)
Constant	3817,16	19,6753	3,01975e-07	62,616
H	477,189	8,5929	1,28621e-05	27,3466
M	-108,36	8,43227	0,00101697	26,8354
H^2	-51,0983	14,6051	0,0395194	46,4803
M^2	-147,938	20,2687	0,00531021	64,5043
M×H	4,39473	9,92223	0,687817	31,5771

Source: Authors, (2025).

Table 4: The Analysis of Variance (ANOVA) summary.

Numerical Contact Force	**DF**	**SS**	**MS (variance)**	**F**	**p**	**SD**
Total	9	1,21625e+08	1,35139e+07			
Constant	1	1,20171e+08	1,20171e+08			
Total corrected	8	1,45394e+06	181742			426,312
Regression	5	1,45266e+06	290532	681,008	**0,000**	539,01
Residual	3	1279,86	426,62			20,6548
	N = 9	Q2 =	0,994	Cond. no. =	5,759	
	DF = 3	R2 =	0,999	RSD =	20,65	
		R2 adj. =	0,998			

Source: Authors, (2025).

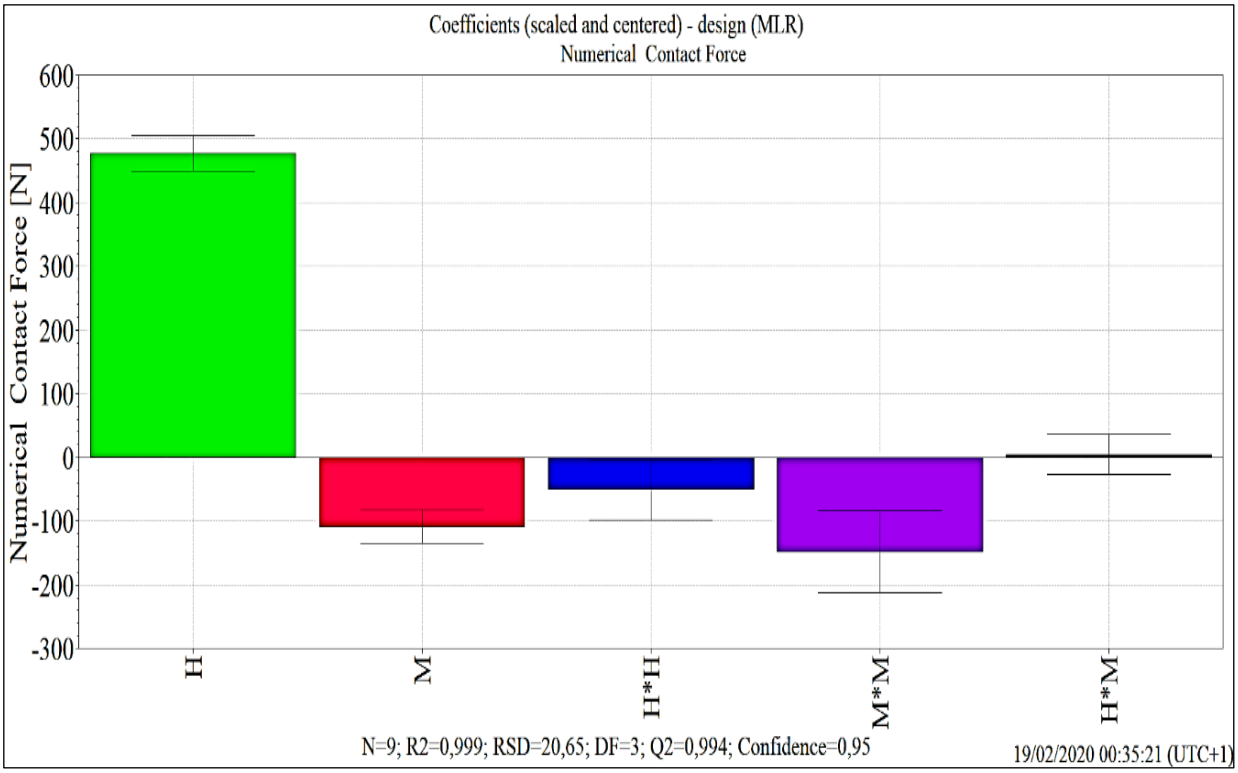

Figure 7: Factors influencing the contact force.
Source: Authors, (2025).

Finally, the proposed model to predict the contact force and covering both the experimental tests and numerical modelling as function as the height H and the mass of absorbed moisture M in the design space is expressed by:

$$F = 3817.16 + 477.189H - 108.36M + 4.39H \times M - 51.0983H^2 - 147.938M^2 + e \quad (2)$$

III. 1.2 GRAFICAL CONTOURS OF THE RESPONSE

- The mathematical representation of the function given earlier in Eq. (2) is presented in Figure 8. The graphed function shows the contour plots of the response i.e. the response surface corresponding to the contact force as function as the two parameters H and M.
- The graphical representation of the model constitutes an important and interesting part of this powerful and judicious DOE method. It reveals that the combined effect of increasing the absorbed moisture and a decrease in the drop height reduces the contact force. The absorbed moisture in this situation gives the material some suppleness (Spongious effect) which results in a decrease in the contact force.
- However, it is noticed that after a certain threshold of absorption noticed when $M \in [0.30 - 0.35]\%$ the contact force decreases with the increasing of M for the same applied level of the impact energy. The results of the study are comforted by other investigations [8],[12]. Moisture swelling of the matrix may alter the state of residual stresses introduced during processing of the composite [5].
- On the other hand, the fibber/matrix interface and interlayers region are commonly target by environmental attack, this is generally due to the difficulties in achieving of a perfect chemical bond between the fibbers and matrix and layers [4],[8] and [10].

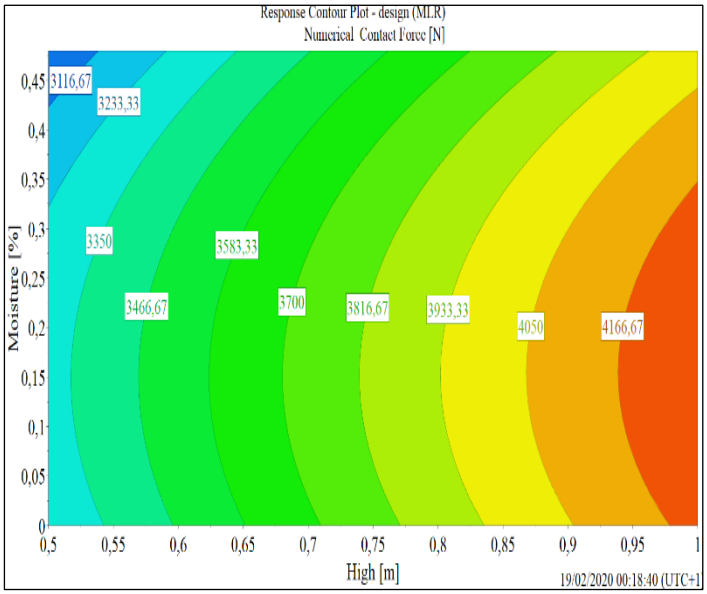

Figure 7: Contours of the response surface according to each level of drop high and moisture absorption.
Source: Authors, (2025).

Predicted force:

- On Figure 9 the evolution of the predicted force is shown according to each factor. The predictive model gives very close results of the impact force to those obtained numerically and experimentally.
- Its observed that when the predicted contact force according to drop height changes is stored, the contact force present linearly evolution with this last parameter Figure 9(a). In the other hand, when predicted contact force is registered according to moisture changes the mathematical graph changes on a non-linear shape function.

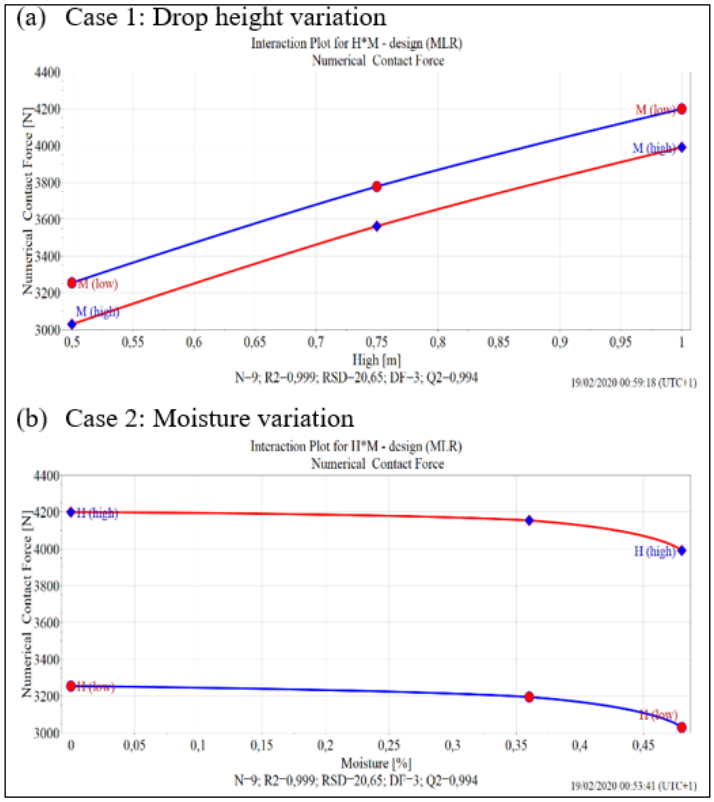

Figure 9: Predicted force as function as the influent parameters (H: case 1; M: case 2).
Source: Authors, (2025).

IV. CONCLUSION

The general conclusions of this study are summarized as follows:

- We have analyzed by the finite element method (FEM) the effect of impact at low energy in S-Glass/Polyester composite laminate.
- The computed time history of the contact force acting in the axial direction on the S-Glass/Polyester plate agrees well with the experimental data in the two studied cases of aged and a non-aged model.
- The absorption of the moisture leads to a decrease in contact force which it can represent an interest point.
- However, it was seen that after threshold of moisture the contact force decreases with the increasing of M for the same applied level of the impact energy.

From the outcome of our investigation on the application of the DOE it is possible to conclude that:

- The proposed method permits the establishment of an analytical model of the impact force.
- The interaction of the two parameters H and M is illustrated.
- A predictive model of impact force is exposed.

V. AUTHOR'S CONTRIBUTION

Conceptualization: Kamel Zouggar and Mustapha Rabouh.
Methodology: Mustapha Rabouh and Kamel Zouggar.
Investigation: Mustapha Rabouh and Kamel Zouggar.
Discussion of results: Mustapha Rabouh, Kamel Zouggar and Khelifa Guerraiche.
Writing – Original Draft: Mustapha Rabouh.
Writing – Review and Editing: Kamel Zouggar and Mustapha Rabouh.
Resources: Mustapha Rabouh, Khelifa Guerraiche.
Supervision : Khelifa Guerraiche and Kamel Zouggar.
Approval of the final text: Mustapha Rabouh, Kamel Zouggar and Khelifa Guerraiche.

VI. REFERENCES

[1] J. Shrestha, T. Ueda, and D. Zhang, "Durability of FRP concrete bonds and its constituent properties under the influence of moisture conditions", ASCE, vol. 27, no. 2, pp. 01-13, Jul. 2014. https://doi.org/10.1061/(ASCE)MT.1943-5533.000109

[2] G. Mirzaei, B. Mohebby, and G. Ebrahimi, "Glulam beam made from hydrothermally treated poplar wood with reduced moisture induced stresses", Construction and Building Materials, vol. 135, no. 15, pp. 386-393, March 2017. DOI: 10.1016/j.conbuildmat.2016.12.178 (2017)

[3] M. A. Zenkour, A. R. Alghanmi, "Bending of symmetric cross-ply multilayered plates in hygrothermal environments", MME, Vol. 2, no. 2, pp. 94-107, Dec 2016. https://doi.org/10.21595/mme.2016.17405

[4] T. Bandyopadhyay, A. Karmakar, "Low-Velocity Impact Response of Delaminated Composite Conical Shells in Hygrothermal Environment due to Time-Delay", Procedia Engineering, vol 173, pp 463-470, 11th International Symposium on Plasticity and Impact Mechanics, Implast, 2016. https://doi.org/10.1016/j.proeng.2016.12.064

[5] L. Rongrong et al, "Experimental and Numerical Study of Moisture-induced Stress Formation in Hexagonal Glulam Using X-ray Computed Tomography and Finite-element Analysis", BioResources, vol. 13, no. 4, pp. 7395-7403, Aug 2018. DOI: 10.15376/biores.13.4.7395-7403

[6] Z. Li, J. Zhang, and Y. Sun, "Influence of accelerated aging tests on properties of glued-laminated timber", Journal of Forestry Engineering vol. 29 no. 1, pp. 94-97, 2015. DOI: 10.13360/j.issn.1000-8101.2015.01.027.

[7] Systèmes, D. (2017). "Abaqus 6.17 online documentation", Abaqus User Subroutines Reference Manual.

[8] B.F. Boukhoulda, L. Guillaumat, J.L. Lataillade, E. Adda-Bedia and A. Lousdad, "Aging-impact coupling based analysis upon glass/polyester composite material in hygrothermal environment", Materials and design, Vol. 32, no. 7, pp. 4080-4087, Aug 2011. https://doi.org/10.1016/j.matdes.2011.03.009

[9] User Guide to MODDE By Umetrics Version 5, www.umetrics.com/modde.

[10] K. Zouggar, F.B. Boukhoulda, B. Haddag, M. Nouari, "Numerical and experimental investigations of S-Glass/Polyester composite laminate plate under low energy impact", Composites Part B, vol. 89, pp. 169-186, 2015. http://dx.doi.org/10.1016/j.compositesb.2015.11.021

[11] Jacques Goupy. "Introduction aux plans d'expériences - Organisation des essais et de l'interprétation des résultats". 5e édition. Dunod, 416 pages ; ISBN :978-2-10-077802-7

[12] K. Imielinska, L. Guillaumat, "The effect of water immersion ageing on low-velocity impact behaviour of woven aramid-glass fiber/epoxy composites", Journal of Composites Science and Technology, vol. 64, no13.14, pp.2271-2278, Oct 2004. https://doi.org/10.1016/j.compscitech.2004.03.002.

Journal of Engineering and Technology for Industrial Applications

ISSN ONLINE: 2447-0228

ITEGAM-JETIA

Manaus, v.11 n.53, p. 76-80. May/June., 2025.

DOI: https://doi.org/10.5935/jetia. v11i53.1555

RESEARCH ARTICLE OPEN ACCESS

DELINEATION OF GROUNDWATER POTENTIAL ZONES USING INTEGRATED VERTICAL ELECTRICAL SOUNDING AND GEOSPATIAL TECHNIQUES IN THE BASEMENT COMPLEX OF IJESHA ISU EKITI, SOUTHWESTERN NIGERIA

Taofeek O. Ewumi[1], Funmilola O. Ogunlana[2] and A. Akinola Oyedele[*3]

[1,3]Department of Physics, Ekiti State University, Ado – Ekiti, Nigeria
[2]Department of Physics, Bamidele Olumilua University of Education, Science and Technology, Ikere - Ekiti, Nigeria

[1] http://orcid.org/0009-0009-1724-155X , [2] http://orcid.org/0000-0001-9024-273X , [3] http://orcid.org/0000-0003-0428-7566

Email: taofik.ewumi@eksu.edu.ng, ogunlana.funmilola@bouesti.edu.ng, *akintunde.oyedele@eksu.edu.ng

ARTICLE INFO

Article History
Received: January 12, 2025
Revised: February 20, 2025
Accepted: May 15, 2025
Published: May 31, 2025

Keywords:
Geoelectrical characteristics,
GIS model,
Groundwater potential,
MCE, Weighting,
Electrical resistivity.

ABSTRACT

A combination of multi-criteria evaluation parameters has been deployed to delineate groundwater potential zones using integrated Vertical Electrical Sounding and geospatial techniques in the basement complex of Ijesha Isu Ekiti, Southwestern Nigeria. The area is underlain by migmatite-gneiss, amphibolities, biotite gneiss and the granitic components of the basement complex terrain with suspect groundwater prospects. Wenner vertical electrical soundings (VES) were conducted at 22 stations. The VES interpretation delineated the topsoil, weathered basement / partly weathered/fractured basement and the fresh basement bedrock with resistivity values ranging from 19 - 304, 16 - 417 and 8 - 2784 Ω-m, respectively. Integration of the attributes of the bedrock resistivity, weathered basement resistivity and the overburden thickness in a GIS environment enabled the classification of the study area into very low, low, medium and high groundwater potential zones covering areal extent of 0.004 km^2, 0.18 km^2, 1.85 km^2, and 1.32 km^2, respectively. A weighted combination of attributes would enhance the hitherto low success rate of groundwater targeting in a typical hard rock terrain.

I. INTRODUCTION

Ijesha Isu Ekiti is underlain by the Precambrian basement complex rocks of Southwestern Nigeria. The town depends on rain water, surface water and groundwater for water supplies. The surface water is usually not available all year round owing to the seasonal flow regime of rivers draining the area; and where available and accessible, cannot guarantee the required water quality status required for most domestic activities. Most homes depend on water from wells whose overall yield and quality are influenced by the alternating wet and dry seasons among other factors [1-3].

In a typical hard rock terrain, groundwater is restricted to the fractures and the weathered zones. The hydraulic properties are characterized by extreme variations over short distances which often limit water development in the area to low-yielding well [4-6]. With the marked low success ratio of drilling for potable water in hard rock terrain the use of Geophysics is often compelling, particularly in the absence of lineaments extracted from imagery [1],[7],[8].

According to [6] the poor understanding of the hydrogeological characteristics of the Basement Complex environment is significantly responsible for borehole failures in the terrain. The groundwater potential of a basement complex area is influenced by a complex inter-relationship involving the geology, post emplacement tectonic history, weathering processes and depth, nature of the weathered layer, groundwater flow pattern, recharge and discharge processes [9],[10]. Improvements in the understanding of this relationship will be fundamental to the planning and management of groundwater resources in crystalline basement terrain and reduction of development cost [4]. It is important to evaluate the overall resource and aquifer occurrence more precisely to assist development efficiency and longer-term sustainability.

The study area lies between latitudes 7º45'N and 7º 46'N and longitudes 5º 25'E and 5º 26'E in Ikole Local Government area of Ekiti, State, Southwestwern Nigeria (Figure 1). The area enjoys high annual rainfall of about 1500mm being within the tropics. The area is underlain by migmatite-gneiss, the amphibolities, biotite gneiss and the granitic components of the Precambrian basement complex of southwestern Nigeria. The regolith and fractured bedrocks constitute the aquifers for groundwater. Development of the bedrock component requires interaction with storage available in overlying or adjacent saturated regolith, or other suitable formations such as alluvium [1],[12],[13].

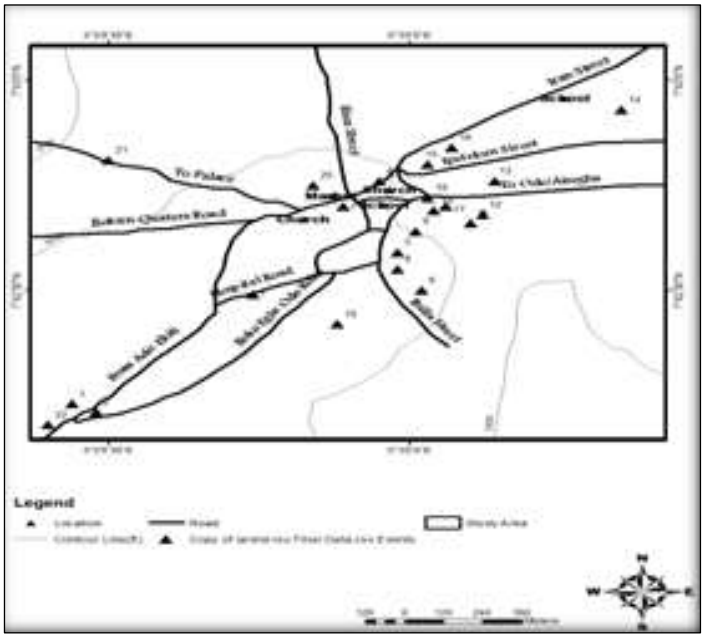

Figure 1: Study Area Map showing the VES Points.
Source: Authors, (2025).

II. THEORETICAL REFERENCE

Electrical Resistivity Method is a non-invasive geophysical technique developed to interpret the nature of the subsurface without altering the dynamic status of the soil mass [10],[11],[16]. Vertical Electrical Resistivity Sounding (VES) technique offers a compact tool for locating promising areas for water boreholes/wells amidst prevailing structural disposition. It has proved very popular with groundwater studies due to the simplicity of the technique, the ruggedness of the instrumentation and the success rate [5],[9]. Geographic Information System (GIS) provides an efficient integration environment. With the implementation of GIS, large volume of geospatial data and information are maintained in a standard format, revised and updated with additional features. Sustainable development and management are thus facilitated at real time [1],[11].

This integrated approach presents a detailed evaluation of the groundwater prospects of Ijesha Isu Ekiti using geoelectric data in a GIS environment.

III. MATERIALS AND METHODS

The geoelectric data acquisition was carried out using Wenner array of Vertical Electrical Sounding (VES) to delineate the subsurface lithological configuration, aquifer characteristics and depth to bedrock. Twenty Two (22) VES points (Figure 1) were fully occupied for data acquisition. The instrument used for the resistance measurement was the ABEM Terrameter SAS 300 B with ABEM 2000 Booster. A Garmin 12-Channel Global Positioning System (GPS) handheld receiver was used to obtain the Eastings (Longitude), Northings (Latitude) and Elevation above mean sea level of each point of interest during the fieldwork. The VES data were interpreted quantitatively by partial curve matching and 1-D computer iteration using the computer algorithm RESIST Version 1.0 [14] to obtain the layer resistivity values and corresponding thicknesses. The curves were inspected to determine the number and nature of the layering [15],[16]. ArcMap 10.2.2 was employed for derivation and re-classification of the thematic layers for spatial analysis. Different classes in each thematic map were assigned a knowledge-based hierarchy of weights [17]. These weights ranged from 1 to 4 for groundwater potential evaluation. In each thematic map, highest weight is given to the class that is most favourable to potential and lowest weight is given to the class that is least favourable for groundwater accumulation.

IV. RESULTS AND DISCUSSIONS

The geoelectric type curves in the study area are presented in Figure 2. They are A, H, KH, HA and Q type curves with the H-curve being the most predominant accounting for 45.4%. This is a consequence of the degree of weathering and fracturing as typical of the basement complex terrain. The analysis of the type curves indicated that the area under study has both weathered layer aquifers and fractured layer aquifers [18],[19].

The geoelectric characteristics are summarized in Table 1. The spatial distributions of the geoeletric parameters are presented in Figures 3 - 8. The resistivity of the topsoil varies from 19 Ω-m to 304 Ω-m with a mean of 79.8 Ω-m and Standard Deviation of 68.7 Ω-m. The skewness of 1.7 shows that the spatial distribution is not uniform. The wide resistivity range is a consequence of the variable composition of this layer.

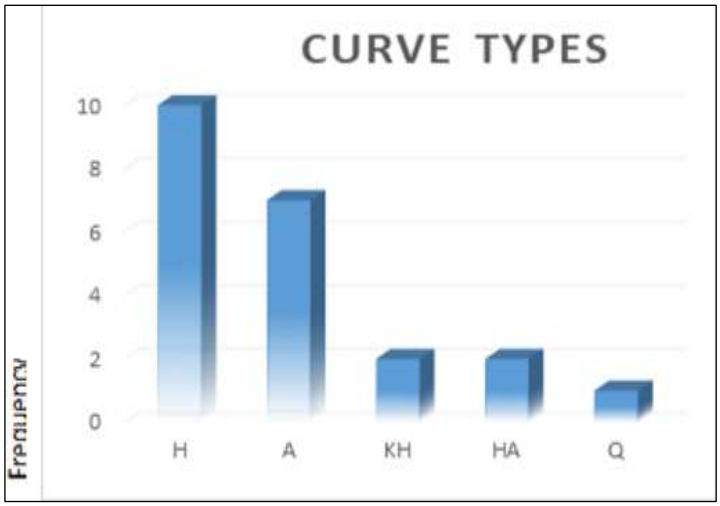

Figure 2: Geoelectric Curve Types.
Source: Authors, (2025).

Table 1: Summary of Geoelectric Characteristics.

Parameters	Min	Max	Mean	Std. Deviation	Skewness
Anisotropy	1	1.8	1.2	0.2	1.9
Top soil Resistivity (Ω-m)	19	304	79.6	68.7	1.7
Top soil Thickness (m)	1.1	8.6	3.9	2.6	0.6

Weathered Basement Resisitivity (Ω-m)	16	417	103.27	103.83	1.7
Weathered Basement Thickness (m)	3.2	19.6	10	3.9	0.4
Overburden Thickness (m)	4.3	25.3	14.5	4.7	0.1
Bedrock Resistivity (Ω-m)	8	2784	645.6	706.3	2.1

Source: Authors, (2025).

The thickness of the topsoil varies from 1.1 m to 8.6 m with a mean of 3.9 ± 2.6 m. The Weathered Basement Resistivity values range from 16 Ω-m to 417 Ω-m. The values indicate varying degree of weathering/fracturing and water saturation. The thickness of the layer ranges from 3.2 – 19.6 m.

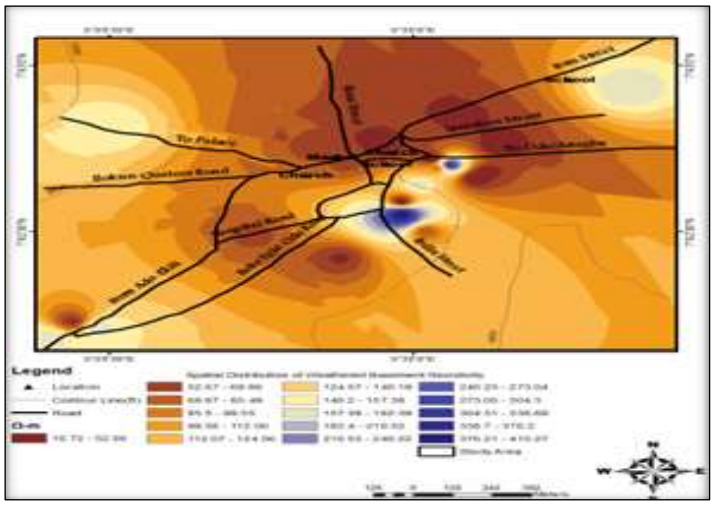

Figure 3: Spatial distribution of Weathered Basement Resistivity.
Source: Authors, (2025).

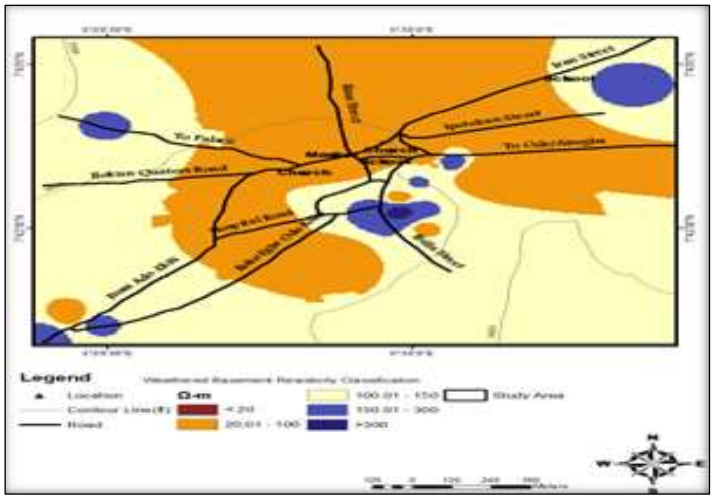

Figure 4: Classification of Weathered Basement Resistivity.
Source: Authors, (2025).

The bedrock resistivity varies from 8 Ω-m to 2784 Ω-m; indicating decreasing impact of weathering/fracturing with corresponding reduction of the groundwater potentials. Localized variations may be attributed to differences in the bedrock mineralogy and structures.

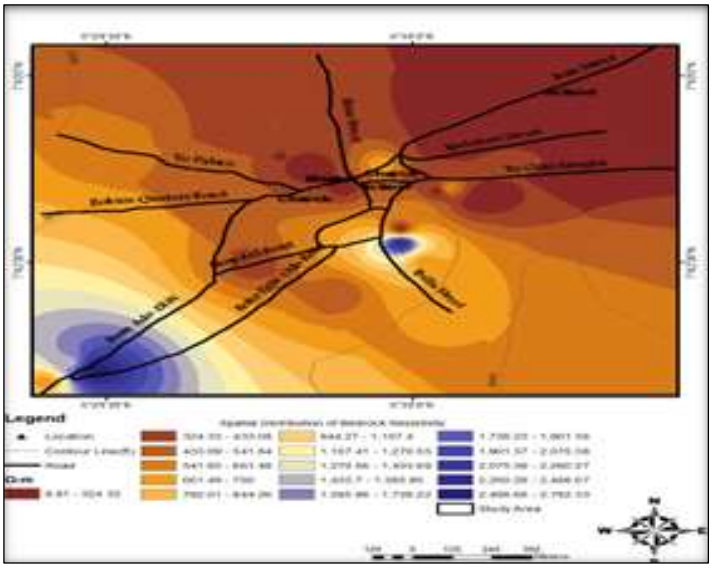

Figure 5: Spatial Distribution of Bedrock Resistivity.
Source: Authors, (2025).

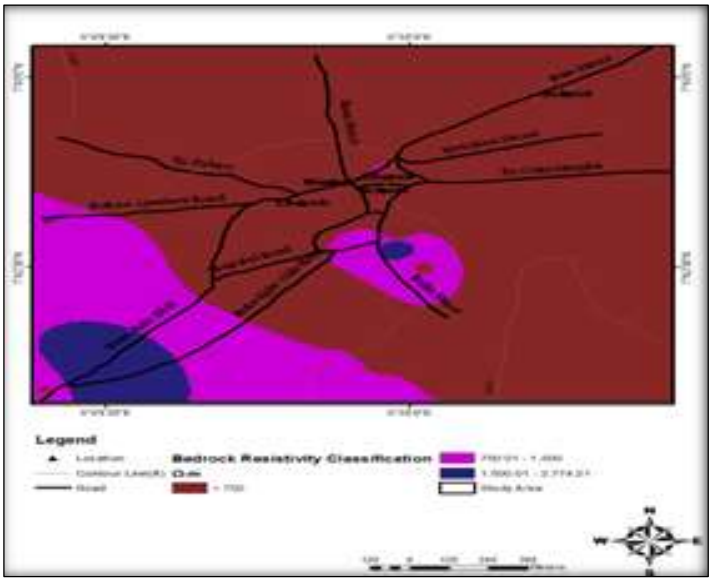

Figure 6: Classification of Bedrock Resistivity.
Source: Authors, (2025).

The overburden thickness varies from 4.3 to 25.3 m. The isopach map of overburden, Figure 7, shows that the southwestern and southeastern regions are characterized by basement highs/ridges with thin overburden cover generally less than 10m. Thresholding produced three classes of overburden thickness of < 10m, 10 - 20m and 20 - 30m with poor, medium and high groundwater potential respectively (Figure 8). The northern flank records increasing value of overburden thickness towards the central portion of the study area thus creating basement depressions at the central portion and Irepodun. An isolated depression has been demarcated along the southern flank of the area. Basement depressions are diagnostic of troughs which are groundwater collecting centres [9],[20].

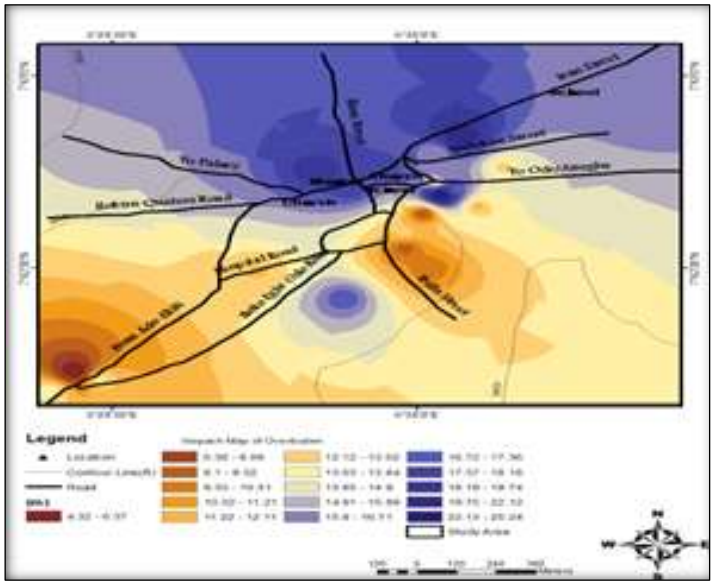

Figure 7: Isopach Map of Overburden.
Source: Authors, (2025).

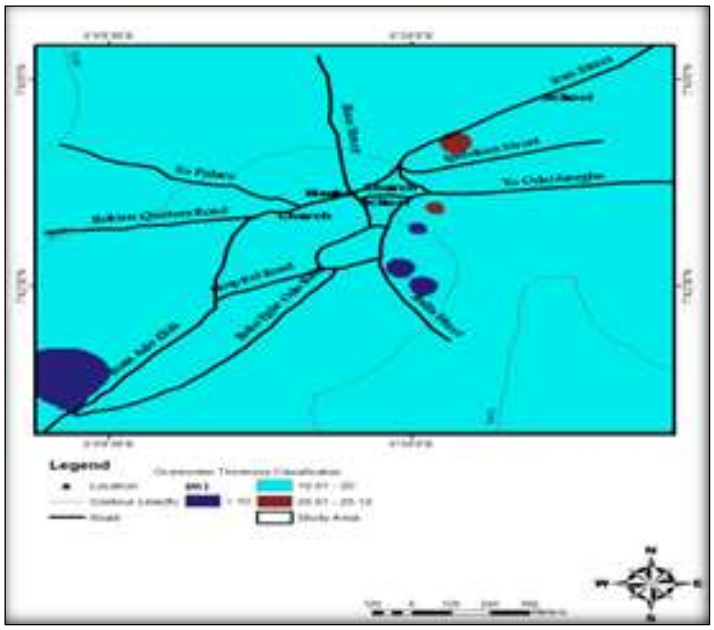

Figure 8: Classification of Overburden Thickness
Source: Authors, (2025).

Maximum possible regolith thickness is required for adequate storativity, transmissivity, and greater drawdown. Optimum weathering offers optimum conditions and groundwater potential [17],[19]. Basement fractures contribute significantly to groundwater yield in a typical basement complex terrain. Fractures readily offer enhanced porosity and permeability and hence increasing the well yield [16],[18],[20]. Bedrock resistivity of less than 750 Ω-m is indicative of high fracture and permeability as a result of weathering with high aquifer potential.

An integration of geoelectric parameters according to the relative importance to groundwater occurrence and accumulation is facilitated in a GIS environment [9], [22-24]. The themati maps were synthesized using the weighting combination (Table 2) for the resulting groundwater potential map, Figure 9. The map classifies the study area into very low, low, medium and high groundwater potential zones covering areal extent of 0.004 km2, 0.18 km2, 1.85 km2, and 1.32 km2, respectively.

Table 2: Multi-criteria evaluation parameters for generation of groundwater potential.

Geoeletric Parameters	Classes	Scale value	Weight
Bedrock Resistivity (Ω-m)	<750 750-1500 1500-3000 >3000	4 3 2 1	45
ouWeathered Basement Resistivity (Ω-m)	<20 20-100 100-150 150-300 >300	3 4 3 2 1	30
Overburden Thickness (m)	<10 10-20 20-30 >30	1 2 3 4	25

Source: Authors, (2025).

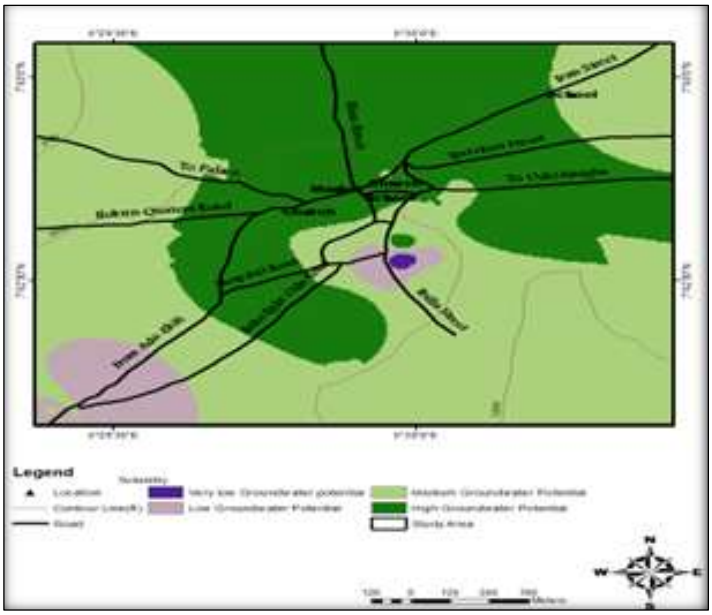

Figure 9: Groundwater Potential Map of the Study Area.
Source: Authors, (2025).

Table 3: Classification of groundwater potential zones (after integration of thematic layer).

Groundwater Potentiality	Area in (km^2)	Percentage
Very Low	0.004	0.1
Low	0.18	5.4
Medium	1.85	55.2
High	1.32	39.3

Source: Authors, (2025).

V. CONCLUSIONS

A geoelectric assessment of the groundwater potentials of Ijesha Isu Ekiti has been conducted in a GIS platform. Integration of attributes in a GIS environment enabled the categorization of the study area into very low, low, medium and high groundwater potential zones. Significant hydro-geologic structures delineated from of the subsurface resistivity distribution included basement ridges and depressions. The basement depressions being the groundwater collecting centres are priority areas for groundwater development. The study provides regional overview of the groundwater resources in the area. It would guide the planning and design of hydrogeophysical investigations for site specific

groundwater development. Data density can be improved for further studies.

VI. AUTHOR'S CONTRIBUTION

Conceptualization: Ewumi and Ogunlana.
Methodology: Oyedele, Ewumi and Ogunlana.
Investigation: Oyedele, Ewumi and Ogunlana.
Discussion of results: Oyedele, Ewumi and Ogunlana.
Writing – Original Draft: Ewumi and Ogunlana.
Writing– Review and Editing: Ewumi and Ogunlana.
Resources: Oyedele, Ewumi and Ogunlana.
Supervision: Ewumi and Ogunlana.
Approval of the final text: Oyedele, Ewumi and Ogunlana.

VIII. REFERENCES

[1] Popoola K, Talabi AO, Afolagboye LO, Oyedele AA, Ojo AA, (2020). Groundwater potential evaluation in the basement complex terrain of Ekiti East Local Government Area, Southwestern Nigeria. International Journal of Energy and Water Resources, https://doi.org/10.1007/s42108-019-00053-5 Springer

[2] Talabi AO, (2018). Estimated volume of water in shallow wells of Ekiti State, Southwestern Nigeria: implications on groundwater sustainability. Arabian Journal of Geoscience, 11, 1–9. https ://doi.org/10.1007/s1251 7-018-4031-3.

[3] Rahaman MA, (1988). Recent advances in the study of the Basement Complex of Nigeria. In Oluyide et.al. (eds) Precambrian Geology of Nigeria Publication. Geological Survey of Nigeria, Kaduna, p. 157-163.

[4] Wright CP, (1992). The hydrogeology of crystalline basement aquifers in Africa. In: CP Wright and W C Burgess (eds). Hydrogeology of crystalline basement aquifer in Africa. Geological Society of London Special Publication. 66, p. 1–27.

[5] Oyedele AA, Ayodele OS, Olabode OF, (2019). Groundwater quality assessment and characterization of shallow basement aquifers in parts of ado ekiti metropolis, Southwestern Nigeria. SN Applied Sciences, https://doi.org/10.1007/s42452-019-0683-1 Springer Nature

[6] Ojo JS, Olorunfemi MO, Akintorinwa OJ, Bayode S, Omosuyi GO, Akinluyi FO, (2015). GIS Integrated Geomorphological, Geological and Geoelectrical Assessment of the Groundwater Potential of Akure Metropolis, Southwest Nigeria. Journal of Earth Sciences and Geotechnical Engineering, 5(14) p. 85-101.

[7] Oyedele AA, (2019). Use of remote sensing and GIS techniques for groundwater exploration in the basement complex terrain of Ado Ekiti, SW Nigeria. Springer Applied Water Science. p. 9:51 https://doi.org/10.1007/s13201-019-0917-9.

[8] Bayewu OO, Oloruntola MO, Mosuro GO, Laniyan TA, Ariyo SO, Fatoba JO, (2017). Geophysical evaluation of groundwater potential in part of southwestern basement complex terrain of Nigeria. Applied Water Science, 7(8) p. 4615–4632. https ://doi. org/10.1007/s1320 1-017-0623-4.

[9] Olorunfemi MO, Ojo JS, Akintunde OM, (1999). Hydrogeophysical Evaluation of the Groundwater Potential of Akure Metropolis, South-Western Nigeria. Journal of Mining and Geology, 35(2) p. 207 – 228.

[10] Prabu P, Rajagopalan B, (2013). Mapping of Lineaments for Groundwater Targeting and Sustainable Water Resource Management in Hard Rock Hydrogeological Environment Using RS- GIS, Climate Change and Regional/Local Responses, Chapter 10 p. 235 – 247.

[11] Hagos Y, Bedaso Z, Kebede M, (2024). Delineating groundwater potential zones using geospatial and analytical hierarchy process techniques in the upper omo-gibe basin, Ethiopia. Revue Internationale de Géomatique, 33(1), 399-425. https://doi.org/10.32604/rig.2024.053975

[12] Clark L, (1985). Groundwater abstraction from basement complex area of Africa. Quarterly Journal of Engineering Geology and Hydrogeology, 18 p. 25–34. https ://doi.org/10.1144/GSL. QJEG.1985.018.01.05.

[13] Bayowa OG, Olorunfemi MO, Akinluyi FO, Ademilua OL, (2014). Integration of Hydrogeophysical and Remote Sensing Data in the Assessment of Groundwater Potential of the Basement Complex Terrain of Ekiti State, Southwestern Nigeria. Ife Journal of Science, 16(3) p. 353 – 363

[14] Vander-Velpen BPA, (2004). Win RESIST Version 1.0. MSc Research Project, ITC, Deft, Netherlands.

[15] Ariyo SO, Adeyemi GO, (2011). Integrated geophysical approach for groundwater exploration in hard rock terrain-A case study from Akaka area of southwestern Nigeria. International Journal of Advanced Scientific and Technical Research, 2(1) p. 376–395.

[16] Olayinka AI, Amidu SA, Oladunjoye MA, (2004). Use of electromagnetic profiling and resistivity sounding for groundwater exploration in the crystalline basement area of Igbeti, southwestern Nigeria. Global Journal of Geological Sciences, 2(2) p. 243–253.

[17] Oyedele EA, Olayinka AI, (2012). Statistical evaluation of groundwater potential of Ado-Ekiti Southwestern Nigeria. Transnational Journal of Science and Technology, 2(6) p. 110–127.

[18] Ademilua LO, Olorunfemi MO, (2000). A Geoelectric/Geologic Estimation of the Groundwater Potential of the Basement Complex area of Ekiti and Ondo States of Nigeria. The Journal of Technoscience, 4: 4-18.

[19] Oladapo MI, Akintorinwa OJ. (2007). Hydrogeophysical study of Ogbese, southwestern Nigeria. Global Journal of Pure and Applied Science, 13(1) p. 55–61.

[20] Jayeoba A, Oladunjoye MA, (2013). Hydro-geophysical evaluation of groundwater potential in hard rock terrain of southwestern Nigeria. RMZ – M&G, 60 p. 271–285.

[21] Sharma SP, Baranwal VC (2005). Delineation of groundwater-bearing fracture zone in a hard rock area integrating Very Low Frequency electromagnetic and resistivity data. Journal of Applied Geophysics, 57 p. 155–166.

[22] Chatterjee S, Dutta S, (2022). Assessment of groundwater potential zone for sustainable water resource management in south-western part of Birbhum District, West Bengal. Applied Water Science, 12(3):40. doi:10.1007/s13201-021-01549-4.

[23] Kedir EG, (2023). Groundwater potential assessment and sustainable management. Environmental monitoring and assessment, 195(7):891. doi:10.1007/s10661-023-11521-1.

[24] Ajayi OG, Nwadialor IJ, Odumosu JO, Adetunji OO, Abdulwasiu IO, (2022). Assessment and delineation of groundwater potential zones using integrated geospatial techniques and analytic hierarchy process. Appied Water Science, 12(12):276. doi:10.1007/s13201-022-01802-4.

Journal of Engineering and Technology for Industrial Applications

ITEGAM-JETIA

Manaus, v.11 n.53, p. 81-86. May/June., 2025.

DOI: https://doi.org/10.5935/jetia. v11i53.1571

ISSN ONLINE: 2447-0228

RESEARCH ARTICLEOPEN ACCESS

ANALYSIS OF LORA SIGNAL PROPAGATION IN URBAN ENVIRONMENT

David Alan de Oliveira Ferreira[1]

[1]Federal University of Amazonas, Brazil.

[1]https://orcid.org/0000-0001-5717-4018

Email: ferreirad08@gmail.com

ARTICLE INFO

Article History
Received: January 12, 2025
Revised: February 20, 2025
Accepted: May 15, 2025
Published: May 31, 2025

Keywords:
Long Range,
Signal Propagation,
Log-normal Shadowing,
Quadratic Approximation.

ABSTRACT

This paper analyzes LoRa signal propagation in an urban environment, based on RSSI collections conducted at various distances ranging from 10 to 1610 meters. The data were analyzed using the log-normal shadowing model, allowing the generation of path loss graphs. The coefficient of determination (R^2) for the log-normal model was 0.9764, with an RMSE of 3.2872 and an MAE of 2.4020, indicating an excellent fit to the data. As a comparison between regression methods, the quadratic approximation presented an R^2 of 0.9117, RMSE of 6.1397, and MAE of 5.2137, reflecting lower performance. These results highlight the impact of distance on signal attenuation and confirm the effectiveness of the log-normal shadowing model in representing propagation in urban scenarios. The research contributes to understanding LoRa performance in dense environments, providing valuable insights for the planning and optimization of LoRa networks, as well as serving as a practical guide for future applications in the Internet of Things context.

I. INTRODUCTION

LoRa® technology (Long Range) has become one of the main solutions for IoT (Internet of Things) networks, offering long-distance communication with low energy consumption [1], [2]. Its applications span areas such as smart cities (as shown in Figure 1), precision agriculture, and environmental monitoring. This paper investigates the performance of the LoRa signal in an urban environment, focusing on signal propagation at various distances. The research validates the results using the log-normal shadowing and quadratic approximation models, contributing to the development of more accurate propagation models and the optimization of LoRa networks in dense urban scenarios.

The propagation analysis is essential to optimize LoRa technology in urban environments, ensuring the efficiency and reliability of data transmissions in projects proposed in the literature, despite the presence of obstacles.

The study in [3] proposes a Vehicle Monitoring System (VMS) based on IoT to collect environmental and vehicle performance data in urban areas. The system uses sensors to monitor parameters such as air quality (PM2.5, NO2, CO, O3), temperature, and humidity, as well as vehicle information via OBD-II and GPS location. The data is transmitted to a cloud server via LoRa technology. The system provides a graphical interface for real-time data visualization, which can be used by both drivers and government authorities for traffic planning and environmental decision-making. Expanding the LoRa gateway infrastructure in the city could enhance transmission stability and contribute to the development of smart cities.

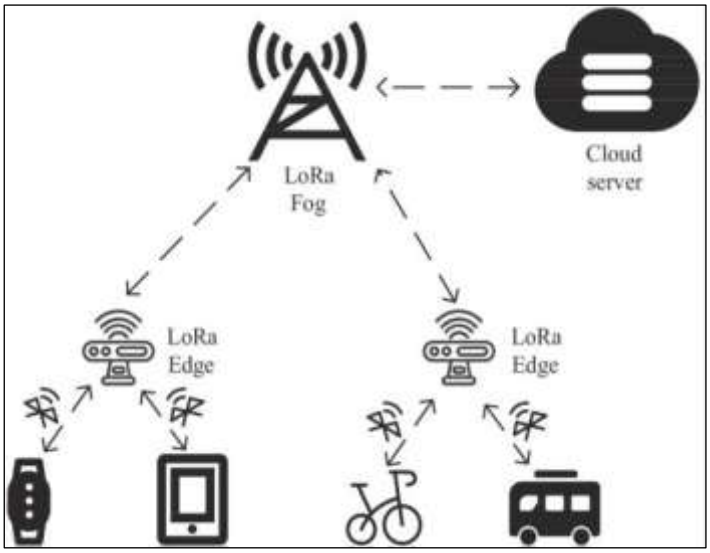

Figure 1: A hybrid LoRa and Bluetooth city network.
Source:[1].

The article [4] presents a collaborative sensor network based on LoRa for pollution monitoring in smart cities. The system uses geo-located nodes to measure temperature, relative humidity, and CO2 concentration, while also considering citizens' opinions. Using the collected data and city policies, the system controls traffic flow and advises citizens to avoid polluted areas. Tested in a real environment, the low-cost system proved effective in detecting CO2 levels. Future work aims to expand the application to larger areas and include additional parameters such as CO and vehicle volume.

The work done in [5] proposes a Fleet Management and Tracking System using LoRa, a low-power, long-range solution for monitoring and managing vehicle fleets. Each vehicle is equipped with a transmitter that includes an Arduino Nano, GPS module, switch, buzzer, and LoRa module. The GPS provides real-time location data, which is sent to the receiver unit at the management center via LoRa, where it is displayed on an LCD screen. The system also allows for emergency alerts and audible notifications in case of unauthorized movements or route deviations, enhancing security. It is scalable, easy to integrate with additional vehicles, and suitable for remote areas where traditional cellular networks are limited. This system offers a reliable and cost-effective alternative to traditional tracking, improving safety and operational efficiency, especially in challenging and remote locations.

In the present work, RSSI (Received Signal Strength Indicator) data collection was conducted practically at distances ranging from 10 to 1610 meters, covering different propagation conditions. The comparative analysis between the log-normal shadowing and quadratic approximation models allowed for a better understanding of signal attenuation and the challenges posed by urban obstacles such as buildings and interference.

Unlike other studies focused on rural environments [6] or line-of-sight scenarios, this paper focuses on the particularities of an urban environment, providing valuable insights for planning LoRa networks in areas with high construction density. The results obtained can be applied to improve coverage and efficiency of IoT networks, which is essential for future implementations in smart cities and other urban contexts.

This article is organized into the following sections: Section II presents the relevant concepts for conducting the studies. Section III presents the materials and methods addressed in this study. Section IV outlines the results obtained, and Section V presents the conclusion of the research.

II. THEORETICAL REFERENCE

II.1 LONG RANGE

LoRa (Long Range) is a wireless communication technology designed to transmit data over long distances with low power consumption. Based on Chirp Spread Spectrum (CSS) modulation, it offers high reception sensitivity, making it ideal for sensor networks and Internet of Things (IoT) applications. Operating in unlicensed frequency bands such as ISM (Industrial, Scientific, and Medical), it uses specific bands that vary by region: 433 MHz, 868 MHz (Europe), and 915 MHz (Americas) [7].

This operational flexibility allows LoRa to be applied in both urban and rural environments, even in locations with physical barriers or large distances. LoRa can reach distances of up to 15 km in rural areas and 2 to 5 km in urban environments, depending on the conditions [8]. Additionally, LoRa offers a relatively low data transmission rate but is sufficient for many IoT applications, ranging from 0.3 kbps to 27 kbps. This ensures efficient communication on a large scale, even in challenging network conditions.

LoRa is an integral part of LoRaWAN networks, which offer advanced security features, device management, and support for thousands of connected devices. LoRaWAN networks are highly scalable, making them suitable for projects involving large numbers of connected devices without overloading the network infrastructure. The CSS modulation used by LoRa also provides greater resilience to interference, ensuring communication in crowded environments or areas with many interference sources.

The technology is widely used in areas such as smart agriculture, smart cities, remote metering, and logistics tracking, standing out for its combination of range, energy efficiency, robustness, and compatibility with different frequency regulations worldwide.

II.2 LOG-NORMAL SHADOWING

The log-normal shadowing model is widely used to analyze the impact of obstacles on the propagation of radiofrequency signals [9]. This model is described by the equation:

$$PL(d) = PL(d_0) + 10\,n \log_{10}\left(\frac{d}{d_0}\right) + X_\sigma \qquad (1)$$

where $PL(d)$ is the path loss at a distance d, $PL(d_0)$ is the reference path loss at a distance d_0, n is the path loss exponent, and X_σ is the normal deviation component (shadowing variability).

According to the model, after determining the values of n and σ, the received power at distances not included during the collection can be estimated using the following equation [10]:

$$P_r(d) = P_r(d_0) - 10n \log_{10}\left(\frac{d}{d_0}\right) \qquad (2)$$

where $P_r(d) + X_\sigma$ is the estimated received power at the distance of interest d, and $P_r(d_0)$ is the received power at the reference distance d_0.

II.3 QUADRATIC APPROXIMATION

The quadratic approximation is capable of establishing a function using only a few points from a curve. Therefore, it can be used to estimate parameters of a semi-deterministic model and/or predict values for that model [11]. In other words, it can be used to create an equation that describes a curve between five points from a reading (e.g., RSSI), allowing the estimation of RSSI for any distance.

The quadratic approximation is easily applied in experiments that use RSSI, which decreases exponentially with the increase in distance, exhibiting second-order behavior. In this context, the number of observed points n can be greater than the degree of the polynomial g [11].

$$U_g(x) = b_0 + b_1 x + b_2 x^2 + \cdots + b_g x^g \qquad (3)$$

since $g < n - 1$.

The equations can be appropriately described in matrix form, as in the system below:

$$X^T X a = X^T f \quad (4)$$

where

$$X = \begin{pmatrix} 1 & x_1 & x_1^2 & \dots & x_1^m \\ 1 & x_2 & x_2^2 & \cdots & x_2^m \\ \vdots & \vdots & \vdots & \ddots & \vdots \\ 1 & x_n & x_n^2 & \cdots & x_n^m \end{pmatrix},$$

X^T is the transpose of the matrix X, which, for example, contains the distance values related to their respective RSSI

values present in the matrix $f = \begin{pmatrix} f_1 \\ \vdots \\ f_n \end{pmatrix}$. The matrix $a = \begin{pmatrix} a_0 \\ a_1 \\ \vdots \\ a_m \end{pmatrix}$

represents the coefficients of the quadratic approximation polynomial that is to be determined. The equations of this system are referred to as normal equations. This nomenclature arises because the system can be written as:

$$X^T(Xa - f) = 0 \quad (5)$$

The components of the vector $(Xa - f)$ are given by the residuals of the approximation, and according to the previous equation, this vector is orthogonal to the vectors formed by the elements of the rows of the matrix X^T, which are in the form

$$\begin{pmatrix} x_1^l \\ x_2^l \\ \vdots \\ x_n^l \end{pmatrix} \text{ with } l = 0, 1, 2, \dots, m.$$

III. MATERIALS AND METHODS

The tests were conducted using a Kerlink indoor LoRaWAN Gateway [12], positioned at a height of 7 meters, while the transmitter (LoRa® module) [13], powered by 3.6V derived from a 12V and 1.2Ah battery, was transported by car, starting 10 meters from the Gateway.

The Kerlink LoRaWAN indoor gateway, illustrated in Figure 2, connects LoRa sensors to cloud servers, enabling indoor IoT networks with Ethernet, Wi-Fi, or cellular connectivity, and is used in applications such as smart cities and automation. The LoRa® module, illustrated in Figure 3, is a low-power wireless technology for long-distance point-to-point communication. Widely used in IoT networks, it enables smart applications like energy management, natural resource control, environmental monitoring, and disaster prevention, operating via AT commands through the serial port (9600 bps).

To better model the collected data, a performance comparison was made between the log-normal shadowing model [10, 14] and quadratic fitting [15], using the metrics coefficient of determination (R^2), Root Mean Squared Error (RMSE), and Mean Absolute Error (MAE) [16]. The coefficient of determination R^2 evaluates the proportion of data variance explained by the model, ranging from 0 to 1, with higher values indicating better fit, as shown in equation 6.

Figure 2: Gateway LoRaWAN indoor.
Source: Kerlink, (2024).

Figure 3: Módulo LoRa®.
Source: Iot-Labs, (2024).

$$R^2 = 1 - \frac{\sum_{i=1}^{n}(y_i - \hat{y}_i)^2}{\sum_{i=1}^{n}(y_i - \bar{y}_i)^2} \quad (6)$$

where y_i are the observed real values, $\hat{y}_i$ are the values estimated by the regression model, $\bar{y}$ is the mean of the real values, and n is the total number of observations.

RMSE measures the average error between observed and predicted values, penalizing larger deviations more heavily, as shown in equation 7.

$$RMSE = \sqrt{\frac{1}{n}\sum_{i=1}^{n}(y_i - \hat{y}_i)^2} \quad (7)$$

where y_i are the observed real values, $\hat{y}_i$ are the values predicted by the regression model, and n is the total number of observations.

MAE calculates the mean of the absolute errors, being less influenced by outliers compared to other metrics like RMSE. The formula for MAE is:

$$MAE = \frac{1}{n}\sum_{i=1}^{n}|y_i - \hat{y}_i| \quad (8)$$

where y_i are the observed real values, $\hat{y}_i$ are the values predicted by the model, and n is the total number of observations.

These metrics were employed complementarily, allowing for a detailed analysis of the fit quality and error magnitude, contributing to the evaluation of model performance under different conditions.

IV. RESULTS

To analyze the propagation of the LoRa signal, the log-normal shadowing model was applied to the collected data. Table 1 summarizes the collected data, presenting the distance (in meters) and the corresponding RSSI (in dBm).

Table 1: Data collected.

Distance (m)	RSSI (dBm)
10	-65
110	-86
310	-108
510	-112
1010	-121
1610	-123

Source: Authors, (2025).

From approximately 2 km onward, no packets were received, highlighting the limitations of the indoor Gateway in urban environments.

The log-normal shadowing model is a widely used statistical model to describe signal attenuation in urban environments. It accounts for random variations caused by obstructions and the dispersion of the signal around an average value. In the log-normal propagation model, the path loss (PL) can be expressed by the equation 1.

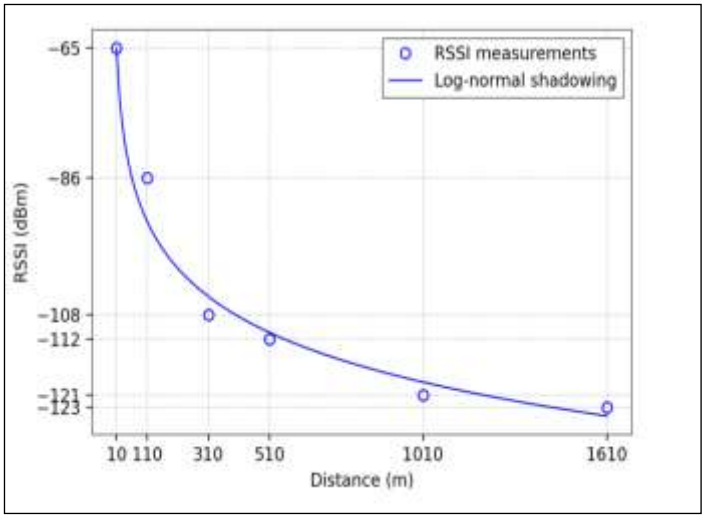

Figure 4: RSSI as a function of distance.
Source: Authors, (2025).

In short distances between 10 and 110 meters, the initial RSSI of -65 dBm gradually decreased, reaching -86 dBm at 110 meters, as shown in Figure 4. This loss suggests that, even at short distances, the urban environment impacts signal propagation due to the presence of obstacles and interference. At longer distances between 310 and 1610 meters, the signal loss became more pronounced, ranging from -108 dBm to -123 dBm.

The observed behavior reflects the additional challenges imposed by urban obstacles such as buildings, vegetation, and constructions, which intensify signal fading. For the log-normal shadowing model, the coefficient of determination (R^2) was 0.9764, the RMSE was 3.2872, and the MAE was 2.4020.

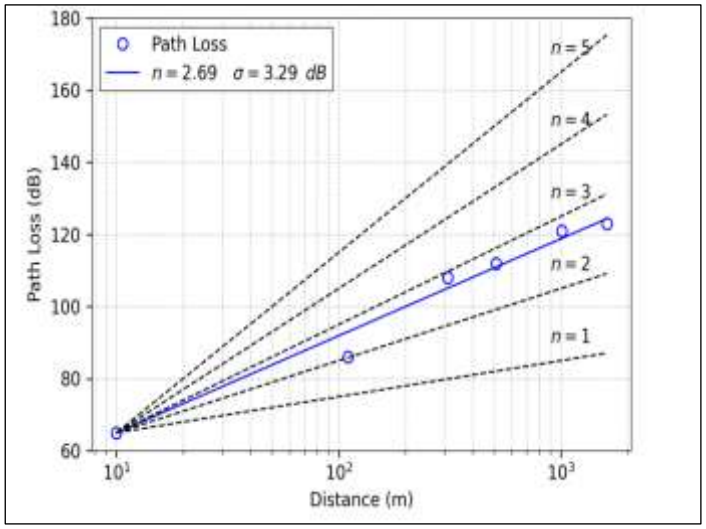

Figure 5: Path Loss as a function of distance.
Source: Authors, (2025).

Path loss (PL) was calculated for distances from 10 meters to 1610 meters, as shown in Figure 5. The propagation model applied in the urban test resulted in a path loss exponent (n) value of 2.69 and a standard deviation (σ) of $\sigma = 3.29$ dB. These values indicate signal attenuation and path loss variability in the studied urban scenario, contributing to the understanding of LoRa signal behavior at different distances and conditions.

Additionally, a quadratic curve fitting was applied to the collected RSSI data. The fitted curve can be observed in Figure 6.

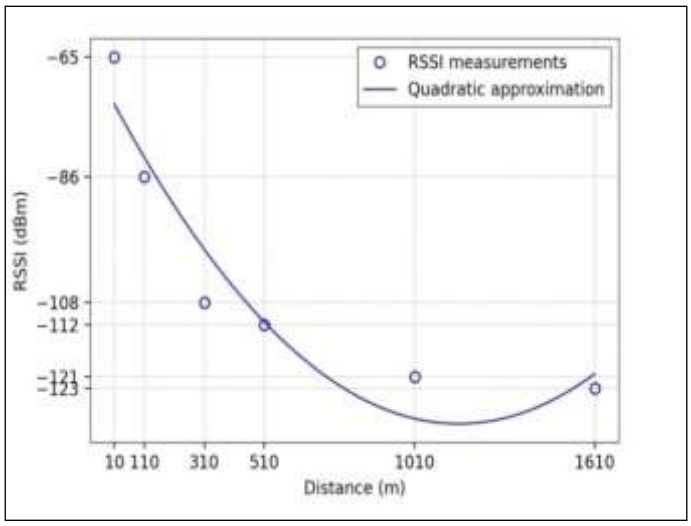

Figure 6: Quadratic approximation of measurements.
Source: Authors, (2025).

The fitting resulted in the equation 9.

$$y = 0.0000425669261x^2 - 0.0984761724x - 72.3111221 \quad (9)$$

The coefficient of determination (R^2) for the quadratic approximation was 0.9117, the RMSE was 6.1397, and the MAE was 5.2137, indicating that the quadratic model fits the collected data well, reflecting the behavior of the signal as a function of distance. For example, path loss increased significantly as the

distance grew, demonstrating the communication challenges in dense urban areas.

Table 2 presents the statistics of the metrics evaluated for the two models compared.

Table 2: Metrics.

Model	R^2	RMSE	MAE
Log-normal Shadowing	0.9764	3.2872	2.4020
Quadratic Approximation	0.9117	6.1397	5.2137

Source: Authors, (2025).

The analysis revealed that signal attenuation followed the expected behavior, with a marked decrease as the distance increased. Obstacles such as buildings and vegetation areas generated variability in the RSSI behavior, characterizing the urban environment as challenging for LoRa communication.

By using an outdoor LoRaWAN Gateway, designed for external environments, better performance is expected, including greater range and better packet reception rate. This upgrade should mitigate the limitations identified in this study.

The log-normal shadowing model outperformed the quadratic approximation. It obtained a higher coefficient of determination (R^2), indicating a greater ability to explain the variance of the data. Additionally, it had a lower RMSE, reflecting a smaller influence of outliers, and a lower MAE, showing reduced mean absolute errors. These results reinforce the higher precision and suitability of the log-normal shadowing model.

V. CONCLUSIONS

Based on the obtained results, the log-normal shadowing model demonstrated significantly better performance compared to the quadratic approximation. The coefficient of determination (R^2) of the log-normal shadowing model was 0.9764, indicating a greater ability to explain the variance of the data compared to the R^2 of the quadratic approximation, which was 0.9117.

Additionally, the log-normal shadowing model showed lower values of RMSE (3.2872) and MAE (2.4020), reflecting lower average errors and less influence from outliers. In contrast, the quadratic approximation had an RMSE of 6.1397 and an MAE of 5.2137, indicating a less precise fit. Therefore, it can be concluded that the log-normal shadowing model is more effective and reliable for representing the signal propagation data analyzed, proving to be a superior choice compared to the quadratic approximation.

The analysis highlights that LoRa communication is viable in urban scenarios, but the signal quality is significantly affected by distance and the presence of physical obstacles. The implementation of equipment optimized for outdoor use and strategies to mitigate urban effects will be essential to improve performance and extend the range of LoRa communication in dense environments.

In future work, it is proposed to evaluate the propagation of the LoRa signal in multiple urban locations across the city, aiming to assess the overall path loss. Additionally, the delay spread will be analyzed to better understand the multipath effects of the propagated signal.

VI. AUTHOR'S CONTRIBUTION

Conceptualization: David Alan de Oliveira Ferreira.
Methodology: David Alan de Oliveira Ferreira.
Investigation: David Alan de Oliveira Ferreira.
Discussion of results: David Alan de Oliveira Ferreira.
Writing – Original Draft: David Alan de Oliveira Ferreira.
Writing – Review and Editing: David Alan de Oliveira Ferreira.
Supervision: David Alan de Oliveira Ferreira.
Approval of the final text: David Alan de Oliveira Ferreira.

VII. REFERENCES

[1] H. H. R. Sherazi, L. A. Grieco, M. A. Imran and G. Boggia, "Energy-Efficient LoRaWAN for Industry 4.0 Applications," in IEEE Transactions on Industrial Informatics, vol. 17, no. 2, pp. 891-902, Feb. 2021, doi: 10.1109/TII.2020.2984549.

[2] Yao, F., Ding, Y., Hong, S., & Yang, S.-H. A Survey on Evolved LoRa-Based Communication Technologies for Emerging Internet of Things Applications. International Journal of Network Dynamics and Intelligence. 2025, 1(1), 4–19. doi: https://doi.org/10.53941/ijndi0101002.

[3] Hsieh, C. L., Ye, Z. W., Huang, C. K., Lee, Y. C., Sun, C. H., Wen, T. H. & Jiang, J. A. (2017). A vehicle monitoring system based on the LoRa technique. International Journal of Transport and Vehicle Engineering, 11(5), 1100-1106.

[4] Sendra, S., Garcia-Navas, J. L., Romero-Diaz, P., & Lloret, J. (2019). Collaborative lora-based sensor network for pollution monitoring in smart cities. In 2019 Fourth International Conference on Fog and Mobile Edge Computing (FMEC) (pp. 318-323), doi: 10.1109/FMEC.2019.8795321.

[5] Rahim, A., Sadhvi, M., Preethi, N., & Maheshwari, M. (2024). Fleet Management and Tracking System Using Lora. International Journal of Multidisciplinary Research in Science, Engineering and Technology, vol. 7, doi: 10.15680/IJMRSET.2024.0710040.

[6] N. H. Abd Rahman, Y. Yamada, M. H. Husni and N. H. Abdul Aziz, "Analysis of Propagation Link for Remote Weather Monitoring System through LoRa Gateway," 2018 2nd International Conference on Telematics and Future Generation Networks (TAFGEN), Kuching, Malaysia, 2018, pp. 55-60, doi: 10.1109/TAFGEN.2018.8580479.

[7] C. Susen, P. Nenninger, C. Fimmers, S. Storms and W. Herfs, "Comparison of Frequency Bands for Wireless Communication in Forests Using LoRa Modulation," 2022 IEEE 46th Annual Computers, Software, and Applications Conference (COMPSAC), Los Alamitos, CA, USA, 2022, pp. 1368-1374, doi: 10.1109/COMPSAC54236.2022.00216.

[8] Benjamín Arratia, Erika Rosas, Carlos T. Calafate, Juan-Carlos Cano, José M. Cecilia, Pietro Manzoni, AlLoRa: Empowering environmental intelligence through an advanced LoRa-based IoT solution, Computer Communications, Volume 218, 2024, Pages 44-58, ISSN 0140-3664, https://doi.org/10.1016/j.comcom.2024.02.014.

[9] S. Kurt and B. Tavli, Path-Loss Modeling for Wireless Sensor Networks: A review of models and comparative evaluations, in IEEE Antennas and Propagation Magazine, vol. 59, no. 1, pp. 18-37, Feb. 2017, doi: 10.1109/MAP.2016.2630035.

[10] Rappaport, T. S. (2002). Wireless communications: Principles and practice. (2nd ed.) (Prentice Hall communications engineering and emerging technologies series). Prentice Hall.

[11] Campos Filho, F. F. Algoritmos Numéricos, Ed. 2, LTC Editora, Belo Horizonte, 2007.

[12] Kerlink (2024). Wirnet iFemtoCell LoRaWAN Gateway. https://www.kerlink.com/product/wirnet-ifemtocell/. [Online; accessed 06-January-2025].

[13] Iot-Labs (2024). Módulo Long-Range (LoRa). https://iot-labs.iopportifoliomodulo-lorawan-smart-modular-technologies/. [Online; accessed 06-January-2025].

[14] Ferreira, D., Souza, R., & Carvalho, C. (2020). QA-kNN: Indoor Localization Based on Quartile Analysis and the kNN Classifier for Wireless Networks. Sensors, 20(17), 4714. https://doi.org/10.3390/s20174714.

[15] Ferreira, D. A. and Carvalho, C. (2019) "Localization In Indoor Environments Using Virtualized Three Dimensional Matrix", ITEGAM-JETIA, 5(18), pp. 120-127, doi: https://dx.doi.org/10.5935/2447-0228.20190037.

[16] Tatachar, A. V. (2021). Comparative assessment of regression models based on model evaluation metrics. International Journal of Innovative Technology and Exploring Engineering, 8(9), 853-860.

Journal of Engineering and Technology for Industrial Applications

ITEGAM-JETIA

Manaus, v.11 n.53, p. 87-94. May/June., 2025.
DOI: https://doi.org/10.5935/jetia. v11i53.1574

ISSN ONLINE: 2447-0228

RESEARCH ARTICLE
ACCESS

OPEN

HEALTH CLASSIFICATION OF PUMPS USING TRANSFORMER-BASED DEEP LEARNING

Arunachalam Shivaa T V [1], Jayaprasanth D [2] and Arunshankar J [3]

[1,2,3] Department of Instrumentation and Control Systems Engineering, PSG College of Technology, Coimbatore, Tamil Nadu 641004, India.

1http://orcid.org/0009-0004-3385-2928, 2http://orcid.org/0009-0009-2189-4908, 3http://orcid.org/0000-0001-8244-0875

Email: arunachalam7shiva@gmail.com, djp.ice@psgtech.ac.in, jas.ice@psgtech.ac.in

ARTICLE INFO

Article History
Received: January 20, 2025
Revised: February 20, 2025
Accepted: May 15, 2025
Published: May 31, 2025

Keywords:
Pumps,
Health classification,
Sensor data,
LSTM,
Transformer.

ABSTRACT

This paper develops a health classification system for pumps to enhance operational efficiency and reduce unplanned downtime, crucial for manufacturing and water treatment industries. Leveraging real-time data from temperature sensors and industrial accelerometer, the system captures vital pump health indicators. Data is collected via Data Acquisition (DAQ) modules and by using Deep Learning (DL) techniques such as Long Short-Term Memory (LSTM) networks and Transformers; the pump health classification is achieved. These DL models excel at understanding complex temporal and spatial patterns in sensor data, essential for accurate fault detection. Through a comparative analysis of LSTM and Transformer models, their efficacy in pump health classification is assessed. This approach emphasizes the importance of sophisticated data analysis and deep learning in industrial maintenance practices. By providing fault detection, the system aims to significantly reduce maintenance costs, optimize resource usage, and enhance the safety and reliability of industrial operations.

I. INTRODUCTION

In the realm of industrial machinery and manufacturing, ensuring the seamless operation of critical components is of paramount significance. Industrial pumps, the workhorses in numerous sectors, including energy production, water treatment, and manufacturing processes, are indispensable for the continuous flow of materials. However, these mechanical workhorses are susceptible to wear, tear, and potential malfunctions. The application of data analytics has emerged as a transformative force in the sphere of predictive maintenance, offering the capacity to proactively assess and maintain the health of these pumps in real-time.

Pump failure detection is a critical task in many industrial applications, as it can help to prevent costly downtime and catastrophic failures. In recent years, deep learning methods have been shown to be effective in pump failure detection, achieving state-of-the-art results. Deep learning methods, particularly Long Short-Term Memory (LSTM) and Transformer models, have excelled in this task. LSTM is suitable for sequential data like sensor readings obtained from the pumps, but have limitations in capturing long-range dependencies. In contrast, Transformers, a newer neural network type, can process data in parallel, enhancing efficiency and the ability to model long dependencies.

This study encompasses the real-time data collected on-site, thereby presenting a comprehensive approach to formulating a dependable and efficient health classification system, for these indispensable components of industrial operations.

II. RELATED WORKS

The need for advanced fault detection and predictive maintenance in industrial systems has led to significant research into sensor technologies, Machine Learning (ML) and Deep Learning (DL). Pioneered this effort by utilizing smart sensors for monitoring centrifugal pumps, demonstrating the potential of real-time data in early fault detection [1]. This study set a precedent for integrating diverse sensor data with analytical models to

enhance predictive maintenance strategies. Expanding on this foundation, the utility of vibration and motor current signature analysis (MCSA) in detecting faults in centrifugal pumps were carried out [2]. This work highlighted the complexity of interpreting the signals associated with mechanical failures, advocating for more nuanced diagnostic tools. A novel approach of using infrared thermography for predictive maintenance was introduced offering a non-invasive technique to monitor temperature variations indicative of underlying conditions, thereby broadening the spectrum of fault detection methods [3]. In the realm of ML, demonstrated the effectiveness of MLP and SVM algorithms in fault prediction within the oil and gas industry [4]. This study emphasized the critical role of algorithm selection in developing predictive models tailored to specific industrial contexts and data characteristics. A data-driven approach to predict pump failures, leveraging correlation analysis and empirical data was developed [5]. This methodology underscored the importance of integrating expert insights with analytical models to improve predictive accuracy.

The advancement of DL in fault diagnosis was significantly marked by Gamboa and utilized LSTM networks for time-series analysis. This approach addressed the challenges of analyzing temporal data, providing a robust framework for anomaly detection and forecasting [6]. Sabir *et al.* further validated the effectiveness of LSTM networks in diagnosing bearing faults in electrical machines, showcasing these models' capability to capture complex, time-dependent patterns characteristic of mechanical faults [7]. Diffusion-convolutional neural network (DCNN) was used for diagnosing pump faults from vibration data and high diagnostic accuracy was achieved in [8]. This work illustrated the potential of combining spatial analysis with traditional diagnostic data. The transformative potential of the Transformer model for fault diagnosis was introduced in [9]. The Anomaly Transformer model demonstrating the applicability of advanced DL models in industrial systems for fault identification was developed [10].

Further research by [11] and [12] expanded the application of ML and DL in industrial pump anomaly detection and bearing fault diagnosis, respectively. These studies highlighted the enhanced detection accuracy and efficiency afforded by advanced models. A comprehensive review of ML approaches for diagnosing faults in rotating equipment, emphasizing the superior performance of DL networks over traditional algorithms was carried out [13].

Sunal *et al*. reviewed ML-based fault detection for centrifugal pump induction motors, illustrating the ongoing advancements in the field and the importance of data quality and model selection [14]. The integration of CNNs with LSTMs marked a significant advancement in fault diagnosis, combining spatial and temporal data analysis for accurate fault identification [15],[16]. A transformer-based approach for novel fault detection was introduced showcasing the real-world applicability of advanced DL techniques in manufacturing and the effectiveness of these models in diverse applications [17]. Studies on centrifugal pump impeller crack detection, DL applications in rotating machinery fault diagnosis, and DL-based fault diagnosis of main pumps in converter stations were carried out [18-20].

The use of time series transformers for fault diagnosis in rotating machinery, demonstrating these models' ability to directly process time-series data and enhance fault identification accuracy was achieved [21],[22]. Reference [23] focused on fault classification of three-phase induction motors using Bi-LSTM networks, underscoring the potential of DL models in developing accurate and efficient fault classification systems. Markov parameters for fault detection in centrifugal pumps, presenting an innovative approach to fault diagnosis based on vibration data analysis was utilized in [24]. Applied a Transformer Neural Network for AC series arc-fault detection, illustrating the specific applications of DL models in addressing critical fault detection challenges in electrical systems [25].

Collectively, these studies form a comprehensive foundation for the development of advanced fault detection and predictive maintenance systems in industrial contexts. From the initial integration of sensor data with analytical models [1] to the application of advanced DL techniques for real-time fault identification [10],[17],[25], this field of research significantly advances the capabilities for fault detection, thereby enhancing operational efficiency, reducing maintenance costs, and improving safety across various industrial domains.

This paper is organized as follows: Section 3 gives description on the hardware setup. Proposed methodology is presented in Section 4. The performance of LSTM and Transformer models in classifying the health status of pump are discussed in Section 5. Finally, conclusions are drawn in Section 6.

III. HARDWARE DESCRIPTION

Figure 1 depicts the hardware setup developed for this work. The setup contains four similar centrifugal pumps. The leftmost pump is the healthy pump and the other three pumps are faulty. The second pump from the left has a bearing fault, and the third pump from the left has an impeller fault. The rightmost pump has both bearing and impeller faults. These faults are purposefully induced for destructive testing. Temperature and vibration sensors are mounted on these pumps to collect temperature and vibration data for fault detection. In this work, the leftmost pump (healthy) and rightmost pump (faulty) are considered for health classification problem using deep learning techniques.

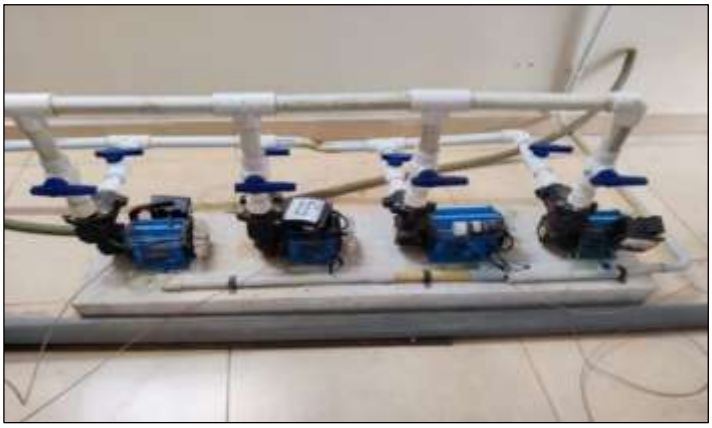

Figure 1: Hardware setup.
Source: Authors, (2025).

The closer view of one of the pumps with sensors mounted is shown in Figure 2. An industrial accelerometer is mounted on top of the pump’s casing, while a J-type thermocouple is placed inside the pump's body and sealed in such a way that the thermocouple lead touches the bearings. The outputs of these sensors are connected to the respective signal conditioning modules, which are then acquired and stored in a computer running data logging software. The logged data is analysed subsequently. This strategic assembly of sensors and modules collectively captures a detailed picture of the pumps operational

health, enabling a targeted and effective maintenance regime that bolsters industrial efficiency and reliability.

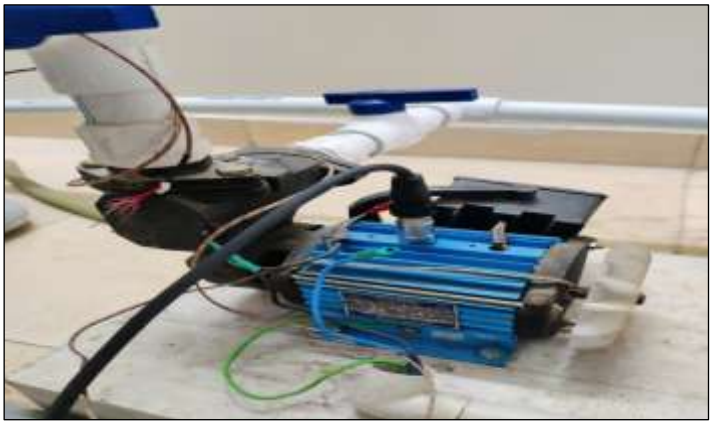

Figure 2: Closer view of a pump with sensors.
Source: Authors, (2025).

IV. PROPOSED METHODOLOGY

This section deals with the step-by-step implementation of the proposed method. It also briefly explains the DL algorithm implementation.

IV.1 FLOW DIAGRAM

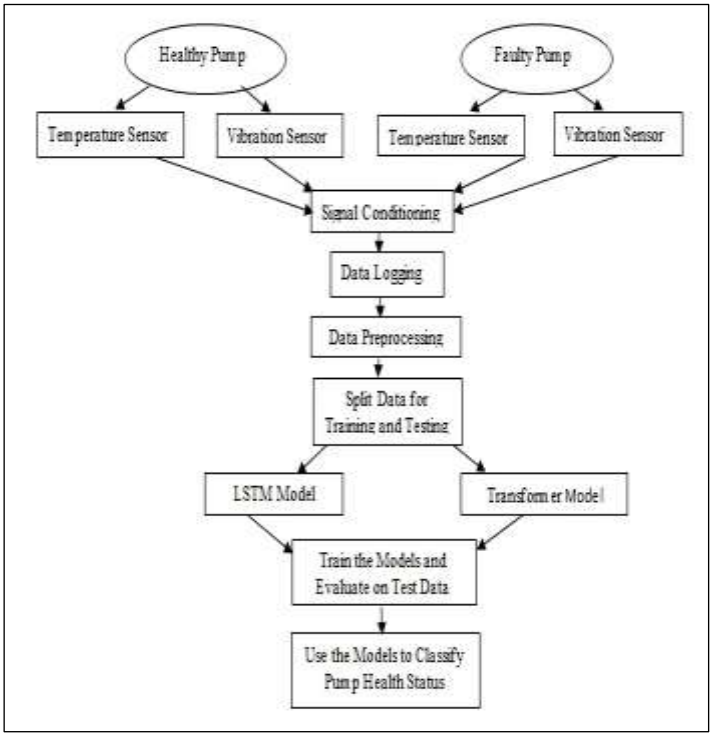

Figure 3: Work flow diagram.
Source: Authors, (2025).

Figure 3 shows the flow diagram that illustrates a process flow for a pump health monitoring system using deep learning models. The system differentiates between healthy and faulty pumps by analyzing the data collected from temperature and vibration sensors connected to the pumps. The process begins with signal conditioning, where the raw sensor data is filtered and transformed to a usable format using the DAQ modules. This is followed by data logging, where the conditioned sensor signals are stored and then data preprocessing is performed.

The preprocessed data is then divided into two sets: one for training the models and another for testing their performance. Two types of deep learning models are used: Long Short-Term Memory models and Transformer models. These models are trained separately with the training data set. After training, the models are evaluated using the test data to determine their accuracy and effectiveness in fault classification. Finally, the trained models are used to classify the health status of pumps in real-time or within a monitoring period, determining whether they are operating correctly (healthy) or have anomalies that suggest faults (faulty). The outcome of this process informs maintenance decisions, potentially leading to proactive interventions that can prevent breakdowns and maintain operational efficiency.

IV.2 ALGORITHM IMPLEMENTATION

Deep learning models like Long Short-Term Memory and Transformer have gained widespread popularity and proven to be highly effective for time series problems, surpassing traditional models for several key reasons.

IV.2.1 LONG SHORT-TERM MEMORY MODEL

Long Short-Term Memory is a type of recurrent neural network (RNN) architecture that has revolutionized the field of deep learning, particularly in the domain of sequential data processing. LSTMs address the vanishing gradient problem, which often hindered the training of traditional RNNs, by introducing a sophisticated memory mechanism that enables them to capture and remember long-range dependencies in sequences. LSTMs achieve their ability to learn long-term dependencies by using a combination of forget, input, and output gates that control the flow of information within the network. The forget gate determines what information from the previous state to forget, the input gate controls what new information to add, and the output gate controls what information to output. This allows LSTMs to selectively update, store, or discard information as they process data over time [15],[23].

The LSTM model design steps are as follows:

Step 1: Determine the number of LSTM layers: The number of LSTM layers depends on the complexity of the task and the size of the dataset. For small datasets, it is typically best to start with one or two LSTM layers. For larger datasets, or for more complex tasks, it may be necessary to use three or more LSTM layers.
Step 2: Determine the number of units in each LSTM layer: The number of units in each LSTM layer represents the complexity of the model. For small datasets, it is typically best to start with a small number of units. For larger datasets, or for more complex tasks, it may be necessary to use a larger number of units.
Step 3: Determine the activation function for the LSTM layers: The activation function for the LSTM layers controls the information flow through the network. The most common activation function for LSTM layers is the hyperbolic tangent (tanh) function. However, other activation functions, such as the sigmoid and rectified linear unit (ReLU) function, can also be used.
Step 4: Determine the optimizer for the LSTM model: The optimizer controls the parameters of the LSTM model which are updated during training. Some popular optimizers for LSTM models include Adam and RMSprop.
Step 5: Determine the loss function for the LSTM model: The loss function measures how well the LSTM model is performing

on the training data. Some common loss functions for LSTM classification tasks include cross-entropy and binary cross-entropy.

Step 6: Determine the batch size for the LSTM model: The batch size controls how many samples are processed by the LSTM model at each training step. A larger batch size can improve the efficiency of training, but it can also lead to overfitting. A smaller batch size can help to prevent overfitting, but it can also make training slower.

Step 7: Determine the number of epochs for the LSTM model: The number of epochs controls how many times the LSTM model is trained over the entire training dataset. A larger number of epochs can improve the performance of the model, but it can also lead to overfitting. A smaller number of epochs can help to prevent overfitting, but it may not allow the model to learn the training data fully.

IV.2.2 TRANSFORMER MODEL

The Transformer model represents a significant breakthrough in deep learning. Its fundamental innovation lies in the attention mechanism, enabling the simultaneous capture of long-range dependencies in input sequences through self-attention layers, resulting in more efficient computation, faster training, and improved accuracy. Furthermore, transformers have found utility in time series analysis, as demonstrated by models like Informer. Informer leverages self-attention to capture long-range temporal dependencies and incorporates positional encoding to discern the temporal order within time series data. This adaptability showcases the far-reaching impact of Transformer-based models in diverse fields, including time series forecasting [12],[25].

The transformer model design steps are as follows:

Step 1: Determine the number of encoder layers: The number of encoder layers depends on the complexity of the task and the size of the dataset.

Step 2: Determine the number of attention heads: The number of attention heads also depends on the complexity of the task and the size of the dataset.

Step 3: Determine the embedding dimension: The embedding dimension should be chosen to be large enough to capture the complexity of the input and output data.

IV.2.3 DESIGN PARAMETERS

Two deep learning models, LSTM and Transformer, were developed to classify the health status of industrial pumps based on separate temperature and vibration datasets. Table 1 and Table 2 represent the design parameters of the LSTM model and transformer model respectively.

The LSTM model is constructed with one layer containing 50 units, employing a sigmoid activation function, with Adam optimizer, and binary cross entropy as the loss function. It is trained over 5 epochs with a batch size of 128, processing 100,000 vibration data points and 23,701 temperature data points for both healthy and faulty pump conditions. The transformer model, designed for capturing complex dependencies, includes 2 encoder layers with 2 attention heads, and an embedding dimension of 128. It follows the same training regimen of 5 epochs and uses an identical dataset structure as the LSTM model. These design parameters enable the models to learn from the temporal and spatial patterns inherent in the sensor data, aiming to provide accurate fault classification to enhance industrial maintenance practices.

Table 1: Design parameters for LSTM model.

Design Parameters	Values/Function
No. of LSTM layers	1
No. of units in each layer	50
Activation function	Sigmoid
Optimizer	Adam
Loss function	Binary Cross Entropy
Batch Size	128
No. of epochs	5
Vibration data points	100000 (for each Healthy and Faulty Pump)
Temperature data points	23701 (for each Healthy and Faulty Pump)

Source: Authors, (2025).

Table 2: Design parameters for transformer model.

Design Parameters	Values/Function
No. of encoder layers	2
No. of attention heads	2
Embedding dimension (Head size)	128
No. of epochs	5
Vibration data points	100000 (for each Healthy and Faulty Pump)
Temperature data points	23701 (for each Healthy and Faulty Pump)

Source: Authors, (2025).

V. RESULTS AND DISCUSSIONS

V.1 LSTM MODEL FOR VIBRATION DATASET

The vibration data obtained from industrial accelerometer is used for training the model. Figure 4 represents the accuracy of the LSTM model for vibration data. It is inferred from Figure 4 that the initial high peak indicates that the model is learning well from the training data and performs effectively on both the training and validation datasets. The downturn in both training and validation accuracy implies a common issue affecting generalization which could be due to overfitting or a sudden change in the data distribution. The subsequent steady increase in accuracy for both datasets suggests that the model is recovering and adapting to the challenges presented during the downturn. As the number of epochs increases, the accuracy also increases.

A confusion matrix in binary classification provides a detailed breakdown of the model's performance by categorizing the predictions into four categories: True Positives (TP), True Negatives (TN), False Positives (FP) and False Negatives (FN).

Figure 5 represents the confusion matrix of the LSTM model for the predictions made upon the test data. The TP and FP are 18,537 and 19,959 respectively. The TN and FN are 1,484 and 0 respectively. These values are used to find several other performance indicators of the model, such as Precision, Recall, and F1 Score.

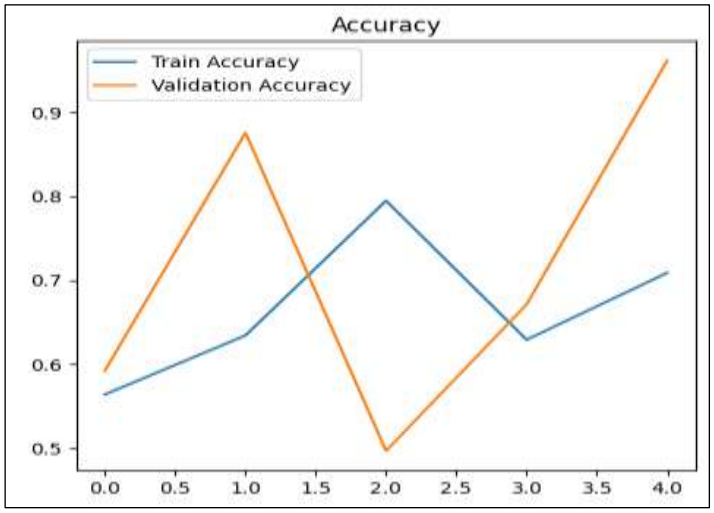

Figure 4: Accuracy of LSTM for vibration dataset.
Source: Authors, (2025).

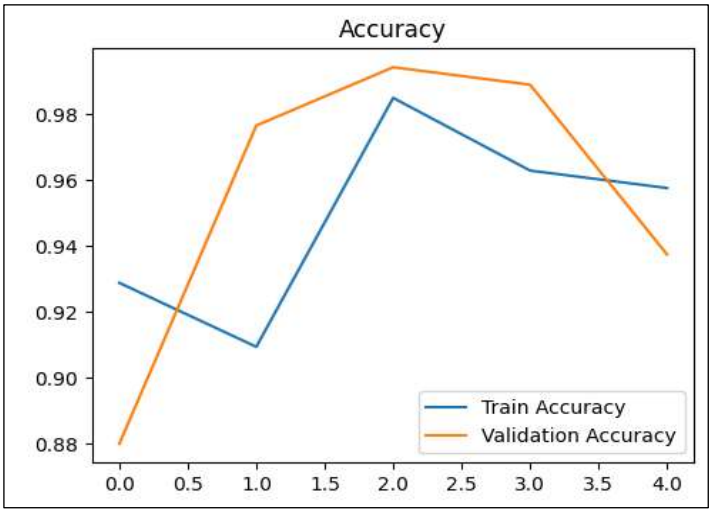

Figure 6: Accuracy of LSTM for temperature dataset.
Source: Authors, (2025).

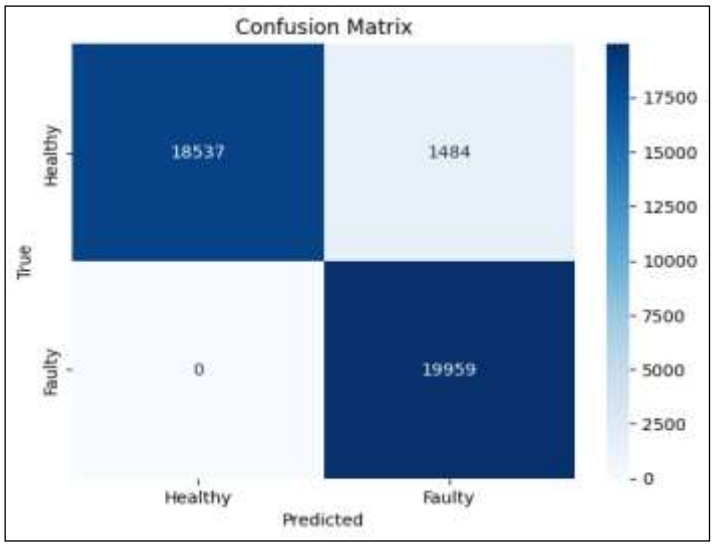

Figure 5: Confusion matrix of LSTM for vibration dataset.
Source: Authors, (2025).

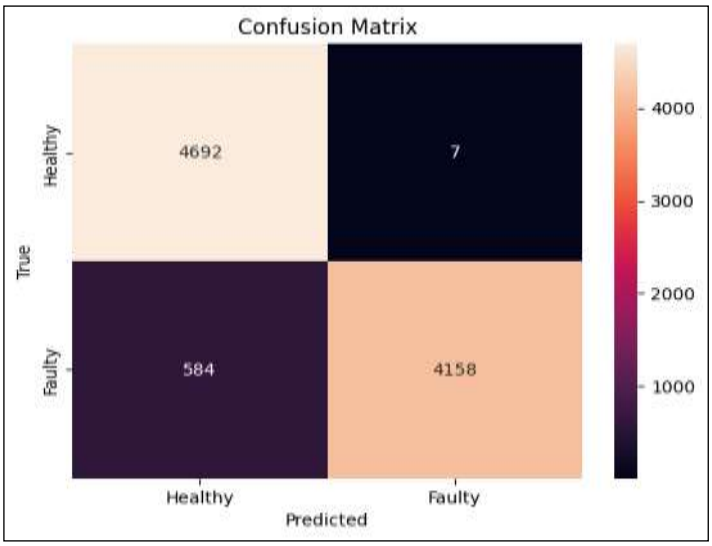

Figure 7: Confusion matrix of LSTM for temperature dataset.
Source: Authors, (2025).

Table 3 shows the classification report of the LSTM model indicating the key performance indicators. It also provides a comprehensive summary of various performance metrics such as precision, recall and F1-score for each class in a classification problem.

Table 3: Classification report of LSTM for vibration dataset.

Class	Precision	Recall	F1-score	Support
Faulty	1.00	0.93	0.96	20021
Healthy	0.93	1.00	0.96	19959
Accuracy			0.96	39980
Macro average	0.97	0.96	0.96	39980
Weighted average	0.97	0.96	0.96	39980

Source: Authors, (2025).

V.2 LSTM MODEL FOR TEMPERATURE DATASET

Figure 6 represents the accuracy of the LSTM model for temperature data. Figure 7 represents the confusion matrix of the predictions made upon the test data.

Table 4 shows the classification report of the LSTM model indicating the key performance indicators. It is observed that the model made a good number of correct predictions of the pump status on the test data with an accuracy of 94%.

Table 4: Classification report of LSTM for temperature dataset.

Class	Precision	Recall	F1-score	Support
Faulty	0.89	1.00	0.94	4699
Healthy	1.00	0.88	0.93	4742
Accuracy			0.94	9441
Macro average	0.94	0.94	0.94	9441
Weighted average	0.94	0.94	0.94	9441

Source: Authors, (2025).

V.3 TRANSFORMER MODEL FOR VIBRATION DATASET

Figure 8 represents the accuracy of the transformer model for vibration data. It shows a higher level of accuracy in classifying the status of the pump. Figure 9 represents the confusion matrix of the predictions made upon the test data.

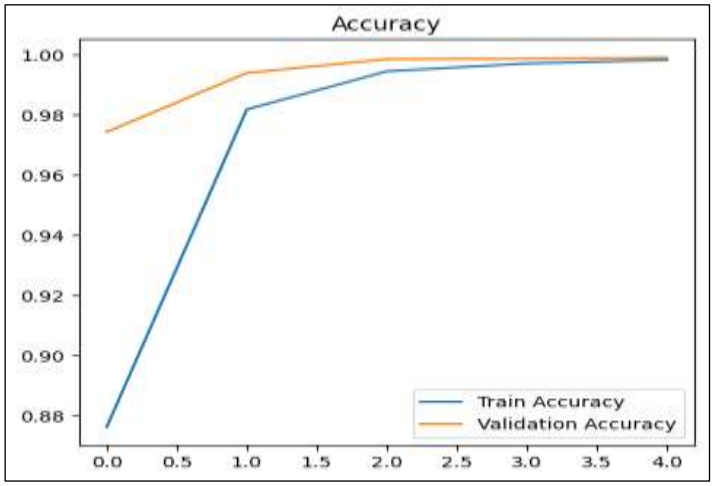

Figure 8: Accuracy of transformer model for vibration dataset.
Source: Authors, (2025).

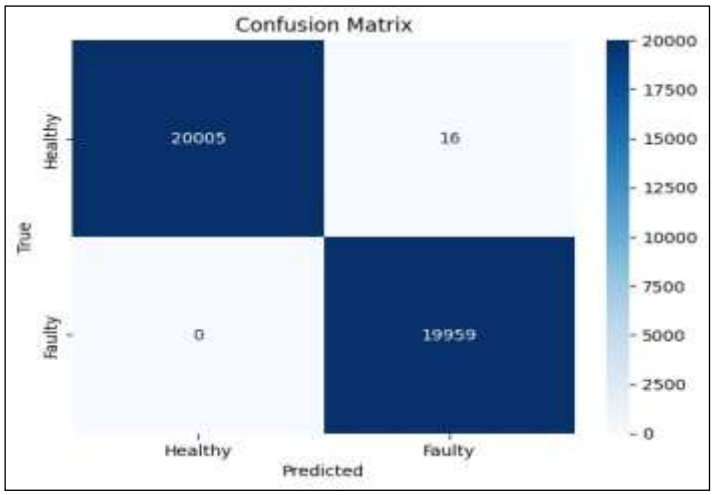

Figure 9: Confusion matrix of transformer model for vibration dataset.
Source: Authors, (2025).

Table 5 shows classification report of transformer model indicating key performance indicators. It is inferred that transformer model for vibration dataset achieved an extremely high accuracy of around 100% in classifying the pump health status.

Table 5: Classification report of transformer model for vibration dataset.

Class	Precision	Recall	F1-score	Support
Faulty	1.00	1.00	1.00	20021
Healthy	1.00	1.00	1.00	19959
Accuracy			1.00	39980
Macro average	1.00	1.00	1.00	39980
Weighted average	1.00	1.00	1.00	39980

Source: Authors, (2025).

V.4 TRANSFORMER MODEL FOR TEMPERATURE DATASET

Figure 10 represents the accuracy of transformer model on temperature data. It shows that greater accuracy is achieved in classifying the status of the pump compared to LSTM model. Figure 11 represents confusion matrix of the predictions made upon the test data.

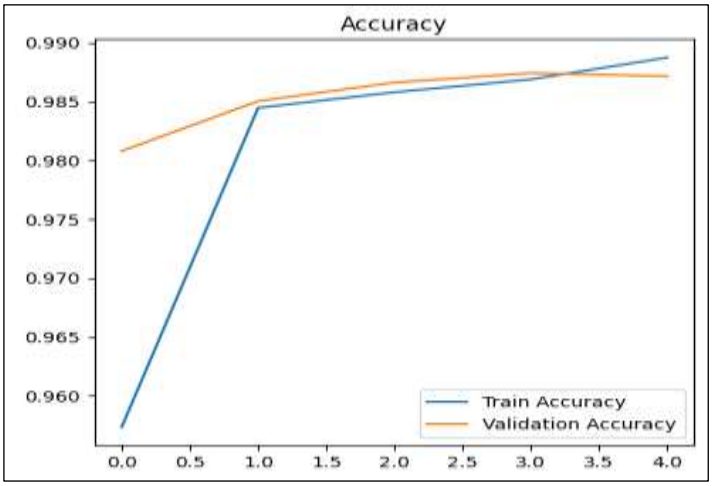

Figure 10: Accuracy of transformer model for temperature dataset.
Source: Authors, (2025).

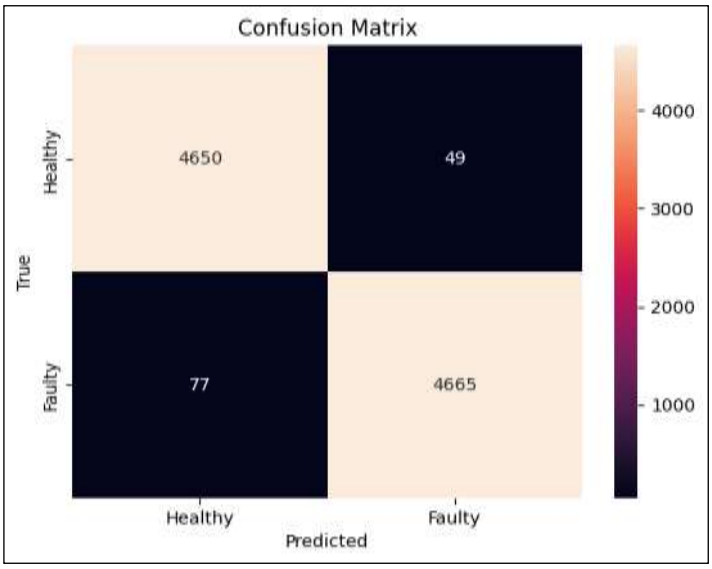

Figure 11: Confusion matrix of transformer model for temperature dataset.
Source: Authors, (2025).

Table 6 shows the classification report of the transformer model indicating the key performance indicators. The transformer model for temperature dataset achieved a very good accuracy of 99% in classifying the pump health status.

Table 6: Classification report of transformer model for temperature dataset.

Class	Precision	Recall	F1-score	Support
Faulty	0.99	0.99	0.99	4699
Healthy	0.99	0.99	0.99	4742
Accuracy			0.99	9441
Macro average	0.99	0.99	0.99	9441
Weighted average	0.99	0.99	0.99	9441

Source: Authors, (2025).

V.5 COMPARATIVE ANALYSIS OF LSTM AND TRANSFORMER MODELS

It is inferred that from Table 7 and Table 8, the classification accuracy obtained with the Transformer model is comparatively better than LSTM model. Hence, the Transformer

model outperforms the LSTM model for pump health classification.

Table 7: Comparison of LSTM and Transformer model for vibration dataset.

Performance Metrics	LSTM	Transformer
Accuracy	0.9629	0.9996
Precision	0.9308	0.9992
Recall	0.9995	1.0000
F1-score	0.9642	0.9996

Source: Authors, (2025).

Table 8: Comparison of LSTM and Transformer model for temperature dataset.

Performance Metrics	LSTM	Transformer
Accuracy	0.9374	0.9867
Precision	0.9983	0.9896
Recall	0.8768	0.9858
F1-score	0.9336	0.9867

Source: Authors, (2025).

V. CONCLUSIONS

The comparative performance analysis of the LSTM and Transformer models for pump health classification using vibration and temperature datasets reveals a distinct advantage in favor of the Transformer model. These findings underscore the effectiveness of the Transformer architecture in handling sequential data, benefitting from its attention mechanisms that capture long-range dependencies more effectively than LSTM's gated recurrent units. Consequently, the Transformer model proves to be a robust and highly accurate tool for predictive maintenance in industries, offering significant potential to reduce downtime and maintenance costs through timely and precise fault detection.

In conclusion, the empirical evidence from this study strongly supports the Transformer-based models over LSTMs for monitoring the health of industrial pumps using sensor data. The higher accuracy and precision of the Transformer model can enable more reliable and effective predictive maintenance strategies, contributing to the advancement of smart monitoring practices.

VI. AUTHOR'S CONTRIBUTION

Conceptualization: Arunachalam Shivaa T V , Jayaprasanth D and Arunshankar J
Methodology: Arunachalam Shivaa T V , Jayaprasanth D and Arunshankar J
Investigation: Arunachalam Shivaa T V , Jayaprasanth D and Arunshankar J
Discussion of results: Arunachalam Shivaa T V , Jayaprasanth D and Arunshankar J
Writing Original Draft: Arunachalam Shivaa T V , Jayaprasanth D and Arunshankar J
Writing Review and Editing: Arunachalam Shivaa T V , Jayaprasanth D and Arunshankar J
Supervision: Arunachalam Shivaa T V , Jayaprasanth D and Arunshankar J
Approval of the final text: Arunachalam Shivaa T V , Jayaprasanth D and Arunshankar J

VII. ACKNOWLEDGMENTS

This work is funded by All India Council for Technical Education (AICTE) - Research Promotion Scheme (RPS) under File No. 8 – 73/ FDC/ RPS (POLICY – 1)/ 2019 – 20.

VIII. REFERENCES

[1] Lei Chen, Lijun Wei, Yu Wang, Junshuo Wang, and Wenlong Li, "Monitoring and predictive maintenance of centrifugal pumps based on smart sensors", *Sensors*, vol. 22, no. 6, p. 2106, 2022. https://doi.org/10.3390/s22062106

[2] A. R. Mohanty, P. K.Pradhan, N. P. Mahalik, and S. G. Dastidar, "Fault detection in a centrifugal pump using vibration and motor current signature analysis", *Int. J. Autom. Control*, vol. 6, no. 3–4, pp. 261–276, 2012. https://doi.org/10.1504/IJAAC.2012.051884

[3] A. D. Marinescu, C. Cristescu, T. C. Popescu, and C. A. Safta, "Assessing the opportunity to use the infrared thermography method for predictive maintenance of hydrostatic pumps", in *Proc. Int. Conf. on Energy and Environment (CIEM)*, 2017, pp. 270–274. https://doi.org/10.1109/CIEM.2017.8120790

[4] Orrù, Pier Francesco, Andrea Zoccheddu, Lorenzo Sassu, Carmine Mattia, Riccardo Cozza, and Simone Arena, "Machine learning approach using MLP and SVM algorithms for the fault prediction of a centrifugal pump in the oil and gas industry", *Sustainability*, vol. 12, no. 11, p. 4776, 2020. https://doi.org/10.3390/su12114776

[5] A. Mohammed, "Data driven-based model for predicting pump failures in the oil and gas industry", *Eng. Fail. Anal.*, vol. 145, p.107019, 2023. https://doi.org/10.1016/j.engfailanal.2022.107019

[6] J. C. B. Gamboa, "Deep learning for time-series analysis", arXiv preprint arXiv:1701.01887, 2017. https://doi.org/10.48550/arXiv.1701.01887.

[7] R. Sabir, D. Rosato, S. Hartmann, and C. Guehmann, " LSTM based bearing fault diagnosis of electrical machines using motor current signal", in *Proc. Int. Conf. on Machine Learning and Applications (ICMLA)*, 2019. https://doi.org/10.1109/ICMLA.2019.00113

[8] S. Manikandan, and K. Duraivelu, "Vibration-based fault diagnosis of broken impeller and mechanical seal failure in industrial mono-block centrifugal pumps using deep convolutional neural network", *J. Vib. Eng. Technol.*,vol. 11, no.1, pp. 141-152, 2023. https://doi.org/10.1007/s42417-022-00566-0

[9] A. Vaswani, N. Shazeer, N. Parmar, J. Uszkoreit, L. Jones, A. N. Gomez, L. Kaiser, and Polosukhin, "Attention is all you need" *Adv. Neural Inf. Process. Syst.*, vol. 30, pp. 5998-6008, 2017. https://doi.org/10.48550/arXiv.1706.03762

[10] J. Xu, H. Wu, J. Wang, and M. Long, "Anomaly transformer: Time series anomaly detection with association discrepancy", in *Proc. Int. Conf. on Learning Representations (ICLR)*, 2022. https://doi.org/10.48550/arXiv.2110.02642

[11] N. Dutta, P. Kaliannan, U. Subramaniam, "Application of machine learning algorithm for anomaly detection for industrial pumps. Machine Learning Algorithms for Industrial Applications", *Springer*, pp. 237-263, 2021. https://doi.org/10.1007/978-3-030-50641-4_14

[12] Z. Yang, J. Cen, X. Liu, J. Xiong, and H. Chen, "Research on bearing fault diagnosis method based on transformer neural network", *Meas. Sci. Technol.*, vol. 33, no. 8, p. 085111, 2022. https://doi.org/10.1088/1361-6501/ac66c4

[13] S. Manikandan, and K. Duraivelu, "Fault diagnosis of various rotating equipment using machine learning approaches–A review", *Proc. Inst. Mech. Eng., Part E: J. Process Mech. Eng.*, vol. 235, no. 2, pp. 629-642, 2021. https://doi.org/10.1177/0954408920971976

[14] C. E. Sunal, V. Dyo, and V. Velisavljevic, "Review of machine learning based fault detection for centrifugal pump induction motors", *IEEE Access*, vol. 10, pp. 71344-71355, 2022. https://doi.org/10.1109/ACCESS.2022.3187718

[15] H. Pan, X. He, S. Tang, F. Meng, "An improved bearing fault diagnosis method using one-dimensional CNN and LSTM", *Stroj. Vestn./J. Mech. Eng.*, vol. 64, pp. 443-452, 2018. https://doi.org/10.5545/sv-jme.2018.5249.

[16] H. Sun, and S. Zhao, "Fault diagnosis for bearing based on 1DCNN and LSTM", *Shock Vib.*, pp.1-17, 2021. https://doi.org/10.1155/2021/1221462

[17] H. Wu, M. J. Triebe, and J. W. Sutherland, "A transformer-based approach for novel fault detection and fault classification/diagnosis in manufacturing: A rotary system application", *J. Manuf. Syst.*, vol. 67, pp. 439-452, 2023. https://doi.org/10.1016/j.jmsy.2023.02.018

[18] Abdulkarem, Waleed, R. Amuthakkannan, and Khalid F. Al-Raheem, "Centrifugal pump impeller crack detection using vibration analysis", in *Proc. Int. Conf. on Research in Science, Engineering and Technology*, 2014, pp. 206-211. http://dx.doi.org/10.15242/IIE.E0314606.

[19] W. Jiang , C. Wang , J. Zou, and S. Zhang, "Application of deep learning in fault diagnosis of rotating machinery", *Processes*, vol. 9, no. 6, p. 919, 2021. https://doi.org/10.3390/pr9060919

[20] Q. Zhao, G. Cheng, X. Han, D. Liang, X. Wang, "Fault diagnosis of main pump in converter station based on deep neural network", *Symmetry*, vol. 13, no. 7, p. 1284, 2021. https://doi.org/10.3390/sym13071284

[21] Y. Jin, L. Hou, and Y. Chen, "A time series transformer based method for the rotating machinery fault diagnosis", *Neurocomputing*, vol. 494, pp. 379-395, 2022. https://doi.org/10.1016/j.neucom.2022.04.111

[22] Z. Lu, L. Liang, J. Zhu, W. Zou, and L. Mao, "Rotating machinery fault diagnosis under multiple working conditions via a time series transformer enhanced by convolutional neural network", *IEEE T. Instrum. Meas.*, vol. 72, pp. 1-11, 2023. https://doi.org/10.1109/TIM.2023.3318707

[23] J. Vanga, D. P. Ranimekhala, S. Jonnala, J. Jamalapuram, B. Gutta, S. R. Gampa, and A. Alluri, "Fault classification of three phase induction motors using Bi-LSTM networks", *J. Electr. Syst. Inf. Technol.*, vol. 10, no. 1, pp. 1-15, 2023. https://doi.org/10.1186/s43067-023-00098-x

[24] J. P. S. Gonçalves, F. Fruett, J. G. Dalfré Filho, and M. Giesbrecht, "Fault detection and classification in a centrifugal pump from vibration data using markov parameters", *Mech. Syst. Signal Process.*, vol. 158, p. 107694, 2021. https://doi.org/10.1016/j.ymssp.2021.107694

[25] A. Chabert, M. C. Bakkay, P. Schweitzer, S. Weber S, and J. Andrea, "A transformer neural network for AC series arc-fault detection", *Eng. Appl. Artif. Intell.*, vol.125, p. 106651, 2023. https://doi.org/10.1016/j.engappai.2023.106651

Journal of Engineering and Technology for Industrial Applications

ISSN ONLINE: 2447-0228

ITEGAM-JETIA

Manaus, v.11 n.53, p. 95-102. May/June., 2025.
DOI: https://doi.org/10.5935/jetia. v11i53.1577

RESEARCH ARTICLE OPEN ACCESS

ENERGY IMPACT OF LIGHTING SYSTEM REPLACEMENT IN A PUBLIC EDUCATION INSTITUTION

Fernando A. Benger[1], Cristian R. Ruschetti [2], Matias Meira [3], Silvano R. Rossi[4], Juan P. Pendones [5].

[1,2,5] Universidad Nacional del Centro de la Pcia. de Buenos Aires, Facultad de Ingeniería, Núcleo INTELYMEC. Olavarría, Bs. As., Argentina.
[3,4] CIFICEN (UNCPBA-CICPBA-CONICET), Argentina.

[1]https://orcid.org/0009-0001-2093-5976, [2]https://orcid.org/0000-0002-3183-7247, [3]https://orcid.org/0000-0002-6332-1915, [4]https://orcid.org/0000-0002-3835-4467, [5]https://orcid.org/0009-0007-4206-8782.

Email: fbenger@fio.unicen.edu.ar, cruschet@fio.unicen.edu.ar, matias.meira@fio.unicen.edu.ar srossi@fio.unicen.edu.ar, jpendones@fio.unicen.edu.ar

ARTICLE INFO

Article History
Received: January 21, 2025
Revised: February 20, 2025
Accepted: May 15, 2025
Published: May 31, 2025

Keywords:
Energy efficiency,
Energy consumption,
Environmental impact,
Lighting,
LED technology.

ABSTRACT

Lighting loads represent a significant percentage of global energy consumption, becoming an important issue to analyze in order to contribute to a more efficient use of electrical energy. This work presents an analysis of the lighting energy demand in the buildings of the College of Engineering - UNCPBA along with a proposal for improvement using LED technology. A survey of each of the buildings and spaces has been carried out to identify the current lighting conditions of the different College work areas and the associated energy consumption. The analysis includes the impact in terms of energy and lighting quality, replacement costs and return on investment. The calculation of greenhouse gases (GHG) and their environmental impact is also presented. The results of the study indicate that the transition to LED lighting would result in approximately 60% savings in electrical energy consumption at the College. The study draws conclusions regarding the efficiency of the lighting process and the reduction of environmental impact.

I. INTRODUCTION

The global trend towards a more efficient use of natural resources leads to the analysis and restructuring of energy-consuming systems. The world's population growth entails a marked increase in electricity consumption in all areas of demand since electricity has greatly improved the population's quality of life. However, on multiple occasions, excessive energy consumption, improper energy use and electrical installations / electrical machines working in poor conditions are situations that directly or indirectly involve Energy Efficiency (EE) [1]. On the one hand, EE involves making a series of changes and/or improvements in different consumption sectors to reduce the energy used for certain services or activities [2],[3]. On the other hand, EE is closely aligned with the necessary investments and policies to make the changes that lead to improvements in energy-consuming systems [4],[5].

The energy demand has grown due to various factors [6]. In addition, electrical energy has a higher relative cost compared with other energies [7]. Therefore, focusing on increasing the EE of electrical systems is a relevant issue as one of the ways to face the situation. In particular, lighting loads represent an important percentage of the electrical energy consumption in different areas [8],[9], and represent approximately up to 20% of the global energy consumption [10],[11]. Therefore, analyzing the problem of energy demand due to lighting loads becomes a matter of great importance in the context of EE. Light Emitting Diodes (LED) lights have higher efficiency compared to other technologies such as incandescent bulbs, halogen lamps, and Compact Fluorescent Lights (CFL). In comparative terms, the required energy to supply a given luminous flux is lower in the case of using lighting through LED technology [9],[12],[13]. Moreover, LED lamps have a duration 5 times longer than CFL lamps and their electrical consumption is around 50% lower [14].

LED lamps also limit the flickering effect produced in fluorescent lamps with conventional ballast, constituting another positive aspect [15]. This phenomenon can produce headaches and visual and neurological effects on humans [16], affecting their health and work environments. So, it should be considered among the factors that determine the decision to move to LED lighting. However, unlike fluorescent lamps, LED lamps are powered by DC current, from a rectification process. Two wave characteristics

influence the flickering. These are the ripple voltage and the frequency at which the ripple occurs [17]. This can lead to intermittency or oscillations in light intensity, which also affect the human eye. According to [18] have analyzed and quantified the flickering effect in commercial LED lights. According to the study, percentage differences can be found between commercially known brand lamps and low-cost generic lamps. However, the flickering effect is considered to be almost completely reduced in LED lamps. To mitigate these effects, international organizations such as the IEEE makes recommendations on maximum flicker levels to avoid harmful effects on human health [19]. Furthermore, the lifespan of LED light sources is not affected by the switching frequency. In general, unlike fluorescent lamps that emit light in all directions, LED light sources radiate in one direction (depending on the position of the lamp); therefore, their optical efficiency is better. Thus, LED lights have better electrical characteristics and, in addition, a positive environmental impact compared with fluorescent ones [20].

In particular, activities that are developed in different areas, such as residential, educational, administrative, industrial, among others, require a certain light level on the work plane.

Several authors have presented studies to characterize the work areas, identifying the conditions in which the activities are developed. These studies allow taking action to improve the results in relation to EE and to verify the illumination levels according to regulations and standards. For example, there are studies aimed at saving energy by replacing of conventional lamps with LED technology in commercial areas and public buildings [21-23]. Others focused on the techno-economic considerations derived from the replacement in offices building [24], and methodologies to verify the illumination levels in offices, classrooms, laboratories and other spaces in educational institutions to consider permissible values [24-27]. Other studies are aimed at safeguarding the safety and health of workers in industrial installations [28], or to evaluate the use of LED lamps in residential environments [29], among others.

This work presents a case study in the buildings of the College of Engineering – UNCPBA, including the analysis of lighting energy demand and an improvement proposal using LED lamps. The analysis comprises the impact of energy and lighting quality, replacement cost and return on investment, the calculation of greenhouse gas (GHG) emissions and its environmental impact.

The paper is organized as follows. The materials and methods section describes the situation before the replacement of the fluorescent tubes with LED technology, together with the energy savings achieved, considering the same buildings. Subsequently, the method used to measure the light levels is described. The results section presents the results obtained, an analysis of the economic issues and the environmental impact. This is followed by a discussion of the results and contributions to the sustainable development goals promoted by the United Nations. Finally, the conclusions of the work are presented.

II. MATERIALS AND METHODS

The indoor lighting system in the building facilities at the College of Engineering - UNCPBA, has been characterized by the use of fluorescent tubes. The system has a non-optimized distribution. This means that the proper illumination levels recommended by Federal Law no. 19587 on occupational health and safety cannot be properly achieved [30]. In view of this situation, the goal is to introduce improvements in the efficiency/energy savings variables, to achieve comfortable lighting for users, and to estimate the necessary investment to restructure the lighting system. In order to identify the current indoor lighting conditions of the different sectors and the associated energy consumption, a survey of each of the College's buildings and areas was conducted. Table 1 summarizes the current situation based on this survey. It is observed that the equipment used are all 36 W fluorescent tubes. If losses in electronic ballasts, reactances, and auxiliary ignition devices are considered, the total consumption per element is 40 W.

II.1 MOVING TOWARDS LED TECHNOLOGY

This subsection shows, through a calculation example, the energy savings achieved by using LED tubes instead of traditional fluorescent tubes. It is proposed to replace the existing devices with LED tubes of 16W, considering similar light level conditions and geometrical disposition of the previous one. This replacement means that with 40 % of the energy of traditional fluorescent tubes, it is possible to obtain the same performance with LED tubes. With this new electrical power reference value, the total power installed on each building is calculated once again. Table 2 shows the electrical power with LED technology and the potential power savings.

The analysis carried out in the main buildings of the College, shows that the installed capacity is reduced by 60%, as expected. This means that 13968W of electrical power can be saved. Figure 1 shows the representation of the current installed power and the potential savings incorporating LED technology.

II.2 ELECTRICAL ENERGY SAVINGS

From the analysis carried out in the previous subsections, it is possible to quantify the electrical energy saved on a daily, monthly and annual basis as a result of replacing traditional fluorescent tubes with LED tubes. For this purpose, an estimation of the average hours of daily usage is utilized, considering that the activities begin at 8:00 a.m. and end at 8:00 p.m. during weekdays. It should be clarified that this time distribution does not apply to all sectors. There are some sectors where the lighting is on for less time, others where it is on for longer, and sectors where it is on 24 hours a day, even on weekends or non-working days.

Table 1: Installed power in the College buildings.

Building	Number of lamps	Installed power (W)
Main Building	241	9640
Students' Center	4	160
Civil Engineering	84	3360
Electromechanical Engineering	62	2480
Industrial Engineering	52	2080
Chemical Engineering	118	4720
Laboratory of Microparticles	21	840
Total	582	23280

Source: Authors, (2025).

Based on the above, an estimate of 12 hours of daily use is appropriate. Table 3 presents the electrical energy savings obtained, considering the lights on 12 hours a day on average, during 5 days a week.

In most of the Argentinean territory, a reference value for electricity consumption of 150 kWh per month has been established, which corresponds to the social tariff and from which

the reference prices for electricity are determined by the Ministry of Energy and Mining – Argentina [31],[32]. Therefore, if the aforementioned value is taken as a reference, it can be deduced that the monthly electrical energy savings would be equivalent to the approximate consumption of 22 households with social tariffs, just by replacing the existing lighting system in the College with LED technology. However, the average electrical energy consumption is considered to be higher than this threshold value. According to Larrere [33] the most frequent consumption is around 150 kWh per month and the average consumption would be around 230 kWh per month taking into account the residential demand in Argentina. Considering this last value as the average monthly consumption of a household, the savings would be equivalent to the monthly consumption of 15 households, which clearly indicates the importance of replacing the lighting system in the College buildings.

Table 2: Electrical power in the College buildings using LED technology and electrical power savings.

Building	Electrical power with LED light (W)	Electrical power savings (W)
Main Building	3856	5784
Students' Center	64	96
Civil Engineering	1344	2016
Electromechanical Engineering	992	1488
Industrial Engineering	832	1248
Chemical Engineering	1888	2832
Laboratory of Microparticles	336	504
Total	9312	13968

Source: Authors, (2025).

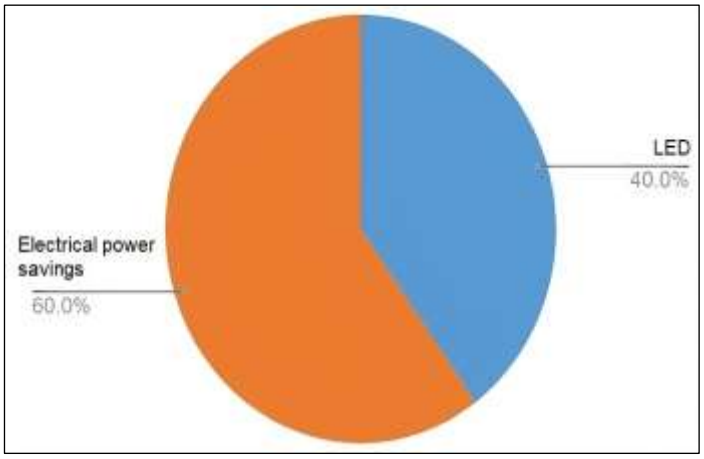

Figure 1: Representation of current installed electrical power vs. potential savings by using LED technology.
Source: Authors, (2025).

Table 3: Electrical energy savings in the College buildings using LED tubes.

Electrical power savings (W)	Daily energy savings - 12 h (kWh)	Weekly energy savings - 5 days (kWh)	Monthly energy savings - 20 days (kWh)
13968	167.6	838.1	3352.3

Source: Authors, (2025).

II.3 LIGHT LEVEL MEASUREMENTS – PREMISES AND GUIDELINES

Lighting conditions achieved with LED lights must be measured through a standardized method to meet the requirements of federal rules on occupational health and safety, and occupational hazards.

Various manufacturers of lighting equipment provide the photometric data for their products. Based on this data, it is possible to evaluate the luminous flux reaching the working plane. There are two alternatives for this: a) analysis through simulation, and b) by experimental tests. Simulation is useful when the lighting device is not available or when different alternatives need to be evaluated.

In this work, the verification of the lighting conditions was carried out experimentally through different tests. According to the manufacturer's specification, a lighting system based on fluorescent tubes has a lower luminous flux utilization when compared to LED tubes, so this is a premise for this work.

This situation is illustrated in Figure 2. In Figure 2(a), corresponding to a fluorescent tube, the luminous flux is emitted in all directions, and must be reflected by the surface of the luminaire to direct it towards the work plane. Figure 2(b) depicts a tube with LED technology. In this case, the luminous flux is mostly emitted directly to the work plane due to its constructive shape.

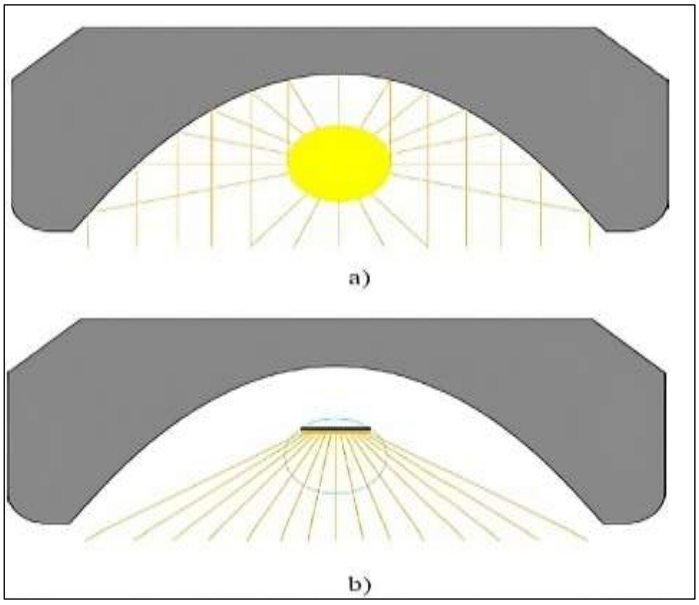

Figure 2. Luminous flux utilization, a) fluorescent lamps, and b) LED tubes.
Source: Authors, (2025).

II.4 MEASUREMENT METHOD

To properly characterize a certain sector, it is necessary to measure the luminous flux per unit area, that is, the light level or illuminance, in lx. In other words, the luminous flux that reaches

the work plane. To exemplify the applied method, the case of light level measurements in a typical office commonly used by professors is presented.

The method is divided into two stages to measure, 1) illuminance on the work plane to obtain a first approximation and choose the more convenient luxmeter scale, and subsequently, 2) illuminance using a measurement point grid covering all the analyzed zone, according to the illumination measurement protocol in work environments that is part of the Resolution SRT no. 84/2012 of the Occupational Hazards Superintendence – Argentina [34]. This protocol is mandatory to measure the light level according to the foresight of the Federal Law no. 19587 on Hygiene and Safety at Work – Argentina [30].

An analog portable luxmeter model 3281 from Yokogawa Electric Corporation, available in our electrical and electronics laboratory, was used to perform the measurements on the work plane. This instrument contains a selenium cell sensor with a plastic covering, connected to a passive instrument built on a linear scale with a measuring range of 0 to 3000 lx divided into three ranges, and an accuracy of ± 7% of reading (23°C ± 2°C).

As part of the first stage, the measurement was made on the work plane considering a conventional fluorescent tube of 36 W. Subsequently, the same measurement procedure was carried out, but replacing the fluorescent tube with a 16 W LED technology tube. Both measurements were made without the presence of natural light.

Both values were below 200 lx, so the 300 lx scale was used to perform the measurement. As expected, once the measurement was made, it was found that the illuminance using LED technology was higher than that reached by the fluorescent tube. The obtained measurements with both technologies are presented in Figure 3.

For fluorescent tube lighting, the illuminance was 150 lx (Figure 3 a)), while with LED tube, 170 lx was reached (Figure 3 b)). Considering the luxmeter specification, the measurement error is ± 10.5 lx in the first case and ± 11.9 lx in the second case, respectively.

As part of the second stage, a point grid covering all the analyzed zone was used to obtain the average illuminance. The method is based on the division of the considered area into several equal areas, each of them ideally square. Figure 4 shows the grid and their dimensions, corresponding to a typical office taken as an example. Thus, the illuminance at the center of each subarea is measured at the altitude of 0.8 m over the floor level (work plane) to calculate the average illuminance (I_{L0}).

The precision in average light level measurement is influenced by the number of points being used. Equation (1) was used to determine the minimum number of measurement points (N_{mp}) as a function of the location index (L_i) [34]:

$$N_{mp} = (L_i + 2)^2 \quad (1)$$

The location index (L_i) was determined through Equation (2) where l and w are the length and the width of the considered area, respectively, and Mh is the mounting height, that is, the vertical distance between the center of light source and the work plane.

$$L_i = \frac{l \times w}{Mh \times (l + w)} \quad (2)$$

The value of the location index is rounded to the upper integer number, except for values equal to or greater than 3, in which case 4 is taken. The measurement method is complemented with a table for each of the college buildings.

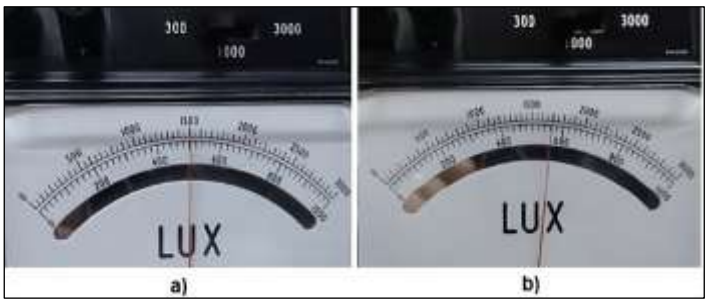

Figure 3: Comparison of the light level on the work plane, a) fluorescent tube, and b) LED tube.
Source: Authors, (2025).

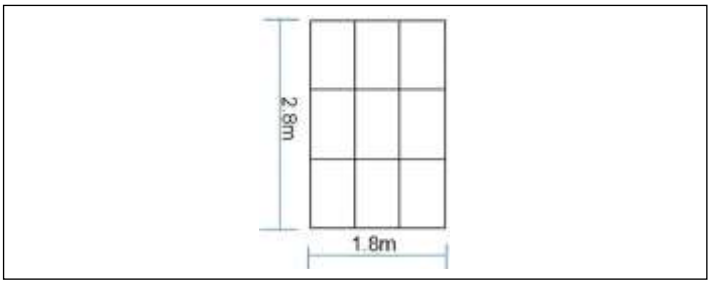

Figure 4: Grid used for measuring average illuminance.
Source: Authors, (2025).

III. RESULTS AND DISCUSSIONS

When calculating the average value resulting from the 9 measurements for both cases, an average illuminance value (I_{L0}) of 145 lx with fluorescent tube and 165 lx with LED tube were obtained, respectively.

It should be highlighted that due offices' dimensions, and the arrangement and length of the luminaire that contains the tube, the measured values were all very close to the average value in both cases, resulting in a high level of uniformity. Table 4 summarizes the measured values obtained for the analyzed case.

III.1 ECONOMIC ISSUES

The return-on-investment time and potential economic advantages of the proposal were estimated using the Simple Payback Time (SPBT) indicator [35]. This estimation has been carried considering the electrical energy consumption analysis made in materials and methods section, the costs associated with the replacement of existing lights with LED technology, and the electrical energy consumed (cost provided by local energy distributor). The bonus per kWh was taken into account to estimate the composition of the electrical energy cost, and all those costs related to provincial and municipal taxes directly impacting the final expense paid by the user.

Table 5 presents the calculation of the electrical energy savings achieved by using LED tubes instead of fluorescent ones. The recorded values take into account the total values of annual energy demand in terms of lighting in the College of Engineering per year, with both types of technologies.

Currently, the acquisition costs of both types of tubes are comparable. This is due to the important development and massive commercialization of LED technology, which allowed the reduction of its cost. However, for its replacement, all labor costs must be taken into account for the adaptation of existing systems. In this case, an adaptation cost equal to the cost of the LED tube

was considered, so the new lighting system requires an investment of twice the acquisition value of the tube, for each tube.

With the aforementioned considerations, the calculation of the return-on-investment time was carried out without considering the annual interest rate, that is, accumulating the energy savings per year to cover the additional value of the investment. Equation (3) used for the calculation of the indicator, corresponds to the static method SPBT [35].

$$SPBT = \frac{i_i}{A_{es}} \quad (3)$$

Where SPBT is the Simple Payback Time in [years], i_i is the additional investment corresponding mainly to the adaptation cost of the installation in [U$S], and A_{es} is the annual energy savings due to the lighting system replacement in [U$S].

Table 4: Illuminance in an office using the measurement point grid method.

Variable	Value
L	2.8 m
W	1.8 m
Mh	1.7 m
L_i	0.64 (rounded to 1)
N_{mp}	9
I_{L0} with fluorescent tube	145 lx
I_{L0} with LED tube	165 lx
L	2.8 m

Source: Authors, (2025).

To obtain the SPBT, two possible scenarios were proposed. The first one (scenario I), corresponds to the current lighting system appropriately working. Therefore, the investment to be made corresponds to the LED tube cost plus the adaptation cost. In the second one (scenario II), the criterion adopted was that the existing tube had reached the end of its lifetime. Therefore, regardless of the technology to be used, the cost of the lamp must be considered within the building maintenance cost. Under this condition only the adaptation cost of the installation was considered. This means that the cost associated with scenario II is equivalent to half that of scenario I.

In Table 6, the obtained SPBT are presented for the two proposed scenarios. As can be seen from Table 6, for the most unfavorable condition, the time needed to recover the additional investment is less than one year, making the replacement proposal economically viable. Alternatively, if the total investment is not available, a gradual replacement plan can be carried out.

III.2 ENVIRONMENTAL IMPACT

The energy savings as a result of technology replacement directly contributes to the optimization of natural resources, since most of the energy matrix in Argentina is composed of natural gas. In this Section, the reduction in the volume of greenhouse gases, product of the decrease in electrical energy consumption, was exclusively analyzed.

In order to estimate the volume of CO_2 production, the emission factors corresponding to the Argentine grid of electrical energy, provided by the Secretariat of Energy were taken into account [36]. These factors consider the amount of CO_2 emissions resulting from the production of a unit of electrical energy from the Argentine grid. The data of the last report accessible on the platform correspond to the year 2023.

Table 5: Annual electrical energy demand and savings in the College buildings.

Energy demand – fluorescent tubes (kWh)	Energy demand – LED tubes (kWh)	Energy savings (kWh)
67046.4	26818.6	40227.8

Source: Authors, (2025).

Table 6: SBPT obtained for the proposed scenarios.

Scenario	i_i (U$S)	SPBT (years)	SPBT (months)
1	1315.8	0.96	11.6
2	657.9	0.48	5.8

Source: Authors, (2025).

Figure 5 presents data from the report, considering the 2007-2023 period. Until 2019, a decrease in emission factors is observed as a result of the advance of renewables in the energy matrix in recent years. However, in 2020 and 2021, the emission factor shows an increasing trend, which is reversed from 2023 onwards. The value of the emission factor in 2023 is similar to that of 2019, and considering the behavior of the curve and the previous trends, as well as the actions taken in recent years regarding energy generation, electric mobility, and others, the emission factor could decrease again.

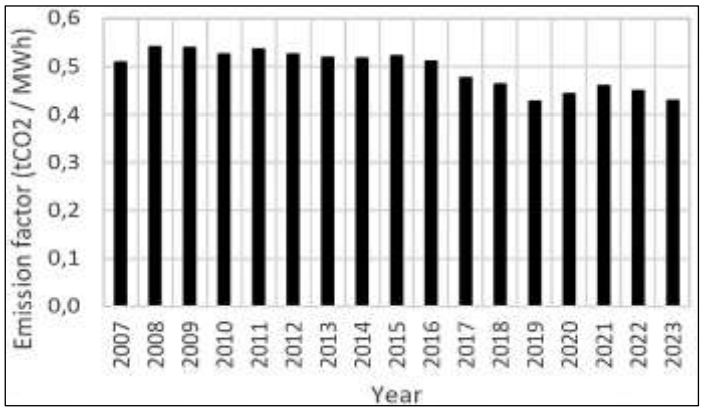

Figure 5: Emission factor during 2007-2023 – Argentine grid of electrical energy.
Source: [36].

It should be pointed out that the factors are closely related to the operating margin and construction of power plants. Depending on the technology of each of them, a weighting is made to obtain a combined margin emission factor.

Thus, the emission factor corresponding to the operating margin of the year 2023, whose value is 0.429 tCO_2/MWh, was used for the analysis. Considering the annual energy saved, affected by the emission factor, a value of 17.2 tCO_2 was obtained for this case study.

The effect of greenhouse gas reduction on climate change is significant. This becomes even more important if its projection to other local or national buildings and institutions is considered.

The 60 % energy consumption reduction in lighting is a unique opportunity, enabled by more efficient lighting technologies.

In addition, it should be noted that fluorescent tubes, at the end of their lifetime, are transformed into hazardous waste. This is due to the presence mainly of mercury mixed with argon in the vapor state, which can cause serious environmental and human health problems when broken [37-39]. When a mercury leakage occurs, it can remain in the atmosphere for a long time before being

deposited on the surface, and can be transported to places far from the emission source [40].

III.3 DISCUSSION

The contributions of this work should be analyzed in the context of indoor lighting systems, more specifically in classrooms and offices. Ongoing research shows similar results for the replacement of fluorescent lighting systems with LED technology lighting. It is clear that electrical energy savings can be achieved through replacement. In this sense, several studies have been carried out in recent years.

In [10] the energy savings that would be obtained if all CFL lamps were replaced by LED technology is analyzed, taking a commercial building as a case study. The economic feasibility of the project is also analyzed. In [23] electrical energy consumption levels between conventional lamps and LED lights were compared, measuring the savings in terms of power and energy efficiency, taking a commercial area as a case study. An economic analysis of the project was carried out in the work. A few years later, in [22], the energy efficiency using LED lighting in a bank building was analyzed. The illumination levels were analyzed and contrasted with the values indicated by international standard. In [21] a case study that considers the replacement of the lighting system in a Navy building was presented. Through the analysis of three different scenarios, the possible energy savings are shown. On the other hand, the simulation results and the energy diagnostic related to the modification of the layout showed satisfactory results in relation to the local technical standard.

However, to be more specific, the present work should be compared with lighting system replacements carried out in educational institutions. The works [24-26] can be cited in this regard. In [24] an analysis was carried out considering the technical-economic aspects of the lighting system replacement, taking as a case study the offices of a building of a university institution. The analysis showed that the replacement allowed a reduction in lighting energy consumption of more than 50%, which results in a reduction of annual operating costs. In [25], the effects of replacing lighting technology in indoor environments were studied. One of the study cases corresponds to the replacement of lighting system of indoor environments in a university building. The results indicate energy savings of more than 50 % associated to a reduction in installed power. Illumination levels were also verified according to local standard. In [26], the illumination levels in the work areas corresponding to a career in an institution of higher education were analyzed. These levels were compared with those specified in the local standard. The work provides recommendations for improving lighting energy efficiency and compliance.

In contrast, in this work an electrical energy saving value of approximately 60 % is achieved in the buildings analyzed. This may be due to the technological advancement of LED lighting systems. As a complement, the economic analysis shows that the time needed to recover the additional investment is less than one year, making the replacement proposal economically feasible. Furthermore, as a contribution, an analysis of the environmental impact has been made, presenting the calculation of GHG, although limited to the case of emissions in Argentina.

The opportunity to quantify the possible savings and make a more efficient use of electrical energy through concrete actions by the use of LED lighting, and especially in a public education institution, can be an incentive for this type of actions to be replicated in other areas. There is another potential opportunity derived from the previous one and it is closely related to increasing awareness of energy usage. This can be achieved if parallel to the technology replacement, an information campaign is carried out in order to raise awareness among the university community so as not to leave lights on unnecessarily. In other words, a campaign to achieve a change in people's attitudes and customs, taking advantage of technological change.

From the technological point of view, these actions can be complemented by incorporating auxiliary equipment, such as motion detectors, sensing of lighting levels, and use of timers, among others. These aspects correspond to the second implementation stage as part of the lighting system replacement policy in this case study.

In terms of electrical energy, it is clear that replacing conventional lighting technology by LED technology have significant advantages. However, the harmonic disturbances that the new system cause on the grid must be monitored. Depending on the quality of the devices, this impact may be different due to the filtering systems they contain.

As final remarks of this work, it can be said that this type of action is also directly in line with the United Nations Sustainable Development Goals for Latin America [41]. It supports Goal 7, "Affordable and Clean Energy," by improving energy efficiency. It is also in line with Goal 12, "Responsible Consumption and Production," by promoting the sustainable management and efficient use of natural resources. Moreover, this action contributes in part to several other goals. It supports Goal 8, "Decent Work and Economic Growth," by enhancing economic productivity through technological upgrades, since the proposed replacement of luminaires improves labor productivity. It also contributes to Goal 11, "Sustainable Cities and Communities," by reducing the adverse environmental impact of hazardous waste. Finally, it supports Goal 13, "Climate Action," by incorporating climate change measures into national policies, strategies, and planning through the replacement of lighting systems in public institutions.

Concerning the effects on human health, as mentioned in Section I, the flickering effect depends on the grid frequency and the equipment used to control the power supply of LED lights. The measurement of these variations and their attenuation is one of the problems facing LED technology in the immediate future, since each person may present symptoms of different intensity, or even not perceive them, although this does not mean that they do not affect its health.

IV. CONCLUSIONS

The replacement of the lighting systems technology in the buildings of the College of Engineering - UNCPBA allows to save approximately 60% of the electrical energy used for such purposes. This saving is equivalent to the consumption of 15 average households.

It is also verified that the light levels obtained with LED tubes are higher than those obtained with the existing system. However, the complete installation should be adapted to the lighting levels established by the regulations.

Furthermore, in relation to the electricity generation process, more than 17.2 tCO_2 can be reduced annually with this replacement. In addition to the reduction of greenhouse gases, the use of LED technology allows to reduce the volume of hazardous waste produced at the end of the LED light’s useful life.

In economic terms, the estimated cost to implement the technological replacement proposal and the return-on-investment time were quantified in a simplified fashion. Based on the obtained results, the SPBT is less than one year, indicating the proposal’s viability.

Based on the above factors and indicators it can be concluded that this first phase of replacement of the lighting system could be gradually extended to all the buildings of the College, and even to other public institutions, causing a positive energy and environmental impact. The action should be complemented with the addition of auxiliary devices for sensing the associated physical variables, and together with an awareness campaign in order to obtain a more comprehensive results derived from replacement action.

Finally, this action contributes to the sustainable development goals for Latin America, according to the United Nations agenda.

V. AUTHOR'S CONTRIBUTION

Conceptualization: Fernando A. Benger and Cristian R. Ruschetti
Methodology: Fernando A. Benger, Cristian R. Ruschetti, Matias Meira, and Silvano R. Rossi
Investigation: Fernando A. Benger, Cristian R. Ruschetti, Matias Meira and Silvano R. Rossi.
Discussion of results: Fernando A. Benger, Cristian R. Ruschetti, Matias Meira, and Silvano R. Rossi
Writing – Original Draft: Fernando A. Benger and Cristian R. Ruschetti
Writing – Review and Editing: Fernando A. Benger, Matias Meira, Silvano R. Rossi and Juan P. Pendones
Resources: Fernando A. Benger, Cristian R. Ruschetti, Matias Meira, and Silvano R. Rossi
Supervision: Cristian R. Ruschetti, Matias Meira and Silvano R. Rossi.
Approval of the final text: All authors.

VII. ACKNOWLEDGMENTS

The authors would like to acknowledge the authorities and personnel of the College of Engineering (UNCPBA) and the Scientific Research Commission of the Province of Buenos Aires (CIC).

VIII. REFERENCES

[1] J. A. Potschka, M. O. Oliveira, M. A. Mazzoletti and R. C. Brazzola, "Energy efficiency in technological education buildings: a study case at UNaM," in 2020 IEEE Biennial Congress of Argentina (ARGENCON), Argentina, 2020, pp. 1-6, Doi:10.1109/ARGENCON49523.2020.9505515.

[2] B. Soroczyński and J. Szkutnik, "New possibilities in electrical energy efficiency," in 16th International Scientific Conf. on Electric Power Engineering (EPE), Czech Republic, 2015, pp. 13-16, doi:10.1109/EPE.2015.7161088.

[3] D. Maheswaran, V. Rangaraj, K. K. J. Kailas and W. A. Kumar, "Energy efficiency in electrical systems," in IEEE Int. Conf. on Power Electronics, Drives and Energy Systems (PEDES), Bengaluru, India, 2012, pp. 1-6, doi:10.1109/PEDES.2012.6484460.

[4] N. Kaur and R. Kaur, "An analytical study of policies for promoting energy efficiency in India with reference to industrial sector," Journal of Economic Policy & Research, vol. 15, no. 2, pp. 54-70. Sep. 2020.

[5] K. Gillingham, R.G. Newell and K. Palmer, "Energy efficiency economics and policy," Annu. Rev. Resour. Econ., vol. 1, pp. 597-620, 2009, doi: 10.1109/PEDES.2012.6484460.

[6] O. Ayan and B. E. Turkay, "Comparison of lighting technologies in residential area for energy conservation," in 2nd Int. Conf. Sustainable and Renewable Energy Engineering (ICSREE), Hiroshima, Japan, 2017, pp. 116-120, doi: 10.1109/ICSREE.2017.7951523.

[7] K. Hansen, "Decision-making based on energy costs: comparing levelized cost of energy and energy system costs," Energy Strategy Reviews, vol. 24, pp. 69-82, 2019, doi:10.1016/j.esr.2019.02.003

[8] F.S. Sanvia, I. Garniwa, G. Alvianingsih and D. R. Aryani, "Study of energy saving performance contracts application for electrical energy efficiency in industrial and commercial sectors," 2020 IOP Conf. Ser.: Mater. Sci. Eng., pp. 1-8, 2020, doi: 10.1088/1757-899X/722/1/012079.

[9] D. Sadhvani and M. A. Musleh, "Moving from CFL to LED lighting: Case study: University laboratory in Dubai," in Proc. Int. Conf. on Intelligent Sustainable Systems (ICISS), Palladam, Thirupur, India, 2017, pp. 725-730, doi: 10.1109/ISS1.2017.8389268.

[10] M. F. Siddiqui, T. J. Soleja and A. Waseem, "A calculation of the cost and energy savings resulting from the replacement of conventional lighting with led lighting for Karachi, Pakistan," in 2017 Asian Conf. on Energy, Power and Transportation Electrification (ACEPT), Singapore, 2017, pp. 1-3, doi: 10.1109/ACEPT.2017.8168605.

[11] M. Franz and F.P. Wenzl, "Critical review on life cycle inventories and environmental assessments of LED-lamps," Critical Reviews in Environmental Science and Technology, vol. 47, no. 21, pp. 2017-2078, Dec. 2017, doi: 10.1080/10643389.2017.1370989.

[12] A. Rahman, A. R. Hafeez, A. Faizan and I. Kanwal, "The impact of domestic energy efficiency: retrofit study of lights & fans using deemed saving method," in Proc. 3rd Int. Conf. on Energy Conservation and Efficiency (ICECE), Lahore, Pakistan, 2019, pp. 1-7, doi: 10.1109/ECE.2019.8921020.

[13] O. Leelakulthanit, "The factors affecting the adoption of LED lamps," International Bussines & Economics Research Journal, vol. 13, no. 4, pp. 757-768, 2014, doi: 10.19030/iber.v13i4.8684.

[14] S. Gil, "Sector residencial. Análisis del servicio energético de iluminación," Eficiencia Energética en Argentina, GFA Consulting Group, pp. 2-11, Apr. 2011.

[15] R. Dubnička, L. Lipnický, M. Barčík and D. Gašparovský, "Comprehensive view of LED products in luminaires," in Proc. Diagnostic of Electrical Machines and Insulating Systems in Electrical Engineering (DEMISEE), Papradno, Slovakia, 2016, pp. 66-70, doi: 10.1109/DEMISEE.2016.7530467.

[16] R. Inger R, J. Bennie, T.W. Davies and K.J. Gaston, "Potential biological and ecological effects of flickering artificial light," PLoS ONE, vol. 9, no. 5, pp. 1-11, May 2014, doi: 10.1371/journal.pone.0098631.

[17] F. Deco, "Incidencia del flicker en el ser humano," Luminotecnia, no. 151, pp. 10-13, 2021.

[18] A. Nagi, R. Manohar and A. Srivastava, "The study of flickering effect present in commercial LED lights, studies of their optical power and driver circuitry. Awareness towards the danger," Int. Journal of Scientific Research and Engineering Development, vol. 3, no. 4, pp. 455-458, July – Aug. 2020.

[19] IEEE Recommended Practices for Modulating Current in High-Brightness LEDs for Mitigating Health Risks to Viewers, IEEE Standard 1789, 2015.

[20] A. M. Estrela Pereira, V. A. Teixeira, M. Zambotti Fortes, G. Martins Tavares and V.H. Ferreira, "Power quality analysis of domestic lamps available in the Brazilian market," WSEAS Trans. On Circuits and Systems, vol. 4, pp. 389-399, 2015.

[21] V. Pereira Cruz, A. C. Soares de Paula Campos, K. Rezende Cardoso, M. Zamboti Fortes, B. Soares Moreira Cesar Borba and A. C. Colombini, "Improving the efficiency of lighting energy in an office building in Brazil," Proc. of the Institution of Civil Engineers - Energy, vol. 175, no. 1, pp: 2-10, 2022, doi:10.1680/jener.20.00013.

[22] P. Parjiman, I. A. Rahardjo, M. Subekti and A. Sunawar, "Analysis of electrical energy efficiency using LED in the bank building (Study case in Bank X)," 2021 IOP Conference Ser.: Mater. Sci. Eng. 1098 042030, doi: 10.1088/1757-899X/1098/4/042030.

[23] A. Khaliq, R. Fahad, J. Shafique and M. Iqbal, "Study of energy saving in a commercial setup by replacing conventional bulbs with LED lights," Int. Journal of Advancements in Technology, vol. 8, no. 4, pp. 1-5, 2018, doi: 10.4172/0976-4860.1000192.

[24] F. Fantozzi, L. Le Bail, F. Leccese, M. Rocca and G. Salvadori, "General lighting in offices building: techno-economic considerations on the fluorescent tubes replacement with LED tubes," International Journal of Engineering and Technology Innovation, vol. 7, no. 3, pp:143-156, 2021

[25] E. B. dos Santos, G. C. M. Azeredo, P. P. C. Resende and J. S. Costa, “Effects of technology replacement on indoor lighting - case studies,” Brazilian Journal of Development, vol. 8, no. 4, pp. 30785-30792, 2022, doi:10.34117/bjdv8n4-523

[26] A. C. Nochebuena Cruz, “Review of the lighting conditions of the work areas of an environmental career in an institution of higher education,” Revista Iberoamericana de Producción Académica y Gestión Educativa, vol. 4, no. 7, pp. 1-26, 2017.

[27] R. Narayanan, A. Kumar, C. Mahto and L. Omshivam, Ramesh, “Illumination level study and energy assessment analysis at university office,” In P. Deiva Sundari, S. Dash, S. Das, B. Panigrahi (Eds), Proc. of 2nd Int. Conf. on Intelligent Computing and Applications. Advances in Intelligent Systems and Computing, 467, (Singapore: Springer, 2016, 399-412, 2016), doi: 10.1007/978-981-10-1645-5_34.

[28] R.A. Victoria Bonilla, N. Sandoval Castro and R. Gamboa Suárez, “Evaluación de los niveles de iluminación en empresas de explotación de rocas fosfóricas para la elaboración de productos agroindustriales en el departamento del Huila,” Ingeniería Industrial, no. 39, pp. 35-49, Dec. 2020, doi: 10.26439/ing.ind2020.n039.4914.

[29] M. Zalesinska, S. Szwedek and A. Pawlak, “Evaluation of lighting parameters at the workplace with the use replacements for incandescent lamps,” in VII Lighting Conf. of the Visegrad Countries (Lumen V4), Czech Republic, 2018, pp. 1-5, doi: 10.1109/LUMENV.2018.8521106.

[30] PEN - Poder Ejecutivo Nacional, Argentina, Ley no. 19587 (1972). [Online]. Available: http://servicios.infoleg.gob.ar/infolegInternet/anexos/15000-19999/17612/norma.htm

[31] Secretaría de Energía, Ministerio de Energía y Minería, Argentina, Res. no. 111/2016, 2016. Available: http://servicios.infoleg.gob.ar/infolegInternet/anexos/260000-264999/262394/norma.htm

[32] Ministerio de Energía y Minería, Argentina, Res. no. 6/2016, 2016. Available: http://servicios.infoleg.gob.ar/infolegInternet/verNorma.do?id=258201

[33] G. Lerrere, “Hacia la normalización del Sistema eléctrico argentino; un análisis de la demanda residencial,” Licenciatura en Economía, Universidad de San Andrés, Argentina, 2017.

[34] Superintendencia de Riesgos del Trabajo, Argentina, Res. No. 84/2012, 2012. Available: http://servicios.infoleg.gob.ar/infolegInternet/anexos/190000-194999/193616/norma.htm

[35] J. Hickiewicz, K. Macek-Kamińska, M. Kamiński, and A. Gardecki, “The application of high-efficiency motors for fan mill drives,” in XIX International Conference on Electrical Machines - ICEM 2010, Rome, Italy, 2010, pp. 1-5, doi: 10.1109/ICELMACH.2010.5608043.

[36] Secretaría de Energía, Argentina, Cálculo del factor de emisión de CO_2 de la Red Argentina de Energía Eléctrica. Available: http://datos.minem.gob.ar/dataset/calculo-del-factor-de-emision-de-co2-de-la-red-argentina-de-energia-electrica

[37] C. C. L. Leopoldino, F. M. de Mendonça, P. H. L. Siqueira, E. L. Borba, “The disposal of fluorescent lamps of industries of the metropolitan region of Belo Horizonte – MG,” Journal of Cleaner Production, vol. 233, pp.1486-1493, Jun. 2019, doi: 10.1016/j.jclepro.2019.06.192.

[38] J. R. Miranda-Mejía, S. Martínez-Gómez, and J.F.K. Hernández-Miranda, “Análisis del tratamiento y nivel de contaminantes por lámparas fluorescentes en El Salvador,” Revista Entorno, no. 59, pp. 97-110, Aug. 2015, doi: 10.5377/entorno.v0i59.6207.

[39] L. N. Leanza, J. R. Parente, “Fundamentos para el tratamiento y disposición de tubos fluorescentes residuales,” Avances en Energías Renovables y Medio Ambiente, vol. 13, pp. 5-10, 2009.

[40] H. Gonzalez-Raymat, G. Liu, C. Liriano, Y. Li, Y. Yin, J. Shi, G. Jiang and Y. Cai, “Elemental mercury: its unique properties affect its behavior and fate in the environment,” Environment Pollution, vol. 229, pp. 69-86, 2017, doi:10.1016/j.envpol.2017.04.101

[41] United Nations - Department of Economic and Social Affairs - Sustainable Development. Accessed: Feb. 2023. [Online]. Available: https://sdgs.un.org/goals

Journal of Engineering and Technology for Industrial Applications

ITEGAM-JETIA

Manaus, v.11 n.53, p. 103-109. May/June., 2025.
DOI: https://doi.org/10.5935/jetia. v11i53.1666

ISSN ONLINE: 2447-0228

RESEARCH ARTICLEOPEN ACCESS

ANALYTICAL AND NUMERICAL MODELING OF THE TRANSIENT BEHAVIOR OF AN EARTH CONNECTION DURING THE INJECTION OF AN ELECTROMAGNETIC WAVE

Mohammed chebout[1], Hakim Azizi[2], Daoud Sekki[3], Mohammed Charif Kihal[4] and Marouane Kihal[5]

[1] Applied Automation and industrial Diagnostic Laboratory, Ziane achour university, Djelfa, Algeria.
[2] Renewable Energy Systems Applications Laboratory, Ziane achour university, Djelfa, Algeria.
[3] Faculty of technology Mohamed Cherif Messaadia University - Souk Ahras, Algeria.
[4] L2EI Laboratory, Mohamed Seddik Ben Yahia University, Jijel, Algeria.
[5] Faculty of Exact Sciences, Bejaia University, Bejaia, Algeria.

[1]http://orcid.org/0009-0006-2798-5411, [2]http://orcid.org/0009-0003-4895-6327, [3]http://orcid.org/0009-0003-2204-7459, [4]http://orcid.org/https://orcid.org/0000-0002-2075-2491, [5]http://orcid.org/0000-0002-6675-7087

Email: 1 m.chebout@univ-djelfa.dz, 2 h.azizi@univ-djelfa.dz, 3 daoud.sekki@univ-soukahras.dz, 4 mc.kihal@univ-jijel.dz, 5 kihal@univ-bejaia.dz

ARTICLE INFO

Article History
Received: February 27, 2025
Revised: March 20, 2025
Accepted: May 15, 2025
Published: May 31, 2025

Keywords:
Transmission line,
Buried electrode,
Current and voltage,
Agrawal model,
Electromagnetic coupling,

ABSTRACT

This paper is devoted to the study and modeling of the behavior of a grounding system. The latter is used for the protection of electrical installations and equipment against surges and various disturbances affecting these systems. The methods used for modeling are multiple for this, an analysis and a synthesis of these methods has been made. In this work, the Agrawal model was used, which is based on the line theory. The finite integration technique was used under the CST Software for the purpose of verifying the first results. At the end, the different factors that influence the response of grounding systems were studied to evaluate the impulse performance. First, we start by determining the current distribution along the excited electrode in order to characterize the grounding radiation over time. The last part of this work is based on a parametric study that takes into account the electrode burial depth as well as the resistivity jump between the electrode and the surface. The results obtained by our analytical model are compared and validated by the CST/EMC software. Good agreements are found between these approaches.

I. INTRODUCTION

Many Several problems in the electrical engineering, electronics or telecommunications industries are due to short circuits or the direct impact of lightning waves on their networks, which put them in a disturbed state, for this reason the analysis of the behavior of grounding in disturbed conditions remains among the main concerns. Short circuits or the direct impact of lightning waves on networks can put certain metal parts equipping a THT or TH station under voltage and for the protection of these devices is the earth network which must limit the duration of this voltage and allow a rapid flow of charges into the ground [1-3].

This discharge into the ground of an overhead station has the following effects: to bring the masses of the latter to a certain potential which risks causing return sparks between the masses and other circuits entering the station to generate radiation likely to disturb the electromagnetic environment (EM) of local electrical systems (self-pollution), and to generate a coupling with neighboring lines [4].

The measurement of earthing is still affected by problems that often lead to considerable uncertainty when interpreting the measured values [5-8].This leads researchers to approach this problem by mathematical calculation using some simplifying assumptions [9]. In this work, we are interested in the transient modeling of a buried electrode, and then we will study the radiation and the coupling of this one with an aerial structure [10-12].

II. LINE THEORY

In It is known that it is necessary to build the line theory on the properties of the electromagnetic field that is to say on Maxwell's equations. We seek solutions in the form of a wave propagating parallel to the line and compatible with the boundary conditions, then we try to find an "equivalent scheme" which gives the same solutions from Ohm's law, which is more convenient to use than Maxwell's equations. Due to the wire geometry of the ground electrodes, it is possible to study them using line theory [1]. The advantage of this theory is that it facilitates the determination of input impedance at the end of the antenna (Figure 1). This is characterized by its impedance per unit length Z and its admittance per unit length Y.

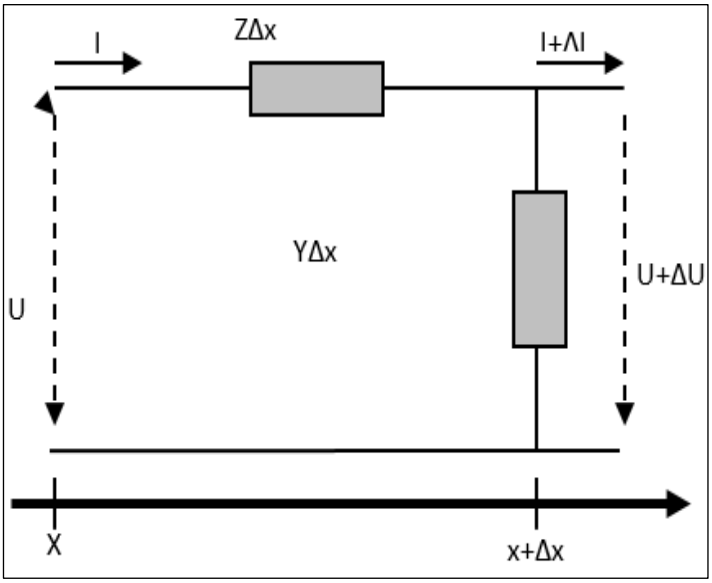

Figure 1: Equivalent schema of a line section.
Source: Authors (2025).

The assumption required for such modeling is that any propagation effect is negligible for each wire element of the structure. The main step is therefore the characterization of the elementary section of the line for which the circuit laws (node law, mesh law, Ohm's law, etc.) can be written locally [2].

For this, each section taken separately must be independent of its neighbors; consequently it is necessary to consider a wire structure of infinite length located in an infinite medium. The introduction of a finite length will be carried out a posteriori as a discontinuity at each end. Since the transverse dimensions of the line are small compared to the wavelength, this discontinuity can be taken into account by writing a local condition [3].

The line equivalent to a straight wire structure of infinite length, immersed in an infinite medium, is now well determined by its primary parameters Z and Y which are independent of the propagation and characteristic of the physical model, and by its secondary parameters k and Zc. The ground electrode is then considered as a transmission line with losses. In frequency for an infinitesimal element of the electrode, the current and voltage equations are given by [4]:

$$\begin{cases} \dfrac{dU}{dx} = -ZI \\ \dfrac{dI}{dx} = -YU \end{cases} \quad (1)$$

The following telegraphist equations:

$$\begin{cases} \dfrac{d^2U}{dx^2} = \gamma^2 U \\ \dfrac{d^2I}{dx^2} = \gamma^2 I \end{cases} \quad (2)$$

Are satisfied by two independent solutions that represent waves moving in positive and negative directions:

$$\begin{cases} U(x) = \left(Ae^{-\gamma x} + Be^{\gamma x}\right) Z_c \\ I(x) = \left(Ae^{-\gamma x} - Be^{\gamma x}\right) \end{cases} \quad (3)$$

A and B are constants of integration.

$$\begin{aligned} Z &= R + j\omega L \\ Y &= G + j\omega C \end{aligned} \quad (4)$$

With:

$Z_c = \sqrt{\dfrac{Z}{Y}}$: Characteristic impedance

$\gamma = \sqrt{ZY} = \alpha + j\beta$: Wave propagation coefficient

α : Linear attenuation

β : Linear phase delay

In this research work we will present a semi-analytical formalism to quantify the coupling of a buried electrode, subjected to excitation, with a piece of overhead line. This formalism is a combination of several methods: First, we start by determining the distribution of the current along the excited electrode and this by using the theory of transmission lines. To characterize the radiation of a grounding in time, we used the dipole method for the quantification of the electromagnetic field radiated by the latter in a free space and the modified image method to take into account the effect of the interface. In the last step, which consists of the study of the electromagnetic coupling, which manifests itself by induced currents and voltages, we will use the Agrawal model [9].

This model does not lack precision and lends itself better to numerical modeling. . Since the soil is relatively poorly understood (its properties change with temperature and humidity), the treatment of earthing by rigorous formalisms is only fortuitous.

III. COUPLING EQUATION FOR THE CASE OF AN IDEAL CONDUCTOR ABOVE A PERFECTLY CONDUCTING GROUND

It is known that the theory of lines is built on the properties of the electromagnetic field, i.e. Maxwell's equations. Under certain approximations and assumptions, it is then possible to translate equations linking the electric and magnetic fields into expressions directly showing the current and voltage. The basic assumptions of the approximation of transmission lines are [5].

- The geometry of the line is reasonably uniform;
- The transverse dimensions of the line are smaller than the minimum significant wavelength;
- The conservation of current (sum of the forward and reverse currents is equal to zero);

- The quasi-transverse electromagnetic (quasi-TEM) propagation mode is predominant along the line. Consider a transmission line formed by a conductor of radius a located at a height h above a perfectly conducting ground (Figure 2).
-

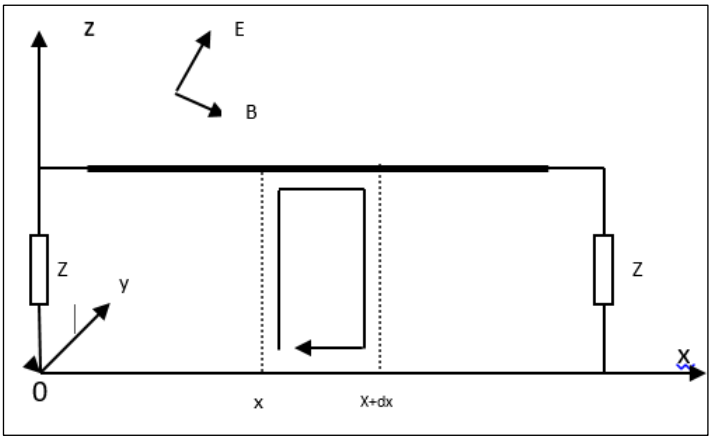

Figure 2: Geometry of a line formed by a conductor illuminated by an electromagnetic field.
Source: Authors (2025).

The exciting electromagnetic fields $\mathbf{E}^e$ and $\mathbf{B}^e$ are defined as the sum of the incident fields $\mathbf{E}^{inc}$, $\mathbf{B}^{inc}$ and the fields reflected by the ground $\mathbf{E}^{ref}$, $\mathbf{B}^{ref}$ in the absence of the conductor [7],[8].

$$\mathbf{E}^e = \mathbf{E}^{inc} + \mathbf{E}^{ref} \tag{5}$$

$$\mathbf{B}^e = \mathbf{B}^{inc} + \mathbf{B}^{ref} \tag{6}$$

The total fields E and B are obtained by adding the exciting fields $\mathbf{E}^e$, $\mathbf{B}^e$, and the diffracted fields, $\mathbf{E}^s$, $\mathbf{B}^s$ which represent the reaction of the line to the exciting field.

$$\mathbf{E} = \mathbf{E}^e + \mathbf{E}^s \tag{7}$$

$$\mathbf{B} = \mathbf{B}^e + \mathbf{B}^s \tag{8}$$

IV. AGRAWAL MODEL

In this formulation, the two equations introduced by Agrawal et al [9]. deduced from equations (2) and (8), are expressed in terms of diffracted voltage and total currents:

$$\frac{dU^s(x,t)}{dx} + L\frac{\partial I(x,t)}{\partial t} = E_x^e(x,h,t) \tag{9}$$

$$\frac{dI(x,t)}{dx} + C\frac{\partial U^s(x,t)}{\partial t} = 0 \tag{10}$$

With :
$E_x^e(x,h,t)$ is the horizontal component of the exciting electric field along the axis at the height h of the conductor;
$U^s(x,t)$ is the vertical component of the diffracted magnetic field

$$U^s(x,t) = -\int_0^h E_z^s(x,z,t)\,dz \tag{11}$$

With:
$E_z^s(x,z,t)$ is the vertical component of the diffracted electric field.

The total voltage induced on the line $U(x,t)$ can be expressed as a function of the diffracted voltages $U^s(x,t)$ and the exciting voltages $U^e(x,t)$ by the following relation:

The boundary conditions for the diffracted voltage are:

$$U^s(0,t) = -Z_A\, I(0,t) + \int_0^h E_z^e(0,z,t)\,dz \tag{12}$$

$$U^s(L,t) = Z_B\, I(L,t) + \int_0^h E_z^e(L,z,t)\,dz \tag{13}$$

In the Agrawal model, the horizontal component of the exciting field along the line and the exciting vertical electric field at the vertical ends of the line are terms that appear explicitly in the equations to produce the diffracted voltage. Agrawal et al proposed an equivalent coupling circuit described by the two equations (7) and (8). This circuit is shown in Fgure 3

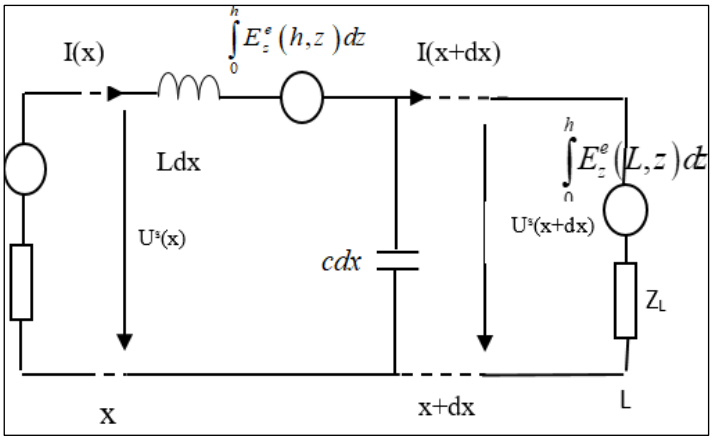

Figure 3: Equivalent differential coupling diagram according to the Agrawal et al model.
Source: [9].

Although the Agrawal model is the most suitable according to the literature [6], it is important to observe that an equivalent formulation of the transmission line coupling equations had been proposed by [10]:

$$\frac{dU(x,t)}{dx} + L\frac{\partial I(x,t)}{\partial t} = -\frac{\partial}{\partial t}\int_0^h B_y^e(x,z,t)\,dz \tag{14}$$

$$\frac{dI(x,t)}{dx} + C\frac{\partial U(x,t)}{\partial t} = -C\frac{\partial}{\partial t}\int_0^h E_z^e(x,z,t)\,dz \tag{15}$$

The boundary conditions for tension are:

$$U(0,t) = -Z_A\, I(0,t) \tag{16}$$

$$U(L,t) = Z_B\, I(L,t) \tag{17}$$

Agrawal's model is numerically more interesting than the others, because it involves only one source term in one of the two

equations; and this source term does not contain any differentiation with respect to time and space.

IV.1. COUPLING EQUATION FOR THE CASE OF A LINE WITH FREQUENCY LOSSES

Consider the same configuration of Figure 2 but taking into account the losses in the conductor and in the ground. The conductivity of the conductor is σ_w and the ground is characterized by a conductivity σ_g and a relative permittivity ε_{rg}.

After correction due to the effect of the ground (finite conductivity) which consists in taking the latter as a dissipative half-medium, the frequency coupling equations in this case become [11].

$$\frac{dU^s(x)}{dx} + ZI(x) = E_x^e(x,h) \tag{18}$$

$$\frac{dI(x)}{dx} + YU^s(x) = 0 \tag{19}$$

With:

$$Z = j\omega L + Z_w + Z_g \tag{20}$$

$$Y = \frac{(G + j\omega C)Y_g}{G + j\omega C + Y_g} \tag{21}$$

$$Y_g = \frac{(G + j\omega C)\, j\omega L}{Z_g} \tag{22}$$

With : Z_w is the linear internal impedance of the conductor given:

$$Z_w = \frac{\gamma_w I_0(\gamma_w a)}{2\pi a \sigma_w I_1(\gamma_w a)} \tag{23}$$

$$\gamma_w = \sqrt{j\omega\mu_0}\left(\sigma_w + j\omega\varepsilon_0\varepsilon_{rw}\right) \tag{24}$$

With:

γ_w Propagation constant of the conductor medium, I_0 and I_1 are the modified Bessel functions.

Z_g Ground impedance given by a logarithmic approximation which was developed by sunde [12].

$$Z_g = \frac{j\omega\mu_0}{2\pi}\ln\left(\frac{1+\gamma_g h}{\gamma_g h}\right) \tag{25}$$

With: γ_g Propagation constant in the ground.

$$\gamma_g = \sqrt{j\omega\mu_0}\left(\sigma_g + j\omega\varepsilon_0\varepsilon_{rg}\right) \tag{26}$$

IV. 2. COUPLING EQUATION FOR A LINE IN THE TIME DOMAIN

The coupling equations in the time domain are obtained by the Fourier transformation of equations (18) and (19). The convolution product highlights the frequency dependence of the correction terms [13].

$$\frac{dU^s(x,t)}{dx} + L\frac{\partial I(x,t)}{\partial t} + \int_0^t Z(t-\tau)I(x,t)\,d\tau = E_x^e(x,h,t) \tag{27}$$

$$\frac{dI(x,t)}{dx} + \int_0^t y(\tau)U^s(x,t-\tau)\,d\tau = 0 \tag{28}$$

Where:

$Z(t)$ and $Y(t)$ are respectively the inverse Fourier transforms of $Z_g + Z_w$ and $\boldsymbol{Y}$.

For practical cases, equation (28) can be approximated by:

$$\frac{dI(x)}{dx} + GU^s(x) + C\frac{\partial U^s(x)}{\partial t} = 0 \tag{29}$$

V. CST SOFTWARE

Generally speaking, the sequence of CST Software programs, equipped with an interface schematized by figure.4 [14-17].

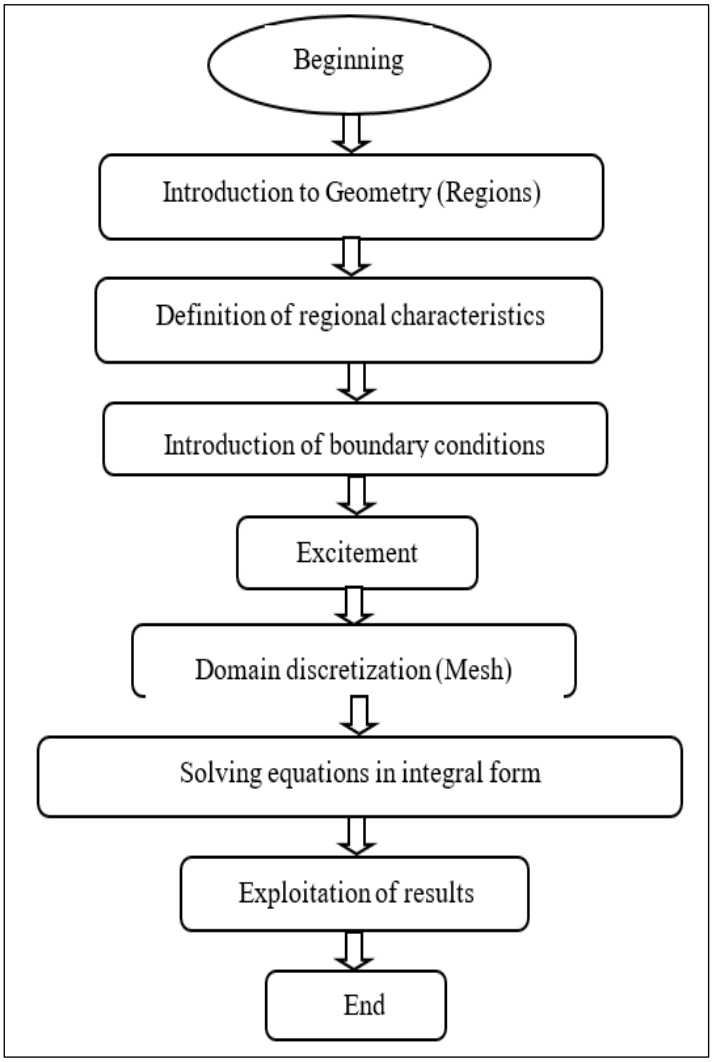

Figure 4: Flowchart of the different modules of the CST software.
Source: Authors (2025).

VI. RESULTS AND APPLICATIONS

VI.1. THE CURRENT AND THE POTENTIAL AT SEVERAL POINTS OF THE ELECTRODE

This is a rectilinear electrode of radius “a” and length “l” (figure 5), buried at a depth “h” in a soil of resistivity ρ, homogeneous and isotropic linear, and supplied at one of its extrinsics by a “lightning wave” generator.

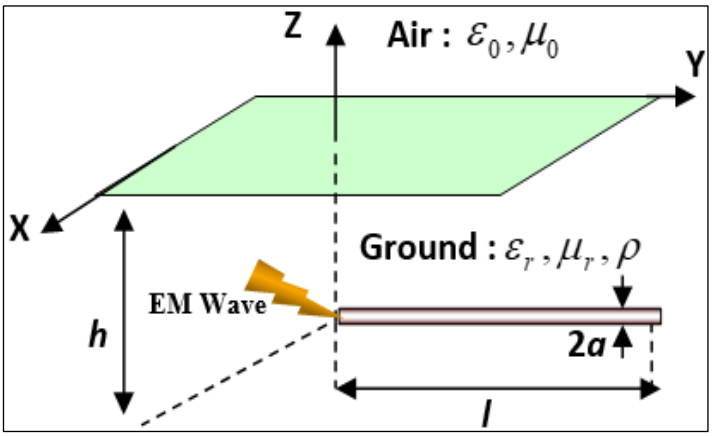

Figure 5: Electrode buried horizontally.
Source: Authors (2025).

For the validation of the computer implementation of the resolution of the equations of the Agrawal model, we consider a rectilinear electrode of radius 7 mm, of a length of 20 m, buried in a linear, homogeneous and isotropic ground at a depth of 0.8 m, the soil has resistivity ρ = 320 Ω.m, electrical permittivity εr = 36 and magnetic permeability μr = 1 as shown in figure 4. The electrode is attacked by a source of disturbance

- $V(t) = V_0(\exp(-\alpha t) - \exp(-\beta t))$
- $V_0 = 30\ KV, \alpha = 45099 \mu s^{-1}, \beta = 9022879 \mu s^{-1}$

To validate this first work, we compare the results obtained with the Agrawal model with those obtained using the CST Software which uses the rigorous antenna formalism. Let us recall that the antenna formalism consists in solving an integral equation in the electric field E or in the magnetic field H by the numerical finite element method.

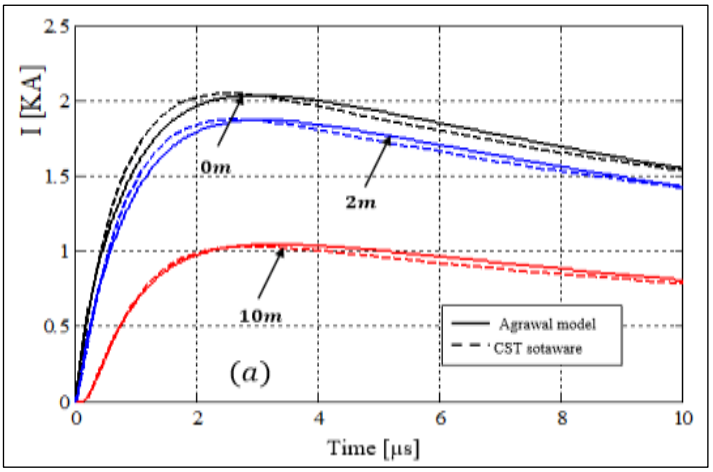

Figure 6: Variation of the current at several points of the electrode.
Source: Authors (2025)

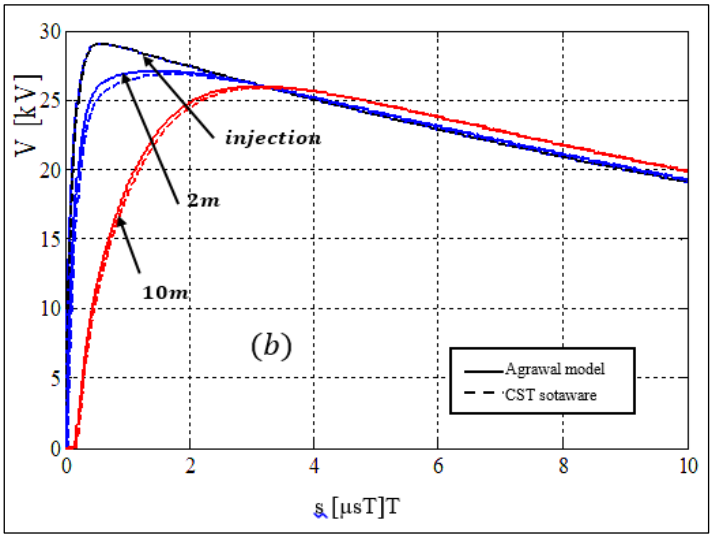

Figure 7: Variation of the potential at several points
Source: Authors (2025)

VI. 2. VARIATION OF THE ELECTRIC AND THE MAGNETIC FIELD

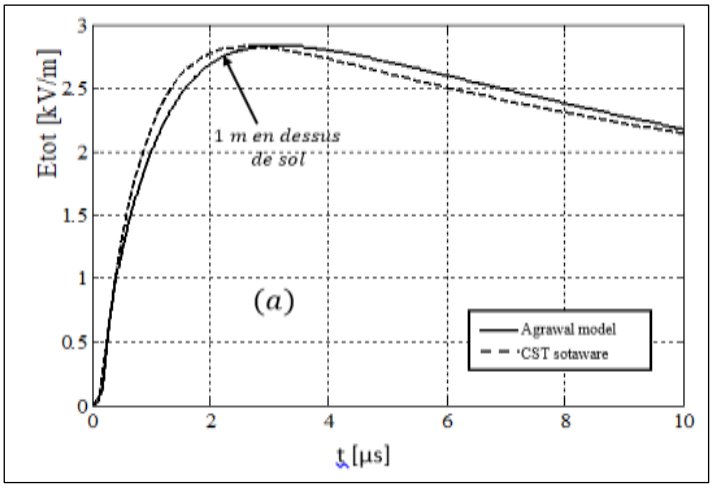

Figure 8: Variation of the electric field at 1m above the ground.
Source: Authors (2025).

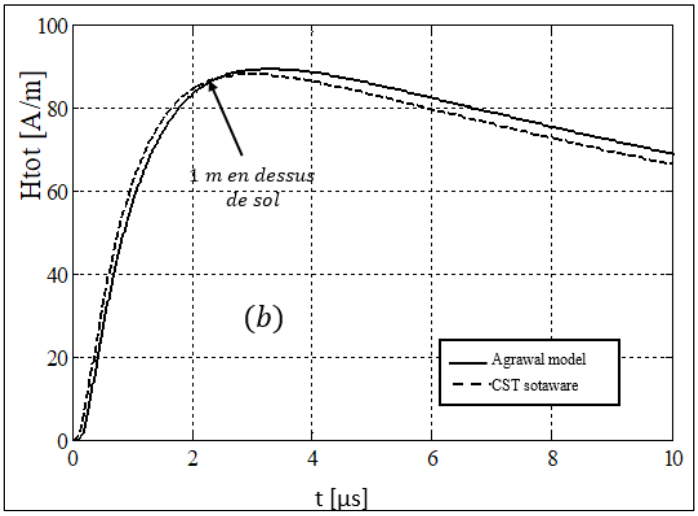

Figure 9: Variation of the magnetic field at 1m above the ground.
Source: Authors (2025).

Figures 6 to 9 show respectively the temporal variation of the current and voltage at several points of the electrode (0, 2 and

10 m) (Figure 6 and 7), as well as the temporal variation of the electromagnetic field at 1 m above the ground considered (Figure 8 and 9). These results in these figures clearly show that the results obtained by the Agrawal analytical model are very close to those obtained by the finite element method by the commercial CST software, the slight difference is mainly related to the use of time-frequency passages by fast Fourier transform when we use the CST Software software.

VI.3. PARAMETRIC STUDY

To consolidate our modeling which consists in associating the concept of apparent resistivity with the topological formalism, we propose a parametric study which takes into account the burial depth of the electrode as well as the resistivity jump between the two layers (ρ1>ρ2 and ρ1<ρ2).

VI.3.1. THE FIRST CASE

In the first case, the resistivity of the upper layer is fixed at ρ1=200 Ω.m and the resistivity of the lower layer successively takes the following values:

- $\rho_2 = 1000\ \Omega.m$
- $\rho_2 = 2000\Omega.m$
- $\rho_2 = 4000\Omega.m$

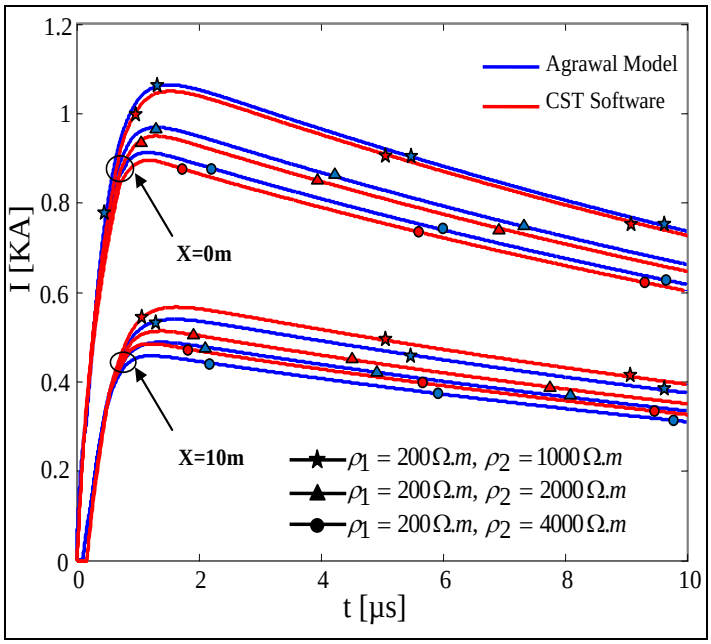

Figure 10: Temporal variation of the current at two points of the electrode (x=0m and x=10m).
Source: Authors (2025).

VI.3.2 THE SECOND CASE

In the second case, the value of the resistivity of the upper layer is fixed at ρ1=1000 Ω.m and the resistivity of the lower layer ρ2 successively takes the following values:

- $\rho_2 = 50\ \Omega.m$
- $\rho_2 = 100\Omega.m$
- $\rho_2 = 200\Omega.m$

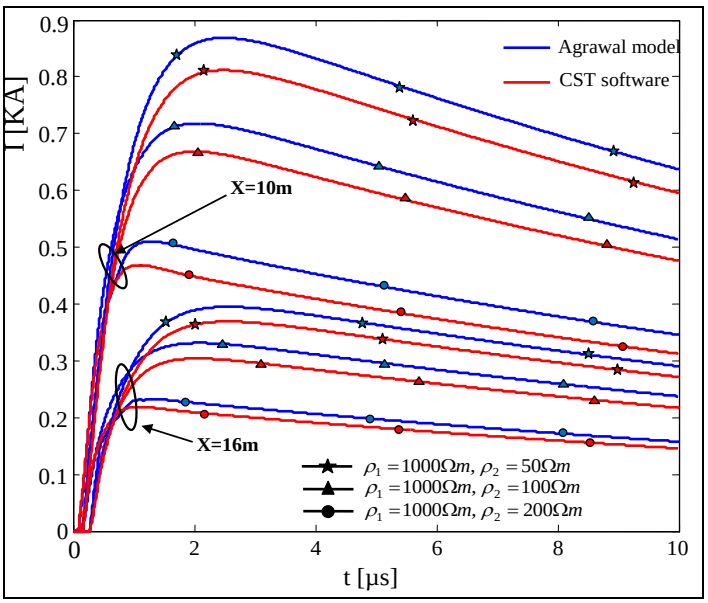

Figure 11: Temporal variation of the current at two points of the electrode (x=0m and x=10m).
Source: Authors (2025).

VI.3.3 THE THIRD CASE

For the third case, we consider a stratified soil with ρ1=200 Ω.m and ρ2=1000 Ω.m, but the burial depth of the electrode successively takes the following values:

- $h = 0.4\ m$
- $h = 0.8\ m$
- $h = 1.2\ m$

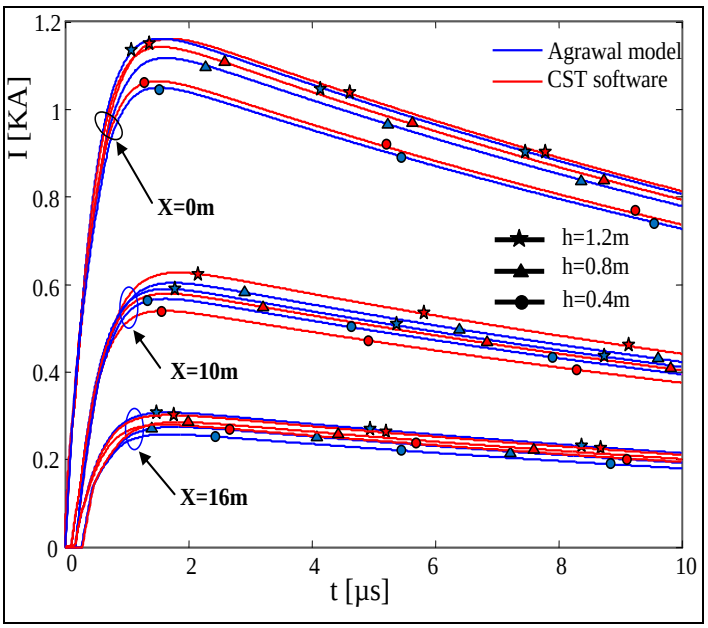

Figure 12: Temporal variation of the current at different points of the electrode.
Source: Authors (2025).

The temporal variations of the currents in Figures 10 to 12 clearly show that the resolution of the Agrawal equations for a two-layer laminated soil in the presence of an electrode as well as the CST Software simulation software lead to comparable results in amplitude and shape. These results confirm that the concept of

apparent resistivity is not affected by the jumps in conductivity or by the depth of burial of the electrode.

VII. CONCLUSION

Our research work focuses on the calculation of the transient electromagnetic field emitted by a buried electrode (electromagnetic pollution) and the induced currents and voltages generated in an overhead line that lead to electromagnetic coupling. In this work we propose the use of a semi-analytical formalism allowing the quantification of the coupling between a horizontally buried electrode and excited by a current in the form of a lightning wave with an overhead wire structure, directly in time.

This quantification was done in several steps. The first step consists in determining the distribution of the current and the potentiel along the buried electrode, for this we used the modeling by the theory of transmission lines. The second step consists in the quantification of the electric and magnetic field radiated by the excited electrode. The last step consists in determining the distribution of the current and the potential induced by electromagnetic coupling, along the piece of line and this by using the Agrawal coupling model and CST Software.

The comparison of the results obtained by this analytical formalism (Agrawal model) with those obtained by the CST Software software, showed a fairly good agreement both in shape and amplitude. We can therefore say that this model constitutes a fast and fairly simple way to evaluate the electromagnetic coupling between two structures.

V. AUTHOR'S CONTRIBUTION

Conceptualization: Mohammed chebout, Hakim Azizi, Daoud Sekki, Mohammed Charif Kihal and Marouane Kihal.
Methodology: Mohammed chebout, Hakim Azizi and Daoud Sekki.
Investigation: Hakim Azizi, Mohammed chebout and Mohammed Charif Kihal.
Discussion of results: Mohammed chebout, Hakim Azizi and Daoud Sekki.
Writing – Original Draft: Mohammed chebout, Hakim Azizi, Mohammed Charif Kihal and Marouane Kihal**.**
Writing – Review and Editing: Hakim Azizi, Mohammed Charif Kihal and Marouane Kihal**.**
Resources: Mohammed chebout, Hakim Azizi, Daoud Sekki, Mohammed Charif Kihal.
Supervision: Hakim Azizi, Mohammed Charif Kihal and Marouane Kihal**.**
Approval of the final text: Mohammed chebout, Hakim Azizi, Mohammed Charif Kihal and and Daoud Sekki.

VI. ACKNOWLEDGMENTS

The authors of this article would like to thank the General Directorate of Scientific Research and Technological Development (DGRSDT) in Algeria for their technical support and the specific research budget allocated to this program.

VII. REFERENCES

[1] A. M. Moussa, 'The sol Ionisation Gradient Associated with Discharge of High Currents into Concentrated Electrode'', IEEE, Trans. On PWRD, vol.9, pp 1669-1977, 1994.

[2] F. Dawalibi, N. Barbeito, ''Measrements and computation of the performance of Grounding Systems Buried in Multilayer soils'', IEEE Trans on PWRD, vol 6 N°4m, pp 1483-1489, October 1999

[3] Z. Wróbel, ''Surge threats appear in railway devices feeding lines'', In Proceedings of the 34th International Conference on Lightning Protection, ICLP2018, Rzeszow, Poland, 2018.

[4] R.. Koszaluk, D. Mukhedkar, ''Experimental Study of Transient Ground Impedances'', IEEE Trans on PWRD, vol pas-100, pp 4653-4660, 1981.

[5] A. Harun, M. Osman, A.M. Ariffin, M. Zainal Abidin Ab Kadir., ''Effect of AC Interference on HV Underground Cables Buried Within Transmission Lines Right of Way'', In Proceedings of the 2021 IEEE International Conference on the Properties and Applications of Dielectric Materials (ICPADM), Johor Bahru, Malaysia, 11–15, pp. 73–76, 2021.

[6] A.S. Al shahri, N.-K.C. Nair, ''Mitigation system for protecting buried pipeline located close to HV OHTL/power cable'', In Proceedings of the 2016 IEEE International Conference on Power System Technology (POWERCON), Wollongong, NSW, Australia, 28 September–1 October, pp. 1–6, 2016.

[7] R. D. Antonje, K. S . Tapan, F. H. Roger, ''Time-domain Response of Multiconductor Transmission line'', proceeding of the IEEE, vol.75, pp.743-761, 1987.

[8] C. Azzetti, M. Veca, ''Impulse Behaviour of Grounding Electrodes'', IEEE Tran on PWRD and S.vol pas-102, pp. 3148-3156, 1983.

[9] A.K. Agrawal, H.J. Price, S.H. Gurbaxani, ''Transient response of multiconductor transmission lines excited by a nonuniform electromagnetic field'', IEEE Transactions on electromagnetic compatibility, vol. 2, pp:119-129, 1980.

[10]C.D. Taylor, R. Satterwhite, C.W. Harrison, ''The Response of Terminated Two-Wire Transmission Line Excited by Nonuniform Electromagnetic Field. Sandia Corporation'', IEEE Transactions on Antennas and Propagation, vol. 13, pp. 987-989, 1965

[11]F. Awalibi and N. Barbeito, ''Measrements and computation of the performance of Grounding Systems Buried in Multilayer soils'', IEEE Trans on PWRD, vol 6, pp 1483-1489, 1999.

[12]M. Einer, ''Electromagnetic Analysis Using Transmission Line Variables'', World Scientific Publishing, Singapore, 2001.

[13]M. Hen, S. Shah, R. Eftekhari, ''Study of electromagnetic interference on distribution conductors from parallel transmission line and practical mitigation solutions'', In Proceedings of the 2014 IEEE PES T&D Conference and Exposition, Chicago, IL,USA, 14–17, pp. 1–9, 2014.

[14]M. Clemens, S. Feight, T. Weiland, "Geometric Multigrid Algorithms Using the Conformal Finite Integration Technique", IEEE Transactions on Magnetics, vol 40, N°. 2, pp. 1065-1068, Mar 2004.

[15]M. Clemens and T. Weiland, "Discrete Electromagnetism with the Finite Integration Technique", Progress in Electromagnetic Research, PIER 32, pp.65-87, 2001.

[16]G. Albertier, Y. Le Menach, J-P. Ducreux, F. Piriou, "Consideration of the coupling of magnetic and electric equations with Finite Integration Technique (FIT)", European Physical Journal, APPLIED PHYSICS, vol. 30, pp 17-22, 2005.

[17]J. Korecki, Y. Le Menach, J-P. Ducreux, F. Piriou, "Numerical solutions in primal and dual mesh of magnetostatic problem solved with the Finite Integration Technique", COMPEL, vol. 27, n°1, pp. 47-55, 4-2008.

Journal of Engineering and Technology for Industrial Applications

ITEGAM-JETIA

Manaus, v.11 n.53, p. 110-116. May/June., 2025.
DOI: https://doi.org/10.5935/jetia. v11i53.1667

ISSN ONLINE: 2447-0228

RESEARCH ARTICLE OPEN ACCESS

AI-DRIVEN FIRE DETECTION AND SUPPRESSION SYSTEM WITH REAL-TIME REMOTE MONITORING

Metahri Dhiyaeddine[1], Dekar Amina[2], SettingsKadi Halima Bouchra[3]

[1] Institute of maintenance and Industrial Safety, University of Oran 2 Mohamed Ben Ahmed, B.P 170, El M'Naouer, Oran, Algeria
[2,3] Production Engineering and Industrial Maintenance Laboratory (LGPMI), University of Oran 2 Mohamed Ben Ahmed, B.P 170, El M'Naouer, Oran, Algeria

[1]https://orcid.org/0000-0002-4188-5525, [2]https://orcid.org/0009-0004-8472-5574, [3]https://orcid.org/0009-0004-6392-3619

Email: metahri.dhiyaeddine@univ-oran2.dz, kacem363@hotmail.fr, belkacem38a@gmail.com

ARTICLE INFO

Article History
Received: February 28, 2025
Revised: March 20, 2025
Accepted: May 15, 2025
Published: May 31, 2025

Keywords:
Intelligent Fire Prevention,
Safety Management,
Sensor-Based System,
Building Automation,
AI-Powered Monitoring.

ABSTRACT

Fire detection and suppression are essential for the safety of monitored environments. Our project aims to develop an intelligent solution using artificial intelligence AI to optimize these processes. We integrate algorithms to process signals from gas and flame sensors via Arduino and use AI to analyze camera signals to improve accuracy. When a fire detected, a signal sent to an automatic extinguisher for immediate intervention. Additionally, we have designed a remote monitoring platform in Python, enabling real-time system management from a control center. This platform offers proactive management and instant visibility into the status of monitored environments, thereby enhancing overall security. A thorough analysis confirms that our Fire detection System FDS is robust and effective for fire detection and management, ensuring rapid and precise responses, and thus contributing to the safety and peace of mind of users. This system is particularly suited for deployment in high-risk and high-occupancy buildings such as hotels, shopping markets, office complexes, industrial facilities, and residential apartments, ensuring enhanced safety and peace of mind for users.

I. INTRODUCTION

Technological advancements have led to the development of various automatic fire detection and suppression systems aimed at protecting lives and property [1-3]. However, despite their widespread use, these systems face challenges such as false alarms and inaccurate detections, compromising their reliability and effectiveness [4],[5]. False alarms can cause unnecessary panic and resource mobilization, while inaccurate detections can lead to delayed responses, resulting in significant damage and losses [6-8]. To address these challenges, this study proposes an intelligent approach using artificial intelligence (AI) techniques to enhance fire detection and suppression. The integrated solution utilizes algorithms to process and encode signals from various sensors, including gas and flame sensors, via the Arduino platform. It also employs AI processing to analyze signals captured by cameras, thereby improving the accuracy of fire detection and automatically triggering suppression measures. Additionally, this research introduces a remote monitoring platform using Python programming, enabling real-time monitoring and management of the fire detection and suppression system from a centralized point. The primary objective of this study is to resolve issues related to false alarms and inaccurate fire detection while enhancing the overall efficiency and reliability of automatic fire detection and suppression systems.

II. ADVANCEMENTS IN AI-INTEGRATEDD FIRE DETECTION AND SUPPRESSION SYSTEMS

Contemporary advancements in security system development integrate extensive automation across residential buildings, offices, and enterprises, aiming to automate life support management and operational functions. This evolution has led to integrated security systems (ISS) with comprehensive functionalities, automating engineering system management within buildings. Fire alarm systems (FAS) are globally mandated components for all structures. Artificial intelligence (AI) utilizing

trained neural networks (NN) shows promise in designing integrated fire alarm and evacuation control systems. NNs, interconnected artificial neurons, resolve complex problems through signal transmission and image classification [9-11]. Researchers apply NNs for pattern recognition and fire classification, using mathematical, empirical, and theoretical methods [12-17] AI effectively classifies fire scenarios using object-monitoring data, enhancing real-time decision-making by identifying critical fire characteristics. However, adapting NN learning algorithms to dynamic changes, such as combustion processes, remains a challenge.

There are several examples of projects with the same concept as our project:

II.1 PROJECT FIRE-GRID

The Connected Firefighter Platform integrates cloud-based connectivity for seamless data transmission [18],[19], enhancing communication and decision-making during firefighting. It manages device and incident data, personnel, and equipment records, offering real-time monitoring locally via Fire-Grid Monitor and remotely through Remote Monitoring. Automated data generation supports post-scene evaluation, training, and maintenance, optimizing firefighting effectiveness.

II.2 DRONE-BASED FIRE MONITORING AND SUPPRESSION

Firefighting drones provide early detection and access to inaccessible areas, crucially saving lives. They deploy fire-extinguishing balls using remote sensing and drones from safe locations [20-25]. These drones detect flame length, enhancing firefighting efficiency, with AI-enabled models using computer vision for smoke and fire detection, leveraging advanced camera systems.

II.3 SMART BUILDING FIRE SAFETY SYSTEMS

Smart buildings integrate cyber-physical systems to enhance daily user routines and optimize building management across health, energy, and security domains [26-29]. These systems operate interactively or autonomously, aiming to address recurring building issues and enhance safety through AI, IoT, and automated response technologies, surpassing traditional fire safety methods by predicting, detecting, and responding to fire hazards efficiently.

II.4 WILDFIRE PREDICTION AND MANAGEMENT

Wildfire prediction and management employ advanced technologies such as predictive analytics using weather, fire history, and vegetation data to forecast fire behavior and spread. Remote sensing through satellite imagery and drones enables real-time detection and assessment, with AI analyzing data to enhance decision-making [30-34]. IoT integrates sensors and cameras for early warning systems, while GIS maps fire-prone areas to plan effective evacuations. These technologies, including automated drones and AI-driven robots, improve fire containment efforts, complemented by community preparedness programs to bolster fire safety and resilience..

III. PROPOSED SYSTEM ARCHITECTURE AND OPERATIONAL WORKFLOW

Due to identified shortcomings in fire detection and extinguishing systems, a solution proposed to mitigate false alarms and ensure swift fire detection in residential, commercial, and industrial sectors, thanks to the architectural design of this system. This automatic system provides a solution to well-known issues in the fire detection and extinguishing systems market. It relies on an intelligent approach, utilizing artificial intelligence (AI) for detection, as well as processing and encoding signals from sensors (such as gas and flame sensors) via the Arduino software. Additionally, it incorporates AI processing for analyzing signals captured by the camera. This solution also offers a remote monitoring platform, facilitated by the use of Python.

Our system integrates three main components: detection, extinguishing, and a control unit. Detection features gas and flame sensors alongside a camera for quick risk assessment. Automatic extinguishers in the system ensure immediate response to fires. The control unit acts as a central platform for fire management, facilitating efficient coordination and swift action during incidents.

Connected sensors, managed by a microcontroller (Arduino Python), process data through specialized algorithms to make informed decisions. Notifications issued via a web portal and local alert system for timely response. The system's block diagram (Figure 1) illustrates sensor data processing, camera integration, and essential components.

Software algorithms dedicated to fire detection interpret sensor and camera inputs to activate or deactivate alerts. In fire emergencies, signals trigger automatic doors for extinguisher activation. The system functions autonomously, potentially supported by a central control unit for remote management. AI integration enhances camera capabilities for precise and rapid-fire detection.

A schematic depicts sensor and camera connections with microcontrollers and the control unit, ensuring scalable deployment across large areas if needed.

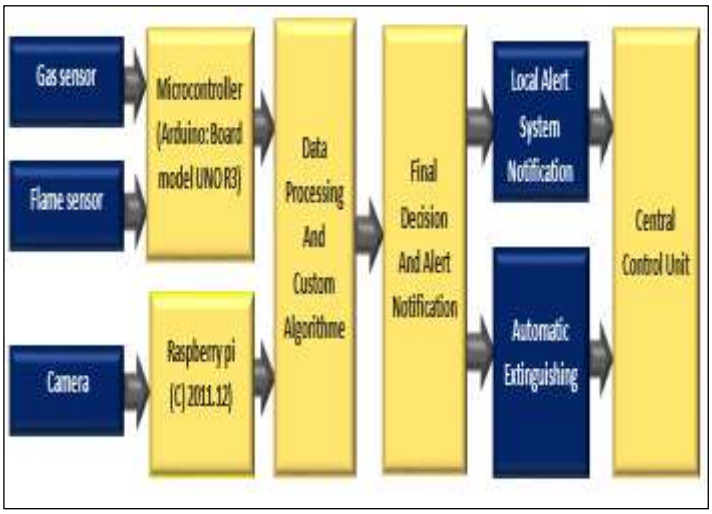

Figure 1: Block diagram of the system.
Source: Authors, (2025).

III.1 DETECTION

Our Fire Detection System (FDS) integrates the MQ135 gas sensor, KY-026 flame sensor, and a camera managed by Python (AI) on a Raspberry Pi microcontroller, all connected to an Arduino Uno R3. This setup sends signals to the serial monitor for cross-validation with camera data, minimizing false alarms and enhancing reliability for prompt fire detection and response.

III.2 GAS SENSOR

We selected the MQ135 sensor for our FDS project due to its ability to detect a wide range of gases including LPG, smoke,

carbon monoxide, ammonia, nitrogen oxides, alcohol, benzene, and carbon dioxide. Its high sensitivity, detecting concentrations as low as 10 to 300 ppm for ammonia, 10 to 1000 ppm for benzene, and 10 to 300 ppm for alcohol, makes it ideal for early fire detection.

III.3 FLAME SENSOR

We chose the KY-026 flame sensor for our FDS project based on its high infrared sensitivity (760 to 1100 nm), dual analog and digital signal outputs, and adjustable detection threshold. Operating on 0 to 15 V DC power, it offers a versatile 60-degree detection angle and compact size, facilitating easy integration into diverse environments. This sensor's primary function swiftly and accurately detect flames, enabling prompt fire response.

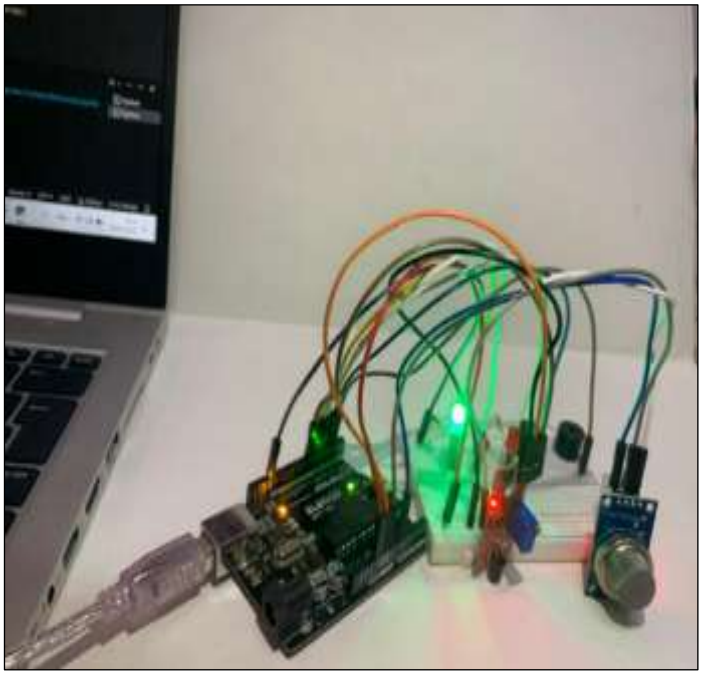

Figure 2: System In A Safe Condition with No Fire Detected.
Source: Authors, (2025).

III.4 LED AND BUZZER

In our FDS project, we use LEDs and a buzzer to ensure a quick and effective response in case of a fire alert. The LEDs provide an immediate visual indication of the presence of smoke or abnormal heat, allowing occupants quickly become aware of the danger. The buzzer emits a loud and distinctive sound to alert people, even if they are not in direct view of the LEDs. This combination of visual and auditory indicators ensures comprehensive coverage, increasing the likelihood of a fast and safe evacuation, thereby minimizing risks to human lives and property.

III.5 ARDUINO ARCHITECTURE

As part of our FDS project, the use of the Arduino Uno R3 proves to be crucial. This versatile tool, based on an Atmega328P architecture, features 14 digital input/output pins (6 of which can be used as PWM outputs), 6 analog inputs, a 16 MHz quartz crystal oscillator, a USB connection, a power jack, and a reset button. These characteristics allow for efficient processing of data from various sensors, particularly those for gas and flame detection. The architecture of the Arduino Uno R3 facilitates the quick and precise processing of incoming signals thanks to its interrupt capabilities and analog-to-digital conversion. In the event of detecting flammable gases or flames, the Arduino Uno R3 activates an LED to indicate the presence of danger and triggers a buzzer to alert the occupants.

III.6 CAMERA

In our Fire Detection System (FDS), a USB Digital PC Webcam (model OEM-CS0138) enhances accuracy by capturing infrared radiation to detect temperature variations and hotspots, enabling early fire detection. This 720p, 30 fps camera with a high-sensitivity CMOS sensor allows real-time monitoring and rapid response, crucial for minimizing damage and ensuring safety.

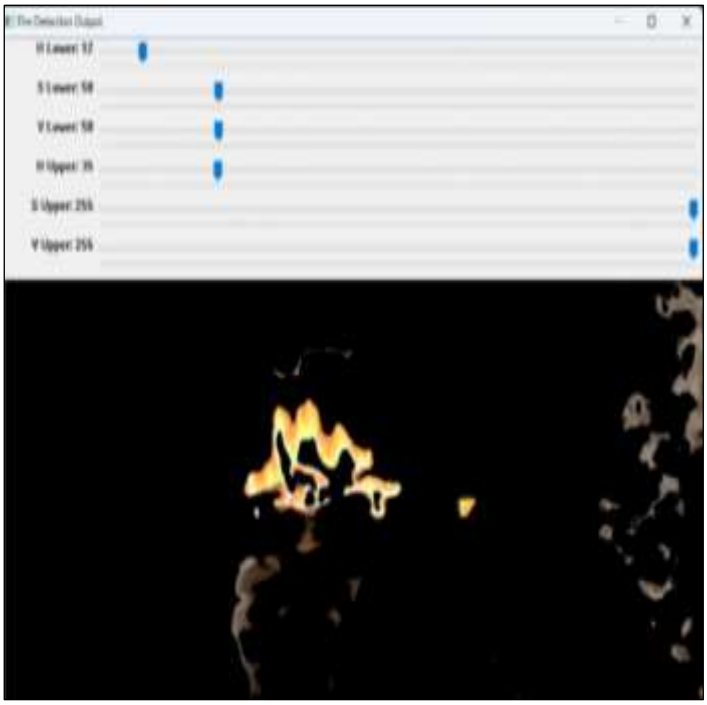

Figure 3: Triggering of an alarm after the detection by the camera.
Source: Authors, (2025).

III.7 ARDUINO SOFTWARE (IDE 2.3.2)

In our FDS project, the use of the Arduino Integrated Development Environment (IDE) is of paramount importance for effectively managing the data captured by our gas and flame sensors. Through this integrated development environment, we can precisely program and calibrate our sensors reliably detect potentially hazardous gas levels and the presence of flames. The Arduino IDE, as officially supported software by the Arduino platform, provides a user-friendly interface for writing, editing, and compiling the code required for our detection system. Compatible with both C and C++ languages, this environment enables us to develop sophisticated algorithms to interpret sensor data and trigger appropriate actions in the event of fire detection, such as activating alert LEDs or buzzers. By fully integrating the Arduino IDE into our development process, we ensure a professional and efficient approach to realizing our project.

III.8 RASPBERRY PI ARCHITECTURE

The architecture of the Raspberry Pi, first launched in 2011-2012, stands out for its unique combination of computing power and versatility, making it an ideal choice for our FDS project for automatic fire detection. Equipped with a high-performance ARM processor and ample RAM, the Raspberry Pi provides the resources needed effectively execute the complex artificial intelligence algorithms required for thermal image analysis. Its extensive

connectivity, including USB ports, GPIO interfaces, and wireless connections, facilitates the integration of various modules and sensors, including cameras, essential for our application. Furthermore, its compact size and low power consumption make it suitable for large-scale deployments while ensuring efficient resource management.

III.9 PYTHON SOFTWARE (3.12 (64 BITS))

Python 3.12 (64 bits) plays a pivotal role in programming the camera for our FDS project, which dedicated to automatic fire detection. With its clear syntax and extensive library ecosystem, Python provides an ideal development environment for integrating artificial intelligence into our detection system. Leveraging specialized libraries such as Open CV and Tensor-Flow, Python simplifies the manipulation and analysis of thermal images captured by the camera. The breadth of Python's features enables the implementation of sophisticated machine learning algorithms and image processing techniques to detect thermal anomalies associated with fires. Moreover, Python's portability across various platforms, including the Raspberry Pi, makes it an optimal choice for our project, offering flexibility and performance for precise and rapid-fire detection.

III.10 VISUAL STUDIO CODE SOFTWARE

Visual Studio Code (VS Code) proves to be an essential element in the programming process of the camera for our FDS project focused on automatic fire detection. With its array of sophisticated features and intuitive user interface, VS Code provides an optimal development environment for code creation, debugging, and deployment. The versatility of VS Code in programming languages, notably its strong compatibility with Python, a widely used language in artificial intelligence projects, makes it a strategic choice for our application. The available extensions for VS Code allow seamless integration of AI-specific tools and libraries, such as TensorFlow or PyTorch, which are crucial for thermal image analysis.

III.11 EXTINGUISHING

In our project, we integrated automatic fire extinguishers with our advanced detection system, using sensors to identify smoke or heat and automatically activating the extinguishers to minimize property damage and ensure occupant safety. These extinguishers feature ultra-fast activation, extensive suppression capacity, and compatibility with various agents like water, foam, chemical powders, and inert gases. Equipped with mechanisms for optimal distribution, they provide continuous protection, reduce fire reaction times, and enhance system reliability and efficiency. This integration ensures a rapid, coordinated emergency response, maximizing safety and minimizing losses.

III.12 SURVEILLANCE PLATFORM

Our FDS system features an integrated surveillance platform that offers real-time visibility into the status of monitored environments, enabling proactive management and prompt intervention in case of fire. This enhances overall site security and ensures efficient responses. In-depth analysis confirms that our FDS system is a comprehensive and robust fire detection and management solution, capable of delivering rapid and accurate responses. This significantly contributes to the safety of monitored environments, providing users with peace of mind.

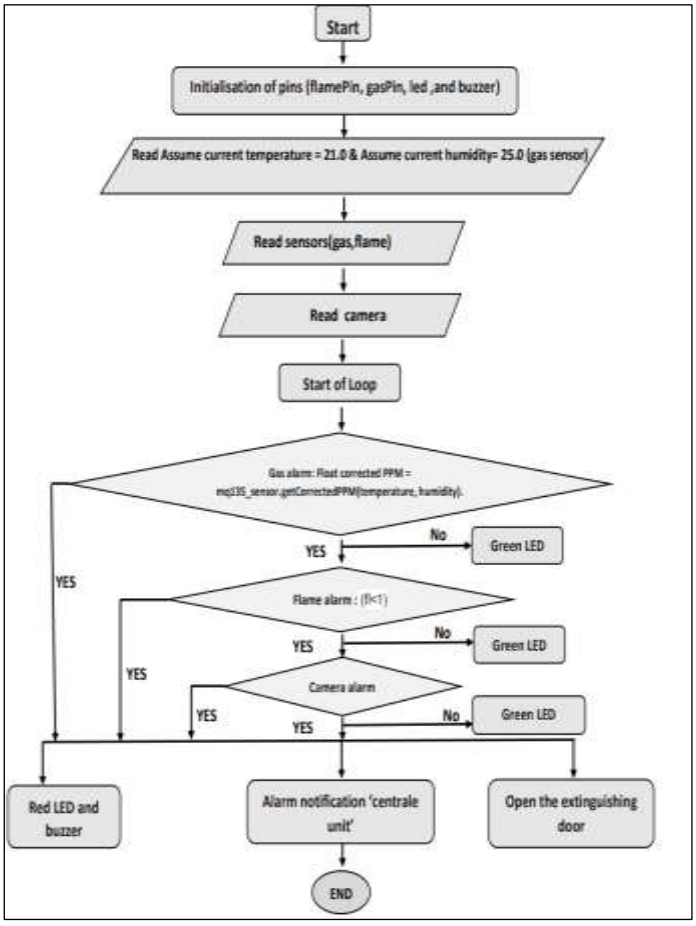

Figure 4: FDS Code flowchart.
Source: Authors, (2025).

Figure 5: Platform design.
Source: Authors, (2025).

IV. TESTING AND RESULTS

The analysis of the results of our FDS project highlights several key aspects of its operation and effectiveness. Firstly, comprehensive testing of the sensors demonstrated the system's reliability in real-time data collection, which is essential for accurate fire detection. The correlation between sensor data and camera signals enhanced continuous surveillance and the system's

ability to react promptly. During this phase, the sensors underwent a series of tests to evaluate their reliability in real-time data collection. These tests verified the accuracy of measurements and the sensors' effectiveness in detecting fire signals.

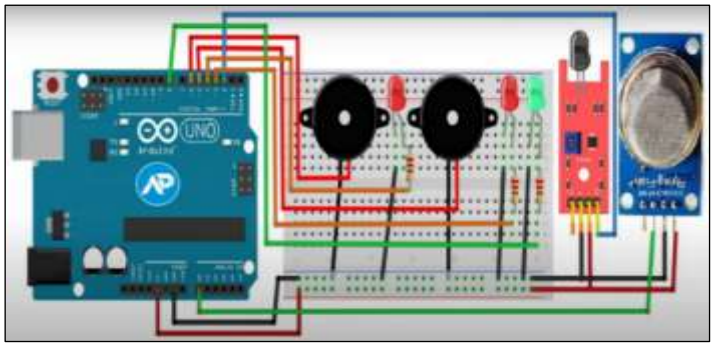

Figure 6: fire detection system circuit diagram.
Source: Authors, (2025).

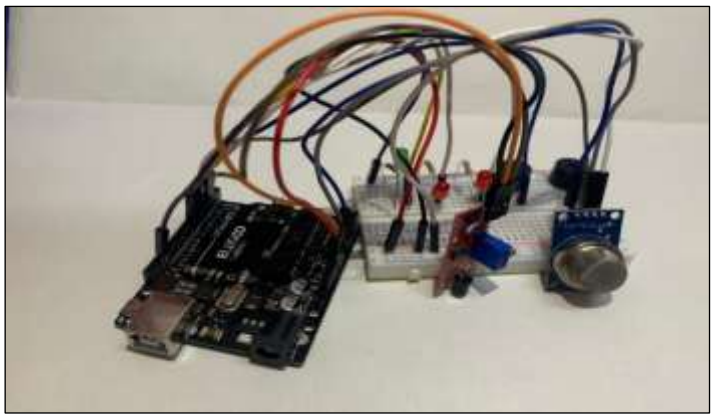

Figure 7: The Actual Installation of Our Project.
Source: Authors, (2025).

IV.1 SIGNAL RECORDING

The system configured to record distinct signals based on the presence or absence of a fire. This functionality was crucial for triggering appropriate emergency measures, such as visual and auditory alerts, as well as automatic activation of extinguishers, ensuring a swift response in case of fire.

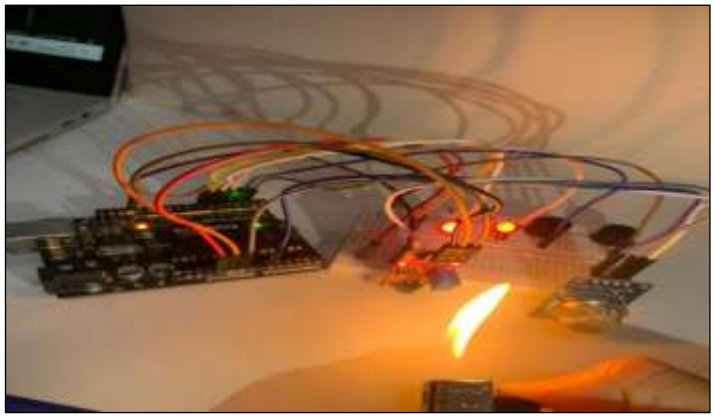

Figure 8: Fire alarm detection.
Source: Authors, (2025).

IV.2 INTEGRATION OF SURVEILLANCE PLATFORM

Integrating the surveillance platform enabled proactive management of the situation by providing users with real-time visibility into the status of each monitored environment. This feature facilitated prompt and efficient intervention in the event of a fire, thereby enhancing overall site security. The in-depth analysis of the results confirms that our FDS system is a comprehensive and robust solution for fire detection and management. Its ability to deliver a rapid and accurate response significantly contributes to the safety of monitored environments, providing users with peace of mind.

Figure 9: In terms of security status.
Source: Authors, (2025).

The security status is indicated by a green color in the absence of anomalies and a red color in case of fire detection, accompanied by an alarm sound. However, the yellow room was not identified correctly, requiring a system reevaluation.

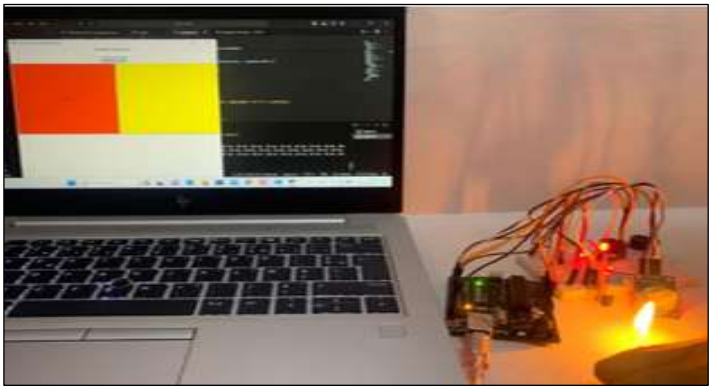

Figure 10: Fire detection.
Source: Authors, (2025).

V. FUTURE WORK

In our project, we plan to add various improvements and future proposals to further develop it, increase its efficiency, and enhance its functionalities. To improve the effectiveness and functionality of our Fire Detection System (FDS) project, we must focus on several key areas. First, it is essential to explore advancements in sensor technology to increase the accuracy and responsiveness of fire detection, by integrating more sensitive sensors or adopting emerging technologies like machine learning algorithms for more precise detection. Next, integrating the FDS with smart building systems can enhance automation and response capabilities, such as automatically shutting down heating systems, unlocking emergency exits, or sending notifications to building occupants. Additionally, developing a robust remote monitoring and control system is crucial, allowing users to access real-time data and control the FDS from anywhere through a mobile application or web interface. Implementing predictive analytics algorithms to anticipate potential fire hazards based on historical data and environmental conditions represents a proactive approach

to fire prevention. Furthermore, exploring options for integrating the FDS with local emergency services to accelerate response times in the event of a fire is necessary, including automatically alerting fire departments and providing them with real-time data.

Finally, the FDS should be designed to be scalable and adaptable to different types of buildings and environments, requiring the development of modular components that can be easily customized and expanded to meet the specific needs of different applications. By focusing on these areas for future work, we can continue to improve fire safety and protection in various environments..

VI. DISCUSSIONS

The following assembly represents the electronic circuit operation of our project. Once the sensor data is collected, it is compared to signals recorded by the camera. This correlation strengthens system surveillance by providing a coherent overview of the monitored environment, enabling rapid and accurate fire detection. The system is configured to record distinct signals based on the presence or absence of a fire. This functionality is crucial for triggering appropriate emergency measures, such as visual and auditory alerts, as well as the automatic activation of extinguishers, ensuring a swift response in case of fire.

The integration of the camera plays a pivotal role in enhancing detection accuracy by capturing real-time visual data, which complements the information gathered by other sensors. The thermal camera, in particular, provides critical insights by detecting heat signatures that might indicate a fire, even in its early stages. This capability is essential for early intervention, potentially preventing small incidents from escalating into major fires. Additionally, the implementation of the FDS (Fire Detection System) platform facilitates remote monitoring and control, offering a comprehensive interface for real-time management. The platform is designed to allow users to access live feeds from the cameras and sensor data from any location, providing immediate insights into the status of the monitored environments.

This real-time visibility is crucial for proactive management, as it enables users to quickly assess and respond to potential fire threats. The combination of sensor data, camera inputs, and the FDS platform creates a robust system for fire detection and management. The in-depth analysis of the results confirms that our FDS system is a comprehensive and reliable solution, capable of delivering rapid and accurate responses to fire incidents. This system significantly contributes to the safety of monitored environments, providing users with peace of mind by ensuring that any fire threat is detected and addressed promptly and effectively.

VII. CONCLUSIONS

This study has demonstrated the effective design and successful integration of an advanced fire detection and management system. Utilizing an integrated approach with cutting-edge sensors and a proactive surveillance platform, our system has shown its ability to swiftly and accurately detect fires while minimizing false alarms. The results have confirmed the reliability and efficiency of our solution, highlighting its potential to enhance the security of monitored environments and provide a prompt and appropriate emergency response. These advancements represent a significant contribution to ongoing efforts aimed at improving fire safety and risk management.

VIII. AUTHOR'S CONTRIBUTION

Conceptualization: Metahri Dhiyaeddine, Dekar Amina, SettingsKadi Halima Bouchra.
Methodology: Metahri Dhiyaeddine, Dekar Amina, SettingsKadi Halima Bouchra.
Investigation: Metahri Dhiyaeddine, Dekar Amina, SettingsKadi Halima Bouchra..
Discussion of results: Metahri Dhiyaeddine, Dekar Amina, SettingsKadi Halima Bouchra..
Writing – Original Draft: Metahri Dhiyaeddine, Dekar Amina, SettingsKadi Halima Bouchra..
Writing – Review and Editing: Metahri Dhiyaeddine, Dekar Amina, SettingsKadi Halima Bouchra..
Resources: Metahri Dhiyaeddine, Dekar Amina, SettingsKadi Halima Bouchra..
Supervision: Metahri Dhiyaeddine, Dekar Amina, SettingsKadi Halima Bouchra..
Approval of the final text: Metahri Dhiyaeddine, Dekar Amina, SettingsKadi Halima Bouchra..

IX. REFERENCES

[1] Donia M, Aly S, Omran S. Automatic fire detection based on early recognition using deep features. The International Journal for Engineering and Modern Science. 2024;3:ID-24013.

[2] Vignesh S, Vishnupriya G, Swetha P, Elakkiya B. Fire detection and extinguisher system using image processing. International Research Journal of Engineering and Technology. 2023;10(6).

[3] Pittman W, McNay J. Applying intelligent visual flame detection in military aircraft hangars. 2023.

[4] Choutri K, Lagha M, Meshoul S, Batouche M, Bouzidi F, Charef W. Fire detection and geo-localization using UAV's aerial images and YOLO-based models. Applied Sciences. 2023;13(20):11548.

[5] Geng X, Su Y, Cao X, Li H, Liu L. YOLOFM: an improved fire and smoke object detection algorithm based on YOLOv5n. Scientific Reports. 2024;14(1):4543.

[6] Zhao X. Design and implementation of intelligent fire detection and alarm system in electrical safety system. In: 2024 International Conference on Telecommunications and Power Electronics (TELEPE); 2024 May; p. 455-459. IEEE.

[7] Awatade A, Pawar P, Lakshmi D. The power of machine learning in forest fire risk analysis and resilience: navigating best practices, challenges, and opportunities. Geospatial Technology to Support Communities and Policy: Pathways to Resiliency. 2024;149-170.

[8] Dilshad N, Khan SU, Alghamdi NS, Taleb T, Song J. Towards efficient fire detection in IoT environment: a modified attention network and large-scale dataset. IEEE Internet of Things Journal. 2023.

[9] Jahanaray, S., Ezoji, M., Imani, Z. EEG-based Feature Space for Supporting Deep Neural Networks in Image Classification. International Journal of Engineering, 2025; 38(6): 1264-1273. doi: 10.5829/ije.2025.38.06c.01

[10] Shakerian, R., Yadollahzadeh-Tabari, M., Bozorgi Rad, S. Y. Recognizing the Type of Human Activities using Inferred Deep Learning Networks and and Intuitive Fuzzy Sets. International Journal of Engineering, 2025; 38(5): 1213-1222. doi: 10.5829/ije.2025.38.05b.20

[11] Sonjaiyout, B., Sunthornpan, N., Peasura, P. Application of Convolutional Neural Networks to Control Quality of Resistance Spot Welding of Galvanized Steel Sheet. International Journal of Engineering, 2025; 38(3): 637-646. doi: 10.5829/ije.2025.38.03c.12

[12] Andreev A, Doronin A, Kachenkova V, Norov B, Mirkhasilova Z. Fire alarm systems construction on artificial intelligence principles. In: E3S Web of Conferences; 2023;365:04028. EDP Sciences.

[13] Reis HC, Turk V. Detection of forest fire using deep convolutional neural networks with transfer learning approach. Applied Soft Computing. 2023;143:110362.

[14] De Venâncio PVA, Lisboa AC, Barbosa AV. An automatic fire detection system based on deep convolutional neural networks for low- power, resource-constrained devices. Neural Computing and Applications. 2022;34(18):15349-15368.

[15] Huang L, Liu G, Wang Y, Yuan H, Chen T. Fire detection in video surveillances using convolutional neural networks and wavelet transform. Engineering Applications of Artificial Intelligence. 2022;110:104737.

[16] Nguyen MD, Vu HN, Pham DC, Choi B, Ro S. Multistage real-time fire detection using convolutional neural networks and long short-term memory networks. IEEE Access. 2021;9:146667-146679.

[17] Roy SS, Goti V, Sood A, Roy H, Gavrila T, Floroian D, et al. L2 regularized deep convolutional neural networks for fire detection. Journal of Intelligent & Fuzzy Systems. 2022;43(2):1799-1810.

[18] Fire Grid Part of the MSA Connected Firefighter Platform. (n.d.). Retrieved May 11, 2024, from MSA Safety: https://us.msasafety.com/connected-firefighter/firegrid?locale=en

[19] Rebai M, Snoussi H, Hnaien F, Khoukhi L. Sensor deployment optimization methods to achieve both coverage and connectivity in wireless sensor networks. Computers & Operations Research. 2015;59:11-21.

[20] Jahan N, Niloy TBM, Silvi JF, Hasan M, Nashia IJ, Khan R. Development of an IoT-based firefighting drone for enhanced safety and efficiency in fire suppression. Measurement and Control. 2024;00202940241238674.

[21] Rahman HI, Saad AF, Yani A. Drone-based fire detection system based on convolutional neural network. International Journal of Artificial Intelligence. 2024;11(1):26-36.

[22] Luan T, Zhou S, Liu L, Pan W. Tiny-object detection based on optimized YOLO-CSQ for accurate drone detection in wildfire scenarios. Drones. 2024;8(9):454.

[23] Lee J, Jeong K, Jung H. Development of a forest fire detection system using a drone-based convolutional neural network model. International Journal of Fire Science and Engineering. 2023;37(2):30-40.

[24] Baruah RL, Dagar SB. Fire fighter drone with robotic gripper. Materials Today: Proceedings. 2023;79:334-337.

[25] Shamsoshoara A, Afghah F, Razi A, Zheng L, Fulé P. Aerial images for pile fire detection using drones (UAVs). 2020.

[26] Santos G, Morais H, Pinto T, Corchado JM, Vale Z. Intelligent energy systems ontology to support markets and power systems co-simulation interoperability. Energy Conversion and Management: X. 2023;20:100495.

[27] Zeng Y, Huang X. Smart building fire safety design driven by artificial intelligence. In: Interpretable Machine Learning for the Analysis, Design, Assessment, and Informed Decision Making for Civil Infrastructure; 2024. p. 111-133. Woodhead Publishing.

[28] Zeng Y, Huang X. Artificial intelligence powered building fire safety design analysis. In: Intelligent Building Fire Safety and Smart Firefighting; 2024. p. 101-124.

[29] Krutskikh VV, Ushkov AN, Trofimov AY, Chukashov DS. Industrial Internet of Things algorithms for fire safety system control. In: 2024 International Conference on Industrial Engineering, Applications and Manufacturing (ICIEAM); 2024 May; p. 853-858. IEEE.

[30] Sayad YO, Mousannif H, Al Moatassime H. Predictive modeling of wildfires: A new dataset and machine learning approach. Fire Safety Journal. 2019;104:130-146.

[31] Gomes PP, Cardoso T. AI-driven wildfire prediction and response in Portugal. In: Cases on AI-Driven Solutions to Environmental Challenges; 2025. p. 115-144. IGI Global Scientific Publishing.

[32] Kanwal R, Rafaqat W, Iqbal M, Weiguo S. Data-driven approaches for wildfire mapping and prediction assessment using a convolutional neural network (CNN). Remote Sensing. 2023;15(21):5099.

[33] Valarmathi V, Ramkumar J. Modernizing wildfire management through deep learning and IoT in fire ecology. In: Machine Learning and Internet of Things in Fire Ecology; 2025. p. 203-230. IGI Global Scientific Publishing.

[34] Nocerino M, Ghosh S. Maximizing prediction accuracy in wildfire severity: A comprehensive analysis of machine learning models using environmental features. In: 2023 IEEE Global Humanitarian Technology Conference (GHTC); 2023 Oct; p. 448-455. IEEE..

Journal of Engineering and Technology for Industrial Applications

ISSN ONLINE: 2447-0228

ITEGAM-JETIA

Manaus, v.11 n.53, p. 117-126. May/June., 2025.

DOI: https://doi.org/10.5935/jetia. v11i53.1755

RESEARCH ARTICLE OPEN ACCESS

USING BAYESIAN NETWORKS AND FUZZY LOGIC TO PREDICT WAREHOUSE PLANNING DISRUPTION RISKS

Kerouich Abdelilah[1], Azmani Abdellah[2], Azmani Monir[3]

[1,2, 3] UAE-Tetoun-Morocco – FST- Tangier, Intelligent Automation & BioMed Genomics Laboratory. Morocco.

[1]http://orcid.org/0009-0000-9208-881X, [2]http://orcid.org/ 0000-0003-4975-3807, [3]http://orcid.org/0000-0002-7434-3781

Email: kerouich@gmail.com, a.azmani@uae.ac.ma, m.azmani@uae.ac.ma

ARTICLE INFO

Article History
Received: March 23, 2025
Revised: April 20, 2025
Accepted: May 15, 2025
Published: May 31, 2025

Keywords:
Risk management,
Warehouse Planning Disruption Risks,
Predictive analysis,
Bayesian network,
Fuzzy logic.

ABSTRACT

The main role of warehouse managers is to establish a schedule adapted to different circumstances. Late arrival of vehicles, lack of handling resources and shortage of packaging supplies all affect this schedule. This is why one of the requirements of quality management in warehousing operations is to anticipate the various likely situations. This article focuses on analysing the risks that can be associated with handling goods in a warehouse, from receipt to delivery. Each risk has two negative effects: the first is the addition of extra costs and the second is the loss of customer confidence. With this in mind, the research presented in this article focuses on the creation of a predictive model to anticipate these risks, using an approach that estimates the degree of disruption to the pre-established schedule, based on a predictive analysis combining Bayesian networks (BN) and fuzzy logic. The model was validated and the parameters influencing the risk studied were identified by analysing the specialist literature and examining scenarios derived from a survey of professionals in the warehousing sector. The results help planners to minimise the impact of disruptions, thereby reducing the time taken to process goods in the warehouse.

I. INTRODUCTION

The effectiveness of warehouse governance is always impacted by unforeseen disruptions. Indeed, the management of tasks of goods processing operations in a warehouse always encounters disruptions at the level of their pre-established planning. These are often unforeseen disruptions due to unfavorable conditions coming from different sources [1],[2]. Applying the principle of regulation or control to them requires an almost total knowledge of the components involved in the warehouse management system, as well as the sources responsible for the disruption or the correct estimation of their values.

For a long time, warehouse management has been a major source of conflicts and problems between customers and suppliers in the absence of effective collaboration or cooperation between them [3], given the difficulty in making a good estimate of unforeseen disruptions. This is further accentuated with the supply chains of e-Commerce and Industry 4.0, as well as during health, ecological and energy crises [4].

The estimation of these disruptions must converge towards values closer to reality for solving this problem.

According to a large study in the literature, we distinguish two types of data processing, the one that is generally done by exact methods [5], when it comes to the existence of exactly defined parameters, and the one based on approximate values, estimated following the analysis of a survey carried out among experts [6]. In this article, our problem is studied by applying two artificial intelligence methods, namely Bayesian networks and fuzzy logic. The first method produces exact numerical results, while the second produces results in the form of intervals or degrees of membership to an interval [7].

The rest of the article is structured as follows: - a first section gives an overview of the literature on planning disruption in the field of warehouse management and a real case study as an application; - a second section provides a brief review of Bayesian networks and presents the construction of our model; - a final section reserved for the discussion of the results obtained; - the

article ends with a conclusion and perspectives of the work presented in this article.

II. RELATED WORK

According to a literature review, risks due to disruptions in supply chains are the most frequent compared to other risks in the industrial environment [8]. More selectively, some of the most relevant research focuses on the study of disruption at the warehouse level [9].

Overall, the management of supply chain disruption risks is becoming necessary [10], and particularly the management of planning disruptions within warehouses is a crucial topic that has been addressed in several research works and case studies [11]. Disruptions also increase the fragility of the supply chain, which leads to an increase in the operational and financial impact of supply chain disruptions [12].

Disruptions to warehouse planning can have significant impacts on several aspects of processing operations:

- Delays in order preparation and delivery operations, these disruptions can lead to delays in receiving or shipping orders, affecting delivery times to customers.
- Increased order processing costs, and disruptions can require overtime or temporary resources to compensate for delays.
- Impact on customer satisfaction, disruptions involve delays or errors in order processing that can affect customer satisfaction.

With over 56% of warehouses worldwide experiencing a disruption in their supply chains at the warehouse level each year, warehouses have started to take these disruptions more into account [13].

Disruptions are linked to internal or external causes, the analysis of different disruptions, such as vehicle delays [14], unexpected breakdowns related to handling equipment, infrastructure events [15] or other sources of problem, allows a delimitation of major problems and convergence towards the application of feasible solutions. The use of statistical and simulation methods allows anticipation of the impacts of disruptions on operating operations. This study will be applied to a real case through the collection and analysis of testimonies and experiences of warehouse experts. These research axes and methods allow a better understanding and management of disruptions in warehouses, thus contributing to better operational efficiency and cost reduction.

III. PROBLEM AND OBJECTIVE

A good planning of loading/unloading allows to reduce costs considerably [16], and demand planning allows to develop the order plan according to the forecasts [17]. On the other hand, a disruption in planning leads to additional costs, which result in:

- A delay in receiving goods.
- A delay in delivering orders.
- A total or partial shutdown of warehouse operations, leading to the shutdown of all parties related to the warehouse.

For this reason, and according to [18], planning can be the most difficult step. According to [19] highlight several criteria for the analysis of the Supply Chain, including the analysis and measurement of the performance of demand planning.

In general, the major problem of the organization and management of warehouse operations lies in the disruption of the planning of functional processes, given its impact on the various stakeholders of the warehouse.

This article seeks to determine the probability of occurrence of disruptions in the functional planning of a warehouse. To do this, identifying the elements, triggers, or amplifiers, responsible for such disruptions is essential. These are elements, presented in the following, that we have identified through the analysis of the literature that focuses on the efficient use of resources and their availability to minimize costs [20] relating to the processing of logistics operations within a warehouse. These elements and their causal links make it possible to create a knowledge base to apply an approach based on Bayesian networks and fuzzy logic theory. This to:

- eliminate their effects as soon as possible.
- update, if necessary, the logistics operations schedule.
- postpone tasks that can be rescheduled.
- inform customers and suppliers of possible delays caused by possible disruptions in planning.

In the event of unacceptable delays [21], planning consists of finding a solution that best meets this requirement, as illustrated in Figure 1.

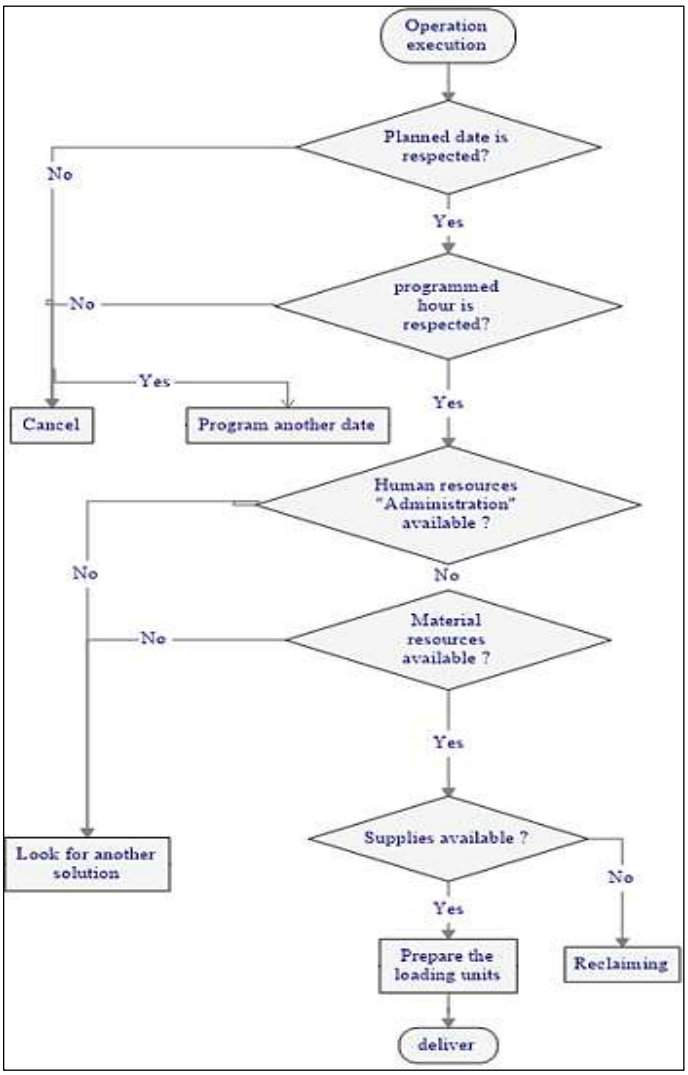

Figure 1: Process of executing an operation.
Source: Authors, (2025).

The use of a causal network of the Bayesian or fuzzy Bayesian network type involves the quantification of variables and the choice of conditional probabilities to build a predictive model. To do this, we can either rely on algorithms from artificial intelligence, which are very complex and have a considerable cost and which must rely on often confidential data, or call on experts to weight their responses and prepare a model close to reality. Developing solutions that can be applied in reality requires the study of a problem situation that also arises from reality.

The model proposed in this article is based on the opinions of several 10 experts, through the analysis of their responses about a questionnaire that we proposed to them (See below), developed in coordination with 3 of the aforementioned experts.

IV. MODELLING THE RISK OF DISRUPTION TO PLANNING BY APPLYING FUZZY BAYESIAN

This section presents the method applied in this study, as well as the variables or parameters used to simulate the scenarios.

IV.1 PRINCIPE OF BAYESIAN NETWORKS

A Bayesian network is a graphical probabilistic model that combines artificial intelligence with statistics to represent uncertain information and reason from data that is incomplete. A Bayesian network consists of two components [22]: A causal acyclic-oriented graph, (see Figure 2), whose nodes are variable and whose arcs characterize the dependency relations between these variables. It is a form of qualitative representation of knowledge. The probability entity contains three branches, conditional probability, total probability, and static independence.

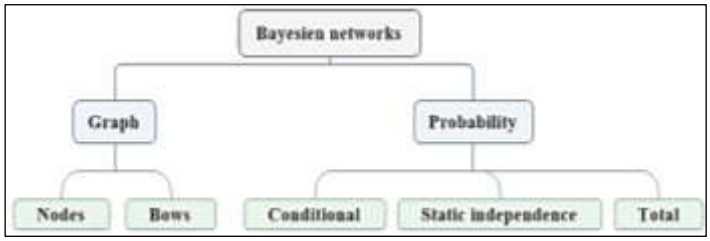

Figure 2: Bayesian network components.
Source: Authors, (2025).

The conditional probability is the degree of occurrence of an event knowing the probability of the second event that corresponds to it, and the total probability, each event of the set of possible events corresponds to a single degree of occurrence, on the other hand. Static independence is the occurrence of an event dependent on, or independent, of another event.

Table 1: Ranking of warehouse parameters.

Space	Material resources	Personal resources
Saturated zone - Saturated parking - Inaccessibility to the warehouse	- Blocked door - Lateness of vehicle - Vehicle puncture - Lack of equipment - Information system failure - Lack of packaging supply	- Lack of staff resources

Source: [23].

IV.2 ELABORATION OF INITIAL PARAMETERS OF BAYESIAN NETWORKS

According to a study carried out by [23], the basic parameters governing the operation of a warehouse are classified into three categories (space, material resources, and personnel resources) presented in Table 1.

The parameters listed in this table are more general, the following part presents the most primary parameters in the form of Bayesian networks.

IV.2.1 DETERMINING THE PRIMARY NODES OF BAYESIAN NETWORKS

In the following, our study focused on determining the main nodes disrupting workflows planning in a warehouse. This section considers the identification and study of the most initial nodes.

Figure 3 gives an overview of the primary nodes responsible for inaccessibility to the warehouse. This criterion is conditioned by the infrastructure and climatic conditions.

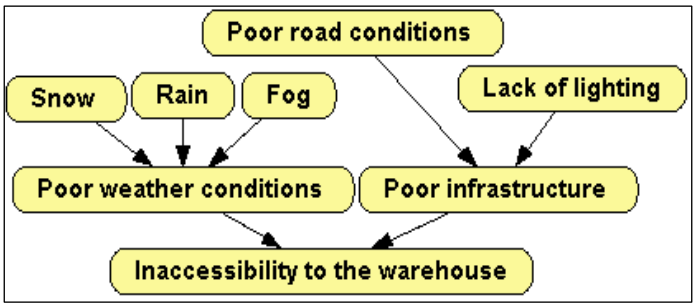

Figure 3: Diagram of inaccessibilité to the warehouse.
Source: Authors, (2025).

Climatic conditions occur periodically during the year with varying proportions depending on the existence of snow, rain, or fog. Infrastructure is measured by two criteria, the condition of the road and lighting.

Figure 4. Deals with the causes of car park saturation (drivers' strike, and vehicle blockage). Vehicle blocking occurs either because of the mechanical condition of the vehicle due to overloading, lack of maintenance, or misuse by the driver.

The energy entity can translate into the battery being discharged due to lack of fuel or exhaustion if the vehicle is electric or hybrid, also the self-degradation of the batteries affects its range [24]. The driver is involved in blocking the vehicle in cases where the driver leaves the vehicle and goes elsewhere for reasons related to the warehouse (administrative document, claim, etc.), or related to personal occupations (eating, smoking, talking on the phone, etc.). A driver's strike is generally linked to working conditions, which involves the total blocking of traffic in parking lots (or absence of traffic).

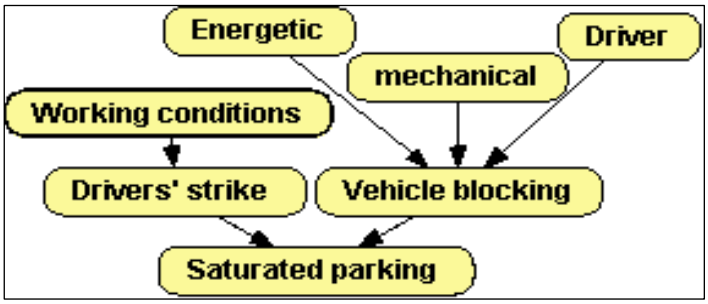

Figure 4: Vehicle Park saturation network.
Source: Authors, (2025).

The saturation of the zones is the result of different factors, as shown in Figure 5, such as:

Blockage of machines in the area, whatever the cause, causes saturation of the area.

Leaving the goods, after storage in the areas, for a considerable time causes saturation of the area.

The dispersion of products in the work areas causes saturation of the area.

Programming zones as temporary passages (dynamic zones) also increases the risk of blocking zones.

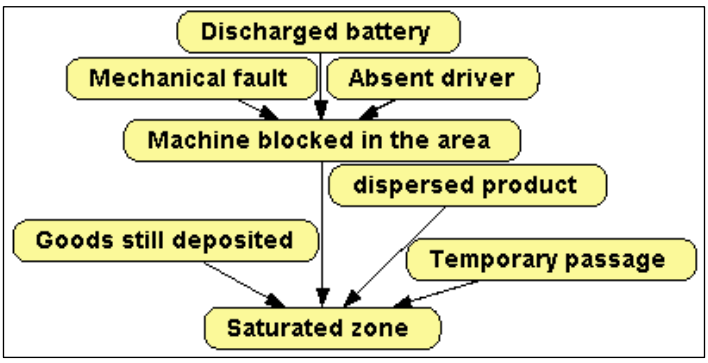

Figure 5: Zones saturation network.
Source: Authors, (2025).

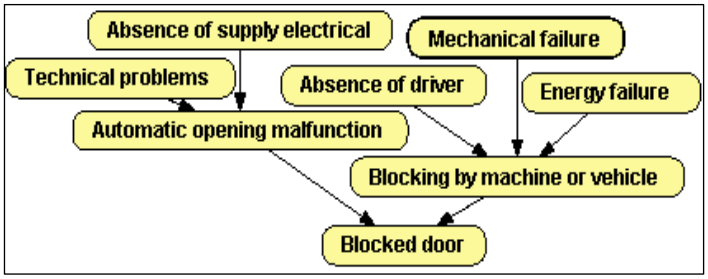

Figure 6: Door blocking network.
Source: Authors, (2025).

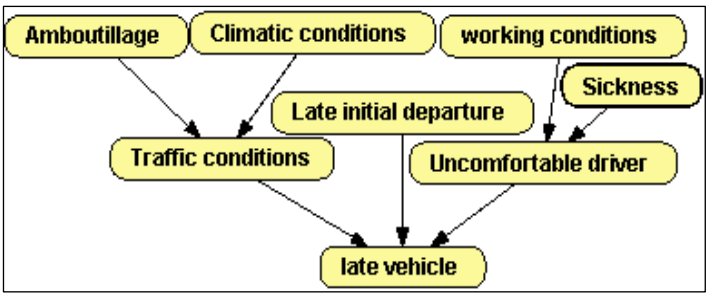

Figure 7: Network showing vehicle delay.
Source: Authors, (2025).

Figure 7. Shows the causes responsible for the door jamming, which can be explained by:

- Blocking of the door operation management: According to the problem diagnosis system [25], this results from the absence of a power supply, or a technical or physical problem (connection, programming, or component degradation).
- The parking or blocking of vehicles in front of the doors is one of the factors contributing to the doors not operating properly, whatever the cause (mechanical failure, electrical failure, driver absence).

Material resources are the main element for handling goods in the warehouse, so their absence or lack disrupts normal operations. For that purpose, we need to study the causes of this lack. Figure 8 lists the different scenarios that lead to a lack of material resources.

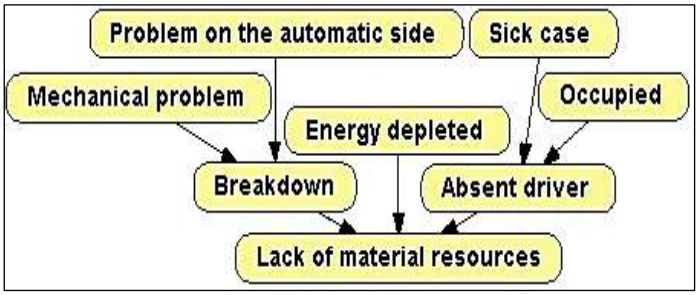

Figure 8: Network of lack of material resources
Source: Authors, (2025).

A vehicle's late arrival causes a double disruption, the first in relation to the reception operation and the second about the departure after unloading. For this reason, identifying the causes of this disruption helps to find an optimal solution, as shown in Figure 8. Since vehicles are not the only users of the road network, they must share it with others [24], and the sources causing this delay are increasing, among other things.

Human resources are the main players or brains of the warehouse [26], influencing all warehouse stakeholders. To ensure the smooth operation of the supply chain, human resources must be at the top of the warehouse's priorities. This architecture enables optimized warehouse management by helping staff to work under better conditions [1].

Figure 9. Gives a clearer vision by identifying the causes responsible for the lack of human resources, such as:

- Staff absence can be caused by illness, strikes, or demonstrations [27].
- Delays can be caused by a lack of motivation or overload at work which leads to fatigue [28].

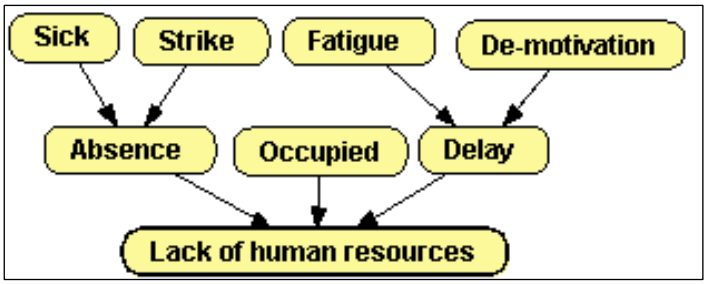

Figure 9: Network of lack of human resources.
Source: Authors, (2025).

In the warehouse, goods are reorganized, dissociated, packed, or repacked [29]. Hence, packaging supply is an essential tool [30] for order processing or storage. Figure 10 helps to avoid any possible lack of supply.

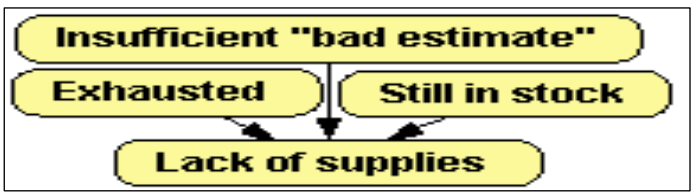

Figure 10: Network of lack of supplies.
Source: Authors, (2025).

The lack of supply, Figure 10, translates to three situations: The first is when the need is underestimated.

The second is when a large number of unexpected orders are received.

The third is when the supply exists in the warehouse, but is still in stock and not available for immediate use.

As shown in Figure 11, a vehicle can break down due to: Lack of energy, discharged battery, or low fuel level. A mechanical problem with parts and components.

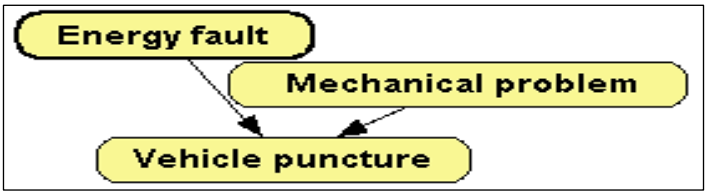

Figure 11: Vehicle puncture.
Source: Authors, (2025).

The information system is the nerve center of the warehouse [31], managing all activities within the warehouse. The phenomenon of saturation of the management system, which cannot adapt and grow ad infinitum to meet the needs of new users [24]. Blocking the latter blocks activities in the warehouse or slows them down if we switch to manual processing and recording. Figure 12. clearly shows the inputs that can contribute to blocking the information system.

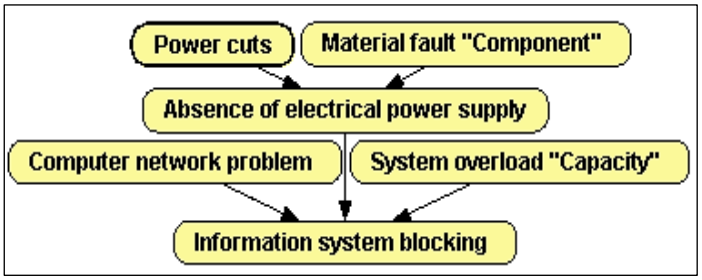

Figure 12: Information system blockage.
Source: Authors, (2025).

With a high volume of information (Intense), the computer network can have complications processing it.

The absence of power to the system due to a power failure or problems [29] with the components used causes the system to come to a complete standstill.

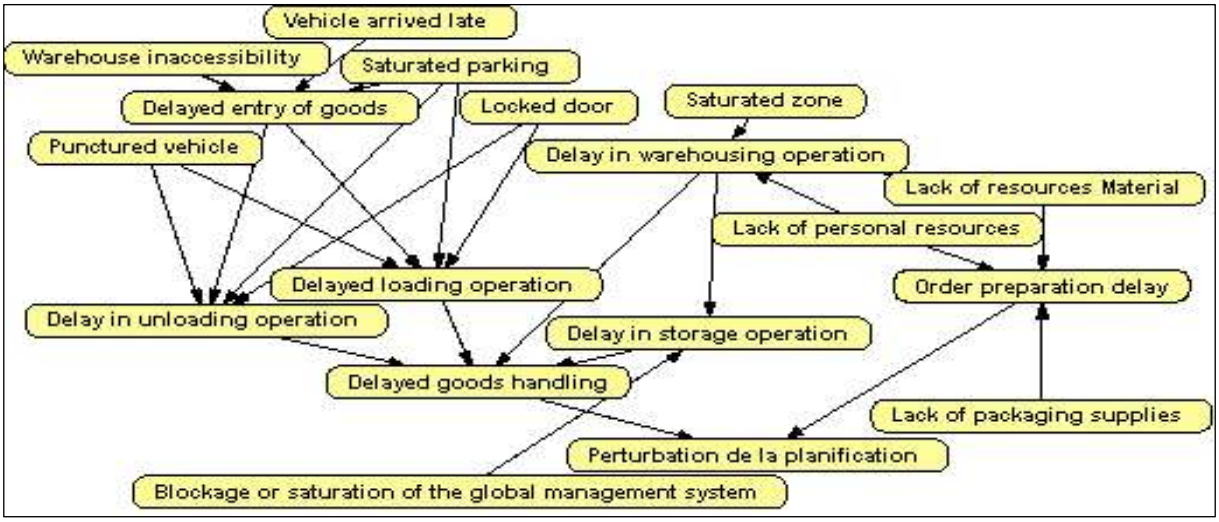

Figure 13: Global Bayesian network representation.
Source: Authors, (2025).

V. GLOBAL BAYESIAN NETWORK

Elaborating the primary nodes of different problems participating in the planning disturbance helps to establish a global Bayesian network, see Figure 13.

Once the global Bayesian network of different sources of disturbance has been constructed, it remains to assign suitable values to each variable to calculate the conditional probabilities. Databases containing rich values and useful information are insufficient or generally of a private nature [32]. For the generation of probabilities systematically, we call upon the application of fuzzy logic which is characterized by its force of reasoning which resembles the reasoning of human beings and natural languages [33].

V.1 QUESTIONNAIRE (PARAMETERS VALUE ATTRIBUTION)

To feed our Bayesian network, we sent a questionnaire to experts in the field of warehouse management (the following section) Table 2.

This questionnaire concerns the absence of a problem concerning the criterion concerned.

Table 2: Example of questionnaire.

Question	Possible answer (single choice)
Saturation of the area	1. Low 2. medium 3. high
Car's park Saturation	1. Low 2. medium 3. high
Inaccessibility to the warehouse	1. Low 2. medium 3. high
Blocked doors	1. Low 2. medium 3. high
Door blockage	1. Rarely 2. Often 3. Frequently
Vehicle delays	1. Rarely 2. Often 3. Frequently
Vehicle punctures	1. Rarely 2. Often 3. Frequently
Lack of equipment	1. Rarely 2. Often 3. Frequently
Information system failure	1. Rarely 2. Often 3. Frequently
Lack of packaging supply	1. Rarely 2. Often 3. Frequently
Lack of personal resources	1. Rarely 2. Often 3. Frequently

Source: Authors, (2025).

As mentioned in the previous section, Bayesian networks are used to represent the knowledge of a system through the simulation of its behavior, this is done through data analysis.

It is therefore necessary to have data to feed our Bayesian network. These data or more generally, the conditional probabilities can be generated from two different methods:

- Objective method: By using a database for automatic learning of probabilities. The latter requires a large data size, and that the database contains exactly the parameters considered in our case study. As a result, we did not find a database that was complete enough and that met these criteria. Therefore, we returned to the subjective methods.
- Subjective methods: by extracting knowledge from warehousing experts in the field of warehouse logistics. We opted for this method by sending a questionnaire to 10 Warehouse's managers in Tangier Free Zone in Morocco.

We used decimal scales from 1 to 9, which indicate the following meaning, Table 3:

Table 3: Correlation between questionnaire values.

Value at %	Interval	Linguistic values
[1%-30%]	[1-3]	Faible or Rarement
]30%-60%]	]3-6]	Moyenne or Souvent
]60%-99%]	]6-9]	Elevé or Fréqement

Source: Authors, (2025).

Note that the starting value is 1% because a parking lot will never be empty in reality, and we stop at 99% because a parking lot will never be full.

The result obtained by this questionnaire is indicated in Table 4, Table 5, Table 6, Table 7, and Table 8.

Table 4: Spatial entity.

	Saturated zone	Saturated parking	Inaccessibility to the warehouse
Present	[1-30]	[6-9]	[7-9]
Absent	[6-9]	[1-30]	[1-3]

Source: Authors, (2025).

30% temporally and spatially, i.e. most of the time the zones are 30% saturated, and temporally we find that 30% of the time the zones are 90% saturated.

Table 4 shows that the saturation of the areas is present with a coefficient ranging from 1 to 3, while the saturation of the parking lot and the inaccessibility to the warehouse are present with a variable factor between 7 and 9.

Table 5: Material resources entity.

	Blocked door	late vehicle	vehicle puncture	lack of machine
Present	[7-9]	[7-9]	[7-9]	[7-9]
Absent	[1-3]	[1-3]	[1-3]	[1-3]

Source: Authors, (2025).

Table 5 shows that the coefficient of the presence of constraints at the material resources entity is between 7 and 9.

Table 6 shows that the value that reflects the lack of personal resources is present with a factor ranging from 7 to 9.

Table 6: Personal resource entity.

	Lack of staff resources
Present	[7-9]
Absent	[1-3]

Source: Authors, (2025).

Table 7: Blockage or saturation of the global management system.

	Blockage or saturation of the global management system
Present	[1-3]
Absent	[7-9]

Source: Authors, (2025).

Table 7 shows that the management system blocking problem is low, it is between 1 and 3.

Table 8: Lack of packaging supply.

	Lack of packaging supply
Present	[1-3]
Absent	[7-9]

Source: Authors, (2025).

Table 8, shows that the lack of supply is less dominant, it is given by a factor ranging from 1 to 3.

VI. FUZZY LOGIC AGGREGATION WITH THE PREVIOUS APPROACH

According to [34], fuzzy logic is considered one of the rare techniques capable of modeling fuzzy and ambiguous knowledge derived from experts. Therefore, it is applied to problems not linearly defined. This application is based on two principles [35]:

- Linguistic variables that take qualitative or nominal values;
- Conditional rules "if-then", which establish a connection between input variables to produce an output or consequence, known as the mechanism called "fuzzy inference system".

VI.1 FUZZIFICATION

The fuzzification is used to transform real input values into fuzzy values by determining their degree of membership in each fuzzy set via the membership function [36].

Table 9 presents the fuzzy variables and their linguistic values highlighted to address our problem statement.

VI.2 INFERENCE

Inference is the implementation of fuzzy rules, which are also called fuzzy implications or fuzzy conditional instructions [37], are represented in the form 'IF... Then.' The number of these rules in a fuzzy inference system depends on the number of variables (input and output) and the number of zones in each of them [38].

To synthesize the approach applied, we will present the generation of the total conditional probabilities of the 'planning disruption' node following the events linked to the state of the primary nodes: Goods handling and Order preparation.

Table 9: Fuzzy variables and linguistic values.

Variables	Linguistic values
Inaccessibility to the warehouse	Low, medium, high
Vehicle arrives late	Low, medium, high
Overcrowded car park	Low, medium, high
Door blocked	Low, medium, high
Punctured vehicle	Low, medium, high
Lack of personal resources	Low, medium, high
Lack of material resources	Low, medium, high
Saturated area	Low, medium, high
Saturation of the global management system	Low, medium, high
Lack of packaging supplies	Low, medium, high
Delayed entry of goods	Low, medium, high
Delay in warehousing operation	Low, medium, high
Delay in unloading operation	Low, medium, high
Delay in loading operation	Low, medium, high
Delay in storage operation	Low, medium, high
Delay in order preparation	Low, medium, high
Delay in goods handling	Low, medium, high
Disruption to planning	Low, medium, high

Source: Authors, (2025).

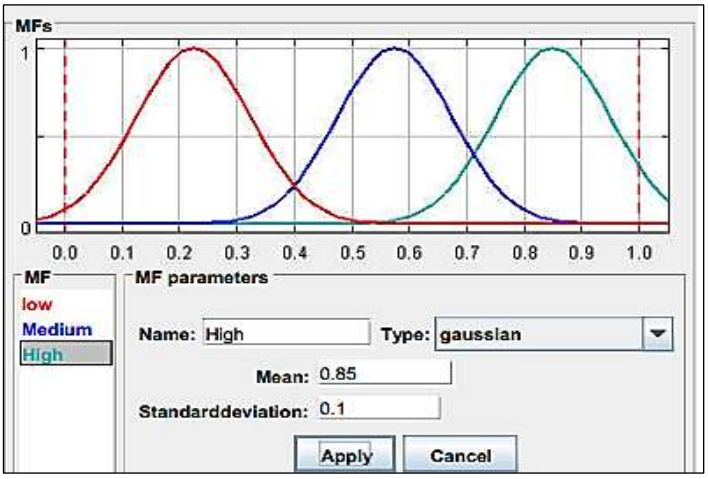

Figure 15: Representation of the Gaussian function, order picking delay.
Source: Authors, (2025).

The membership functions most commonly used in the literature for this type of problem are the triangular function, the trapezoidal function, and the Gaussian function, which will be applied in our case, for the different nodes. Because it generates fewer errors than the others [39]. Figure 14 shows the shape of the Gaussian function used. Subsequently, our work focuses on the study and application of the inference method to the last 'planning disruption' field. Table 10 gives the fuzzy rules for the 'planning disruption' node.

Table 11 shows the numerical values corresponding to the fuzzy variables.

Table 10: Fuzzy rules.

Rules	If Delayed goods handling	And order-picking delays	So Planning disruption
R1	Low	Low	Low
R2	Low	medium	Low
R3	Low	high	Low
R4	medium	Low	medium
R5	medium	medium	medium
R6	medium	high	medium
R7	High	Low	high
R8	High	medium	high
R9	High	high	high

Source: Authors, (2025).

Table 11: Fuzzy and numerical values.

Disruption to planning	Discrete value
Low	0.2
Medium	0.5
High	0.8

Source: Authors, (2025).

VI.3 STUDY AND ANALYSIS USING FUZZY LOGIC

This stage concerns the aggregation of conclusions triggered by activated rules. Table 12 shows an example case extracted from the simulation carried out during the study, Figure 15.

Applying the max operator between the different situations activated gives a single value.

Table 12: Presentation of activated rules.

Rule activated	Linguistic value	Degree of belonging
5	Medium	0.458
6	High	0.135
8	Medium	0.325
9	High	0.135

Source: Authors, (2025).

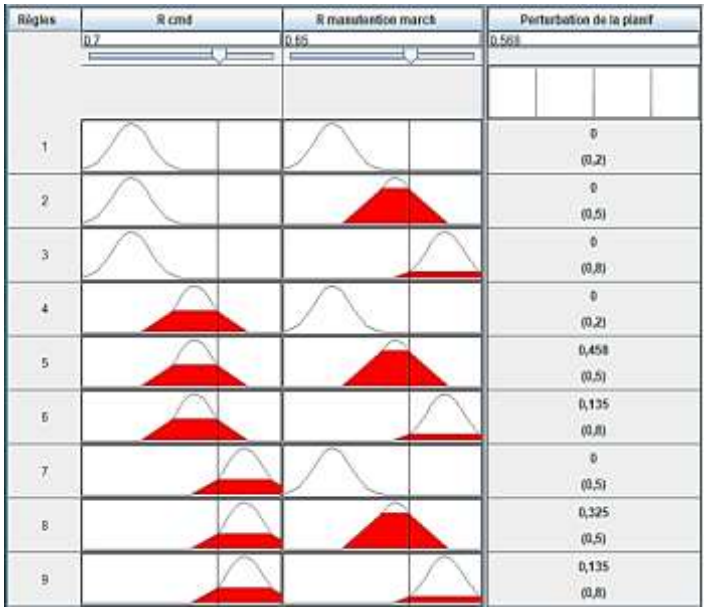

Figure 15: Global Bayesian network representation.
Source: Authors, (2025).

According to this scenario, the values of the 'planning disruption' output variable are as follows:

- For medium linguistic value: 0.458 and 0.325
- For high linguistic value: 0.135

The weak variable has not appeared in this configuration, so we assign it the value 0.001, because each case is possible to be present even if with a very weak degree of presence that is strictly positive.

- Disruption to planning (Low) = 0.001
- Disruption to planning (medium) = Max (0.458; 0.325) = 0.458
- Disruption to planning (high) = 0.135

Take the case of rule number 6 where the input variables have the following linguistic values:

- R. handling = Medium, and R. cmd= High, then:
- P (Perturbation=Low/ R. handling = Medium, R. cmd= High) = (0.001/0.001+0.458+0.135) =0.0016
- P (Disturbance=Medium/ R. handling = Medium, R. cmd= High) = (0.458/0.001+0.458+0.135) =0.771
- P (Disturbance=High/ R. handling = Medium, R. cmd= high) = (0.135/0.001+0.458+0.135) = 0.2273

The rest of the calculation of different situations concerning the conditional probabilities of the output variables (planning perturbation) from the values of the primary nodes is presented in Table 13.

Table 13: Calculation results for different situations.

					Perturbation de la planification		
Rules	**Handling delay**	**Values**	**order delay**	**Values**	**Low**	**Medium**	**High**
1	Low	0.1	Low	0.3	0.950	0.048	0.002
2	Low	0.1	Medium	0.45	0.148	0.850	0.002
3	Low	0.1	High	0.75	0.001	0.320	0.679
4	Medium	0.55	Low	0.3	0.766	0.233	0.001
5	Medium	0.55	Medium	0.45	0.148	0.850	0.002
6	Medium	0.55	High	0.75	0.001	0.262	0.737
7	High	0.70	Low	0.3	0.584	0.415	0.001
8	High	0.7	Medium	0.45	0.148	0.850	0.002
9	High	0.7	High	0.75	0.001	0.320	0.679

Source: Authors, (2025).

VI.3 RESULTS OF GRAPHICAL SIMULATION

Simulating the response of the fuzzy system under the 'Section' option produces two graphs leading to a comparative study between the two input variables. Each of these two variables (order delay & goods handling delay) is studied as a function of the output variable (planning disruption), (figure 16) and (figure 17).

Interpretation of the graphs: Fig. 16 shows the variation in planning disturbance as a function of the variation in order picking delay. When the order delay is in the range [0-15%], the variation between the two variables is proportional or linear. Above 15%, the impact of R.cmd remains constant even if its value increases and this is reflected in the fact that the order picking function is linear within the warehouse and the number of operators remains small, so this delay can be recovered in the order picking line. Figure 17, on the other hand, shows the disruption of planning as a function of goods-handling delays in three intervals:

[0-30%]: The merchandise handling delay has a 20% coefficient on planning disruption. This is because, in this phase, the disruption to planning generally shows a linear relationship with the order-picking delay.

[30-90%]: The variation is almost linear and proportional to the order-picking delay.

Above 90%, the disruption to planning no longer depends on either the order-picking delay or the goods-handling delay, as there are always unforeseen factors influencing the normal operation of the warehouse.

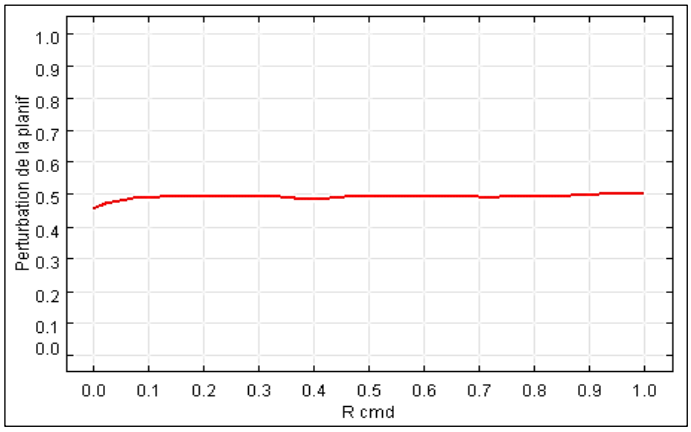

Figure 16: Planning disruption based on order delay
Source: Authors, (2025).

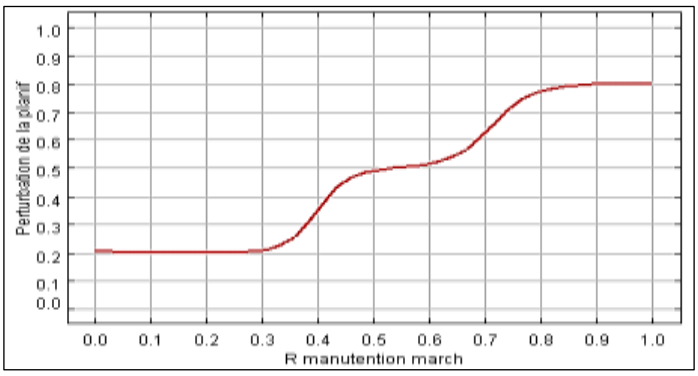

Figure 17: Disruption to planning due to delayed goods handling
Source: Authors, (2025).

VII. DISCUSSION

In this paper, a study of possible scheduling disruptions is developed by applying the Bayesian fuzzy model. The application of Bayesian networks is widely used in studies carried out for the analysis of disruption risks caused by delays in the marine and air navigation domains [40-42], or railways [43]. Our model focuses on the study of disruptions to the planning of order processing tasks in an industrial warehouse. This study considers several internal and external factors at the origin of the disruption.

Exploration and analysis of the results obtained from the study of the 'planning disruption' entity reveals that the influence of factors internal to the warehouse on the stability of pre-planning task progress is greater than that of external factors. This indicates that the decisions taken within the warehouse by the decision-makers in terms of designating materials or personnel to carry out the tasks have a more important factor in compliance with planning and, consequently, in meeting the deadlines for processing goods and orders.

So intelligent planning will be coherent planning between the programmed tasks and the resources designated for this purpose.

VIII. CONCLUSIONS

Respecting the order processing schedule in a logistics warehouse is crucial to ensuring the quality of logistics services. Unfortunately, this planning is often not respected, leading to more or less unfortunate consequences. This study focuses on forecasting the risks of planning disruption, anticipating them, avoiding them, or being prepared to reduce the consequences of a negative disruption to the plan.

In order to achieve this objective, this article proposes a fuzzy Bayesian model that combines the Bayesian approach and fuzzy logic to monitor disturbances in planning. This model is based on a series of causes that lead to the disruption of task planning and their causal relationships represented by a causality graph. Fuzzy logic is used to create fuzzy rules based on conditional probability tables.

A model like this is compelling, particularly for the problem discussed in this article. It is an alternative approach to Deep Learning for prediction when there is a lack of massive data.

One of the limitations of the proposed model is the elaboration of all the factors that influence the disruption of planning. The lack of integration of all these factors may affect the effectiveness of this model in correctly predicting possible disruptions. The application of this model to the treatment of all risks that may occur in the disruption of planning tasks is a potential perspective. A comparative study between a Bayesian fuzzy model and a model from Deep-Learning to predict the risks of disruption of planning tasks is a very promising avenue of research.

IX. AUTHOR'S CONTRIBUTION

Conceptualization: Kerouich Abdelilah, Azmani Abdellah, Azmani Monir.
Methodology: Kerouich Abdelilah, Azmani Abdellah, Azmani Monir.
Investigation: Kerouich Abdelilah, Azmani Abdellah, Azmani Monir.
Discussion of results: Kerouich Abdelilah, Azmani Abdellah, Azmani Monir.
Writing – Original Draft: Kerouich Abdelilah, Azmani Abdellah, Azmani Monir.
Writing – Review and Editing: Kerouich Abdelilah, Azmani Abdellah, Azmani Monir.
Resources: Kerouich Abdelilah, Azmani Abdellah, Azmani Monir.
Supervision: Kerouich Abdelilah, Azmani Abdellah, Azmani Monir.
Approval of the final text: Kerouich Abdelilah, Azmani Abdellah, Azmani Monir.

X. ACKNOWLEDGMENTS

This research is supported by the Ministry of Higher Education, Scientific Research and Innovation, the Digital Development Agency (DDA), and the National Center for Scientific and Technical Research (CNRST) of Morocco (Smart DLSP Project - AL KHAWARIZMI IA-PROGRAM).

XI. REFERENCES

[1] Gharbi S. La réalité augmentée au service de l'optimisation des opérations de picking et putting dans les entrepôts [Internet] [phdthesis]. Ecole Centrale de Lille; 2015.

[2] V.Zeimpekis, Chaînes et réseaux agroalimentaires intelligents, 2011, https://doi.org/10.1002/9781444339895.fmatter

[3] Nogatchewsky G. Le contrôle dans la relation client-fournisseur. Rev Fr Gest. 2003 Dec 1;29(147):173–83. https://doi.org/10.3166/rfg.147.173-183

[4] Soleilhac G. Optimisation de la distribution de marchandises avec sous-traitance du transport : une problématique chargeur [Internet] [phdthesis]. Ecole nationale supérieure Mines-Télécom Atlantique; 2022.

[5] Kaddoussi A. Optimisation des flux logistiques : vers une gestion avancée de la situation de crise [Internet] [phdthesis]. Ecole Centrale de Lille; 2012 [cited 2024 May 30].

[6] Liu KF-R, Yeh K, Chen C-W, Liang H-H, Shen Y-S. Using Bayesian Belief Networks and Fuzzy Logic to Evaluate Aquatic Ecological Risk. Int J Environ Sci Dev. 2013;419–24. https://doi.org/10.7763/IJESD.2013.V4.385

[7] Roodbergen KJ, De Koster R, Van Voorden R. Reduction of Walking Time in the Distribution Center of De Bijenkorf. In: Speranza MG, Stähly P, editors. New Trends in Distribution Logistics [Internet]. Berlin, Heidelberg: Springer Berlin Heidelberg; 1999 [cited 2024 May 30]. p. 215–34. (Fandel G, Trockel W, editors. Lecture Notes in Economics and Mathematical Systems; vol. 480). https://doi.org/10.1007/978-3-642-58568-5_11

[8] Thun, J. H. et Hoenig, D. (2011). Une analyse empirique de la gestion des risques de la chaîne d'approvisionnement dans l'industrie automobile allemande. *Revue internationale d'économie de production, 131*(1), 242-249.

[9] Sanjoy kumar et al. Modéliser les impératifs de l'industrie 5.0 basés sur l'intelligence artificielle vers des chaînes d'approvisionnement résilientes : une perspective post-pandémie de COVID-19, 2023, DOI : 10.1016/j.cie.2023.109055

[10] Kleindorfer, P. R. et Saad, G. H. (2005). Gérer les risques de perturbation dans les chaînes d'approvisionnement. *Gestion de la production et des opérations, 14*(1), 53-68.

[11] Hassan_et_al. Business_Strategy_and_the_Environment, 2020.

[12] Zsidisin, G. A., Melnyk, S. A. et Ragatz, G. L. (2005). Une perspective théorique institutionnelle de la planification de la continuité des activités pour la gestion des achats et des approvisionnements. *Revue internationale de recherche sur la production, 43*(16), 3401-3420. https://doi.org/10.1080/00207540500095613.

[13] BCI-Business Continuity Institute. (2019). Supply chain resilience 10-year trend analysis. 2009–2018. *Zurich Insurance Group* https://www.b-c-training.com/img/uploads/resources/Supply-Chain-Resilience-10-year-trend-analysis.pdf

[14] Ivanov, D., Dolgui, A., Sokolov, B. et Ivanova, M. (2017). Revue de la littérature sur la reprise après les perturbations dans la chaîne d'approvisionnement. *Revue internationale de recherche sur la production*, *55*(20),61586174. https://doi.org/10.1080/00207543.2017.1330572.

[15] Zsidisin, G. A., Petkova, B. N. et Dam, L. (2016). Examen de l'influence des problèmes de la chaîne d'approvisionnement sur la richesse des actionnaires : la raison est-elle importante ? *Revue internationale de recherche sur la production*, *54*(1), 69-82. https://doi.org/10.1080/00207543.2015.1015751

[16] Yaagoubi AE. Contribution à l'optimisation du chargement et du déchargement des conteneurs dans le cas des transports routier et fluvial [Internet] [phdthesis]. Normandie Université; Université Sidi Mohamed ben Abdellah (Fès, Maroc). Faculté des Sciences et Techniques; 2019.

[17] Ding D, Chou MC. Stowage planning for container ships: A heuristic algorithm to reduce the number of shifts. Eur J Oper Res. 2015 Oct;246(1):242–9. https://doi.org/10.1016/j.ejor.2015.03.044

[18] Wallace T, Stahl B. The demand planning process in executive S&OP. J Bus Forecast. 2008;27(3):19.

[19] Wang H, Tong L, Takeuchi R, George G. Corporate Social Responsibility: An Overview and New Research Directions: Thematic Issue on Corporate Social Responsibility. Acad Manage J. 2016 Apr;59(2):534–44. https://doi.org/10.5465/amj.2016.5001

[20] Kande S. Etude et résolution de problèmes de planification dans des réseaux logistiques multi-échelons [Internet] [phdthesis]. Université de Technologie de Troyes; 2015.

[21] Sabah B. Outils de planification de la production et de la distribution des produits en vrac : cas de l'OCP Maroc, 2021. Thèse

[22] Choi J, Johnson DW, Johnson R. Relationships Among Cooperative Learning Experiences, Social Interdependence, Children's Aggression, Victimization, and Prosocial Behaviors: INTERDEPENDENCE, AGGRESSION, AND PROSOCIAL BEHAVIOR. J Appl Soc Psychol. 2011 Apr;41(4):976–1003. https://doi.org/10.1111/j.1559-1816.2011.00744.x

[23] Kerouich A, Azmani A, Azmani M. Reorganization of the Warehouse Activities Processes with the Framing of their Problems and Solutions. Int J Prof Bus Rev. 2023 Nov 17;8(11):e03805. https://doi.org/10.26668/businessreview/2023.v8i11.3805

[24] Romet P. SURATRAM - Système de Transport Intelligent pour la gestion du fret de marchandises en zone urbaine [Internet] [phdthesis]. Université Bourgogne Franche-Comté; 2022.

[25] Raoult O. Diagnostic de pannes des systèmes complexes [Internet] [phdthesis]. Institut National Polytechnique de Grenoble - INPG; 1989.

[26] Nathan B. La zone d'activité logistique comme levier de développement économique des territoires, 2017.

[27] Mahmoudi J. Simulation et gestion des risques en planification distribuée de chaînes logistiques : application au secteur de l'électronique et des télécommunications.

[28] Marylene Mouketou m. Etude des determinants environnementaux du stress professionnel, 2020.

[29] Gwynne RichardsWarehouse Management: A complete guide to improving efficiency and minimising costs in the modern warehouse.

[30] Bessouat J. Un modèle de référence pour lapplication de l'ABC dans le cadre de la réorganisation des activités de l'entrepot , une recherche - inventaire chez FM Logistic, 2019.

[31] Sakli L. Modélisation et évaluation des vulnérabilités et des risques dans les chaînes logistiques. [Internet] [phdthesis]. Aix Marseille Universitè; 2016.

[32] S. Renooij, « Probability elicitation for belief networks: issues to consider », The Knowledge Engineering Review, 2001, doi: 10.1017/S0269888901000145

[33] Khalfaoui H, Azmani A, Farchane A, Safi S. Symbiotic Combination of a Bayesian Network and Fuzzy Logic to Quantify the QoS in a VANET: Application in Logistic 4.0. Computers. 2023 Feb 14;12(2):40. https://doi.org/10.3390/computers12020040.

[34] Garmendi, L. Razonamiento Aproximado y Con Incertidumbre, 2010.

[35] Zadeh LA, Klir GJ, Yuan B. Fuzzy sets, fuzzy logic, and fuzzy systems: selected papers. Vol. 6. World Scientific; 1996.

[36] Enache, IOAN CONSTANTIN."Marketing a Web-Site Using a Fuzzy Logic Approach." In Proceedings of the International Conference on Risk Management, Assessment And Mitigation Marketing, 2010.

[37] Jyh-Shing R.J. "Neuro-Fuzzy and Soft Computing. Estados Unidos: Prentice-Hall." 1997: 1–164. Kacioui-Maurin, Elodie. 2011. "Exploration et Exploitation, Les Formes d'ambidextrie Organisationnelle Dans l'innovation de Services: Le Cas Des Prestataires de Services Logistiques." AIX-MARSEILLE UNIVERSITE (UNIVERSITE DE LA MEDITERRANEE)

[38] Claude, Théorêt. "Élaboration D'un Logiciel D'enseignement Et D'application De La Logique Floue Dans Un Contexte D'automate Programmable." Ecole de technologie supérieure, université du Québec, 2009.

[39] S. Mandal, J. Choudhury, et S. Bhadra Chaudhuri, « In Search of Suitable Fuzzy Membership Function in Prediction of Time Series Data », International Journal of Computer Science Issues, vol. 9, mai 2012.

[40] J. Wang et al. « Predicting a Containership's Arrival Punctuality in Liner Operations by Using a Fuzzy Rule-Based Bayesian Network (FRBBN) », The Asian Journal of Shipping and Logistics, vol. 33, p. 95-104, juill. 2017

[41] F. Goerlandt et al. « A Bayesian Network risk model for estimating coastal maritime transportation delays following an earthquake in British Columbia », Reliability Engineering & System Safety, vol. 214, p. 107708, oct. 2021, doi: 10.1016/j.ress.2021.107708.

[42] K. Law et al. « Modelling the delay propagation effects of multiple resource connections in an airline network using a Bayesian network model », Transportation Research Part E: Logistics and Transportation Review, vol. 122, p. 62-77, févr. 2019.

[43] F. Corman et al. « Stochastic prediction of train delays in realtime using Bayesian networks », Transportation Research Part C: Emerging Technologies, vol. 95, p. 599-615, oct. 2018, doi: 10.1016/j.trc.2018.08.003

Journal of Engineering and Technology for Industrial Applications

ITEGAM-JETIA

Manaus, v.11 n.53, p. 127-135. May/June., 2025.
DOI: https://doi.org/10.5935/jetia. v11i53.1830

ISSN ONLINE: 2447-0228

RESEARCH ARTICLE
OPEN ACCESS

PATCHDETECT: BREAST CANCER DETECTION COMBINING UNET-RESNET-50 AND PATCH EMBEDDING LSTM.

Hadj Ahmed BOUARARA [1], Kadda BENYAHIA [2]

[1,2] GeCoDe Laboratory, University of Saida Dr Moulay Tahar Algeria

[1]http://orcid.org/0000-0002-4973-4385, [2]http://orcid.org/0000-0002-6394-0855,

Email: bouararaahmed1990@gmail.com , benyahiak@gmail.com

ARTICLE INFO

Article History
Received: April 4, 2025
Revised: May 2, 2025
Accepted: May 15, 2025
Published: May 31, 2025

Keywords:
bidi-LSTM,
Recurrent Neural Network,
Convolutional Neural Network,
breast cancer detection,
ResNet50.

ABSTRACT

This study presents a novel framework for breast cancer detection, combining patch embedding, feature extraction using a pre-trained Convolutional Neural Network (CNN) model (ResNet50), Long Short-Term Memory (LSTM) networks for image sequence analysis, and Fully Connected Layers for final classification. The model's performance was optimized using various hyperparameters, achieving an accuracy of 94%, recall of 93%, precision of 92%, and F-measure of 92% while maintaining a minimal error rate of 6%. The findings emphasize the importance of integrating pre-trained CNNs with sequential analysis via LSTMs for feature-rich and temporal data like mammographic patches. The study also highlights the impact of parameter tuning on classification performance, paving the way for more accurate, automated, and non-invasive breast cancer diagnostic tools.

I. INTRODUCTION

Breast cancer remains a major public health problem worldwide. In 2022, there were 2.3 million new cases among women, making it the most common cancer in many countries. In the same year, around 670,000 deaths from breast cancer were recorded, underlining the urgent need to improve screening and diagnosis strategies [1].

Mammography (see figure 1), currently considered the gold standard for screening, can detect abnormalities before clinical symptoms appear. However, it is not without its limitations, including false-negative or false-positive results, which can lead to unnecessary invasive biopsies or delays in diagnosis [2].

These technical and clinical limitations of mammography have prompted researchers to explore the solutions offered by artificial intelligence (AI) techniques. Recent literature highlights the growing impact of machine learning (ML) and deep learning (DL) approaches on breast cancer screening. According to Yao et al [3], these approaches have considerably improved the processing of mammographic images, particularly in terms of mass detection, segmentation and classification.

However, these techniques still face significant challenges, such as the need for large datasets for training, the high costs of advanced algorithms, and the difficulty of achieving accurate lesion recognition, particularly in dense breast tissue.

In response to these obstacles, we suggest the incorporation of recurrent neural networks, particularly Long Short-Term Memory (LSTM) networks, as a promising alternative. In contrast to conventional methods, which typically rely on Convolutional Neural Networks (CNNs), our approach enables the sequential analysis of images after they have been segmented into regions. This segmentation, when combined with patch embedding and position encoding techniques, improves the capacity to identify subtle patterns that are indicative of malignancy, which are frequently imperceptible to the human eye. This innovative approach seeks to enhance the quality-of-care pathways and increase the likelihood of patient survival by decreasing the dependence on invasive biopsies and enhancing diagnostic accuracy.

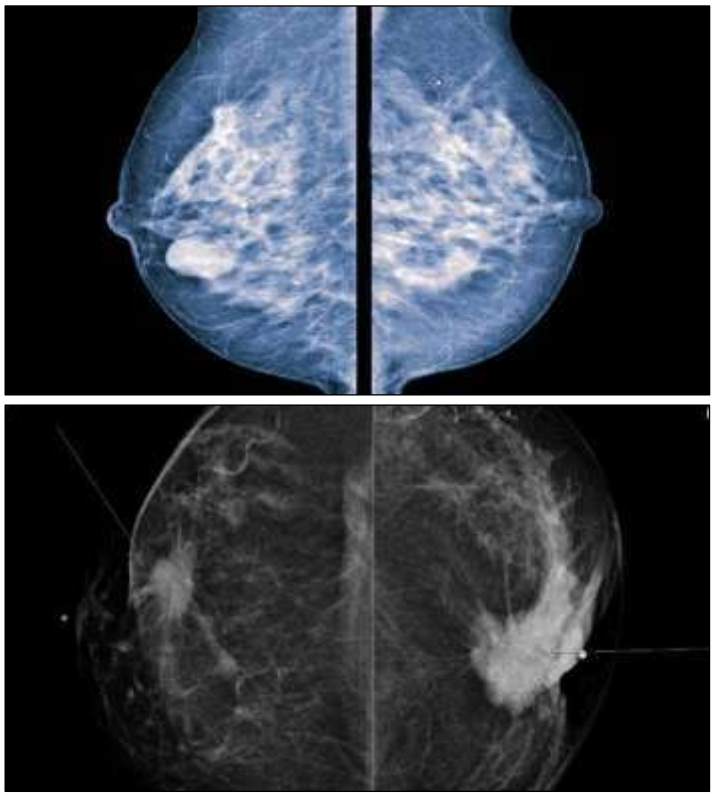

Figure 1: Screening mammography for breast cancer
Source: [1].

The structure of this paper will be organized as follows: We will begin with a review of the essential works on this topic to establish a state-of-the-art foundation. Next, we will detail our approach and the proposed components. Following that, we will conduct an experimental and comparative study to present the best results obtained. Finally, we conclude with a discussion of the key challenges and unresolved questions in the field, as well as potential directions for future research. We also reflect on the broader implications of our findings and the opportunities for advancing the state-of-the-art in this area.

II. REVIEW OF LITERATURE

The most important works around the problem of breast cancer detection are detailed in this section:

Breast cancer detection has improved significantly over the years, as many studies have employed machine learning techniques to enhance diagnostic accuracy. These advancements demonstrate how computer models can facilitate early detection and improve treatment outcomes. For instance, in 2011, Rakhi Malpani and his team[4] used the WEKA API to analyze mammography data from the Digital Database for Screening Mammography (DDSM), achieving an accuracy of 79.36%. Although there was room for improvement, this early work proved that rule-based methods can be useful in analyzing medical images. Building on this foundation, Vikas Chaurasia and Saurabh Pal in 2017 applied boosting techniques like IBK, SMO, and BFtree with the same WEKA API and DDSM dataset [5]. Their model achieved a higher accuracy of 86.2%, showing that combining different classifiers can yield more reliable predictions by addressing the limitations of individual models. Similarly, Gouda Salama in 2012 adopted methods such as SMO, J48, MLP, and IBK to classify data from the WDBC and WPBC datasets, attaining an accuracy of 77.32% [6] While this result was lower than Chaurasia and Pal's, it underscored the potential of ensemble methods to work well across diverse datasets. These variations in performance highlighted the importance of selecting models that best align with dataset characteristics to optimize accuracy.

In another innovative approach, Jahanvi Joshi and her team in 2014 [7] utilized a clustering method called 2-means in WEKA to analyze the UCI dataset. They achieved an accuracy of 83%, emphasizing the effectiveness of unsupervised learning techniques like k-means clustering, especially in scenarios with limited labeled data. Furthermore, in 2019, Xuan Tran and colleagues highlighted that while many AI applications in cancer research outperform traditional methods, thorough evaluation and clinical validation are necessary to substantiate these findings[8]. This insight emphasized the critical need for assessing AI technologies within clinical settings.

In 2021, Kumar and colleagues reviewed various AI cancer prediction models and noted the increasing adoption of deep learning techniques, particularly Convolutional Neural Networks (CNNs), to improve diagnostic accuracy[9] . However, they also pointed out persistent challenges in the early detection of less-explored cancers, such as head and neck cancers, thereby calling for further research in these areas. Similarly, Munir Shah and his team, in a 2021 review[10], focused on breast cancer detection and observed that traditional imaging is prone to human errors. They highlighted the growing reliance on AI for automated image analysis, which not only reduces errors but also enhances accuracy in identifying cancer [11].

Meanwhile, in 2015, Nerea Matamala investigated the use of microRNAs for early breast cancer detection, contributing to the trend of exploring molecular markers for non-invasive cancer detection. While specific datasets or accuracy metrics were not provided, her work involved analyzing miRNA expression in tissue samples from 122 breast tumors and 11 healthy controls. Additionally, she validated the results in a larger cohort, demonstrating the potential of combining molecular markers with traditional imaging for comprehensive diagnostic approaches [12]. Manjurul Ahsan and Siddique in 2021[13] discussed the advantages of machine learning in disease diagnosis. They highlighted how these algorithms can accelerate diagnostic processes, particularly in resource-limited settings, while addressing the limitations of traditional methods. Their work reinforced the importance of adopting machine learning systems to improve both diagnostic accuracy and efficiency. Koh in [14] reviews the expanding role of AI and ML in cancer imaging, highlighting the need for multidisciplinary collaboration to ensure effective tool development and validation.

Annother reviews prenented by Hunter et all [15] discusses the role of artificial intelligence in enhancing early cancer diagnosis, a priority outlined by the World Health Organization. The review outlines how AI can assist in screening asymptomatic individuals, triaging symptomatic patients, and detecting cancer recurrence. It highlights the use of various AI approaches—from logistic regression to deep learning—across multiple data types, such as medical records, imaging, pathology, and blood samples. The study also explores current clinical applications, while addressing challenges like ethical concerns, data security, and the strain on diagnostic resources.

Musa and his team [16] conducted a bibliometric analysis of the top 100 most-cited articles on AI and ML in cancer research, highlighting key technologies such as ANN, CNN, and deep learning models. The study emphasizes the role of these innovations in improving cancer detection, diagnosis, and prevention, guiding future research efforts.

Zajnulina [17] reviewed the growing role of AI in enhancing cancer diagnostics, particularly through MRI, CT, and emerging spectroscopy-based techniques. The study highlights how AI-integrated spectroscopy can enable fast, low-invasive, and chemical-free tissue classification, marking a promising direction for safer and more efficient cancer diagnosis.

Habchi and his team[18] present a comprehensive review of AI in thyroid cancer diagnosis, analyzing supervised, unsupervised, and ensemble learning techniques including deep learning and probabilistic models. The study highlights key datasets, feature extraction methods, evaluation metrics, and outlines current challenges and future research directions.

In the studies of Bechelli [19], a comprehensive review is provided on the use of machine learning and deep learning for cancer diagnosis, examining the steps involved in developing efficient algorithms for cancer detection, classification, and prediction, while addressing the challenges and advancements in utilizing various imaging techniques.

Aamir et all [20] conducted a comprehensive review on the integration of Artificial Intelligence (AI) in healthcare, emphasizing its growing role in disease diagnosis. The study highlights the use of machine learning and deep learning techniques to enhance diagnostic accuracy and clinical efficiency.

Building upon the existing body of work in cancer detection through machine learning and deep learning, our study introduces a novel framework for breast cancer detection. Unlike traditional methods, which often rely on standalone techniques, our approach integrates patch embedding, feature extraction via a pre-trained Convolutional Neural Network (CNN) model (ResNet50), and Long Short-Term Memory (LSTM) networks for analyzing image sequences. Additionally, we employ Fully Connected Layers for the final classification step, optimizing the model's performance using a variety of hyperparameters. This combination of advanced techniques aims to improve the accuracy and efficiency of breast cancer detection, marking a significant advancement in the field.

With this foundational understanding of the existing methods and their limitations, we now turn to the details of our proposed approach. The following section outlines the novel framework developed for breast cancer detection, emphasizing the integration of cutting-edge techniques such as patch embedding, Unet-ResNet50 for seglentation and feature extraction, LSTM networks for image sequence analysis, and Fully Connected Layers for classification. We will also explore the optimization process, including the hyperparameter tuning that was crucial for enhancing the model's performance.

III. PROPOSED SOLUTION

Our solution (see figure 3) combines U-Net-ResNet50 segmentation to identify regions of interest (ROIs) in mammography images, extracts and embeds patches from these ROIs, and uses an LSTM to model spatial dependencies between patches before final classification with DenseNet . By integrating localized patch-level analysis with global image features, the approach enhances the accuracy of breast cancer classification while leveraging the strengths of sequential modeling and hierarchical feature extraction.

III.1 DATASET USED

Curated Breast Imaging Subset of DDSM (CBIS-DDSM): The CBIS-DDSM is an updated and standardized subset of the Digital Database for Screening Mammography (DDSM) , which originally consisted of 2,620 scanned film mammography studies as illustrated in figure 2. While the DDSM includes normal, benign, and malignant cases with verified pathology information, its non-standard format and lack of precise annotations limited its usability. The CBIS-DDSM addresses these challenges by curating a targeted selection of DDSM data, decompressing images into DICOM format, and providing updated ROI segmentations, bounding boxes, and pathologic diagnoses for training. This enhanced dataset includes approximately 1,566 unique participants (though metadata suggests 6,671 due to multiple patient IDs) and encompasses a wide range of cases: normal cases with no abnormalities, benign cases featuring non-cancerous lesions, and malignant cases with cancerous tumors or anomalies. These are distributed across cranio-caudal (CC) and mediolateral oblique (MLO) projections, ensuring comprehensive coverage of breast structures. With thousands of annotated images spanning hundreds of cases per class the CBIS-DDSM provides a robust foundation for developing and testing decision support systems, including CADx and CADe algorithms, for accurate breast cancer detection and diagnosis [21].

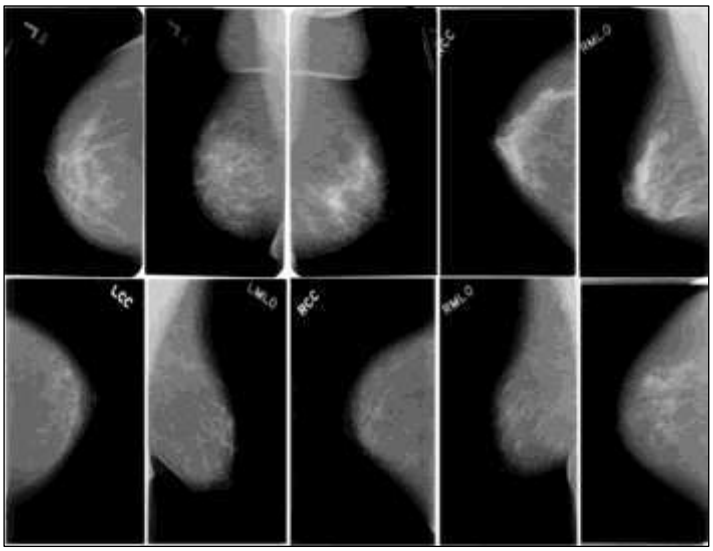

Figure 2: image mammography from CBIS-DDSM dataset. Source: [21].

III.2 DATA PREPROCESSING AND AUGMENTATION

The DDSM images, often large and containing noise or lighting variations, require rigorous pretreatment. Normalization is used to homogenize contrasts and reduce the variability in medical equipment quality. Image augmentation techniques like rotation, zoom, and contrast adjustment are also used to maximize data diversity and ensure the model's robustness against slight variations in images.

III.3 SEGMENTATION AND FEATURES EXTRACTION

In this step (figure 4) , we use U-Net with ResNet-50 Backbone , where the encoder part of U-Net is replaced by ResNet-50 to enhance feature extraction. To use U-Net with ResNet-50 for the segmentation of mammography breast cancer images, the process involves leveraging the strengths of both architectures to achieve precise pixel-level annotations. ResNet-50 serves as the encoder in the U-Net framework, replacing the default convolutional layers typically used for feature extraction. The pre-trained ResNet-50 backbone extracts high-level features from the mammography images, capturing intricate patterns such

as masses, calcifications, or other abnormalities. These features are then passed through the decoder part of the U-Net, which uses upsampling and skip connections to reconstruct the segmentation map at the original image resolution. The skip connections ensure that spatial information lost during downsampling in the encoder is reintegrated, enabling accurate localization of lesions. During training, the model is fed annotated mammography images from datasets like CBIS-DDSM , where ground truth masks highlight regions of interest (e.g., benign or malignant tumors). A loss function such as Dice Loss or Binary Cross-Entropy is used to optimize the network for pixel-wise predictions. Once trained, the U-Net-ResNet50 model can segment suspicious regions in new mammograms(figure 5), aiding radiologists by providing detailed delineations of potential cancerous areas for further analysis and diagnosis. This approach combines the hierarchical feature extraction capabilities of ResNet-50 with the precise localization strengths of U-Net, making it highly effective for medical image segmentation tasks.

ResNet-50 offers several advantages when adapted for segmentation tasks. Its pretrained weights , often trained on large datasets like ImageNet, provide a strong starting point for transfer learning in segmentation tasks. The deep architecture of ResNet-50 allows it to learn rich, hierarchical features, which are critical for distinguishing fine details in segmentation tasks. Moreover, its versatility enables integration into various segmentation frameworks, making it adaptable to different applications and datasets. These strengths make ResNet-50 a popular choice as a backbone in segmentation models, especially in medical imaging applications. The residual blocks in ResNet50 enable the network to learn more complex features and deeper representations, which are crucial for accurate segmentation

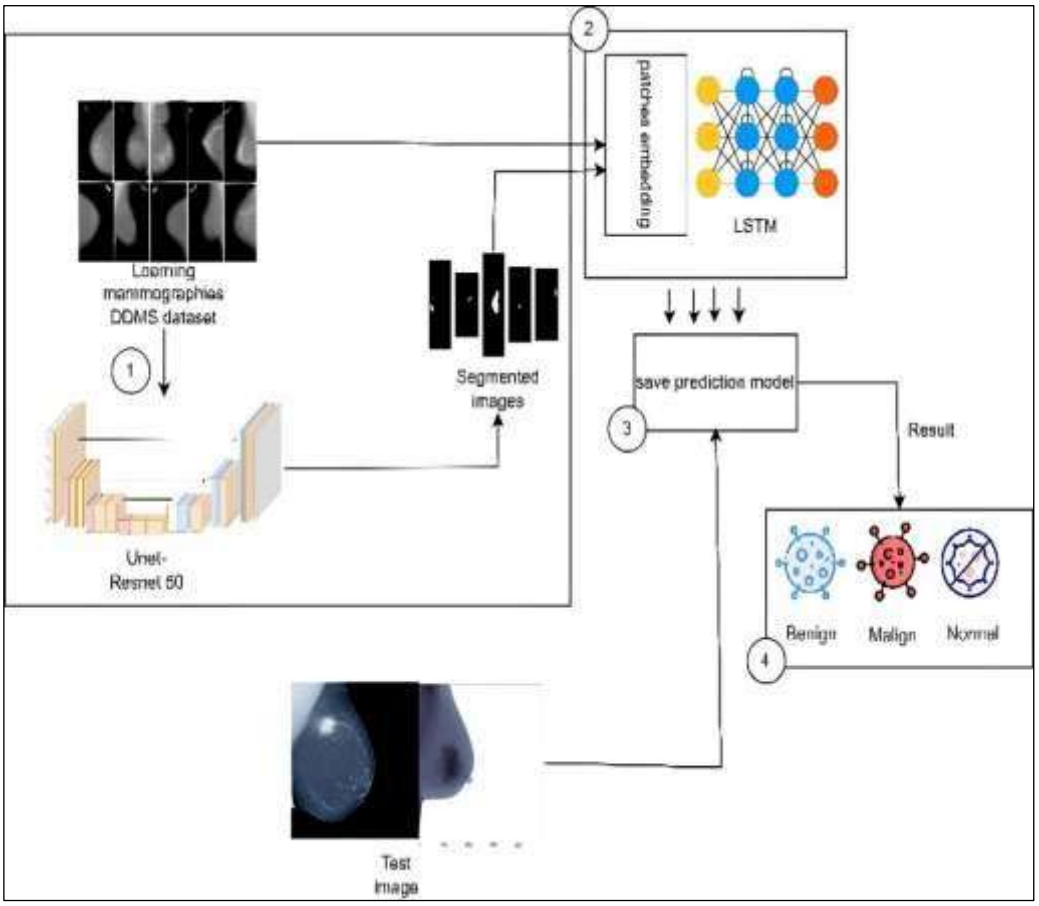

Figure 3: Generale process of the proposed solution. 1)features and ROI extraction using Unet-Resnet50.2). 2) patches+LSTM for learning step and classification part. 3) prediction model saved. Classification of test image.
Source: Authors, (2025).

III.4 PATCHES EMBEDDING + LSTM BLOCKS

III.4.1.PATCHES EMBEDDING + LSTM MODEL

The solution leverages U-Net-ResNet50 for precise segmentation of mammography images, identifying regions of interest (ROIs) such as masses or calcifications, which are then divided into localized patches. These patches are processed by a Patch_Embedding_Model , a CNN-based sub-model that extracts hierarchical features and reduces them to compact embeddings. The sequential relationships between these embedded patches are captured using an LSTM (figure 7), which models spatial dependencies and contextual information across patches, while dense layers perform the final classification into categories like benign, malignant, or normal. By combining U-Net-ResNet50's localization accuracy, CNN feature extraction, and LSTM's sequential learning, the pipeline ensures both fine-grained details and broader contextual relationships are utilized for robust breast cancer diagnosis.

To prevent overfitting, Dropout regularization is applied to the LSTM layers, enhancing generalization. The entire process integrates patch-level analysis with global modeling, treating patches as sequences to capture complex spatial relationships and improve diagnostic accuracy. This hybrid approach enables comprehensive mammography analysis, effectively leveraging spatial and temporal dependencies for more reliable cancer detection and classification.

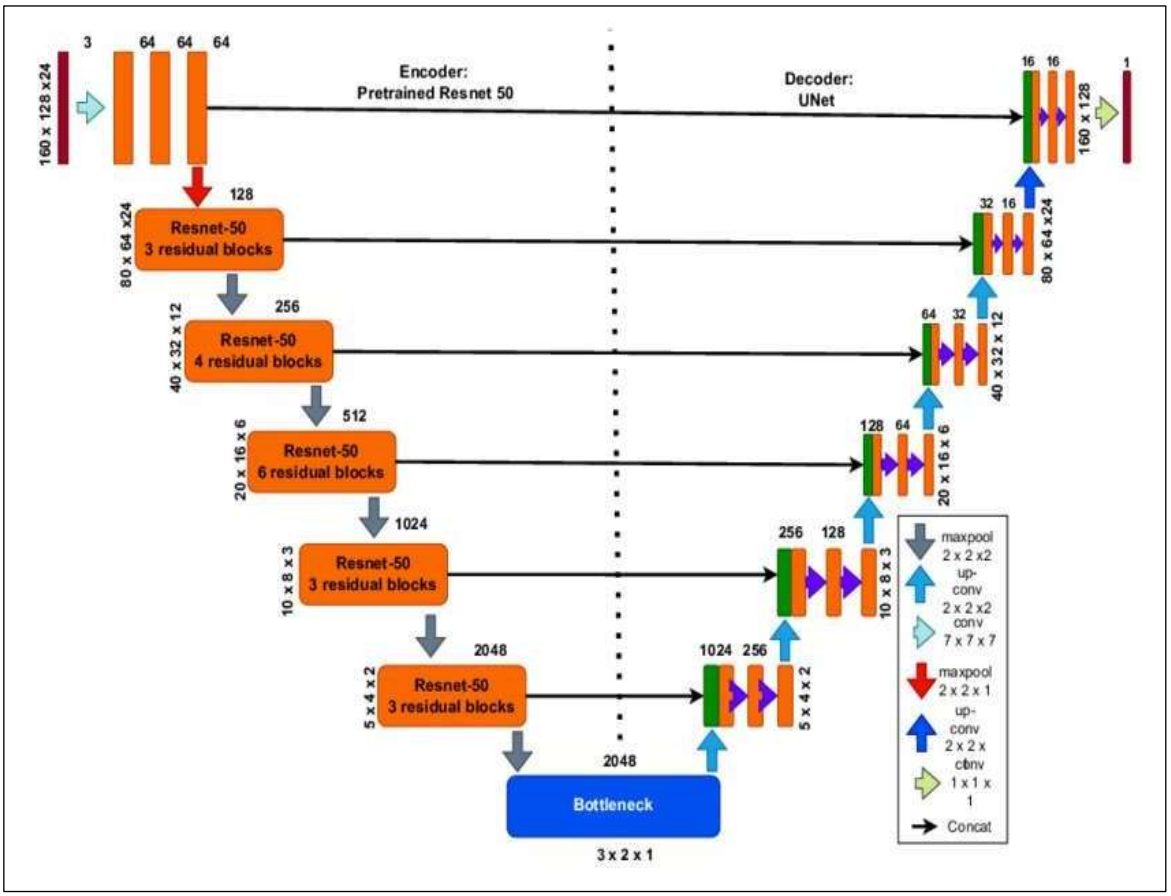

Figure 4: The Segmentation architecture of Unet with pretrained Resnet50 as backbone
Source: Authors, (2025).

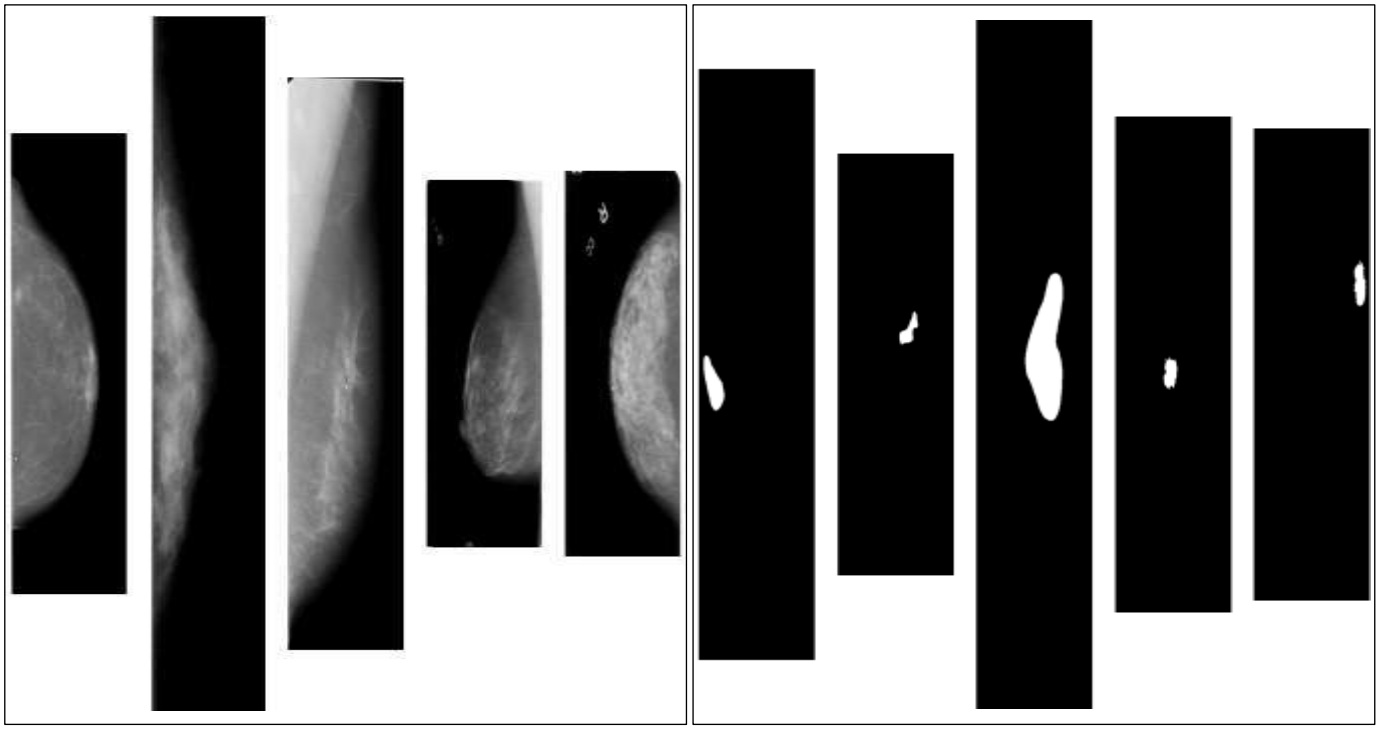

(a) (b)

Figure 5: mammography breast cancer segmentation using Unet-Resnet50 to extract ROI. a) Original image from dataset DDSM b)segmented image after applying Unet-Resnet50
Source: Authors, (2025).

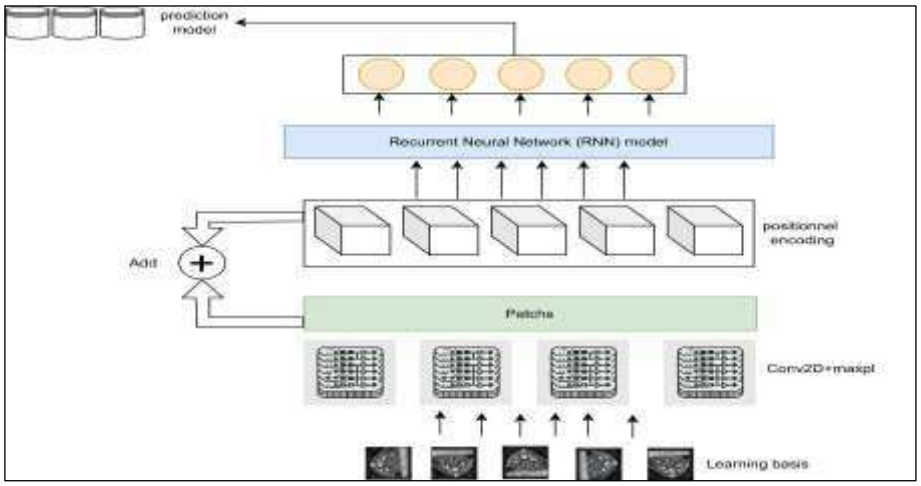

Figure 6: General architecture of patches RNN for breast cancer detection.
Source: Authors, (2025).

Layer (type)	Output Shape	Param #
Sequence_Input (InputLayer)	[(None, None, 64, 64, 1)]	0
TimeDistributed_Patch_Embedding	(None, None, 1600)	73792
| Patch_Embedding_Model |		
| Conv2D_1 (Conv2D)	(None, 64, 64, 32)	320 |
| MaxPooling2D_1 (MaxPooling2D)	(None, 32, 32, 32)	0 |
| Conv2D_2 (Conv2D)	(None, 32, 32, 64)	18496 |
| MaxPooling2D_2 (MaxPooling2D)	(None, 16, 16, 64)	0 |
| Flatten (Flatten)	(None, 1600)	0 |
LSTM (LSTM)	(None, 128)	885248
Dense_1 (Dense)	(None, 64)	8256
Dropout (Dropout)	(None, 64)	0
Output (Dense)	(None, 3)	195

Total params: 967,491
Trainable params : 967,491
Non-trainable params : 0

Figure 7: LSTM model with patch embedding and positional encoding.
Source: Authors, (2025).

III.4.2. PATCHES EMBEDDING + Bidirectional LSTM

In our second combination we have applied a Bidirectional LSTM for the classification step. It is particularly advantageous in the context of breast cancer detection, as it allows the relationships between patches to be captured in both directions (forward and backward). This improves contextual understanding, particularly useful for subtle anomalies and complex dependencies in imaging data. (figure 8)

Layer (type)	Output Shape	Param #
Sequence_Input (InputLayer)	[(None, None, 64, 64, 1)]	0
TimeDistributed_Patch_Embedding	(None, None, 1600)	73792
| Patch_Embedding_Model |		
| Conv2D_1 (Conv2D)	(None, 64, 64, 32)	320 |
| MaxPooling2D_1 (MaxPooling2D)	(None, 32, 32, 32)	0 |
| Conv2D_2 (Conv2D)	(None, 32, 32, 64)	18496 |
| MaxPooling2D_2 (MaxPooling2D)	(None, 16, 16, 64)	0 |
| Flatten (Flatten)	(None, 1600)	0 |
Bidirectional_LSTM (Bidirectional	(None, 256)	1802240
Dense_1 (Dense)	(None, 64)	16448
Dropout (Dropout)	(None, 64)	0
Output (Dense)	(None, 3)	195

Total params: 1,896,675
Trainable params: 1,896,675
Non-trainable params: 0

Figure 8**:** Breast Cancer Detection Model With BiLSTM.
Source: Authors, (2025).

III.5 FULLY CONNECTED LAYERS FOR CLASSIFICATION

After the RNN model analyzes the spatial relationships in an image, it combines the outputs from different patches to make a global prediction. This is done using Fully Connected Layers that take the summarized information from the RNN to create a final classification. The model uses several dense layers with ReLU activation functions to improve these predictions. The final layer applies a Softmax activation function, allowing the model to clearly show the probability that the image represents malignant cancer.

III.6 VALIDATION AND LEARNING MODEL

A rigorous training and validation phase is essential to ensure the model's performance. The dataset is divided into three parts: a training set to adjust the model weights, a validation set to evaluate performance during training, and a test set toz assess final performance. Based on the targeted classes, an appropriate loss function, such as Categorical Cross entropy, is employed. Optimization is carried out using algorithms like Adam or Stochastic Gradient Descent (SGD), which adjust the model parameters to minimize the loss.

IV. RESULTS AND DISCUSSIONS

To present the results of the two RNN models mentioned (Breast Cancer Detection Model with BiLSTM and LSTM with Patch Embedding) on the CBIS-DDMS dataset, we used the evaluation metrics (Recall, Precision, F-measure, Accuracy, Error). Experiments may vary according to the parameters (Learning rate, Batch size, Number of units in the LSTM/BiLSTM layers, Dropout %, Number of epochs. All the obtained results and configuration of parameters are illustrated in detail in the tables 1 and 2.

Table 1: Result of breast cancer detection using our solution with **simple LSTM RNN** model for the classification and variation of parameters (learning rate, batch size, LSTM UNIT, DropOut, Recall , Precision, Accuracy, Error).

Learning Rate	Batch Size	LSTM UNIT	Dropout	Recall	Precision	F-measure	Accuracy	Error
0.001	32	256	0.3	0.91	0.89	0.90	0.92	0.08
0.001	64	256	0.5	0.88	0.87	0.87	0.90	0.10
0.0005	32	128	0.3	0.93	0.91	0.92	0.93	0.07
0.001	32	128	0.3	0.89	0.88	0.88	0.91	0.09
0.001	64	128	0.5	0.87	0.86	0.86	0.89	0.11
0.0005	32	256	0.3	0.91	0.90	0.91	0.92	0.08
0.001	16	256	0.3	0.92	0.90	0.91	0.94	0.06
0.0005	16	128	0.3	0.88	0.87	0.87	0.90	0.10
0.0001	64	256	0.5	0.93	0.92	0.92	0.94	0.06
0.0001	64	128	0.5	0.86	0.85	0.85	0.88	0.12

Source: Authors, (2025).

Table 2: Result of breast cancer detection using our solution with bidirectionnel-LSTM RNN model for the classification and variation of parameters (learning rate, batch size, LSTM UNIT, DropOut, Recall , Precision, Accuracy, Error)

Learning Rate	Batch Size	LSTM UNIT	Dropout	Recall	Precision	F-measure	Accuracy	Error
0.001	32	128	0.3	0.88	0.86	0.87	0.89	0.11
0.001	64	128	0.5	0.86	0.84	0.85	0.88	0.12
0.0005	32	128	0.3	0.90	0.88	0.89	0.91	0.09
0.0005	64	128	0.3	0.89	0.87	0.88	0.90	0.10
0.0001	32	128	0.3	0.91	0.90	0.91	0.92	0.08
0.001	16	256	0.3	0.87	0.85	0.86	0.88	0.12
0.001	32	256	0.5	0.85	0.83	0.84	0.87	0.13
0.0005	64	256	0.3	0.88	0.86	0.87	0.89	0.11
0.0001	32	256	0.3	0.90	0.89	0.89	0.91	0.09
0.0001	64	256	0.5	0.88	0.87	0.87	0.89	0.11

Source: Authors, (2025).

This study explored the impact of key hyperparameters on model performance, including learning rates ranging from 0.0001 to 0.001 to analyze their effect on convergence, batch sizes of 16, 32, and 64, as well as LSTM units with varying complexities of 128 and 256. Dropout was also utilized to regulate overfitting and improve generalization.

The results indicate that BiLSTM models tend to outperform standard LSTM models in metrics such as recall and F-measure, although they require higher computational resources. Conversely, the LSTM model with Patch Embedding achieves slightly lower performance but remains more efficient due to its lighter parameter footprint. For optimal configurations, recall and precision stabilize around 0.88, with a balanced F-measure ranging between 0.87 and 0.91, suggesting consistent performance across all classes. The accuracy reaches up to 0.92, showcasing the model’s strong predictive capabilities on the tested data.

These findings highlight how hyperparameter variations influence the precision and robustness of the model. If specific analyses, additional parameters, or further refinements are required, they can be tailored to meet particular objectives or resource constraints.

COMPARATIVE STUDY

To give our result more reference in literature we have conduct a comparaison with existed techniques in literature such as vgg16, VGG19, Inception V3, MobileNET, DensNet201, ResNEt101, ResNet152,[22] GoogleNet[23]

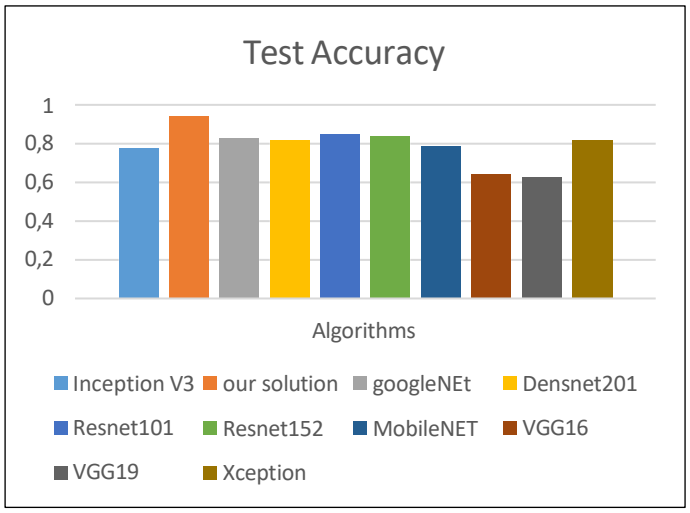

Figure 9: comparative study between our solution and existed solution in literature for breast cancer detection.
Source: Authors, (2025).

After analyzing the results in figure 9, We remark clearly that our model achieves an exceptional test accuracy close to 1.0, significantly outperforming other state-of-the-art architectures like Inception V3, Resnet101, Xception, GoogleNet, MobileNet, and VGG variants. This remarkable performance can be attributed to the innovative design of our pipeline. The UNET-Resnet50 architecture excels in segmentation tasks, enabling precise localization of regions of interest within medical images. By breaking down images into patches and embedding them, we ensure that local features are captured effectively while maintaining computational efficiency. The inclusion of a bidirectional LSTM further enhances the model's ability to analyze sequential dependencies and contextual information across patches, which is particularly valuable in understanding the spatial structure of tumors. Finally, the DenseNet-based classification layer aggregates these features to make robust predictions, benefiting from DenseNet's ability to preserve feature richness through dense connections.

In contrast, other architectures like Inception V3, Resnet101, and Xception, while powerful, may lack the specialized design needed for the nuances of breast cancer detection. Models such as GoogleNet and Densenet201 exhibit moderate performance but do not match the tailored approach of our pipeline. Simpler architectures like VGG16 and VGG19, known for their shallow designs, struggle to capture the complexity of medical images. MobileNet, optimized for lightweight applications, sacrifices depth and detail, making it less suitable for high-stakes tasks like cancer detection.

Several factors contribute to the superior performance of our solution. The UNET-Resnet50 segmentation step ensures accurate identification of suspicious regions, providing a strong foundation for subsequent analysis. Patch embedding allows the model to focus on localized features while reducing computational overhead, ensuring scalability. The bidirectional LSTM adds temporal and contextual understanding, enabling the model to interpret relationships between different parts of the image. DenseNet's dense connectivity pattern ensures efficient feature propagation and reuse, enhancing classification accuracy. Additionally, the pipeline likely benefits from pre-training on large-scale medical datasets, fine-tuning on domain-specific data, and rigorous optimization techniques such as advanced learning rate scheduling and regularization methods.

V. CONCLUSIONS

In this study, we developed an effective framework for breast cancer detection by combining patch embedding with feature extraction using a pretrained ResNet-50 model and sequential analysis through LSTM networks. Our approach demonstrated robust classification performance, achieving a high accuracy of 94% with optimized hyperparameters. These results emphasize the potential of integrating deep learning techniques for precise and automated breast cancer diagnostics. Furthermore, the use of patch embedding allowed for localized feature analysis, enhancing the system's ability to detect patterns indicative of malignancies.

Despite the promising outcomes, challenges remain, such as the computational cost associated with training deep learning models on large-scale datasets and the potential need for domain-specific dataset augmentation to address imbalances. Future work will focus on optimizing the framework further by exploring lightweight architectures and reducing computational overhead. Additionally, integrating explainable AI (XAI) techniques could enhance the interpretability of predictions, making the system more applicable in clinical settings.

Expanding the dataset diversity, including different imaging modalities and demographic factors, will also be prioritized to improve the generalizability of the model. Moreover, real-world validation through clinical trials will be crucial to ensure the reliability and practical utility of the proposed system for early and accurate breast cancer detection.

VI. AUTHOR'S CONTRIBUTION

Conceptualization: hadj ahmed bouarara
Methodology: hadj ahmed bouarara
Investigation: hadj ahmed bouarara and kadda benyahia.
Discussion of results: hadj ahmed bouarara
Writing – Original Draft: hadj ahmed bouarara
Writing – Review and Editing: hadj ahmed bouarara and kadda benyahia.
Resources: hadj ahmed bouarara .
Supervision: kadda benyahia.
Approval of the final text: kadda benyahia.

VII. REFERENCES

[1] Oakeshott, Andrew. "World Health Organisation." (2023).

[2] Jiao, S., Chen, J., Shen, J., Peng, A., Chen, R., Lai, B., ... & Pei, X. (2024). Case report: Triple-negative breast cancer with low tumour-infiltrating lymphocytes infiltration and good prognosis: a case of Tall Cell Carcinoma with

Reversed Polarity and review of the literature. Frontiers in Oncology, 14, 1455893.

[3] Yao, L., Zhang, Z., Keles, E., Yazici, C., Tirkes, T., & Bagci, U. (2023). A review of deep learning and radiomics approaches for pancreatic cancer diagnosis from medical imaging. ncbi.nlm.nih.gov

[4] R. Malpani, M. Lu, D. Zhang and W. K. Sung, "Mining transcriptional association rules from breast cancer profile data," *2011 IEEE International Conference on Information Reuse & Integration*, Las Vegas, NV, USA, 2011, pp. 154-159, doi: 10.1109/IRI.2011.6009538.

[5] Chaurasia, D. V., & Pal, S. (2017). A novel approach for breast cancer detection using data mining techniques. *International journal of innovative research in computer and communication engineering (An ISO 3297: 2007 Certified Organization) Vol*, *2*.

[6] Salama, Gouda I., M. Abdelhalim, and Magdy Abd-elghany Zeid. "Breast cancer diagnosis on three different datasets using multi-classifiers." Breast Cancer (WDBC) 32.569 (2012): 2.

[7] Joshi, J., Doshi, R., & Patel, J. (2014). Diagnosis and prognosis breast cancer using classification rules. *International Journal of Engineering Research and General Science*, *2*(6), 315-323.

[8] Xuan Tran, B., A Latkin, C., Sharafeldin, N., Nguyen, K., Thu Vu, G., W S Tam, W., Cheung, N. M., Lan Thi Nguyen, H., S H Ho, C., & C M Ho, R. (2019). Characterizing Artificial Intelligence Applications in Cancer Research: A Latent Dirichlet Allocation Analysis. ncbi.nlm.nih.gov. Diagnosis: Techniques, Trends, and Future Directions.

[9] Kumar, Y., Gupta, S., Singla, R., & Hu, Y. C. (2021). A Systematic Review of Artificial Intelligence Techniques in Cancer Prediction and Diagnosis. ncbi.nlm.nih.gov

[10] Munir Shah, S., Ahmed Khan, R., Arif, S., & Sajid, U. (2021). Artificial Intelligence For Breast Cancer Detection: Trends & Directions.

[11] Shah, Shahid Munir, et al. "Artificial intelligence for breast cancer analysis: Trends & directions." Computers in Biology and Medicine 142 (2022): 105221.

[12] Matamala, Nerea, et al. "Tumor microRNA expression profiling identifies circulating microRNAs for early breast cancer detection." Clinical chemistry 61.8 (2015): 1098-1106.

[13] Manjurul Ahsan, M. & Siddique, Z. (2021). Machine learning based disease diagnosis: A comprehensive review.

[14] Koh, D. M., Papanikolaou, N., Bick, U., Illing, R., Kahn Jr, C. E., Kalpathi-Cramer, J., ... & Prior, F. (2022). Artificial intelligence and machine learning in cancer imaging. *Communications Medicine*, *2*(1), 133.

[15] Hunter, B., Hindocha, S., & Lee, R. W. (2022). The role of artificial intelligence in early cancer diagnosis. Cancers, 14(6), 1524.

[16] H. Musa, I., O. Afolabi, L., Zamit, I., H. Musa, T., H. Musa, H., Tassang, A., Y. Akintunde, T., & Li, W. (2022). Artificial Intelligence and Machine Learning in Cancer Research: A Systematic and Thematic Analysis of the Top 100 Cited Articles Indexed in Scopus Database. ncbi.nlm.nih.gov.

[17] Zajnulina, M. (2022). Advances of artificial intelligence in classical and novel spectroscopy-based approaches for cancer diagnostics. A review. *arXiv preprint arXiv:2208.04008*.

[18] Habchi, Y., Himeur, Y., Kheddar, H., Boukabou, A., Atalla, S., Chouchane, A., Ouamane, A., & Mansoor, W. (2023). AI in Thyroid Cancer

[19] Bechelli, S. (2022). Computer-aided cancer diagnosis via machine learning and deep learning: a comparative review. arXiv preprint arXiv:2210.11943.

[20] Aamir, A., Iqbal, A., Jawed, F., Ashfaque, F., Hafsa, H., Anas, Z., Olatunde Oduoye, M., Basit, A., Ahmed, S., Abdul Rauf, S., Khan, M., & Mansoor, T. (2024). Exploring the current and prospective role of artificial intelligence in disease diagnosis. ncbi.nlm.nih.gov

[21] Lee, R. S., Gimenez, F., Hoogi, A., Miyake, K. K., Gorovoy, M., & Rubin, D. L. (2017). A curated mammography data set for use in computer-aided detection and diagnosis research. Scientific data, 4(1), 1-9.

[22] Falconi, L. G., Perez, M., Aguilar, W. G., & Conci, A. (2020). Transfer learning and fine tuning in breast mammogram abnormalities classification on CBIS-DDSM database. Adv. Sci. Technol. Eng. Syst. J, 5(2), 154-165.

[23] Murty, P. S. C., Anuradha, C., Naidu, P. A., Mandru, D., Ashok, M., Atheeswaran, A., ... & Saravanan, V. (2024). Integrative hybrid deep learning for enhanced breast cancer diagnosis: leveraging the Wisconsin Breast Cancer Database and the CBIS-DDSM dataset. Scientific Reports, 14(1), 26287.

Journal of Engineering and Technology for Industrial Applications

ITEGAM-JETIA

Manaus, v.11 n.53, p. 136-139. May/June., 2025.
DOI: https://doi.org/10.5935/jetia. v11i53.1886

ISSN ONLINE: 2447-0228

RESEARCH ARTICLE OPEN ACCESS

SUSTAINABLE SOLUTIONS FOR URBAN INFRASTRUCTURE: THE ENVIRONMENTAL AND ECONOMIC BENEFITS OF USING RECYCLED CONSTRUCTION AND DEMOLITION WASTE IN PERMEABLE PAVEMENTS

Eliomar Gotardi Pessoa

UFRJ -Universidade Federal do Rio de Janeiro- Rio de Janeiro-RJ, Brazil.

http://orcid.org/0009-0008-7713-4740

Email: eliomar.pessoa@coc.ufrj.br

ARTICLE INFO

Article History
Received: April 17, 2025
Revised: May 2, 2025
Accepted: May 15, 2025
Published: May 31, 2025

Keywords:
Permeable pavements,
Construction and demolition waste,
Recycled aggregates,
Sustainable infrastructure,
Environmental impact.

ABSTRACT

This study explores the economic and environmental implications of using recycled construction and demolition waste (CDW) in permeable pavements, presenting it as a viable solution for promoting sustainable urban development. As urbanization intensifies, both the volume of CDW and the demand for resilient, flood-mitigating infrastructure are rising. Permeable pavements made from recycled concrete, ceramic bricks, reclaimed asphalt, and industrial waste offer a dual benefit—minimizing environmental degradation and enhancing pavement performance. The findings from various studies indicate that these materials, when properly processed and chemically stabilized, can replace virgin aggregates in pavement base and subbase layers without compromising structural integrity. The paper highlights improvements in mechanical properties, stormwater infiltration, and pollutant removal when using permeable systems, even when recycled materials are incorporated. In particular, innovations such as the use of geopolymer concrete and secondary aluminum dross (SAD) fillers have shown to enhance compressive strength and moisture resistance in asphalt mixes containing RCA. Moreover, life cycle assessment (LCA) methods validate the environmental gains of these practices, from reduced carbon emissions to lower resource extraction rates. Despite these advantages, technical challenges such as pore clogging, leaching risks, and material variability persist. Addressing these through standardization, further field trials, and continued innovation will be key to expanding the adoption of CDW in permeable pavements. Ultimately, the integration of recycled materials into urban infrastructure emerges as a promising strategy to reduce construction waste, conserve natural resources, and build cities that are both sustainable and resilient.

I. INTRODUCTION

The growing urbanization has generated increasingly significant challenges for the management of construction and demolition (C&D) waste. These wastes, primarily composed of concrete, bricks, wood, metals, and asphalt, represent a significant portion of solid waste generated in urban areas. The reuse of these materials in the construction of permeable pavements offers an innovative and sustainable solution to two crucial problems: the growing amount of waste and the need for urban infrastructure that minimizes environmental impacts such as urban flooding and excessive stormwater runoff.

Permeable pavements, which allow rainwater infiltration into the soil, have increasingly been used as an ecological alternative to traditional asphalt, which contributes to the increase in urban land impermeability. When made from recycled

demolition materials, such as recycled concrete, broken bricks, and reclaimed asphalt, these pavements not only play a vital role in urban drainage but also promote the circular economy by reintroducing materials that would otherwise be discarded. This process reduces the demand for new natural resources and decreases the need for waste disposal areas.

From an economic perspective, the reuse of demolition materials in permeable pavements offers several benefits. First, the use of recycled waste can significantly reduce the production cost of pavements, as recycled materials are often cheaper than new ones. Furthermore, disposal costs for demolition waste are reduced, as many of these materials can be directly reused in construction, minimizing the need for transportation and disposal in landfills. Another relevant economic benefit is the creation of new market opportunities and jobs, especially in the recycling sector and sustainable construction industry. The demand for technologies that improve C&D waste reuse, such as the chemical stabilization of recycled materials and innovation in construction methods, can generate new investments and stimulate the local economy. Additionally, by adopting sustainable practices, cities can attract investments related to green infrastructure, promoting long-term urban resilience.

From an environmental perspective, permeable pavements made from recycled materials contribute to the mitigation of significant environmental issues. The primary advantage of these pavements is the reduction in soil impermeabilization, which allows for better rainwater absorption, reducing the risk of urban flooding and the overload of drainage systems. Furthermore, by promoting the infiltration of rainwater, these pavements help recharge groundwater tables and reduce water pollution, as the water passing through them can be filtered of impurities. The reuse of demolition materials also plays an essential role in reducing the carbon footprint of the construction industry. The production of new construction materials, such as cement and asphalt, is an energy-intensive process that generates greenhouse gas emissions. By replacing these materials with recycled options, permeable pavements help reduce the demand for natural resources and the emission of pollutants, contributing to climate change mitigation.

However, the reuse of C&D materials also presents challenges, such as variations in the quality of recycled materials and the possibility of pore clogging in permeable pavements over time. These issues can be minimized through ongoing research to improve processing and stabilization methods for the waste, ensuring that these pavements are both durable and effective.

The reuse of demolition materials in the construction of permeable pavements is a promising solution that combines economic and environmental benefits. By adopting this practice, cities not only face the challenges of C&D waste management more effectively but also promote sustainability by improving urban infrastructure and the quality of life for their inhabitants. The continuous advancement of recycling technologies and the encouragement of sustainable practices are critical to the success of this approach, which could become an essential strategy for the future of more resilient and environmentally responsible cities.

II. THEORETICAL REFERENCE

The research conducted by [1] evaluates and contrasts the environmental and economic impacts of permeable bricks and concrete pavement bricks, focusing on China's "sponge city" initiative. By employing a life cycle assessment within a "cradle-to-gate" framework, the study identifies the primary environmental and cost implications of both materials. The results show that concrete pavement bricks have a lower environmental impact and economic cost when the water-saving benefits of permeable bricks are not factored in. Notable contributors to the environmental footprint of concrete bricks are basalt powder and cement, whereas permeable bricks primarily involve cement and crushed gravel. The study underscores the numerous advantages of permeable bricks, including groundwater preservation, reduced waterlogging, and cost savings on drainage system construction and maintenance. These insights are particularly valuable for shaping policies and strategies for sustainable urban development, such as the promotion of sponge cities.

In a similar vein, [2] examines the potential of reusing recycled construction and demolition (C&D) waste, specifically mortars, concrete, and ceramic bricks, as aggregates for making interlocking blocks. This study simulates the characteristics of conventional blocks used in civil construction. Six concrete load specimens were cast using varying proportions of coarse and fine aggregates—50% and 25%, respectively—following NBR 5738 standards. The findings reveal that interlocking pavements created from C&D waste significantly enhance land permeability, benefiting sidewalks and streets. Additionally, the study emphasizes that ordinary people can produce and apply these sustainable blocks in their homes, offering a practical and environmentally friendly solution for urban construction.

The research by [3] provides a thorough review of the use of recycled concrete aggregate (RCA), a major component of C&D waste, in base and subbase layers of pavements. The paper explores the impact of crushing RCA particles, particularly in terms of resilient modulus, permanent deformation, and the California Bearing Ratio. It also compares RCA with natural aggregate (NA) and discusses the consumption and disposal policies of these materials in various countries. The study highlights the environmental and economic benefits of using RCA, emphasizing that when processed correctly, RCA can perform as well as or better than virgin aggregates for many pavement applications. However, it is advised that full-scale tests be conducted to ensure the mechanical properties and durability of RCA before its widespread use. The findings offer valuable guidance for contractors and engineers seeking sustainable alternatives in construction while reducing the environmental impact of C&D waste.

The work of [4] addresses the global challenges associated with the increasing demand for non-renewable natural resources in the construction and maintenance of hot mix asphalt pavements. Simultaneously, the growing volume of C&D waste has raised significant environmental and economic concerns. However, the study suggests that C&D waste, once converted into raw materials, holds substantial potential in the market. Through an extensive literature review, the paper explores alternative methods for incorporating C&D waste in asphalt paving projects, aiming to encourage highway authorities to create new technical guidelines and specifications for CDW recycling. The review also stresses the importance of verifying the safety, effectiveness, and feasibility of using these materials by supporting larger-scale production and suitability testing. The research envisions a new era of economic innovation in pavement engineering, driven by the sustainable application of C&D waste.

Finally, [5] focuses on the recycling and reuse of Construction and Demolition Waste (CDW), which results from debris generated during the construction, renovation, and demolition of buildings, roads, and bridges. Recycling these materials is essential for achieving sustainability, particularly from an environmental standpoint. Despite the inclusion of recycled aggregates in some technical specifications, their widespread use is

still hindered by a lack of knowledge about their technical applications. This paper consolidates the recommendations found in the "Catalogue of Road Pavements with Recycled Aggregates," supported by experimental sections. The study proposes various structural configurations for road pavements using recycled aggregates, aiming to encourage broader adoption of these sustainable materials in road construction projects.

III. METHODOLOGY

The methodology adopted for this study was based on an extensive bibliographic research in major scientific databases, aiming to collect relevant information on the use of recycled materials, such as construction and demolition waste, in permeable pavements. The research was conducted through consulting specialized journals, conference papers, theses and dissertations, as well as technical reports available in academic repositories. The sources consulted were selected based on their relevance and scientific quality, prioritizing studies that presented experimental analyses, literature reviews, or case studies applied to sustainable infrastructure projects.

In addition, databases such as Google Scholar, Scopus, Web of Science, and ScienceDirect were extensively used to ensure the breadth and quality of the gathered information. The publication selection process involved searching for specific keywords, such as "permeable pavements," "construction waste recycling," "recycled aggregates," and "environmental impact of pavements." Through reading abstracts and full articles, the main advancements in the use of recycled materials in paving were identified, along with the experimental methodologies employed in different geographical and climatic contexts.

Finally, the collected data were analyzed both qualitatively and quantitatively to identify patterns and trends in the results found. The bibliographic research allowed for an in-depth understanding of the techniques used, the challenges faced, and the solutions proposed to optimize the use of recycled materials in permeable pavements. This approach contributed to the development of a critical view on the environmental and economic impact of using these materials, providing a basis for recommendations and suggestions for future research in the field.

IV. RESULTS AND DISCUSSIONS

The research carried out by [6] delves into the advancement of permeable pavement systems (PPS), especially regarding their function in sustainable urban drainage systems (SUDS) for managing stormwater. Utilizing a bibliometric analysis and a systematic literature review of studies published between 2000 and 2021, the authors identified trends, knowledge gaps, and innovations in the field. Their findings suggest that small design modifications or the use of novel filtering layers can improve the removal of pollutants. However, factors such as low-permeability soils and inadequate pore sizes remain as primary challenges to infiltration efficiency. Additionally, the study emphasizes that combining different maintenance techniques can successfully address clogging—mostly occurring in the top 1.5–2.5 cm of the system. Although recycled aggregates improved permeability, they caused a slight reduction in compressive strength. The study provides useful directions for future innovations aimed at enhancing water quality and incorporating recycled materials into PPS designs.

In the study conducted by [7], the pressing issue of construction and demolition waste (CDW), which exceeds 10 billion tonnes annually, is addressed through the development of sustainable pavement solutions. The researchers assessed the use of CDW fines to create recycled cement, optimized with well-graded crushed stone (WGCS), for use in pavement base layers. The project included scaling up the methodology with materials from a local recycling plant and constructing pilot pavement sections to measure field performance. Results indicated that the CDW cement achieved substantial heat accumulation and compressive strength, while pavement sections using this cement exhibited unconfined compressive strength and resilient modulus values comparable to conventional alternatives. Deflections reduced over time due to pozzolanic reactions, proving the feasibility of CDW in creating sustainable, structurally sound pavements.

Focusing on sustainable construction, [8] explored the viability of reusing CDW materials—such as crushed concrete, asphalt mix, and ceramic waste aggregates—in the construction of pavement base layers. The research aimed to minimize landfill use and reduce dependence on natural aggregates. A field investigation tested pavement sections under actual traffic loads, confirming the structural adequacy of the recycled materials. The results demonstrated satisfactory load-bearing performance, reinforcing the potential for CDW to serve as a sustainable and technically sound alternative in road construction.

The investigation by [9] tackles the environmental consequences of urban development by proposing a novel approach combining pervious surfaces, recycled concrete aggregates (RCA), and industrial waste to produce pervious geopolymer concrete. With a target porosity of 15%, the study assessed the performance of pervious geopolymer recycled aggregate concrete (PGRAC) using two binder blends—slag:fly ash in 1:0 and 1:1 ratios—and varying RCA contents (0% and 100%). The concrete made with natural aggregates and a 1:0 binder blend delivered significantly higher compressive strength compared to its 1:1 counterpart. Although permeability remained relatively unchanged with binder variation, full RCA replacement reduced strength, while the 1:1 mix offered slightly better permeability. These findings support the potential use of PGRAC in sustainable pavement applications.

The study presented by [10] contributes to the ongoing efforts to mitigate environmental harm caused by the accumulation of industrial waste. By recycling materials like concrete, brick, and breeze blocks from demolished structures, the research explores their potential application in the base layers of flexible pavements. The mechanical behavior of these recycled materials was evaluated through experimental methods, revealing promising results. The use of such materials helps preserve natural resources, reduce transportation-related emissions, and lower energy consumption. This approach not only optimizes pavement design but also offers a cost-effective solution that avoids the use of expensive surface layers like bituminous concrete.

In research by [11], attention is drawn to the challenge of improving the performance of asphalt mixtures that incorporate recycled concrete aggregates (RCA). Given the limitations of RCA in traditional asphalt applications, this study investigates the use of secondary aluminum dross (SAD) as an alternative filler. SAD was substituted for limestone dust in varying proportions (10%, 20%, and 30%), and its effects on mixture properties were evaluated using the Marshall method, as well as tensile and compressive strength tests. Results showed that SAD enhanced mechanical performance, with 20% being identified as the most effective dosage. When applied to mixtures containing 25% RCA, this dosage significantly improved both the tensile strength ratio (TSR)

and the index of retained strength (IRS). The findings underline the potential of industrial by-products to strengthen asphalt pavements while contributing to sustainable waste management.

Lastly, the work developed by [12] highlights the importance of integrating C&D waste into sustainable infrastructure practices, particularly in road construction. It addresses both the environmental burden caused by the excessive generation of waste and the depletion of natural aggregate resources by the transportation sector. The study promotes the use of recycled C&D materials in pavement layers, which not only reduces landfill volumes but also minimizes resource extraction. A life cycle assessment (LCA) was employed to evaluate the environmental performance of recycled aggregate use, considering risks related to chemical composition and leaching. The research advocates for broader adoption of C&D waste in roadworks, offering a viable pathway toward zero-waste construction and eco-efficient infrastructure development.

V. CONCLUSIONS

The reuse of construction and demolition waste (CDW) in permeable pavements presents a significant opportunity for integrating sustainability into urban infrastructure. This practice effectively addresses two of the most pressing challenges in civil construction: the growing volume of waste materials and the environmental impacts of impermeable surfaces in cities. By substituting traditional materials with recycled alternatives such as concrete, brick, and asphalt, permeable pavements contribute to improved urban drainage, reduced flood risks, and the circular use of resources that would otherwise burden landfills.

Moreover, the studies reviewed indicate that permeable pavements made with recycled materials not only meet technical performance standards but also offer tangible environmental and economic advantages. Benefits include enhanced water infiltration and quality, reduced greenhouse gas emissions from the manufacturing of virgin materials, and significant cost savings in waste disposal and raw material extraction. The inclusion of industrial by-products, such as secondary aluminum dross, further amplifies these benefits, offering a path toward more efficient and eco-friendly pavement technologies.

However, challenges remain. Variability in the quality of recycled aggregates, risks of pore clogging, and slight reductions in compressive strength demand further research and innovation. Standardization, long-term performance evaluations, and continued investment in recycling technologies are essential to fully realize the potential of CDW in permeable pavements. With proper policy support and technical refinement, this approach holds promise for transforming urban infrastructure into a more resilient, cost-effective, and environmentally responsible system.

VI. AUTHOR'S CONTRIBUTION

Conceptualization: Eliomar Gotardi Pessoa.
Methodology: Eliomar Gotardi Pessoa.
Investigation: Eliomar Gotardi Pessoa.
Discussion of results: Eliomar Gotardi Pessoa.
Writing – Original Draft: Eliomar Gotardi Pessoa.
Writing – Review and Editing: Eliomar Gotardi Pessoa.
Resources: Eliomar Gotardi Pessoa.
Supervision: Eliomar Gotardi Pessoa.
Approval of the final text: Eliomar Gotardi Pessoa.

VII. REFERENCES

[1] Yuan, Xueliang, et al. "Environmental and economic impacts assessment of concrete pavement brick and permeable brick production process-a case study in China." *Journal of Cleaner Production* 171 (2018): 198-208.

[2] dos Santos Teixeira, Willians, et al. "Use of RCDs in the Making of Interlocked Pavements With Waste Collected at the Federal Institute of Amazonas – CMC". *International Journal for Innovation Education and Research*, vol. 7, no. 10, Oct. 2019, pp. 90-96, https://doi.org/10.31686/ijier.vol7.iss10.1749.

[3] Aytekin, Burcu, and Ali Mardani-Aghabaglou. "Sustainable materials: A review of recycled concrete aggregate utilization as pavement material." *Transportation research record* 2676.3 (2022): 468-491.

[4] Gedik, Abdulgazi. "A review on the evaluation of the potential utilization of construction and demolition waste in hot mix asphalt pavements." *Resources, Conservation and Recycling* 161 (2020): 104956.

[5] Barbudo, Auxi, et al. "Catalogue of pavements with recycled aggregates from construction and demolition waste." *Proceedings*. Vol. 60. No. 1. MDPI, 2018.

[6] Singer, Mohamed N., et al. "Permeable pavement systems for effective management of stormwater quantity and quality: A bibliometric analysis and highlights of recent advancements." *Sustainability* 14.20 (2022): 13061.

[7] Pereira, Valdir M., et al. "Thermoactivated cement from construction and demolition waste for pavement base stabilization: A case study in Brazil." *Waste Management & Research* 43.1 (2025): 121-132.

[8] Herrador, Rosario, et al. "Use of recycled construction and demolition waste aggregate for road course surfacing." *Journal of transportation engineering* 138.2 (2012): 182-190.

[9] Anwar, Faiz Habib, et al. "MECHANICAL AND HYDRAULIC PERFORMANCE OF PERVIOUS RECYCLED AGGREGATE GEOPOLYMER CONCRETE." *Proceedings of International Structural Engineering and Construction* 11.2 (2024).

[10] Hocine, Hadidane, Djebbari Zina, and Tioua Tahar. "Mechanical behavior of recycled materials used in the base layers of bituminous pavements." *Studies in Engineering and Exact Sciences* 5.2 (2024): e11892-e11892.

[11] Ugla, Sarah Khalid, and Mohammed Qadir Ismael. "Evaluating the moisture susceptibility of asphalt mixtures containing RCA and modified by waste alumina." *Civil Engineering Journal* 9 (2023): 250-262.

[12] Khan, Zainul Abedin, Umashankar Balunaini, and Susanga Costa. "Environmental feasibility and implications in using recycled construction and demolition waste aggregates in road construction based on leaching and life cycle assessment–A state-of-the-art review." *Cleaner Materials* (2024): 100239.

Journal of Engineering and Technology for Industrial Applications

ITEGAM-JETIA

Manaus, v.11 n.53, p. 140-145. May/June., 2025.
DOI: https://doi.org/10.5935/jetia. v11i53.1887

ISSN ONLINE: 2447-0228

RESEARCH ARTICLE OPEN ACCESS

ANALYSIS OF THE PERFORMANCE OF HELICAL PILES UNDER VARIOUS LOAD AND GEOMETRY CONDITIONS

Eliomar Gotardi Pessoa[1]

[1] UFRJ- Universidade Federal do Rio de Janeiro-RJ, Brazil.

[1]http://orcid.org/0009-0008-7713-4740

Email: eliomar.pessoa@coc.ufrj.br

ARTICLE INFO

Article History
Received: April 17, 2025
Revised: May 2, 2025
Accepted: May 15, 2025
Published: May 31, 2025

Keywords:
Helical piles,
Load capacity,
Helical plate configuration,
Pull-out resistance,
Combined loads

ABSTRACT

The study by [7] analyzed the load capacity of moderately sized helical piles, considering configurations such as shaft diameter, plate diameter, and penetration depth. The results showed that increasing the shaft diameter and modifying the helical plates significantly improved load capacity. The configuration of the plates had a greater impact on performance than the shaft diameter. Other studies complemented these findings, such as [8], which emphasized the importance of plate position for pull-out resistance. Study [9] highlighted the impact of helix pitch on lateral load capacity, while [10] examined the spacing between the helices and its effect on load distribution. Helix deflection, as shown by [11], was also a critical factor in pile performance. Additionally, studies on pile groups [13] and pressure grouted helical piles [14] provided valuable insights for optimizing the design of these foundations. Research by [15] on combined loads revealed a positive correlation between helix diameter and load capacity. Overall, the studies demonstrated that geometric factors and soil characteristics are essential for optimizing the performance of helical piles, especially in applications in challenging environments like offshore wind platforms.

I. INTRODUCTION

The load-bearing capacity of helical piles is strongly influenced by various factors, with installation depth and helix diameter being two of the most significant parameters. The depth determines the reach of the piles into the soil, directly affecting the interaction between the soil and the pile. The helix diameter, on the other hand, is related to the area of contact between the pile and the soil, which impacts the load transfer capacity and pullout resistance.

The depth of the helical pile influences both compressive and tensile resistance. The deeper the pile, the greater the resistance provided by the soil in deeper layers, which can increase the load-bearing capacity. However, the depth must also be optimized, as very deep piles can result in higher installation costs and logistical complications. Choosing the ideal depth depends on the soil type, layer distribution, and load conditions, making it essential to consider these variables in foundation design to maximize pile efficiency.

On the other hand, the helix diameter has a direct impact on the area of contact between the pile and the soil. Piles with larger helices generate a greater area of resistance to both pullout and compression, resulting in higher load-bearing capacity, especially in looser soils or conditions of high liquefaction potential.

However, increasing the helix diameter can also lead to higher costs and challenges during installation, such as requiring more torque for drilling. Therefore, balancing the diameter with other pile parameters is crucial to ensure good performance without compromising the economic feasibility of the project.

Thus, the interaction between the depth and the helix diameter is crucial for determining the load-bearing capacity of helical piles. Adjusting these parameters, taking into account local geotechnical conditions and project requirements, allows for the optimization of foundation performance, ensuring greater stability and durability.

II. THEORETICAL REFERENCE

Helical piles have gained recognition as an advanced and versatile foundation solution in both onshore and offshore engineering applications, providing numerous advantages over traditional pile systems. They are particularly appreciated for their ease of installation, minimal environmental impact, and impressive load-bearing capacity. One of the most critical aspects affecting the performance of helical piles is their bearing capacity, which is significantly influenced by various design parameters. Among these, the depth of installation and the diameter of the helical plates are considered key factors that govern the efficiency of these foundations.

According to [1], helical piles are defined as a type of pile foundation equipped with one or more helices that are attached to the shaft at specific intervals. These helices serve to enhance the load distribution and resistance of the pile by engaging a larger volume of soil compared to conventional piles. The geometry of the helical plates, including their diameter and spacing, plays a direct role in influencing the load transfer mechanism, which ultimately affects the overall bearing capacity of the pile. The arrangement of the helix diameters is particularly important; experimental studies by [1] showed that a progressive increase in helix diameter, such as 6 cm, 8 cm, and 10 cm from top to bottom, leads to a more effective load transfer and improved bearing capacity compared to a decreasing diameter configuration. This progressive design allows for a more optimal distribution of end-bearing and shaft friction contributions, resulting in superior overall performance in comparison to other configurations.

Further studies have examined the influence of the number of helices and the spacing between them on the bearing capacity and failure mechanisms of helical piles. In a numerical study conducted by [2], the effects of helix diameter and spacing were investigated, revealing that both parameters play a critical role in the transition between different failure modes, such as cylindrical shear to individual bearing failure. When the spacing-to-diameter ratio approached two, the pile transitioned to an individual bearing failure mechanism, which significantly increased the efficiency of the pile. This transition was shown to enhance the load-bearing capacity, particularly in piles with a larger number of helices and greater spacing. The study further emphasized that conventional methods of calculating bearing capacity often fail to account for these geometric parameters, suggesting the need for advanced modeling techniques to more accurately predict the behavior of helical piles. These findings underscore the importance of considering the geometric configuration of helical plates when designing pile foundations.

Depth is another critical factor that plays an essential role in optimizing the performance of helical piles. As the pile is embedded deeper into the soil, it engages denser and more stable soil strata, thereby enhancing both compressive and tensile resistance. Studies by [3] have highlighted the importance of increasing the embedded depth of helical piles, especially in loose sandy soils, where deeper embedment leads to improved interaction between the helix and surrounding soil. This deeper engagement helps distribute the load more efficiently, contributing to enhanced pile stability and reduced settlement. Numerical simulations have corroborated these findings, revealing that deeper installation depths result in lower displacement and improved load-carrying capabilities, particularly when combined with optimal helix spacing and diameter configurations. In these cases, the pile's ability to resist both vertical and lateral forces is enhanced, making them more reliable and effective for use in a variety of soil conditions.

Additionally, research by [4] examined the impact of the number of helices on the bearing capacity of helical piles. This study involved static loading tests on different types of helical piles, including single shaft piles, piles with identical diameter helices, and piles with helices of varying diameters. The study concluded that adding more helices significantly increased the bearing capacity, with helical piles exhibiting a 252% to 369% increase in capacity compared to the single shaft. Furthermore, the research compared the performance of helical piles with the same diameter helices to those with varying diameters, highlighting how the configuration of helices can further influence pile performance. These findings are significant for understanding how to optimize the number and arrangement of helices in order to maximize the load-bearing capabilities of helical piles.

The performance of helical piles in partially saturated soils has been a subject of limited research compared to their performance in dry or fully saturated conditions. The study by [5] focused on this gap by testing small-scale models of steel piles with single, double, and triple helices embedded in cohesionless soils under varying soil saturation conditions. The results indicated that helical piles in partially saturated soils exhibited an increased bearing capacity, ranging from 1.5 to 1.8 times greater than that of piles in fully saturated soils. Additionally, the study demonstrated that the addition of helices significantly improved bearing capacity, with single, double, and triple helix configurations showing improvements of 33.3%, 45.0%, and 108.3%, respectively, over the shaft pile only. This research underscores the potential advantages of using helical piles in soils with intermediate levels of saturation, offering insights into their performance in real-world conditions that may not always be fully saturated or dry.

Lastly, a study conducted by [6] explored the behavior of helical piles in Iraq using the finite element method. This study used Plaxis 3D software to model the geometry of helical piles and performed parametric analyses to examine the effects of various factors such as the number of helices, spacing between helices, helix diameter, and helix configuration. The results showed that increasing the number of helices significantly enhanced the bearing capacity, with the maximum pile capacity for a three-helix configuration increasing by 115.4% compared to the case without helices. The study also found that increasing the spacing between the helices led to a 130.7% increase in pile capacity when the spacing was increased from 0.5D to 3.5D. Furthermore, the study highlighted that displacement values decreased with increasing spacing between the helices, which suggests that optimal helix spacing can improve pile performance by reducing settlement.

Overall, the literature consistently highlights the importance of geometric factors such as helix diameter, pile depth, and helix configuration in determining the bearing capacity of helical piles. These factors, when optimized according to the specific soil conditions and load requirements, contribute significantly to the stability and efficiency of helical pile foundations. The studies also emphasize the need for advanced modeling techniques and experimental validation to accurately predict the behavior of helical piles, ensuring their reliable performance in a variety of engineering applications.

III. MATERIALS AND METHODS

.The methodology adopted in this study was primarily based on a bibliographic research approach, aimed at gathering and analyzing the main studies and scientific articles that address the behavior and performance of helical piles. The research was conducted across major scientific databases such as Google

Scholar, Scopus, Science Direct, and Web of Science, focusing on recent and relevant publications on the subject. The selection of articles was made with great care, considering the quality of the publications, the reputation of the journals, and the relevance of the studies regarding the load-bearing capacity and performance of helical piles under various soil conditions. Additionally, research analyzing different design parameters, such as helix diameter, embedment depth, and the number of helices, was included.

This study is characterized as exploratory and qualitative research, focusing on the analysis of secondary data from previously conducted studies. The exploratory research allows for an in-depth examination of various aspects of the behavior of helical piles, including variables such as helix geometry and installation conditions, providing a broad view of the different analysis methodologies and experimental tests applied to the subject. Furthermore, the qualitative nature of the research enabled the identification of key trends and gaps in the literature on the performance of helical piles, highlighting the importance of specific parameters, such as helix configuration and installation depth, for the success of these foundations in various soil types.

Finally, the bibliographic research conducted was not limited to a simple data collection but involved a critical and comparative analysis of the methodologies used in the selected studies. Not only were the results obtained evaluated, but also the experimental and numerical approaches employed to simulate the loading conditions and behavior of helical piles in different scenarios. This analysis allowed for the identification of best practices and the suggestion of recommendations for the application of helical piles in foundation projects, considering the particularities of sandy, cohesive, and partially saturated soils, among others.

IV. RESULTS AND DISCUSSIONS

The study conducted by [7] aimed to estimate the load capacity of moderately sized helical piles, considering various configurations such as shaft diameter, plate configuration, and penetration depth. Six different types of helical piles were constructed with shaft diameters ranging from 73 mm to 114 mm, support plate diameters varying from 400 mm to 250 mm, and different numbers of helical plates (one or three). Field loading tests were carried out to assess the impact of these configurations on the load capacity of the helical piles. The results indicated that both the increase in shaft diameter and changes in the number or diameter of the helical plates significantly improved the load capacity of the pile. Notably, the configuration of the helical plates was found to be more critical than the shaft diameter in enhancing the pile's load capacity.

In another study, [8] analyzed the load capacity and resistance to pull-out of helical piles. The research used both model tests and numerical modeling to investigate the impact of factors such as the number, size, and position of the helices on pile performance. The results showed that increasing the number and diameter of the helices improved both the load capacity and pull-out resistance of the pile. Furthermore, when the helix was installed near the base of the pile, performance was significantly improved. The study also included an economic analysis, highlighting the importance of considering the installation position of the helix to optimize performance and cost-effectiveness of the helical piles. Based on these findings, the research suggested that the helical pile design could be substantially enhanced by adjusting these parameters.

The research conducted by [9] focused on the influence of thread pitch and helix diameter on the lateral load capacity of a single-helix helical pile, with an emphasis on installation effects. This study, which included laboratory tests, revealed that the helix diameter had a negligible effect on the lateral load capacity of the pile. However, the thread pitch significantly influenced pile performance due to the increased soil disturbance around the pile. The results from the single-helix pile were compared with those of steel tube piles and other foundation methods, offering valuable insights into the behavior of helical piles for applications such as offshore wind turbine foundations. The study reinforced the importance of considering thread pitch when designing helical piles for optimal lateral load performance.

In another study, [10] investigated the effects of helix spacing on the behavior of helical piles through compressive axial load tests on instrumented piles with strain gauges. The test piles, which had two helices with variable spacing between them, were installed in a homogeneous clay layer with an average undrained shear strength of 65 kPa. Failure mechanisms of the piles were determined by comparing the measured load distributions with those predicted by cylindrical shear and individual load models. The results indicated that for piles with a helix spacing-to-diameter ratio of 1.5 or greater, the individual load model dominated the pile behavior. The study also evaluated the load capacity factor of the helices and the shaft adhesion factor, comparing measured resistances with theoretical estimates, and concluded that the recalculated load capacity and adhesion factors were lower than those typically used in helical pile design. Additionally, the research analyzed the impact of the soil setup on pile behavior by comparing load and settlement responses of piles tested immediately after installation with those tested days later.

Another relevant study by [11] investigated the effect of helix deflection on the load-settlement behavior and ultimate load capacity of helical piles. Recognizing that these piles have greater ultimate load capacity due to the presence of larger helices relative to the central shaft, the study aimed to understand the limitations imposed by helix deformation under high load conditions. To this end, load tests were performed on models with different helix-to-shaft diameter ratios and varying helix thicknesses to assess the behavior of the piles with and without significant deformations. The tests were conducted on dense, dry Toyoura sand. The results showed that helix deflection began to negatively affect the load-settlement response once it exceeded a critical value. It was further observed that the ratio of critical deflection to projection length decreased as the helix-to-shaft diameter ratio increased, and this relationship was presented in the study. Furthermore, Roark's formula for flat circular plates under uniform load on a very small area with fixed edges showed good agreement with the measured helix deflection, enabling the development of a modified equation to estimate the optimal helix thickness based on the critical deflection.

The study conducted by [12] investigated the geotechnical behavior of helical piles through experiments using the frustum confining vessel (FCV) method. This device was chosen due to its special geometry, which allows for a linear distribution of vertical and lateral stresses along its height, effectively simulating field conditions. The research focused on small-scale helical piles made of 4 mm thick steel plates, with a shaft diameter of 32 mm and helices ranging from 64 to 89 mm in diameter. The results indicated that the performance of helical piles strongly depends on geometric characteristics such as the spacing ratio between helices (S/D) and helix diameter. It was observed that failure could occur either near the individual helices or along a cylindrical shear surface, directly

affecting the load capacity. Additionally, the helical piles demonstrated the ability to support axial uplift loads comparable to conventional steel piles with the same helix diameter, and their compressive load capacity was sufficient to classify them as medium-capacity piles.

In the study conducted by [13], the results of a field load testing program were presented to investigate the group effects on the pull-out capacity of deep single-helix helical piles installed in sand. Due to their high pull-out capacity and quiet installation process, helical piles have become a viable alternative to conventional deep foundations, especially in offshore applications for renewable energy structures. Considering new applications in marine environments, the use of helical pile groups to resist structural loads is being evaluated. While it is known that group interaction effects occur in this type of foundation, there is still a lack of field data on performance in sand under pull-out loading. The study involved the installation and load testing of round-shaft piles with a 152 mm diameter, tested individually and in groups, embedded at depths equivalent to 12 and 18 times the helix diameter. Variables such as pile spacing, group configuration (number of piles), and soil strength (determined by CPT tests) were analyzed. The results showed group efficiencies ranging from 0.6 to 1.0 for horizontal spacings of 2 to 3 times the helix diameter, in sands with friction angles between 39° and 44°. The obtained data are also valuable for calibrating and validating numerical models to further analyze group interactions in helical pile systems.

The study by [14] investigated the performance of pressure grouted helical piles (PGHPs), which are reinforced piles installed using the simultaneous drilling and grouting technique. This method promotes the formation of a soil-cement column around the pile, whose geometry is influenced by various installation parameters, such as the number and size of the helices and the drilling speed. To analyze the axial behavior of these piles and the load transfer mechanism, small-scale model tests were conducted in clay. The results showed that the final compressive load capacity of PGHPs was between 260% and 293% greater than that of ungrouted helical piles. Additionally, the load capacity increased proportionally with the number and size of the helices but decreased with an increase in drilling speed. The adhesion between the soil-cement column and the surrounding clay varied between 0.8 and 1.2, and the diameter of the cement column was approximately 1.26 to 1.35 times the size of the helix. These results demonstrate the effectiveness of the simultaneous drilling and grouting technique in improving the axial performance of helical piles compared to traditional ungrouted piles.

The study conducted by [15] investigated the performance of hollow-shaft and single-helix helical piles under combined loading, a common condition in offshore structures due to the simultaneous action of wind, waves, currents, and the structure's own weight. Although these piles are widely used in onshore foundations due to their quick installation and high load capacity, their behavior under combined loading is not well understood. To address this gap, the study used finite element method (FEM) analysis in 561 different cases, considering various ratios of helix to shaft diameter, as well as helix positions. The results showed a positive linear correlation between the helix-to-shaft diameter ratio and load capacity, while the influence of helix position exhibited a more complex and nonlinear behavior. Based on these analyses, a predictive formula was developed to estimate the load capacity of helical piles under combined loading, significantly contributing to their application as an alternative to monopile foundations in offshore wind turbines.

Finally, the study by [16] investigated the uplift capacity of helical piles, focusing on the effect of helix size. Helical piles, widely used for low-load applications, consist of helical plates attached to a central shaft, with both the shaft and helix diameters varying in size. When installed in appropriate soil layers, helical piles can resist both compressive and tensile loads. The total capacity of the pile is defined as the sum of the capacities of each individual helical plate. This study specifically explored the influence of helix size on uplift capacity, performing uplift load tests on two types of helical piles — with uniform and variable-sized plates — installed in clayey soil. The helix diameters used in the tests were 15 cm, 20 cm, and 25 cm, with a spacing ratio (S/D) of less than 3 for the larger helix diameters. The results revealed that variations in helix size significantly influenced the uplift capacity, with capacity increasing by up to 50% as the helix diameter increased. This study provides valuable insights into the effect of helix size on the uplift capacity of helical piles.

The results presented by the studies discussed above provide a comprehensive view of the performance of helical piles under various loading conditions and geometric variables. While each study focused on different aspects of helical piles, they all converge on the idea that the geometric configuration and soil characteristics have a significant impact on the load-bearing capacity and behavior of the piles.

The study by [7] emphasizes the importance of the configuration of the helical plates, showing that both an increase in the shaft diameter and variations in the number or diameter of the helical plates result in significant improvements in load capacity. However, a crucial finding was the observation that the configuration of the helical plates is more critical to the pile's performance than the shaft diameter, an important insight for the design of helical piles in terms of optimizing load capacity.

In a complementary study, [8] not only investigated the load capacity but also the pull-out resistance of helical piles, analyzing how the number and size of the helices influence these properties. The study also highlighted the importance of the helix position to improve pile performance, emphasizing that installing the helices closer to the base resulted in significant improvements in pull-out resistance and load capacity. This suggests that optimizing the design of piles should consider the position of the helices, in addition to their number and size, for optimal performance under different soil conditions.

The research by [9], in turn, revealed that the pitch of the screw has a more significant impact on the lateral load capacity of the pile than the helix diameter. This study is particularly relevant for applications in terrains with high lateral loads, such as offshore wind farm foundations, where helical piles are frequently used. The discovery that increasing the pitch results in greater soil disturbance and consequently better performance under lateral load provides valuable guidance for the design of these foundations.

Another relevant study by [10] investigated the effect of helix spacing on the behavior of helical piles. The results indicated that the pile behavior can be more accurately modeled when the ratio of helix spacing to helix diameter is greater than 1.5. This finding suggests that optimizing the spacing between helices can directly influence load distribution and performance efficiency, especially in homogeneous soil conditions like clay.

Studies by [11] and [12] analyzed the deflection of the helices and the impact of geometric characteristics on the load capacity of helical piles. Study [11] concluded that excessive deflection of the helices can compromise pile performance, with important implications for the design of the helices and the sizing of their thicknesses. On the other hand, [12] investigated the

geometric characteristics of small-scale piles, revealing that failure in helical piles can occur both near individual helices and along a cylindrical shear surface, reinforcing the importance of helix distribution and size.

Regarding the performance of helical piles in groups, study [13] provided valuable insights into the group effects on the performance of helical piles installed in sand. The research indicated that group efficiencies vary with pile spacing and soil resistance, with direct implications for the design of foundations in high-traction environments, such as offshore structures.

Additionally, the study by [14] on pressure grouted helical piles (PGHPs) highlighted the impact of the grouting technique on pile load capacity, showing that combining larger helices with grouting can result in a substantial increase in load capacity. This offers an interesting alternative to enhance the performance of helical piles in soils with low resistance.

Finally, the study by [15] addressed combined loading, an important condition for offshore structures, showing that the ratio of helix diameter to shaft diameter has a positive correlation with load capacity, while the position of the helices has a more complex effect. These findings are essential for the design of helical piles for applications in structures subjected to multiple types of simultaneous load.

In summary, the studies discussed demonstrate the importance of a detailed analysis of geometric variables, soil characteristics, and group effects on helical piles, highlighting that pile design should be carefully adjusted to optimize performance under different loading and soil conditions. The combination of different optimization strategies, such as adjusting the number and size of the helices, modifying the screw pitch, and considering the spacing between the helices, is essential to ensure the success of helical piles in modern foundation projects, including those in challenging environments such as offshore wind farms and other submerged structures.

V. CONCLUSIONS

The research on the performance of helical piles under various load conditions and geometric characteristics reveals that factors such as shaft diameter, helix configuration, and penetration depth play crucial roles in the load capacity of these piles. The studies showed that both increasing the shaft diameter and modifying the number and size of the helical plates significantly improved load capacity. However, the configuration of the helical plates was found to be more important than the shaft diameter in optimizing the pile's load-bearing capacity.

Additionally, the results indicated that positioning the helical plates near the base of the pile improves pull-out resistance, which is an important consideration for designs in more challenging soils. The research also highlighted the importance of the spacing distribution between the helical plates and the shaft thickness, as factors that can negatively impact pile performance if not properly dimensioned.

In specific conditions, such as soils subject to high lateral loads, modifying the helix pitch was crucial to improving lateral load capacity. This finding is particularly relevant for the use of helical piles in offshore wind turbine foundations, where lateral load conditions dominate.

Studies on helix deflection indicated that excessive deformations could compromise pile efficiency, emphasizing the need to consider critical deflection limits during design. The combination of different optimization strategies, such as adjusting the number and size of the helical plates, and a detailed analysis of group interactions, ensures more efficient and safer performance.

In summary, these studies provide valuable insights into improving the design of helical piles, being essential for applications in challenging environments, such as offshore platforms and submerged structures. Ongoing research on the behavior of helical piles will allow for the adaptation of foundations to different soil types and load conditions.

VI. AUTHOR'S CONTRIBUTION

Conceptualization: Eliomar Gotardi Pessoa.
Methodology: Eliomar Gotardi Pessoa.
Investigation: Eliomar Gotardi Pessoa.
Discussion of results: Eliomar Gotardi Pessoa.
Writing – Original Draft: Eliomar Gotardi Pessoa.
Writing – Review and Editing: Eliomar Gotardi Pessoa.
Resources: Eliomar Gotardi Pessoa.
Supervision: Eliomar Gotardi Pessoa.
Approval of the final text: Eliomar Gotardi Pessoa.

VII. REFERENCES

[1] Amalia, G., M. M. Iqbal, and R. Dewi. "The influence of helix diameter configuration on helical pile bearing capacity." IOP Conference Series: Earth and Environmental Science. Vol. 1173. No. 1. IOP Publishing, 2023. https://doi.org/10.1088/1755-1315/1173/1/012020.

[2] Pratama, Ignatius Tommy, Anastasia Sri Lestari, and Ivan Oktavianus. "Numerical Study on the Effects of Helix Diameter and Spacing on the Helical Pile Axial Bearing Capacity in Cohesionless Soils." Journal of the Civil Engineering Forum, p. 173-182.

[3] Emirler, Buse. "Physical and finite element models for determining the capacity and failure mechanism of helical piles placed in weak soil." *Applied Sciences* 14.6 (2024): 2389.

[4] Kurniawan, Yofy, M. Iqbal, and Ratna Dewi. "Effect of helical geometry on the axial compressive capacity." *International Journal of Innovative Science and Research Technology* 5.6 (2020): 717-723.

[5] Mahmood, Mahmood R., Nahla M. Salim, and Ammar A. Al-Gezzy. "Effect of soil saturation conditions and helical configurations on compression capacity of screw piles." *IOP Conference Series: Materials Science and Engineering*. Vol. 1058. No. 1. IOP Publishing, 2021.

[6] Ali, Ahmed S., Nahla M. Salim, and Husam H. Baqir. "Numerical Modelling of Axially Loaded Helical Piles: Compressive Resistance." *E3S Web of Conferences*. Vol. 318. EDP Sciences, 2021.

[7] Lee, Jongwon, et al. "Effect of configuration of shaft and helix plate on bearing capacity of moderate-size helical pile: I. Test-bed construction and field loading test." *Journal of the Korean Geosynthetics Society* 13.2 (2014): 31-39.

[8] Jun, Sanghyun, Hyungho Lee, and Byungsoo Park. "Experimental and numerical study for analyzing applicability of helical piles." *Journal of the Korean Society of Hazard Mitigation* 20.3 (2020): 215-223.

[9] Ding, Hongyan, et al. "Study on the lateral bearing capacity of single-helix pile for offshore wind power." *International Conference on Offshore Mechanics and Arctic Engineering*. Vol. 51302. American Society of Mechanical Engineers, 2018.

[10] Lanyi-Bennett, Stephen A., and Lijun Deng. "Effects of inter-helix spacing and short-term soil setup on the behaviour of axially loaded helical piles in cohesive soil." *Soils and Foundations* 59.2 (2019): 337-350.

[11] Malik, Adnan Anwar, et al. "Effect of helix bending deflection on load settlement behaviour of screw pile." *Acta Geotechnica* 14 (2019): 1527-1543.

[12] Khazaei, Javad, and Abolfazl Eslami. "Geotechnical behavior of helical piles via physical modeling by Frustum Confining Vessel (FCV)." *International Journal of Geography and Geology* 5.9 (2016): 167-181.

[13] Bradshaw, Aaron S., Lindsay Cullen, and Zachary Miller. "Field study of group effects on the pullout capacity of “deep” helical piles in sand." *Canadian Geotechnical Journal* 59.4 (2022): 538-545.

[14] Zhuang, Xiaoxuan, et al. "Analysis of the installation effect on the axial performance of pressure-grouted helical piles in clay by small-scale model tests." *Buildings* 12.7 (2022): 992.

[15] Wang, Le, et al. "The Study of the Failure Envelopes of Hollow Shaft Single-Plate Helical Piles in Clay." *Journal of Marine Science and Engineering* 11.7 (2023): 1323.

[16] Mulyanda, Dhevi, Maulid M. Iqbal, and Ratna Dewi. "The effect of helical size on uplift pile capacity." *Int. J. Sci. Technol. Res* 9.2 (2020): 4140-4145.

Journal of Engineering and Technology for Industrial Applications

ISSN ONLINE: 2447-0228

ITEGAM-JETIA

Manaus, v.11 n.53, p. 141-144. May/June., 2025.
DOI: https://doi.org/10.5935/jetia. v11i53.1519

RESEARCH ARTICLE OPEN ACCESS

DEVELOPMENT OF HYBRID EXEMPLAR BASED DLSRGAN MODEL FOR RESTORATION OF THE DISTORTED SIGNALS

Tammineni Shanmukha Prasanthi[1], Swaraiya Madhuri Rayavarapu[2], Gottapu Sasibhushana Rao[3] and Rajkumar Goswami[4]

[1,2] Department of Electronics and Communication Engineering, Research Scholar, Andhra University college of engineering, Visakhapatnam, India.
[3]Department of Electronics and Communication Engineering, Professor, Andhra University college of engineering, Visakhapatnam, India.
[4]Gayatri vidya parishad college of engineering for women, Visakhapatnam, India

[1]http://orcid.org/0009-0000-5352-2265, [2]http://orcid.org/0000-0001-6346-8274
[3]http://orcid.org/0000-0001-6346-8274, [4]http://orcid.org/0000-0002-0651-6783

E-mail: prashanthitammineni.rs@andhrauniversity.edu.in, madhutirayavarapu.rs@andhrauniversity.edu.in
sasigps@gmail.com, rajkumargoswami@gmail.com

ARTICLE INFO

Article History
Received: January 1, 2025
Revised: February 20, 2025
Accepted: June 15, 2025
Published: June 30, 2025

Keywords:
Signal,
Inpainting,
SRGAN,
PSNR,
MSE,
SSIM.

ABSTRACT

This research focuses on the Development of a Hybrid Exemplar-based Deep Learning SRGAN Model for the restoration of distorted signals. Traditional signal restoration techniques often struggle with noise and distortion, leading to loss of critical information. The proposed model integrates Super-Resolution Generative Adversarial Networks (SRGAN) with exemplar-based method to enhance the quality and fidelity of degraded signals. By leveraging the adversarial training framework, the generator learns to produce high-resolution outputs while the discriminator ensures perceptual realism. Initial results indicate significant improvements in signal clarity and detail recovery, outperforming conventional methods in metrics such as Peak Signal-to-Noise Ratio (PSNR), Structural Similarity Index Measure (SSIM) and Mean Squared Error (MSE). This hybrid approach not only restores signals more effectively but also preserves essential features, making it a valuable tool for applications in telecommunications and audio processing. Future work will focus on optimizing the model for real-time applications and expanding its use across various types of signal degradation scenarios.

I. INTRODUCTION

Signal inpainting is an essential modern technique used for restoring and enhancing visual data. It plays a critical role in data recovery, maintaining the integrity of information affected by loss or corruption. By filling in missing areas, inpainting [1] improves the visual quality of images, making them more coherent and aesthetically pleasing. This technique is particularly valuable in areas such as signal processing and digital content creation. In addition to visual enhancement, inpainting facilitates the recovery of lost or obscured information, which aids in better analysis and decision-making. It also contributes to data compression by reconstructing missing parts of signals, thereby reducing overall data size without compromising quality. In medical imaging, for instance, it can restore corrupted scans, leading to more accurate diagnoses and improved patient care. Overall, signal inpainting is vital across various fields, providing solutions for data restoration and information recovery. This paper introduces a Hybrid Exemplar-based Deep Learning Super Resolution Generative Adversarial Network (DLSRGAN) specifically designed for recovering deteriorated signals. The proposed method demonstrates superior performance across key metrics higher Peak Signal-to-Noise Ratio (PSNR), lower Mean Squared Error (MSE) and higher Structural Similarity Index Measure (SSIM) compared to the exemplar method.

Recovering deteriorated signals is equally important in domains such as audio restoration, seismic data processing and communication systems. In audio restoration, eliminating noise and artifacts enhances the quality of historical recordings. For seismic data processing, addressing noise and interference is crucial for accurately interpreting subsurface structures and identifying hydrocarbon reservoirs. Advanced techniques like deconvolution and filtering can help recover original signals and improve interpretation accuracy. In communication systems, effective signal recovery ensures reliable data transmission through

methods like error-correction codes and adaptive filtering. Overall, investing in advanced signal processing techniques enhances the quality, accuracy and reliability of processed data.

II. DEVELOPMENT OF HYBRID EXEMPLAR BASED DLSRGAN INPAINTING TECHNIQUE

This section offers an in-depth look at the proposed Hybrid Exemplar based DLSRGAN Inpainting method, which combines the advantages of exemplar-based techniques with Deep Learning Super Resolution Generative Adversarial Networks (DLSRGAN) [2] to achieve high-quality image inpainting. The hybrid approach starts with exemplar-based inpainting, which effectively fills in missing areas with coherent textures and structures. Subsequently, DLSRGAN enhances the resolution of the inpainted image, particularly targeting regions that lack detail.

Exemplar-based inpainting is a technique that fills missing regions of an image by propagating similar patches from known areas [3]. The process involves patch matching through data propagation and confidence propagation [4]. In this method, the confidence propagation ascertains the presence of known information. This process is repeated iteratively until the entire patch or hole is filled. However, exemplar-based inpainting has limitations such as the inability to synthesize novel content and blending artifacts. It is highly sensitive to patch size. This method will give inaccurate results if the patch size is large. Further this method lacks the semantic understanding.

The Super-Resolution Generative Adversarial Network (SRGAN), introduced by Ledig et al. in 2017, aims to improve the resolution of images. SRGANs employ adversarial training to produce high-resolution images from low-resolution inputs, resulting in a substantial enhancement in image quality and the level of detail. Later studies have expanded upon SRGAN to further improve its effectiveness [5]. The perceptual loss function of SRGAN enables the production of high-fidelity, aesthetically attractive and lifelike images. The model also utilizes residual blocks to extract features, capturing complex details and textures, hence improving the authenticity of the image. The discriminator in SRGAN distinguishes between super-resolved photos and genuine high-resolution images, guaranteeing their close resemblance to real-world data [6-9]. Furthermore, SRGAN integrates a content loss that relies on perceptual similarity, resulting in high-resolution images that preserve the visual attributes and intricacies of the original material.

The integration of these two techniques provides several benefits over traditional inpainting methods, including enhanced resolution and better texture and structure propagation. Initially, the input image is processed using exemplar-based inpainting to enhance texture coherence. This is then followed by the application of DLSRGAN to improve overall resolution and recover finer details in low-resolution areas. This hybrid method has a wide range of applications in video processing, including image video inpainting and video outpainting.

Key features of the hybrid Exemplar-based DLSRGAN technique include its capacity to combine the strengths of both methods for improved image reconstruction and quality. It employs a tensor-based data term for more effective pixel selection when filling in missing regions, surpassing conventional techniques.

]Additionally, a fast patch lookup strategy is utilized to ensure improved geometric coherence in the results. The hybrid approach also addresses common issues faced by traditional methods, such as blurriness in large damaged areas, by leveraging both exemplar-based and deep learning advantages. The limitations of conventional inpainting methods are well-recognized and include problems like blurriness in large damaged regions, high computational complexity, insufficient perceptual similarity between inpainted areas and their surroundings, and challenges in handling complex structures and textures. While traditional methods often yield blurry results for extensive missing areas, the hybrid technique alleviates this issue through a tensor-based data term for better pixel selection and a fast patch lookup strategy to enhance coherence. Moreover, although traditional methods can be resource-intensive, literature suggests modifications that can reduce processing time without significantly affecting quality. The hybrid method demonstrates potential for producing more realistic results by utilizing deep neural networks to replicate complex textures. By merging exemplar techniques with DLSRGAN, this new approach referred to as Hybrid Exemplar-based DLSRGAN aims to effectively address these limitations.

III. RESULTS AND DISCUSSIONS

In this work, the proposed Hybrid Exemplar based DLSRGAN technique is applied to recover the deteriorated signals. To analyze the performance of Hybrid technique for signal inpainting, Received Signal Strength Indicator (RSSI) signal is wantedly distorted in three ways; large, medium and small. This RSSI signal is taken as input from RSSI dataset for Indoor Positioning Fingerprinting [10].

Dataset:

The RSSI Dataset for Indoor Localization Fingerprinting is a comprehensive dataset created by Petros Spachos to support research in indoor localization using fingerprinting techniques. The dataset aims to improve the accuracy and robustness of localization systems relying on Received Signal Strength Indicator (RSSI) values. The dataset includes RSSI readings from three different wireless technologies such as Zigbee, Bluetooth Low Energy (BLE) and Wireless Fidelity (Wi-Fi). The dataset was collected in diverse indoor environments to provide a realistic testing environment for algorithms that need to operate under different conditions and interferences typical of indoor spaces.

The dataset is suitable for research and development, testing and validation and machine learning, as it enhances indoor localization algorithms and techniques, provides a benchmark for evaluating the performance of different localization methods, and trains models to predict locations based on RSSI values. The dataset is available on Institute of Electrical and Electronics Engineers (IEEE) Data port and can be accessed via the provided DOI (Digital Object Identifier) link. By making this dataset available, Petros Spachos has contributed a valuable resource to the research community, enabling advancements in indoor localization technologies.

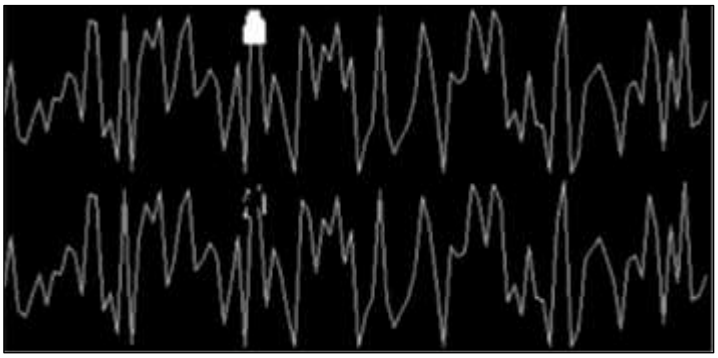

Figure 1: Output of Exemplar based signal inpainting for less distorted signal.
Source: Authors, (2025).

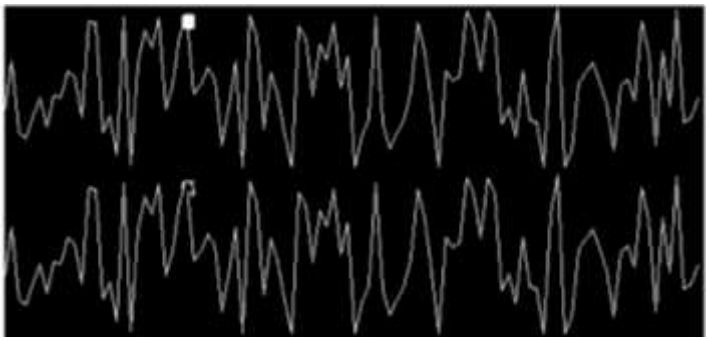

Figure 2: Output of Exemplar based signal inpainting for medium distorted signal.
Source: Authors, (2025).

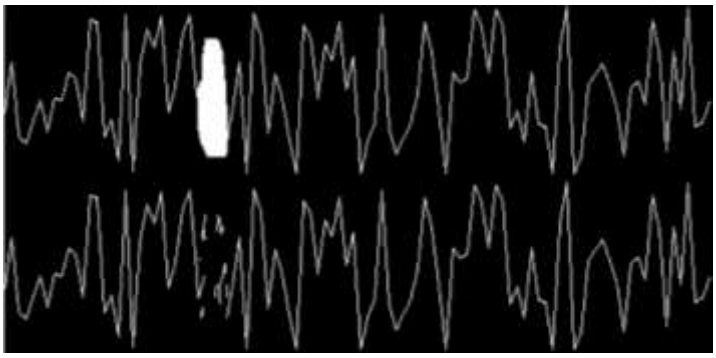

Figure 3: Output of Exemplar based signal inpainting for more distorted signal.
Source: Authors, (2025).

The resultant processed signals through Exemplar technique for corresponding input signals are shown in upper part of the Figure 1, Figure 2 and Figure 3 are respectively presented in lower part of Figgure 1, Figure 2 and Figure 3.

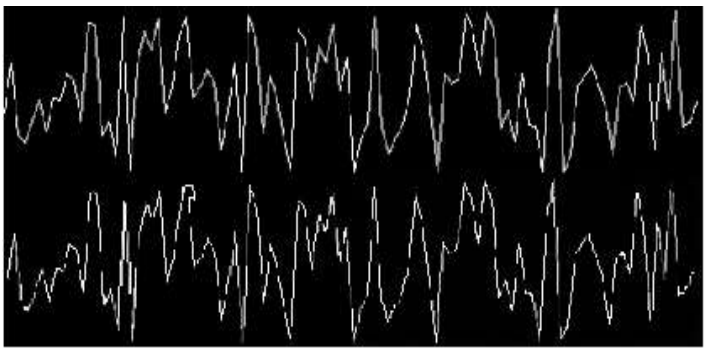

Figure 4: Output of Hybrid DLSRGAN based signal inpainting for less distorted signal.
Source: Authors, (2025).

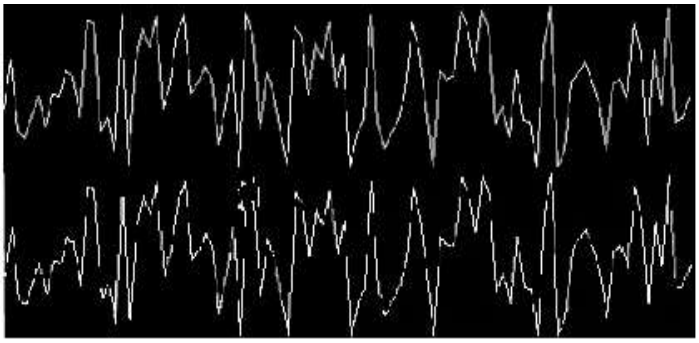

Figure 5: Output of Hybrid DLSRGAN based signal inpainting for medium distorted signal.
Source: Authors, (2025).

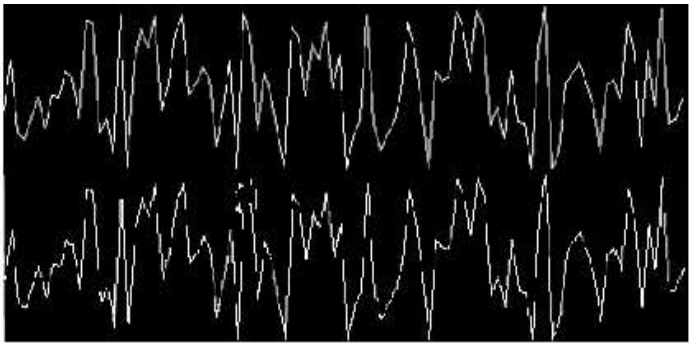

Figure 6: Output of Hybrid DLSRGAN based signal inpainting for more distorted signal.
Source: Authors, (2025).

The upper signals shown in the Fig. 4, Fig. 5 and Fig. 6 correspond to the distorted signal and the lower signals corresponds to their respected super resolution signals. The resultant processed signals through hybrid technique are shown in Fig. 4, Fig. 5 and Figure 6.

Table 1: Comparison of various metrics of Exemplar technique and Hybrid method for inpainted signals.

Sl. No	Metrics	Inpainting Method					
		Exemplar Method			Hybrid GAN		
		More distortion	Medium distortion	Less distortion	More distortion	Medium distortion	Less distortion
1.	PSNR	10.67	11.7	12.0	13.7	14.5	15.2
2.	MSE	5565	4118	4088	2805	2465	1958
3.	SSIM	0.46	0.57	0.59	0.71	0.75	0.785

Source: Authors, (2025).

The metrics MSE, PSNR and SSIM are used to evaluate the performances of the hybrid and exemplar techniques [11]. Results are tabulated for all these distorted signals in Table 1.

From Table 1, it is very clear that signal with less distortion has high PSNR, high SSIM and low MSE. To explore this for more distorted signals deeper studies should be carried on by assessing more number of variants.

IV. CONCLUSIONS

Signal inpainting is an essential process for accurately repairing images in Signal Processing and Biomedical applications. The hybrid method effectively improves the resolution, quality, and visual coherence of images by integrating exemplar-based inpainting which fills in missing areas by replicating similar patches from known regions with the super-resolution capabilities of Generative Adversarial Networks (GANs). This combined approach seeks to address the challenges of signal enhancement and restoration by leveraging the strengths of both inpainting and super-resolution techniques, leading to better inpainting results.

The proposed hybrid exemplar-based DLSRGAN Signal Inpainting method for less distortion demonstrates significant improvements, achieving a 26.6% increase in Peak Signal-to-Noise

Ratio (PSNR), a 52.1% reduction in Mean Squared Error (MSE) and a 33% enhancement in Structural Similarity Index Measure (SSIM) compared to traditional exemplar method. Further research in signal inpainting using GANs is anticipated to bring advancements in signal processing, data recovery and information extraction in diverse fields.

V. AUTHOR'S CONTRIBUTION

Conceptualization: Tammineni Shanmukha Prasanthi, Swaraiya Madhuri Rayavarapu, Gottapu Sasibhushana Rao and Rajkumar Goswami.
Methodology: Tammineni Shanmukha Prasanthi, Swaraiya Madhuri Rayavarapu, Gottapu Sasibhushana Rao and Rajkumar Goswami.
Investigation: Tammineni Shanmukha Prasanthi, Swaraiya Madhuri Rayavarapu, Gottapu Sasibhushana Rao and Rajkumar Goswami.
Discussion of results: Tammineni Shanmukha Prasanthi, Swaraiya Madhuri Rayavarapu, Gottapu Sasibhushana Rao and Rajkumar Goswami.
Writing – Original Draft: Tammineni Shanmukha Prasanthi, Swaraiya Madhuri Rayavarapu, Gottapu Sasibhushana Rao and Rajkumar Goswami.
Writing – Review and Editing: Tammineni Shanmukha Prasanthi, Swaraiya Madhuri Rayavarapu, Gottapu Sasibhushana Rao and Rajkumar Goswami.
Resources: Tammineni Shanmukha Prasanthi, Swaraiya Madhuri Rayavarapu, Gottapu Sasibhushana Rao and Rajkumar Goswami.
Supervision: Tammineni Shanmukha Prasanthi, Swaraiya Madhuri Rayavarapu, Gottapu Sasibhushana Rao and Rajkumar Goswami.
Approval of the final text: Tammineni Shanmukha Prasanthi, Swaraiya Madhuri Rayavarapu, Gottapu Sasibhushana Rao and Rajkumar Goswami.

VI. REFERENCES

[1] M. Bertalmio, G. Sapiro, V. Caselles, and C. Ballester, "Image inpainting," in Proceedings of the 27th annual conference on Computer graphics and interactive techniques, 2000, pp. 417–424.

[2] Ian J. Goodfellow, Jean Pouget-Abadie, Mehdi Mirza, Bing Xu, David Warde-Farley, Sherjil Ozair, Aaron Courville, and Yoshua Bengio. Generative Adversarial Networks. 2014.

[3] W.-H. Cheng, C.-W. Hsieh, S.-K. Lin, C.-W. Wang, and J.-L. Wu, "Robust algorithm for exemplar-based image inpainting," in Proceedings of International Conference on Computer Graphics, Imaging and Visualization, 2005, pp. 64–69.

[4] A. Criminisi, P. Perez, and K. Toyama. Object removal by exemplar-based inpainting. Proceedings of the IEEE Computer Society Conference on Computer Vision and Pattern Recognition, 2, 2003.

[5] Ledig, Christian, et al. "Photo-realistic single image super-resolution using a generative adversarial network." *Proceedings of the IEEE conference on computer vision and pattern recognition*. 2017.

[6] B. Z. Demiray, M. Sit, and I. Demir, "D-SRGAN: DEM super resolution with generative adversarial networks," *SN Computer Science*, vol. 2, no. 1, pp. 1–11, 2021.

[7] R. Sood, B. Topiwala, K. Choutagunta, R. Sood, and M. Rusu, "An application of generative adversarial networks for super resolution medical imaging," in *2018 17th IEEE International Conference on Machine Learning and Applications (ICMLA)*, 2018.

[8] Q. Delannoy *et al.*, "SegSRGAN: Super-resolution and segmentation using generative adversarial networks-Application to neonatal brain MRI," *Computers in Biology and Medicine*, vol. 120, 2020.

[9] Rezayi, H., & Seyedin, S. A. (2015). Simultaneous Methods of Image Registration and Super-Resolution Using Analytical Combinational Jacobian Matrix. *Journal of Information Systems and Telecommunication (JIST)*, *3*(11), 1.

[10] P. Spachos, "RSSI Dataset for Indoor Localization Fingerprinting," IEEE Dataport, 17-Apr-2020.

[11] K. Kipli et al., "Full reference image quality metrics and their performance," 2011 IEEE 7th International Colloquium on Signal Processing and its Applications, Penang, Malaysia, 2011, pp. 33-38, doi: 10.1109/CSPA.2011.5759838.

Journal of Engineering and Technology for Industrial Applications

ITEGAM-JETIA

Manaus, v.11 n.53, p. 145-153. May/June., 2025.
DOI: https://doi.org/10.5935/jetia. v11i53.1605

ISSN ONLINE: 2447-0228

RESEARCH ARTICLE OPEN ACCESS

DESIGN AND IMPLEMENTATION OF A SCALABLE LORA-BASED IOT IRRIGATION SYSTEM WITH DUAL CONTROL MECHANISMS

Salahedin Rehan[1], Esra Alhame[2], Esra Hassan[3]

[1]Advanced Technology and Communication Research Group, Department of Electrical and Electronic Engineering, Faculty of Engineering, University of Zawia, Libya
[2,3]Al-Asas Al-Mateen for Technology and Modern Systems, R&D, Zawiya, Libya

[1]https://orcid.org/0000-0003-0869-7933, [2]https://orcid.org/0009-0004-2569-9644, [3]https://orcid.org/0009-0002-0802-5344

Email: s.rehan@zu.edu.ly, e.alhame@asas.com.ly, e.hassan@asas.com.ly.

ARTICLE INFO

Article History
Received: February 02, 2025
Revised: May 20, 2025
Accepted: June 15, 2025
Published: June 30, 2025

Keywords:
Precision Agriculture,
Irrigation System,
Scalability,
LoRa,
IoT.

ABSTRACT

Efficient water management is a critical challenge in large-scale agriculture, especially in remote areas where manual monitoring and control of irrigation systems are impractical. This paper presents the design and implementation of a scalable, LoRa-based Internet of Things irrigation system with dual control mechanisms, offering both local and remote control of irrigation processes. The system comprises field sensor nodes that transmit environmental data—such as soil moisture, temperature, and pump status—to both a local control node and a cloud gateway. Users can manage irrigation remotely via a cloud-based dashboard, while local control is achieved through manual intervention at the control node. A synchronization mechanism ensures that changes in actuator states are reflected across the system, regardless of where the control originates. By employing Long Range technology for extended communication distances and MQTT (Message Queuing Telemetry Transport) for efficient cloud connectivity, the system supports reliable, low-power operation over distances of up to 5.76 kilometers. Field tests validate its effectiveness, showcasing its potential to enhance water use efficiency in agriculture and reduce the need for constant human oversight in irrigation management. The scalable design ensures the system can adapt to various agricultural field sizes, making it practical for wide-area irrigation management.

I. INTRODUCTION

Efficient water management in agriculture is increasingly critical due to growing water scarcity and the need for sustainable practices. Agriculture accounts for approximately 70% of global freshwater withdrawals, emphasizing the importance of optimizing irrigation systems [1]. Traditional irrigation methods often require significant human intervention and are inefficient, leading to water wastage and suboptimal crop yields [2]. These challenges are exacerbated in remote or large-scale agricultural settings where manual monitoring and control are impractical. The Internet of Things (IoT) offers transformative solutions by enabling automation and optimization of irrigation processes through interconnected, low-power devices that communicate wirelessly [3]. IoT-based systems facilitate real-time monitoring and control, allowing for precision agriculture where inputs like water are applied only when and where needed, enhancing sustainability and productivity [4]. Scalability is a crucial aspect of these systems, designed to accommodate the expansive and varying sizes of agricultural fields [5].

One primary challenge in deploying IoT for agriculture is maintaining wide-area coverage while keeping energy consumption low. Traditional wireless technologies like Wi-Fi are limited in range and consume significant power, making them unsuitable for large-scale agricultural applications [6]. Technologies like Zigbee and Bluetooth are more energy-efficient but are not optimized for long-range communication, which is often necessary in rural environments [7]. Low-Power Wide-Area Networks (LPWAN) have emerged as a solution for IoT applications requiring extended communication range and low energy consumption [8]. Among LPWAN technologies, LoRa stands out due to its ability to provide reliable data transmission over many kilometers while operating on minimal power [9]. LoRa employs chirp spread spectrum modulation, which is robust against

interference and can achieve long-range communication with low power consumption [10]. This makes it ideal for large agricultural areas with complex terrains, where maintaining connectivity is challenging. LoRa's scalability features are particularly advantageous for accommodating a growing number of devices in expansive fields [11].

Previous studies shows that precise control over irrigation can significantly reduce water consumption while maintaining crop health [12]. An IoT-based smart irrigation system was proposed by H. Zhang et al. [13] utilizing wireless sensor networks to monitor soil moisture and environmental conditions in real time, reducing the need for manual intervention and improving water use efficiency. A. Kumar and B. Singh [14] emphasized the importance of designing scalable IoT solutions that can expand to accommodate varying field sizes, ensuring that the benefits of IoT technologies are accessible to farms of all scales. M. Ali, S. Khan, and L. Wang [15] designed and implemented an IoT-based smart irrigation system using LoRaWAN technology, demonstrating enhanced energy efficiency and reliable data transmission over long distances suitable for large agricultural fields. Additionally, integrating advanced data analytics into IoT-based irrigation systems has shown promise in optimizing irrigation scheduling. M. Patel and D. Roy [16] demonstrated how predictive analysis using historical and real-time data can improve water use efficiency and crop yield. While previous studies have made significant strides in developing IoT-based irrigation systems, several challenges remain unaddressed, particularly concerning energy efficiency, the integration of local and remote-control mechanisms, and the seamless scalability of such systems in remote or large-scale agricultural settings. Existing solutions often focus primarily on either local control or cloud-based management but rarely provide a unified approach that combines both effectively.

This paper presents the design and implementation of a scalable, LoRa-based IoT agricultural irrigation system that integrates both local and cloud-based control mechanisms. The system's dual approach adds robustness and flexibility. The local control node provides real-time, on-site decision-making and allows manual intervention when needed, crucial in environments where internet access is intermittent or unavailable. Simultaneously, cloud integration enables users to monitor and control irrigation remotely, providing a broader scope for managing the system from any location. The modular and scalable design allows for easy addition of field sensor nodes, ensuring the system can expand to cover larger agricultural areas.

By incorporating these features, the system is well-suited for large-scale agricultural applications, addressing challenges related to water management, energy efficiency, and the need for automation. The scalable architecture ensures that the system can adapt to various field sizes and complexities, making it a practical cost-effective solution for wide-area irrigation management.

II. SYSTEM ARCHITECTURE

The system architecture includes three core components: a field sensor node, a local control node, and a gateway node connected to a cloud platform. The field node collects real-time environmental data such as soil moisture, temperature, and humidity. This data is transmitted to both the control node and the gateway node using a point-to-multipoint communication scheme. The control node enables local decision-making, and the gateway facilitates remote monitoring via a cloud-based control and monitoring platform. The platform, named Kolibrio, has been developed for the purpose of this application.

The system is designed with scalability at its core. The modular architecture allows for the easy addition of field sensor nodes and actuators without significant reconfiguration.

The MQTT protocol plays a key role in enabling efficient communication between the gateway node and the Kolibrio dashboard, ensuring lightweight, reliable data transmission for remote management [17]. The use of MQTT protocols supports scalability by efficiently managing increased data traffic from additional nodes. By employing LoRa technology for long-range, low-power communication, the system can cover extensive agricultural areas in an energy efficient manner.

II.1 LORA MODULE CONFIGURATION

The E32-433T20DC LoRa module is pivotal in enabling long-range communication in an energy-efficient manner. Firmware was created to manage the configuration of parameters such as frequency, spreading factor, bandwidth, and power output, ensuring optimal performance in long-range, low-power data transmission [18], [19]. In all nodes, communication between the microcontroller and the LoRa module is established through the UART interface, using the E32LoRa open-source library [20]. This library simplifies data encapsulation for transmission and handles the module's operation modes, including Normal, Wake-up, Power-Saving, and Sleep, to optimize energy efficiency in wide-area deployment.

As detailed in our previous study [21] and shown in Figure (1), the power consumption pattern of the E32-433T20DC was analyzed to understand its impact on battery life. While in sleep mode, the module consumes only 4.6 µA, before transitioning to a wake-up phase where it draws 15.4 mA for approximately 410 ms. During transmission, the current spikes to 102 mA for 820 ms as it sends a 58-byte packet at 2.4 Kbps. This analysis informs the current system's design, ensuring efficient operation within the constraints of battery powered IoT deployments.

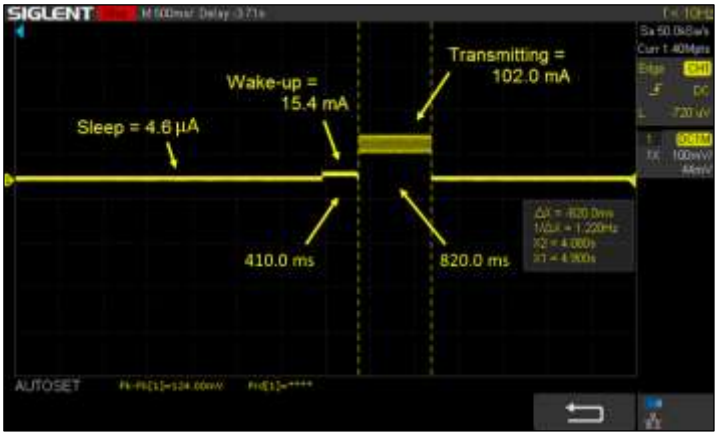

Figure 1: Signal of transmitted data while in the Sleep mode. Source: [21].

II.2 SENSORS AND ACTUATORS

The system integrates two primary environmental sensors: the DHT11 for temperature and humidity monitoring [22] and a soil moisture sensor to measure soil water content [23], [24]. The firmware initializes these sensors and processes the data collected, ensuring reliable transmission of environmental data to both local and cloud systems.

- DHT11 Sensor: Provides 40-bit humiture data via a digital signal, measuring temperature and humidity.

- Soil Moisture Sensor: Outputs analog signals corresponding to soil moisture levels.

The system controls a low-cost submersible water pump using a relay, which is activated based on sensor data and user commands. The pump's operation is crucial for automating irrigation based on environmental analysis, and the relay ensures efficient, reliable activation/deactivation of the pump [25].

II.3 FIRMWARE AND MICROCONTROLLER OPERATIONS

The system's functionality is driven by firmware that handles interactions among sensors, actuators, microcontrollers, and communication modules. The Arduino platform is utilized due to its versatility and ease of use for rapid prototyping [26]. Firmware was developed for both the Arduino Nano and the NodeMCU v3 boards, each selected for its suitability in specific parts of the system.

The Arduino Nano microcontroller specifically handles the field sensors and actuators. It processes sensor readings and communicates with the LoRa module for transmitting data to both the local control node and the gateway, allowing real-time decision-making at the local level [26]. Communication between the Arduino Nano and the OLED display occurs via the I2C interface, providing real-time feedback on sensor readings, actuator status, and system conditions. The NodeMCU v3 board [27], acts as the gateway, connecting to the Kolibrio dashboard via Wi-Fi. It manages data exchange between the field sensor and the cloud platform, allowing for remote monitoring and control through the Kolibrio platform. The microcontroller firmware is designed to support scalability by allowing easy integration of additional sensors or nodes, as illustrated in Section III, which describes the nodes.

II.4 COMMUNICATION MANAGEMENT

The communication architecture integrates both local and cloud-based systems using LoRa and Wi-Fi. The communication protocols and network topology are designed to support scalability, efficiently managing increased data traffic as more nodes are added.

• **Field Node Communication:** The field node transmits environmental data and actuator status in a point-to-multipoint configuration. Data is broadcasted to all addresses within a specific channel, allowing simultaneous data exchange. See Figure (2) [18]. Both the control node and the gateway, identified by their common channel, can receive the data. The field node sends the status of the actuator with every transmission, ensuring synchronization between local and remote controllers.

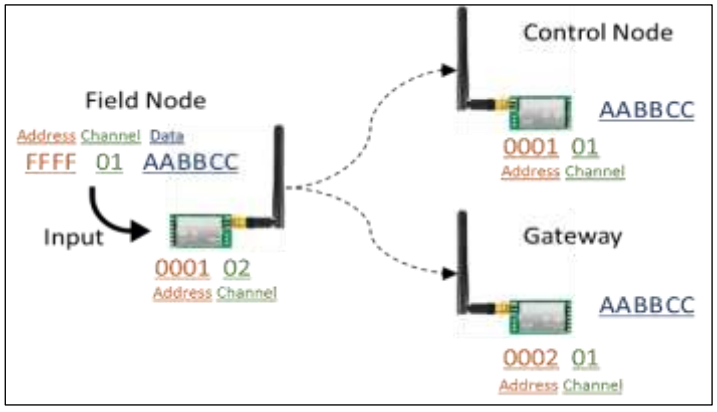

Figure 2: Transmission of field data.
Source: Authors, (2025).

• **Control Node and Gateway Communication:** Both the control node and gateway node communicate with the field node in a point-to-point manner using specific address and channel configurations. See figure (3) [18].

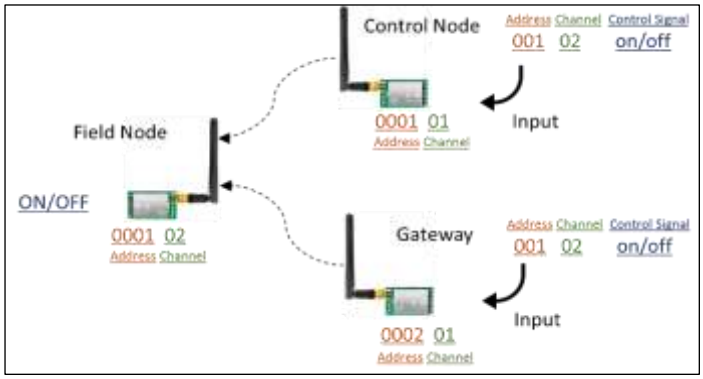

Figure 3: Transmission of control commands.
Source: Authors, (2025).

• **MQTT Protocol for Cloud Integration:** The NodeMCU board, serving as the gateway, communicates with the Kolibrio platform based on a publish-subscribe model using the MQTT protocol [17]. Figure (4) illustrates the communication architecture using the MQTT protocol.

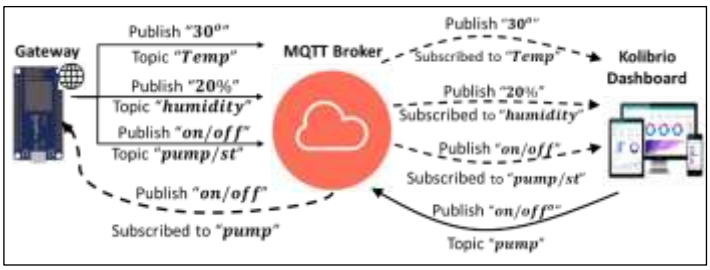

Figure 4: Communication architecture using the MQTT protocol.
Source: Authors, (2025).

The gateway connects to the local Wi-Fi network and acts as the intermediary between the field sensors and the cloud dashboard. It gathers sensor readings and publishes this data to specific MQTT topics: `/FieldNode1/temperature`, `/FieldNode1/humidity`, and `/FieldNode1/soil_moist`. This data is serialized into JSON format using the ArduinoJson library before being sent via the `mqtt_client.publish()` function [28]. The Kolibrio dashboard, subscribed to these MQTT topics, visualizes the sensor data, allowing the user to monitor environmental conditions in real time. The dashboard also provides a control interface, enabling users to turn the pump on or off remotely by publishing to the `/FieldNode1/pump` topic. The NodeMCU, subscribed to these control topics, listens for incoming commands, and forwards them to the field node using LoRa.

The system's bidirectional communication is robust; the NodeMCU sends updates about the actuator status back to the Kolibrio dashboard by publishing actuator states to the `/FieldNode1/pump_st` topic. This ensures the cloud platform is always synchronized with the local system, regardless of where the control action originates. Additionally, the system publish-subscribe model as well as the two-level MQTT topic design ensures flexibility and scalability for larger agricultural deployments. For instance, the addition of a field node would only require the addition of a topic such as `/FieldNode2/temperature`, and

`/FieldNode3/temperature` and so on. The gateway matches the first level to the appropriate field node address, and the second level to the sensor data.

III. SYSTEM COMPONENTS

The system is a robust energy-efficient IoT-based LoRa irrigation solution with cloud integration, designed for both local and remote control in large-scale agricultural irrigation.

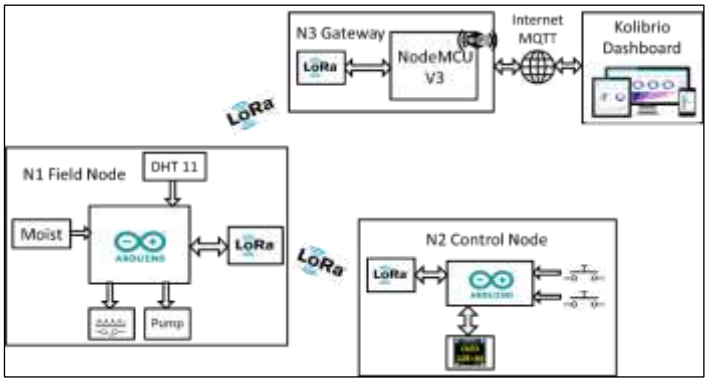

Figure 5: System diagram.
Source: Authors, (2025).

The architecture integrates a field node, a control node for local decision-making, and a gateway node for cloud-based management through the Kolibrio platform. Each component is designed with scalability in mind, ensuring the system can grow without significant reconfiguration. Figure (5) illustrates the system and corresponding components of the nodes. The system can be scaled with minimal intervention to incorporate additional field nodes. Sensors and actuators can also be easily integrated into the respective nodes, as illustrated in the schematics and flowcharts below, where a redundant actuator is incorporated in the form of a relay to demonstrate the scalability of the system.

III.1 FIELD NODE

The field node is responsible for gathering real-time environmental data and executing actuator control. Equipped with the DHT11 sensor for temperature and humidity measurement and a soil moisture sensor, it monitors key environmental parameters.

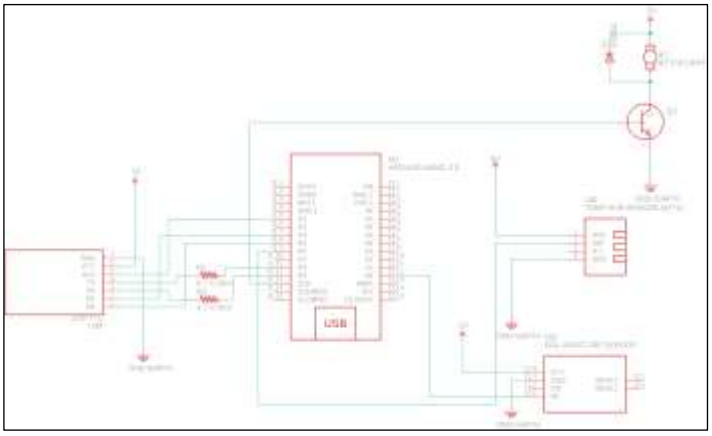

Figure 6: Schematic diagram of Field Node (N1).
Source: Authors, (2025).

Figure (6) shows the schematic of the field node, including sensor connections and communication pathways. The node incorporates the E32-433T20DC LoRa module, which facilitates long-range communication between the field node, control node, and gateway. Data collected by the sensors is transmitted to both the local control node and the cloud gateway. Field node is designed for easy replication and deployment, allowing the system to scale by adding more nodes to cover larger agricultural areas. Simply adding a replica having a distinct address and channel configurations, configured to transmit data to the same gateway channel.

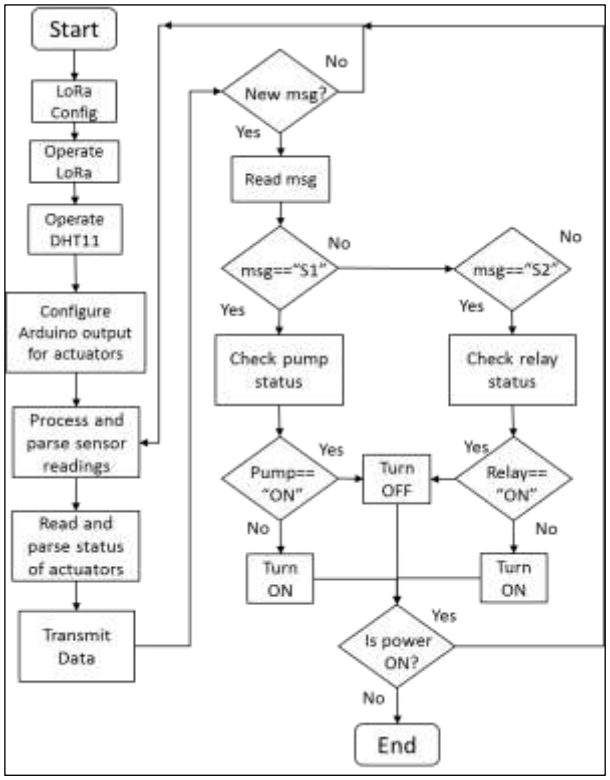

Figure 7: Flowchart of Field Node (N1).
Source: Authors, (2025).

Figure (7) illustrates the flowchart of how the node processes sensor readings and determines whether to activate the water pump, relaying the pump's status to both the control node and the cloud. The figures demonstrate how additional actuators (or sensors), such as a redundant relay, can be incorporated to enhance functionality and scalability.

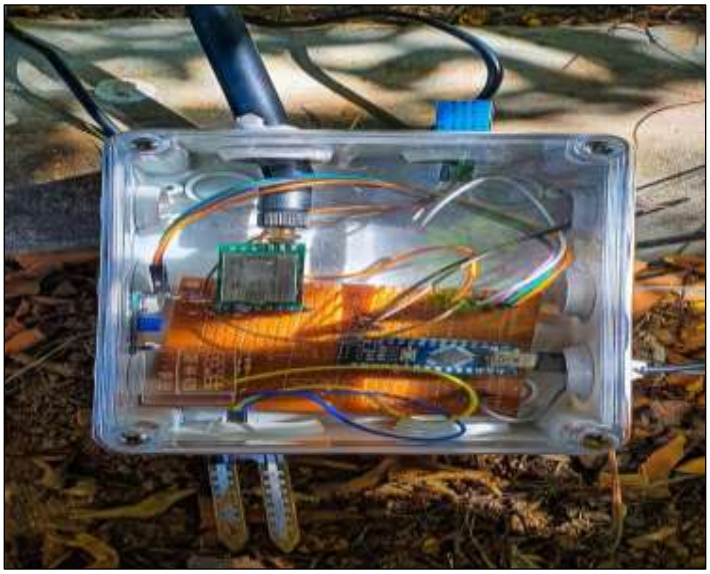

Figure 8: actual deployment of the field node.
Source: Authors, (2025).

Figure (8) shows the actual deployment of the field node, demonstrating the connected sensors, LoRa module, and actuator control setup. The picture provides a visual representation of how the components are laid out in the field, ensuring the reader has a practical understanding of the system's physical layout.

III.2 CONTROL NODE

The control node provides localized decision-making capabilities, enabling manual intervention when necessary. It is equipped with an OLED screen displaying real-time environmental data and pump status, allowing on-site monitoring without relying on cloud access.

The control node, as described in section II, sends specific commands to the field node via a point-to-point link such as activating or deactivating the irrigation pump. It also listens for broadcasted data from the field node, including sensor readings (e.g., soil moisture, temperature) and pump status. Users can manually control the irrigation pump through the control node using push buttons that issue commands to the field node. With minor adjustments, the node can manage data from multiple field sensor nodes and control multiple actuators, ensuring seamless scalability as the number of nodes increases.

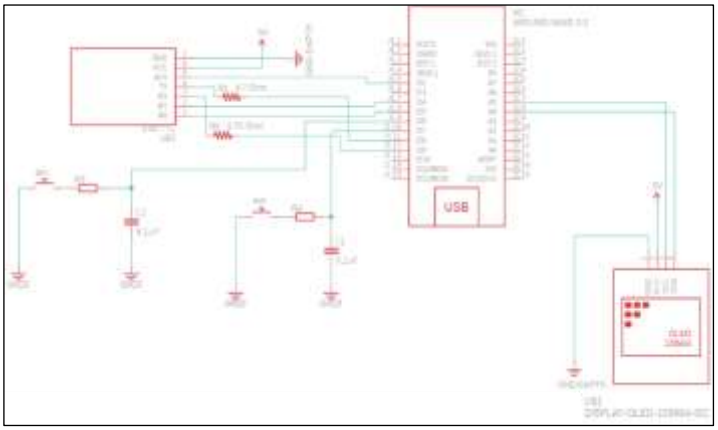

Figure 9: Schematic diagram of control node (N2).
Source: Authors, (2025).

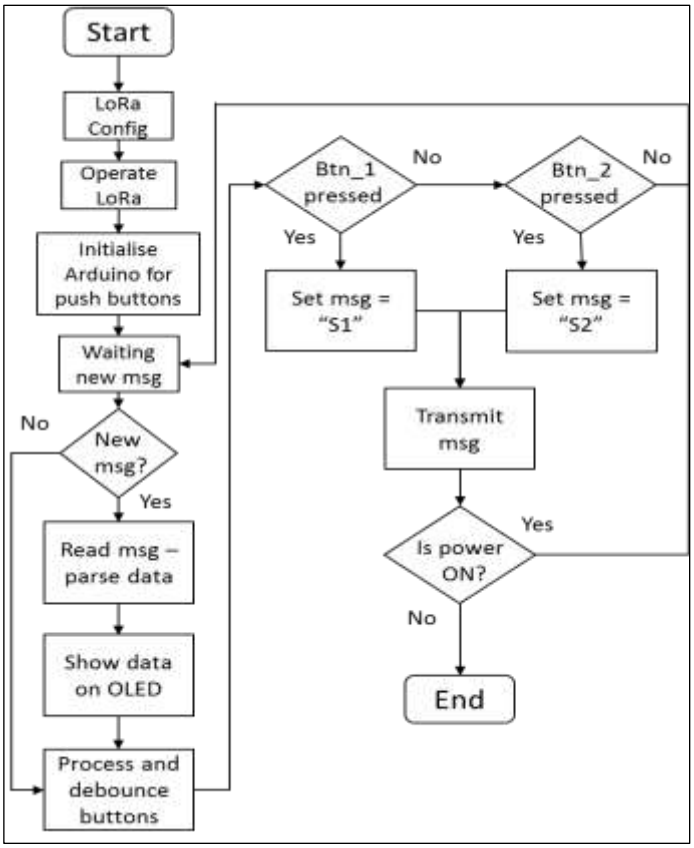

Figure 10: Flowchart of Control Node (N2).
Source: Authors, (2025).

Figure (9) details the schematic of the control node, highlighting the OLED display, buttons, and LoRa communication module. Figure (10) explains the flowchart of how the control node processes incoming data and allows for manual override.

As illustrated, the system is scalable to control multiple actuators by merely increasing the physical number of push buttons and minimal modification to the firmware. The addition of a redundant actuator in the form of a relay is illustrated in both figures below. Different buttons can be dedicated to specific field nodes; hence, the control of actuators in different field nodes can be easily enabled, scaling the system to incorporate several field nodes.Figure (11) shows a picture of the control node setup featuring an OLED screen displaying live environmental data and buttons used for manual control of actuators.

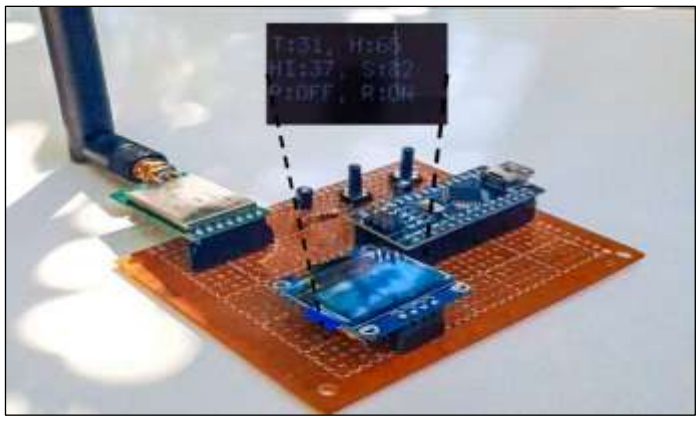

Figure 11: Control node.
Source: Authors, (2025).

III.3 GATEWAY

The gateway node bridges the local irrigation system and the cloud-based Kolibrio platform. Built on the NodeMCU v3 board with an integrated ESP8266 Wi-Fi module, it collects data from the field node and sends it to the cloud. It is designed to handle communication with multiple field nodes, supporting network expansion. This is realized by transparently relaying any received message regardless of the transmitter and publishing it based on the first level of the MQTT topic, as discussed in Section II. The gateway is also responsible for relaying control commands from the Kolibrio platform and transmits them back to the appropriate field node depending on the first level of the MQTT topic.

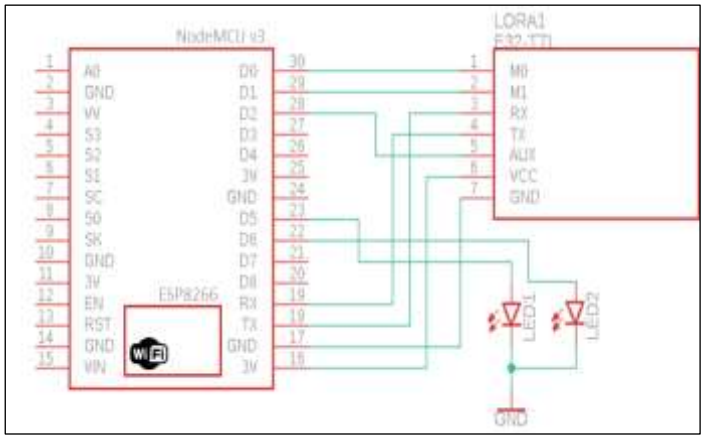

Figure 12: Schematic circuit diagram of gateway.
Source: Authors, (2025).

Figure (12) demonstrates the schematic of the gateway node, showing its connections.

Figure (13) explains the communication flow between the gateway and the cloud, including data transmission and processing of control commands. Figure (14) illustrates an image of the gateway node in operation.

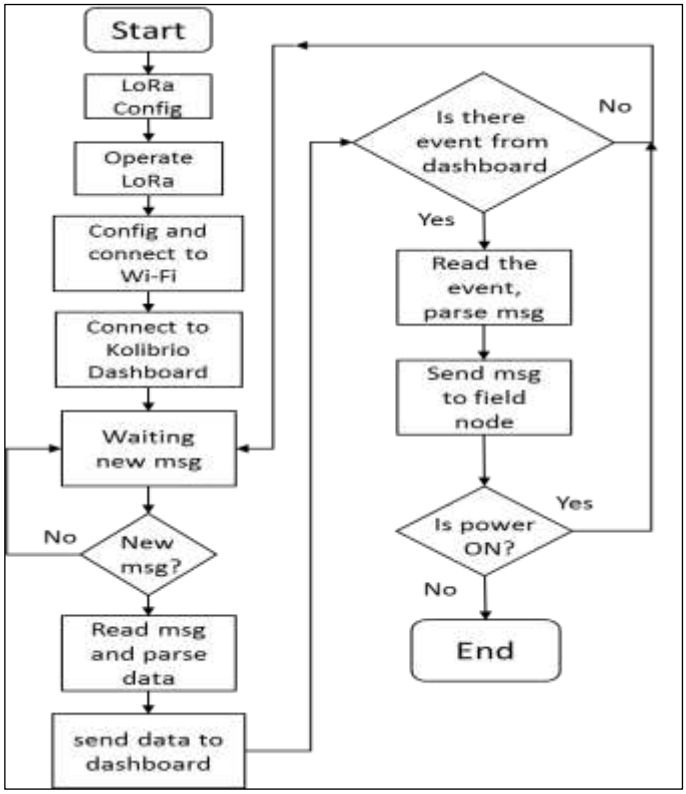

Figure 13: Flowchart of the gateway.
Source: Authors, (2025).

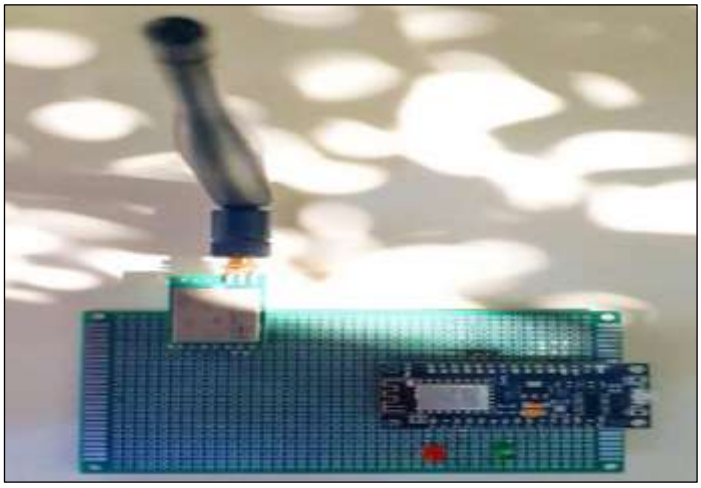

Figure 14: Gateway node.
Source: Authors, (2025).

III.4 KOLIBRIO DASHBOARD

The Kolibrio dashboard, developed specifically for this application, serves as the cloud-based user interface for the irrigation system. It is an open-source platform providing customizable dashboards to monitor sensor data and control actuators remotely. Features include:

- Real-Time Visualization: Live sensor readings such as soil moisture, temperature, and humidity.
- Historical Data Analysis: Graphs displaying historical data trends, allowing users to identify patterns and optimize irrigation schedules.
- Remote Control: Toggle switches to control actuators like the irrigation pump.
- Accessibility: Accessible from any internet-connected device, including computers, smartphones, and tablets.
- Scalability Support: The dashboard can handle data from multiple field sensor nodes, making it suitable for larger deployments.

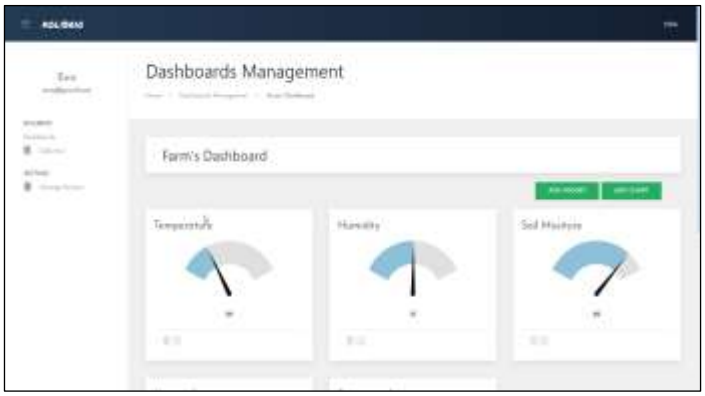

Figure 15: Example of the Kolibrio dashboard.
Source: Authors, (2025).

Communication between the gateway and Kolibrio is handled using the MQTT protocol, as discussed in section II, ensuring reliable and efficient data transmission. The dashboard is customizable, allowing users to create multiple dashboards with widgets tailored to their needs. As the number of field nodes increases, the dashboard can be easily configured to include additional data streams and control elements. An example of the Kolibrio dashboard is illustrated in figure (15).

IV. RESULTS AND DISCUSSIONS

IV.1 RANGE MEASUREMENTS

The range performance of the E32-433T20DC LoRa module was tested to assess its capability in long-range data transmission under various configurations.

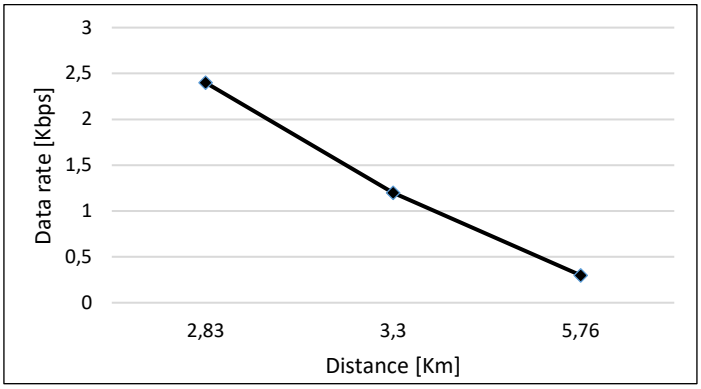

Figure 16: Data Rate vs. Communication Range.
Source: Authors, (2025).

As shown in Figure (16), LoRa technology, renowned for its extended range, confirms that the module can transmit data up to 5.76 kilometers at a data rate of 0.3 Kbps under ideal line-of-sight conditions. As the data rate increases, the effective communication range decreases; however, reliable transmission was sustained over several kilometers even at higher rates. This confirms the system's suitability for large-scale agricultural fields, ensuring reliable monitoring over extensive areas, which is ideal for spatially distributed farms and environmental monitoring in remote locations (see Table 1). The long-range capability reduces the need for additional infrastructure, supporting scalability by allowing more nodes to connect over wide areas without significant network changes.

Table 1: coverage areas for various air data rates.

Air Data Rate [Kbps]	Communicaition Distance [km]	Range Area [Hectares]
0.3	5.76	10,418
1.2	3.30	3,420
2.4	2.83	2,516

Source: Authors, (2025).

IV.2 SYSTEM FUNCTIONALITY

The IoT-based irrigation system effectively manages and monitors environmental conditions in real time. The system employs point-to-multipoint communication from the field sensor node to both the gateway and the local control node. Meanwhile, point-to-point communication between the gateway and control node ensures bidirectional control and feedback.

Data Flow and System Responsiveness

Field nodes, equipped with moisture and temperature sensors, gather critical environmental data, and transmit these values to both the local control node and the gateway. The data is visualized in real time via the Kolibrio cloud dashboard on any connected device (laptop, mobile, etc.). This facilitates remote management and analysis of environmental conditions and system statuses, such as pump operation. The cloud integration ensures real-time synchronization between the local control node and the cloud, allowing for seamless irrigation management regardless of network availability.

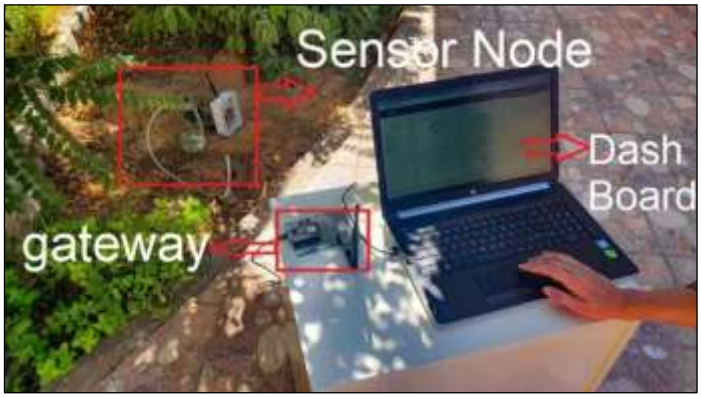

Figure 17: Real-world deployment.
Source: Authors, (2025).

Figure (17) illustrates the real-world deployment of the system, showing how the sensor nodes, control node, and gateway interact. This demonstrates the system's practical setup, emphasizing its robustness and flexibility in field operations. To clarify, the cloud-based control platform can be accessed from anywhere in the world via internet. Accessing the Kolibrio dashboard using the laptop as in figure (17) is only for demonstration purposes.

Real-Time Monitoring and Control

The Kolibrio dashboard, as shown in Figure (18), provides users with live sensor readings such as soil moisture, temperature, and humidity levels. In addition, the dashboard showcases the status of actuators, enabling remote control of the irrigation pump. Users can toggle the pump's operation through the cloud platform, which is immediately reflected on both the cloud dashboard and the OLED display of the local control node, maintaining synchronization between remote and local control.

Figure 18: Live sensor readings with control switch.
Source: Authors, (2025).

Historical Data and Analysis

The system stores historical environmental data in the cloud, accessible through the Kolibrio dashboard's graph widget as illustrated in figure (19). This feature allows for trend analysis over time, enhancing irrigation scheduling. By analyzing past sensor data, users can identify patterns in moisture levels and other parameters, enabling optimization of irrigation schedules and reduction of water consumption.

As more field sensor nodes are added, the system can handle increased data volumes. The cloud-based storage and processing capabilities ensure that historical data from additional nodes can be managed effectively, supporting scalability in data analysis. Figure (19) demonstrates the graph widget's capability to display historical data trends, empowering users to optimize long-term irrigation strategies.

Figure 19: Graph displaying historical temperature data.
Source: Authors, (2025).

V. CONCLUSIONS

This paper presents the development and implementation of a scalable, IoT-based LoRa-Cloud Integrated irrigation system designed to address the challenges of water management in remote agricultural areas. By integrating low-power, long-range communication with cloud connectivity, the system provides a robust, energy-efficient, scalable solution for monitoring and controlling irrigation processes both locally and remotely.

The real-time data acquisition, control capabilities, and historical data analysis make it a valuable tool for optimizing water usage in agriculture. Field tests confirmed the system's ability to maintain reliable communication over distances up to 5.76 kilometers, making it suitable for large-scale agricultural deployments. The system's architecture, with dual control options, ensures continued operation even during network outages, demonstrating adaptability in both connected and disconnected environments.

The scalable design of the system ensures that it can be expanded to accommodate larger agricultural areas, making it a practical and adaptable solution for wide-area irrigation management. The modular components, efficient communication protocols, and flexible software support growth without significant reconfiguration or increased complexity.

Future research could explore enhancements such as renewable energy integration, advanced data analytics, and the implementation of adaptive transmission intervals to further improve resource efficiency. Additionally, scalability can be further tested by deploying the system in larger networks and integrating more diverse sensor types to monitor additional environmental parameters.

VI. AUTHOR'S CONTRIBUTION

Conceptualization: Salahedin Rehan, Esra Alhame, Esra Hassan.
Methodology: Salahedin Rehan, Esra Alhame, Esra Hassan.
Investigation: Salahedin Rehan, Esra Alhame, Esra Hassan.
Discussion of results: Salahedin Rehan, Esra Alhame, Esra Hassan.
Writing – Original Draft: Salahedin Rehan, Esra Alhame, Esra Hassan.
Writing – Review and Editing: Salahedin Rehan, Esra Alhame, Esra Hassan.
Resources: Salahedin Rehan, Esra Alhame, Esra Hassan.
Supervision: Salahedin Rehan, Esra Alhame, Esra Hassan.
Approval of the final text: Salahedin Rehan, Esra Alhame, Esra Hassan.

VII. REFERENCES

[1] Food and Agriculture Organization of the United Nations, "The State of the World's Land and Water Resources for Food and Agriculture," FAO, Rome, Italy, 2011.

[2] Food and Agriculture Organization of the United Nations (FAO). (2020). *The State of Food and Agriculture 2020: Overcoming water challenges in agriculture*. Rome: FAO.

[3] A. A. AlZubi and K. Galyna, "Artificial Intelligence and Internet of Things for Sustainable Farming and Smart Agriculture," in IEEE Access, vol. 11, pp. 78686-78692, 2023, doi: 10.1109/ACCESS.2023.3298215

[4] Prakash, C., Singh, L. P., Gupta, A., & Lohan, S. K. (2023). Advancements in smart farming: A comprehensive review of IoT, wireless communication, sensors, and hardware for agricultural automation. Sensors and Actuators A: Physical, 362, 114605. https://doi.org/10.1016/j.sna.2023.114605

[5] M. Jawad, M. N. A. Khan, A. Ahmad, and N. Imran, "Scalability Analysis of IoT Enabled Smart Irrigation System," Journal of Network and Computer Applications, vol. 157, p. 102589, Mar. 2020.

[6] A. Lavric, V. Popa, and I. Finis, "Performance evaluation of LoRaWAN communication scalability in large-scale wireless sensor networks," Wireless Communications and Mobile Computing, vol. 2018, Article ID 6730719, 9 pages, 2018.

[7] Soussi A, Zero E, Sacile R, Trinchero D, Fossa M. Smart Sensors and Smart Data for Precision Agriculture: A Review. Sensors (Basel). 2024 Apr 21;24(8):2647. doi: 10.3390/s24082647. PMID: 38676264; PMCID: PMC11053448.

[8] A. Raza, M. A. Zahid, G. Asadullah Shah, A. Wahid, H. Ning, and H. Ur Rehman, "A Critical Analysis of Research Potential, Challenges, and Future Directives in Industrial Wireless Sensor Networks," IEEE Communications Surveys & Tutorials, vol. 20, no. 1, pp. 39–95, First quarter 2018.

[9] LoRa Alliance, "A Technical Overview of LoRa and LoRaWAN," Nov. 2015. Available: https://lora-alliance.org/resource-hub/lorawan-specification.

[10] F. Adelantado et al., "Understanding the limits of LoRaWAN," IEEE Communications Magazine, vol. 55, no. 9, pp. 34–40, Sept. 2017.

[11] A. Augustin, J. Yi, T. Clausen, and W. M. Townsley, "A study of LoRa: Long range & low power networks for the Internet of Things," Sensors, vol. 16, no. 9, p. 1466, Sept. 2016.

[12] K. Evans and L. T. Sadler, "Irrigation management strategies for improved water use efficiency," Agricultural Water Management, vol. 96, no. 11, pp. 1499–1504, 2009.

[13] H. Zhang et al., "Implementation of an IoT-Based Smart Irrigation System," Proceedings of the ACM Conference on Embedded Networked Sensor Systems, 2023, pp. 120–131.

[14] A. Kumar and B. Singh, "Scalable IoT Solutions in Agriculture for Real-Time Monitoring," Journal of Sensor Networks, vol. 15, no. 2, pp. 100–110, 2023.

[15] M. Ali, S. Khan, and L. Wang, "Design and Implementation of an IoT-Based Smart Irrigation System Using LoRaWAN," IEEE Internet of Things Journal, vol. 10, no. 4, pp. 2501–2510, 2023.

[16] M. Patel and D. Roy, "Machine Learning Integration in IoT-Based Irrigation Systems for Predictive Analysis," International Journal of Advanced Computer Science, vol. 14, no. 3, pp. 200–210, 2023.

[17] Usmani, M. F. (2021). MQTT Protocol for the IoT - Review Paper. Technical Report, Frankfurt University of Applied Sciences. DOI: 10.13140/RG.2.2.26065.10088

[18] EBYTE "E32-433T20DC LoRa Module User Manual. Available: https://www.ru-ebyte.com/pdf-down.aspx?id=1350

[19] Semtech Corporation, "LoRa and LoRaWAN: A Technical Overview," [Online]. Available: https://www.semtech.com/uploads/technology/LoRa/lora-and-lorawan.pdf.

[20] E. Xreef, "E32 LoRa Series Library for Arduino." GitHub Repository. Available: https://github.com/xreef/EByte_LoRa_E32_Series_Library.

[21] S. Rehan A. Alkabair, E. Hassan, "Energy Efficiency Evaluation of the E32-433T20DC Ebyte LoRa Module in Battery-Powered IoT Applications," International Science and Technology Journal, vol. 25, pp. 342-359, 2021.

[22] ASAIR (Aosong Electronics Co., Ltd.). (2018). DHT11 Humidity & Temperature Sensor Datasheet (Translated Version). Retrieved from Mouser Electronics: https://www.mouser.com/datasheet/2/758/DHT11-Technical-Data-Sheet-Translated-Version-1143054.pdf.

[23] DataSheetHub. FC-28 Soil Moisture Sensor Module. Available at: https://www.datasheethub.com/fc-28-soil-moisture-sensor-module/

[24] T. D. N. Nguyen and V. K. Bui, "IoT-Based Smart Agriculture: A Low-Cost and Energy-Efficient Soil Moisture Monitoring System," Sensors, vol. 21, no. 4, p. 1572, Feb. 2021.

[25] Omron Electronics LLC, "G5LE PCB Power Relay Datasheet." Available: https://omronfs.omron.com/en_US/ecb/products/pdf/en-g5le.pdf.

[26] Arduino: The Open-Source Prototyping Platform, Arduino.cc, available at: https://www.arduino.cc.

[27] NodeMCU Documentation Contributors. (n.d.). NodeMCU Lua Reference Manual. Retrieved from https://nodemcu.readthedocs.io/en/dev/nodemcu-lrm/

[28] B. Blanchon, "ArduinoJson: Efficient JSON serialization for embedded C++." Available: https://arduinojson.org.

Journal of Engineering and Technology for Industrial Applications

ISSN ONLINE: 2447-0228

ITEGAM-JETIA

Manaus, v.11 n.53, p. 154-161. May/June., 2025.

DOI: https://doi.org/10.5935/jetia. v11i53.1640

RESEARCH ARTICLE OPEN ACCESS

TIYPE 2 FUZZY CONTROL OF DFIG FOR WIND ENERGY CONVERSION SYSTEMS

Kouadria Mohamed Abdeldjabbar[1], Kouadria Selman[2] and Bouzid Mohamed Amine [3]

[1] Department of Electrical Engineering Abdelhamid Ibn Badis University Mostaganem, Algérie.
[2] Laboratoire de Génie électrique et des plasmas, Université Ibn Khaldoun Tiaret, Algérie.
[3] Laboratory Computer Engineering and Energy Engineering Ibn Khaldoun University, Algérie.

[1]https://orcid.org/0000-0002-5001-4131, [2]https://orcid.org/0000-0001-7179-2146, [3]https://orcid.org/0000-0002-1696-8388

Email: mohamedabdeldjabbar.kouadria@univ-mosta.dz, kouadria.selman@univ-tiaret.dz, bouzid19amine@gmail.com

ARTICLE INFO

Article History
Received: February 14, 2025
Revised: May 20, 2025
Accepted: June 15, 2025
Published: June 30, 2025

Keywords:
Wind Energy Conversion System (WECS),
Doubly Fed Induction Generator (DFIG),
Direct control,
Indirect control,
Type-2 fuzzy logic controller,

ABSTRACT

This study develops and designs a Type 2 fuzzy controller technique for application in wind turbines directly linked to the grid and incorporating variable-speed doubly fed induction generators (DFIG).

Type 2 fuzzy theory is proposed with the aim of enhancing system performance. Unlike Type 1 fuzzy systems, it accommodates a wide range of uncertainties and dynamic nonlinearities that may constrain the system's operational efficiency.

Type 2 fuzzy logic provides an effective approach to managing linguistic uncertainty by modeling the ambiguity and limited reliability of information, thereby reducing the overall level of uncertainty within the system.

Both Type 1 Fuzzy Logic Control (T1FLC) and Type 2 Fuzzy Logic Control (T2FLC) techniques were employed in direct and indirect modes. The two control methods were developed, their performances were evaluated, and the most effective control method in terms of reference tracking and robustness was identified. This comparative analysis is derived from a series of tests performed under identical conditions during both transient and steady-state operations of the system.

The simulation results demonstrate that the proposed method exhibits significant resilience to parameter variations and unstructured uncertainties.

I. INTRODUCTION

Over the past few decades, global interest in renewable energy sources has grown considerably. At this stage, electricity generation using wind turbines is among the most promising sustainable energy alternatives [1].

Wind energy is a promising technology for electricity generation due to its well-known environmental advantages over conventional generation systems [2]. To effectively exploit the potential of wind energy, Doubly Fed Induction Generators (DFIGs) play a crucial role [3]. With their advanced technology and design, DFIGs are specifically designed to convert wind energy into electrical energy with remarkable efficiency [4]. They achieve this by using a rotor or blade system that interacts with the force of the wind, converting its kinetic energy into usable electricity [5]. The electricity generated by DFIGs is intelligently integrated into the existing grid.

Type-2 fuzzy sets have recently been included into Fuzzy Logic Systems (FLS) across a range of application fields.

This study focuses on controlling the electrical power produced by the DFIG using a Type-2 Fuzzy Logic Controller (T2FLC). The control method aims to manage the active and reactive power transfer between the stator and the grid, considering variations in rotor resistance, inductance, tip speed ratio, and power coefficient [6-8].

When handling external disturbances, uncertainties, and nonlinearities in nonlinear systems like WEC Systems, robust control is an essential component of renewable energy technology [9].

In recent years, various control methodologies based on T2FLC theory for DFIG have been proposed. In this section, several studies will be presented to show the different applications.

In [10], the authors offer an innovative control technique that employs interval type-2 fuzzy sets for enhanced grid synchronization of DFIG-based wind energy conversion systems. The methodology's distinctive three-dimensional membership function architecture provides parametric adaptability to accommodate stochastic variations and measurement inaccuracies inherent in distributed generation environments.

In [11], the authors presents an adaptive control architecture for DFIG rotor-side converters, where interval type-2 fuzzy logic dynamically optimizes proportional-integral (PI) controller parameters. This methodology demonstrates enhanced robustness against generator parameter variations and grid disturbances compared to conventional PI implementations.

Another method proposed in [12], where a neuro-fuzzy controller for DFIG that uses adaptive sliding mode to regulate power. To improve the efficiency of the suggested control technique, the parameters of the type-2 fuzzy system membership functions are trained online using sliding mode control (SMC) theory.

In [13], the authors use a Type 2 adaptive fuzzy controller approach to evaluate the efficiency of the system in maximizing power generation from wind turbines with variable-speed doubly-fed induction generators connected directly to the grid. The control technique is employed to sustain the optimal value of the stator's reactive power.

Another method for regulating a DFIG in hyposynchronous mode has been discussed in [14]. The approach relies on maximum power point tracking (MPPT). To regulate Ird and Irq, a novel class of fuzzy logic known as adaptive type-2 fuzzy logic control has been created as an alternative to standard proportional integral derivative (PID) controllers. A three-level neutral point clamped (NPC) converter was used to provide power to the rotor side converter (RSC).

Another architecture combines type-2 fuzzy logic control with sliding mode control (SMC) has been presented in [15]. It was used to control effectively the active and reactive powers of the DFIG. This technique reduces chattering and increase the system's performance in speed monitoring and stator side power regulation.

In this work, we will propose a T2FLC strategy. The structure of this paper is organized as follows: In Section II, we present the mathematical model of the wind turbine system, which comprises DFIG driven by a variable pitch turbine. This system is regulated through rotor variables using two bidirectional Pulse Width Modulation (PWM) converters, allowing for effective management of power output and operational efficiency. In Sections III and IV, the control strategy and synthesis of the type 2 fuzzy logic control algorithm (direct and indirect modes) is discussed. Section V presents and discusses the simulation results, using Matlab/Simulink software, along with an evaluation of the proposed controller's effectiveness. Finally, we conclude the reported work.

II. SYSTEM MODELLING

The wind energy conversion system examined in this study utilizes a Doubly Fed Induction Generator (DFIG). From a system perspective, the conversion chain consists of three key interacting components, each modeled separately: the wind turbine, gearbox, and DFIG topology. As illustrated in Figure 1, the rotor is linked to the grid through a back-to-back AC-DC-AC PWM converter, while the stator is directly connected to the grid.

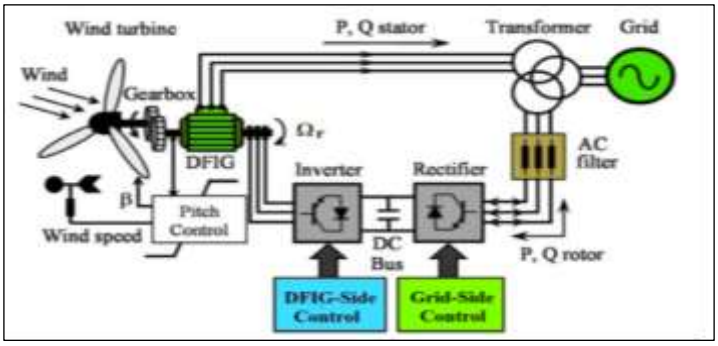

Figure 1: Wind energy conversion system.
Source: Authors :[16].

II.1 WIND TURBINE

The aerodynamic power generated by a wind turbine is determined by several key factors, including wind speed, turbine design, and its geometric characteristics. The relationship can be mathematically described using the following equation[17],[18]:

$$P_{aer} = \frac{1}{2}\rho\pi R^2 C_p(\lambda,\beta)v^3 \quad (1)$$

Then the aerodynamic torque is given by:

$$T_{aer} = \frac{P_{aer}}{\Omega_t} \quad (2)$$

In this context, ρ denotes the air density, which has a value of ρ = 1.225 kg/m³. R refers the length of the blade in meters (m), and V indicates the wind velocity in meters per second (m/s). The power coefficient C_p (λ, β), depends on two factors: the pitch angle of the turbine (β, in degrees°) and the tip speed ratio (TSR), represented as λ.

The tip speed ratio (λ) is expressed as:

$$\lambda = \frac{\Omega_t R}{v} \quad (3)$$

where Ω_t represents the angular shaft speed of the wind turbine.

The power coefficient C_p and the tip speed ratio λ are related by the following function:

$$C_p(\lambda,\beta) = 0.5176\left(\frac{116}{\lambda_i} - 0.4\,\beta - 5\right)e^{\frac{-21}{\lambda_i}} + 0.0068 \quad (4)$$

$$\frac{1}{\lambda_i} = \frac{1}{\lambda+0.08.\beta} - \frac{0.035}{\beta^3+1} \quad (5)$$

The turbine is connected to the generator shaft via a gearbox, which has a gear ratio G selected to ensure that the generator shaft operates within a specified speed range:

$$\begin{cases} T_g = \frac{T_{aer}}{G} \\ \Omega_t = \frac{\Omega_m}{G} \end{cases} \quad (6)$$

Where T_g the driving torque of the generator and Ω_m is the generator shaft speed, respectively.

II.2 DYNAMIC MODEL OF A DFIG

The electrical expressions in the (d, q) reference frame are written as follows [19], [20]:

$$\begin{cases} V_{ds} = R_s.I_{ds} + \dfrac{d\Phi_{ds}}{dt} - \omega_s\Phi_{qs} \\ V_{qs} = R_s.I_{qs} + \dfrac{d\Phi_{qs}}{dt} + \omega_s\Phi_{ds} \\ V_{dr} = R_r.I_{dr} + \dfrac{d\Phi_{dr}}{dt} - (\omega_s - \omega)\Phi_{qr} \\ V_{qr} = R_r.I_{qr} + \dfrac{d\Phi_{qr}}{dt} + (\omega_s - \omega)\Phi_{dr} \end{cases} \quad (7)$$

Where R_s and R_r stand for the phase resistances of the stator and rotor, respectively.
ω = Ω p. is the electrical speed and p is the number of pair poles.
The expressions for the stator and rotor fluxes in the (d, q) reference frame are:

$$\begin{cases} \Phi_{ds} = L_s I_{ds} + M I_{dr} \\ \Phi_{qs} = L_s I_{qs} + M I_{qr} \\ \Phi_{dr} = L_r I_{dr} + M I_{ds} \\ \Phi_{qr} = L_r I_{qr} + M I_{qs} \end{cases} \quad (8)$$

Where L_s and L_r represent the stator and rotor self-inductances, respectively, while M denotes the mutual inductance between windings. Additionally, I_{ds} , I_{qs},I_{dr}, and I_{dr}correspond to the direct and quadrature components of the stator and rotor currents, respectively.

The following expression expresses the electromagnetic torque of the DFIG:

$$Tem = \frac{PM}{Ls}\left(\Phi_{qs} I_{dr} - \Phi_{ds} I_{qr}\right) \quad (9)$$

The model of the DFIG can be represented using state equations in the synchronous reference frame, with the d-axis aligned with the orientation of the stator flux, as indicated in the equation below:

$$\begin{cases} \mathrm{V_{ds}} = 0 \\ \mathrm{V_{qr}} = \mathrm{V_s} = \omega_s \Phi_{ds} \end{cases} \quad (10)$$

The stator's active and reactive powers, together with those that are provided to the grid, are described as follows:

$$\begin{cases} \mathrm{P_s} = \mathrm{V_{ds}}.\mathrm{I_{ds}} + \mathrm{V_{qs}}.\mathrm{I_{qs}} \\ \mathrm{Q_s} = \mathrm{V_{qs}}.\mathrm{I_{ds}} - \mathrm{V_{ds}}.\mathrm{I_{qs}} \end{cases} \quad (11)$$

Here are the formulas for rotor voltages as a function of rotor currents:

$$\begin{cases} \mathrm{V_{dr}} = \mathrm{R_r}.\mathrm{I_{dr}} + \sigma.\mathrm{L_r}.\dfrac{\mathrm{dI_{dr}}}{\mathrm{dt}} - \mathrm{g}.\omega_s.\sigma.\mathrm{L_r}.\mathrm{I_{qr}} \\ \mathrm{V_{qr}} = \mathrm{R_r}.\mathrm{I_{qr}} + \sigma.\mathrm{L_r}.\dfrac{\mathrm{dI_{qr}}}{\mathrm{dt}} + \mathrm{g}.\omega_s.\sigma.\mathrm{L_r}.\mathrm{I_{dr}} + \mathrm{g}.\dfrac{\mathrm{M.V_s}}{\mathrm{L_s}} \end{cases} \quad (12)$$

where the DFIG's dispersion coefficient is denoted by

$$\sigma = \left(1 - \frac{M^2}{\mathrm{L_s L_r}}\right).$$

III. CONTROL OF THE STUDIED SYSTEM

This section will discuss the utilization of a Type 2 Fuzzy Logic controller (T2FLC)to manage the active and reactive power DFIG.

III.1 DIRECT CONTROL OF THE DOUBLY FED INDUCTION GENERATOR

Figure 2 illustrates the block design of the DFIG that shows the direct control technique. By using separate regulators on each axis and ignoring the coupling factors, this method allows the active and reactive powers to be separately controlled.

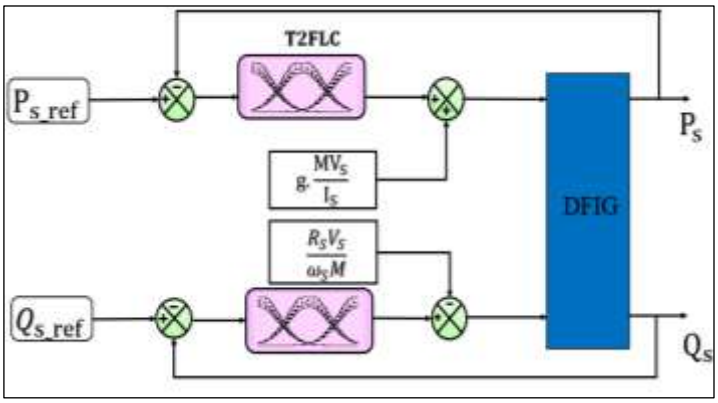

Figure 2: Direct control of the DFIG.
Source: Authors, (2025).

III.2 INDIRECT CONTROL OF THE DOUBLY FED INDUCTION GENERATOR

The indirect control strategy for the DFIG is depicted in Figure. 3. This method focuses on addressing the coupling terms and compensating for them by utilizing a dual-loop system designed to regulate both power output and rotor currents. This technique, referred to as the indirect method, facilitates the management of rotor currents, which is crucial for safeguarding the DFIG by limiting excessive currents and enhancing the operational flexibility of the machine.

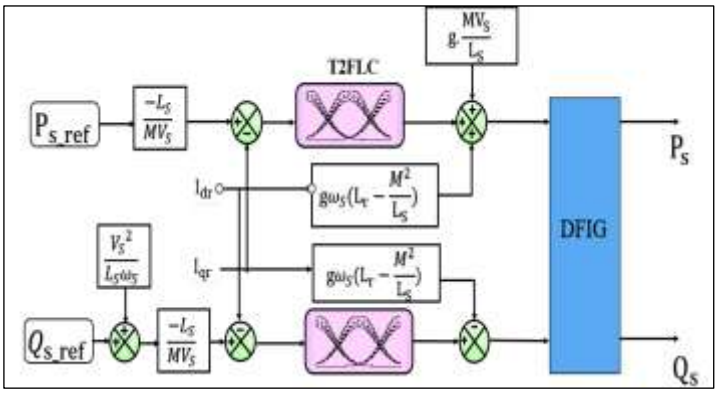

Figure 3: Indirect control of the DFIG.
Source: Authors, (2025).

IV. TYPE-2 FUZZY LOGIC CONTROL SYNTHESIS

Artificial intelligence methods are widely recognized for their significant potential in addressing industrial process challenges, especially in areas such as control, parameter estimation, and system identification [21]. Fuzzy logic, a notable technique within artificial intelligence, is increasingly utilized for controlling induction machines and adapting their vector control -

[22]. The overarching goal of artificial intelligence is to develop systems capable of emulating human reasoning behavior in various cognitive tasks [23].

Type-2 fuzzy logic is an advancement of classical fuzzy logic that expands upon type-1 fuzzy logic. This novel logic will allow us to integrate uncertainties into the regulations, positively influencing the system's output under examination [24]. Type-2 fuzzy logic is particularly efficacious in scenarios when establishing precise membership functions for a fuzzy system proves challenging.

A Type 2 fuzzy system is structured similarly to a Type 1 fuzzy system, consisting of a fuzzification block, a rule base, and an inference mechanism. The primary difference lies in the output, which introduces a reduction block before the defuzzification block in Type 2 systems [25], [26].

Figure 4 shows the Type-2 fuzzy logic controller's structure:

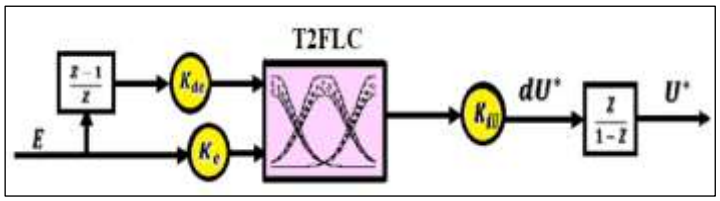

Figure 4: Schematic diagram of T2FLC.
Source: Authors, (2025).

The controller continuously analyzes the error signal and its derivative within the active and reactive power control loops. Based on this analysis, it adjusts the output U to ensure that the active power Ps aligns with its desired reference value P_s^*, while also ensuring that the reactive power Qs matches its corresponding reference value Q_s^*. Each Type-2 fuzzy controller processes two input signals: the error signal E and its derivative dE/dt. These signals undergo normalization using their specific scaling factors, K_e for the error and K_{de} for its derivative. The control output signal U is computed by multiplying the rate of change du/dt by the output scale factor K_{dU}, followed by integration to produce the final command signal.

The primary goal of this control method is to enhance the effectiveness of the results obtained through Type-1 fuzzy control. By implementing this advanced approach, the system can achieve significantly lower static errors, ensuring a more accurate response. Additionally, it provides a robust and swift reaction to changes, which is crucial for maintaining stability and efficiency in dynamic operating conditions.

The defuzzification employs the center of gravity method, and the controller block is founded on a Mamdani-type inference system. A distinctive set of criteria was established to ascertain the appropriate defuzzification procedure according to the quantity of input/output parameters. We implemented this control utilizing the Type-2 fuzzy control technique and integrated it into our system. Three Gaussian fuzzy sets represent the error and its variance in the membership functions of the fuzzification block. Our choice of three Gaussian fuzzy sets aligns with the defuzzification block, which determines the order variation.

Figure 5a illustrates the error, Figure 5b depicts the rate of change of the error, and Figure 5c presents the corresponding control action. Table 1 offers a comprehensive summary of the inference rules employed to identify the control variable.

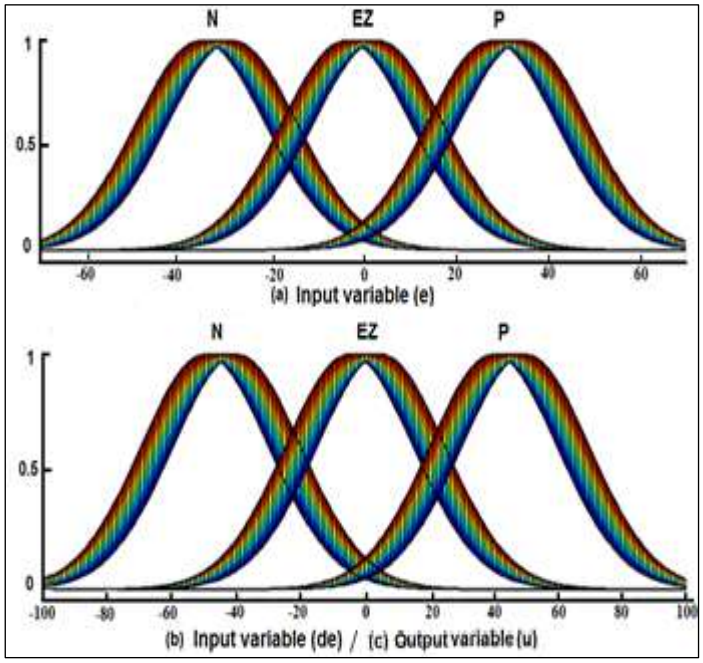

Figure 5: T2FLC membership functions.
Source: Authors : [25].

Table 1: Inference Rules for the T2FLC.

Control		**Error**		
		N	**EZ**	**P**
Rate of change of error	N	N	N	EZ
	Z	N	EZ	P
	P	Z	P	P

Source: Authors : [26].

V. SIMULATIONS AND RESULTS

We conduct comparative MATLAB/Simulink simulations to evaluate the dynamic performance of Type-1 (T1FLC) and Type-2 (T2FLC) fuzzy logic controllers in achieving decoupled active/reactive power regulation for DFIG-based wind turbines. The experimental framework utilizes the wind turbine specifications and DFIG electrical parameters detailed in Appendix A, with particular focus on transient response characteristics during grid interconnection scenarios.

Case I: Setpoint Tracking Test

This evaluation investigates DFIG performance under controlled rotational speed (1440 rpm) during bidirectional active/reactive power transitions:
At t = 3 sec: an active power step (P_{ref}) changes from 1M W to -1MW.

At t=2 sec: a reactive power step (Q_{ref}) changes from 0 var to -5000 var

Concerning this initial test, Figures 6 and 7 illustrate the results of the simulations for the two DFIG power control methods, the direct and indirect techniques.

The results indicate that the DFIG effectively rejects disturbances and maintains to the power set points for both active and reactive power for both control methods.

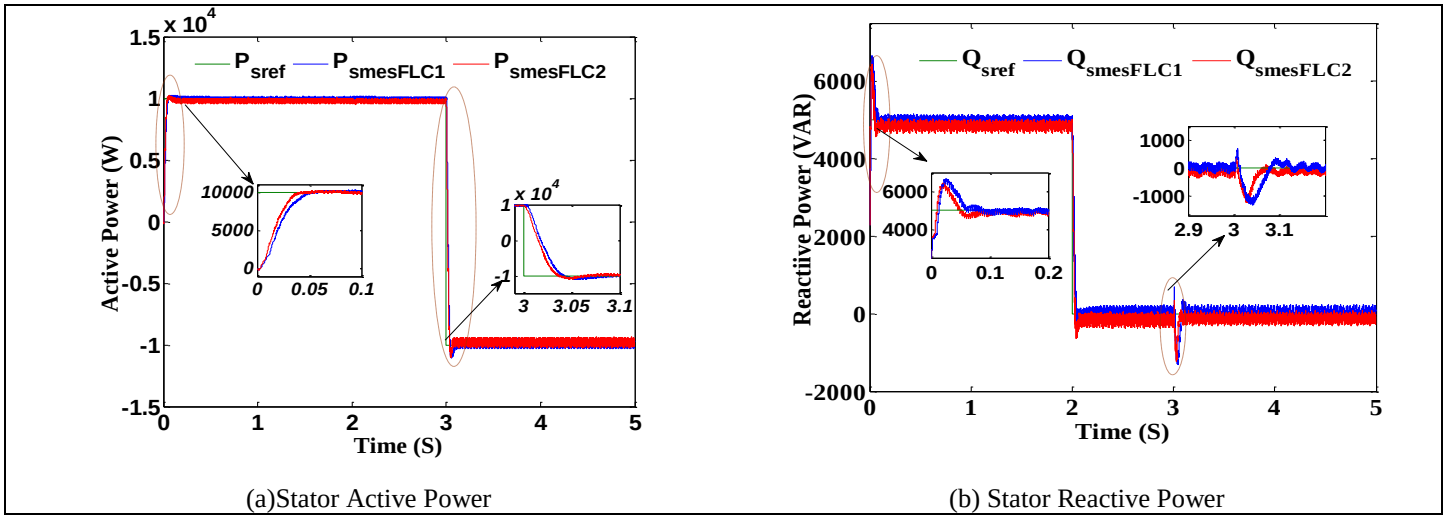

(a)Stator Active Power (b) Stator Reactive Power

Figure 6: Direct control of the DFIG (setpoint tracking).
Source: Authors, (2025).

As shown in Figure 6, for both power control methods (T2FLC and T1FLC), the reactive and active powers of the DFIG closely follow their reference values. However, in the direct control approach using the T1FLC controller, the coupling effect between the two axes is evident. In contrast, the T2FLC controller effectively ensures decoupling between them.

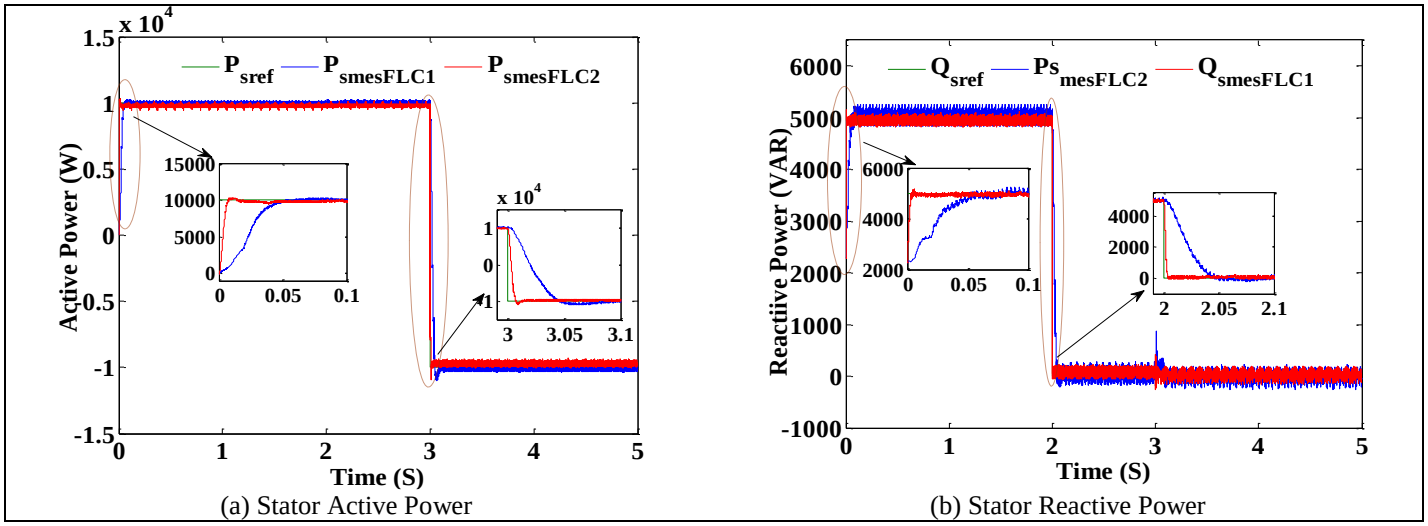

(a) Stator Active Power (b) Stator Reactive Power

Figure 7: Indirect control of the DFIG (setpoint tracking).
Source: Authors, (2025).

The simulation results show in Figure 7 demonstrate that both controllers effectively achieve decoupling, power regulation, and accurate tracking of the reference values. Consequently, the suggested control technique for each converter, as well as the established simulation model, can be validated. Furthermore, a comparison between the results of the T2FLC and T1FLC controllers reveals a strong similarity in their dynamic behavior.

Table 2 provides a comprehensive summary of the controllers' performance, highlighting factors such as decoupling, response time, and power tracking ability.

Table 2: Step response of the controllers.

Active power				
Performances	**Direct control**		**Indirect control**	
	T1FLC	**T2FLC**	**T1FLC**	**T2FLC**
Rise time(s)	1.5758e+3	1.3501e+3	148.9657	271.6274
Overshoot (%)	13.3101	13.0162	33.6529	13.8152
SettlingTime	4.9956e+5	4.9990e+5	3.0140e+5	4.9413e+4
Reactive power				
Performances	**Direct control**		**Indirect control**	

	T1FLC	**T2FLC**	**T1FLC**	**T2FLC**
Rise time(s)	1.4752e+3	0.4000e+3	77.8339	149.6292
Overshoot (%)	5.8596e+3	2.4317e+3	4.1447e+3	3.7551e+3
SettlingTime	4.9998e+5	4.9998e+5	5.000e+5	4.9998e+5

Source: Authors, (2025).

The simulation results, under nominal conditions of operation show that the designed T2FLC and T1FLC control strategy can achieve satisfactory performance. It is possible to individually regulate active and reactive power, with the power responses closely following their reference values.

Case II: Real wind profile

To assess the system's dynamic behavior, regulating the DFIG with a realistic wind speed profile is crucial. This simulation was conducted using the wind profile presented in Fig. 8, where the mean wind velocity fluctuates between 7.5 m/s and 15 m/s. This wind speed profile was rescaled and processed over 5 seconds, as illustrated in Fig. 9 and 10, to align with the simulation and ensure

the controllers operated at maximum efficiency. The T2FLC controller exhibited a faster response time and reduced undershoot compared to the T1FLC controller.

Figures 9 and 10 depict the simulation results obtained from direct and indirect control implemented on the DFIG, utilizing the MPPT control technique for the complete wind turbine system.

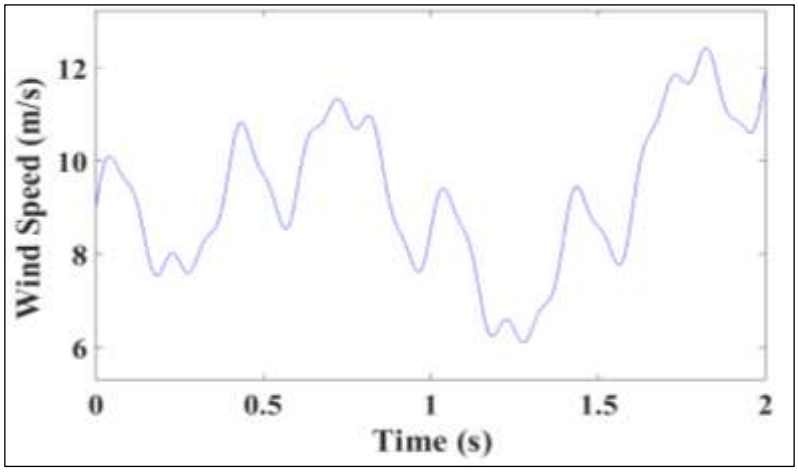

Figure 8: Wind Profile.
Source: Authors, (2025).

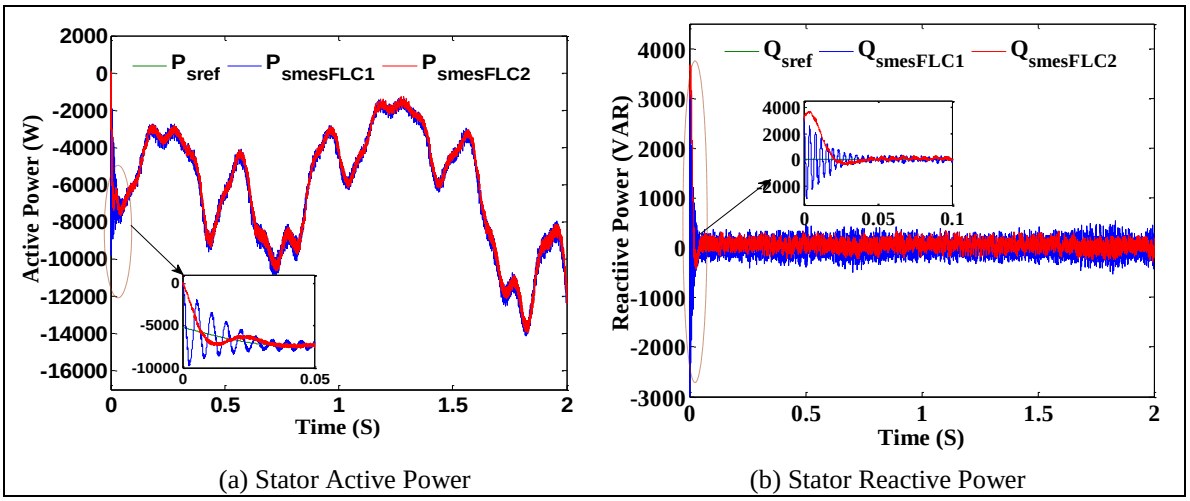

(a) Stator Active Power (b) Stator Reactive Power

Figure 9: Direct control of the DFIG (Real wind profile).
Source: Authors, (2025).

As illustrated in Fig. 9b, the reactive power waveforms for the evaluated control techniques maintain a reference value of Q_{ref} = 0 Var. The T2FLC demonstrated improved performance, featuring lower overshoot, minimal undershoot, and better damping characteristics compared to the T1FLC.

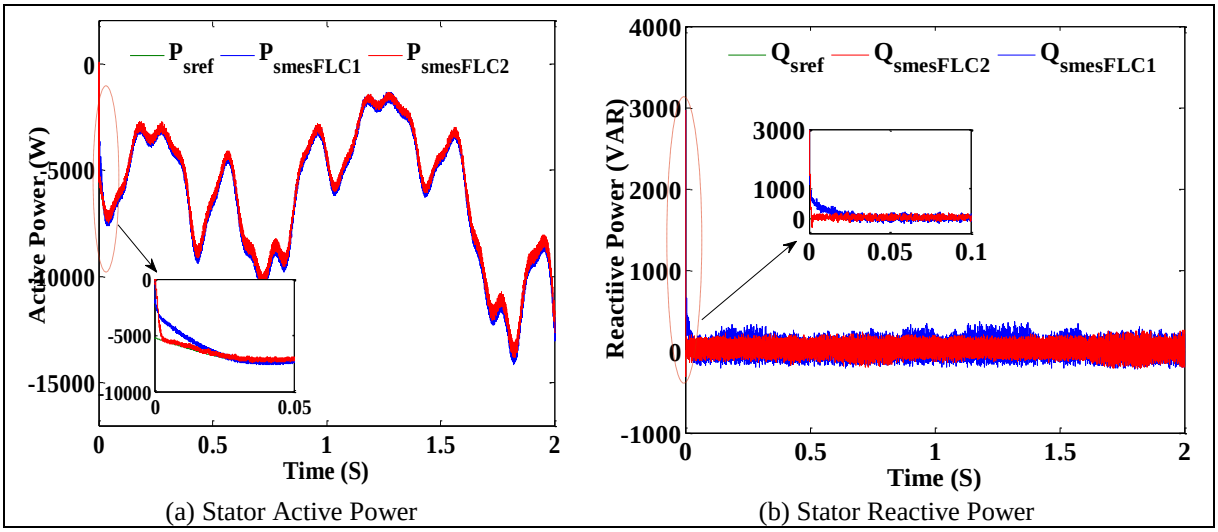

(a) Stator Active Power (b) Stator Reactive Power

Figure 10: Indirect control of1 the DFIG (Real wind profile).
Source: Authors, (2025).

We assessed the decoupling of reference active and reactive powers under varying wind speed conditions by obtaining suitable dynamics.

To optimize wind turbine efficiency, the MPPT control method enables the stator's active power to correspond with the turbine's mechanical power, which fluctuates with wind variations. The reactive power is null as we aim for operating at a unity power factor.

The results clearly indicate that the T2FLC provides enhanced performance regarding maximum power tracking and system stability restoration.

Compared to the two controllers, the T2FLC demonstrates exceptional performance in terms of rise time, overshoot, and settling time. It is particularly notable for its low overshoot when compared to the T1FLC controller. However, it does show a noticeable undershoot.

Table 3 provides a summary of the dynamic and static performances of the two controllers.

Table 3: Step response of the controllers.

Active power				
Performances	**Direct control**		**Indirect control**	
	T1FLC	**T2FLC**	**T1FLC**	**T2FLC**
Rise time(s)	1.7018e+5	7.0800e+4	1.7006e+5	1.7003e+5
Overshoot (%)	14.7001	21.6464	15.1533	16.3602
SettlingTime	1.9997e+5	1.9990e+5	1.9997e+5	1.9995e+5
Reactive power				
Performances	**Direct control**		**Indirect control**	
	T1FLC	**T2FLC**	**T1FLC**	**T2FLC**
Rise time(s)	83.5158	951.5273	170.5732	77.8431
Overshoot (%)	2.1221e+3	0.8012e+3	1.7387e+3	1.7233e+3
SettlingTime	2.0000e+5	2.0000e+5	2.0000e+5	2.0000e+5

Source: Authors, (2025).

VI. CONCLUSIONS

This study designs a Type-2 Fuzzy Logic Controller (T2FLC) to independently regulate active and reactive power exchange in a Doubly Fed Induction Generator (DFIG)-based Wind Energy Conversion System (WECS). The research further evaluates and contrasts the efficacy of Type-1 and Type-2 fuzzy logic control strategies to identify optimal solutions for maintaining reliability and adaptability amid parameter fluctuations and shifting operational setpoints. Rigorous testing was conducted under consistent operating conditions, analyzing both steady-state and transient behaviors of the system. The primary objective is to identify controllers that deliver consistent stability and high performance across varying scenarios. Results conclusively demonstrate that the T2FLC outperforms its Type-1 counterpart (T1FLC) in the examined WECS, exhibiting superior dynamic response, robustness, and operational effectiveness under diverse conditions.

VII. APPENDIX

Table 4: Wind power parameters.

Components	Parameter Name	Rated Value
P	Nominal power	1.5 MW
U	Nominal voltage	380/690 V
F	Frequency	50 HZ
n	Rotation speed	1440 tr/min
R	Wind Radius	35.25 m
G	speed multiplier gain	90
Rs	Stator Resistance	0.455 Ω
Rr	Rotor Resistance	0.62 Ω
l_{0s}	Stator leakage inductance	0.084 H
l_{0r}	Rotor Leakage Inductance	0.081 H
M	Main inductance	0.078 H
j	Inertial	0.3125 kg m^2
f	Viscous coefficient	6.73.10^{-3}N.m.s^{-1}
p	Pole pairs number	2

Source: Authors : [19].

VIII. AUTHOR'S CONTRIBUTION

Conceptualization: Kouadria Mohamed Abdeldjabbar, Kouadria Selman and Bouzid Mohamed Amine.
Methodology: Kouadria Mohamed Abdeldjabbar, Kouadria Selman and Bouzid Mohamed Amine.
Investigation: Kouadria Mohamed Abdeldjabbar, Kouadria Selman and Bouzid Mohamed Amine.
Discussion of results: Kouadria Mohamed Abdeldjabbar, Kouadria Selman and Bouzid Mohamed Amine.
Writing – Original Draft: Kouadria Mohamed Abdeldjabbar.
Writing – Review and Editing: Kouadria Mohamed Abdeldjabbar and Bouzid Mohamed Amine.
Resources: Kouadria Selman.
Supervision: Kouadria Selman and Bouzid Mohamed Amine.
Approval of the final text: Kouadria Mohamed Abdeldjabbar, Kouadria Selman and Bouzid Mohamed Amine.

IX. REFERENCES

[1] Bošnjaković, M., Katinić, M., Santa, R., & Marić, D. (2022). Wind Turbine Technology Trends. Applied Sciences, 12(17), 8653. https://doi.org/10.3390/app12178653

[2] Sukanta Roga, Shawli Bardhan, Yogesh Kumar, Sudhir K. Dubey, Recent technology and challenges of wind energy generation: A review, Sustainable Energy Technologies and Assessments, Volume 52, Part C, 2022, 102239, https://doi.org/10.1016/j.seta.2022.102239.

[3] SINGH, Pradeep, ARORA, Krishan, et RATHORE, Umesh C. Energy Storage Systems with Artificial Intelligence Techniques in Doubly Fed Induction Generator Based Wind Energy Conversion System—An Overview. Intelligent Circuits and Systems for SDG 3–Good Health and well-being, p. 403-418.

[4] B. Desalegn, D. Gebeyehu, et B. Tamrat, « Wind energy conversion technologies and engineering approaches to enhancing wind power generation: A review », Heliyon, vol. 8, nº 11, nov. 2022, https://doi:10.1016/j.heliyon.2022.e11263.

[5] Tan, J. D., Chang, C. C. W., Bhuiyan, M. A. S., Nisa'Minhad, K., & Ali, K. (2022). Advancements of wind energy conversion systems for low-wind urban environments: A review. Energy Reports, 8, 3406-3414. https://doi.org/10.1016/j.egyr.2022.02.153

[6] S. R. Mosayyebi, S. H. Shahalami and H. Mojallali, "Fault Ride-Through Capability Improvement in a DFIG-Based Wind Turbine using Modified ADRC," in Protection and Control of Modern Power Systems, vol. 7, no. 4, pp. 1-37, October 2022, https://doi:10.1186/s41601-022-00272-9

[7] Verma, P., K., S., & Dwivedi, B. (2021). Comprehensive investigation on doubly fed induction generator-Wind farms at fault ride through capabilities: technical difficulties and improvisations. Energy Sources, Part A: Recovery, Utilization, and Environmental Effects, 47(1), 3621–3653. https://doi.org/10.1080/15567036.2020.1857476

[8] Sonam Gupta, Anup Shukla, Improved dynamic modelling of DFIG driven wind turbine with algorithm for optimal sharing of reactive power between converters, Sustainable Energy Technologies and Assessments, Volume 51, 2022, https://doi.org/10.1016/j.seta.2022.101961.

[9] Sahu, S., & Behera, S. (2022). A review on modern control applications in wind energy conversion system. Energy & Environment, 33(2), 223-262. https://doi.org/10.1177/0958305X21995929

[10] S. Krishnama Raju and G. N. Pillai, "Design and Implementation of Type-2 Fuzzy Logic Controller for DFIG-Based Wind Energy Systems in Distribution Networks," in IEEE Transactions on Sustainable Energy, vol. 7, no. 1, pp. 345-353, Jan. 2016, https://doi:10.1109/TSTE.2015.2496170.

[11] Kanasottu Anil Naik, Chandra Prakash Gupta, Eugene Fernandez, Design and implementation of interval type-2 fuzzy logic-PI based adaptive controller for DFIG based wind energy system, International Journal of Electrical Power & Energy Systems, Volume 115, 2020, https://doi.org/10.1016/j.ijepes.2019.105468.

[12] Moradi, H., Alinejad-Beromi, Y., Yaghobi, H. and Bustan, D. (2019), Sliding mode type-2 neuro-fuzzy power control of grid-connected DFIG for wind energy conversion system. IET Renewable Power Generation, 13: 2435-2442. https://doi.org/10.1049/iet-rpg.2019.0066

[13] Hosseini, S. M., & Manthouri, M. Type 2 adaptive fuzzy control approach applied to variable speed DFIG based wind turbines with MPPT algorithm. Iranian Journal of Fuzzy Systems, 19(1), 31-45. (2022), https://doi:10.22111/ijfs.2022.6549

[14] F. Amrane, A. Chaiba and B. Francois, "Suitable power control based on type-2 fuzzy logic for wind-turbine dfig under hypo-synchronous mode fed by multi-level converter," 2017 5th International Conference on Electrical Engineering - Boumerdes (ICEE-B), Boumerdes, Algeria, 2017, pp. 1-6, https://doi:10.1109/ICEE-B.2017.8191983.

[15] Zouggar, E. O., Chaouch, S., Abdeslam, D. O., & Abdelhamid, L. (2019). Sliding control with fuzzy type-2 controller of wind energy system based on doubly fed induction generator. Instrumentation, Mesure, Métrologie, 18(2), 137-146. https://doi:10.18280/i2m.180207

[16] Kouadria, Selman, et al. "Improved control strategy of DFIG-based wind turbines using direct torque and direct power control techniques." Journal of Renewable and Sustainable Energy 10.4 (2018).

[17] Balat, M. (2009). A Review of Modern Wind Turbine Technology. Energy Sources, Part A: Recovery, Utilization, and Environmental Effects, 31(17), 1561–1572. https://doi.org/10.1080/15567030802094045

[18] Kouadria, Abdeldjabbar Mohamed, et al. Power Quality Enhancement in Off-Grid Hybrid Renewable Energy Systems Using Type-2 Fuzzy Control of Shunt Active Filter. In: Bi, Y., Kapoor, S., Bhatia, R. (eds) Intelligent Systems and Applications. Studies in Computational Intelligence, vol 650. Springer, Cham 2016. https://doi.org/10.1007/978-3-319-33386-1_17

[19] Kouadria, M. A., Kouadria, S., & Chaib, H. (2024). Sliding mode control for doubly fed induction generators system-based a wind turbine. STUDIES IN ENGINEERING AND EXACT SCIENCES, 5(2), e7199. https://doi.org/10.54021/seesv5n2-139

[20] X. Liu and X. Kong, "Nonlinear Model Predictive Control for DFIG-Based Wind Power Generation," in IEEE Transactions on Automation Science and Engineering, vol. 11, no. 4, pp. 1046-1055, Oct. 2014, https://doi:10.1109/TASE.2013.2284066

[21]I. Ahmed, G. Jeon and F. Piccialli, "From Artificial Intelligence to Explainable Artificial Intelligence in Industry 4.0: A Survey on What, How, and Where," in IEEE Transactions on Industrial Informatics, vol. 18, no. 8, pp. 5031-5042, Aug. 2022, https://doi:10.1109/TII.2022.3146552.

[22] M. A. Hannan, J. A. Ali, P. J. Ker, A. Mohamed, M. S. H. Lipu and A. Hussain, "Switching Techniques and Intelligent Controllers for Induction Motor Drive: Issues and Recommendations," in IEEE Access, vol. 6, pp. 47489-47510, 2018, https://doi:10.1109/ACCESS.2018.2867214
.
[23] VERNON, David. Artificial cognitive systems: A primer. MIT Press, 2014.

[24] N. N. Karnik, J. M. Mendel and Qilian Liang, "Type-2 fuzzy logic systems," in IEEE Transactions on Fuzzy Systems, vol. 7, no. 6, pp. 643-658, Dec. 1999, https://doi:10.1109/91.811231.

[25] Kouadria, M. A., Allaoui, T., & Denaï, M. (2015). High performance shunt active power filter design based on fuzzy interval type-2 control strategies. Int. Rev. Autom. Control (I. RE. A. CO.), 8(5), 322.

[26] Kouadria, A. M., Allaoui, T., Denaï, M., & Pissanidis, G. (2015, November). Grid power quality enhancement using fuzzy control-based shunt active filtering. In 2015 SAI Intelligent Systems Conference (IntelliSys) (pp. 646-650). IEEE.

Journal of Engineering and Technology for Industrial Applications

ITEGAM-JETIA

Manaus, v.11 n.53, p. 162-169. May/June., 2025.
DOI: https://doi.org/10.5935/jetia. v11i53.1652

ISSN ONLINE: 2447-0228

RESEARCH ARTICLE OPEN ACCESS

APPLICATION OF MACHINE LEARNING FOR REAL-TIME PHISHING ATTACK DETECTION

Andrina Dsouza[1], Jimit Mehta[2], Prajwal Naik[3], Akshay Agrawal[4], Sanketi Raut [5]

[1,2,3] Department of Information Technology, Universal College of Engineering, University of Mumbai, Vasai, India.
[4,5] University of Mumbai, Mumbai. India.

[1]https://orcid.org/0009-0006-2743-840X, [2]https://orcid.org/0009-0009-1689-2158, [3]https://orcid.org/0009-0008-7885-3210, [4]https://orcid.org/0000-0002-8722-7181, [5]https://orcid.org/0009-0007-1511-8019

Email: andrinarosanne05@gmail.com, jimitmehta553@gmail.com, naikprajwal20@gmail.com, akshay1661@gmail.com, sanketiraut28@gmail.com

ARTICLE INFO

Article History
Received: February 20, 2025
Revised: May 20, 2025
Accepted: June 15, 2025
Published: June 30, 2025

Keywords:
Phishing,
Machine Learning,
Python,
Random Forest,
Real-time detection.

ABSTRACT

Over the years, the Internet has been exploited to carry out a range of cyber attacks, with phishing being the most prominent one. Increasingly sophisticated techniques of phishing have threatened the security of many Internet-based systems. To be able to detect suspicious websites is a potential first step in reducing the amount of phishing attacks occurring daily. This paper outlines the development and implementation of a platform to detect phishing websites. It highlights the pressing need for early detection of possible phishing attacks to prevent data theft, frauds, etc. The system uses machine learning algorithms to distinguish legitimate websites from phishing websites and generate a prediction to be used for the platform. A user interface is implemented to have two parts. The first part includes a text field for entering a URL, which the ML model processes to give a prediction that gets displayed to the user. Another module gathers URLs as they arrive from an API and scans them for potentially suspicious websites. The final ML model, a Random Forest classifier with 27 estimators, had an accuracy of 96.12% and F1 score of 95.94%. Future enhancements and research directions are also discussed for further development of the system.

I. INTRODUCTION

A phishing attack is a form of fraud in which attackers lure victims into a fake website, manipulating them to enter sensitive details so they can be stolen. It is a prominent cyber attack, responsible for huge financial losses, data theft, users losing trust over Internet services [1], [2] and damaging the reputation of well-known industries [3]. Moreover, such attacks have shown a drastic increase in recent years [4], [5].

In the modern landscape, the Internet is being used for a wide variety of tasks, including conducting transactions between a retailer and a buyer of a product, mobile banking, healthcare, entertainment, social networking and education [6]. All such domains share one aspect in common: they require the user's data in order to operate properly. Usually, web platforms or mobile applications are used to facilitate communication between different parties, and allow sharing and storing important information so they can be accessed anywhere at any time [7]. In a phishing attack, attackers seek to exploit the trust that users have to certain entities, particularly banks and government websites [8], [9].

Although most attackers employ fake emails for phishing, there are many different types of phishing, such as:

1) **Smishing**: Uses SMSs to lure victims to fake websites.
2) **Spear Phishing**: Highly targeted phishing; the target can be an individual or an organization [8].
3) **Vishing**: Steals sensitive data through voice calls.
4) **Whaling**: Targets high-profile individuals, such as celebrities or higher authorities in an organization [8].
5) **Pop-up Phishing**: Uses fake pop-ups with a seemingly urgent tone (eg. a security flaw detected in the victim's computer) to trick victims into downloading malware.
6) **Social Engineering**: Pressures the victim into revealing sensitive information.

Figure 1 depicts a typical phishing attack, which takes place as follows: (1) A fake email or SMS is sent to the victim. The attacker, posing as a genuine entity like a well-known brand or the victim's bank, sends the victim a message that has false offers or an urgent action to be taken, that involves entering sensitive credentials (eg. credit card numbers, account numbers, passwords, etc.). (2) The victim inherently trusts the bank or the brand, making them inadvertently open the email and read it. (3) The victim then opens the attached link.]

They are sent to a fake website that was carefully constructed by attackers to make it indistinguishable from the real website [10]. There, the victim enters their credentials as demanded. (4) The credentials are sent to the attackers and hence, they get stolen. (5) The attacker may use the stolen credentials to impersonate the victim and log in to another website to possibly carry out malicious activities.

These may include making a transaction of a very large amount, posting explicit or offensive messages on social media sites or even tampering with stored data in online repositories like Google Drive. The outcome of phishing attacks can range from identity theft to severe organization-level losses. The attacker can use stolen credentials of the victim to impersonate the victim and conduct fraudulent transactions using them [10]. If employee credentials, especially those of higher-level employees are stolen, the attacker can gain access to highly sensitive organizational data and cause data breaches.

The rise of evolving phishing techniques makes it extremely difficult to develop a reliable security system to work against all of them [8], [11]. Detecting suspicious websites before the victim loses their data can ensure safer browsing. Hence, there is a need to develop an automated system that can reliably distinguish between genuine websites and phishing websites [9]. Machine Learning (ML) is one of the techniques by which phishing URLs can be inspected for their authenticity.

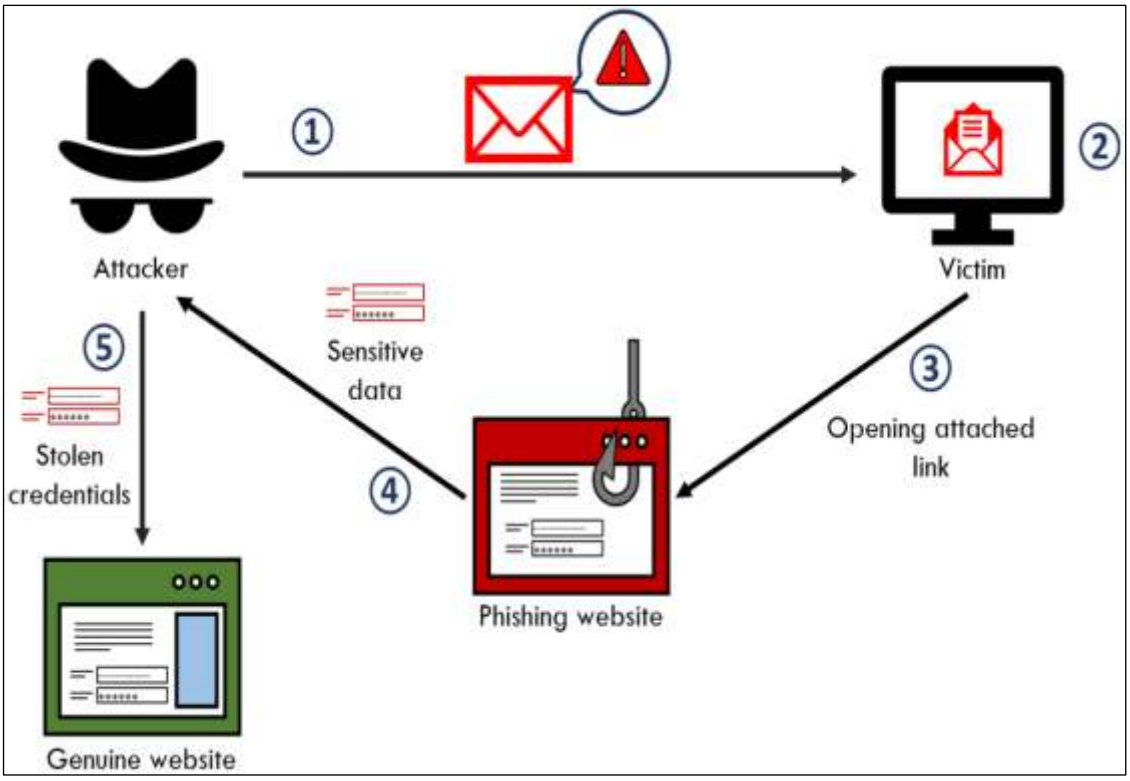

Figure 1: A Typical Phishing Attack.
Source: Authors, (2025).

I.1 OBJECTIVES

The objectives of this paper are as follows:

1. **To utilize website URL data using appropriate datasets**: Finding the best dataset that has all the necessary attributes to describe website URLs, while also allowing for appropriate ML usage.
2. **To implement an ML algorithm to distinguish phishing websites from genuine ones**: Finding the appropriate algorithm that gives optimal performance, particularly accuracy, to allow the system to be as reliable as possible.
3. **To design and develop a User Interface (UI)**: Using Python Flask to develop an application that allows users to enter a potentially suspicious URL to check whether it is a genuine or a phishing URL.
4. **To develop a platform for real-time phishing detection**: To utilize API calls from a source of website URLs to display phishing URLs as they arrive in real time.
5.

I.2 LITERATURE SURVEY

The paper [1] proposes a hybrid model for phishing detection. Its aim is to counter the problems of relying on a single model for classification, since different models have their own benefits and problems. The two best algorithms were found, then combined into a hybrid model. The top-performing models were found to be SVM (Simple Vector Machine), Gradient Boost, Random Forest (RF) and Neural Networks. The approach used is better than traditional approaches for detection; the weaknesses of one algorithm would be balanced by the strengths of another algorithm, hence stacking these together created a better-performing approach.

The study [2] explores different ML algorithms to detect spam emails. The dataset included nine features to distinguish legitimate emails from spam and phishing emails. Each of these features described emails and their content by presence of specific words (eg. 'bank', 'paypal'), the number of attached links, hidden JavaScript and other relevant features. Of the five algorithms tested, SVM and RF were the best-performing models. The method offers high accuracy, and limits the number of features to the most important ones, giving good performance.

The study [3] proposes a stacked model to detect phishing websites, combining multiple ML algorithms. The most important features were selected through feature reduction. The obtained features were then fed to a multitude of algorithms, including Random Forest, Neural Network, Bagging and SVM. The best-performing models were then stacked. The results were two stacked models: Stacking1, a combination of RF, bagging and Neural Network; and Stacking2, a combination of RF, bagging and k-Nearest Neighbour. Both gave high classification accuracy, but Stacking1 proved to be the best stacked model, giving the highest accuracy of 97.4%.

Paper [4] explores different ML algorithms to develop a phishing detection model and designs a user interface implementing the model. The algorithms tested were RF, ANN and KNN. All tested models showed extremely high accuracy. The best algorithm, the RF model, was then integrated into a Django-based web application. The interface displays a field for the user to enter a URL, which would then be processed by the ML model to return a prediction. A feedback mechanism was also implemented, allowing the user to directly state if the prediction was correct or not, and how can the site be further improved. In this way, the website facilitates real-time phishing detection and allows user feedback to further refine future predictions.

The study [5] aimed to develop an improved dataset intended for URL-based phishing detection. It focused on features within URLs to distinguish malicious websites. The dataset was developed by combining various reliable sources, including OpenPhish. 41 features were generated: 31 from previous studies and 10 novel features. These features describe the characteristics of the URL itself, the domain, and any subdomains. They also include Shannon entropies (degree of randomness of characters) of the URL and domain. They, too, can help identify phishing websites, as they tend to have higher Shannon entropies. The dataset does not include features related to the actual content of the web pages, which makes it faster to process while sacrificing some accuracy. However, it can still be relied on for research.

I.3 EXISTING SYSTEMS

Given the particularly common occurrence of email phishing [3],[4], email clients employ spam filtering to discard any suspicious emails. Email content is analyzed, especially links and attachments, to verify the authenticity of the email being received [6]. Such systems have a major drawback: they may miss targeted emails from social engineering attacks. These attacks seek a specific target rather than mass-sending to a large number of receivers.Hence, the email filter may pass the malicious emails as legitimate, especially ones that appear to be so. Moreover, attackers can adjust the language and content of their phishing email to avoid detection by many email filters.

Identifying phishing websites has multiple approaches. Some systems rely on examining the domain of the website, checking whether the secure HTTPS protocol is used instead of HTTP [6]. While some phishing websites do use the insecure HTTP protocol, attackers are increasingly switching to HTTPS to avoid detection and appear trustworthy.

The most common phishing detection approach is called 'Blacklisting' [1], [6], [8], [10]. Here, a list of suspicious websites is created and maintained. It uses up heavy amounts of computing resources, since each website must be first registered and then verified to be a phishing website. Moreover, with the constant emergence of new phishing websites, a blacklist would continue to grow and become difficult to maintain [8]. A similar approach called 'Whitelisting' lists all authentic sites, but is similarly difficult to maintain.

Anti-phishing sites like PhishTank allow users to identify suspicious websites that then get added into the growing list of phishing websites. However, as of today, new users cannot register into the site; the site was abused in 2020, leading to the removal of this feature. Existing users can continue submitting potential phishing websites.

The popularity of ML algorithms and availability of multiple datasets of phishing websites makes it possible to explore the best-performing algorithms and implement a predictive detection based on the characteristics of the URL or web page content, depending on the requirements [8], [11].

I.4 PROBLEM STATEMENT

Phishing attacks continue to evolve and become increasingly difficult to detect. Many phishing attacks occur as a result of the user having poor knowledge of phishing websites, emails, or SMSs. They do not always check for the authenticity of domains, or whether any organization actually sends them urgent messages. If a victim is unable to recognize a phishing website at the earliest, the loss of valuable data cannot be avoided.

It should be possible to scan URLs in real-time and detect phishing websites without the risk of opening suspicious links. There are numerous features of URLs that would have to be examined in order to distinguish a genuine website from phishing sites [10]. Also, the user should be alerted to any detected phishing websites.

This paper aims to utilize Machine Learning to predict whether a URL is genuine or phishing. The choice of dataset, algorithm used and its performance are important factors in accurately predicting the nature of the URL. A probability-based prediction method can help users identify the likelihood that a website is phishing or genuine. The UI consists of two simple modules: one for predicting the nature of a user-entered URL, and another for real-time fetching of URLs from an API to detect phishing websites.

II. PROPOSED SYSTEM

The system contains two web pages. The first page features an input field to accept user-entered URLs. The second page collects website URLs from an API, namely OpenPhish. In both cases, the ML model returns a probability-based prediction, which is displayed as a percentage likelihood that a URL is genuine or phishing. The system is developed using Python, Flask, HTML, CSS and Bootstrap. The main structure of the web page is developed using HTML, CSS and Bootstrap. Python code for the ML model was implemented using Jupyter Notebook. The model and front-end code were integrated using Python Flask to develop a simple web interface.

The choice of ML algorithm is made to be suitable for large data, have good accuracy, and the minimum possible false negative rate. The dataset was obtained from paper [5].

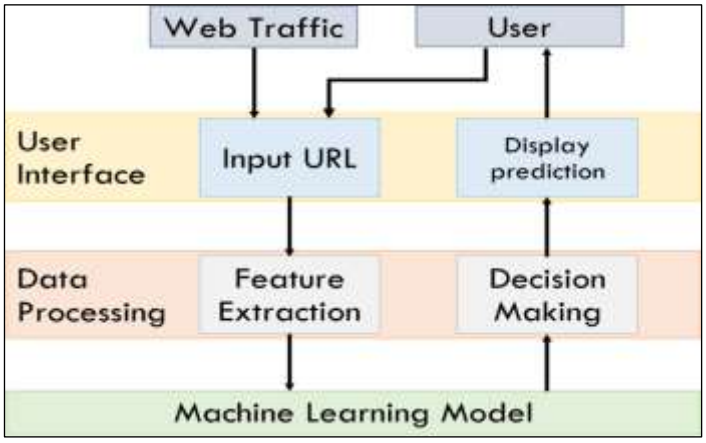

Figure 2: System Architecture.
Source: Authors, (2025).

In Figure 2, the system architecture of the proposed system is shown. The User Interface (UI) features two separate modules to obtain input URLs: in one module, the user manually enters a URL into an input field, and in the second, URLs are fetched from OpenPhish API. The URLs are then passed into the Data Processing layer, where the features of the URL are extracted.

These extracted features are passed to the ML algorithm, which returns a probability-based prediction: the likelihood that a given website link is phishing or genuine. Based on this value, the label for the website URL is decided. The predicted value lies between 0 and 1, so it is then converted into a percentage value which is then displayed to the user along with the label for the URL (either 'Genuine' or 'Phishing').

III. METHODOLOGY

III.1 DATASET CHARACTERISTICS

The dataset, obtained from [5], has 41 features, encompassing the entire URL, its domains, and subdomains. The target feature is 'Type', which labels each tuple as '1' for phishing and '0' for legitimate.

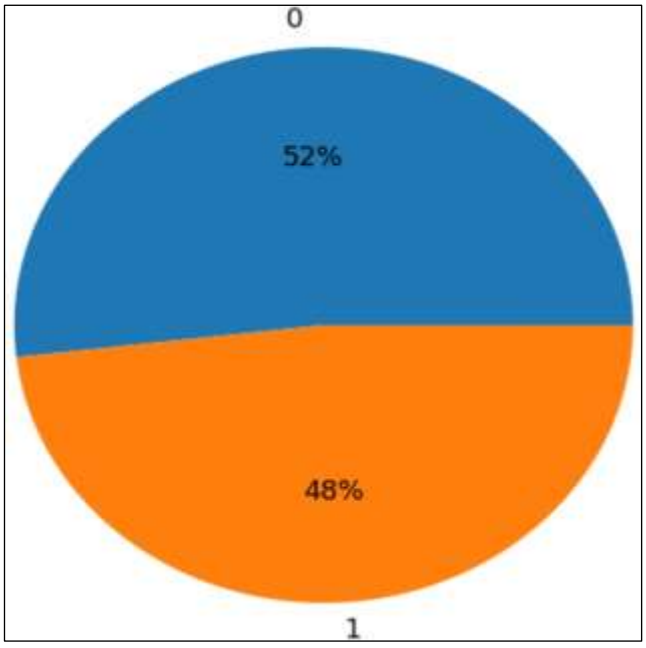

Figure 3: Data Distribution in Obtained Dataset.
Source: Authors, (2025).

The dataset has 247,950 tuples; 128,541 of them are of type 0, while the remaining 119,409 are of type 1. Figure 3 shows the distribution of the data within the dataset. It shows that the dataset is nearly balanced, with type 0 comprising 52% of the dataset, and type 1 comprising the remaining 48%. This reduces the chances of biased ML results. Hence, the dataset can be used without resorting to any sampling techniques.

The dataset contains 10 new features in total, but two particular ones are the Shannon Entropies of the URL and the domain. Shannon Entropy is defined as the randomness or uncertainty of the domain. If P_i is the probability of the i^{th} character in the domain, Shannon Entropy is given by:

$$H(i) = -\sum P_i * \log_2(P_i) \quad (1)$$

The dataset was free from null or missing values, eliminating the need for any steps to handle missing values. However, the dataset contained three attributes that had no non-zero values:
1) having_hyphen_in_subdomain,
2) average_number_of_hyphens_in_subdomain
3) having_path.

To compare the performance of each ML algorithm, two versions of the dataset were created:
1) **dataset_A**: the original dataset, with all 41 attributes.
2) **dataset_B**: the dataset with the above three attributes removed, leaving 38 attributes.

Each dataset was split in a 70:30 ratio for training and testing tuples, leaving 74,385 testing tuples.

III.2 ML ALGORITHMS TESTED

On each of the two versions of the dataset, the following ML models were tested:

1) **Decision Tree Classifier**: This is a supervised classification algorithm that creates a tree-like structure to classify tuples. Each non-leaf node is a feature that is tested, each branch is the result of testing that feature, and each leaf node is a class label (in this case, 0 or 1). Since this dataset contains purely numerical values, the nodes are split based on a threshold value for each feature, such as $>$ $\geq$, $\leq$ or $<$.

2) **AdaBoost**: This is a popular variant of the Boosting algorithm; it combines together a number of 'weak learners', which are ML models trained incrementally on the dataset [12]. Each tuple is assigned a weight, which indicates how difficult it is to classify. All weights are equal at the start of the training. When a model has been trained and tested, the weights of misclassified tuples are increased, while those of tuples that were correctly classified are decreased. The tuples with updated weights are used to train the next model. Once all the base models have been trained, they will have a weight assigned to their vote based on how well they performed. To classify an unknown URL, each model will return a vote for its class label, which is combined with its weight. The class with the highest weighted sum will be labelled final. Here, the algorithm was used with 100 estimators and a learning rate of 1.

3) **Gradient Boosting**: It is another variant of the Boosting algorithm, where each new base model must reduce the errors produced by the previous model. Since there are only two class labels in this dataset, the loss function used is log-loss, determining the deviation of the predicted label from the actual label.

4) **Artificial Neural Network**: This supervised learning technique relies on Artificial Neurons, which are information processing systems analogous to biological neurons. The three main layers in an ANN are the input layer which accepts raw inputs, hidden layers which process the input to pass to subsequent layers, and output layers which yield the final class label. Here, three hidden layers were used, each using Rectified Linear Unit (ReLU) as their activation function, and having 40, 30, and 20 neurons respectively. The output layer used the Sigmoid activation function. The number of training epochs was chosen as 100.

5) **Random Forest Classifier**: It is a popular ensemble method for ensuring high accuracy while balancing the variances introduced by individual classifiers. It is a variation of the Bagging (Bootstrap Aggregating) algorithm. The base classifiers, which are decision trees, are trained in parallel on the dataset. To implement it for this dataset, an appropriate number of decision trees must be discovered so that the maximum accuracy can be achieved. Then the ensemble can be trained and tested to predict a label based on majority voting; each base decision tree returns a class label for the URL, and the label with the highest votes is the final label. Here, dataset_A was used to repeatedly train the algorithm using different numbers of estimators from 1 to 40 trees. The training and testing accuracies were then plotted to find the best number of estimators.

After each model was trained on the datasets, their performance metrics were computed. Since the task performed is a binary classification, the tuples with phishing URLs (Type '1' in the dataset) are considered as the 'positive' tuples denoted by 'P'. The genuine URLs (Type '0' in the dataset) are considered 'negative' tuples, denoted by 'N'. There are four possibilities of a prediction of the model:

1) **True Positive (TP)**: The given URL was correctly labelled as 'Phishing' or '1'.
2) **True Negative (TN)**: The given URL was correctly labelled as 'Not Phishing' or '0'.
3) **False Positive (FP)**: A genuine URL was incorrectly labelled as 'Phishing' or '1'.
4) **False Negative (FN)**: A phishing URL was incorrectly labelled as 'Not Phishing' or '0'.

False negatives have potentially disastrous consequences, since a phishing URL may be marked as genuine. Hence, they should be minimized as much as possible. Hence, the choice of the final ML model will not just factor in accuracy, but also the false negative rate. A model of a small size is preferred to allow it to be loaded faster in the web page. In Python, when an ML model is used to give a prediction, there are two possible ways to get a prediction: a class label, achieved using the predict() method, and a probability-based prediction, achieved using the predict_proba() model. For this system, the latter is used.

III.3 DEVELOPING THE USER INTERFACE

Once the best model is obtained, it is to be used to predict a URL's nature based on its features. This means that for every URL being inputted by the user or obtained from the API, all features of the URL must be extracted, matching their order in the original dataset. Hence, a Python program was written to perform the following:

1) **Compute Shannon Entropy of Input**: The formula from Equation (1) is applied to obtain the Shannon Entropy of the input URL or extracted domain.
2) **Check for Repeated Digits**: The URL is examined for repeated digits, returning '1' if they exist, otherwise '0'.
3) **Extract all URL Features**: Each of the 40 features are extracted from the URL; the first two functions are called to return their respective features. These are formed into a Python dictionary, i.e. as key-value pairs. The values are appended into a Python list, and finally converted into a Pandas DataFrame.
4) **Fetch URLs from an API**: The OpenPhish API is used to obtain URLs in real-time to be run through the algorithm.

The interface web pages are developed using HTML, CSS, Bootstrap and JavaScript. The input-based page is developed as a simple input field, with the results of the prediction to be displayed below the field. The real-time detection page implements JavaScript and Bootstrap to render cards displaying the URLs and their nature.

The application is developed using Python Flask. First, the final ML model is loaded into the application. Then, as the user interacts with the application, it displays the input and output to the user.

III.4 SYSTEM FLOW

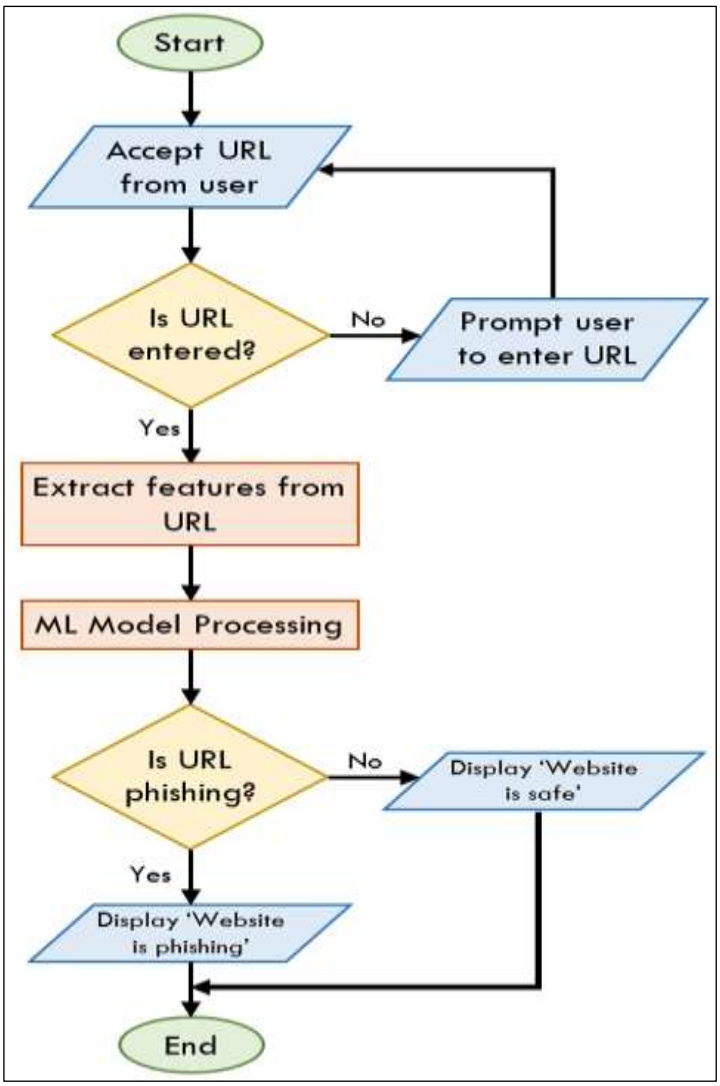

Figure 4: System Flowchart.
Source: Authors, (2025).

Figure 4 shows the system flow for the input-based phishing detection. First, a user has to enter a URL that they think is suspicious. The system checks for the field being filled, sending an alert to fill the field if left empty. The URL entered is

forwarded to the feature extraction process, which creates a complete list of URL features. These are passed to the ML model, which returns a prediction. This prediction is represented as two probabilities: the probability of the website being genuine, and the probability of the website being phishing. The prediction is based on the probability that is greater; the user is shown the prediction and the two probabilities.

IV. RESULTS AND DISCUSSIONS

IV.1 PERFORMANCE METRICS

All six ML algorithms were tested on the two created datasets to determine the one with the best classification metrics. The metrics computed for each model were as follows:

1) **Accuracy**: This is the proportion of test tuples that were labelled correctly, i.e. out of the total test tuples, how many of them were correctly labelled 0 or 1. Accuracy is given by:

$$Accuracy = \frac{TP + TN}{P + N} \quad (2)$$

2) **Recall**: This is the proportion of positive tuples that were labelled correctly, i.e. out of the total phishing URLs, how many of them were correctly labelled 1. Recall is given by:

$$Recall = \frac{TP}{P} \quad (3)$$

3) **Precision**: It is a measure of exactness, and is the proportion of tuples labelled positive by the model that are actually positive. In other words, since the ML model labels TP+FP tuples as 1, precision measures the proportion of TP tuples. Precision is given by:

$$Precision = \frac{TP}{TP + FP} \quad (4)$$

4) **F1 Score**: This measure combines the Recall and Precision to give a single result. It is the harmonic mean of the Recall and Precision, and is given by:

$$F1\ Score = \frac{2 * Precision * Recall}{Precision + Recall} \quad (5)$$

As the classification task involved two classes, a confusion matrix was developed after each algorithm was tested. This structure compares the actual class of the tuple to the labels predicted by the model. It includes each of the four labelling types, which are TP, FP, FN and TN.

Table 1: Performance Metrics of Tested Algorithms.

Algorithm	dataset_A				dataset_B			
	Accuracy	Precision	Recall	F1 Score	Accuracy	Precision	Recall	F1 Score
AdaBoost	80.98%	81.94%	77.6%	79.71%	80.98%	81.94%	77.6%	79.71%
Gradient Boost	86.31%	88.1%	82.75%	85.34%	86.31%	88.1%	82.74%	85.34%
ANN	90.41%	93.01%	86.57%	89.68%	90.08%	91.15%	87.95%	89.52%
Decision Tree	94.55%	94.5%	94.16%	94.33%	94.57%	94.56%	94.14%	94.36%
Random Forest	96.12%	96.56%	95.33%	95.94%	96.1%	96.59%	95.27%	95.93%

Source: Authors, (2025).

Table 1 shows the final performance metrics of all the tested algorithms. Out of the five, the only algorithms to give an accuracy of 90% or higher were ANN, Decision Tree, and Random Forest with 27 estimators.

The Random Forest Classifier was initially tested with 10 estimators. The accuracies shown for dataset_A and dataset_B were 95.52% and 95.61% respectively. Given the high initial accuracy, the model was then tested using dataset_A with varying numbers of estimators. The graph of accuracies for the tested classifier is shown in Figure 5. The testing accuracy peak occurs between 25 and 30 estimators, and the position of the peak implied that the best number of estimators is 27.

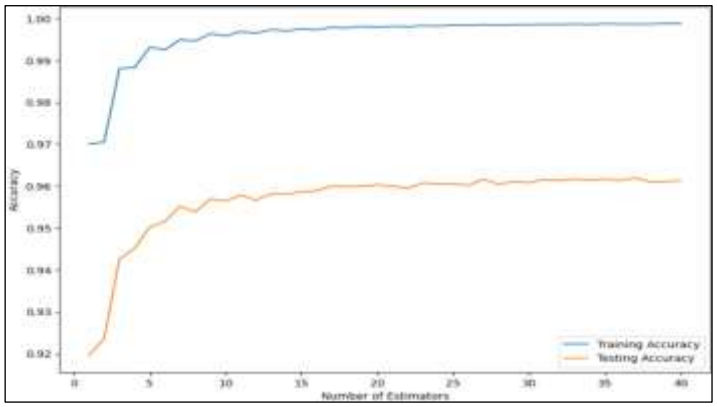

Figure 5: Accuracy Graph for Random Forest Classifier Measured from 1 to 40 Estimators
Source: Authors, (2025).

Using 27 estimators, a Random Forest Classifier was developed for each dataset. This was followed by testing the classifier and generating a confusion matrix.

Figure 6 shows the confusion matrix generated for the Random Forest for dataset_A, indicating that most tuples were correctly classified. There were 1,217 false positives and 1,672 false negatives.

Figure 7 shows the confusion matrix for dataset_B. It has a similar amount of false positives and false negatives, at 1,166 and 1,701 respectively.

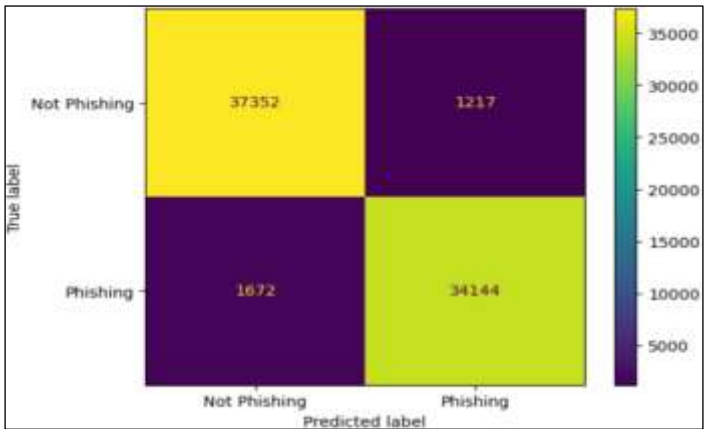

Figure 6: Confusion Matrix for Random Forest for dataset_A
Source: Authors, (2025).

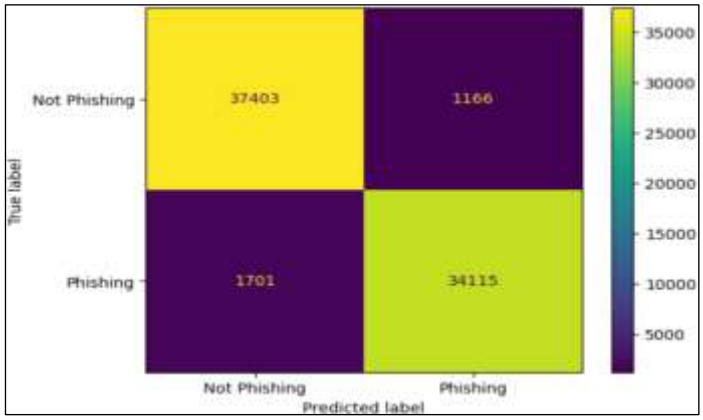

Figure 7: Confusion Matrix for Random Forest for dataset_B
Source: Authors, (2025).

For dataset_B, Random Forest showed a slightly better accuracy, precision and F1 score than for dataset_A. However, the Recall metric was slightly lower, at 95.27%, compared to 95.33% for dataset_A. This was also reflected in the confusion matrices, showing that the false negative rate was slightly lower for the original dataset. Based on the good performance and overall lower false negative rates, the final classification model chosen was Random Forest, using all 41 attributes and 27 base classifiers.

IV.2 USER INTERFACE INTERACTION

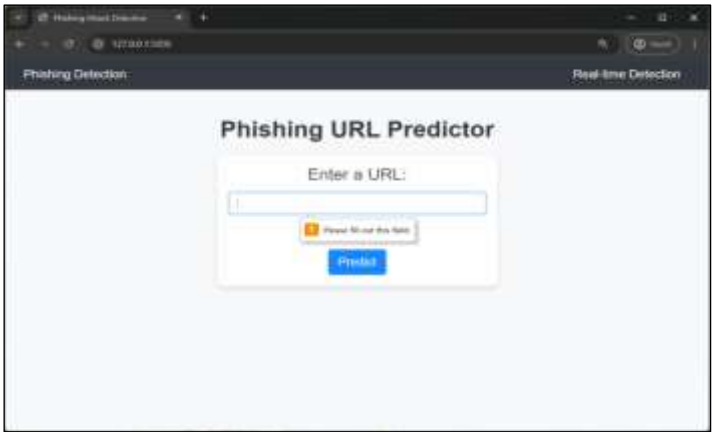

Figure 8: User Interface with a Prompt to Enter a Website URL.
Source: Authors, (2025).

Figure 8 shows the screen displayed upon opening the application, featuring a simple form-like window with an input field to accept a URL. Should the user leave the field blank and press 'Submit', they are prompted to fill out the field.

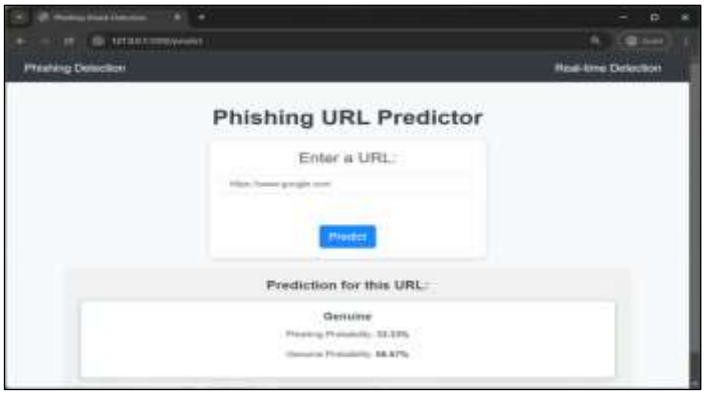

Figure 9: Prediction for a Genuine Website
Source: Authors, (2025).

Figure 9 shows the results shown when the ML model predicts a website as genuine, in this case, Google. The probability of the website being genuine is higher than its phishing probability, accordingly causing the 'Genuine' prediction to be shown.

In Figure 10, the prediction of a phishing website is shown. It displays a higher probability of the website being a phishing site, causing it to be labelled as such.

Figure 11 shows the real-time detection module, where URLs are fetched and then run through the ML model. It shows the predicted nature of the website detected and their probabilities of being phishing.

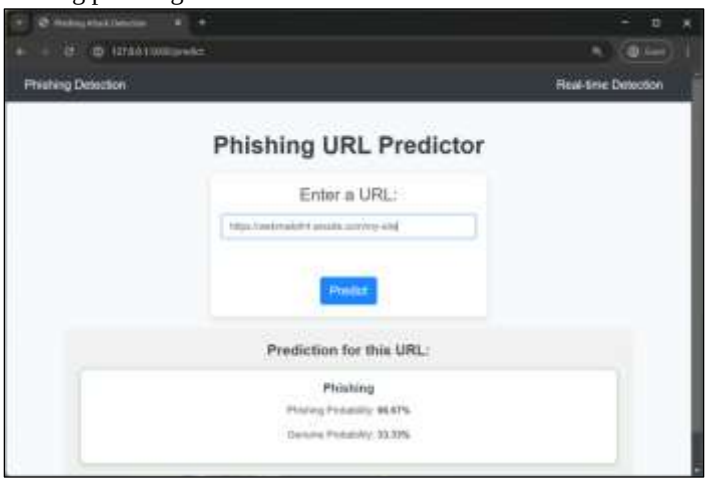

Figure 10: Prediction for a Phishing Website
Source: Authors, (2025).

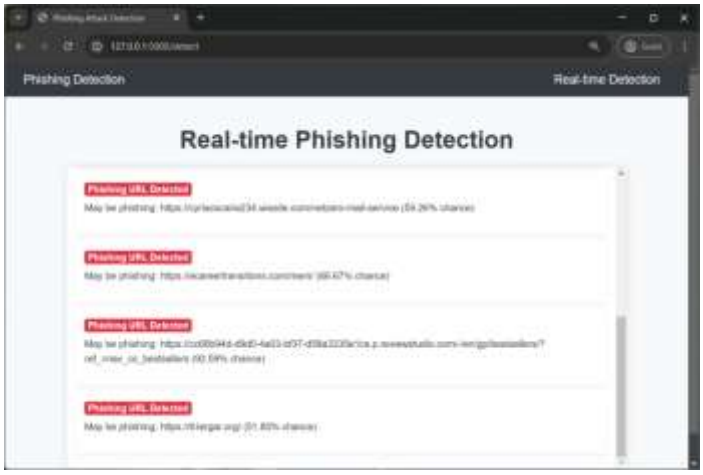

Figure 11: Real-time Phishing Detection Page
Source: Authors, (2025).

IV.3 COMPARATIVE ANALYSIS

Table 2: Comparative Analysis of Other Proposed Methodologies.

Sr. no.	Title of Paper	Proposed Methodology	Drawbacks
1	Application of machine learning for real-time phishing attack detection	Integrate the best ML algorithm into a Python Flask application, use probability-based prediction, and include a URL fetching module	May be affected by user's input, possibility of incorrect predictions
2	Machine learning approach for	Hybrid model combining well-performing ML	High False Positive rates, slower

	phishing website detection: A literature survey [1]	algorithms	in some cases
3	Phishing Detection in E-mails using Machine Learning [2]	Use only the most relevant email features and the best-performing ML algorithm	Poor adaption to evolving phishing emails
4	Phishing web site detection using diverse machine learning algorithms [3]	Find a combination of the best ML algorithms to create a stacked model	Potentially slow to execute
5	Phishing Detection Using Machine Learning: A Model Development and Integration [4]	Integrate the best-performing ML algorithm into a Django-based application	User errors may affect prediction results

Source: Authors, (2025).

The Python Flask application thus developed is capable of performing real-time detection of potentially harmful URLs. However, the ML model is not without its flaws. Given that the dataset was purely focused on the features of the URL, and that the ML model was not fully accurate, it is easy to miss potentially harmful websites and return the wrong prediction, or mislabel a known genuine website as phishing. The user may enter the same URL in many ways, and that can further lead to varying predictions. This would require mechanisms to validate user input, like checking for the presence of certain characters typical of a URL. The fetching of URLs is also limited based on the rate at which it can be performed and ethical considerations. It is possible to explore different sources to fetch URLs, but adhering to their terms of service is vital to ensure proper functioning of such applications while avoiding ethical issues.

V. CONCLUSIONS

The development of a phishing attack detection has numerous approaches, but usage of ML algorithms opens the possibility to automate such a process. A number of datasets were available online, including the one from [5] which was sufficiently large, nearly balanced and included novel attributes. The availability of updated datasets is very important in training any ML algorithm; outdated data leads to a much poorer accuracy. The final choice of the algorithm, the Random Forest Classifier, proved to have the best performance out of the five tested algorithms.

The Python Flask application integrated the algorithm, using it to predict the nature of the site by showing how likely it was to be a phishing website. Some improvements that can be made include improving input validation for the URL and experimenting with a variety of ML algorithms with different combinations of hyperparameters. The most reliable model not only provides highly accurate predictions on the dataset itself, but also on real-world data. This raises the need for development of large and updated datasets that also represent real-world websites to the highest accuracy.

VI. AUTHOR'S CONTRIBUTION

Conceptualization: Andrina Dsouza, Jimit Mehta and Prajwal Naik.
Methodology: Andrina Dsouza and Prajwal Naik.
Investigation: Andrina Dsouza, Jimit Mehta and Prajwal Naik.
Discussion of results: Andrina Dsouza, Jimit Mehta, Prajwal Naik and Akshay Agrawal.
Writing – Original Draft: Andrina Dsouza.
Writing – Review and Editing: Andrina Dsouza and Akshay Agrawal.
Resources: Andrina Dsouza.
Supervision: Akshay Agrawal.
Approval of the final text: Akshay Agrawal.

VII. REFERENCES

[1] R. R. Patil, G. Kaur, H. Jain, A. Tiwari, S. Joshi, K. Rao and A. Sharma."Machine learning approach for phishing website detection : A literature survey", Journal of Discrete Mathematical Sciences & Cryptography, Vol. 25 (2022), No. 3, pp. 817–827, April 2022, DOI: 10.1080/09720529.2021.2016224.

[2] S. Rawal, B. Rawal, A. Shaheen and S. Malik. "Phishing Detection in E-mails using Machine Learning", International Journal of Applied Information Systems (IJAIS), Vol. 12 – No. 7, October 2017, DOI:10.5120/ijais2017451713.

[3] A. Zamir, H. U. Khan and T. Iqbal, N. Yousaf, F. Aslam, A. Anjum and M. Hamdani. "Phishing web site detection using diverse machine learning algorithms", The Electronic Library, Vol. 38 No. 1, pp. 65-80, 2020, DOI: 10.1108/EL-05-2019-0118.

[4] V. A. Onih. "Phishing Detection Using Machine Learning: A Model Development and Integration", International Journal of Scientific and Management Research, Vol. 7, No. 04, pp. 27-63, April 2024.

[5] M. A. Tamal, M. K. Islam, T. Bhuiyan, A. Sattar. "Dataset of suspicious phishing URL detection", Front. Comput. Sci., Vol. 6, Mar 2024, DOI: 10.3389/fcomp.2024.1308634.

[6] G. Prasaath M, I. Khan I, M. Lingam K, R. Ramya. "Phishing website detection system using machine learning algorithms", IJCRT, Vol. 11, No. 11, November 2023.

[7] F. P. E. Putra, Ubaidi, A. Zulfikri, G. Arifin, R. M. Ilhamsyah. "Analysis of Phishing Attack Trends, Impacts and Prevention Methods: Literature Study", Brilliance Research of Artificial Intelligence, Vol. 4, No. 1, May 2024. DOI: https://doi.org/10.47709/brilliance.v4i1.4357

[8] S. S. M. Aldaham, O. Ouda, A. A. Abd El-Aziz, "Improved Detection of Phishing Websites using Machine Learning", International Journal of Intelligent Systems and Applications in Engineering, Vol. 12, No. 21, pp. 4619-4633, March 2024.

[9] N. N. Sakhare, J. L. Bangare, R. G. Purandare, D. S. Wankhede, P. Dehankar. "Phishing Website Detection Using Advanced Machine Learning Techniques", International Journal of Intelligent Systems and Applications in Engineering, Vol. 12, No. 12, pp. 329-, January 2024.

[10] A. Garje, N. Tanwani, S. Kandale, T. Zope, S. Gore. "Detecting Phishing Websites Using Machine Learning", IJCRT, Vol. 9, No. 11, pp. 243-246 November 2021.

[11] M. A. Saedi, N. A. Flayh. "Phishing Website Detection Using Machine Learning: A Review", Wasit Journal of Pure Sciences, Vol. 2, No. 2, pp. 270-281, June 2023, DOI: 10.31185/wjps.145.

[12] S. Alnemari, M. Alshammari. "Detecting Phishing Domains Using Machine Learning", Vol. 13, No. 8, DOI: https://doi.org/10.3390/app13084649.

Journal of Engineering and Technology for Industrial Applications

ISSN ONLINE: 2447-0228

ITEGAM-JETIA

Manaus, v.11 n.53, p. 170-176. May/June., 2025.

DOI: https://doi.org/10.5935/jetia. v11i53.1654

RESEARCH ARTICLE OPEN ACCESS

PLANNING OF DISTRIBUTED GENERATION SOURCES WIND AND PV IN IEEE 33-BUS SYSTEM

Karar Shaker Al-Ibrahimi [1] and S.M.H. Hosseini [2]

[1, 2] Department of Electrical Engineering, South Tehran Branch, Islamic Azad University, Tehran, Iran.

[1] https://orcid.org/0009-0004-4626-3313, [2] https://orcid.org/0000-0002-3686-0702

Email: eng.karar@gmail.com , Smhh110@azad.ac.ir

ARTICLE INFO

Article History
Received: February 21, 2025
Revised: May 20, 2025
Accepted: June 15, 2025
Published: June 30, 2025

Keywords:
Microgrid, wind turbine, photovoltaic, optimization, planning, GAMS.

ABSTRACT

To mitigate the impacts of rising power consumption and new technologies for distributed generation, microgrids are being developed. Another consequence of this is the expansion of the distribution network to include more microgrids, often known as multi-microgrid systems. Undoubtedly, renewable generators contribute to today's electrical energy networks. However, when it comes to scheduling, this might introduce uncertainty into the entities' mathematical models. Therefore, the future of a multi-day microgrid is planned using chance-constrained programming in this study. A system operating in an unpredictable setting. The traditional units are being utilized alongside the renewable energy units, which might have negative effects on the environment, such as increasing greenhouse gas emissions.

I. INTRODUCTION

Cost savings, improved economics, and environmental advantages from reduced greenhouse gas emissions have contributed to a rise in the adoption of renewable-based DGs in the last decade [1]. Using MGs (Microgrids) may solve a number of problems that this growth is causing in the functioning electrical power networks.

Anyway, as a result of the integration of a range of new technologies with MGs, their structures are growing more complicated, potentially exposing them to a slew of new issues, such as high investment costs, market challenges, and regulation challenges [2].

The advancements in technology section and industry, population expansion, and increasing economic comfort all contribute to a rise in energy use. Investments and planning based on accurate estimates are essential for the well-being and economics of both the producer and the consumer as energy demand rises [3].

Electrical energy consumption may be influenced by differences between developed and developing nations in socio-economic factors including population, energy exports and imports, and gross domestic product. For instance, studies comparing the established economy of the United States with that of Iran (a developing economy) found that, in 2030, Iran's EEC would be 2.73 times higher than in 2009, while the United States' EEC will be 1.09% lower [4].

In order to discover real-time optimum energy management solutions for a standalone hybrid wind-microturbine (MT) energy system, the particle swarm optimization algorithm (PSO) was used. PSO is a biologically driven direct search approach [5]. Unfortunately, the power flow limits and uncertainties were disregarded. Optimizing the control process of microgrid batteries while ignoring uncertainties and security limitations was also achieved by [6] by modifying the PSO algorithm for real-time optimum energy management.

According to [7] In order to control demand response and optimize costs, this study proposes a broad definition of the optimal operating strategy. To develop an energy management system for optimization objectives, a multi-period imperialist competition algorithm-based expert heuristic technique is used, but the network constraints are not taken into account. Also, the multi-layer ant colony optimization algorithm was used as a metaheuristic method to solve the day-ahead scheduling problem of microgrids.

Researchers are currently trying to pin down the exact advantages of metaheuristic techniques, such as their capacity to solve complicated issues and the optimality of the solutions they uncover. Consequently, methods such as mixed integer non-linear programming, liner programming, non-liner programming, mixed

integer liner programming, mixed integer non-linear programming (LP, MILP, NLP, and MINLP) have been tested for energy management of isolated MGs in [8], ignoring the penetration of renewable-based distributed generation (DG) and uncertainties. In contrast, the authors of [9] addressed energy management on two levels: optimum power flow and unit commitment.

The biggest problem with these two books was that they didn't address the presence of uncertainty. Uncertainties in electrical power system are resulted because of load changing, solar radiation and wind speed variations which lead to unstable output power of the renewable energy power plants and problem was introduced under the name of stochastic programming optimization problem.

A plethora of models and methods, including CCP and the Resource-Based Model for Expected Value, were proposed to address this issue. A method for managing the energy consumption of a mixed-generation (MG) system that includes renewable power sources, batteries, diesel generators, and loads has been suggested in [10].

However, the limitations of the network and the unpredictability of renewable energy sources were disregarded in this study. In their study, the researchers from [11] introduced a microgrid system that uses combined heat and power units that are based on biomass.

The goal of the algorithm is to minimize operational costs by using an anticipated value model. Both electrical and thermal loads have been subjected to a demand response program in this issue. In this study, the computations have been done without the power flow limitations. With a limited model of the uncertainties and neglecting the network constraints [12] presented a mixed integer linear programming (MILP) method for energy management for MGs in the means of expected value form to model the uncertainties.

According to [13] Have introduced a fresh method for managing energy that makes use of updated mathematical models to account for a wide range of unpredictable demands. In order to determine the best operating points while taking into account diverse sources of uncertainty, stochastic scheduling for MGs with WTs, fuel cells as combined heat and power units, energy storage devices, and variable loads has been proposed [14]. For day-ahead scheduling of an MG disregarding security restrictions, a two-stage stochastic robust model-based optimization method was suggested in [15].

For energy management for the next day, the rigorous optimization may be too cautious. Using conditional value at risk, the authors of [16] provide a data-driven charging strategy for EVs that takes into account EV behavior and demand levels as sources of uncertainty. This approach has the potential to be refined for usage in MGs.

A different way to represent the unknowns is using Chance Constraints Programming (CCP), which solves all the issues mentioned. The optimization issue in CCP may be handled utilizing several ways that transform chance-constraints into deterministic ones, given a reliability level that is set for certain uncertain constraints [17].

As a result, CCP increases system stability and dependability by keeping the likelihood of breaching certain unknown requirements at the desired level. Solving nonlinear problems with uncertainty is also possible with the help of deterministic CCP counterparts. Stochastic power system challenges have so attracted the attention of several scholars who have used CCP. An optimization model for MG energy management that is data-driven and nonparametric is provided in [17]. Taking into account network and security limits might enhance the value of the job, notwithstanding the noble intentions.

The presence of greenhouse gases in the atmosphere is typically responsible for the emergence of environmental concerns over global warming, which is now one of the most pressing issues facing our planet. It is important to reduce the use of traditional units and replace them with cleaner manufacturing methods in order to reduce emissions. Therefore, a penalty cost associated with emissions has been taken into account in several researches. In [18], the authors provide a CCP-based methodology for managing the energy consumption of MGs that are linked to the grid. The authors have made nice work with this reference; however the research may be much better if they took into account energy storage devices and network restrictions, two crucial tools in MGs. For power system planning, [19] have laid out a multi-stage CCP framework to help in dealing with various types of uncertainty.

The researchers in [20] proposed an improved particle swarm optimization (PSO) algorithm is proposed to solve a multi-objective optimal load dispatch model of microgrid with the stochastic access of electric vehicles. Then they have discussed the dispatch results under three different scheduling scenarios, i.e., uncoordinated charging scenario, coordinated charging scenario with and without DGs.

The task will be of higher quality if many microgrids are considered. Additionally, a multi microgrid system is a high-level structure that is formed by the presence of several dispersed generating units and loads in the distribution system. In [21], a hybrid stochastic-robust framework for MMGs system optimum scheduling is suggested. Energy management takes both the current and future cost of energy into account.

As an additional tool for improved MG operation, time-of-use demand response programs are being considered. Stochastic programming is also used to simulate energy pricing, electric cars, PV systems, WTs, and other sources of uncertainty. In order to minimize the overall cost of the system, which includes the cost of power generation by units as well as the cost of power exchange among the interconnected MGs and the main grid, the authors of this research have presented a new stochastic framework for optimal energy management of interconnected MGs [22].

One method for managing energy in MMG systems that takes contingencies into account is shown in [23]. This method takes the possibility of a contingency into account and uses energy management as a tool for addressing MMG-style contingency situations. Energy management of MMG-based DNs in the context of demand response programs and uncertainties related to renewable energy supplies, loads, and pricing is addressed in a new way by the authors of [24].

We use a meta-heuristic method called NSGA-II to solve the energy management issue, which is modeled as a multi-objective problem. The authors of [25] laid forth a unified strategy for managing energy consumption in MMG systems. In this paper, a novel metric is proposed for evaluating energy management procedures in conditions of uncertainty, including those involving load, WTs, and PV systems.

We can summaries the conclusion of the previous works in the following points:

- The ignorance of uncertainties caused by wind and solar units and load changes.

- Power flow constraints was not included in the calculations in one paper.
- Network and security constraints of have been ignored.
- Only the presence of one MG has been studied in most of the studies.

As a conclusion there is no research that took into account the uncertainties resulted by load, PV and wind turbines with the emission consideration in multi microgrid systems in solving the day-ahead scheduling problem using chance constrained programming approach.

II.MATHEMATICAL MODELING OF THE SYSTEM

Within microgrids are one or more kinds of distributed energy (solar panels, wind turbines, combined heat and power, generators) that produce its power. In addition, many newer microgrids contain energy storage, typically from batteries. Some also now have electric vehicle charging stations Figure 1.

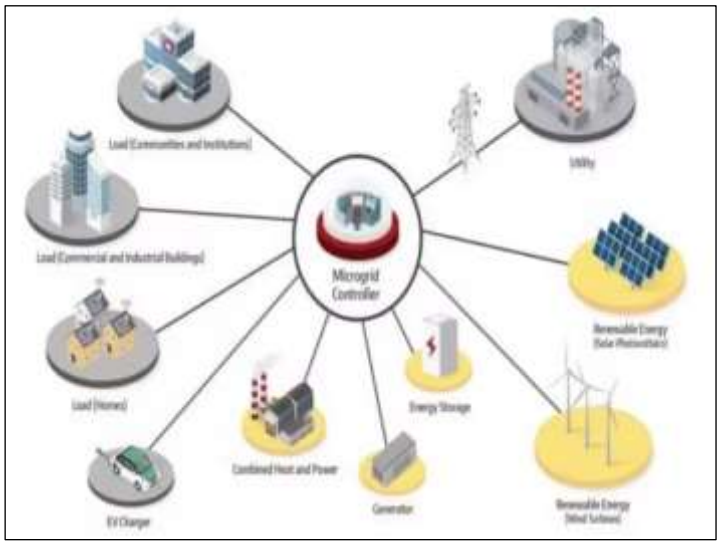

Figure 1: Microgrid scheme.
Source: Authors, (2025).

II.1 INTERNAL COMBUSTION GENERATORS:

The internal combustion (IC) unit technology transforms the fuel-based source of energy into electricity. The production costs are calculated as a quadratic function of the output power of the unit P during a time period t.

$$Cost_{IC,t}^{operation} = \alpha_1 P_{IC,t}^2 + \alpha_2 P_{IC,t} + \alpha_3 \quad (1)$$

Where:

α_1, α_2, α_3 Cost function coefficients of diesel generator, besides to the operation cost there is the unit startup cost:

$$Cost_{IC,t}^{stup} = \gamma_{IC,t} \times C_{IC}^{SU} \quad (2)$$

Where:

γ First, the total cost, followed by a binary variable representing the unit's status:

$$Cost_{IC,t} = Cost_{IC,t}^{operation}(P_{IC}) + Cost_{IC,t}^{stup} \quad (3)$$

The complicated power limits and the ramp up pace of the generating units are the limitations of these sorts of units:

$$0 \le P_{IC,t} \le v_{IC,t} P_{IC}^{max} \;\; v_{IC,t} \in 0,1 \quad (4)$$

$$-ramp_{IC} \times P_{IC}^{max} \le P_{IC,t} - P_{IC,t-1} \le ramp_{IC} \times P_{IC}^{max} \quad (5)$$

$$P_{IC,t}^2 + Q_{IC,t}^2 \le S_{IC}^2 \quad (6)$$

II.2 WIND GENERATORS

When it comes to harnessing renewable energy sources for electrical power, wind production units are among the most exciting and rapidly evolving technology. They include wind turbines, which convert the wind's kinetic energy into electricity. Because its output power is dependent on the wind speed, an inherently stochastic variable, the amount of electrical energy that is produced is never guaranteed.

Below is an example of how the wind speed follows a Weibull PDF, which uses two WT-site characteristics, called the shape factor and the scale factor:

$$f_V(v) = \left(\frac{k}{\delta}\right)\left(\frac{v}{\delta}\right)^{k-1} e^{-\left(\frac{v}{\delta}\right)^k} \; 0 \le v \le \infty \quad (7)$$

The following shows the relationship between wind speed and the electrical power produced by the wind system:

$$P_{wt} = \begin{cases} 0 & v \le v_{in}, \;\; v \ge v_o \\ \frac{v - v_{in}}{v^{rated} - v_{in}} P_{wt}^{rated} & v_{in} \le v \le v^{rated} \\ P_{wt}^{rated} & v^{rated} \le v \le v_o \end{cases} \quad (8)$$

II.3 SOLAR POWER GENERATION

One of the most prevalent and straightforward methods of generating renewable energy is the use of photovoltaic (PV) devices to convert sunlight into electricity. The rapid expansion of PV panel installations may be attributed to their compact design and reduced price tag as compared to WTs.

Solar irradiance is a stochastic phenomenon that affects the power output of PV systems. This relationship is often represented by the lognormal PDF, which looks like this:

$$f_{Ir}(Ir) = \frac{1}{Ir \,.\sigma\,.\sqrt{2\pi}} exp\left[\frac{-(lnIr - \mu)^2}{2\sigma^2}\right] \;\; I_r \ge 0 \quad (9)$$

Depending on the amount of sunlight reaching the PV system, its output power is proportional to the following:

$$P_{PV} = \begin{cases} P_{PV}^{rated} \times \left(\frac{Ir^2}{Ir_{std}\,.Ir_{cer}}\right), \; Ir \le Ir_{cer} \\ P_{PV}^{rated} \times \left(\frac{Ir^2}{Ir_{std}}\right), \; Ir_{cer} \ge Ir \end{cases} \quad (10)$$

II.4 ENERGY STORAGE SYSTEM

Energy storage system is considered as a battery, charging and discharging power limitations:

$$0 \le P_{ch,t}^{bat} \le v_{ch,t}^{bat} P_{cap}^{bat} \quad (11)$$

$$0 \leq P_{disch,t}^{bat} \leq v_{disch,t}^{bat} P_{cap}^{bat} \quad (12)$$

The limitation on not charging and discharging at the same time:

$$v_{ch,t}^{bat} + v_{disch,t}^{bat} \leq 1 \quad v_{ch,t}^{bat}, v_{disch,t}^{bat} \in 0,1 \quad (13)$$

Battery system limitations with respect to charge or energy level:

$$SOC_t = SOC_{t-1} - \frac{1}{P_{cap}^{bat}} \left(P_{disch,t}^{bat} - P_{ch,t}^{bat}\right) \quad (14)$$

$$0 \leq SOC_t \leq 1 \quad (15)$$

$$SOC_{T_0} = SOC_{int} \quad (16)$$

$$SOC_{T_{final}} = SOC_{final} \quad (17)$$

The stored/released power constraints:

$$P_t^{bat} = P_{ch,t}^{bat} - P_{disch,t}^{bat} \quad (18)$$

II.5 LOADS

One source of uncertainty in electrical power system modeling is loads, which are a result of users' stochastic behavior. When trying to model the load's uncertainty, the normal distribution function is often used:

$$f_{load}(load) = \frac{1}{\sigma.\sqrt{2\pi}} exp\left[\frac{-(load-\mu)^2}{2\sigma^2}\right] \quad load \geq 0 \quad (19)$$

II.6 NETWORK MODELING

Radial networks are the standard representation for MGs and distribution systems. Assumption #1 in this thesis is that Bus #1 is upstream-connected to the grid and has a 1 P. u. apparent power flexible power injection:

$$S_{k,t} = S_{k,t}^{bat} + S_{k,t}^{load} - S_{k,t}^{gen} \quad (1)$$

II.7 EMISSION MODELING

May learn how much pollution a typical unit produces as a function of fuel used by looking at the following equation:

$$Em_{IC,t} = \Psi_{IC}. \frac{Cost_{IC,t}^{operation}}{\xi_{fuel,IC}} \quad (21)$$

The emission coefficient:

$$\Psi_{IC} = PTV_{IC}. EC_{IC}. OC_{IC} \quad (2)$$

Where: PTV: Pure thermal value, EC: Emission factor OC: Oxidation factor

To calculate the emission cost the amount of emission is multiplied to a penalty factor ħ:

$$Cost_{IC,t}^{emission} = ħ_{IC} \times Em_{IC,t} \quad (23)$$

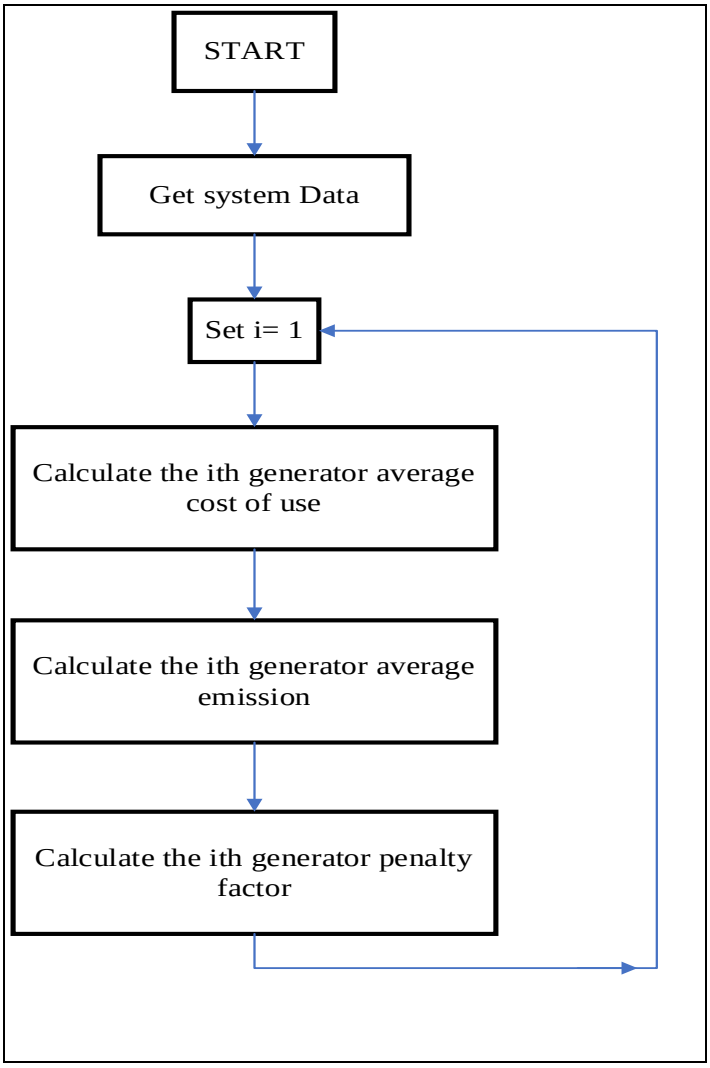

Figure 2: calculating penalty factor algorithm.
Source: Authors, (2025).

Objective function:

$$min\ O.F._{MG,\omega} = \sum_{t=T_0}^{T_f} \left(\sum_{IC=1}^{n_{IC,\omega}} \left[Cost_{IC,t} + Cost_{IC,t}^{Emission}\right] + \lambda_t^{buy}.P_{\omega,t}^{sh} - \lambda_t^{sell}.P_{\omega,t}^{sur}\right) \quad (24)$$

Simulation results

The electrical energy prices in the distribution network estimated in $ for MWh are shown in Figure 3.

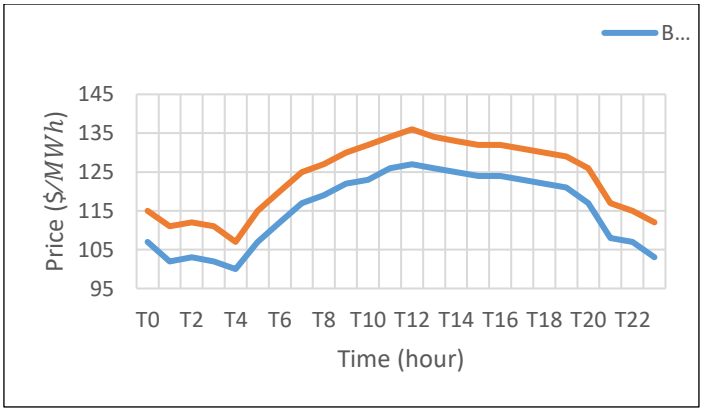

Figure 3: Electrical energy prices.
Source: Authors, (2025).

```
VARIABLE Xpv.L  binary variable fot PV placement
18 1.000,   33 1.000

VARIABLE Xwt.L  binary variable fot PV placement
```

In the simulation of the deterministic case the distributed generation units weren't taken into account. The results for this simulation:

```
PARAMETER SS_PV        =      0.000  Total PV Capacity

PARAMETER SS_WT        =      0.000  Total WT Capacity

VARIABLE Cost.L        =  1935517.665  Totall Cost($)

VARIABLE EM.L          =    15090.772  Totall Emission (ton)
VARIABLE C_Ploss.L     =    68185.147  Cost of Loss Power
VARIABLE Ploss.L       =        1.825  power Loss
VARIABLE DG_Cost.L     =        0.000  DG Investement and operation Cost
VARIABLE C_energy.L    =  1799147.371  Energy Price that Purchase from Grid
```

According to the above results the losses in one day are 1.825 MWh and the cost of these losses is 68185.1 dollars. The amount of pollution emission related to the power purchased from the grid in one year is 15090 tons and the cost of buying energy from the net for one year is 1799147 dollars. For this case the voltage range for the busses in every hour is shown in Fig. 4. In this figure every curve is related to one hour of the day. It's clear that the worst case for the voltage value 0.918 pu. The amount of the purchased power from the net in every hour is depicted in Fig. 5, and it can be noticed that the maximum limit is equal to 3.8 MW in the hour 17.

The second case is related to the uncertainty case. The results of this case are as follow. And it's clear that in this case a 0.787 MVA PV and a 1.969 MVA WT are installed.

```
PARAMETER SS_PV        =      0.787  Total PV Capacity

PARAMETER SS_WT        =      1.969  Total WT Capacity

VARIABLE Cost.L        =  2490654.824  Totall Cost($)

VARIABLE EM.L          =     7216.941  Totall Emission (ton)
VARIABLE C_Ploss.L     =    40973.710  Cost of Loss Power
VARIABLE Ploss.L       =        1.103  power Loss
VARIABLE DG_Cost.L     =  1579681.979  DG Investement and operation Cost
VARIABLE C_energy.L    =   829025.425  Energy Price that Purchase from Grid
```

In this case the energy loss in one day is equal to 1.103 MWh which is 40 % decreased compared to the previous case (without DG). The amount of pollution in one year has also reached 7216 tons, which has decreased by 52% compared to the previous situation. The cost of exchanging energy with the grid in one year is 829025 dollars, which has decreased by 53% compared to the previous state.

In this case, the location and capacity of PV and WT sources are obtained as follows. It is clear that two PVs are installed in 18 and 33 buses and two wind turbines are also installed in 15 and 30 buses. The capacities are also stated below that for PV it is equal to 0.301 and 0.486 megavolt ampere (MVA) respectively. For wind turbine capacities are 0.726 and 1.243 megavolt ampere.

```
15 1.000,   30 1.000

VARIABLE Spv.L  MVA OF PV
18 0.301,   33 0.486

VARIABLE Swt.L  MVA OF WT
15 0.726,   30 1.243
```

For this case, the bus voltage range is shown in Fig. 6 and the amount of power exchanged with the network is shown in Fig.7. Is. It is clear that the minimum voltage range is equal to 0.95 pu, which is improved compared to before. The maximum power received from the network is also 2.6 megawatts, which shows a decrease of 1.2 megawatts compared to the previous state.

And finally, the uncertainty of the PV and WT is taken into account, 2.778 MVA PV and 0.115 MVA WT were installed. The amount of installation Scattered production has not changed significantly compared to the previous state, but the amount of PV installation has increased and the amount of turbine installation has increased Badi is greatly reduced. The reason for choosing more PV is also due to the coincidence of its production hours with peak demand which makes its uncertainty management easier than wind turbine.

```
PARAMETER SS_PV        =      2.778  Total PV Capacity

PARAMETER SS_WT        =      0.115  Total WT Capacity

VARIABLE Cost.L        =  2665961.310  Totall Cost($)

VARIABLE EM.L          =     7586.545  Totall Emission (ton)
VARIABLE C_Ploss.L     =    57994.843  Cost of Loss Power
VARIABLE Ploss.L       =        1.554  power Loss
VARIABLE DG_Cost.L     =  1740191.645  DG Investement and operation Cost
VARIABLE C_energy.L    =   809779.978  Energy Price that Purchase from Grid
```

In this case, the loss is equal to 1.554 megawatts, which is 15% compared to the first case (without DGs). The amount of contamination in one year has also reached 7586 tons, which has decreased by 49% compared to the first case.

The cost of exchanging energy with the network in one year is 809779.9 dollars, which has decreased by 54% compared to the first case.

In this case, the location and capacity of the resources are obtained as follows. It is clear that 5 PV in buses 16, 17, 18, 32 and 33 are installed. The capacities of these resources are respectively 0.235, 0.292, 0.425, 1.417 and 0.408 MVA. One wind turbine is also installed in bus 15 with a capacity of 0.155 megavolt ampere.

```
VARIABLE Xpv.L  binary variable fot PV placement
16 1.000,   17 1.000,   18 1.000,   32 1.000,   33 1.000

VARIABLE Xwt.L  binary variable fot PV placement
15 1.000

VARIABLE Spv.L  MVA OF PV
16 0.235,   17 0.292,   18 0.425,   32 1.417,   33 0.408

VARIABLE Swt.L  MVA OF WT
15 0.115
```

For this case, the average voltage range of the buses is shown in Fig. 8. Based on this figure the minimum voltage range is equal to 0.96 pu, which is improved compared to the first case. Also, the amount of energy exchanged with the network every hour and every scenario are shown in Fig. 9. From this figure we can notice that from hour 7 to 20 when PV sources produce power, the amount of energy exchanged with the grid is also decreased. The maximum amount of demand from the network is 2.8 megawatts, which is a decrease compared to the first case (1MW).

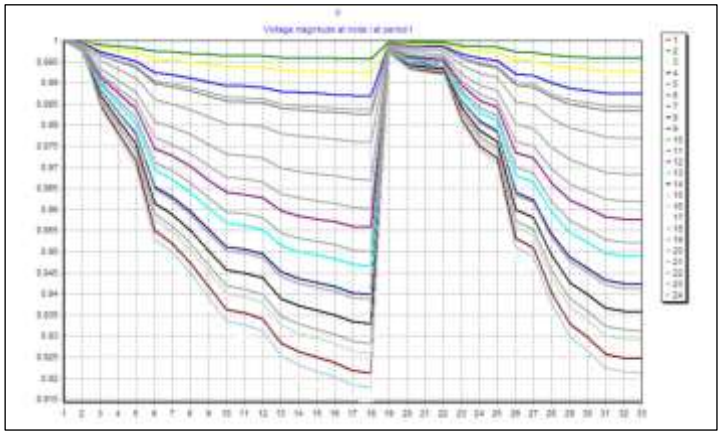

Figure 4: Voltage range of each bus per hour for deterministic case without distribution generation.
Source: Authors, (2025).

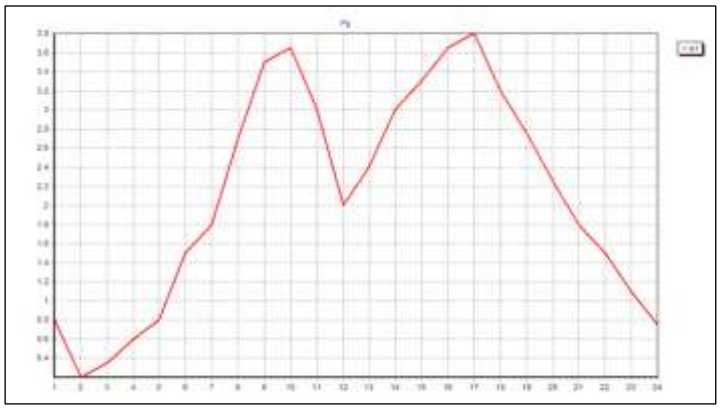

Figure 5: The amount of energy purchased from the grid every hour.
Source: Authors, (2025).

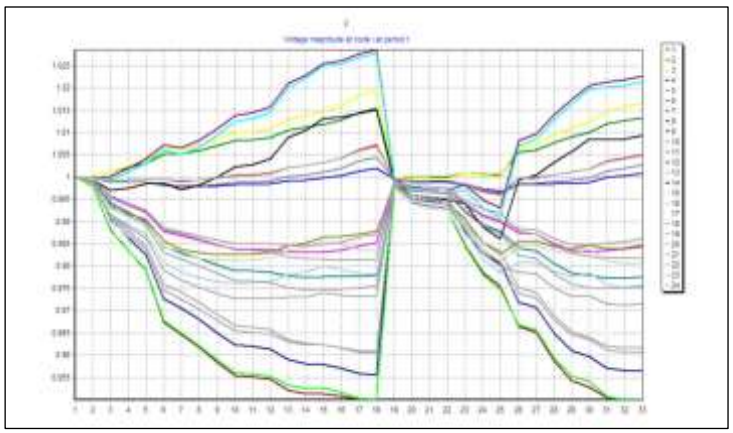

Figure 6: Voltage range of each bus per hour for deterministic case without distribution generation.
Source: Authors, (2025).

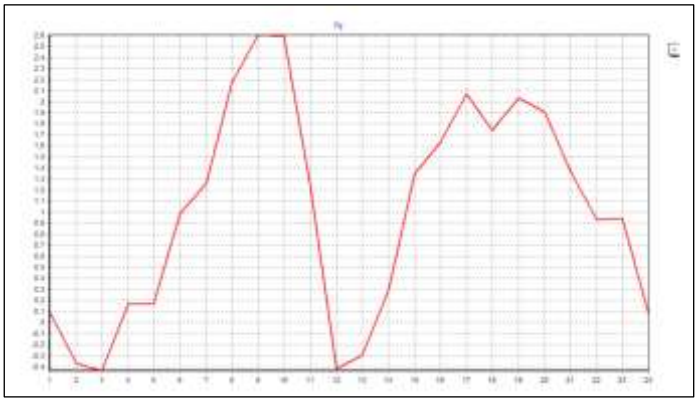

Figure 7: The amount of energy purchased from the grid every hour in the deterministic case.
Source: Authors, (2025).

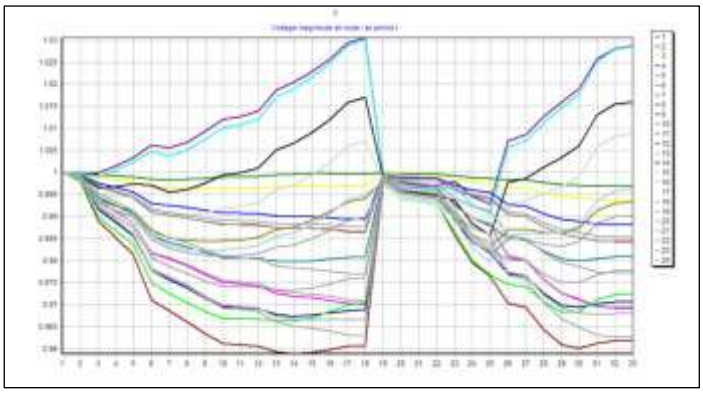

Figure 8 Average voltage range of each bus per hour for contingency mode.
Source: Authors, (2025).

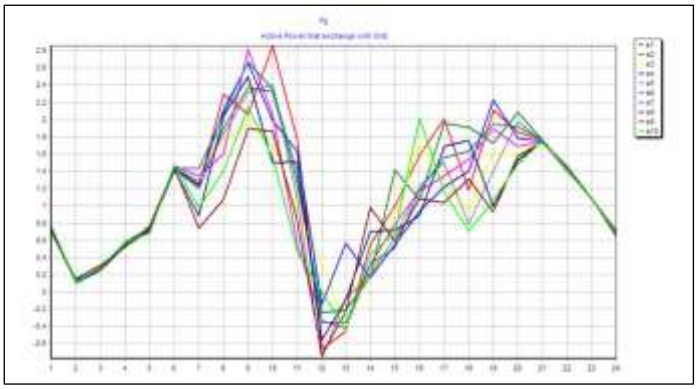

Figure 9: The amount of energy exchanged with the network per hour and per scenario for the probability case.
Source: Authors, (2025).

V. CONCLUSION

All the researches and the results of this work indicates to the increasing importance of the renewable energy. And the new electrical system which includes the microgrid (MMG system in the case of many MGs) is associated with more complicated energy management problems. In this work a day ahead scheduling of a 33-bus system containing 3 microgrids with renewable resources PV and wind turbine optimization problem was solved using GAMS software in 3 cases: deterministic, and with renewable energy penetration in tow levels.

The results show that the more penetration of the renewable energy the total cost and the energy purchased from the network decrease besides to the pollution reduction. So, the only problem

is the associated difficulty in the energy management calculation which can be solved using the powerful optimization algorithms and software. A linearization to represent the issue as a linear problem and find a global optimum is proposed for use in future investigations. Additionally, it may be very intriguing for future research to suggest a method of bidding for the MMG system that takes emissions and CCP modeling into account. To further improve optimization while protecting MG privacy, a decentralized approach to the issue in a CCP context should be considered.

VI. REFERENCES

[1] Huenteler, J., Niebuhr, C., & Schmidt, T. S. (2016). The effect of local and global learning on the cost of renewable energy in developing countries. Journal of Cleaner Production,128,6–21. https://doi.org/10.1016/j.jclepro.2014. 06.056

[2] Bellido, M. H., Rosa, L. P., Pereira, A. O., Falcão, D. M., & Ribeiro, S. K. (2018). Barriers, challenges and opportunities for microgrid implementation: The case of Federal University of Rio de Janeiro. Journal of Cleaner Production,188,203–216. https://doi.org/10.1016/j.jclepro.2018.03. 012.

[3] Unutmaz, Y. E., Demirci, A., Tercan, S. M., & Yumurtaci, R. (2021). Electrical Energy Demand Forecasting Using Artificial Neural Network. 2021 3rd. International Congress on Human-Computer Interaction, Optimization and Robotic Applications (HORA), 1–6. https://doi.org/10.1109/HORA52670.2021.9461186.

[4] Ardakani, F. J., & Ardehali, M. M. (2014). Long-term electrical energy consumption forecasting for developing and developed economies based on different optimized models and historical data types. Energy, 65, 452–461. https://doi.org/10.1016/j.energy.2013.12.031.

[5] Pourmousavi, S. A., Nehrir, M. H., Colson, C. M., & Wang, C. (2010). RealTime Energy Management of a Stand-Alone Hybrid Wind-Microturbine Energy System Using Particle Swarm Optimization. IEEE Transactions on Sustainable Energy, 1(3), 193–201. https://doi.org/10.1109/TSTE.2010.2061881.

[6] Hossain, M. A., Pota, H. R., Squartini, S., & Abdou, A. F. (2019). Modified PSO algorithm for real-time energy management in grid-connected microgrids. Renewable Energy,136,746–757. https://doi.org/10.1016/j.renene.2019.01.005

[7] Marzband, M., Parhizi, N., & Adabi, J. (2016). Optimal energy management for stand-alone microgrids based on multi-period imperialist competition algorithm considering uncertainties: Experimental validation. International Transactions on Electrical EnergySystems,26(6),1358–1372. https://doi.org/10.1002/etep.2154

[8] Marzband, M., Sumper, A., Domínguez-García, J. L., & Gumara-Ferret, R. (2013). Experimental validation of a real time energy management system for microgrids in islanded mode using a local day-ahead electricity market and MINLP. Energy ConversionandManagement,76,314–322. https://doi.org/10.1016/j.enconman.2013.07.053

[9] Olivares, D. E., Cañizares, C. A., & Kazerani, M. (2014). A Centralized Energy Management System for Isolated Microgrids. IEEE Transactions on Smart Grid, 5(4), 1864–1875. https://doi.org/10.1109/TSG.2013.2294187

[10] Shen, J., Jiang, C., Liu, Y., & Wang, X. (2016). A Microgrid Energy Management System and Risk Management Under an Electricity Market Environment. IEEE Access, 4, 2349–2356. https://doi.org/10.1109/ACCESS.2016.2555926

[11] Zheng, Y., Jenkins, B. M., Kornbluth, K., Kendall, A., & Træholt, C. (2018). Optimization of a biomass-integrated renewable energy microgrid with demand side management under uncertainty. Applied Energy, 230, 836–844. https://doi.org/10.1016/j.apenergy.2018.09.015

[12] Silvente, J., Papageorgiou, L. G., & Dua, V. (2017). Optimal management of microgrids under uncertainty using scenario reduction. In A. Espuña, M. Graells,& L. Puigjaner (Eds.), Computer Aided Chemical Engineering (Vol.40, pp. 2257–2262). Elsevier. https://doi.org/10.1016/B978-0-444-63965- 3.50378-0

[13] Giaouris, D., Papadopoulos, A. I., Patsios, C., Walker, S., Ziogou, C., Taylor, P., Voutetakis, S., Papadopoulou, S., & Seferlis, P. (2018). A systems approach for management of microgrids considering multiple energy carriers, stochastic loads, forecasting and demand side response. Applied Energy, 226, 546–559. https://doi.org/10.1016/j.apenergy.2018.05.113

[14]n Alipour, M., Mohammadi-Ivatloo, B., & Zare, K. (2015). Stochastic Schduling of Renewable and CHP-Based Microgrids. IEEE Transactions on Industrial Informatics, 11(5), 1049–1058. http://doi.org/10.1109/TII.2015.2462296

[15] Zhang, Y., Fu, L., Zhu, W., Bao, X., & Liu, C. (2018). Robust model predictive control for optimal energy management of island microgrids with uncertainties. Energy, 164, 1229–1241.https://doi.org/10.1016/j.energy.2018.08.200

[16] Li, C., Liu, C., Deng, K., Yu, X., & Huang, T. (2018). Data-Driven Charging Strategy of PEVs Under Transformer Aging Risk. IEEE Transactions on Control Systems Technology, 26(4), 1386–1399. https://doi.org/10.1109/TCST.2017.2713321

[17] Ciftci, O., Mehrtash, M., & Kargarian, A. (2020). Data-Driven Nonparametric Chance-Constrained Optimization for Microgrid Energy Management. IEEE Transactions on Industrial Informatics, 16(4), 2447– 2457. https://doi.org/10.1109/TII.2019.2932078

[18] Liu, C., Wang, X., Guo, J., Huang, M., & Wu, X. (2018). Chanceconstrained scheduling model of grid-connected microgrid based on probabilistic and robust optimisation. IET Generation, Transmission & Distribution, 12(11), 2499–2509. https://doi.org/10.1049/iet-gtd.2017.1039

[19] Wang, L., Huang, G., Wang, X., & Zhu, H. (2018). Risk-based electric power system planning for climate change mitigation through multi-stage joint-probabilistic left-hand-side chance-constrained fractional programming: A Canadian case study. Renewable and Sustainable Energy Reviews, 82, 1056–1067. https://doi.org/10.1016/j.rser.2017.09.098

[20] Lu, X., Zhou, K., Yang, S., & Liu, H. (2018). Multi-objective optimal load dispatch of microgrid with stochastic access of electric vehicles. Journal of Cleaner Production, 195, 187–199. https://doi.org/10.1016/j.jclepro.2018.05.190.

[21] Misaghian, M. S., Saffari, M., Kia, M., Nazar, M. S., Heidari, A., Shafiekhah, M., & Catalão, J. P. S. (2018). Hierarchical framework for optimal operation of multiple microgrids considering demand response programs. Electric Power Systems Research, 165, 199–213. https://doi.org/10.1016/j.epsr.2018.09.003

[22] Papari, B., Edrington, C. S., & Vu, T. (2017). Stochastic operation of interconnected microgrids. 2017 IEEE Power & Energy Society General Meeting, 1–5. https://doi.org/10.1109/PESGM.2017.8273898

[23] Hamzeh Aghdam, F., Salehi, J., & Ghaemi, S. (2018). Contingency based energy management of multi-microgrid based distribution network. Sustainable Cities and Society, 41, 265–274. https://doi.org/10.1016/j.scs.2018.05.019

[24] Haddadian, H., & Noroozian, R. (2019). Multi-Microgrid-Based Operation of Active Distribution Networks Considering Demand Response Programs IEEE Transactions on Sustainable Energy,10(4),1804–1812. https://doi.org/10.1109/TSTE.2018.2873206

[25] Arefifar, S. A., Ordonez, M., & Mohamed, Y. A.-R. I. (2017). Energy Management in Multi-Microgrid Systems—Development and Assessment. IEEE Transactions on Power Systems, 32(2), 910–922. https://doi.org/10.1109/TPWRS.2016.2568858

Journal of Engineering and Technology for Industrial Applications

ITEGAM-JETIA

Manaus, v.11 n.53, p. 177-185. May/June., 2025.
DOI: https://doi.org/10.5935/jetia. v11i53.1670

ISSN ONLINE: 2447-0228

RESEARCH ARTICLE OPEN ACCESS

A BIMODAL TECHNIQUE FOR ENHANCEMENT OF PICTURE QUALITY OF MEDICAL IMAGES

Akeem Abimbola Raji[1], Oluwaseun Ibrahim Adebisi[2] Olubunmi Adewale Akinola[3] and Ayoade Benson Ogundare[4]

[1,2,3]Department of Electrical and Electronics Engineering, Federal University of Agriculture, Abeokuta, Nigeria
[4]Department of Electrical and Electronics Engineering, Lagos State University of Science and Technology, Ikorodu, Nigeria

[1]http://orcid.org/0000-0003-4303-4940, [2]http://orcid.org/0000-0001-8958-4951
[3]http://orcid.org/0000-0001-6532-1698, [4]http://orcid.org/0009-0003-7876-6444

Email: rajiakeemabimbola@gmail.com, adebisioluwaseun@funaab.edu.ng, akinolaoa@funaab.edu.ng, ayoadebensonoludare@gmail.com

ARTICLE INFO

Article History
Received: February 28, 2025
Revised: May 20, 2025
Accepted: June 15, 2025
Published: June 30, 2025

Keywords:
Bimodal technique,
Contrast,
Image enhancement,
Medical disorder,
Picture quality.

ABSTRACT

Medical images are useful for diagnosis of medical disorder in human body. Image enhancement has received significant attention in the literature in a bid to help medical personnel in ascertaining the cause of ailment in human body. Conventional techniques for enhancing medical images suffer from over contrast enhancement, noise and poor picture quality. As a result, this work proposes a bimodal technique that combines Histogram Equalization (HE) and Contrast Limited Adaptive Histogram Equalization (CLAHE) for improving the picture quality of medical images. The performance of the proposed model in enhancing the picture quality of gray scale X-ray, Computed Tomography (CT) and Magnetic Resonance Image (MRI) images is compared with HE and CLAHE. It is observed that the proposed bimodal technique performs better than HE and CLAHE in all images used as candidates of investigation. It produces better picture quality and better structural quality than HE and CLAHE. It is found that the proposed model exhibits 59% picture quality while HE and CLAHE, respectively, exhibit 11% and 30% picture qualities.

I. INTRODUCTION

In medical profession, medical images assist health personnel in disease diagnosis with a view to providing comprehensive report about an ailment in the human body. Poor quality medical image may be difficult to examine by the medical person and may lead to wrong diagnosis of the ailment in the internal structure of the body. The presence of noise in medical images hides the essential features which may cause inaccurate diagnosis of medical disorder [1]. In essence, a clear image devoid of noise and artefact is the foundation upon which an accurate diagnosis of medical ailment is built. Image enhancement concerns with increasing the visual appeal of an image by heightening the contrast or brightness and the picture quality of the image [2]. Various traditional methods have been proposed in the literature for improving the contrast content, increasing the picture quality and removing the noise in medical images in a bid to improve their visual representation. These methods include Histogram Equalization (HE) [3] and its variations [4-7], Adaptive Histogram Equalization (AHE) and its variations [8], Contrast Limited Adaptive Histogram Equalization (CLAHE) [9].

Others are Unsharp Masking (UM), sigma filtering, Logarithmic Transformation (LT), wavelet transform and discrete wavelet transform [10], [11], spatial domain methods such as Median filter, Weiner filter [12], fuzzy logic and Fuzzy inference models, Compressed Sensing (CS) methods and machine learning techniques etc. These techniques have been deployed by researchers with mixed performance and varying degree of success. Zhu et al. [13] proposed wavelet transform for enhancing contrast of X-ray images. Zaafouri et al. [14] proposed UM for brightening the dark area of human facial image where high pass filter was used to reduce the noise. Bilcu and Vehvilainen [15] combined UM and sigma filtering for contrast enhancement and removal of noise. Qiu et al. [2] introduced a method based on convolution neural network and frequency band broadening for enhancement of quality of medical images. Mirza et al. [7] utilized different versions of HE for increasing the quality of CoVID-19 Computed Tomography (CT) images. Sarath and Sreejiths [16] employed Fuzzy logic and homographic filtering for enhancement of visual quality of medical

image. Agarkar [17] employed Fuzzy logic to enhance the picture quality of image in submarines and sea while Sharma and Bhatia [18] deployed Fuzzy logic for contrast enhancement in common images. These methods have inherent drawbacks which limit their performance. Though HE and UM enhance the brightness level of the images, the noise in the image is also increased in the process. HE produces images with too much lightening (over contrast) effect while AHE suffers from slow speed and noise. Though CLAHE limits noise level in the image, its contrast level is low. Fuzzy logic is poor when it is deployed to enhance images taken from crowded area. Convolution neutral network enhancement of image may lead to deterioration or distortion in the quality of the image.

Moreover, a number of hybrid models have also been presented by researchers [19],[20] that combined the characteristics of conventional enhancement techniques. These hybrid models require greater amount of computational effort for implementation. Hence, this work introduces a bimodal technique that requires less computational time. It combines the features of HE and CLAHE for enhancing the visual appeal of medical images. While HE is utilized to increase the contrast level in images, CLAHE on the other hand limits the noise level in the image and overly high contrast effect of HE.

II. MATERIAL AND METHODS

II.1 DATASETS

The dataset employed in this study consists of several X-ray, Computed Tomography (CT), and Magnetic Resonance Imaging (MRI) images which are sourced from the public repositories. The sourced images are preprocessed by resizing them to 255×255 pixels in order make them compatible with the models considered as candidate examples of enhancement.

II.2 HISTOGRAM EQUALIZATION (HE)

Histogram equalization is usually employed to increase the brightness or contrast of image. It transforms the pixel value of image into image of uniform distribution. It is useful in images with overly dark area by uncovering the hidden details.. The grayscale distribution of an image assumes expression of the form

$$h(f_n) = d_n \tag{1}$$

where f_n is the nth gray level with $0 \leq n \leq L-1$, in which, L is the total number of gray levels in the image, d_n represents the number of pixels in the image with a grayscale value of f_n. Thus, the probability density of the histogram equalized image can be expressed by

$$P(f_n) = \frac{d_n}{N} \tag{2}$$

in which N represents the total number of pixels in the image, and $P(f_n)$ denotes the proportion of the total number of pixels in the image that has n-th grayscale level. Histogram equalization produces an enhanced image by applying histogram to the entire image via cumulative distribution function expressed by

$$T(f_i) = \sum_{i=1}^{n} P(f_i) = \sum_{i=1}^{n} \frac{d_i}{N} \tag{3}$$

In eq. (3), the input image is mapped into entire range given by $[f_0, f_1, \mathrm{L}\ , f_{L-1}]$ for which cumulative distribution function serves as a transform function [4].

II.3 CONTRAST LIMITED ADAPTIVE HISTOGRAM EQUALIZATION (CLAHE)

Unlike HE that works on the entire image, CLAHE divides the original image into a number of non-overlapping images of equal sizes. It operates on these non -overlapping small portions, otherwise known as tiles. The brightness of each tile is enhanced and adjacent tiles are combined using bilinear interpolation to prevent the creation of artificial boundaries. CLAHE limits the contrast level in homogeneous regions and in such a manner avoids increasing the noise level in the image. The following steps are implemented when using CLAHE to enhance medical images.

Step 1: Start

Step 2: Input X-ray, CT scan, and MRI images

Step 3: Determine the number of regions in images, dynamic range and clip limit

Step 4: Split the images into regions after padding

Step 5: Process each mapped region, and create gray level mapping

Step 6: Carry out interpolation of gray level mapping in order to aggregate CLAHE images

Step 7: Output enhanced image

Step 8: Stop

II.4 PROPOSED BIMODAL TECHNIQUE

The proposed method integrates the concept of HE and CLAHE for improving the visual appeal of medical images. It enhances medical image quality by leveraging on the strength of both techniques. Specifically, the proposed model utilizes HE to enhance brightness level of medical image while CLAHE is used to remove noise and reduce over contrast effect of HE. Thus, the overall visibility and quality are improved without the adverse effect of noise amplification. The steps followed when implementing the proposed technique are as follows:

Step 1: Input X-ray, CT scan, and MRI images

Step 2: Convert the input X-ray, CT scan, and MRI images into Gray level image.

Step 3: Apply HE on the input images to enhance the contrast of the image.

Step 4: Apply CLAHE on the Histogram Equalized images to reduce noise and over contrast enhancement resulting from HE.

Step 5: Output enhanced images.

Step 6: End

Figure 1 illustrates the block diagram for implementing the proposed model

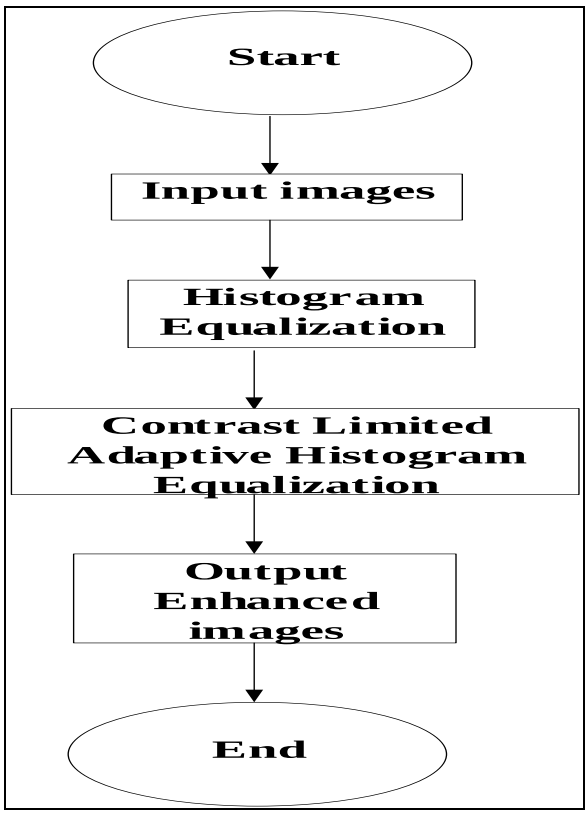

Figure 1: Illustration of steps for implementing the proposed hybrid model.
Source: Authors (2025)

III. RESULTS AND DISCUSSION

Here, simulation results were presented using HE, CLAHE and bimodal technique to enhance the quality of X-ray images showing bone femur with tumour, chest and knee, CT images depicting human kidney, human chest and human brain with tumor, and MRI images showing human lumber spine, human brain and human spine. The results were generated via simulation code written with python and implemented on Intel ® Corre ™ i5-6300U CPU @2.40GHz.. Figures. 2-4 illustrated the results of enhancement of X-ray images via HE, CLAHE and proposed (bimodal) method.

(a)

(b)

(c)

(d)

Figures 2: Simulation results for X-ray image showing bone femur with tumour, (a) original image (b) HE, (c) CLAHE and (d) proposed (bimodal) model
Source: Authors (2025)

(a)

(b)

(c)

(d)

Figure 3: Simulation results for X-ray image showing Human chest, (a) original image, (b) HE, (c) CLAHE and (d) proposed (bimodal) model

Source: Authors, (2025)

(a)

(b)

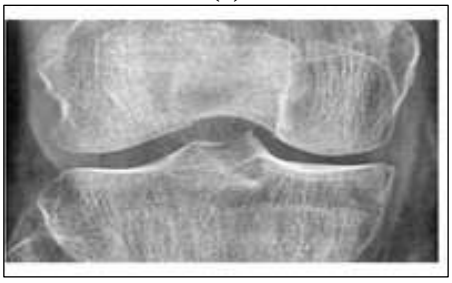

(c)

(d)

Figure 4: Simulation results for X-ray image illustrating Human knee, (a) original image, (b) HE, (c) CLAHE and (d) proposed (bimodal) model

Source: Authors, (2025)

It was found in Figures 2(b) and 4(b) that the brightness level of HE was higher than CLAHE and the proposed model. This was expected as HE has specific application in improving the contrast or brightness of an image. It was found in these images that HE produced images with too much light effect which covered internal structures of the images and which may hinder accurate clinical diagnosis. It was seen also that CLAHE images were a bit darker as seen in Fig 2-4(c). It was however observed that the proposed bimodal technique performed better than HE and CLAHE in enhancing the picture quality of X-ray images as seen in Figures 2-4(d), producing images with little light effect and moderate brightness that maintained important details of the image.

Figsures 5-7 illustrated the results of enhancement of CT images via HE, CLAHE and the proposed model.

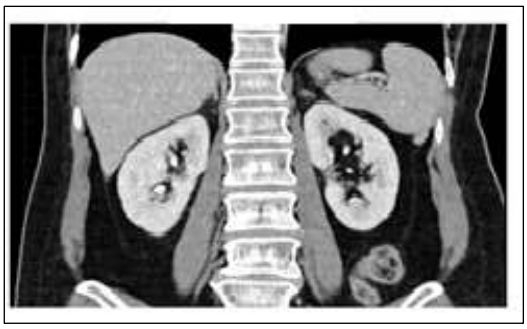

(a)

(b)

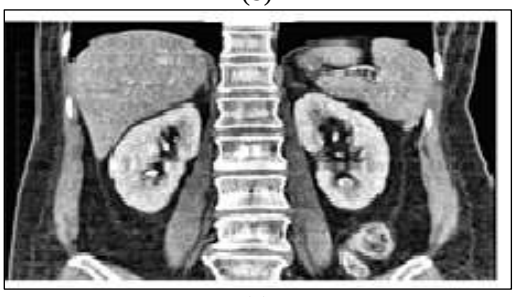

(c)

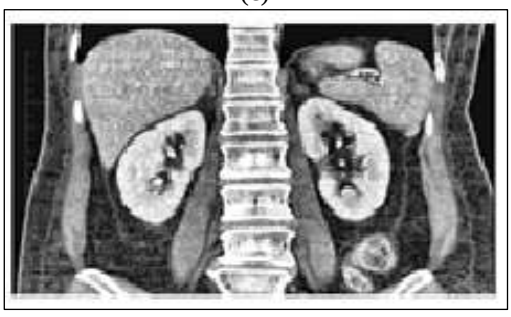

(d)

Figure 5: Simulation results for CT scan of human kidney, (a) original image (b) HE, (c) CLAHE and (d) proposed (bimodal) model

Source: Authors, (2025)

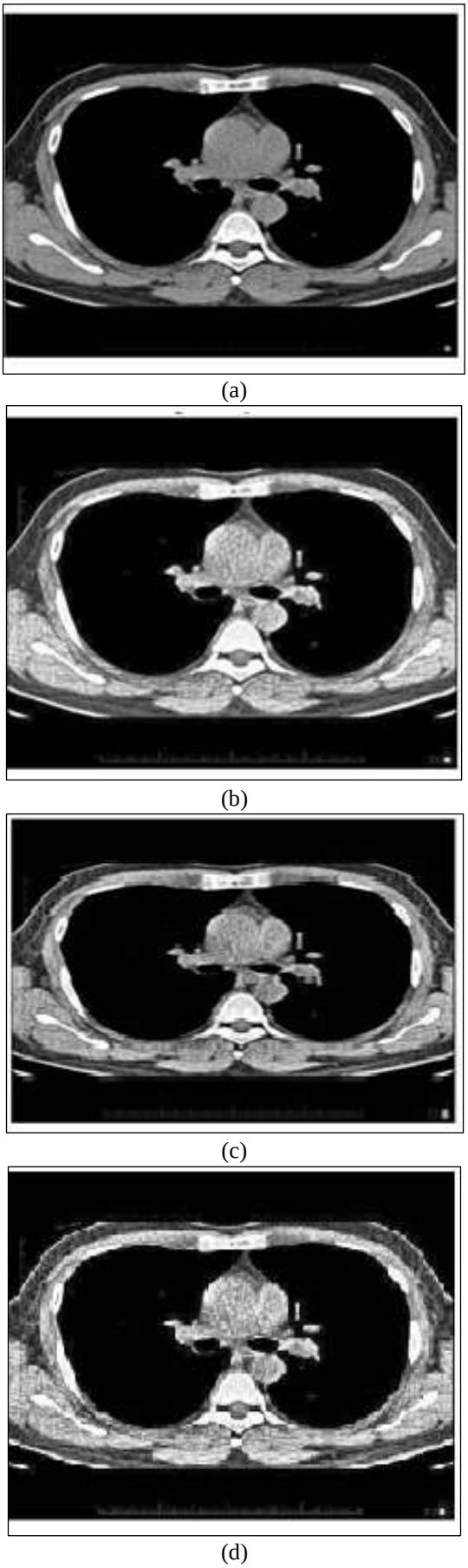

(a) (b) (c) (d)

Figure 6: Simulation results for CT scan of Human chest, (a) original image (b) HE, (c) CLAHE and (d) proposed (bimodal) model
Source: Authors, (2025)

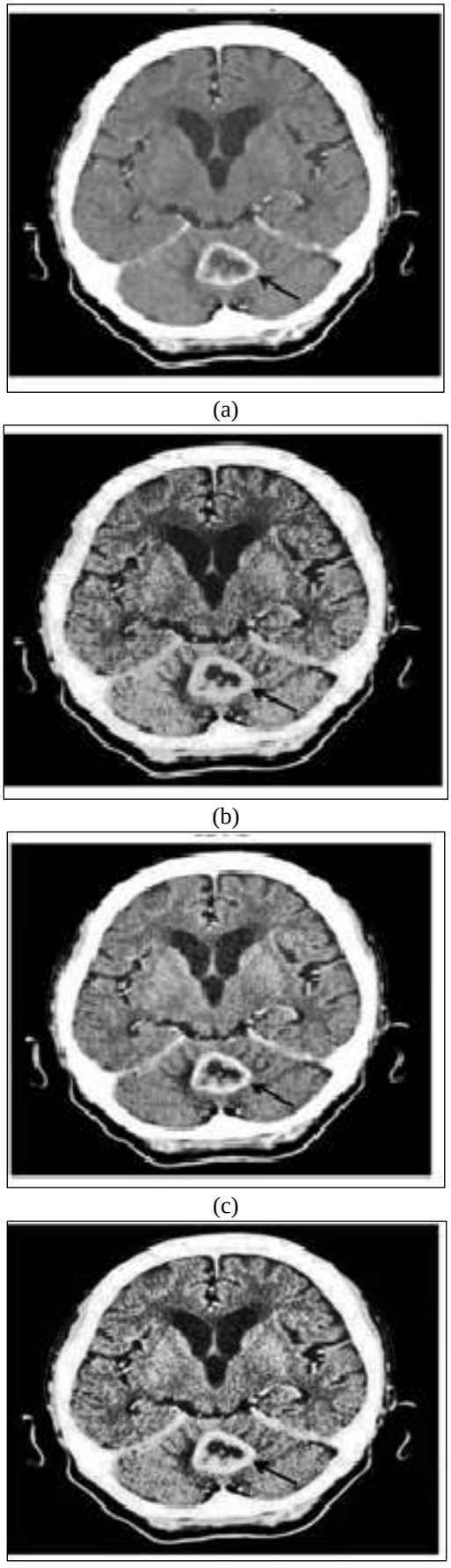

(a) (b) (c) (d)

Figure 7: Simulation results for CT scan of human brain with tumor, (a) original image, (b) HE, (c) CLAHE and (d) proposed (bimodal) model
Source: Authors, (2025)

It was observed in Figures 5-7 that the proposed bimodal technique produced better CT images than other models considered. It revealed internal features and structures of CT images better than HE and CLAHE which made it a better technique for clinical diagnosis. In addition, Figures 8-10 compared the performance of the proposed model with HE and CLAHE for enhancing MRI images.

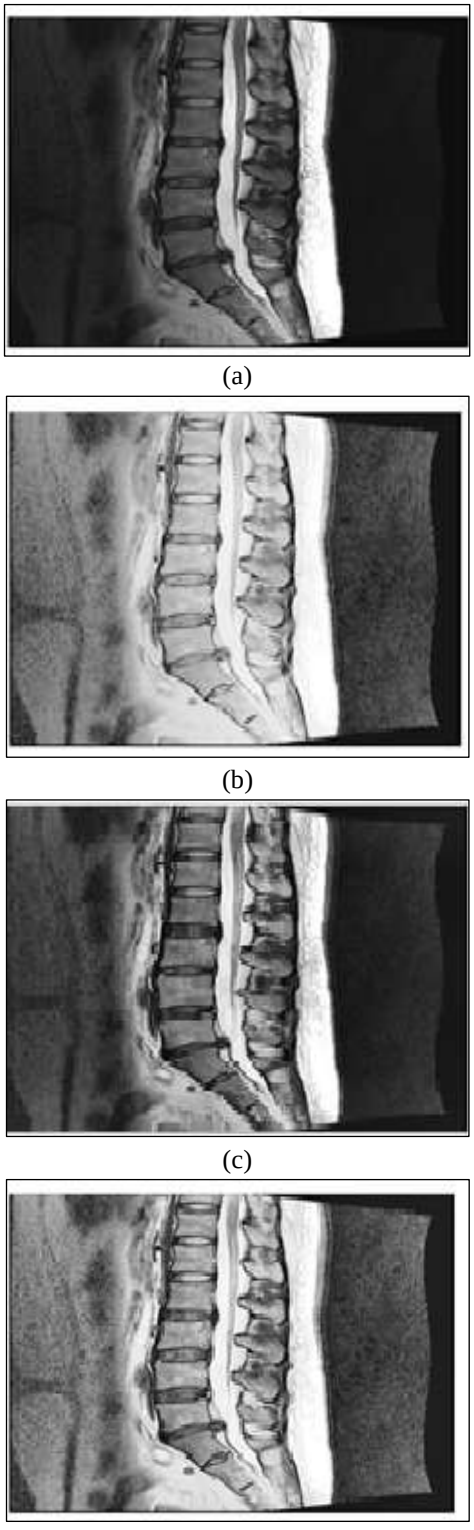

(a) (b) (c) (d)

Figure 8: Simulation results for MRI image of a human lumbar spine, (a) original image, (b) HE, (c) CLAHE and (d) proposed (bimodal) model
Source: Authors, (2025)

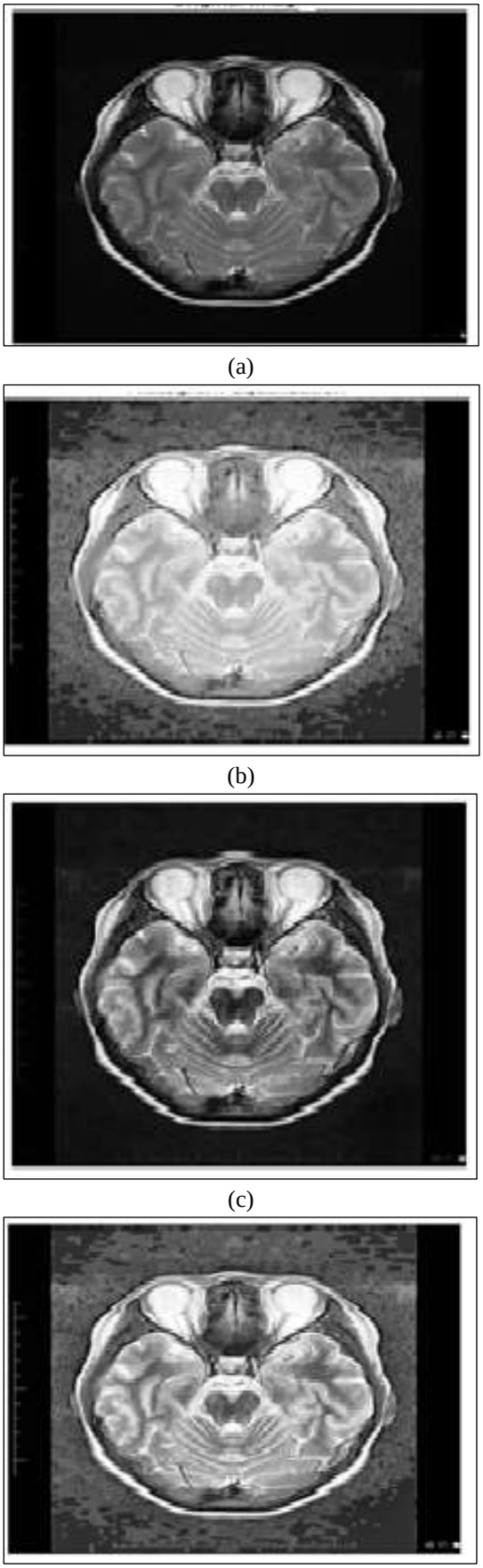

(a) (b) (c) (d)

Figure 9**:** Simulation results for MRI image of human brain, (a) original image (b) HE, (c) CLAHE and (d) proposed (bimodal) model
Source: Authors, (2025)

(a)

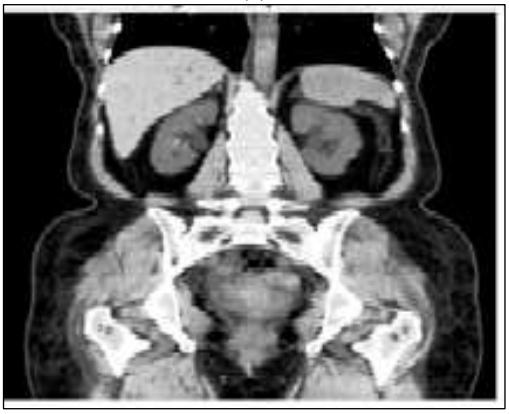

(b)

(c)

(d)

Figure 10: Simulation results for MRI image of human spine, (a) original image, (b) HE, (c) CLAHE and (d) proposed (bimodal) model
Source: Authors, (2025)

It was observed in Figures 8-10 that HE produced images with too much light effect as revealed in Figure 8-10(b) which could obstruct important structural details of the image and consequently affect its performance for clinical diagnosis. In addition, it was found that CLAHE images were better than those produced by HE. It was however observed in Figures 8-10 that the proposed bimodal technique had the best picture quality as seen in Figures 8-10 (d).

Furthermore, nine medical personnel (radiologists) were contacted to assess the quality of enhanced images shown in Figs. 2-10 in terms of brightness level, structural quality and picture quality. The opinion results of this assessment were presented in Table 1.

Table 1: Results of subjective evaluation of HE, CLAHE and the proposed model

Image category	Performance indicators	HE	CLAHE	Proposed (Bimodal) model
Bone femur X-ray	Brightness	9	-	-
	Picture quality	-	6	3
	Structural similarity with original image	6	3	-
Chest X-ray	Brightness	3	3	3
	Picture quality	3	3	3
	Structural similarity with original image	3	3	3
Knee X-ray	Brightness	3	-	6
	Picture quality	-	6	3
	Similarity with original image	3	3	3
Human Kidney CT image	Brightness	9	-	-
	Picture quality	3	-	6
	Structural similarity with original image	3	6	-
Human chest CT image	Brightness	6	-	3
	Picture quality	-	3	6
	Structural similarity with original image	-	-	9
Human brain with tumor CT image	Brightness	-	6	3
	Picture quality	-	3	6
	Structural similarity with original image	3	-	6
Human lumber spine MRI image	Brightness	3	-	6
	Picture quality	-	3	6
	Structural similarity with original image	-	6	3
Human brain MRI image	Brightness	6	-	3
	Picture quality	-	-	9
	Structural similarity with original image age	-	-	9
Human spine MRI image	Brightness	6		3
	Picture quality	3	-	6
	Structural similarity with original image	-	3	6

Source: Authors, (2025)

It was seen in table 1 that 45 radiologists out of 81 possible outcomes, polled HE as producing the brightest image while 9 polled CLAHE as producing the brightest image. On the other hand, 27 out of 81 possible outcomes polled the proposed bimodal technique as generating the brightest image.

The corresponding percentage scores of the subjective evaluations by the medical personnel resulting from the analysis presented in table 1 were illustrated in Figure 11 which revealed the rating of the brighness level of all the models considered for investigation.

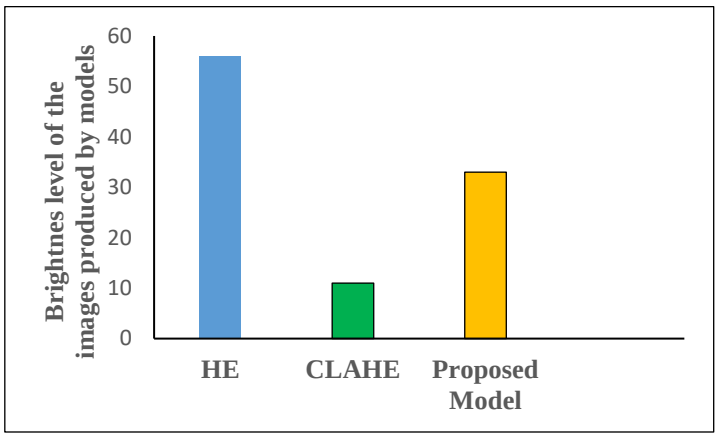

Figure 11: Comparison of brightness level of the models.
Source:Authors, (2025)

It was observed in Figure 11 that HE, CLAHE and the proposed model had the percentage scores of 56%, 11% and 33%, respectively. This implied that majority of the evaluators agreed that HE produced brighter images than others. This is in line with the expectation as the model has specific application in increasing the contrast or brightness level of images but suffer from over contrast enhancement [9]. Images in Figs 2(b), Fig. 8(b) and Fig. 9(b) supported this observation

It was observed in table 1 that the picture quality of the bimodal technique received highest poll with 48 medical personnel out of 81 preferring the model to other models. CLAHE received 24 polls while 9 medical personnel prefered HE to other models. Figure 12 presented the graphical representation of the rating of the picture quality of the images produced by different model.

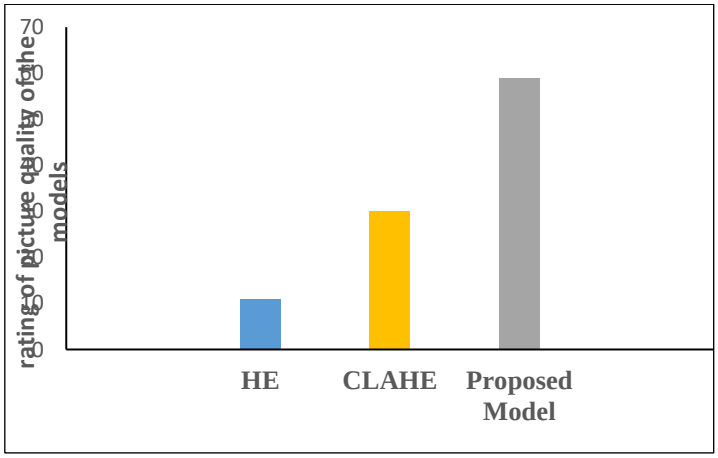

Figure 12**:** Comparison of picture quality of the models.
Source:Authors, (2025).

It was seen in Figure 12 that the picture quality scores of HE, CLAHE and the proposed model were 11%, 30% and 59%, respectively which indicated that the proposed bimodal technique had higher preference than other models. This implied that most evaluators prefered the picture quality of the model to others.

Also, in terms of structural quality when compared with the original image, 39 evaluators indicated that the proposed bimodal technique had the best structural quality while 24 and 18 prefered CLAHE and HE, respectively. Figure 13 therefore compared the evaluators' rating of the structural quality of all the models when compared with original image.

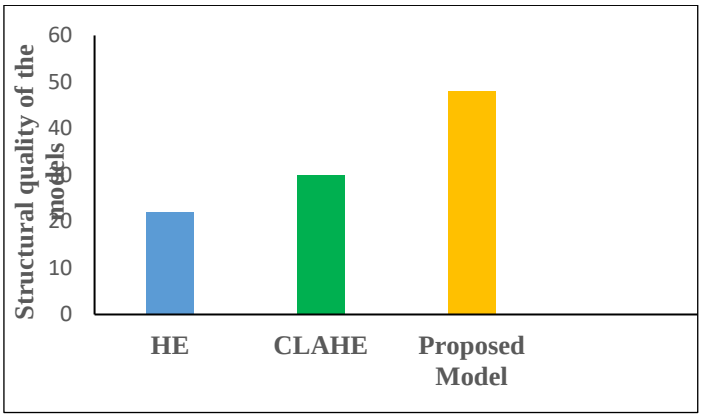

Figure 13: Comparison of the structural quality of the models
Source: Authors, (2025)

Figure 13 revealed that the proposed model had the percentage score of 48% while CLAHE and HE had 30% and 22%, respectively. This implied that majority of the evaluators chose the proposed model as having better structural quality than the other models.

IV. CONCLUSIONS

This work proposed a bimodal technique that combined Histogram Equalization (HE) and Contrast Limited Histogram Equalization (CLAHE) for enhancing the picture quality of medical images. The proposed method utilized the advantage of HE and CLAHE to enhance the picture quality and structural appearance of medical images by reducing the over contrast effect resulting from HE. Nine set of images comprising three modes of CT, X-ray and MRI images were sourced from different repositories and were used as candidates for enhancement.

The performance of the proposed model was compared with HE and CLAHE. It was found that the proposed model produced images with better picture qualities than the other models. Moreover, subjective assessment of the performance of these models by radiologists revealed that HE suffered from over enhancement which was in line with what has been previously reported in the literature. It was observed that the proposed model had better picture quality and better structural similarity with original image than other models considered for assessment and required less computational time when compared with hybrid models existing in the literature.

V. AUTHOR'S CONTRIBUTION

Conceptualization: Akeem Abimbola Raji
Methodology: Akeem Abimbola Raji, Oluwaseun Ibrahim Adebisi, Olubunmi Adewale Akinola, and Ayoade Benson Ogundare
Investigation: Akeem Abimbola Raji, Oluwaseun Ibrahim Adebisi Olubunmi Adewale Akinola, and Ayoade Benson Ogundare

Discussion of results: Akeem Abimbola Raji, Oluwaseun Ibrahim Adebisi Olubunmi Adewale Akinola, and Ayoade Benson Ogundare
Writing – Original Draft: Akeem Abimbola Raji
Writing – Review and Editing: Oluwaseun Ibrahim Adebisi and Olubunmi Adewale Akinola
Resources: Akeem Abimbola Raji, Oluwaseun Ibrahim Adebisi, Olubunmi Adewale Akinola, and Ayoade Benson Ogundare
Supervision: Akeem Abimbola Raji, Oluwaseun Ibrahim Adebisi Olubunmi Adewale Akinola, and Ayoade Benson Ogundare
Approval of the final text: Akeem Abimbola Raji, Oluwaseun Ibrahim Adebisi Olubunmi Adewale Akinola, and Ayoade Benson Ogundare
Supervision: Akeem Abimbola Raji, Oluwaseun Ibrahim Adebisi Olubunmi Adewale Akinola, and Ayoade Benson Ogundare
Approval of the final text: Akeem Abimbola Raji, Oluwaseun Ibrahim Adebisi Olubunmi Adewale Akinola, and Ayoade Benson Ogundare

VI. REFERENCES

[1] S.A. Thepade & P.M. Pardhi, "*Enhancing visibility of nighttime images using wavelet decomposition with Kekre's LuV colour space*," International Journal of Systematic Innovation,vol. 8, no. 2, pp. 17-30, 2024.

[2] T. Qiu, C. Wen, K. Xie, F-Q. Wen, G-Q Sheng, & X-G Tang, " *Efficient medical image enhancement based on CNN-FBB model*", The Institution of Engineering and Technology, vol. 13, no. 10, pp. 1736-1744, 2019.

[3] R. Gang, B. Mittal & S. Gang, " *Histogram equalization techniques for image enhancement*", IJECT, vol. 2, no. 1, pp. 107-111, 2011.

[4] O. Patel, P.S. Yogendra., & S. Sanjeev, "*A comparative study of Histogram Equalization based image enhancement techniques for brightness preservation and contrast enhancement",* Signal and Image Processing: An International Journal (SIPIJ), vol. 4, no. 5, pp. 11-25, 2013.

[5] S. Das, T. Gulati, T., & V. Mittal , "*Histogram equalization techniques for contrast enhancement: A review",* International Journal of Computer Applications, vol. 114, no. 10, pp. 32-36, 2015.

[6] H. Kaur, & J. Rani, " *MRI brain image enhancement using Histogram Equalization techniques*", Proceedings of the IEEE WISPNET 2016 conference, pp. 770-773, 2016.

[7] M.W. Mirza, A. Siddiq, & I.R. Khan, " *A comparative study of medical image enhancement algorithms and quality assessment metrics on CoVID-19 CT images*", Signal, Image and Video Processing, 17, pp. 915-924, 2023.

[8] M.P. Stephen, E.P. Ambun, J.D. Austin, R. Cromartie, R. Gezelowitz, R. Greer, B.H. Romeny, J.B. Zimmerman, & K. Zuiderveld, " *Adaptive histogram equalization and its variation"*, Computer Vision, graphics and Image Processing, 39, pp. 355-368, 1987.

[9] A.M. Reza," *Realization of the Contrast Limited Adaptive Histogram Equalization (CLAHE) for Real-time image enhancement*", Journal of VLSI Signal Processing, 38, 35-44, 2004.

[10] R.P. Pai, S. Halvi, B. & Hiremath, "*Medical color image enhancement using wavelet transform and contrast strengthening technique",* International Journal of Scientific and Research Publications, vol. 15, no. 7, pp. 1-7, 2015.

[11] L. Kong, M. Huang, L. Zhang, & L-W Chi Chan, " *Enhancing diagnostic images to improve the performance of the segment anything model in medical image segmentation*", Bioengineering, vol. 11, no. 270, pp. 1-15, 2024. https: doi.org/10.3390/bioengineering/1103027s.

[12] C. Priya, C. Ramya, P. Gayatri, A.G. Gughan, P.K. Hema, & D. Hemala, " *A significant method for image enhancement*", International Journal of Innovative Technology and Exploring Engineering (IJITEE), vol. 8, no. 65, pp. 271-275, 2019

[13] W. Zhu, H.Jiang, E. Wang, &Y. Hou, " *X-ray image global enhancement algorithm in medical image*", Classification, Discrete and Continuous Dynamical System Series C, vol. 12, no. 485, pp. 1297-1309, 2019.

[14] A.Zaafouri, M. Sauadi, & F. Fnaiech, " *A developed Unsharp Masking method for image contrast enhancement",* 2011 8th International Multi-Conference on Systems, Signals and Devices, 2011

[15] R-C Bilcu & M. Vehvilainen, (2008), "*Constrained Unsharp Masking for image enhancement*", ICISP, pp. 10-19., 2008.

[16] K. Sarath & Sreejiths, " *Low contrast image enhancement using fuzzy logic",* IOSR Journal of Electronics and Communication Engineering (IOSR-JECE), pp. 34-44, 2017

[17] T.Agarkar, "*Underwater enhancement using fuzzy logic*", Turkish Online Journal of Qualitative Inquiry (TOJQI), vol. 11, no. 4, pp. 1362-1369, 2020.

[18] S. Sharma, & A. Bhatia, " *Contrast enhancement of an image using fuzzy logic*", International Journal of Computer Applications, vol. 14, no. 17, pp. 14-20, 2015.

[19] P.C. Zhang, "*Image enhancement method based on deep learning*. Mathematical Problems in Engineering", pp. 1-9, 2002. https: doi.org/10.1155/2022/6797367.

[20] K.A. Amusa, O.I Idowu, I.A. Adejumobi, & G.A. Adebayo, " *Tri-modal technique for medical image enhancement*", International Journal of Advances in Applied Sciences (IJAAS), vol. 11, no. 3, pp. 199-210, 2022.

Journal of Engineering and Technology for Industrial Applications

ISSN ONLINE: 2447-0228

ITEGAM-JETIA

Manaus, v.11 n.53, p. 186-192. May/June., 2025.
DOI: https://doi.org/10.5935/jetia. v11i53.1672

RESEARCH ARTICLE OPEN ACCESS

OPTIMIZED PID TUNING IN LONGITUDINAL CONTROL OF ELECTRIC AUTONOMOUS VEHICLES: A COMPARATIVE STUDY OF JELLYFISH SEARCH AND GENETIC ALGORITHM

Asmaa Guendouz[1], Mustapha Hatti[2], Abdelhalim Tlemçani[3]

[1,3]Electrical Engineering and Automation Research Laboratory (LREA), University of Medea, Medea, Algeria.
[2]UDES, Unit for the Development of Solar Equipment, BP 386, 42004 Bou Ismail, Tipaza, Algeria.

[1]http://orcid.org/0009-0006-9260-833X, [2]http://orcid.org/0000-0002-8645-207X, [3]http://orcid.org/0000-0002-4385-671X

Email: guendouz.asma@univ-medea.dz, mustapha.hatti@ieee.org, tlemcani.abdelhalim@univ-medea.dz

ARTICLE INFO

Article History
Received: February 28, 2025
Revised: May 20, 2025
Accepted: June 15, 2025
Published: June 30, 2025

Keywords:
Metaheuristic Algorithms,
Electric Autonomous Vehicles,
Jellyfish Search optimizer,
Genetic Algorithms,
PID based Longitudinal Control.

ABSTRACT

Tuning PID controllers to enhance longitudinal control and speed planning of Electric Autonomous Vehicles is a challenge, which can be effectively addressed by evolving metaheuristic algorithms. This paper evaluates the performance of the Jellyfish Search (JS) optimizer and Genetic Algorithms (GA) against conventional PID tuning methods in longitudinal control systems. A modified objective function combining Time-weighted Absolute Error (ITAE) and Integral Square Error (ISE) is proposed based on the weighted sum method, aiming to balance performance metrics and overcome the limitations of conventional objective functions. This function is optimized by both genetic and jellyfish techniques. The simulations are conducted through realistic scenarios in accordance with road safety standards, using a sinusoidal profile as speed reference. The results demonstrate the effectiveness of both GA and JS in outperforming conventional PID, achieving zero overshoot, reduced settling times, and lower steady-state errors. Observably, JS optimizer exhibits a slight advantage over GA in the overall performance, especially fast convergence. These outcomes validate the contribution of the proposed approaches in enhancing the field of autonomous driving.

I. INTRODUCTION

Autonomous driving has been the subject of significant research and development for many years to this day. The control system consists of lateral and longitudinal control. This work presents a contribution in longitudinal control for Electric Autonomous Vehicles (EAVs), specifically addressing optimized techniques and speed profiles to ensure safety, comfort and efficiency. A wide array of control strategies has been employed for longitudinal control, including PID control [1]. However, tuning PID gains is a challenging task, as traditional approaches such as trial-and-error methods often fall short. This matter is addressed via optimization-based tuning techniques such as metaheuristic algorithms [2]. In the literature, the Integral Absolute, Square, Time-weighted Squared, and Time-weighted Absolute Errors (IAE), (ISE), (ITSE), and (ITAE), are generally the most used metrics for the cost function [3],[4], which can give suboptimal performance in certain scenarios.

This paper proposes a combination of these performance metrics to build the cost function based on the weighted sum method [5], where ITAE and ISE are combined to build a robust objective function to guarantee a better tuning and high performance. The weights are selected through observation of the output's behavior and performance, including overshoot, settling time and steady-state error. Moreover, the two optimization techniques used to optimize the selected cost function are Genetic Algorithms (GAs) and the Jellyfish Search (JS) optimizer.

GAs are widely used in several applications, being a class of evolutionary algorithms inspired by the principle of natural selection, their contribution is proven effective, in particular in control systems and PID tuning [6]. JS optimizer is a recently developed nature-inspired optimization algorithm that mimics the motion patterns of jellyfish in the sea. It balances exploration and

exploitation to find optimal solutions using passive and active motions. This algorithm demonstrates high performance in certain optimization tasks due to its dynamic adaptation and enhanced global search capability [7].

The configuration of this paper is arranged as follows. The speed control system is presented in section **II**. Section **III** discusses the optimization methods. In section **IV**, simulation results and discussions are given to validate the proposed methods, followed by a conclusion.

II. SYSTEM DESCRIPTION

In this section, the design of the speed control system for an EAV is introduced. The system employs a direct current (DC) motor as the speed actuator and a Proportional-Integral-Derivative (PID) as the main controller.

II.1 DC MOTOR MODELLING

The DC motor is described by the equations given below [8].

DC motor Equations

$$V = R_a \cdot i_a + e + L_a \cdot \frac{di_a}{dt} \quad (1)$$

$$e = k \cdot \Omega \quad (2)$$

$$J \cdot \frac{d\Omega}{dt} = T_{em} - f \cdot \Omega - T_L \quad (3)$$

$$T_{em} = k_{em} \cdot i_a \quad (4)$$

Where, V is the input voltage, e is the back electromotive force (EMF), i_a is the current in the motor winding, T_{em} is the electromagnetic torque, and Ω is the angular velocity.

The parameters of the DC motor are given in Table 1. These latter are selected to approximate the characteristics of a Tesla Model S, with a torque of $T_L = 430Nm$, as specified in the catalog provided in [9].

Table 1: DC Motor Parameters.

Parameter	value
Armature resistance R_a	0.193 Ω
Armature inductance L_a	0.00383 H
Back EMF constant k	2.332232 $V.s$
Torque constant k_{em}	2.1717 $N.m/A$
Moment of inertia J	0.6 $kg \cdot m^2$
Coefficient of friction f	2.632177 $N.m.s$

Source: Authors, (2025).

To simulate the motor's performance, it has been modeled in MATLAB Simulink, as shown in Figure 1.

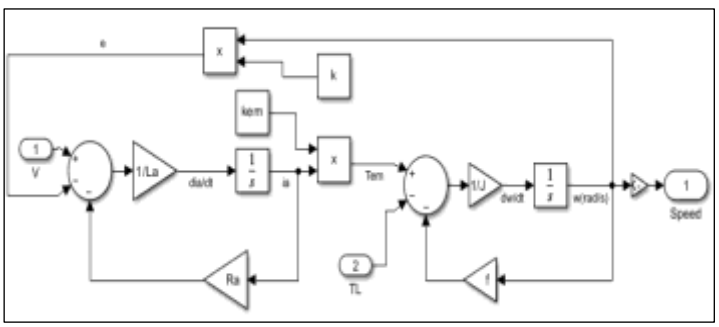

Figure 1: DC motor block diagram.
Source: Authors, (2025).

II.2 PID CONTROLLER

PID controllers are the basis of control systems, they provide a simple yet powerful framework. The transfer function describing a PID controller is given in Equation 5. K_P, K_I, and K_D are the proportional, integral, and derivative gains, respectively [10].

PID transfer function

$$G(s) = K_P + \frac{K_I}{s} + K_D.s \quad (5)$$

The performance of this controller is based on the selection of its gains. However, the outcome of the conventional methods is limited and often demonstrates inadequate disturbance rejection, which highlights the need for more advanced optimization techniques.

III. OPTIMIZATION METHODS

III.1 OBJECTIVE FUNCTION

In order to satisfy the performance criteria, including minimal overshoot, rapid settling time, and low steady-state error. The optimization process focuses on minimizing an objective function (cost function), denoted f, a mathematical expression that quantifies the system's performance for optimization. This latter is formulated based on the performance metrics. IAE, ISE, ITSE, and ITAE [4].

The Integral Absolute Error

$$IAE = \int |e(t)|dt \quad (6)$$

Integral Square Error

$$ISE = \int e^2(t)dt \quad (7)$$

Integral Time-weighted Absolute Error

$$ITAE = \int t|e(t)|dt \quad (8)$$

Integral Time-weighted Squared Error

$$ITSE = \int t\, e^2(t)dt \quad (9)$$

The selection of the cost function in this study is based on the weighted sum method [5], by combining ITAE and ISE. Where $w_1 = 0.2$ and $w_2 = 0.8$. These latter are selected to emphasize steady-state performance, while ensuring reasonable transient performance [11].

Objective function

$$f = w_1 \cdot ITAE + w_2 \cdot ISE \quad (10)$$

III.2 GENETIC ALGORITHM

Genetic Algorithms (GAs) are metaheuristic algorithms inspired by the biological evolution process that employ an intelligent exploitation of a stochastic search. These algorithms evolve a group of potential solutions across multiple generations through selection, recombination, and mutation. [12]. The mechanism's process is illustrated in Figure 2.

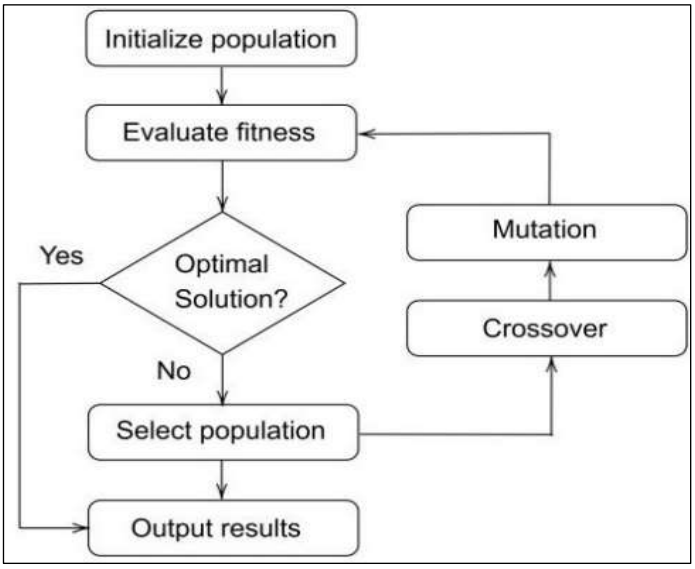

Figure 2: GA process flowchart.
Source:[13].

III.3 JELLYFISH SEARCH OPTIMIZER

The Jellyfish Search (JS) optimizer is a recent metaheuristic optimization algorithm developed by Jui-Sheng Chou et al. [14]. It is built based on an inspiration of the behavior of jellyfish food-seeking process in the ocean. The first step involves following the ocean current to find regions rich in food resources (optimal solutions), this step is called the exploration phase. Over time, a jellyfish swarm is created, and each jellyfish pursues the motion within the swarm to discover a more optimal location, which is translated as active and passive motions, representing the exploitation phase. Meanwhile, time control is introduced to identify the varied motion types and regulate the transition, which makes the optimum phase [15]. The overall process is illustrated in Figure 3.

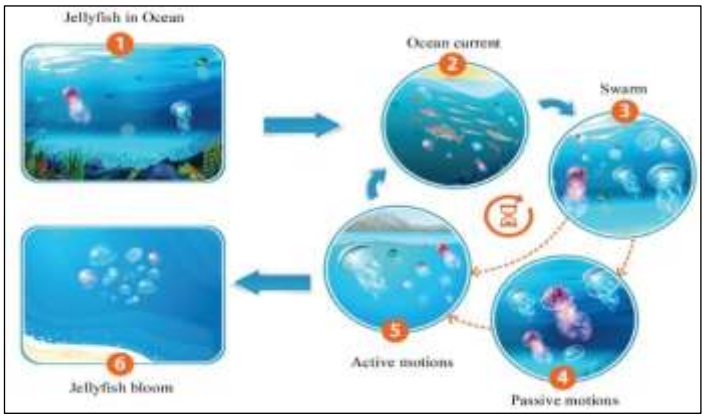

Figure 3: Jellyfish behavior process.
Source: [14].

The mechanism process of the Jellyfish Search (JS) optimizer is governed by a series of mathematical equations given below. These latter are detailed in [14].

Trend Calculation

$$\overrightarrow{tr} = Z^* - \beta \times \text{rand}(0,1) \times \mu \quad (11)$$

Active Motion Update

$$Z_i(t+1) = Z_i(t) + \text{rand}(0,1) \times (Z^* - \beta \times \text{rand}(0,1) \times \mu) \quad (12)$$

Passive Motion Update

$$Z_i(t+1) = Z_i(t) + \gamma \times \text{rand}(0,1) \times (U_b - L_b) \quad (13)$$

Direction Calculation

$$\overrightarrow{\text{Dr}} = \begin{cases} Z_j(t) - Z_i(t), & \text{if } f(Z_i) \geq f(Z_j) \\ Z_i(t) - Z_j(t), & \text{if } f(Z_i) < f(Z_j) \end{cases} \quad (14)$$

Position Update

$$Z_i(t+1) = Z_i(t) + \overrightarrow{\text{Step}} \quad (15)$$

$$\overrightarrow{\text{Step}} = \text{rand}(0,1) \times \overrightarrow{\text{Dr}} \quad (16)$$

Time Control Function

$$c(t) = \left| \left(1 - \frac{t}{\text{I}_{\max}}\right) \times (2 \times \text{rand}(0,1) - 1) \right| \quad (17)$$

Where $\overrightarrow{tr}$ is the direction of the ocean current, $Z_i(t)$ is the location of the i[th] jellyfish at time t, U_b *and* L_b are upper and lower bounds, β is a distribution coefficient, μ is the mean location of all jellyfish, γ is a motion coefficient, and $\text{I}_{\max}$ is the maximum number of iterations.

Algorithm 1 represents the pseudocode of the JS optimization based PID tuning. The corresponding flowchart is illustrated in Figure 4.

Algorithm 1: JS PID tuning pseudo-code
Begin
Intialize **PID** parameters
Objective function **f(Z)** calculation (Equation **10**)
Set: population size $\boldsymbol{n_{pop}}$**=100**
maximum iteration $\text{I}_{\max}$**=50**
Initialization of the population of jellyfish $\boldsymbol{Z_i}$ **(i=1, 2, ...,** $\boldsymbol{n_{pop}}$**)** through logistic chaotic map
Calculation of the quantity of food at each $\boldsymbol{Z_i}$, **f (**$\boldsymbol{Z_i}$**)**
Search of jellyfish at current location with most food (**Z***)
Initialize time: **t = 1**
Repeat
For i = 1: $\boldsymbol{n_{pop}}$ **do**
Calculation of the time control function c(t) (Equation **17**)
If c(t) ≥ 0.5:
Jellyfish pursuit of the ocean current
1. Determination of the ocean current (Equation **11**)
2. New location calculation (Equation **12**)
Else: Jellyfish motion inside a swarm
If rand (0,1) > (1 - c(t)): Passive motions
Location update by Equation **13**
Else: Jellyfish exhibits Active motions
1. Calculation of the direction of jellyfish (Equation **14**)
2. Location of jellyfish is updated by Equation **15**
End If
End If
Boundary check and calculation of the quantity of food at new location
Location update (**$\boldsymbol{Z_i}$, Z***)
End For
Time Update: **t ++**
Until stop criterion is met
Output: convergence iteration
the best results: K_P, K_I, and K_D
the best optimal value of the objective function
End

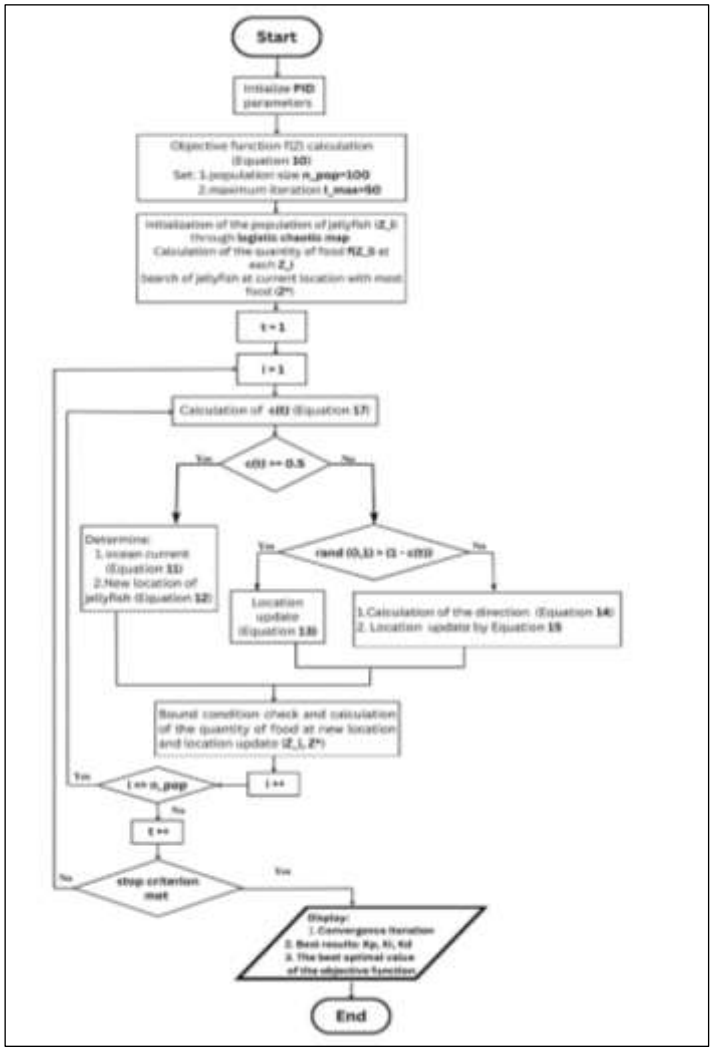

Figure 4: JS Flowchart for PID tuning.
Source: Authors, (2025).

IV. RESULTS AND DISCUSSIONS

The designed PID longitudinal control system is evaluated on a 2 km road segment. Initially, the PID gains are determined using the conventional trial-and-error method. The performance of this approach is then compared to the optimized PID gains via the Jellyfish Search (JS) optimizer and Genetic Algorithm (GA). The overall control system is illustrated in Figure 5.

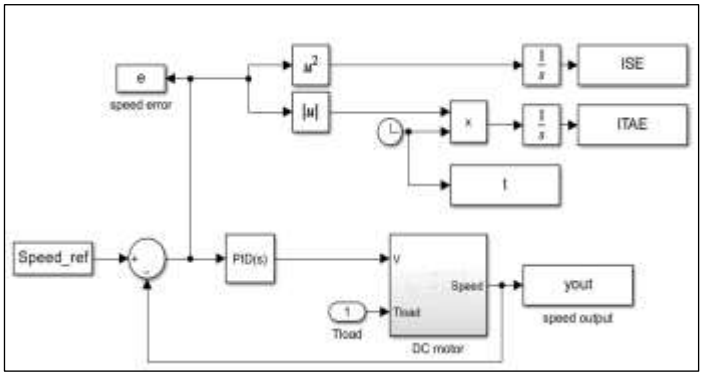

Figure 5: PID longitudinal control system.
Source: Authors, (2025).

The speed input selected for this scenario is the optimized sinusoidal profile (Figure 6), characterized by the following parameters:

A speed limit V_m of $28.8\,km/h\,(8m/s)$, suitable for urban environments as per the ISO 2631 standard**.** An acceleration limit, $A_m = 0.4\,m/s^2$ chosen based on the ISO 22737 standard**.** This speed input considers urban travel whilst maintaining safety, smooth driving, and passenger comfort.

The initialization parameters for both GA and JS optimizer are given in Tables 2 and 3 respectively.

Table 2: GA Parameters.

Parameter	**value**
Number of variables	3
Lower bounds	[0,0,0]
Upper bounds	[20, 500, 10]
Max generation	50
Population size	100
Crossover fraction	0.8
Mutation	Adaptive feasable mutation

Source: Authors, (2025).

Table 3: JS Parameters.

Parameter	**value**
dimensions	3
Lower bounds	[0,0,0]
Upper bounds	[20, 500, 10]
Max Iterations	50
Population size	100
Stopping Condition	Convergence Check
Initialization Method	Logistic Map

Source: Authors, (2025).

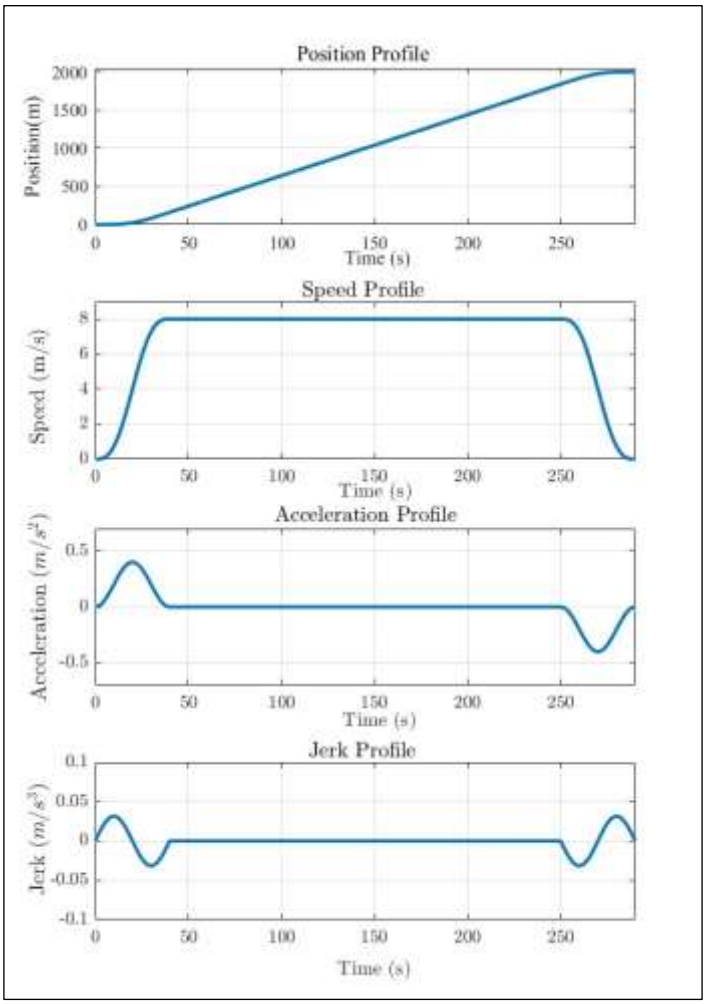

Figure 6: Sinusoidal profiles.
Source: Authors, (2025).

The GA corresponding results are illustrated in Figure 7. The statistical indices of the algorithm's outcome are given in Table 4.

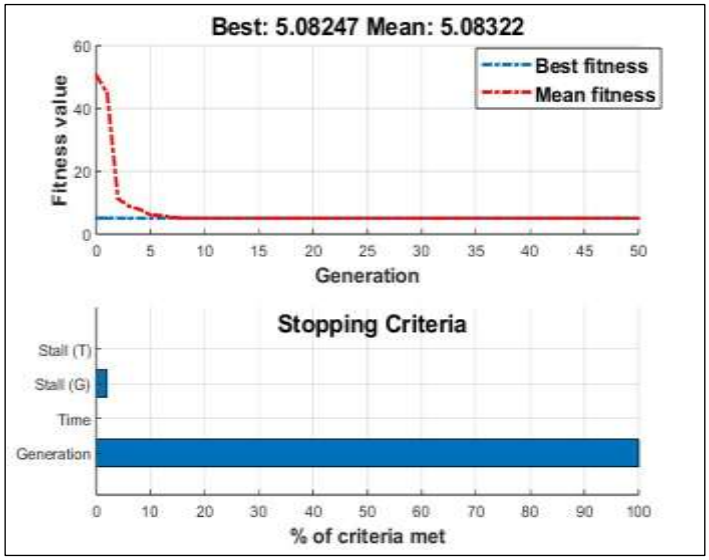

Figure 7: Genetic algorithm results.
Source: Authors, (2025).

Table 4: Progress of the Genetic Algorithm.

Generation	Func-count	Best f(z)	Mean f(z)	Stall Generations
1	200	5.103	44.930	0
2	295	5.094	11.300	0
3	390	5.092	8.905	0
4	485	5.092	7.892	0
5	580	5.092	6.107	1
6	675	5.087	5.937	0
7	770	5.087	5.328	0
8	865	5.087	5.097	0
9	960	5.087	5.095	0
10	1055	5.087	5.094	0
11	1150	5.087	5.093	0
12	1245	5.087	5.093	1
13	1340	5.084	5.092	0
14	1435	5.084	5.091	1
15	1530	5.084	5.087	0
16	1625	5.084	5.087	1
17	1720	5.084	5.086	2
18	1815	5.083	5.086	0
19	1910	5.083	5.086	0
20	2005	5.083	5.086	1
21	2100	5.083	5.085	0
22	2195	5.083	5.084	1
23	2290	5.083	5.084	2
24	2385	5.083	5.083	3
25	2480	5.083	5.083	0
26	2575	5.083	5.083	0
27	2670	5.083	5.083	0
28	2765	5.083	5.084	1
29	2860	5.083	5.083	2
30	2955	5.083	5.083	3
31	3050	5.083	5.083	4
32	3145	5.083	5.083	0
33	3240	5.083	5.083	0
34	3335	5.083	5.083	1
35	3430	5.083	5.083	2
36	3525	5.083	5.083	3
37	3620	5.083	5.083	0
38	3715	5.083	5.083	1
39	3810	**5.082**	5.083	0
40	3905	5.082	5.083	1
41	4000	5.082	5.083	2
42	4095	5.082	5.083	0
43	4190	5.082	5.083	0
44	4285	5.082	5.083	0
45	4380	5.082	5.083	0
46	4475	5.082	5.083	0
47	4570	5.082	5.083	0
48	4665	5.082	5.083	0
49	4760	5.082	5.083	0
50	4855	5.082	5.083	1

Source: Authors, (2025).

The results obtained from the Jellyfish Search (JS) algorithm demonstrate its effectiveness in PID tuning, converging at iteration **7** with optimal parameters. The best cost function value achieved is **5.083**. In Table 5, The performance of the JS optimizer is compared to those of GA and conventional PID.

Table 5: Comparative study of PID gains.

Technique	K_p	K_i	K_d	Objective Function
Convetional PID	19	100	0.5	44.7791
JS optimizer	4.3455	499.998	9.7863	5.083
GA	0.00087	499.999	4.2312	5.082

Source: Authors, (2025).

In terms of objective function optimization, metaheuristic algorithms (JS & GA) effectively improve PID tuning compared to conventional methods. These algorithms, produce very similar performance. However, JS algorithm has a slightly more balanced gain distribution. Furthermore, The GA algorithm converged to the best solution around iteration **39** as it's highlighted in Table 4, while JS optimizer converged at the **7th** iteration, reducing time cost while maintaining optimization quality.

The speed outputs and their corresponding Error plot, of the Jellyfish algorithm (JS), Genetic algorithm (GA), and conventional PID (Conv PID) are depicted in Figures 8 and 9 respectively. All methods perform good tracking performance. However, the zoomed-in inset highlights an overshoot exhibited by conventional PID response while, GA and JS optimizers perform smoother responses with less deviation, indicating better control performance.

Figure 9 shows that the Conv PID output falls short in the transitory phase, with larger transient errors, and also struggles with steady-state accuracy. In contrast, GA and JS are proven effective. Table 6 highlights the results discussed earlier, where both JS Optimizer and GA outperform conventional PID tuning, with zero overshoot, faster settling times, and lower steady-state errors. JS Optimizer slightly outperforms GA in rapidity performance.

Table 6: Performance criteria comparison.

Technique	Overshoot (%)	Settling Time (s)	Rise time (s)	Steady-State Error (m/s)
Convetional PID	0.52	41.64	34.236	10^{-4}
JS optimizer	0	38.93	34.153	10^{-5}
GA	0	40.41	34.156	10^{-5}

Source: Authors, (2025).

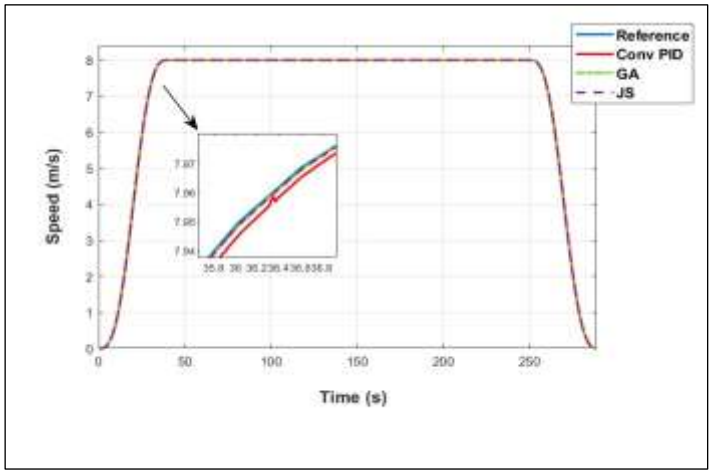

Figure 8: Speed response of the longitudinal PID control system.
Source: Authors, (2025).

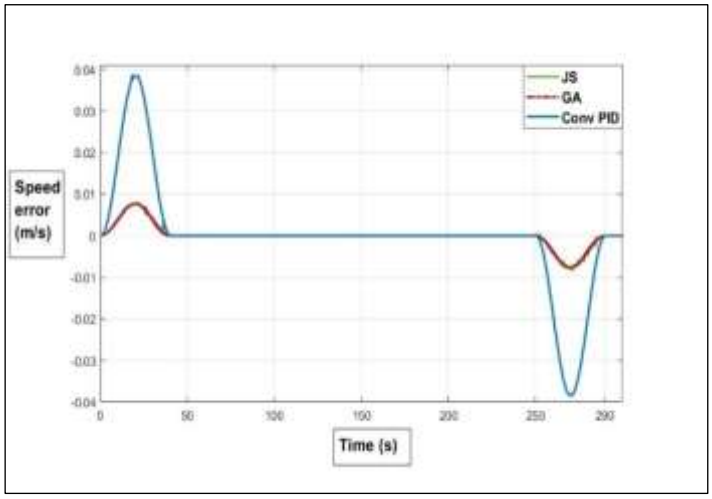

Figure 9: Error plot.
Source: Authors, (2025).

V. CONCLUSIONS

This paper presented a contribution to the implementation of Metaheuristic optimization algorithms in the field of Electric Autonomous Vehicles, by comparing Jellyfish Search (JS) and Genetic Algorithm (GA) to conventional methods in tuning PID controllers for the construction of a robust yet simple longitudinal control system.

Furthermore, simulation results were conducted on a realistic driving scenario using a sinusoidal speed profile, adhering to road standards, leading to smoother, safer, and more efficient driving performance.

The effectiveness of metaheuristic optimization techniques (Jellyfish Search and Genetic Algorithm) has been proven in tuning PID controllers for their significant improvements in key performance metrics such as overshoot, settling time, rise time, and steady-state error.

Both GA and JS eliminated the delay and overshoot exhibited by the conventional PID. Notably, JS provided the fastest convergence and required less computation time due to its ability to balance between exploration and exploitation, making it an excellent metaheuristic algorithm for EAV's speed control.

However, further work should be considered to explore hybrid optimization techniques and real-time implementation to further validate these findings.

VI. AUTHOR'S CONTRIBUTION

Conceptualization: Asmaa Guendouz, Mustapha Hatti, Abdelhalim Tlemçani.
Methodology: Asmaa Guendouz, Mustapha Hatti, Abdelhalim Tlemçani.
Investigation: Asmaa Guendouz, Mustapha Hatti, Abdelhalim Tlemçani.
Discussion of results: Asmaa Guendouz, Mustapha Hatti, Abdelhalim Tlemçani.
Writing – Original Draft: Asmaa Guendouz, Mustapha Hatti, Abdelhalim Tlemçani.
Writing – Review and Editing: Asmaa Guendouz, Mustapha Hatti, Abdelhalim Tlemçani.
Resources: Asmaa Guendouz, Mustapha Hatti, Abdelhalim Tlemçani.
Supervision: Asmaa Guendouz, Mustapha Hatti, Abdelhalim Tlemçani.
Approval of the final text: Asmaa Guendouz, Mustapha Hatti, Abdelhalim Tlemçani.

VIII. REFERENCES

[1] B. Paden, M. Čáp, S. Z. Yong, D. Yershov and E. Frazzoli, "A Survey of Motion Planning and Control Techniques for Self-Driving Urban Vehicles," in *IEEE Transactions on Intelligent Vehicles*, vol. 1, no. 1, pp. 33-55, March 2016, doi: 10.1109/TIV.2016.2578706.

[2] H. R. Moshtaghi, A. T. Eshlaghy, and M. R. Motadel, "A comprehensive review on meta-heuristic algorithms and their classification with novel approach," *J. Appl. Res. Ind. Eng.*, vol. 8, no. 2, pp. 151–174, 2021, doi: 10.22105/jarie.2021.238926.1180.

[3] H. S. Elias, "A longitudinal control for an autonomous vehicle using modified particle swarm optimization method," *Int. J. Eng. Technol.*, vol. 13, no. 1, pp. 123–131, 2024, doi: 10.14419/q6bgfv04.

[4] R. Pazmiño, W. Pavon, M. Armstrong, and S. Simani, "Performance evaluation of fractional proportional–integral–derivative controllers tuned by heuristic algorithms for nonlinear interconnected tanks," *Algorithms*, vol. 17, no. 7, Art. no. 306, Jul. 2024, doi: 10.3390/a17070306.

[5] R. T. Marler and J. S. Arora, "The weighted sum method for multi-objective optimization: new insights," *Struct. Multidisc. Optim*, vol. 41, pp. 853–862, 2010, doi: 10.1007/s00158-009-0460-7.

[6] T. Alam, S. Qamar, A. Dixit, and M. Benaida, "Genetic algorithm: Reviews, implementations, and applications," *Int. J. Eng. Pedagog.*, vol. 10, no. 6, pp. 57–66, 2020, doi: 10.3991/ijep.v10i6.14567.

[7] A. Khare, G. M. Kakandikar, and O. K. Kulkarni, "An insight review on jellyfish optimization algorithm and its application in engineering," *Rev. Comput. Eng. Stud.*, vol. 9, no. 1, pp. 31–40, 2022, doi: 10.18280/rces.090103.

[8] F. Mohamad Farid and P.-W. Hsueh, "Parameters identification of a permanent magnet DC motor: A review," *Electronics*, vol. 12, no. 12, Art. no. 2559, 2023, doi.3201410.3390/electronics12122559.

[9] LEROY-SOMER, "D.C. motors 2 to 750 kW," 2020. [Online]. Available: https://www.leroysomer.com/documentation_pdf/3805_en.pdf.

[10] S. Singh, V. Singh, A. Rani and J. Yadav, "Optimization of PID controller based on various tuning methods," *2023 International Conference on Power, Instrumentation, Energy and Control (PIECON)*, Aligarh, India, 2023, pp. 1-6, doi: 10.1109/PIECON56912.2023.10085805.

[11] J. E. Naranjo, F. Serradilla, and F. Nashashibi, "Speed control optimization for autonomous vehicles with metaheuristics," *Electronics*, vol. 9, no. 4, Art. no. 551, Mar. 2020, doi: 10.3390/electronics9040551.

[12] A. Lambora, K. Gupta and K. Chopra, "Genetic Algorithm- A Literature Review," *2019 International Conference on Machine Learning, Big Data, Cloud and Parallel Computing (COMITCon)*, Faridabad, India, 2019, pp. 380-384, doi: 10.1109/COMITCon.2019.8862255.

[13] Y. Kebbati, N. Ait-Oufroukh, V. Vigneron, D. Ichalal and D. Gruyer, "Optimized self-adaptive PID speed control for autonomous vehicles," *2021 26th International Conference on Automation and Computing (ICAC)*, Portsmouth, United Kingdom, 2021, pp. 1-6, doi: 10.23919/ICAC50006.2021.9594131.

[14] J.-S. Chou and D.-N. Truong, "A novel metaheuristic optimizer inspired by behavior of jellyfish in ocean," *Appl. Math. Comput.*, vol. 389, Art. no. 125535, 2020, doi: 10.1016/j.amc.2020.125535.

[15] A. F. Güven, et al., "Comprehensive optimization of PID controller parameters for DC motor speed management using a modified jellyfish search algorithm," *Optim. Control Appl. Methods*, 2024, doi: 10.1002/oca.3218.

Journal of Engineering and Technology for Industrial Applications

ITEGAM-JETIA

Manaus, v.11 n.53, p. 193-200. May/June., 2025.
DOI: https://doi.org/10.5935/jetia. v11i53.1898

ISSN ONLINE: 2447-0228

RESEARCH ARTICLE OPEN ACCESS

AI-POWERED SIMULTANEOUS MULTI-VEHICLE SPEED ESTIMATION FOR INTELLIGENT TRAFFIC MONITORING IN DEVELOPING REGIONS USING YOLOV7 AND DEEPSORT

Merrad Ahmed[1], Daoud Walid[2], Dalouli Aissa[3], Latrech Boubakeur[4] and Nouri Abdelkader Nabil[5]

[1,2,3,4,5] Laboratory of Computer Science & Applied Artificial Intelligence, Faculty of Exact Sciences & Computer Science, University of Djelfa PO Box 3117, Djelfa 17000, Algeria.

[1]https://orcid.org/0009-0003-4084-4291, [2]https://orcid.org/0009-0005-9609-6645, [3]https://orcid.org/0009-0005-7659-0769
[4]http://orcid.org/ 0009-0007-9367-3368, [5]https://orcid.org/0000-0003-1439-0209

Email: ahmed.merrad@univ-djelfa.dz , waliddaoud230@gmail.com , Dellouliaissa@gmail.com , b.latreche@univ-djelfa.dz, nabil.nouri@gmail.com

ARTICLE INFO

Article History
Received: May 19, 2025
Revised: June 20, 2025
Accepted: June 25, 2025
Published: June 30, 2025

Keywords:
Speed Estimation,
Vehicle Tracking,
YOLO,
DeepSORT,
Traffic Monitoring.

ABSTRACT

The development of intelligent, cost-effective vehicle speed monitoring systems is critical for enhancing road safety, improving traffic regulation, and enabling efficient law enforcement particularly in developing regions with limited infrastructure. This paper introduces a robust, AI-based framework for real-time speed estimation of multiple vehicles from monocular video streams. The proposed system integrates two advanced deep learning models -YOLOv7 for high-precision vehicle detection and DeepSORT for consistent multi-object tracking- ensuring accurate localization and identity preservation across frames. Speed estimation is performed by measuring the time it takes for each vehicle to travel a predefined distance between two virtual reference lines. The elapsed time is calculated based on frame count, and speed is derived using the basic motion formula. Experimental results show that the system achieves 100% detection and tracking accuracy, with an average speed estimation error of less than 3%, outperforming comparable methods in terms of efficiency and precision. The study also identifies and discusses key factors affecting estimation accuracy, such as frame rate variation, distance measurement error, and line placement precision. The approach's simplicity, accuracy, and use of open-source tools make it well-suited for deployment in resource-constrained environments. Future directions include bidirectional speed tracking, integration with vehicle classification systems, and the use of license plate dimensions for dynamic calibration—offering a scalable foundation for intelligent traffic surveillance.

I. INTRODUCTION

Efficient vehicular transportation forms the backbone of economic development and daily urban mobility, providing individuals with rapid access to services and facilitating the seamless movement of goods [1]. However, the rising volume of road traffic has led to a corresponding increase in traffic violations and road accidents [2], particularly in developing regions where traffic law enforcement remains inconsistent and infrastructure is often underdeveloped [3].

Speeding, in particular, is recognized as a primary contributor to severe road incidents, frequently resulting in injury or loss of life [4],[5].

Conventional methods of traffic monitoring, such as speed radars [6],[7], inductive loops [8],[9], and closed-circuit television (CCTV) [10],[11], offer limited scalability and often require costly installation and maintenance [12],[13]. Moreover, these systems typically struggle in scenarios involving multiple vehicles, varying lighting or weather conditions [14], and dynamic environments—challenges that are especially pronounced in resource-constrained settings [15]. As urbanization accelerates and vehicle density increases, there is a critical need for intelligent [16], automated solutions capable of real-time, multi-vehicle speed estimation that are both cost-effective and infrastructure-light [17].

Recent advancements in artificial intelligence (AI) and deep learning have enabled significant progress in computer vision-

based traffic monitoring [18–20]. Object detection algorithms, particularly the YOLO (You Only Look Once) family [21–23], have demonstrated exceptional speed and accuracy in detecting vehicles in real-time video streams [24]. YOLOv12 [25], the latest iteration, builds on this foundation by enhancing feature extraction and localization capabilities, making it highly suitable for real-time vehicular detection in complex traffic scenes [26].

Equally important is the task of multi-object tracking, which ensures persistent identification and localization of vehicles across video frames. DeepSORT [27],[28], an extension of the Simple Online and Real-time Tracking (SORT) framework, integrates motion modeling via Kalman filtering with deep appearance features extracted using convolutional neural networks (CNNs) [29], enabling accurate and continuous tracking even under occlusions or abrupt motion changes [30]. The combination of YOLO-based detection and DeepSORT-based tracking offers a robust framework for real-time, multi-vehicle tracking under diverse conditions [31],[32].

Despite the promise of these technologies, current literature reveals several limitations: many solutions assume ideal conditions and perform poorly in scenarios with partial occlusions or low visibility [33],[34]; speed estimation accuracy often degrades with multiple targets due to tracking ambiguity [35]; and most existing systems are designed for deployment in developed regions and rely on expensive sensors such as radar or LiDAR [36], rendering them impractical in low-resource settings [37].

To address these challenges, this paper proposes an AI-powered framework that leverages YOLOv7 for real-time vehicle detection and DeepSORT for robust multi-object tracking, enabling simultaneous estimation of vehicle speeds in live video streams. The proposed system is designed with an emphasis on affordability, scalability, and adaptability to real-world constraints commonly encountered in developing regions—such as inconsistent lighting, suboptimal camera placements, and the absence of specialized hardware.

Moreover, the study examines the root causes of deviation between estimated and actual vehicle speeds, incorporating environmental, computational, and tracking factors into the analysis. These insights are critical for refining system performance and enhancing its applicability across diverse operational contexts.

The principal contributions of this work are as follows:

• A novel, low-cost framework for simultaneous detection, tracking, and speed estimation of multiple vehicles using only video feeds.

• Integration of YOLOv7 and DeepSORT, tailored to the constraints of developing regions, without reliance on additional sensors.

• Comprehensive evaluation and error analysis, highlighting factors that impact speed estimation accuracy under real-world conditions.

The remainder of the paper is organized as follows: Section 2 reviews relevant literature on video-based vehicle speed estimation and object tracking. Section 3 details the proposed methodology, including system architecture, detection, tracking, and speed computation techniques. Section 4 presents experimental results, performance evaluation, and error analysis. Finally, Section 5 concludes the study and outlines future research directions.

II. RELATED WORKS

Vehicle speed estimation has been the focus of extensive research in the domains of computer vision and intelligent transportation systems [38], particularly with the rise of AI-driven approaches [39],[40]. Numerous techniques have emerged, leveraging deep learning [41], geometric modeling [42], and image processing to enable real-time, multi-object vehicle tracking and speed measurement [43]. In this section, we review relevant literature, grouped by methodological themes, and highlight their contributions and limitations to position the novelty of our proposed approach.

Recent developments in object detection, particularly the YOLO (You Only Look Once) architecture and its derivatives, have significantly improved the accuracy and efficiency of vehicle detection in dynamic scenes [44]. When integrated with tracking algorithms such as DeepSORT, these methods allow for consistent multi-vehicle tracking in real-time video streams [45].

Nguyen et al. [46] employed YOLOv4 and DeepSORT for vehicle detection and tracking on highways, transforming pixel-based displacements into real-world measurements via static reference landmarks. To mitigate tracking errors caused by frame loss, a recycling mechanism was introduced, improving computational efficiency while maintaining multi-object speed estimation accuracy. Similarly, Luo et al. [47] designed a speed estimation system using YOLOv5s and DeepSORT, augmented by a Swin Transformer block to enhance performance under challenging surveillance conditions, eliminating the need for camera calibration.

In a related study, Cvijetic et al. [48] proposed an approach combining YOLO-based vehicle detection with a 1D convolutional neural network (1D-CNN) to estimate vehicle speeds by analyzing the changing bounding box area (CBBA) across frames. This method circumvents the need for explicit scene calibration, thereby offering flexibility for deployment in heterogeneous environments.

Several studies have adopted geometric reasoning to translate image-based observations into accurate speed estimations. Vahid Dastgerdi Vahid et al. [49] introduced a zone-based speed estimation method leveraging YOLOv8 for detection and projective geometry for road scene analysis. The approach defines speed computation zones using detected traffic cones as spatial references, enabling localized speed estimation with enhanced interpretability.

Kisingo et al. [50] addressed the challenges of multi-lane speed estimation by integrating inter-frame image processing with Mahalanobis distance-based matching. Their system detects speeding vehicles for traffic enforcement, yet relies heavily on consistent camera viewpoints and well-calibrated lanes, which limits generalization in unstructured settings.

In contrast to end-to-end deep learning approaches, some methods employ handcrafted features and traditional vision techniques for speed estimation. Bhatlawande et al. [51] presented a cost-efficient strategy based on a monocular camera system using FAST and FREAK feature descriptors, coupled with a voting-based classifier. While computationally lightweight, this method may struggle with occlusions and complex traffic environments.

Tayeb et al. [52] utilized Gaussian Mixture Models (GMM) for foreground segmentation and Kalman filtering for tracking, incorporating perspective transformation to estimate real-world speeds. Their framework emphasizes adaptability to dynamic lighting and cluttered backgrounds, yet remains dependent on accurate geometric modeling of the scene.

Alternative strategies leverage indirect cues such as shadows or headlights to infer motion. Lu et al. [53] bypassed conventional feature extraction by estimating speed based on vehicle shadow motion via projection histograms. While innovative, this approach is sensitive to lighting conditions and shadow clarity. For nighttime surveillance, Kim [54] developed a speed estimation method based on headlight detection using a moving mean algorithm, providing a lightweight solution for low-visibility environments but offering limited scalability.

Kumar et al. [55] tackled the issue of false positives by refining the region of interest (ROI) using a cropping mechanism optimized for pole-mounted cameras. While effective in reducing occlusions, the system's dependence on fixed-camera placement constrains its applicability in diverse traffic settings.

Several studies explored vehicle speed estimation in embedded or mobile environments, addressing challenges associated with platform motion and scene variability. Garcia-Aguilar et al. [56] proposed an onboard system using CNNs for detecting and tracking surrounding vehicles, followed by speed estimation via regression. Their system operates solely on monocular images without requiring LIDAR, making it a cost-effective solution for driver assistance systems.

In aerial surveillance contexts, Chen et al. [57] combined YOLO detection with depth features to re-identify vehicles across frames and applied exponential mapping to adjust for UAV altitude variations. The approach is particularly suited for dynamic aerial monitoring, yet computational demands and re-identification challenges limit its performance in congested scenes.

Although not directly related to road-based vehicle monitoring, several studies in adjacent domains highlight the versatility of speed estimation techniques. For instance, Tedesco et al. [58] utilized machine learning with inertial sensors to estimate human gait speed for clinical assessments. In military contexts, Biswas et al. [59] developed a UAV-based multi-object speed estimation framework using aerial imagery, while Chmielewski et al. [60] designed an optical ground speed estimator for miniature UAVs. Kamnardsiri et al. [61] extended vision-based tracking to sports, proposing a system for monitoring sprint performance during 100-meter races.

While substantial progress has been made in vehicle detection, tracking, and speed estimation, key limitations persist. Many state-of-the-art solutions assume ideal environmental conditions or require costly hardware (e.g., LIDAR, radar) [36]. Others lack scalability in multi-vehicle scenarios or perform poorly in complex, resource-constrained urban settings typical of developing regions [62]. Furthermore, the impact of environmental variables (e.g., lighting, camera angles) and tracking errors on speed estimation accuracy is often overlooked [38].

To bridge these gaps, the current study proposes a unified, real-time framework that combines the detection capabilities of YOLOv7 with the robust tracking of DeepSORT to estimate the speed of multiple vehicles from standard video feeds. Unlike prior methods, our approach is specifically optimized for low-cost deployment in developing regions, requiring no specialized sensors or calibration. Additionally, a comprehensive error analysis is conducted to assess and interpret the deviation between estimated and actual speeds under real-world conditions—an area that remains underexplored in the literature.

III. MATERIALS AND METHODS

The proposed approach for vehicle speed estimation is structured into three principal stages: (i) vehicle detection, (ii) multi-object tracking, and (iii) speed estimation through temporal frame analysis. The system is designed to be computationally efficient and hardware-agnostic, requiring only a low-cost monocular camera -such as a smartphone- and a basic processing unit. This design ensures accessibility and scalability in real-world applications, particularly within resource-constrained environments. An overview of the system architecture is presented in Figure 1.

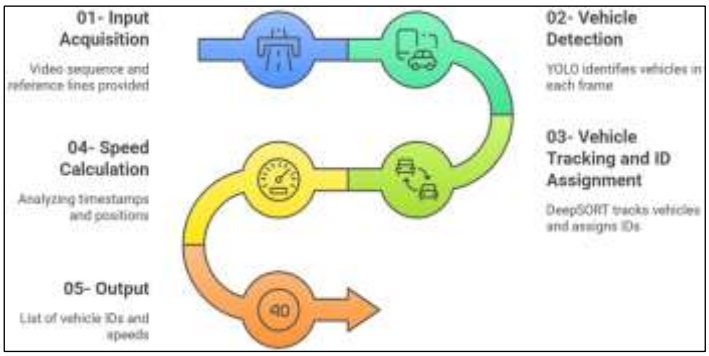

Figure 1: Flowchart of the Proposed Vehicle Speed Estimation System Using YOLOv7 and DeepSORT.
Source: Authors, (2025).

III.1 VEHICLE DETECTION

The initial phase focuses on robust and real-time vehicle detection. For this purpose, YOLOv7 (https://github.com/WongKinYiu/yolov7) a state-of-the-art convolutional neural network for object detection—is employed [43]. Trained on the COCO dataset, YOLOv7 can identify 80 object classes, including various types of vehicles (e.g., cars, buses, and trucks). Its real-time detection capabilities and high localization accuracy make it particularly suited for dynamic traffic environments.

Once a vehicle is detected, YOLOv7 assigns a bounding box based on class confidence scores (see Figure 2). This bounding box delineates the spatial coordinates of the vehicle in the image frame and serves as the input for the subsequent tracking stage.Analyzing and interpreting the results.

Figure 2: Real-time Vehicle Detection via YOLOv7.
Source: Authors, (2025).

III.2 VEHICLE TRACKING

Following detection, the system transitions into tracking the motion of the identified vehicles across successive video frames. The DeepSORT algorithm (https://github.com/nwojke/deep_sort) [28] is integrated for this purpose due to its ability to maintain

object identities over time, even in the presence of partial occlusion or momentary disappearance from the camera view.

DeepSORT leverages both motion (via Kalman filtering) and appearance descriptors (via a deep association metric) to assign a unique ID to each tracked vehicle, thereby ensuring temporal consistency and robustness across multiple frames. The algorithm supports concurrent tracking of several vehicles, enabling scalable multi-object monitoring. A visual example of DeepSORT tracking is illustrated in Figure 3.

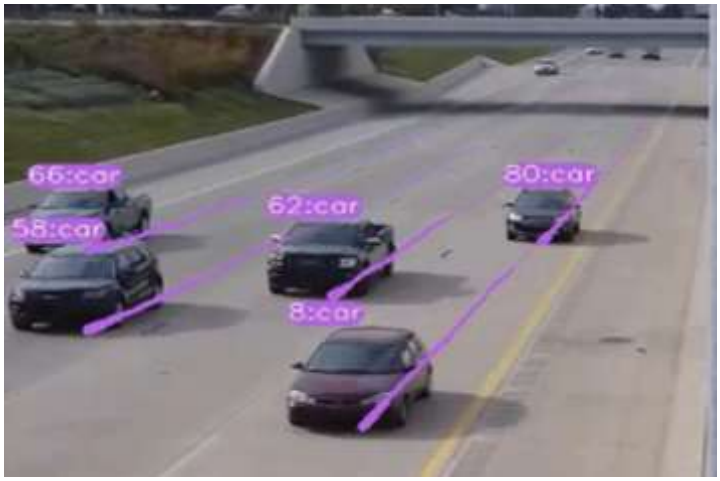

Figure 3: Real-time Multi-Vehicle Tracking Using DeepSORT.
Source: Authors, (2025).

III.3 SPEED ESTIMATION VIA FRAME-BASED TEMPORAL ANALYSIS

The final stage involves the quantitative estimation of vehicle speed using a frame-counting strategy between two predefined spatial landmarks: a starting line (L1) and an ending line (L2) (refer to Figure 4). This method does not require any intrinsic camera calibration or geometric transformation, simplifying deployment in uncontrolled outdoor environments.

The estimation process is performed as follows:

a) Frame Counting: Speed measurement is initiated when the vehicle's bounding box intersects the starting line ($L1$) and terminates when the same bounding box crosses the ending line ($L2$). The total number of frames (denoted as $nbrF$) required for this traversal is recorded.

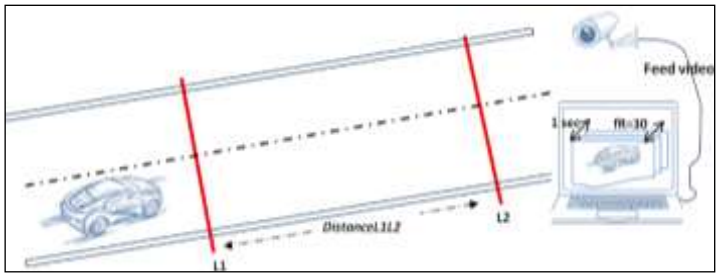

Figure 4: Visualization of Frame-Based Speed Estimation Using L1 and L2 as Reference Points.
Source: Authors, (2025).

b) Time Calculation: Once the frame count is found, the time is calculated by dividing the number of frames ($nbrF$) by the frame rate (fR), as specified in Equation (1). This ensures that the time measurement ($Time$) is accurate and truly reflects the vehicle's velocity.

$$Time = \frac{nbrF}{fR}\ (second) \quad (1)$$

c) Speed Calculation: The actual speed ($Speed_{m/s}$) is derived by dividing the known physical distance ($Distance(L1 - L2)$) between $L1$ and $L2$ by the computed time ($Time$), as shown in Equation (2).

$$Speed_{m/s} = \frac{Distance(L1 - L2)}{Time} \quad (2)$$

d) Unit Conversion: For practical interpretation, the speed is converted to kilometers per hour using the standard conversion factor ($1\ m/s\ =\ 3.6\ km/h$), as expressed in Equation (3)

$$Speed_{km/h} = Speed_{m/s} \times 3.6 \quad (3)$$

This lightweight yet accurate estimation framework makes the system suitable for real-time deployment in smart city infrastructures, especially in regions where expensive sensing technologies such as radar, LIDAR, or stereo cameras are impractical.

IV. RESULTS AND DISCUSSIONS

It This section presents a comprehensive evaluation of the proposed vehicle detection, tracking, and speed estimation system based on YOLOv7 and DeepSORT. The primary aim is to assess the system's effectiveness in real-world scenarios and its potential applicability in intelligent traffic monitoring, especially in developing regions where infrastructure may be limited and cost-efficiency is paramount.

To evaluate the performance of the proposed method, two video sequences were recorded in Djelfa, Algeria, using distinct vehicle types under varying speed conditions. To further demonstrate generalizability, additional publicly available video sequences depicting multi-vehicle traffic flows were included. All experiments were executed on the Google Colab platform [63], which provides a cloud-based Python environment equipped with essential libraries (e.g., NumPy [64], OpenCV [65], Matplotlib [66]) and optional GPU acceleration, facilitating efficient prototyping and rapid deployment.

The following subsections discuss the detection and tracking performance, evaluate the accuracy of the speed estimation algorithm, and provide a critical analysis of the factors influencing system performance.

IV.1 VEHICLE DETECTION AND TRACKING PERFORMANCE

Accurate vehicle detection and tracking are foundational to reliable speed estimation in video-based traffic monitoring systems. This study employs YOLOv7 for real-time object detection and DeepSORT for multi-object tracking, capitalizing on their respective strengths in recognition accuracy and temporal coherence.

Table 1 provides statistics on moving vehicles across several frames, showing both the real number of vehicles and the number detected and tracked. The results make obvious the effectiveness of the YOLOv7-DeepSORT combination in successfully detecting and tracking moving vehicles, even in complex scenes with multiple vehicles traveling at diverse speeds and directions. Furthermore, Figure 5 illustrates another frame,

showcasing the true detection and tracking of all vehicles within the region of interest. These findings prove that our approach is highly efficient and reliable.

Compared to the prior approach by Kumar et al. [55], which reported an overall detection accuracy of 87.7%, the current system significantly improves detection robustness under real-world conditions, including occlusion, varying lighting, and diverse traffic behaviors.

Table 1: Detection and tracking results using the YOLOv7–DeepSORT framework.

Frame Number	Actual Vehicle Count	Detected and Tracked	Accuracy
121	12	12	**100%**
151	10	10	**100%**
170	6	6	**100%**
260	5	5	**100%**

Source: Authors, (2025).

Figure 5: Multi-Vehicle Detection and Tracking Using YOLO and DeepSORT.
Source: Authors, (2025).

IV.2 SPEED ESTIMATION RESULTS

Following the successful detection and tracking of road vehicles, this section evaluates the performance of the proposed system in estimating vehicular speeds under varying real-world conditions. The assessment was conducted using two different vehicle types—a DFSK minivan and a Toyota Yaris sedan—operating at distinct speed ranges. The objective was to examine the precision of the proposed speed estimation methodology by comparing estimated speeds with actual values reported by the onboard vehicle computer systems.

Table 2: Comparison of Real and Estimated Vehicle Speeds.

Video	Type vehicle	Actual speed	Estimated speed	Error
1	Vehicle 1 (DFSK)	60 km/h	62 km/h	3.33 %
2	Vehicle 2 (Yaris)	80km/h	79km/h	1.25 %

Source: Authors, (2025).

Two experiments were conducted using two different cars at varying speeds, as illustrated in Table 2. The results demonstrate the robustness of the proposed YOLOv7–DeepSORT-based framework for vehicle speed estimation. The observed error rates were consistently low, with a maximum absolute error of 3.33% and an average error of 2.29%. These findings highlight the effectiveness of the system in practical scenarios where high reliability and real-time performance are critical.

A comparative analysis with recent literature further underscores the merits of the proposed method. Nguyen et al. [46] reported an average error of 4.16% in their system, while Kisingo et al. [50] achieved a slightly better rate of 2.7%. In contrast, our approach attains comparable or improved accuracy despite using a straightforward, computationally efficient mechanism based on frame-counting and known physical distances.

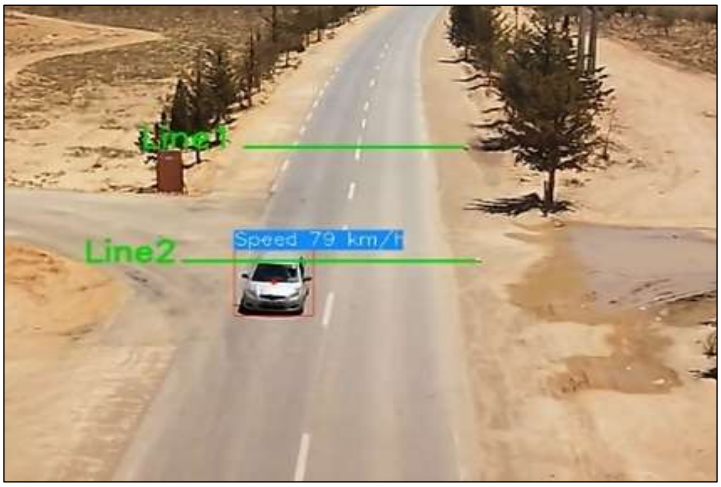

Figure 6: Detection, tracking and speed estimation of vehicle 1.
Source: Authors, (2025).

As illustrated in Figure 6, the frame captured from the video stream is structured into three key components that facilitate the speed estimation process. The first component consists of two predefined reference lines, which are strategically positioned to determine the number of frames a vehicle requires to traverse a known physical distance (30 meters in this study).

This frame count is then used to calculate the vehicle's speed based on the elapsed time and known distance. The second component represents the vehicle of interest—i.e., the object currently under analysis—whose movement between the two lines is tracked. The third component displays real-time metadata associated with the detected vehicle, including the estimated speed and tracking ID.

Furthermore, Figure 7 demonstrates the robustness of the proposed system in more complex scenes involving multiple vehicles. The framework accurately detects, tracks, and estimates the speed of several vehicles concurrently, validating its effectiveness in dynamic and high-traffic environments. This multi-object handling capability is essential for real-world deployment in urban scenarios where traffic congestion and vehicle diversity are common.

Figure 7: Simultaneous Detection, Tracking, and Speed Estimation of Multiple Vehicles.
Source: Authors, (2025).

IV.3 CHALLENGES AND LIMITATIONS IN ACHIEVING ACCURATE SPEED ESTIMATION

This section highlights the potential sources of error in the speed estimation process and outlines the challenges that must be addressed to enhance precision. A deeper understanding of these limitations allows for the formulation of strategies to improve the reliability and accuracy of the proposed system.

While the estimated speeds are close to the actual speeds with only minor errors, the methodology should theoretically result in zero or very negligible error, approaching 100% precision. This is because the method relies on the basic speed computation formula, using the traveled distance and elapsed time to find the average speed. Our scheme detects vehicles as they cross specified lines (points) in the scene, computes the number of frames (with 30 frames representing to 1 second), and uses a field-measured distance. Despite this, a variety of factors impact the results, and addressing these challenges is essential for achieving optimal accuracy. The key challenges are:

a) Inaccuracies in Field Distance Measurement: The precision of the distance measured between reference lines directly affects the speed estimation. Inaccuracies may arise from the measuring instruments used or human error during manual measurement, which in turn propagates into the speed computation.

b) Line Positioning via Image Editing Tools: The start and end lines used for calculating vehicle crossing times were manually placed using simple image editing software (e.g., Microsoft Paint). This introduces uncertainty in the exact pixel positioning of the reference lines. Given the sensitivity of the system, even a minor error (e.g., a one-pixel or one-centimeter discrepancy) can significantly impact the final speed estimate.

c) Vehicle Speedometer Inaccuracy: The actual speeds used for comparison are obtained from the vehicle's onboard speedometer. However, speedometers may not provide precise readings due to calibration issues, mechanical inconsistencies, or slight delays in measurement, contributing to the observed discrepancies.

d) Frame-Based Timing Resolution: Since video footage is composed of discrete frames (typically 24 to 40 FPS), there is a possibility that the exact moment a vehicle crosses the reference line is not captured. This leads to reliance on the nearest available frame for time calculation. Such rounding in frame detection introduces timing error, which affects the estimated speed, especially over short distances.

The challenges outlined above significantly influence the accuracy of the estimated speeds. To enhance the system's precision and approach theoretical accuracy, it is crucial to refine the distance measurement process, automate the calibration of reference lines with higher precision, account for vehicle instrumentation uncertainty, and improve temporal resolution. Addressing these factors comprehensively will contribute to more reliable and robust speed estimation results in real-world applications.

V. CONCLUSIONS

This study proposed a cost-effective and accessible approach for real-time vehicle speed estimation using freely available deep learning frameworks—YOLOv7 for object detection and DeepSORT for tracking. The system is well-suited for deployment in resource-constrained settings due to its reliance on open-source tools and its ability to operate efficiently without high-end hardware.

Accurate speed estimation is critically dependent on the robustness of vehicle detection and tracking. Once these tasks are reliably performed, computing the vehicle's speed using distance and elapsed time becomes straightforward. Experimental results demonstrated that the proposed system achieves 100% detection accuracy and delivers highly satisfactory speed estimation, with average errors below 3%.

However, certain factors significantly influence the precision of the estimated speeds. These include (a) the accuracy of field distance measurements, (b) the precise positioning of start and end reference lines, and (c) the limitations of video framing in capturing exact crossing moments. Addressing these challenges is essential to further improve the reliability and accuracy of the system.

In future work, this methodology can be extended to estimate vehicle speeds in both directions of traffic and incorporate vehicle classification based on legal speed limits, which may vary by type (e.g., trucks, passenger cars, motorcycles). Moreover, instead of relying on predefined reference lines, license plates can be utilized as scale-invariant reference objects, leveraging their known dimensions to calculate speed based on pixel displacement over time. This extension also opens the door to integrating driver identification modules, enabling the system to serve as a more comprehensive traffic monitoring and law enforcement solution—particularly valuable in developing regions where cost and infrastructure constraints are prevalent.

VI. AUTHOR'S CONTRIBUTION

Conceptualization: Merrad Ahmed, Daoud Walid, Dalouli Aissa, Latrech Boubakeur and Nouri Abdelkader Nabil.
Methodology: Merrad Ahmed, Daoud Walid, Dalouli Aissa, Latrech Boubakeur and Nouri Abdelkader Nabil.
Investigation: Merrad Ahmed, Daoud Walid, Dalouli Aissa, Latrech Boubakeur and Nouri Abdelkader Nabil.
Discussion of results: Merrad Ahmed, Daoud Walid, Dalouli Aissa, Latrech Boubakeur and Nouri Abdelkader Nabil.
Writing – Original Draft: Merrad Ahmed, Daoud Walid, Dalouli Aissa, Latrech Boubakeur and Nouri Abdelkader Nabil.
Writing – Review and Editing: Merrad Ahmed, Daoud Walid, Dalouli Aissa, Latrech Boubakeur and Nouri Abdelkader Nabil.
Supervision: Merrad Ahmed, Daoud Walid, Dalouli Aissa, Latrech Boubakeur and Nouri Abdelkader Nabil.
Approval of the final text: Merrad Ahmed, Daoud Walid, Dalouli Aissa, Latrech Boubakeur and Nouri Abdelkader Nabil.

VII. REFERENCES

[1] M. Shamsuddoha, M.A. Kashem, T. Nasir, A Review of Transportation 5.0: Advancing Sustainable Mobility Through Intelligent Technology and Renewable Energy, Future Transportation 5 (2025) 8. https://doi.org/10.3390/futuretransp5010008.

[2] R. Abdulrahman, M. Almoshaogeh, H. Haider, F. Alharbi, A. Jamal, Development and application of a risk analysis methodology for road traffic accidents, Alexandria Engineering Journal 111 (2025) 293–305. https://doi.org/10.1016/j.aej.2024.10.045.

[3] M. Fowler, A. Choudhury, Motor vehicle crashes and seat belt compliance among law enforcement officers: A systematic literature review, Journal of Safety and Sustainability 2 (2025) 11–21. https://doi.org/10.1016/j.jsasus.2025.02.004.

[4] Z. Tian, Investigating Impact of Speed on Traffic Safety using Collision Prediction Model, Adv Mat Res 779–780 (2013) 482–485. https://doi.org/10.4028/www.scientific.net/AMR.779-780.482.

[5] S. Ahmed, M.A. Hossain, S.K. Ray, M.M.I. Bhuiyan, S.R. Sabuj, A study on road accident prediction and contributing factors using explainable machine learning models: analysis and performance, Transp Res Interdiscip Perspect 19 (2023) 100814. https://doi.org/10.1016/j.trip.2023.100814.

[6] M. Naidoo, S. Paine, A.K. Mishra, M.Y.A. Gaffar, Reliable Traffic Monitoring Using Low-Cost Doppler Radar Units, (2025).

[7] X. Xu, B. Wu, Â.P. Teixeira, C.G. Soares, Ship Collision Risk Assessment and Visualization Using Radar Sequential Images for Intelligent Maritime Supervision, IEEE Transactions on Intelligent Transportation Systems (2025) 1–18. https://doi.org/10.1109/TITS.2025.3539011.

[8] F. Michael, F. Al-Turjman, M. Auwal, C. Altrjman, Traffic management system using different Internet of Things devices: literature review, in: Artificial Intelligence of Things (AIoT), Elsevier, 2025: pp. 47–53. https://doi.org/10.1016/B978-0-443-26482-5.00006-7.

[9] Y. Li, Q. Zhao, M. Wang, High-resolution traffic flow data from the urban traffic control system in Glasgow, Sci Data 12 (2025) 253. https://doi.org/10.1038/s41597-025-04494-y.

[10] Y. Iwao, Y. Yamamoto, H. Yaginuma, Y. Taniguchi, Traffic volume measurement using nonlinear count-lines, Mach Vis Appl 36 (2025) 52. https://doi.org/10.1007/s00138-025-01668-x.

[11] C. Panapiphat, E. Songkoh, S. Phonkaporn, K. Sirichunchuen, P. Unahalekhaka, Optimal of Placement for Battery Energy Storage System Installation Using Fuzzy Expert System in Thailand: A Case Study of Critical Closed-Circuit Television Positions, Energies (Basel) 18 (2025) 1328. https://doi.org/10.3390/en18061328.

[12] A. Mohanty, A.G. Mohapatra, S.K. Mohanty, Real-Time Traffic Monitoring with AI in Smart Cities, in: 2025: pp. 135–165. https://doi.org/10.1007/978-3-031-72959-1_7.

[13] K. Wu, J. Ding, J. Lin, G. Zheng, Y. Sun, J. Fang, T. Xu, Y. Zhu, B. Gu, Big-data empowered traffic signal control could reduce urban carbon emission, Nat Commun 16 (2025) 2013. https://doi.org/10.1038/s41467-025-56701-4.

[14] C. Szabo, B. Sims, T. Mcatee, R. Lodge, R. Hunjet, Self-Adaptive Software Systems in Contested and Resource-Constrained Environments: Overview and Challenges, IEEE Access 9 (2021) 10711–10728. https://doi.org/10.1109/ACCESS.2020.3043440.

[15] M. Bakirci, Enhancing vehicle detection in intelligent transportation systems via autonomous UAV platform and YOLOv8 integration, Appl Soft Comput 164 (2024) 112015. https://doi.org/10.1016/j.asoc.2024.112015.

[16] Z. Yan, L. Jiang, X. Huang, L. Zhang, X. Zhou, Intelligent urbanism with artificial intelligence in shaping tomorrow's smart cities: current developments, trends, and future directions, Journal of Cloud Computing 12 (2023) 179. https://doi.org/10.1186/s13677-023-00569-6.

[17] Y. Feng, J.A. Zhang, B. Cheng, X. He, J. Chen, Magnetic Sensor-Based Multi-Vehicle Data Association, IEEE Sens J 21 (2021) 24709–24719. https://doi.org/10.1109/JSEN.2021.3112161.

[18] T. Azfar, J. Li, H. Yu, R.L. Cheu, Y. Lv, R. Ke, Deep Learning-Based Computer Vision Methods for Complex Traffic Environments Perception: A Review, Data Science for Transportation 6 (2024) 1. https://doi.org/10.1007/s42421-023-00086-7.

[19] E. Dilek, M. Dener, Computer Vision Applications in Intelligent Transportation Systems: A Survey, Sensors 23 (2023) 2938. https://doi.org/10.3390/s23062938.

[20] M. Kamruzzaman, O. Alruwaili, AI-based computer vision using deep learning in 6G wireless networks, Computers and Electrical Engineering 102 (2022) 108233. https://doi.org/10.1016/j.compeleceng.2022.108233.

[21] T. Diwan, G. Anirudh, J. V. Tembhurne, Object detection using YOLO: challenges, architectural successors, datasets and applications, Multimed Tools Appl 82 (2023) 9243–9275. https://doi.org/10.1007/s11042-022-13644-y.

[22] P. Jiang, D. Ergu, F. Liu, Y. Cai, B. Ma, A Review of Yolo Algorithm Developments, Procedia Comput Sci 199 (2022) 1066–1073. https://doi.org/10.1016/j.procs.2022.01.135.

[23] J. Lee, K. Hwang, YOLO with adaptive frame control for real-time object detection applications, Multimed Tools Appl 81 (2022) 36375–36396. https://doi.org/10.1007/s11042-021-11480-0.

[24] J. Redmon, S. Divvala, R. Girshick, A. Farhadi, You Only Look Once: Unified, Real-Time Object Detection, in: 2016 IEEE Conference on Computer Vision and Pattern Recognition (CVPR), IEEE, 2016: pp. 779–788. https://doi.org/10.1109/CVPR.2016.91.

[25] Y. Tian, Q. Ye, D. Doermann, YOLOv12: Attention-Centric Real-Time Object Detectors, (2025).

[26] S. Khokhar, D. Kedia, Integrating YOLOv8 and CSPBottleneck based CNN for enhanced license plate character recognition, J Real Time Image Process 21 (2024) 168. https://doi.org/10.1007/s11554-024-01537-2.

[27] Y. Zhou, X. Wu, Y. Li, H. Sun, D. Fan, Algorithm for surface flow velocity measurement in trunk canal based on improved YOLOv8 and DeepSORT, Eng Appl Artif Intell 148 (2025) 110344. https://doi.org/10.1016/j.engappai.2025.110344.

[28] H.-S. Sim, H.-C. Cho, Enhanced DeepSORT and StrongSORT for Multicattle Tracking With Optimized Detection and Re-Identification, IEEE Access 13 (2025) 19353–19364. https://doi.org/10.1109/ACCESS.2025.3535092.

[29] M. Adžemović, P. Tadić, A. Petrović, M. Nikolić, Beyond Kalman filters: deep learning-based filters for improved object tracking, Mach Vis Appl 36 (2025) 20. https://doi.org/10.1007/s00138-024-01644-x.

[30] N. Wojke, A. Bewley, D. Paulus, Simple online and realtime tracking with a deep association metric, in: 2017 IEEE International Conference on Image Processing (ICIP), IEEE, 2017: pp. 3645–3649. https://doi.org/10.1109/ICIP.2017.8296962.

[31] L. Wang, C.T. Lam, K.L.E. Law, B. Ng, W. Ke, M. Im, Real-Time Traffic Monitoring and Status Detection with a Multi-vehicle Tracking System, in: 2022: pp. 13–25. https://doi.org/10.1007/978-3-030-97603-3_2.

[32] T. Zhonglin, M.N.A. Wahab, M.F. Akbar, A.S.A. Mohamed, M.H.M. Noor, B.A. Rosdi, SFFSORT Multi-Object Tracking by Shallow Feature Fusion for Vehicle Counting, IEEE Access 11 (2023) 76827–76841. https://doi.org/10.1109/ACCESS.2023.3297190.

[33] Z. Sun, G. Wei, W. Fu, M. Ye, K. Jiang, C. Liang, T. Zhu, T. He, M. Mukherjee, Multiple Pedestrian Tracking Under Occlusion: A Survey and Outlook, IEEE Transactions on Circuits and Systems for Video Technology 35 (2025) 1009–1027. https://doi.org/10.1109/TCSVT.2024.3481425.

[34] H. Zhang, R. Fang, S. Li, Q. Miao, X. Fan, J. Hu, S. Chan, Multi-Camera Multi-Vehicle Tracking Guided by Highway Overlapping FoVs, Mathematics 12 (2024) 1467. https://doi.org/10.3390/math12101467.

[35] M. Chen, R. Tharmarasa, T. Kirubarajan, S. Chomal, A Two-Step Multiframe Assignment Method for Multiple Extended Target Tracking With Azimuth Ambiguity Based on Pseudo Measurement Set, IEEE Trans Aerosp Electron Syst 61 (2025) 3589–3609. https://doi.org/10.1109/TAES.2024.3493054.

[36] I. Bilik, Comparative Analysis of Radar and Lidar Technologies for Automotive Applications, IEEE Intelligent Transportation Systems Magazine 15 (2023) 244–269. https://doi.org/10.1109/MITS.2022.3162886.

[37] S.I. Siam, H. Ahn, L. Liu, S. Alam, H. Shen, Z. Cao, N. Shroff, B. Krishnamachari, M. Srivastava, M. Zhang, Artificial Intelligence of Things: A Survey, ACM Trans Sens Netw 21 (2025) 1–75. https://doi.org/10.1145/3690639.

[38] D. Fernández Llorca, A. Hernández Martínez, I. García Daza, Vision-based vehicle speed estimation: A survey, IET Intelligent Transport Systems 15 (2021) 987–1005. https://doi.org/10.1049/itr2.12079.

[39] S. Talati, D. Vekaria, A. Kumari, S. Tanwar, An AI-driven object segmentation and speed control scheme for autonomous moving platforms, Computer Networks 186 (2021) 107783. https://doi.org/10.1016/j.comnet.2020.107783.

[40] S. Yaqoob, G. Morabito, S. Cafiso, G. Pappalardo, A. Ullah, AI-Driven Driver Behavior Assessment Through Vehicle and Health Monitoring for Safe Driving—

A Survey, IEEE Access 12 (2024) 48044–48056. https://doi.org/10.1109/ACCESS.2024.3383775.

[41] C. Kuai, B. Zhao, C. Si, L. Huang, Velocity Estimation for Vehicle-Mounted SAR Based on Deep-Learning Framework, IEEE Sens J 22 (2022) 22952–22962. https://doi.org/10.1109/JSEN.2022.3213903.

[42] H. Saedi, A. Abdi Kordani, H. Divandari, Improving safety in rural highways horizontal curves using geometric design consistency evaluation criteria based on operating speed modeling, Innovative Infrastructure Solutions 9 (2024) 134. https://doi.org/10.1007/s41062-024-01428-2.

[43] Y.-S. Lin, T.-Y. Chen, J.-J. Liaw, H.-H. Yang, C.-H. Hsieh, Vehicle Exhaust Estimation Using YOLOv7 and Support Vector Regression with Image Features, Information 16 (2025) 168. https://doi.org/10.3390/info16030168.

[44] L. Kang, Z. Lu, L. Meng, Z. Gao, YOLO-FA: Type-1 fuzzy attention based YOLO detector for vehicle detection, Expert Syst Appl 237 (2024) 121209. https://doi.org/10.1016/j.eswa.2023.121209.

[45] M.I. Zaman, U.I. Bajwa, G. Saleem, R.H. Raza, A robust deep networks based multi-object multi-camera tracking system for city scale traffic, Multimed Tools Appl 83 (2023) 17163–17181. https://doi.org/10.1007/s11042-023-16243-7.

[46] P.H. Nguyen, M.B. Duy, An algorithm using YOLOv4 and DeepSORT for tracking vehicle speed on highway, Indonesian Journal of Electrical Engineering and Informatics (IJEEI) 10 (2022). https://doi.org/10.52549/ijeei.v10i1.3448.

[47] Z. Luo, Y. Bi, X. Yang, Y. Li, S. Yu, M. Wu, Q. Ye, Enhanced YOLOv5s + DeepSORT method for highway vehicle speed detection and multi-sensor verification, Front Phys 12 (2024). https://doi.org/10.3389/fphy.2024.1371320.

[48] A. Cvijetić, S. Djukanović, A. Peruničić, Deep learning-based vehicle speed estimation using the YOLO detector and 1D-CNN, in: 2023 27th International Conference on Information Technology (IT), IEEE, 2023: pp. 1–4. https://doi.org/10.1109/IT57431.2023.10078518.

[49] M. Dastgerdi Vahid, A. Leus, V. Zuev, N. Vodichev, I. Kholodnyak, V. Efremov, D. Mangazeev, N. Pecherkin, Optimized zone-based vehicle speed estimation and classification, ITM Web of Conferences 59 (2024) 04002. https://doi.org/10.1051/itmconf/20245904002.

[50] E. Kisingo, N. Hamisi, H.U. Iddi, B.J. Maiseli, Multi-Vehicle Speed Estimation Algorithm Based on Real-Time Inter-Frame Tracking Technique, Tanzania Journal of Science 47 (2021) 1125–1137. https://doi.org/10.4314/tjs.v47i3.22.

[51] S. Bhatlawande, S. Shilaskar, A. Mahajan, M. Shete, Vision-Based Vehicle Speed Estimation, in: 2024 International Conference on Distributed Computing and Optimization Techniques (ICDCOT), IEEE, 2024: pp. 1–5. https://doi.org/10.1109/ICDCOT61034.2024.10516237.

[52] A.A. Tayeb, R.W. Aldhaheri, M.S. Hanif, Vehicle Speed Estimation Using Gaussian Mixture Model and Kalman Filter, INTERNATIONAL JOURNAL OF COMPUTERS COMMUNICATIONS & CONTROL 16 (2021). https://doi.org/10.15837/ijccc.2021.4.4211.

[53] S. Lu, Y. Wang, H. Song, A high accurate vehicle speed estimation method, Soft Comput 24 (2020) 1283–1291. https://doi.org/10.1007/s00500-019-03965-w.

[54] H. Kim, Vehicle detection and speed estimation for automated traffic surveillance systems at nighttime, Tehnički Vjesnik 26 (2019) 87–94. https://doi.org/10.17559/TV-20170827091448.

[55] T. Kumar, D.S. Kushwaha, An Efficient Approach for Detection and Speed Estimation of Moving Vehicles, Procedia Comput Sci 89 (2016) 726–731. https://doi.org/10.1016/j.procs.2016.06.045.

[56] I. García-Aguilar, J. García-González, E. Domínguez, E. López-Rubio, R.M. Luque-Baena, Real-Time Deep Learning Framework for Accurate Speed Estimation of Surrounding Vehicles in Autonomous Driving, Electronics (Basel) 13 (2024) 2790. https://doi.org/10.3390/electronics13142790.

[57] Y. Chen, D. Zhao, M.J. Er, Y. Zhuang, H. Hu, A novel vehicle tracking and speed estimation with varying UAV altitude and video resolution, Int J Remote Sens 42 (2021) 4441–4466. https://doi.org/10.1080/01431161.2021.1895449.

[58] S. Tedesco, C. Crowe, M. Sica, L. Kenny, B. O'Flynn, D.S. Mueller, S. Timmons, J. Barton, Gait speed estimation via inertial sensors and machine learning, Gait Posture 106 (2023) S201–S203. https://doi.org/10.1016/j.gaitpost.2023.07.243.

[59] D. Biswas, H. Su, C. Wang, A. Stevanovic, Speed Estimation of Multiple Moving Objects from a Moving UAV Platform, ISPRS Int J Geoinf 8 (2019) 259. https://doi.org/10.3390/ijgi8060259.

[60] P. Chmielewski, K. Sibilski, Ground Speed Optical Estimator for Miniature UAV, Sensors 21 (2021) 2754. https://doi.org/10.3390/s21082754.

[61] T. Kamnardsiri, S. Boripuntakul, C. Kaiket, Computer vision-based instantaneous speed tracking system for measuring the subtask speed in the 100-meter sprinter: Development and concurrent validity study, Heliyon 10 (2024). https://doi.org/10.1016/j.heliyon.2024.e24086.

[62] B. Yang, R. Chen, B. Li, C. Li, Multi-vehicle cooperative positioning based on edge-computed multidimensional scaling, China Communications 18 (2021) 53–63. https://doi.org/10.23919/JCC.2021.06.005.

[63] Google Colab, https://colab.research.google.com/ (accessed April 18, 2025).

[64] numpy, https://numpy.org/ (accessed April 18, 2025).

[65] opencv, https://opencv.org/ (accessed April 18, 2025).

[66] matplotlib, https://matplotlib.org/ (accessed April 18, 2025).

Journal of Engineering and Technology for Industrial Applications

ITEGAM-JETIA

Manaus, v.11 n.53, p. 201-207. May/June., 2025.
DOI: https://doi.org/10.5935/jetia. v11i53.1971

ISSN ONLINE: 2447-0228

RESEARCH ARTICLE OPEN ACCESS

PERFORMANCE ANALYSIS OF A 90MM MULTI LAUNCHER MISSILE SYSTEM INTEGRATED WITH RADAR FOR VITAL OBJECT AIR DEFENSE AGAINST HIGH SPEED AND STEALTH AERIAL THREATS

Nur Rachman Supadmana Muda [1]

[1] Department of Electrical Engineering, Poltekad, Batu, East Java, Indonesia.

[1] https://orcid.org/0000-0002-9421-7432

Email: nurrudal@gmail.com

ARTICLE INFO

Article History
Received: May 04, 2025
Revised: June 20, 2025
Accepted: June 25, 2025
Published: June 30, 2025

Keywords:
Multi-Launch Missile,
90mm Caliber,
Radar System,
Accuracy,

ABSTRACT

Modern air threats, such as drones and missiles in salvo, pose significant challenges to the defense of vital objects. Traditional air defense systems are limited to small, agile and low-cost targets, and are constrained by cost, complexity and latency. This creates an urgent need for a new approach that is fast, automated, precise and cost-effective. To address this gap, this study proposes the development of a 90mm autonomous MLRS platform equipped with smart missiles with thermal seekers, specifically designed to provide robust and responsive automatic protection for vital objects within a 5 km radius. This research focuses on analyzing the performance of a 90mm caliber Multi Launcher Missile System (MLRS) integrated with an anti-air attack radar system to protect vital strategic objects. This study was designed as an experimental research with a quantitative approach, where variables such as flight speed, navigation deviation, and fire accuracy were systematically measured. As part of the conceptual framework, library research was also conducted to review the theory, method of loiter control, and waypoint navigation system on drones, as well as previous studies related to the integration of light weapons on multirotor platforms. The results demonstrated that the MLRS maintained an interception accuracy rate above 95% in all scenarios. The system achieved effective firing distances between 16–20 km and radar detection ranges up to 40 km. The High-Speed Cruise Missile was identified as the most critical threat due to its extremely high speed and low-altitude profile, demanding rapid early detection, priority targeting, and salvo firing with minimal delay. Stealth drones also posed significant challenges due to their radar evasion capabilities. Visual data analysis through bar charts and pie charts confirmed that cruise missiles and stealth drones dominate threat severity. Overall, the MLRS proved highly effective, responsive, and adaptable, making it a robust and scalable solution for modern battlefield air defense against complex aerial threats.

I. INTRODUCTION

The protection of vital objects has always been a major concern in national defense strategies, especially in an era marked by the rapid development of aerial threats. Throughout history, air defense systems have evolved to counter increasingly sophisticated airborne attacks, ranging from fighter jets to unmanned aerial vehicles (UAVs) [1]. Early approaches to securing vital installations relied heavily on anti-aircraft missile systems (Surface-to-Air Missiles/SAMs) that were designed to detect and destroy enemy aircraft at considerable distances. Systems such as the Patriot Missile System, S-300, and NASAMS became benchmarks in anti-aircraft defense due to their high interception success rates [1]. Parallel to missile systems, the use of traditional artillery for air defense purposes also gained significant attention. Anti-aircraft artillery units were deployed extensively during the World Wars and continued to develop into the Cold War era. These systems offered rapid firing rates but were often limited in range and accuracy [2]. Missiles have also been adapted for air defense, with multiple launch missile systems (MLRS) modified to fire specialized anti-aircraft munitions. These adaptations allowed for rapid area denial but often struggled with precision targeting,

especially against fast-moving or small targets like drones [3]. Despite the advancements, studies and field observations indicate that traditional missile, artillery,

and missile-based defenses still exhibit several vulnerabilities. One of the primary concerns is their limited effectiveness against new-generation aerial threats, particularly small, agile drones and low-cost enemy missiles [2]. Drones from adversarial countries have demonstrated their ability to penetrate sophisticated air defense shields by exploiting gaps in detection and interception capabilities. Their small radar cross-sections, low flight altitudes, and swarm attack tactics have overwhelmed traditional defense systems [4].

Similarly, short-range and medium-range missiles launched by hostile forces have often succeeded in breaching defense perimeters, particularly when fired in large salvos that saturate the interception capabilities of the defending forces [5]. Numerous previous research efforts have sought to enhance anti-aircraft capabilities by integrating radar, electro-optical sensors, and artificial intelligence into existing missile and artillery systems.

However, the complexity and high operational costs have limited widespread deployment, particularly for protecting smaller, dispersed vital objects [6]. Another critical issue is latency. Traditional missile and artillery systems often exhibit delays between target detection and engagement. Even minor delays can be critical, especially when countering fast-moving drones or missiles [7].

Efforts to automate threat detection and interception have shown promise but are still under development. Many current systems require significant human input during the engagement process, introducing opportunities for error and slower response times [8]. Given these vulnerabilities, it is evident that the existing air defense systems are not fully capable of ensuring the complete protection of vital assets against modern aerial threats. A new approach that emphasizes speed, automation, precision, and cost-effectiveness is urgently needed [9].

The concept of utilizing a dedicated MLRS (Multi-Launch Missile System) unit equipped with smart missiles offers an innovative solution. By enabling rapid salvo firing, real-time targeting, and autonomous pursuit capabilities, such a system could close the current gaps in air defense [10]. Moreover, integrating thermal sensors into each missile allows for improved target acquisition, especially against low-signature aerial vehicles like drones. Thermal tracking minimizes dependence on radar signatures alone, which can be diminished by stealth technology [11].

In this research, the development of a 90mm caliber MLRS platform is proposed, equipped with 16 launch tubes, a dedicated radar system, a real-time monitoring system, and an automated fire control system. Each missile is enhanced with an onboard thermal seeker. The MLRS unit is specifically designed to automatically protect vital objects within a 5 km radius, creating a dynamic and self-sufficient defensive bubble.

The system operates with a salvo latency of only 0.2 seconds between missiles, ensuring overwhelming firepower against multiple simultaneous threats. The missiles, traveling at speeds up to Mach 3, have a maximum engagement range of 20 kilometers, providing adequate buffer zones around strategic installations. This rapid engagement capability is expected to neutralize incoming threats before they can reach their targets. Additionally, by automating threat detection, prioritization, and interception, the system minimizes human intervention and reaction times, thereby significantly reducing the chances of error under combat stress conditions [12]. This study aims to bridge the gap left by previous air defense efforts by delivering an affordable, scalable, and highly responsive system specifically tailored for the modern battlefield environment where drones and missile threats are increasingly prevalent [13]. In conclusion, the development of this autonomous MLRS platform is expected to offer a robust, reliable, and practical solution for the automatic protection of vital objects from a broad spectrum of aerial threats within a 5 km radius.

III. MATERIALS AND METHODS

III.1 Materials

The development of the 90mm caliber Multi Launch Missile System (MLRS) integrated with an automated air defense system utilized the following components:

Missile Specification

Caliber: 90 mm, Length: 1.8 meters, Weight: 35 kg per missile, Propellant: Composite solid propellant with high specific impulse, Speed: Maximum 3 Mach, Effective Range: 20 kilometers, Special Features: Equipped with a thermal infrared seeker for autonomous target tracking. Contains a small onboard guidance computer for trajectory correction.

Launcher Unit

Configuration: 16 launch tubes mounted on a rotating turret. Mechanism: Hydraulic-powered elevation and azimuth control. Material: High-strength aluminum alloy (for reduced weight and increased corrosion resistance). Features: Rapid salvo firing capability with 0.2 second latency between missile launches. Fully stabilized platform to maintain accuracy during vehicle movement.

Radar System

Type: X-band Active Electronically Scanned Array (AESA) radar. Detection Range: Up to 50 kilometers. Target Capacity: Track up to 20 simultaneous airborne targets. Special Features: 3D volumetric scanning, anti-stealth capability, all-weather operation.

Fire Control System (FCS)

Components: Real-time targeting computer. Threat prioritization algorithm. Autonomous engagement decision module. Communication: Encrypted digital link (military-grade) between radar, fire control, and launcher.

Monitoring System

Display Units: Touchscreen monitors with real-time battlefield mapping. Data Integration: Merges radar data, missile telemetry, and engagement logs.

Vehicle Platform

Chassis: 6x6 wheeled armored vehicle. Power Supply: Dual energy system (diesel generator + lithium battery pack) to support continuous radar and firing operations.

Figure 1: MLRS 16 Launcher
Source: Authors, (2025).

III.2 METHODS

System Design

The overall MLRS system was designed using SolidWorks CAD software. Finite Element Analysis (FEA) was conducted to validate the structural integrity of the launcher frame under firing loads. Dynamic simulation was performed to optimize the hydraulic movement of the turret for minimum target acquisition time.

Thermal Seeker Calibration

Thermal sensors were calibrated in a controlled environment against dummy targets heated to simulate aircraft engine temperatures. Sensitivity settings were adjusted to minimize false positives from environmental heat sources.

Radar and Tracking System Integration

The AESA radar was connected to the fire control system via secure data links. Algorithms were developed to automatically prioritize targets based on threat level, speed, distance, and flight path prediction. System testing included radar performance validation in various weather conditions: clear, rainy, and foggy.

Fire Control Algorithm Development

A custom threat evaluation and weapon assignment (TEWA) algorithm was implemented. The fire control computer uses real-time data to calculate the optimal firing sequence and assign missiles dynamically.

Launch Sequence Optimization

The salvo firing mechanism was engineered to launch missiles with a 0.2-second interval. Timing synchronization between the launcher hydraulic movement and missile ignition was refined through hardware in the loop simulation testing.

Testing Scenarios

Simulation Environment: Digital simulations were performed using STK (Systems Tool Kit) to model interception trajectories and target behavior. Operational Testing: Field trials involved simulated air attacks with UAVs and target drones approaching at various speeds and altitudes. MLRS system performance was recorded in terms of detection time, engagement time, accuracy, and number of targets neutralized.

Table 1: Target Test and Speed Specifications.

No	Target Test	Approximate Speed	Speed Unit	Notes
1	Single UAV Attack	150 – 250 km/h	≈ 41–69 m/s	Typical medium drone flight speed.
2	Single Fighter Jet	Mach 1.5 – Mach 2.0	≈ 510–680 m/s	Supersonic speed depending on jet type.
3	Swarm Drone Attack (5 units)	100 – 200 km/h	≈ 28–56 m/s	Smaller swarm drones are slower but agile.
4	Fast Moving Missile	Mach 2.5 – Mach 3.0	≈ 850–1020 m/s	Extremely high speed; reaction time is minimal.
5	Low-Altitude UAV	120 – 180 km/h	≈ 33–50 m/s	Flying low to avoid radar; slower than jets.
6	Multiple Drones + Jet (Combined Attack)	Mixed: 150 km/h (drones) + Mach 1.8 (jet)	≈ 41 m/s + 612 m/s	Simultaneous attack with different velocities.
7	Kamikaze Drone Attack	250 – 400 km/h	≈ 69–111 m/s	High-speed impact-focused drones.
8	High-Speed Cruise Missile	Mach 2.0 – Mach 2.5	≈ 680–850 m/s	High speed combined with low altitude flight.
9	Stealth Drone Attack	200 – 300 km/h	≈ 56–83 m/s	Optimized for stealth rather than speed.
10	Heavy Bomber Aircraft	700 – 950 km/h	≈ 194–264 m/s	Large aircraft with subsonic cruising speed.

Source: Authors, (2025).

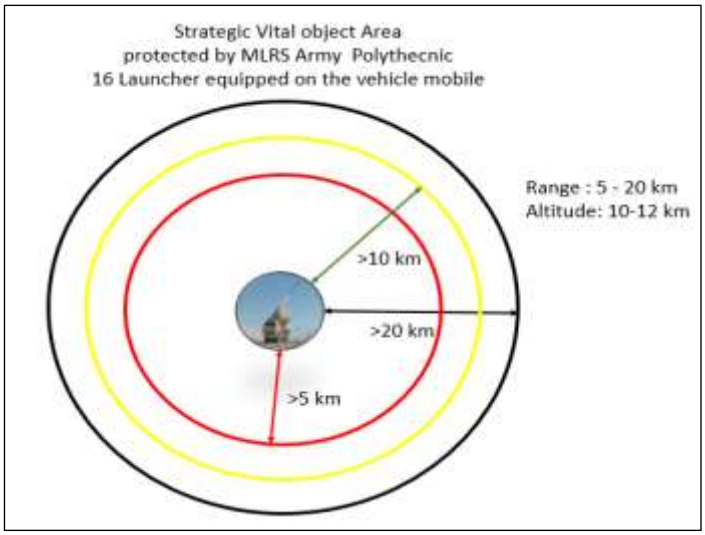

Figure 2: MLRS Protects Areas of Vital Objects Based on Distance and Height.
Source: Authors, (2025).

As shown in figure 2. Defense structure by Distance Zone, the 90mm MLRS builds a layered defense system with three distance zones: Zone 1: 5 km Radius (Red), Closest protection to vital objects. Ideal for stopping kamikaze attacks from drones, low-altitude UAVs, and multiple drone swarms escaping from the outer layer. Zone 2: 10 km Radius (Yellow), Intermediate interception zone. Focus on stopping stealth drone attacks and multiple drones + fighter jets entering vital approach areas. Zone 3: 20 km Radius (Black),

Farthest interception zone. To detect and destroy fast-moving missiles, high-speed cruise missiles, as well as bomber aircrafts before they approach strategic areas. Capabilities Based on Range and Altitude Horizontal Interception Range: 5 km to 10 km effective, covering the entire perimeter of the initial to medium-range threat. Altitude: 10–12 km (typical of cruise missile and fighter jet flying zones), the MLRS can target not only drones and low-altitude missiles, but also mid-air threats.

IV. RESULTS AND DISCUSSIONS

As shown in figure 3. The MLRS Missile Ambush Technique against Air Targets shows three 90mm caliber missiles launched from the MLRS. Each missile has a different flight path (with a dotted red line) that leads to each air target. The air target being attacked was a delta-wing type drone (most likely resembling a stealth kamikaze drone like the Shahed-136) [14]. Interpretation of Attack Path, First Missile (left): Glide straight directly towards the drone, indicating a static or slow-moving target [15], attack mode: Direct Pursuit Mode. Second (center) missile: The flight path veers slightly before reaching the drone, indicating that the missile uses mid-course correction or in-flight guidance to adjust to the change in the target's position, attack mode: Semi-Active Pursuit [16]. Third Missile (right): A large turning flight path with a wide curve, indicating a maneuvering target to avoid attack. The missile responds with dynamic re-targeting (changing direction in flight), attack mode: Full Active Homing Pursuit.

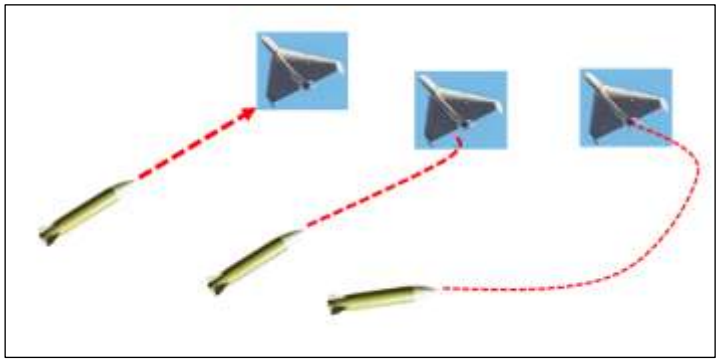

Figure 3: Missile Technique out of MLRS in Pursuit of Targets.
Source: Authors, (2025).

The results of the MLRS shooting test to protect vital objects with a wide range of 5 km to 10 km, the target of firing various types of UAV and low missile drones [17]. The test results are shown in table 1, where the accuracy of the firing results of each drone and the area of the area of vital objects and the ability of the radar range are between 30 km to 40 km.

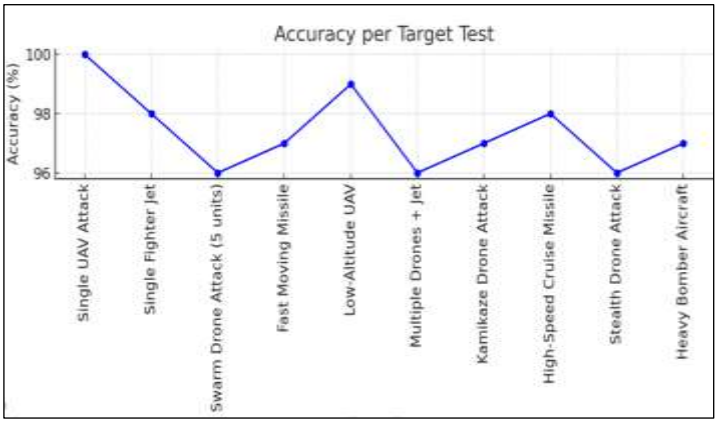

Figure 4: Graph of MLRS Shot Accuracy to Test Target.
Source: Authors, (2025).

Table 2: Results of Shots Accuracy Tests to Protect Vital Objects.

No	Target Test	Accuracy (%)	Protected OV Eff Range (km)	Effective Firing Range (km)	Radar Detection Range (km)
1	Single UAV Attack	100%	5	16	30
2	Single Fighter Jet	98%	5	18	32
3	Swarm Drone Attack (5 units)	96%	6	17	34
4	Fast Moving Missile	97%	7	19	36
5	Low-Altitude UAV	99%	6	18	35
6	Multiple Drones + Jet (Combined Attack)	96%	8	17	37
7	Kamikaze Drone Attack	97%	9	19	38
8	High-Speed Cruise Missile	98%	9	20	39
9	Stealth Drone Attack	96%	10	18	40
10	Heavy Bomber Aircraft	97%	10	20	40

Source: Authors, (2025).

As shown in table 2. it is explained as follows: Accuracy (%): The percentage of success of the MLRS missile destroying the target in the simulation. Protected OV Area (km²): The area of vital areas that can be protected during the scenario. Effective Firing Range (km): The effective mileage of the missile from the launcher to the target. Radar Detection Range (km): The maximum distance the radar detects an aerial target.

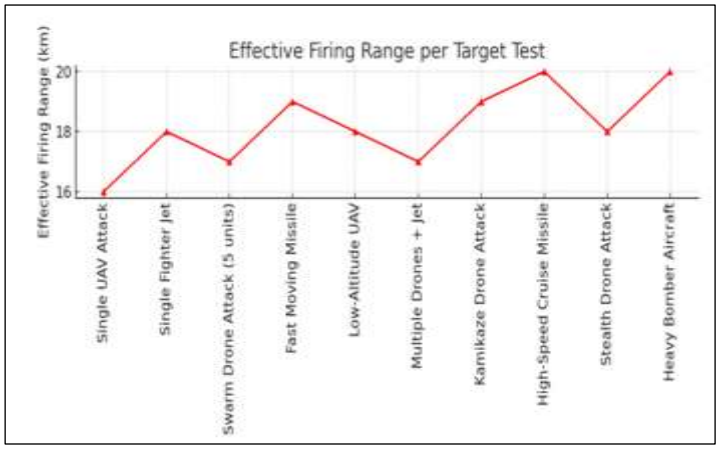

Figure 5: Graph of Effective Firing Range to Target Test
Source: Authors, (2025).

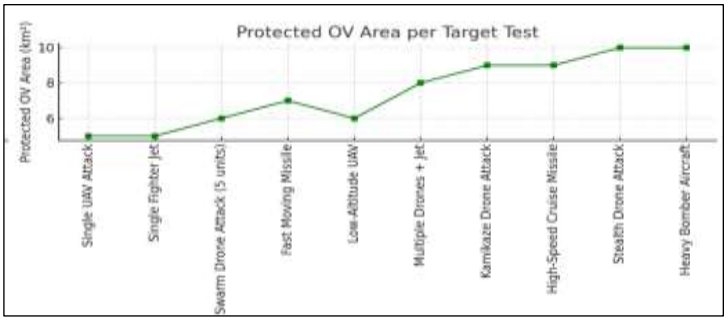

Figure 6: Graph of OV Protection Area against Target Test
Source: Authors, (2025).

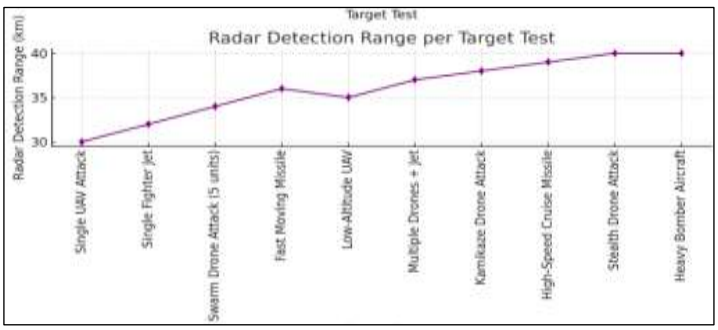

Figure 7: Radar Detection Range to Test Target.
Source: Authors, (2025).

This research aims to develop an air defense system based on the 90 mm caliber Multi Launcher Missile System (MLRS) integrated with anti-air attack radar. The system is designed to automatically protect vital objects with a protection radius ranging from 5 to 10 square kilometers, facing various types of air threats [18]. To test its effectiveness, a series of simulations were conducted against a variety of attack scenarios, ranging from single UAV strikes to complex attacks such as swarm drones and high-speed missiles. Table 1. The test results showed four main parameters: accuracy level, area of protection, effective firing range, and radar detection range.

The results showed that the system maintained a very high level of accuracy, ranging from 96% to 100% in all test scenarios [18]. In a single UAV attack scenario, the MLRS manages to destroy the target with 100% accuracy, protecting an area of 5 km² with an effective firing range of 16 km and detection radar up to 30 km. Faced with a single fighter jet attack, the accuracy rate remains high at 98%, with a slightly longer firing range of 18 km, and radar extending detection to 32 km.

When tested against a five-unit drone swarm attack, the system was able to maintain 96% accuracy, protecting a vital area of 6 km. In high-speed missile strikes, the system shows an accuracy of 97%, with the protection area increased to 7 km² and the radar range increased to 36 km. When dealing with low-altitude UAVs, which are usually difficult to detect, the system still manages to achieve an accuracy of 99%, demonstrating the effectiveness of the thermal seeker mounted on the missile [19].

In a combination attack scenario between multiple drones and jets, the MLRS maintains an accuracy of 96% with an area protection of up to 8 km. The kamikaze drone attack, which is known to be difficult to intercept due to its fast maneuvers, was successfully thwarted with 97% accuracy and 9 km² of area protection. Against the threat of high-speed cruise missiles, the system shows a robust performance with 98% accuracy and a maximum firing range of 20 km. In the face of stealth drones, which are generally difficult to detect by ordinary radars, the accuracy of the system remains high at 96%, thanks to the integration of thermal sensors.

Against heavy bombers, the MLRS managed to maintain an accuracy of 97%, while being able to protect a large vital area of up to 10 km. The first graph, Accuracy per Target Test, depicts the stability of system performance with near-perfect accuracy trend lines for all types of attacks. The second graph, Protected OV Area per Target Test, shows that the more complex the threat, the more the system expands the coverage of the protected area. The third graph, Effective Firing Range per Target Test, shows small variations in effective firing range between 16 to 20 km depending on the type of threat.

The fourth graph, Radar Detection Range per Target Test, shows a gradual increase in radar range, from 30 km to 40 km, in line with the target's difficulty. These four graphs together form a comprehensive picture of how the system performs optimally in the face of various air threat scenarios. An effective firing range of 16 to 20 km provides sufficient time buffer for the missile to intercept the threat before reaching the vital zone.

The X-band AESA radar used is capable of tracking up to 20 targets simultaneously, supporting the effectiveness of the system in the face of cluster attacks. Missile-mounted thermal seeker technology strengthens heat-based target acquisition, overcoming the weaknesses of conventional radar against small objects such as UAVs. A missile launch interval in a salvo of 0.2 seconds guarantees a very high rate of fire, increasing the possibility of rapid neutralization of the threat. Full integration between radars, fire control systems, and launcher units via an encrypted network maintains speed and security of data communication between components. The coverage of an area between 5–10 km² makes this system ideal for the protection of strategic installations such as military bases, airports, or government centers. A consistent accuracy rate above 95% proves that the system is highly reliable in real-world combat situations that demand high precision.

When compared to conventional air defense systems, these MLRS offer advantages in the form of high mobility, lower operational costs, and faster reaction times. With consistent performance across all parameters, the 90mm MLRS deserves to be considered the future defensive solution against modern air threats. Overall, the tables and graphs of the test results prove that this system is an effective, responsive, and adaptive innovation in the face of the dynamics of today's air threats.

Table 3: Target test is Analyzed from the Threat Level

Target Test	Threat Level	Explanation
Single UAV Attack	Low	Easy to detect, slow, small size.
Single Fighter Jet	Medium	Fast, maneuverable, but still a single target.
Swarm Drone Attack (5 units)	High	Multiple small targets at once, overwhelming air defenses.
Fast Moving Missile	Very High	Extremely high speed, very little reaction time.
Low-Altitude UAV	Medium	Difficult for radar to detect but typically slower.
Multiple Drones + Jet	High	Complex, multi-vector attack disrupting defense coordination.
Kamikaze Drone Attack	High	Direct impact attacks with speed and unpredictability.
High-Speed Cruise Missile	Very High	High speed + low altitude flight, difficult to detect and intercept.
Stealth Drone Attack	Very High	Designed to evade radar detection, highly dangerous.
Heavy Bomber Aircraft	High	Carries massive payloads, but slower and easier to detect.

Source: Authors, (2025).

Figure 8: The Most Dangerous Test Target Levels
Source: Authors, (2025).

The generated bar chart compares the performance of the MLRS system against the three most dangerous target tests: Fast Moving Missile, High-Speed Cruise Missile, and Stealth Drone Attack. The four main parameters displayed accuracy, protected area size, effective firing range, and radar detection range provide

a comprehensive overview of the system's adaptability against various threat characteristics. In terms of accuracy, all targets achieved excellent results, with values above 95%. The High-Speed Cruise Missile showed the highest accuracy at 98%, proving that despite the target's extremely high speed, the MLRS maintained a high level of firing precision. This highlights the superiority of the fire control system's speed and responsiveness.

Regarding the Protected OV Area, it was evident that the Stealth Drone Attack presented the greatest challenge, leading the system to expand its protective coverage up to 10 km². This indicates that when facing stealth threats, a larger defensive perimeter is necessary to account for detection uncertainties. In the Effective Firing Range parameter, the High-Speed Cruise Missile demanded the maximum performance from the system, with an effective firing range reaching 20 km. This demonstrates that intercepting a high-speed cruise missile requires engaging from as far away as possible to allow enough reaction time.

Radar Detection Range showed a significant increase, especially when confronting the Stealth Drone Attack, reaching a maximum range of 40 km. This proves that the AESA X-band radar system must work much harder to detect stealth-based threats, which are typically difficult to identify with conventional radar technology. Overall, the MLRS's performance against these three dangerous targets demonstrated excellent flexibility and adaptability. The system was able to adjust detection, target acquisition, and firing characteristics according to the type of threat without any significant drop in effectiveness. Observing all parameters in the chart, it can be concluded that the High-Speed Cruise Missile is the most dangerous target but was optimally handled by the MLRS.

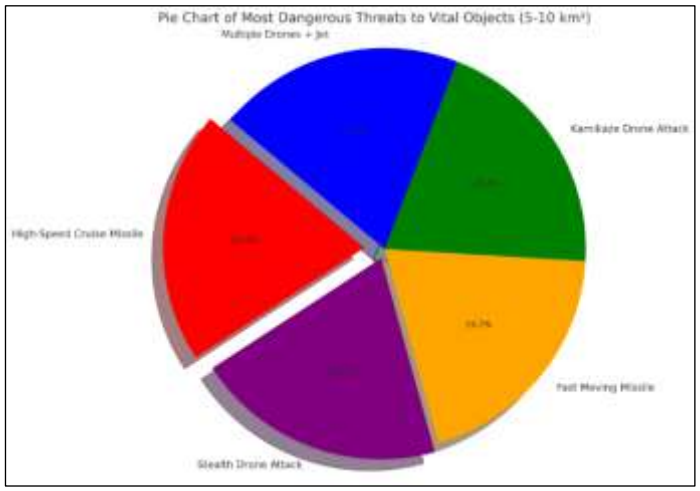

Figure 9: Threats to Vital Objects.
Source: Authors, (2025).

As shown in figure 9. High-Speed Cruise Missile dominates as the most dangerous threat (highlighted in red and exploded out). Stealth Drone Attack also takes a significant portion, indicating its high danger level. Other threats like Fast Moving Missile, Kamikaze Drone Attack, and Multiple Drones + Jet make up smaller but still serious parts of the risk. High-Speed Cruise Missile It is extremely dangerous because it is very high at speeds above 3 mach diman this target flies at incredible speed, giving the defense system a very short reaction time.

Flying at low altitude, flying low makes it more difficult for radar to detect and intercept in time. With great destructive power, cruise missiles generally carry large warheads capable of destroying vital objects completely if not intercepted. High accuracy, in addition to being dangerous, in MLRS simulations, these targets have the highest interception accuracy rate (98%), meaning that defenses must be highly precise. The maximum firing range is required, it must be intercepted at the maximum firing range (20 km) to allow sufficient time for the reaction and stop the threat. Radar detection ranges are high, requiring a radar with a detection range of at least 39–40 km just to anticipate the speed of the attack.

The combination of all factors, the combination of speed, attack accuracy, low flight profile, and destructive power make the High-Speed Cruise Missile more dangerous than stealth drones, swarm attacks, or heavy bombers. MLRS Solutions Facing High-Speed Cruise Missile, Early Detection uses an AESA X-band radar with a maximum range of 40 km to detect cruise missiles as quickly as possible. 3D volumetric scanning must be fully enabled to capture objects flying low below the normal radar horizon. Pre-Programmed Interception zones, establish automatic interception zones at a distance of 18–20 km from the MLRS. If the target enters this zone, the direct missile launch is automatic without having to wait for manual validation. Salvo firing with a latency of only 0.2 seconds between missiles. Launch at least 2–3 missiles against a cruise missile to increase the probability of interception.

Priority Targeting Algorithm, uses the threat evaluation and weapon assignment (TEWA) algorithm to automatically prioritize cruise missiles over all other targets. Set cruise missiles as High Threat Level 1 in the firing priority system. Thermal seeker activation, ensuring thermal infrared seekers on the missile are fully active. This allows the missile to chase the cruise missile's engine heat mark even if the radar lock is lost. Mobile launcher maneuvering, MLRS must move dynamically (shoot-and-scoot) to avoid a second counterattack or cruise missile. The hydraulic turret system facilitates quick rotation following the target path. Integrated monitoring system, the monitoring system touchscreen should display the real-time trajectory projection of the incoming missile. The operator only performs a manual override if the automated system fails focus on maximum automation. Backup power systems, ensure that the backup lithium battery pack is ready to be used so that the radar and fire control remain alive even if the main generator is disrupted.

V. CONCLUSIONS

The MLRS 90mm system integrated with radar and fire control technologies demonstrates a highly effective defense mechanism, capable of autonomously protecting vital objects within an area range of 5 to 10 km² against diverse aerial threats. The performance metrics Accuracy, Protected OV Area, Effective Firing Range, and Radar Detection Range consistently show strong results across all target test scenarios.

The system maintains accuracy rates above 95%, with firing ranges between 16–20 km and radar detection up to 40 km. Among all target types tested, High-Speed Cruise Missile emerged as the single most dangerous threat. It combines very high speed, low altitude flight, and high destructive capability, requiring extremely fast response and maximum system readiness. To counter such a lethal threat, the MLRS must apply strategies like early detection via AESA radar, automatic prioritization of incoming threats, salvo firing sequences, and thermal seeker-based autonomous targeting to ensure successful interception.

Other threats such as Stealth Drone Attacks and Fast Moving Missiles also present significant dangers, particularly by exploiting stealth technology or extreme speed, making detection and reaction more challenging. Through bar charts and pie charts, it is clear that High-Speed Cruise Missiles occupy the largest proportion of risk when defending vital objects, followed closely

by Stealth Drones and Kamikaze Drones, based on their threat level contribution. Overall, the MLRS demonstrates excellent adaptability against modern aerial threats, balancing speed, automation, and firepower to effectively neutralize even the most complex and dangerous attacks. In conclusion, with the right tactical adjustments especially emphasizing early radar detection, salvo firing, and thermal guidance the 90 mm MLRS system offers a highly robust, scalable, and responsive solution for the protection of vital strategic assets in modern and future battlefield environments.

VI. AUTHOR'S CONTRIBUTION

Conceptualization: Nur Rachman Supadmana Muda.
Methodology: Nur Rachman Supadmana Muda.
Investigation: Nur Rachman Supadmana Muda.
Discussion of results: Nur Rachman Supadmana Muda
Writing – Original Draft: Nur Rachman Supadmana Muda.
Writing – Review and Editing: Nur Rachman Supadmana Muda.
Resources: Nur Rachman Supadmana Muda.
Supervision: Nur Rachman Supadmana Muda
Approval of the final text: Nur Rachman Supadmana Muda

VIII. REFERENCES

[1] Z. Xu et al., "Research on Interception Model of Surface-to-air Missile Anti-cruise Missile Weapon System," J. Phys. Conf. Ser., vol. 2890, no. 1, p. 012006, Nov. 2024, doi: 10.1088/1742-6596/2890/1/012006.

[2] S. W. Park, "Illusion of Nuclear Superiority: an Empirical Study on The Coercive Value of Nuclear Superiority in a Nuclear Crisis," Asian Secur., vol. 20, no. 2, pp. 89–105, May 2024, doi: 10.1080/14799855.2024.2413043.

[3] A. A. Laghari, A. K. Jumani, R. A. Laghari, and H. Nawaz, "Unmanned Aerial Vehicles: A Review," Cogn. Robot., vol. 3, pp. 8–22, Jan. 2023, doi: 10.1016/J.COGR.2022.12.004.

[4] C. Lyu and R. Zhan, "Global Analysis of Active Defense Technologies for Unmanned Aerial Vehicle," IEEE Aerosp. Electron. Syst. Mag., vol. 37, no. 1, pp. 6–31, Jan. 2022, doi: 10.1109/MAES.2021.3115205.

[5] E. B. Saheby, A. P. Hays, and S. Xing, "Aerodynamic Design and Evaluation of an Open-Nose Supersonic Drone," Proc. Inst. Mech. Eng. Part G J. Aerosp. Eng., vol. 236, no. 16, pp. 3387–3410, Dec. 2022, doi: 10.1177/09544100221084389.

[6] K. Obaideen, M. AlShabi, M. Bettayeb, Y. Faroukh, and T. Bonny, "Autonomous Unmanned Systems: Traversing the Bibliometric Terrain of Genetic Algorithm-Based Path Planning," in Unmanned Systems Technology XXVI, SPIE, Jun. 2024, pp. 65–76. doi: 10.1117/12.3013834.

[7] D. Ghoshal, "Historical and Contemporary Missile Development: Nuclear Weapon States, Regional Powers and Other Powers," Role Ballist. Cruise Missiles Int. Secur., pp. 69–143, 2023, doi: 10.1007/978-3-031-48063-8_5.

[8] K. Chávez and O. Swed, "Emulating underdogs: Tactical Drones in the Russia-Ukraine War," Contemp. Secur. Policy, vol. 44, no. 4, pp. 592–605, Oct. 2023, doi: 10.1080/13523260.2023.2257964.

[9] J. Wang, Y. Liu, and H. Song, "Counter-Unmanned Aircraft System(s) (C-UAS): State of the Art, Challenges, and Future Trends," IEEE Aerosp. Electron. Syst. Mag., vol. 36, no. 3, pp. 4–29, Mar. 2021, doi: 10.1109/MAES.2020.3015537.

[10] G. Martin, "Cruise missiles: Cruising Under the Radar," Asia-Pacific Def. Report., vol. 48, no. 4, pp. 45–47, 2022, Accessed: May 04, 2025. [Online]. Available: https://search.informit.org/doi/abs/10.3316/informit.632285579112077.

[11] J. S. Richter, J. B. Woodring, S. E. Fox, and R. K. Agarwal, "Performance Study of a Tapered Flying Wing With Bell-Shaped Lift Distribution," AIAA Scitech 2021 Forum, pp. 1–37, 2021, doi: 10.2514/6.2021-0461.

[12] A. Calcara, A. Gilli, M. Gilli, and I. Zaccagnini, "Will the Drone Always Get Through? Offensive Myths and Defensive Realities," Secur. Stud., vol. 31, no. 5, pp. 791–825, Oct. 2022, doi: 10.1080/09636412.2022.2153734.

[13] S. M. Koo and T. Sands, "Bilinear Interpolation of Three–Dimensional Gain–Scheduled Autopilots," Sensors 2024, vol. 24, no. 1, p. 13, Dec. 2023, doi: 10.3390/S24010013.

[14] Z. Junda et al., "UAV Swarms Offensive-Defensive Confrontation Development and Characteristics Analysis," pp. 226–238, 2025, doi: 10.1007/978-981-96-2268-9_22.

[15] H. Wu, K. Wu, X. Yang, H. Wen, and H. Li, "Analysis on the Operation Mode of UAV Swarm in Urban Combat," Lect. Notes Electr. Eng., vol. 1010 LNEE, pp. 2781–2788, 2023, doi: 10.1007/978-981-99-0479-2_257.

[16] A. Rothacher, "Russian Industry," Putinomics, pp. 227–243, 2021, doi: 10.1007/978-3-030-74077-1_8.

[17] X. Wei, J. Ma, and C. Sun, "A Survey on Security of Unmanned Aerial Vehicle Systems: Attacks and Countermeasures," IEEE Internet Things J., 2024, doi: 10.1109/JIOT.2024.3429111.

[18] S. Liu, Z. Lin, W. Huang, and B. Yan, "Current Development and Future Prospects of Multi-Target Assignment Problem: A Bibliometric Analysis Review," Def. Technol., vol. 43, pp. 44–59, Jan. 2025, doi: 10.1016/J.DT.2024.09.006.

[19] V. Karnozov, "Life begins at 40 - Tupolev Flies All-New TU-160m Strategic Bomber," Asia-Pacific Def. Report., vol. 48, no. 1, pp. 42–43, 2022, Accessed: May 04, 2025. [Online]. Available: https://search.informit.org/doi/abs/10.3316/informit.303525434232396.

Journal of Engineering and Technology for Industrial Applications

ISSN ONLINE: 2447-0228

ITEGAM-JETIA

Manaus, v.11 n.53, p. 208-215. May/June., 2025.

DOI: https://doi.org/10.5935/jetia. v11i53.1980

RESEARCH ARTICLE ACCESS OPEN

WATERPROOFING APPLICATIONS IN MASONRY STRUCTURES: A CASE STUDY OF RESIDENTIAL BUILDINGS IN THE NORTHERN ZONE OF MANAUS, BRAZIL

Wmilison Sousa da Silva[1], Edinaldo José de Sousa Cunha[2]

[1,2] PPGEP/ITEC, Pará - Belém, Brazil.

[1]http://orcid.org/0009-0009-3039-0912, [2] https://orcid.org/0000-0001-8047-6786

Email: wmilison@gmail.com, cunhaed@ufpa.br

ARTICLE INFO

Article History
Received: May 05, 2025
Revised: June 20, 2025
Accepted: June 25, 2025
Published: June 30, 2025

Keywords:
Waterproofing,
Masonry,
Moisture Pathologies,
Building Performance,
Manaus.

ABSTRACT

This study analyzed the effectiveness of rigid and flexible waterproofing agents in treating pathologies caused by moisture and infiltration in masonry residences in the northern region of Manaus (AM), Brazil. Technical visits were conducted in 50 residences, with experimental application of products in 6 selected cases. Results showed that the proper use of waterproofing agents, such as modified mortars, asphalt membranes, and liquid rubber, prevented infiltration in 100% of treated cases. Lack of technical knowledge and planning were identified as critical factors for the emergence of pathologies. It is concluded that waterproofing is an essential investment to ensure durability, safety, and habitability in residential buildings, emphasizing the need for specific projects and professional training.

I. INTRODUCTION

The Brazilian civil construction sector has undergone profound transformations over the past few decades, shaped by a complex interplay of socioeconomic development, accelerated urbanization, technological evolution, and the persistent housing deficit that still affects millions of citizens [1]. Driven by government housing programs, private sector investment, and growing demand for urban infrastructure, the industry has expanded rapidly. However, this expansion has not always been accompanied by the necessary structural reforms, regulatory enforcement, or improvements in construction quality. As a result, various systemic issues persist, especially in peripheral urban areas and regions with challenging environmental conditions.

In particular, regions with humid tropical climates, such as the Amazon, present unique challenges to the construction industry. Manaus, the capital of the state of Amazonas, stands as a compelling case study. With an annual rainfall exceeding 2,300 mm and an average relative humidity of 85%, the city experiences intense and prolonged exposure to moisture throughout the year [2], [3]. Under these conditions, the absence of effective waterproofing systems has led to the emergence of recurrent pathologies, especially in masonry buildings. These pathologies, including infiltration, mold, efflorescence, and structural degradation, compromise not only the durability and mechanical stability of constructions but also their habitability, aesthetic integrity, and sanitary conditions.

Waterproofing—defined as the set of techniques, materials, and procedures used to prevent the intrusion of water or moisture into structures—is a critical and strategic stage of the construction process [4]. Its relevance is reinforced by technical standards such as ABNT NBR 15575 [5], which establishes performance criteria for residential buildings, emphasizing the need to ensure water-tightness, resistance to moisture, and long-term structural reliability. Water, in its various states (liquid, vapor, or even ice), is considered one of the most aggressive agents of physical and chemical degradation. It infiltrates buildings through microcracks, capillary rise from the ground, or percolation, leading to pathologies such as efflorescence, corrosion of reinforcement bars, fungal colonization, peeling of

coatings, and eventual compromise of load-bearing elements [6], [7].

These manifestations not only reduce the useful life of buildings but also represent serious health risks, particularly when fungi and mold proliferate in indoor environments. Inhabitants are exposed to respiratory illnesses, allergies, and general discomfort due to poor air quality [8]. Thus, addressing waterproofing failures is not merely a matter of structural maintenance but of public health and social well-being.

Despite the development of advanced materials—such as polymer-modified cementitious mortars, asphalt-based membranes, and liquid-applied elastomeric membranes—the implementation of these solutions often falls short. In Manaus and similar urban centers, the rapid and unregulated expansion of the city has resulted in the proliferation of self-built housing, constructed without adequate planning, inspection, or adherence to building codes [9]. These buildings are often erected by informal labor, using low-quality or incompatible materials, and with little or no technical specification regarding waterproofing. As a result, construction errors, neglect of maintenance, and misuse of materials are common, creating a fertile ground for the emergence of chronic pathologies.

Moreover, many homeowners and small-scale builders underestimate the importance of waterproofing in the lifecycle of a building. Due to its relatively low initial cost, it is often considered dispensable, particularly when budget constraints arise. This short-sighted view, focused on short-term savings, inevitably leads to higher future expenses due to corrective maintenance, deterioration of property value, and even legal disputes. Studies have shown that the cost of preventive waterproofing is significantly lower than that of subsequent repair interventions, especially when damage extends to structural components or finishes [10].

In light of these challenges, the general objective of this research is to investigate the occurrence, causes, and manifestations of moisture-related pathologies in residential buildings located in the northern region of Manaus. The study seeks to identify the most affected building components, evaluate the materials and construction techniques used, and propose practical and technically grounded solutions based on the application of rigid and flexible waterproofing systems adapted to local climatic and soil conditions.

The specific objectives of the study are as follows:

- To identify, classify, and map pathologies such as damp stains, efflorescence, and spalling of concrete layers, particularly in slabs and exterior walls;
- To select and apply appropriate waterproofing systems for various structural elements, including foundations, masonry walls, and roof slabs, considering both static and dynamic performance requirements;
- To analyze the effectiveness of different waterproofing systems—rigid systems such as additive-modified mortars, and flexible systems like asphalt-based membranes or elastomeric coatings—under real-world conditions;
- To formulate technical recommendations for preventive and corrective measures, aligned with the ABNT normative framework, including standards NBR 9575, NBR 15575, and NBR 9952.

This research aims to offer a detailed and contextualized diagnosis of the most common pathologies observed in the region, linking them to construction failures, design oversights, or material inadequacies—particularly in regard to waterproofing. By combining empirical observation, field interviews, and technical analysis, the study demonstrates the feasibility of practical solutions that are cost-effective, sustainable, and locally adaptable.

Furthermore, the contribution of this work lies in bridging the gap between theory and practice, reinforcing the importance of interdisciplinary collaboration between engineers, architects, builders, public agencies, and the communities involved. By raising awareness about the strategic importance of waterproofing, this research encourages stakeholders to view it not as a marginal expense but as an investment in longevity, safety, and environmental performance.

As noted by Jesus [11], preventive maintenance is essential to preserve the intended performance of buildings and avoid premature obsolescence. Buildings are expected to last for decades—often up to 50 years [9] — but without regular inspection and proactive intervention, especially in regard to water control, their lifespan and functionality are drastically compromised.

Finally, this study seeks to address a critical gap in the literature and in applied engineering practice: the lack of systematic research on waterproofing performance in humid equatorial environments, such as the Amazon basin. In these contexts, intense rainfall, high ambient moisture, and clayey, poorly draining soils demand tailored solutions. By focusing on the city of Manaus, this research contributes not only to technical advancement but also to the formulation of more inclusive, sustainable, and resilient construction practices, strengthening the connection between academia, industry, and civil society [12].

II. THEORETICAL REFERENCE

Pathologies in buildings are structural or non-structural anomalies that compromise not only the functionality and performance of constructions but also their safety, comfort, and aesthetic appeal. These manifestations demand a thorough technical diagnosis, careful analysis, and targeted intervention to avoid long-term deterioration and user discomfort [3]. Luduvico [12] compares this process to that of medical treatment: a building, much like a human body, may develop "illnesses" such as cracks, stains, or water infiltration, which require proper identification of causes (diagnosis), prediction of impacts (prognosis), and implementation of corrective measures (therapy).

Thomaz [2] provides a detailed conceptualization of building pathologies, classifying them into categories such as physical deterioration, chemical degradation, and biological attack. He emphasizes the importance of early detection and systematic classification of anomalies to inform the choice of rehabilitation techniques. Among the various strategies for preventing structural degradation, waterproofing stands out as a fundamental line of defense. According to the ABNT NBR 15575 standard [3], waterproofing is a mandatory preventive measure in all types of buildings, especially in regions with high rainfall and humidity indexes, such as Manaus, where annual precipitation exceeds 2,300 mm [13].

One of the most recurrent and impactful pathologies in masonry structures is water infiltration. It occurs when water penetrates through microcracks, poorly sealed joints, or capillary suction from the ground. The consequences are diverse: coating disintegration, paint deterioration, efflorescence (salt

crystallization), mold proliferation, and, eventually, structural compromise [14]. These effects are not only aesthetic or material; as Schreiber [11] warns, persistent moisture within homes and buildings can severely worsen the living conditions of residents, particularly those with pre-existing respiratory conditions.

In specific geological contexts, such as areas with clayey soil, water has the capacity to ascend through masonry by capillary action, a phenomenon that allows groundwater to rise up to 1.5 meters within walls [6]. This leads to dark stains near floor levels, flaking of paint, disaggregation of plaster, and a characteristic musty odor. In buildings with exposed slabs and flat roofs, percolation — the slow migration of water through porous surfaces—is another common mechanism of infiltration. These areas often lack adequate slope for water runoff, requiring the application of flexible waterproofing membranes that can accommodate expansion and contraction caused by thermal cycles [9].

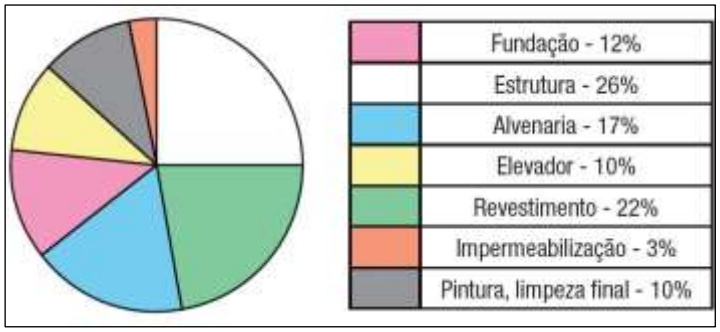

Figure 1: Estimation of the cost of waterproofing on a project.
Source: Authors, (2025).

Despite its critical function, waterproofing is often undervalued, both in financial and technical terms. As shown in Figure 1, waterproofing typically represents only around 3% of a project's overall cost, a proportion that belies its crucial role in ensuring durability and habitability over time. This low investment often results in higher costs later due to repairs, maintenance, or legal disputes with property owners.

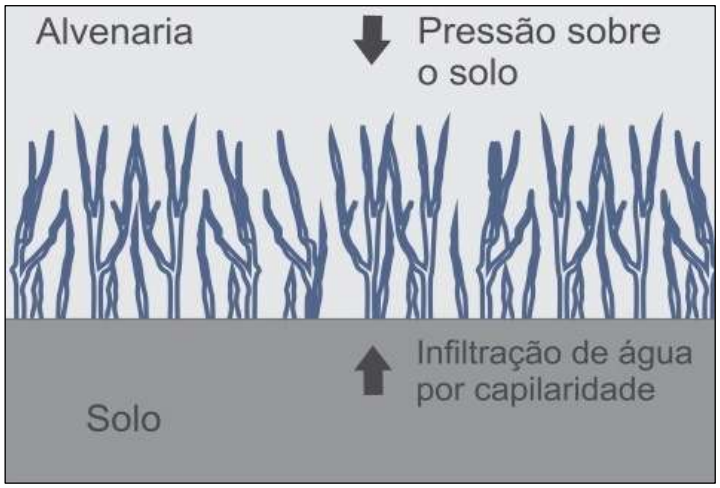

Figure 2: Infiltration rising up the masonry wall through the soil.
Source: Authors, (2025).

Among the visible consequences of infiltration is efflorescence, which presents as white crystalline deposits of salts (mainly calcium carbonate) on the surface of walls or floors. These deposits indicate chronic moisture penetration and are often accompanied by internal pressure caused by salt crystallization, leading to microcracking and weakening of the concrete [5]. More critically, moisture facilitates corrosion of steel reinforcement bars, particularly in beams and columns, which can reduce their service life by up to 20 years in tropical climates with high humidity and aggressive environmental exposure [15].

Additionally, biological agents such as fungi—including Stachybotrys—can proliferate on damp surfaces. These organisms not only affect indoor air quality but also release allergenic spores, increasing the risk of respiratory illnesses and allergic reactions [7]. Cracks themselves can vary in severity: microcracks (less than 0.1 mm wide) are often due to drying shrinkage or thermal fluctuations, whereas fissures (greater than 0.5 mm wide) are typically related to deeper structural problems such as foundation settlement or mechanical overload [16].

Figure 3: Appearance of efflorescence on the masonry wall.
Source: Authors, (2025).

To prevent and mitigate these pathologies, the selection and proper application of waterproofing systems are essential. The ABNT NBR 9575 standard [17] defines waterproofing as the use of materials and techniques to block fluid ingress into building components. These systems are generally classified into three main types:

- Cementitious systems, typically composed of waterproofing mortars mixed with chemical additives, are rigid and recommended for use in foundations and water tanks.
- Asphalt-based systems, such as polymer-modified bitumen membranes (e.g., torch-on membranes), are more flexible and suitable for roofs and terraces.
- Polymeric systems, including PVC membranes and liquid-applied membranes like elastomeric rubber, provide high elasticity and are ideal for areas subjected to constant movement or temperature fluctuations [18].

Rigid systems, while effective in static zones like underground tanks or base walls, often fail when applied to areas that experience structural movement above 0.3 mm. In such cases, flexible waterproofing solutions—such as EPDM membranes—are more appropriate. These materials accommodate expansion and contraction and offer increased durability, though at a slightly higher cost. On average, waterproofing can represent 2% to 5% of a building's total construction value, depending on the system and complexity of application [19].

Standards such as NBR 9952 (focused on asphalt membranes) and NBR 15575 (building performance requirements) provide guidance on the minimum physical, chemical, and mechanical resistance that waterproofing materials must meet to ensure their effectiveness over time [20]. Modern waterproofing strategies also benefit from integration into Building Information Modeling (BIM), where detailed information about materials, compatibility with other systems (e.g., plumbing), and structural joints can be digitally simulated and documented in the design phase [21].

Finally, the success of any waterproofing system depends not only on proper design and material selection but also on professional execution. According to data from VEDACIT [9], the use of trained and certified professionals (e.g., engineers with CREA accreditation) reduces the likelihood of waterproofing failures by up to 80%, underscoring the importance of expertise in both the planning and execution stages.

III. MATERIALS AND METHODS

The research was conducted in the Northern Zone of Manaus (Amazonas State, Brazil), a region marked by rapid urban expansion and a predominance of self-built single-family homes. According to IBGE data (2022), the municipality had an estimated population of 2,063,547 inhabitants, distributed across an area of 11,401.09 km², with a GDP per capita of BRL 45,782.75 [22].

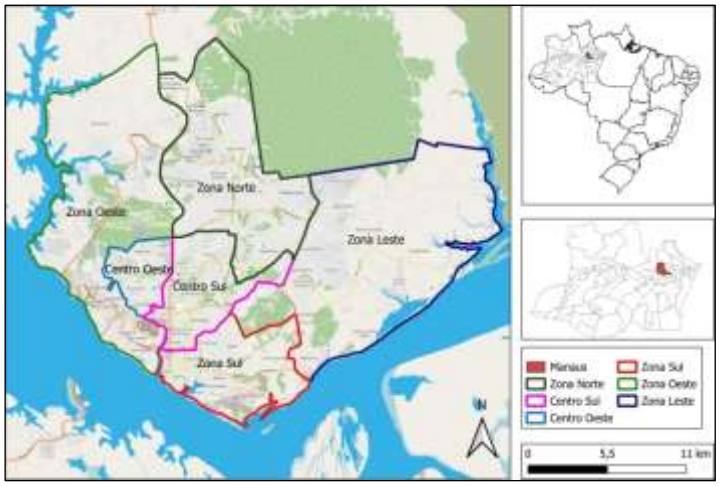

Figure 4: Map of the city of Manaus divided by zones.
Source: [13].

The Northern Zone of Manaus comprises a diverse set of neighborhoods, including Colônia Terra Nova, Novo Israel, Monte das Oliveiras, Cidade Nova, Santa Etelvina, Lago Azul, Piorini, Colônia Santo Antônio, and Fazendinha. These districts are marked by accelerated urban growth, heterogeneous urban morphology, and high rates of self-constructed housing. As such, they provide a relevant and complex field for investigating recurring construction pathologies—particularly those linked to moisture and lack of waterproofing.

The sample for this study consisted of 50 residential buildings, strategically selected along the main thoroughfares of the aforementioned neighborhoods. Selection criteria were defined based on accessibility, typicality, and evidence of deterioration, particularly in structures showing visible signs of moisture-related pathologies, such as damp spots, water infiltration, mold proliferation, efflorescence, and partial degradation of plaster and paint. Homes exhibiting these anomalies were considered as units of analysis, allowing for targeted observation and empirical intervention.

The methodological framework adopted for this research is qualitative in nature, focusing on a comprehensive, exploratory, and interpretive approach. Fieldwork was conducted through on-site technical inspections, developed in collaboration with local civil engineers, construction companies, and building maintenance professionals. These visits allowed the team to identify critical failure points in masonry structures, especially in elements directly exposed to environmental conditions, such as roof slabs, retaining walls, beams, baldrames, and external vertical surfaces.

From the full sample, a subset of six residences was selected to receive experimental application of waterproofing products, enabling practical, in situ evaluation of different systems. The goal was to examine the performance of rigid systems (such as waterproof mortars with chemical additives) and flexible systems (including asphalt membranes, polymeric coatings, and elastomeric products) in the specific environmental conditions of Manaus.

During field assessments, a recurring challenge identified was the residents' limited technical knowledge regarding waterproofing materials and procedures. Many homeowners lacked basic understanding of the causes and consequences of infiltration, leading them to adopt ineffective or inappropriate solutions. Frequently, incompatible or substandard paints, non-certified sealants, or improvised mixtures were found to be applied to problem areas, exacerbating rather than mitigating moisture-related issues. In some cases, additives were improperly dosed, or applied without following manufacturer specifications, resulting in failures of adhesion, coverage, and impermeability.

To facilitate meaningful engagement with the communities involved, the research team adopted an open and participatory communication approach, conducting semi-structured interviews and collaborative discussions with key stakeholders: homeowners, construction workers, site foremen, and local engineers. These conversations provided valuable insights into the decision-making processes related to construction and maintenance, highlighting knowledge gaps, financial limitations, and behavioral patterns. They also allowed for the co-identification of priorities for intervention, fostering a sense of ownership and trust among participants.

To ensure the health and safety of all involved, particularly during the phases of product application and testing, strict Personal Protective Equipment (PPE) protocols were implemented. The use of boots, PVC or rubber gloves, helmets, protective eyewear, solvent-resistant masks, and appropriate clothing (long sleeves and trousers) was mandatory, in line with standard construction site safety regulations [23].

The application of waterproofing products required specific tools and equipment, adapted to each material's nature and intended surface. These included trowels, smooth and notched screeds, wide brushes, paint rollers, torches for torch-on membranes, plastic or metal buckets, and wheelbarrows for material transportation. Tool selection and handling were conducted strictly following technical datasheets and manufacturer guidelines, ensuring optimal performance and accurate assessment of product behavior under field conditions [24].

The sampling strategy was intentionally non-probabilistic, based on purposive sampling techniques. This choice was guided by the need to access buildings that exhibited clear and relevant symptoms of water-related damage, while also ensuring logistical

feasibility for technical interventions. According to established qualitative research practices, purposive sampling allows for the in-depth exploration of complex phenomena within specific contexts, providing rich and meaningful data [25].

The selected buildings were, in most cases, single-story homes built more than ten years prior to the study. A large portion had been constructed by local masons, construction workers, or even by the residents themselves, without the support of qualified professionals or engineering supervision. As such, many of the structures lacked architectural and technical planning, presenting construction deficiencies that directly contributed to the emergence of moisture-related pathologies. These include the absence of foundational sealing systems, inadequate external paving, and misapplication of finishing materials.

Additionally, the lack of investment in skilled labor—often due to financial constraints—was identified as a key factor in the poor implementation of waterproofing solutions. Many households reported that they opted for the cheapest available materials, or skipped the waterproofing step entirely, believing it to be unnecessary or unaffordable.

Post-inspection interviews with residents were essential in complementing the visual diagnoses made during site visits. These interviews were divided into two parts: initially, a structured script with open-ended questions was used to understand residents' general perceptions regarding moisture control, thermal comfort, structural quality, and maintenance practices. In the second phase, targeted follow-up questions were posed, addressing specific topics such as knowledge of waterproofing systems, experience with rigid or flexible products, and familiarity with Brazilian technical standards, notably ABNT NBR 9575 and NBR 15575 [3], [17].

The combination of visual inspections and resident interviews enabled the triangulation of data, reinforcing the validity of the findings. Based on these observations, the team created comparative charts and frequency tables to analyze the recurrence and distribution of pathologies across the sample. The most common anomalies included:

- Accumulation of sludge on external walls due to poor rainwater drainage;
- Moisture infiltration into retaining walls;
- Absence of perimeter pavement, allowing water ingress near the foundations;
- Cracks at beam-column junctions, often caused by differential settlement or thermal stress.

Each pathology was quantified in terms of occurrence rate, allowing the team to identify patterns and critical areas. These insights directly informed the selection of techniques and materials for the experimental applications, as well as the development of a set of technical recommendations for broader application.

The systematized knowledge derived from this study holds the potential to guide construction companies, independent professionals, and public agencies in the implementation of preventive and corrective strategies. By identifying the main technical gaps and behavioral trends affecting waterproofing efficacy, this research promotes the improvement of construction quality standards and the adoption of long-term, sustainable solutions.

Moreover, the findings underscore the urgent need for investment in technical training, capacity-building programs, and public awareness campaigns. Promoting better understanding of waterproofing techniques and their importance is not only essential for improving construction practices but also for encouraging the development of safer, more efficient, and more accessible materials in line with national standards for durability and performance [3], [17], [20].

IV. RESULTS AND DISCUSSIONS

The findings of this research are grounded in empirical evidence and technical concepts previously outlined in specialized literature on waterproofing (Section 2). While this study adhered to technical criteria in the handling and application of waterproofing materials, it is recommended that such services be executed by qualified professionals, strictly following surface preparation, system selection, and application steps in compliance with current technical standards.

The applied systems demonstrated satisfactory performance until the conclusion of the research. However, if end-users lack familiarity with product behavior under specific conditions, preliminary testing is advised prior to definitive application.

As per ABNT NBR 15575 [3], an effective waterproofing system must meet the following performance requirements:

- Resistance to static and dynamic loads;
- Accommodation of substrate expansion and contraction due to thermal variations;
- Resistance to climatic, chemical, and biological agents;
- Watertightness under hydrostatic pressure and soil moisture;
- Adhesion, flexibility, and physico-mechanical stability aligned with design specifications;
- Adequate service life under projected conditions.

Data collection involved technical visits to 50 residences in the Northern Zone of Manaus. Purposive sampling targeted areas with high incidence of moisture-related pathologies, such as leaking slabs, damp walls, and deteriorated retaining walls. Interviews with residents, foremen, masons, and civil engineers enabled a comprehensive analysis of factors contributing to pathological manifestations.

Figure 5: Number of residences per pathology-affected area.
Source: Authors, (2025).

Figure 5 illustrates the profile of those responsible for constructing the surveyed residences, revealing that homeowners predominantly executed or supervised the work. This reality directly impacts the adoption (or absence) of proper waterproofing practices.

Figure 6: Parties responsible for residence construction.
Source: Authors, (2025).

Practical application of waterproofing systems was conducted in six residences, with data organized in Table 1. The table details waterproofing types, building age, and percentage of estimated 50-year residential lifespan achieved [26].

Table 1: Service life of waterproofed residences relative to estimated lifespan.

Residence	Waterproofing Type	Service Life (Years)	Lifespan Achieved (%)
Street A	Rigid	18	36%
Street B	Rigid	15	30%
Street C	Rigid	17	34%
Street D	Rigid	4	8%
Street E	Flexible	12	24%
Street F	Flexible	20	40%

Source: Authors, (2025).

As Ferreira [18] notes, building longevity is directly tied to proper waterproofing system execution, which acts as a protective barrier against infiltration and structural degradation. Absence of such systems leads to pathologies like stains, mold, coating detachment, compromised habitability, and structural instability.

During interviews, residents reported critical infiltration and thermal discomfort issues. Per NBR 15575 [3], such conditions violate minimum habitability and safety requirements, particularly when structural integrity or occupant mobility is compromised.

Resident dissatisfaction with cracks, mold, and infiltration directly impacts physical and psychological well-being, underscoring the need for buildings ensuring long-term performance. Most pathologies stemmed from design flaws, poor execution, lack of technical product knowledge, or absent preventive maintenance.

Figure 7: Root causes of pathologies in surveyed residences.
Source: Authors, (2025).

V. CONCLUSIONS

The findings presented in this case study reaffirm that no building—whether residential, commercial, or industrial—is inherently immune to water infiltration. Regardless of architectural design, construction quality, or intended use, the presence of moisture in masonry structures represents a consistent and latent risk, especially in regions characterized by humid equatorial climates, such as Manaus. When waterproofing systems are improperly designed, inadequately applied, or entirely neglected, pathological manifestations inevitably emerge, compromising both the physical integrity of the structure and the quality of life of its users.

One of the most concerning consequences of moisture infiltration is its direct impact on human health, particularly in households with occupants suffering from respiratory conditions or allergies. The proliferation of mold, mildew, and fungi on interior surfaces, often accompanied by foul odors and visual deterioration, creates environments that are not only

uncomfortable but also clinically unsafe. Additionally, water ingress through slabs has been observed to cause concrete deterioration, corrosion of reinforcement bars, and fragment detachment, leading to safety hazards for the building's inhabitants and visitors.

From a structural and performance standpoint, waterproofing must be treated as a fundamental and non-negotiable element of the construction process. It is not merely a protective finish or optional step, but rather a technical necessity that should be planned and integrated into all phases—from architectural design and material specification, to execution, inspection, and maintenance. Building users and property owners must be educated and empowered to demand compliance with waterproofing standards and to recognize watertightness as a key performance indicator of any construction project.

The study revealed that the application of well-specified waterproofing systems—whether rigid or flexible—can significantly reduce the occurrence of critical anomalies. These systems not only prevent fissures in exposed slabs and enhance the performance of retaining walls and foundation beams, but also block moisture penetration toward steel reinforcements, thus extending the structural life cycle. As a result, indoor comfort improves, the value of the property is preserved, and the maintenance costs associated with deterioration are drastically reduced.

As Gatto [27] insightfully points out, housing plays a foundational role in the development of individuals and communities, especially in developing countries like Brazil, where housing conditions are intrinsically linked to social mobility and urban equity. In this regard, ensuring the quality, safety, and durability of residential construction—through practices such as proper waterproofing—is not just a technical objective, but also a social imperative.

This research also calls attention to the fragmentation within the construction chain, where manufacturers, designers, applicators, and consumers often operate in silos. Overcoming this disconnect requires establishing more integrated workflows, multidisciplinary collaboration, and greater awareness of waterproofing as a specialized subfield within Civil Engineering. This would support not only technical consistency but also innovation in materials, methods, and regulatory frameworks.

The systematic evaluation of 50 residences in the Northern Zone of Manaus revealed a pattern of pathologies that mirror those found throughout the city and across similar climatic regions, largely stemming from economic constraints, lack of technical oversight, and limited understanding of waterproofing systems among both professionals and end users. These conditions are further aggravated by the absence of legal and regulatory mechanisms that mandate the inclusion of waterproofing strategies in standard project documentation. The lack of enforcement and oversight leaves ample room for omission, improvisation, and error, ultimately affecting the safety and longevity of buildings.

Consequently, one of the key conclusions of this study is that waterproofing should be regarded not as a dispensable cost, but as a long-term investment—an integral part of sustainable building design that ensures structural integrity, property valuation, and the well-being of its occupants. Even in cases where waterproofing is successfully applied during construction, its long-term effectiveness is contingent upon regular maintenance and periodic inspections, particularly in high-risk environments subject to intense rainfall and humidity fluctuations.

The current demand for high-performance materials, combined with increasing awareness of building failures, is already fostering positive shifts in the waterproofing sector. New products with enhanced physical, chemical, and environmental resistance are being introduced, alongside growing investments in technical training, certification programs, and digital modeling technologies, such as BIM, that allow for precise waterproofing planning and simulation. These developments signal a broader paradigm shift in construction culture, where quality and performance standards are becoming central rather than peripheral concerns.

Moreover, empirical studies like this one, which document the frequency and distribution of pathological manifestations, have the potential to inform material development, guide public policy, and optimize construction practices. They provide actionable insights for researchers, industry professionals, regulatory bodies, and municipal authorities, contributing to a more robust and resilient building sector.

Through this research, not only were key areas of water-induced deterioration identified, but they were also treated using appropriate products and protocols, reinforcing the importance of evidence-based interventions. The outcomes validate the application of waterproofing systems grounded in technical rigor, local feasibility, and long-term durability.

In conclusion, the pursuit of quality, longevity, and health in civil construction—especially in humid and climatically vulnerable regions such as Manaus—demands a comprehensive, systemic, and interdisciplinary approach. Waterproofing, far from being a minor detail, must be elevated to the status of critical infrastructure within every construction project. Only then will it be possible to safeguard built heritage, promote healthier living environments, and build a more equitable and resilient urban future.

VI. AUTHOR'S CONTRIBUTION

Conceptualization: Wmilison Sousa da Silva
Methodology: Wmilison Sousa da Silva
Investigation: Wmilison Sousa da Silva
Discussion of results: Wmilison Sousa da Silva
Writing – Original Draft: Wmilison Sousa da Silva
Writing – Review and Editing: Wmilison Sousa da Silva
Resources: Wmilison Sousa da Silva
Supervision: Edinaldo José de Sousa Cunha
Approval of the final text: Edinaldo José de Sousa Cunha

VII. ACKNOWLEDGMENTS

To the Galileo Institute of Technology and Education of the Amazon (ITEGAM) and the Federal University of Pará (UFPA), for making this master's degree possible and for encouraging the dissemination of knowledge and the completion of yet another successful project in my career. To my advisor Prof. Dr. Edinaldo José de Sousa Cunha for his support during the experimental research and for his assistance in preparing the research.

VIII. REFERENCES

[1] D. Zechmeister, Estudo para a padronização das dimensões de unidades de alvenaria estrutural no Brasil através do uso da coordenação modular. Dissertação (Mestrado em Engenharia Civil) - Universidade Federal do Rio Grande do Sul, Porto Alegre, 2005.

[2] E. Thomaz, Trincas em edifícios: causas, prevenção e recuperação, 2. ed. São Paulo: Oficina de Textos, 2020.

[3] ABNT - Associação Brasileira de Normas Técnicas, NBR 15575: Desempenho de Edifícios Residenciais. Rio de Janeiro: ABNT, 2013.

[4] IBI - Instituto Brasileiro de Impermeabilização. O que é impermeabilização. 2022. [Online]. Disponível em: https://ibibrasil.org.br/artigos/o-que-e-impermeabilizacao/. Acesso em: 18 maio 2023.

[5] F. Queruz, Contribuição para identificação dos principais agentes e mecanismos de degradação em edificações da Vila Belga. Dissertação (Mestrado em Engenharia) – Universidade Federal de Santa Maria, Santa Maria, 2007.

[6] C. R. K. Moraes, Impermeabilização em lajes de cobertura: levantamento dos principais fatores envolvidos na ocorrência de problemas na cidade de Porto Alegre. Dissertação (Mestrado em Engenharia) - Universidade Federal do Rio Grande do Sul, Porto Alegre, 2002.

[7] E. R. P. Malgueiro, Definição de critérios de avaliação da qualidade de edifícios de habitação em Portugal. Dissertação (Mestrado em Engenharia) - Universidade de Trás-os-Montes e Alto Douro, Vila Real, 2009.

[8] P. C. C. Vieira, Patologias em instalações hidro sanitárias de edifícios residenciais na Zona Centro-Sul de Manaus (AM): diagnóstico e terapia. Dissertação (Mestrado em Engenharia) - Universidade Federal do Pará, Belém, 2016.

[9] Bser Engenharia. A importância da impermeabilização. 2022. [Online]. Disponível em: https://bserengenharia.com.br/postagem/a-importancia-da-impermeabilizacao/. Acesso em: 15 abr. 2023.

[10] C. R. M. Jesus, Análise de custos para reabilitação de edifícios para habitação. Dissertação (Mestrado em Engenharia) - Escola Politécnica da Universidade de São Paulo, São Paulo, 2008.

[11] P. A. A. Schreiber, Impermeabilização de lajes de cobertura: caracterização, execução e patologias. Pós-Graduação em Construção Civil - Universidade Federal de Minas Gerais, Belo Horizonte, 2012.

[12] T. S. Luduvico, Desempenho a estanqueidade à água: interface janela e parede. Dissertação (Mestrado em Engenharia Civil) - Universidade Federal de Santa Maria, Santa Maria, 2016.

[13] IBGE - Instituto Brasileiro de Geografia e Estatística. Panorama da cidade de Manaus. 2022. [Online]. Disponível em: https://www.cidades.ibge.gov.br/brasil/am/manaus/panorama/. Acesso em: 2 fev. 2024.

[14] J. V. Macedo, “Manifestações patológicas causadas pela umidade devido à falha ou ausência de impermeabilização: estudo de caso,” Conferência Nacional de Patologia e Recuperação de Estruturas, Pernambuco, 2017.

[15] G. C. Isaia, Concreto: ciência e tecnologia, 1. ed. São Paulo: Ipsis, 2011.

[16] C. Caporrino, Patologias em alvenaria, 2. ed. São Paulo: Oficina de Textos, 2018.

[17] ABNT - Associação Brasileira de Normas Técnicas, NBR 9575: Impermeabilização - Seleção e projeto. Rio de Janeiro: ABNT, 2010.

[18] R. Ferreira, “Conhecendo os impermeabilizantes,” Equipe de Obra Como Construir na Prática, vol. 44. São Paulo: Pini, 2012.

[19] Fibersals. Impermeabilização de lajes: o guia completo, 2022. [Online]. Disponível em: https://fibersals.com.br/. Acesso em: 22 jul. 2023.

[20] ABNT - Associação Brasileira de Normas Técnicas, NBR 9952: Manta asfáltica para impermeabilização. Rio de Janeiro: ABNT, 2014.

[21] ABNT - Associação Brasileira de Normas Técnicas, NBR 13532: Elaboração de projetos de edificação - Arquitetura. Rio de Janeiro: ABNT, 1995.
[22] VEDACIT, Manual Técnico: Impermeabilização de Estruturas, 6ª ed. Vedacit Impermeabilização, ago. 2023.

[23] Júnior, G. R., Componentes estratégicos para categorias de análises do sistema de gestão ambiental. Tese (Doutorado em Engenharia de Produção) – Universidade Federal de Santa Catarina, Florianópolis, 2006.

[24] E. Thomaz, “Patologia,” in Manual técnico de alvenaria, ABCI – Associação Brasileira de Construção Industrializada, 1. ed. São Paulo, 1990, pp. 97–117.

[25] N. M. Pintan, Manifestações patológicas e estudo da corrosão presente em pontes do Recife. Dissertação (Mestrado em Engenharia Civil) - Universidade de Pernambuco, Recife, 2013.

[26] AECWeb. Impermeabilização de lajes com borracha líquida. AECWeb Notícias Técnicas, 2022.

[27] A. Gatto, A moradia como direito social no Brasil: desafios e possibilidades. São Paulo: Ed. Moderna, 2012..

Journal of Engineering and Technology for Industrial Applications

ISSN ONLINE: 2447-0228

ITEGAM-JETIA

Manaus, v.11 n.53, p. 216-224. May/June., 2025.

DOI: https://doi.org/10.5935/jetia. v11i53.2024

RESEARCH ARTICLE OPEN ACCESS

DESIGN OF PARTICLE SWARM OPTIMIZATION-BASED PID CONTROLLER FOR HIGH-PERFORMANCE PMSM SPEED CONTROL

Ghufran Saad Mohammed[1] and Mohammed Obaid Mustafa[2]

[1] MSc student, Dept. Of Electrical Eng, College of Engineering, University of Mosul, Mosul, Iraq.
[2] Dept. Of Electrical Eng, College of Engineering, University of Mosul, Mosul, Iraq.

[1]https://orcid.org/0009-0004-6298-8146, [2]https://orcid.org/0000-0001-5188-6508

Email: ghufran.22enp41@student.uomosul.edu.iq, mohammed.obaid@uomosul.edu.iq

ARTICLE INFO

Article History
Received: May 11, 2025
Revised: June 20, 2025
Accepted: June 25, 2025
Published: June 30, 2025

Keywords:
Permanent magnet synchronous motor (PMSM
PWM switching strategies,
PSO-optimized PID controllers,

ABSTRACT

The present study shares an appropriate technique for regulating the speed of a Permanent Magnet Synchronous Motor (PMSM) drive system using a PID controller. This approach maintains the main architecture of the PID controller while significantly improving its performance compared to previous controllers. The resulting controller offers great resilience to changes in PMMS settings, fast and precise responses, and necessary noise rejection. Testing revealed that for accuracy, parametric variation, and load torque disturbances the suggested system performs best with proportional gain of 0.0029, integral gain of 0.65, and derivative gain of 0.0012.

Moreover, we utilized Particle Swarm Optimization (PSO) to improve the parameters of the PID controller, leading to significant performance improvements under various scenarios. The proposed method offers simplicity and ease of real-time implementation while providing stability and outstanding efficacy in achieving optimal performance.

I. INTRODUCTION

The remarkable progress in electric motor technology has increased the need for high-efficiency motor control systems. The Permanent Magnet Synchronous Motor (PMSM) is widely used among motor types due to its high power density, excellent efficiency, and precise torque control [1]. The PMSM is now widely regarded as a key drive technology in industrial applications such as robots, electric vehicles, and aircraft. Still, achieving perfect results in Permanent Magnet Synchronous Motor (PMSM) operation remains difficult, especially with relation to energy efficiency, torque ripple reduction, and speed control.

Permanent Magnet Synchronous Motors (PMSMs) are often regulated with traditional Proportional-Integral-Derivative (PID) controllers. They need to be enhanced, nevertheless, to function efficiently with load fluctuations, nonlinearities, and outside disturbances. [2].

However, it is still difficult to precisely and reliably manage PMSM speed, especially when there are external disturbances and parameter deviations. The growing need for dependable, high-performance motor drives in contemporary applications like robotics, industrial automation, and electric cars has led to a great deal of research into the management of PMSMs [3].

The simplicity, ease of implementation, and adequate performance of traditional control techniques—like proportional-integral-derivative (PID) controllers—make them popular in many real-world systems. That being said, the proper choice of a PID controller's gain parameters is crucial to its performance, with performance including overshoot, lengthy settling times, and steady-state error that can be caused by improper tuning. Particularly for nonlinear and time-varying systems like PMSMs, traditional PID tuning techniques like Ziegler-Nichols and trial-and-error procedures frequently fail to achieve optimal performance.

Advanced optimization methods have been investigated to improve and automate the PID tuning procedure in order to overcome this constraint. Particle Swarm Optimization (PSO) is a potential metaheuristic technique among these algorithms because

of its fast convergence features, global search capabilities, and ease of use [4], [5].

For instance, Field-oriented control (FOC) [3] is a common approach of controlling AC motors. FOC separates torque and flux by changing stationary phase currents into a rotating d-q frame. The FOC approach simplifies the AC motor control challenge to a DC motor control problem. FOC is not without its potential failures, significant shortcomings, and restrictions such as relies on accurate motor parameters, variations due to temperature changes and magnetic saturation. Furthermore, FOC needs to know the rotor location. Incorrect commutation due to sensor damage or noise can result in instability and torque ripple [6].

Furthermore, DTC was originally introduced by I. Takahashi and T. Noguchi in (Takahashi and Noguchi (1986)) as a powerful systematic design solution for improving the dynamic torque and speed response without using Park transformation and PI controller. DTC achieves direct control of flux and torque, while it also enjoys design simplicity, and less dependence on parameter values. However, DTC may cause time varying switching frequency, and can also be prone to introduce relatively large torque and flux ripples, since the inverter keeps the same switching sequence as long as the flux and torque hysteresis controller outputs remains the same.[7], [8].

Moreover, many advanced control methods have been proposed to control PMSM including: Model Predictive Control [9], Sliding Mode Control [10], Sliding Mode Control and Artificial Neural Networks [11]. The combined use of predictive algorithms and intelligent control is anticipated to propel additional developments in PMSM control, while enhanced AI and optimization strategies are boosting performance and adaptability. Kumar and Palani (2020) achieved reliable performance under load variation by using a modified PSO method for adaptive PID tuning in electric car applications [12].

Furthermore, utilized a modified PSO technique for adaptive PID tuning in electric vehicle applications, resulting in dependable performance under load variation. For PID tuning in PMSM control, [13] suggested a hybrid GA-PSO algorithm, which produced better optimization accuracy and greater adaptability. In [14] combined fuzzy logic with PSO to produce a fuzzy-PID controller with optimized gains, which provided smoother and more dependable performance.

In this context, the present study proposes a PSO-based PID controller specifically tailored for PMSM speed control with the aim of optimizing both transient and steady-state responses. The controller is evaluated using standard performance indices (e.g., IAE, ITAE) and tested under varying load and disturbance conditions using MATLAB/Simulink, contributing to the growing body of research on intelligent motor control systems.

The rest of this paper is organized as follows: Section 2 presents the mathematical modeling of the PMSM and the control strategy. Section 3 describes the design and implementation of the PSO algorithm for PID tuning. Section 4 discusses the simulation results and performance evaluation. Finally, Section 5 concludes the paper with future directions.

II. THEORETICAL REFERENCE

II.1 Mathematical Modeling of the PMSM:

A mathematical model in the rotating dq-reference frame provides an accurate description of the dynamic behavior of a Permanent Magnet Synchronous Motor (PMSM). By transforming three-phase time-varying values into two steady-state quantities, this transformation streamlines the analysis and enables decoupled torque and flux control, much like in DC machines as shown in figure1[5][6].

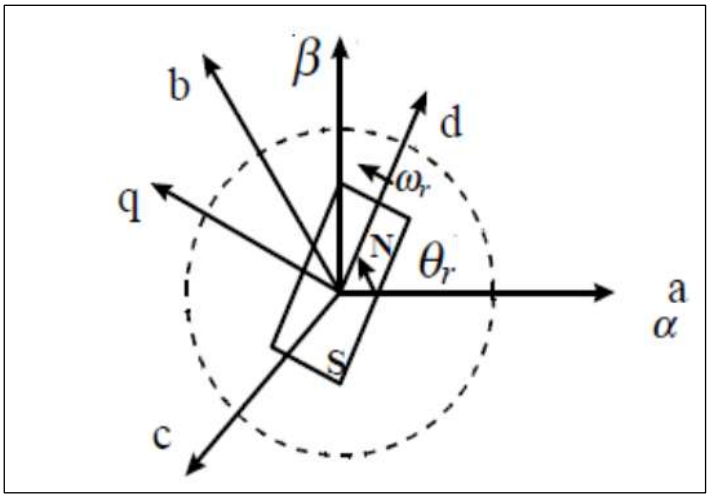

Figure 1: The stationary and synchronous frame.
Source: Authors, (2025).

In PMSM, the d-q axis reference frame (rotating frame of reference) is commonly used for modeling because it simplifies the dynamic equations. The following are the core equations [7]:

Voltage Equations in d-q Frame:

d-axis voltage: $vd = Ri_d + L(\frac{di_d}{dt} - w.iq)$ ..... (1)

q-axis voltage: $vq = Ri_q + L\left(\frac{di_q}{dt} + w.id\right) + w\lambda_m$ .....(2)

Where: v_d & v_q are the voltage components along the d-q axes, i_d & i_q are the current components along the d-q axes, L is the Inductance, R is the Resistance, w is the Angular Speed of the motor, λ_m is the permanent magnet flux linkage (Wb) and L_m is the Magnetizing Inductance.

The electromagnetic torque given by the PMSM is:

$$T = \frac{3}{2}P(\lambda_m i_q + (L - L_m)i_d i_q) \text{..... (3)}$$

Where: T is the torque, λ_m is the flux leakage of the permanent magnet and P is the number of poles in the motor. Also, The mechanical dynamic of the PMSM can be module as:

$$\frac{dw}{dt} = \frac{T_e - T_l}{j} \text{ ..... (4)}$$

Where: w is the angular speed, T_e is the electro-magnetic torque, T_l is the load torque and j moment of inertia.

II.2 CONTROL STRATEGY USING PSO AND PID:

The presented work employs a Particle Swarm Optimization (PSO) in order to -tunning a PID controller to automatically optimize the PID settings for improved performance. Motor control systems have used a traditional PID tuning techniques, including as Ziegler-Nichols, Cohen-Coon, and trial-and-error methods. These techniques might not always provide the

best results because they frequently rely on linear approximations. Additionally, they are usually unavailable and do not adjust to changes in parameters or outside interruptions. Researchers are increasingly using intelligence and optimization-based techniques to get beyond the drawbacks of conventional tuning methods. To adjust PID parameters for a variety of applications, metaheuristic algorithms including Genetic Algorithms (GA), Artificial Bee Colony (ABC), Differential Evolution (DE), and Particle Swarm Optimization (PSO) have been popular in recent years. PSO has become well-known among them because of its powerful worldwide search capabilities, simplicity of use, and computing economy.

The Proportional-Integral-Derivative (PID) controller is a common way to control things, but it needs to be fine-tuned to work well and stay stable, especially when loads change and the system isn't linear [8]. We use the Particle Swarm Optimization (PSO) algorithm to quickly optimize the PID's parameters for enhanced efficiency [15].

The standard PID control law is defined as:

$$u(t) = K_P e(t) + K_i \int_0^t e(\tau)d\tau + K_d \frac{d}{dt} e(t) \quad \ldots\ldots\ldots (5)$$

Where $e(t)$ is the error (difference between the reference and actual values). K_p, K_i, K_d are the proportional, integral and derivative respectively. The proportional, integral, and derivative components of the PID controller then generate a control signal that modifies the PWM duty cycle. By adjusting the PWM inputs, the controller effectively controls the motor's torque and current, thereby matching the motor speed with the reference value. This direct control of the PWM signal allows precise and dynamic speed regulation, allowing quick responses to changes in load or desired

II.3 PSO - PID PARAMETER OPTIMIZING:

Particles Swarm Optimization (PSO) is an optimization method that was created in 1995 by Drs. Eberhart and Kennedy and was motivated by the social behavior of fish schools and flocks of birds. PSO, an optimization technique inspired by nature, enhances the controller's adaptability by minimizing overshoot, accelerating response time, and enhancing system stability. The social behavior of fish schools or flocks of birds, in which a population of particles searches the search space for the best answer, serves as the model for PSO. Based on both its own and its neighbors' experiences, each particle modifies its course.

The Integral of Absolute Error (IAE), Integral of Time-weighted Absolute Error (ITAE), or Integral of Squared Error (ISE) are examples of performance criteria that can be efficiently minimized by using PSO in PID tuning [17]-[16]. The PSO concept uses a swarm of agents, or particles, to move around the search space in pursuit of the optimal answer. Every particle in the search area modifies its "flying" based on both its own and other particles' flying experiences; the best are referred to as "pbest." Additionally, individual particles know the group's values the best (gbest). To adjust their location, each agent uses the data pertaining to their current position (x, y), current velocity (vx, vy), and the distance between their current position and the best group. Equations (18) and (19) below alter each agent's position and velocity.peed while maintaining system stability and performance [9].

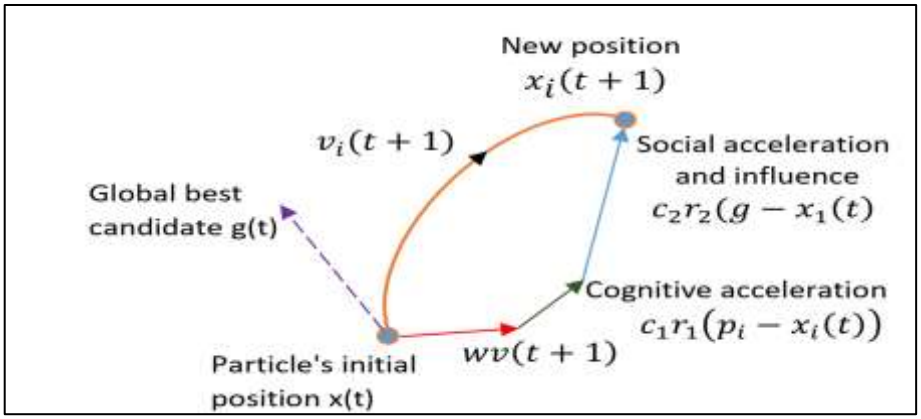

Figure 2: Primary Procedures of PSO.
Source: Authors, (2025).

The update method is as follows [17]:

Position Update:

$$x_i(t+1) = x_i(t) + v_i(t+1) \quad \ldots\ldots\ldots\ldots\ldots (6)$$

Velocity Update:

$$v_i(t+1) = wv_i(t) + c_1r_1\big(p_i - x_i(t)\big) + c_2r_2(g - x_1(t)) \quad (7)$$

Where:

- x_i is the position of the particle (representing the PID parameters).
- v_i is the velocity of the particle.
- w is the inertia weight.
- c_1 and c_2 are the cognitive and social coefficients, respectively.
- r_1 and r_2 are random numbers between the [0, 1] range.
- p_i is the particle's personal best position.
- g is the global best location the swarm discovered.

Usually the Integral of Time-weighted Absolute Error (ITAE) or Integral of Squared Error (ISE), the fitness function is defined as the error in the system evaluated using the current PID settings [16]-[17].

$$Fitness = \int_0^T |e(t)|^p dt \quad \ldots\ldots\ldots\ldots\ldots (8)$$

Where p is a constant typically chosen as 2 for ISE (Integral of Squared Error).

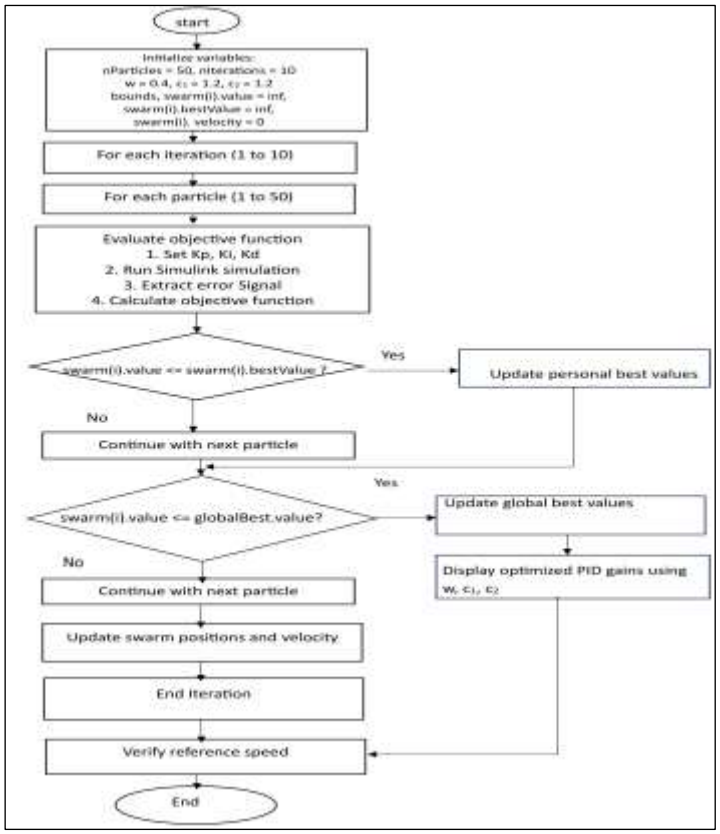

Figure 3: Particle Swarm Optimization (PSO) flowchar.
Source: Authors, (2025).

The flowchart represents the Particle Swarm Optimization (PSO) algorithm applied to optimize the PID parameters [18]. Initially, the necessary variables, including the number of particles (50), iterations (10), and constants w, c1, and c2, are defined. The swarm (population of particles) is initialized, with each particle having an initial value (swarm(i).value), best value (swarm(i).bestValue), and velocity (swarm(i).velocity). For each iteration, each particle evaluates the objective function by calculating its performance based on the PID values. The algorithm compares the particle's value with its personal best (swarm(i).bestValue) and the global best (globalBest.value). If a better value is found, the particle's personal best and the global best are updated. The particle's position and velocity are then updated using the PSO velocity update equation, which incorporates the inertia weight (w), personal attraction constant (c1), and global attraction constant (c2). The process repeats for all particles and iterations. Once the optimization completes, the best PID parameters are displayed, and the reference speed is verified

II.4 PULSE WIDTH MODULATION (PWM):

The PWM technique is applied to control the voltage and current fed to the PMSM. PWM ensures efficient motor performance and enables precise control of speed and torque by adjusting the duty cycle of the switching signals [19], [20]. Pulse Width Modulation (PWM) is also used to control the voltage and current data going to the motor, which gives precise control over how the PMSM works. Using PSO-optimized PID control along with PWM switching methods makes the system more efficient, cuts down on power losses, and boosts motor performance under a range of load conditions. [3] [4]. This study looks at how PSO-optimized PID controls and PWM signal handling affect the performance of PMSMs, focusing on important factors like controlling speed, lowering torque ripple, saving power, and making the system strong. The study's goal is to make it easier to make high-performance motor control systems that use less energy by combining smart optimization and advanced switching methods.

III. MATERIALS AND METHODS

Different load conditions were applied to the system. We operated the Permanent Magnet Synchronous Motor (PMSM) at a reference speed of 750 rpm under the specified circumstances: Case 1 features an open-loop state without a controller, Case 2 has a closed-loop condition with a proportional-integral-derivative controller, Case 3 uses a PSO-PID controller, and Case 4 features a PSO-PID controller with a two-step load.

Table 1: PMSM SPECIFICATION.

Stator Phase Resistance (Rs)	0.0485 ohm
Stator Phase Inductance (Ls)	0.000395 H
Voltage Constant	300[Vrms/krpm]
Moment of Inertia	0.02 J(kg.m^2)
Rated Speed	750 r.p.m

Source: Authors, (2025).

IV. RESULTS AND DISCUSSIONS

A block diagram of a PSO-tuned PID control system for PMSM speed regulation is displayed in Figure (3) . By modifying the PID gains in response to feedback on system performance, the PSO algorithm minimizes a specified objective function.

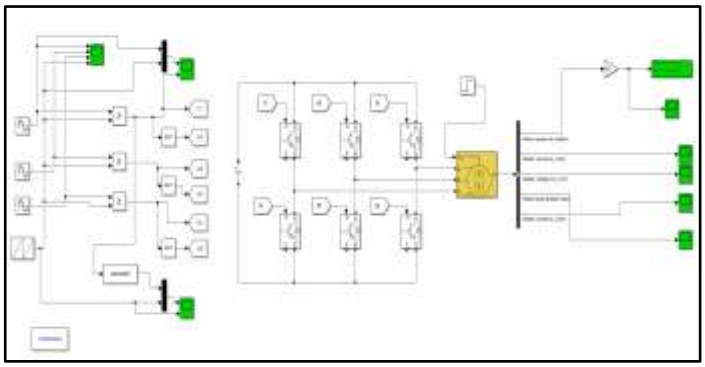

Figure 4: PMSM drive system without controller (open loop)
Source: Authors, (2025).

The diagram represents a Simulink model of a Permanent Magnet Synchronous Motor (PMSM), designed to control and monitor the motor's performance. The system receives control signals such as voltage and current, which are processed through logical gates to regulate the motor's speed and torque. The motor model simulates the behavior of the PMSM, producing outputs like torque, rotor speed, and current in both the stator and rotor. Key parameters such as rotor speed, stator current, stator voltage, rotor

angle, and rotor current are measured to evaluate the motor's efficiency and performance. This model helps in simulating and analyzing motor operation, ensuring optimal control and monitoring of the system in applications like electric vehicles and industrial machinery.

The following figures represent the speed and torque profiles of the PMSM under open-loop control, where no feedback control is applied to adjust the motor's performance. In an open-loop system, the motor operates based on predefined input signals without any real-time adjustments. As a result, the speed and torque may exhibit fluctuations and may not maintain optimal performance, especially under varying load conditions. These profiles highlight the behavior of the motor when it is running in an uncontrolled open-loop configuration, providing a basis for comparison with closed-loop controlled systems, where feedback mechanisms are used to stabilize and optimize

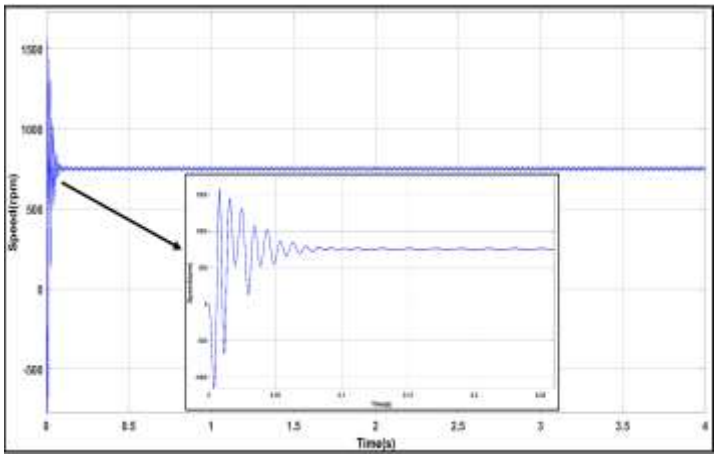

Figure 5: Speed response at open-loop condition.
Source: Authors, (2025).

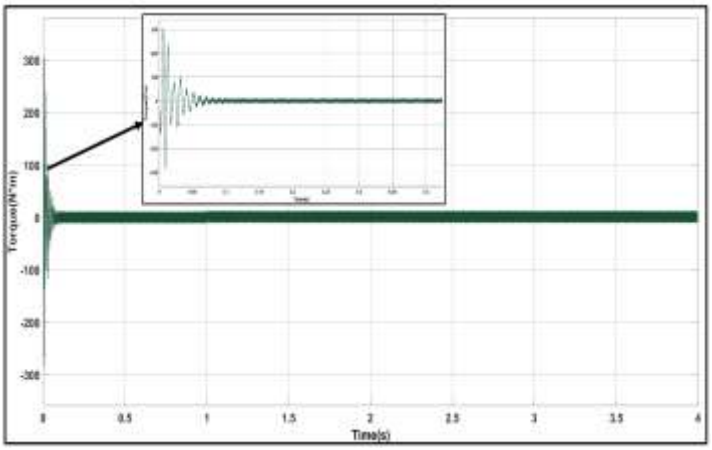

Figure 6: Torque response at open-loop condition.
Source: Authors, (2025).

Figure (7) represents a closed-loop control system for a Permanent Magnet Synchronous Motor (PMSM), where PID control is applied to regulate the motor's performance. The system consists of a PID controller that takes feedback from the motor's performance parameters, such as speed and torque, to adjust the input signals accordingly. The feedback loop ensures that any deviations from the desired motor speed or torque are corrected in real time.

The motor operates under this closed-loop configuration, where the PID controller adjusts the control signals to maintain stable and optimal motor operation, improving performance and reducing the effects of external disturbances or load variations. This system provides enhanced control compared to open-loop configurations, ensuring the motor's speed and torque remain at desired levels throughout operation.

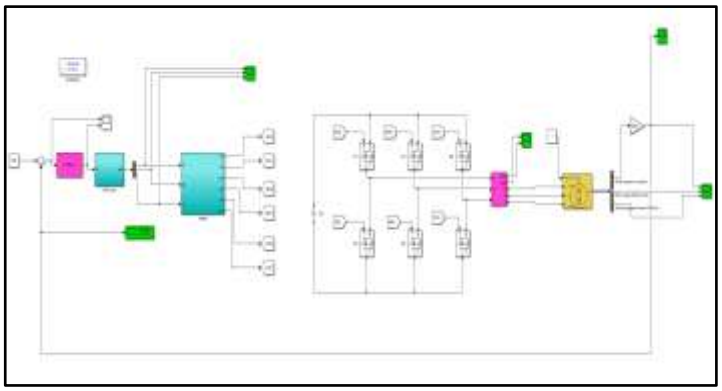

Figure 7: PMSM drive system with PID Controller.
Source: Authors, (2025).

In Fig(7)and Fig(8) respectivly, the speed and torque waveforms of the PMSM are shown under closed-loop PID control. Compared to the open-loop system, where the motor operates without feedback, the closed-loop control significantly improves performance. The speed waveform becomes much more stable and smooth as the PID controller adjusts the input signals to maintain a consistent motor speed, minimizing any fluctuations caused by load variations.

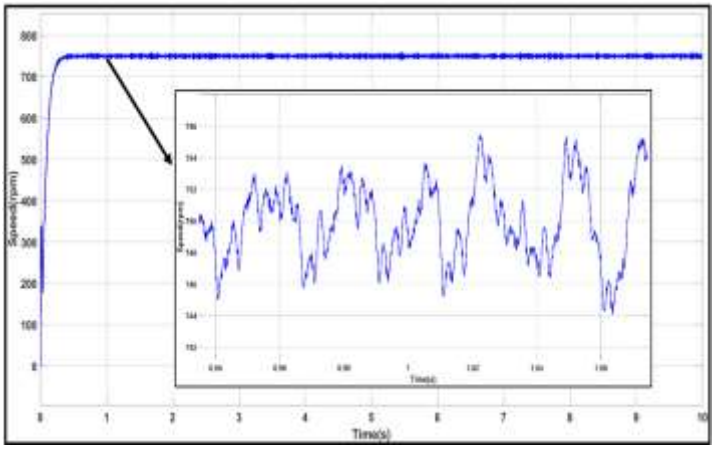

Figure 8: Speed response with PID controller.
Source: Authors, (2025).

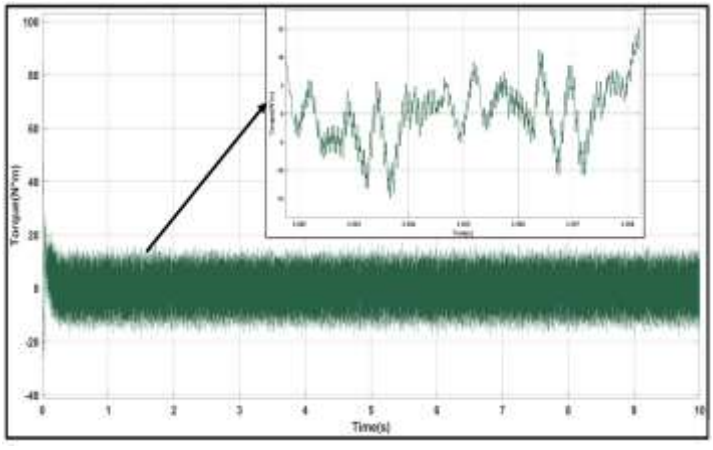

Figure 9: Torque response with PID controller.
Source: Authors, (2025).

PID controller-driven speed control of a Permanent Magnet Synchronous Motor (PMSM) is investigated in this work. Simulated performance of the PMSM drive system in open-loop, that is, without control, and with the PID controller operating to regulate the motor's speed is achieved.

Figure (7) illustrates that the input voltage significantly affects the motor speed in an open-loop condition, as depicted in Figure (4), leading to substantial oscillations and prolonged settling times. The PID controller significantly enhances speed control by minimizing steady-state error, enabling the motor's speed to attain the goal setpoint more swiftly, with less overshoot and expedited settling time. As depicted in Figure (8). The PID controller facilitates the system's transition from a critically damped state to an underdamped state in open-loop settings, thereby optimizing the balance between swift response and minimal overshoot.

The PID controller enhances overall system performance through more precise speed regulation and smoother operation, which are essential for PMSM applications. Adjusting the PID parameters according to motor specifications and control requirements will enhance the system's maximum performance. This study emphasizes the significance of feedback control in motor systems by illustrating the real-time response of the PID controller to variations in motor speed. The PID controller continuously monitors the motor's speed and adjusts the control signal accordingly, thereby stabilizing the system and enhancing its responsiveness.

The comparison of open-loop and closed-loop performance underscores the necessity of employing a controller for accurate and consistent speed regulation in PMSM applications, thereby ensuring the motor operates within its specified range. Particle Swarm Optimization (PSO) was employed to optimize the gains of the PID controller. Inspired by the social behavior of birds flocking and fish schooling, Particle Swarm Optimization (PSO) is an evolutionary algorithm.

The optimal configuration of proportional gain (Kp), integral gain (Ki), and derivative gain (Kd) that minimizes the discrepancy between the reference speed and the actual speed of the PMSM, resulting in an effective control response, was established. A block diagram of a PSO-tuned PID control system for PMSM speed regulation is displayed in Figure(10) By modifying the PID gains in response to feedback on system performance, the PSO algorithm minimizes a specified objective function.

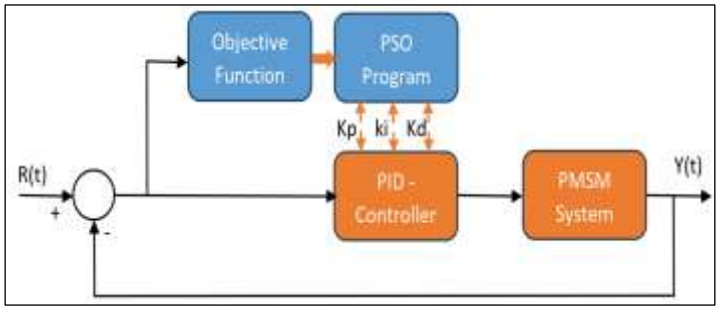

Figure 10: block diagram of PSO-tuned PID control system for PMSM.
Source: Authors, (2025).

In the PSO process, particles (potential solutions) move through the search space, adjusting their positions based on their own experiences and the experiences of neighboring particles. The optimization objective was to minimize the integral of time-weighted absolute error (ITAE) or another similar error metric that quantifies the control system's performance.

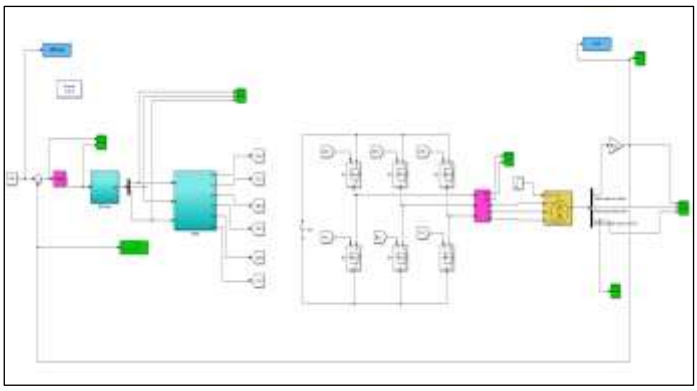

Figure 11: PMSM drive system with PSO-PID Controller.
Source: Authors, (2025).

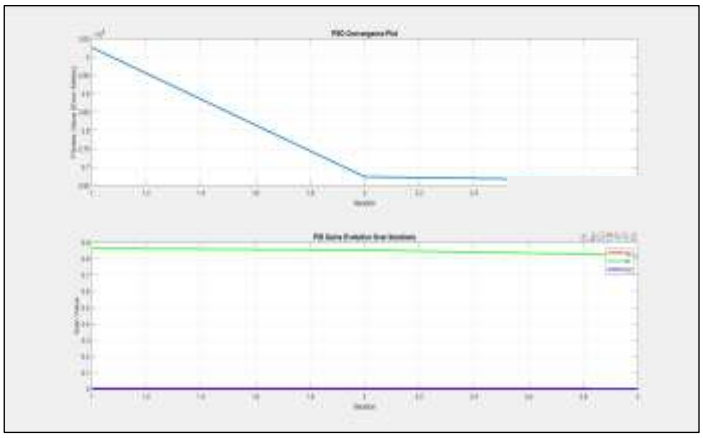

Figure 12: PSO Optimization Results for PID Gains Tuning.
Source: Authors, (2025).

The Particle Swarm Optimization (PSO) results for tuning the PID controller to control the Permanent Magnet Synchronous Motor (PMSM) speed show that the PSO algorithm essentially optimized the PID gains (Kp, Ki, Kd) to minimize the error between the reference speed and the motor's output speed (yout) as shown in Figure (11). The PSO Convergence Plot Figure(12) shows a consistent declining fitness value, therefore validating the effective optimization process.

The PID Gains Evolution Plot shows that while Kp stayed constant after the first adjustments, Ki settled around 0.8 and Kd about 0.0002, and the PID gains stabilized rapidly. Reference speed and motor speed are compared to find that, with some slight oscillations typical of an underdamped system, the motor speed closely after a transitory period follows the reference speed. With minimum steady-state error and regulated transient behavior, the optimized PID controller—tuned by PSO—produced good performance by closely tracking the motor speed from the reference speed.

After applying the PID-PSO (PID controller optimized by Particle Swarm Optimization), the speed response has significantly improved. The waveform now shows a smoother and faster

transition to the desired speed, with minimal overshoot and oscillations. The motor reaches the target speed more quickly, with reduced overshoot and less fluctuation around the steady-state value. This indicates better system control, resulting in a faster settling time, smoother operation, and overall more stable performance. The PID-PSO optimization has thus enhanced both the efficiency and stability of the motor control system.

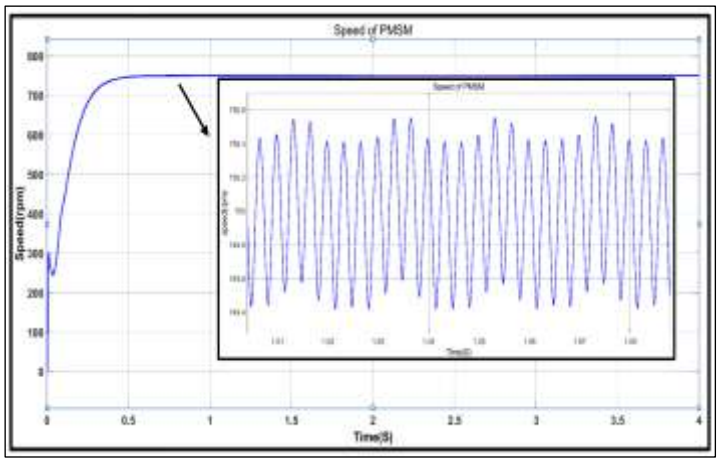

Figure 13: Speed response with PSO-PID Controller.
Source: Authors, (2025).

With a total speed over-shoot of 0.0263%. A low overshoot value indicates that the system responds quickly to changes without excessively exceeding the desired target, which is a sign of a well-tuned system. It ensures stability and minimizes the risk of oscillations, making the system more reliable and efficient in its operation as shown in Figure (13). After applying the PID-PSO optimization, the electromagnetic torque response has significantly improved as well.

The Open-loop waveform shows large fluctuations and oscillations in the torque, indicating instability and poor control. However, in figure(14) after optimization, reveals a much smoother and more stable torque signal. The torque reaches a steady value quickly, with minimal oscillations and fluctuations around the target. This indicates that the PID-PSO optimization has enhanced the torque control by reducing instability, leading to a more efficient and reliable system. The improvements include a faster settling time, reduced overshoot, and a more stable performance overall.

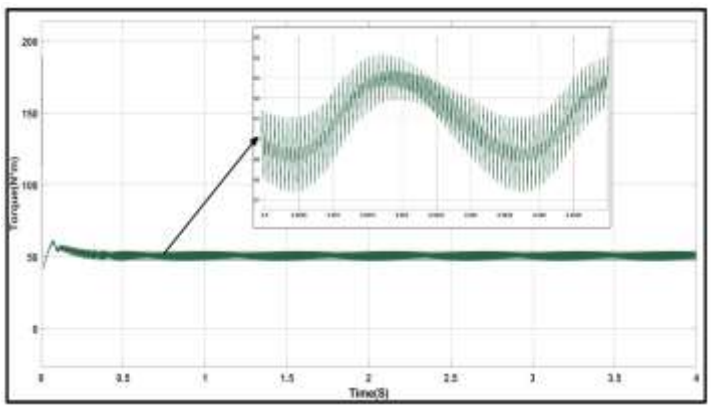

Figure 14: torque response with PSO-PID controller.
Source: Authors, (2025).

The presence of some oscillations in the torque waveform Figure(14) is due to several factors inherent to the system. Firstly, the physical limitations of the motor, such as friction and mechanical imperfections, can introduce small, unavoidable oscillations that cannot be entirely eliminated, even with optimal tuning. Additionally, electrical noise or interference, often generated by the motor or surrounding equipment, can cause minor fluctuations in the torque signal. The non-linear dynamics of the system, where the motor's behavior may change under varying conditions, can also lead to subtle oscillations despite careful optimization. Furthermore, the use of a PWM (Pulse Width Modulation) circuit for motor control can contribute to these oscillations. The switching nature of PWM can introduce high-frequency ripples and voltage variations, which may manifest as slight oscillations in the torque waveform. These factors combined contribute to the persistence of minor oscillations in the system.

ESS Calculation:

The ESS (Steady-State Error) was calculated using the initial PID values and the final values after applying the PSO-PID optimization, based on the equation outlined below. The results obtained from this calculation are as follows:

$$ESS = | {}_{otimizepd}Kp - {}_{initial}Kp | + | {}_{optimized}Ki - {}_{initial}Ki | + | {}_{otimized}Kd - {}_{initial}Kd | \quad .....(9)$$

The initial values of Kp, Ki , and Kd were, respectively, as follows (0.0015 , 0.8 , 0.0006) And the final values of the same parameters after using PSO-PID controller were (0.0029 ,0.65 , 0.0012) so ESS = 0.152 .An ESS value of 0.152 for the PMSM indicates a relatively small steady-state error, which is generally considered acceptable in many applications

Stator Current Response at Constant Load:

In addition to the speed and torque responses, the stator current waveforms for phases a, b, and c at constant load are shown in figure(15)(16) . The currents in each phase exhibit smooth, sinusoidal waveforms, characteristic of steady-state operation in a PMSM. These waveforms indicate that the system has stabilized after initial transients and is now operating under a constant load without significant fluctuations

The currents remain around 200 A for all three phases, reflecting a balanced load distribution across the motor's stator. Figure(15) shows the current waveforms over a longer time span, with consistent oscillations around the steady-state value. This steady current profile is expected in PMSM motors operating at constant load, confirming the system's efficiency and balance figure(16) zooms in to provide a closer view of the current oscillations within one cycle, showing minimal variation and smooth transitions, indicating the motor's stable operating condition. This behavior further confirms that the PSO-PID controller is effectively managing the motor's electrical characteristics to maintain stability and performance, even under constant load conditions

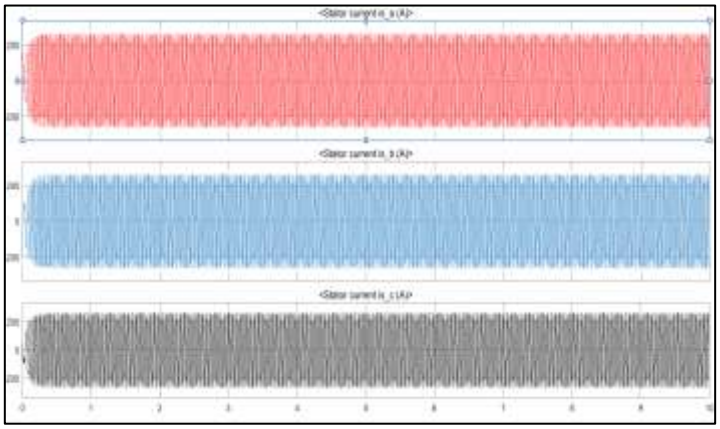

Figure 15: current waveforms.
Source: Authors, (2025).

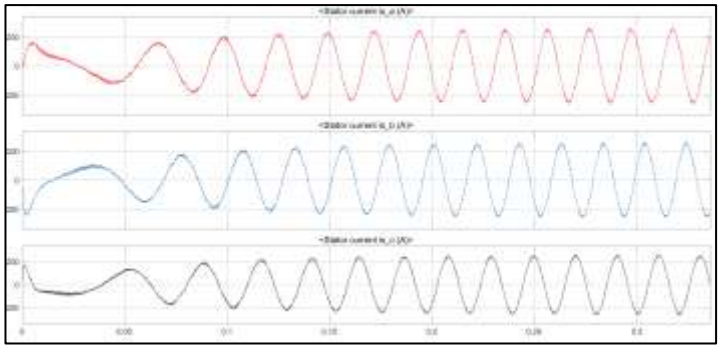

Figure 16: a closer view of the current oscillations within 0.3sec.
Source: Authors, (2025).

PSO-PID Controller and Two step load

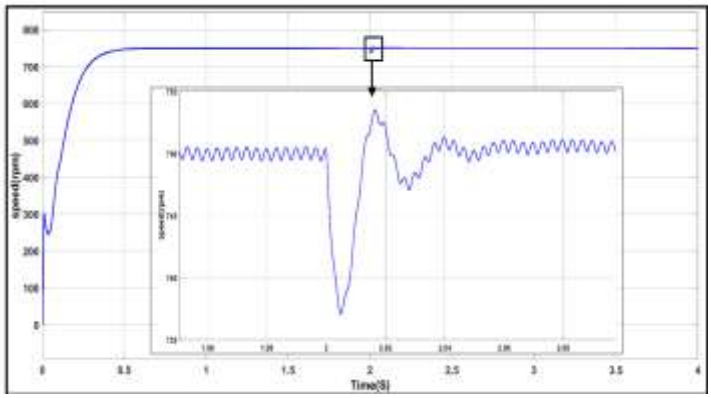

Figure 17: Speed response with PSO-PID Controller and Two step load.
Source: Authors, (2025).

The speed response in Figure (17) shows the behavior of the system with a PSO-PID controller when subjected to a two-step load change. Upon the first load change around 2 seconds, a brief oscillation in the speed is observed as the system reacts to the disturbance. This oscillation can be attributed to the sudden load variation, causing a temporary deviation in the speed. However, the system quickly stabilizes, and the speed returns to its target value.

The settling time after the load change, where the system regains stability, is observed to be approximately 0.06 seconds. Specifically, the speed begins stabilizing around 2 seconds and fully settles by 2.06 seconds, demonstrating a fast and effective recovery of the system from the disturbance with minimal oscillation. This behavior indicates the controller's strong performance in maintaining the desired setpoint even in the presence of sudden load changes

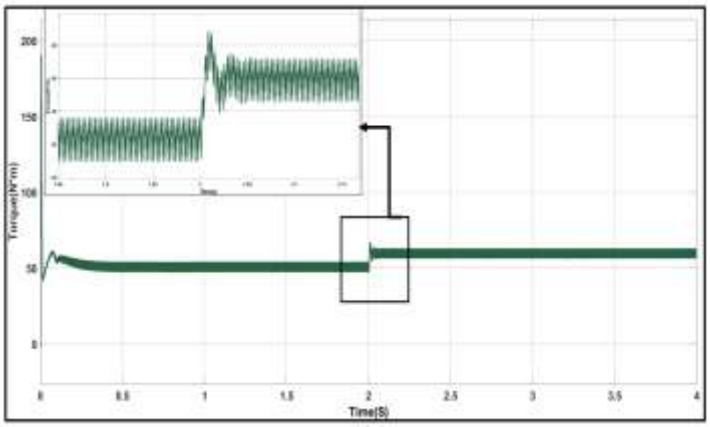

Figure 18: Torque response with PSO-PID Controller and Two step load.
Source: Authors, (2025).

Similarly, in the torque response shown in Figure (18), the system exhibits a sharp spike in torque at exactly 2 seconds due to the load change, followed by oscillations. However, the torque quickly stabilizes and settles back to its target value within about 0.15 seconds by 2.15 seconds. This demonstrates that the PSO-PID controller effectively handles both speed and torque disturbances, ensuring that the system returns to a steady state with minimal fluctuation in both parameters following the load change.

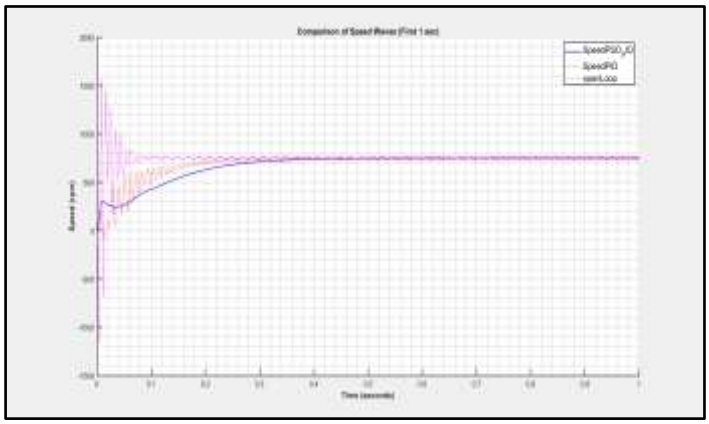

Figure 19: Compression of Speed Waves.
Source: Authors, (2025).

Figure (19) shows three responses from different control systems, with the comparison happening only in the first second. Speed PSO_PID (blue) shows a rapid response and good stability after an initial fluctuation, thanks to the combination of the PSO algorithm with PID control. Speed PID (red) responds more slowly but with excellent stability, showing small oscillations after reaching the desired speed.

In contrast, open Loop (purple) shows an uncontrolled response with large oscillations, as it lacks any form of control, leading to instability. Since the time range was limited to 1 second (X_{lim} [0 1]), the comparison focuses solely on the initial behavior of the systems within this short time frame, highlighting their different response characteristics during the first second after startup.

V. AUTHOR'S CONTRIBUTION

Conceptualization: Ghufran Saad Mohammed and Mohammed Obaid Mustafa.
Methodology: Ghufran Saad Mohammed and Mohammed Obaid Mustafa.
Investigation: Ghufran Saad Mohammed and Mohammed Obaid Mustafa.
Discussion of results: Ghufran Saad Mohammed and Mohammed Obaid Mustafa.
Writing – Original Draft: Ghufran Saad Mohammed and Mohammed Obaid Mustafa.
Writing – Review and Editing: Ghufran Saad Mohammed and Mohammed Obaid Mustafa.
Resources: Ghufran Saad Mohammed and Mohammed Obaid Mustafa.
Supervision: Ghufran Saad Mohammed and Mohammed Obaid Mustafa.
Approval of the final text: Ghufran Saad Mohammed and Mohammed Obaid Mustafa.

VI. REFERENCES

[1] X. Shen (Sherman), L. Mili, and H. Wu, Permanent Magnet Synchronous Machines and Drives: Flux Weakening, Advanced Control Techniques, and Fault Diagnosis. Wiley-IEEE Press, 2020.

[2] Z. Liu and L. Zhang, "Enhanced Torque Ripple Reduction in Permanent Magnet Synchronous Motors Using PI Controllers Integrated with Direct Torque Control," Journal of Electrical Engineering and Technology, 2020.

[3] H. Li, Y. Guo, and Q. Xu, "PMSM Torque Ripple Suppression Method Based on SMA-Optimized ILC," Sensors, vol. 23, no. 23, p. 9317, Dec. 2023.

[4] A. Oubelaid, Y. Berkani, N. Taib, and T. Rekioua, "Speed control and performance analysis of PMSM using Particle Swarm Optimization," International Conference on Applied Automation and Industrial Diagnostics, 2017.

[5] Y. Deng and J. Zhu, "The Improved Particle Swarm Optimization Method: An Efficient Parameter Tuning Method with the Tuning Parameters of a Dual-Motor Active Disturbance Rejection Controller," Entropy, 2023.

[6] J. Smith and L. Zhang, "Challenges in optimizing Permanent Magnet Synchronous Motor (PMSM) performance for speed regulation and energy efficiency," Journal of Electrical Engineering, 2019.

[7] T. Johnson and M. Patel, "Mathematical modeling and control strategies for Permanent Magnet Synchronous Motors," IEEE Transactions on Industrial Electronics, vol. 61, no. 8, pp. 1212-1223, Aug. 2014.

[8] H. Zhao, Z. Wang, and X. Xu, "Modeling of Permanent Magnet Synchronous Motor using the d-q axis reference frame," IEEE Transactions on Power Electronics, vol. 35, no. 2, pp. 229-237, Feb. 2016.

[9] L. Yaohua, Z. Chenghui, Z. Yifan and Q. Yugui, ''Model predictive torque control of PMSM based on data drive'', Energy Reports, Volume 6, Supplement 9, December 2020, P. 1370-1376

[10] F. Zaihidee, S. Mekhilef and M. Mubin , ''Robust Speed Control of PMSM Using Sliding Mode Control (SMC)—A Review, Energies , Volume 12 , Issue 9,May 2019.

[11] S. Wang a, Y. Cao b, T. Huang , Y. Chen, P. Li and S. Wen , "Sliding mode control of neural networks via continuous or periodic sampling event-triggering algorithm", Neural Networks, Volume 121, January 2020, Pages 140-147.

[12] R. Kumar and S. Palani, "Adaptive PID controller tuning using modified PSO method for electric vehicle applications under load variations," International Journal of Electrical and Computer Engineering (IJECE), vol. 10, no. 5, pp. 4857–4865, Oct. 2020.

[13] Y. Chen, L. Zhang, and M. Wang, "A hybrid GA-PSO algorithm for improved optimization accuracy and adaptability," *IEEE Access*, vol. 10, pp. 12345–12354, 2022.

[14] X. Zhao, Y. Liu, and H. Sun, "Fuzzy-PID controller design based on PSO optimization for enhanced system performance," *IEEE Transactions on Industrial Electronics*, vol. 70, no. 4, pp. 3500–3510, Apr. 2023.

[15] Y. Zhang and Q. Li, "Optimal tuning of the Proportional-Integral-Derivative (PID) controller for efficient and stable operation under varying loads and nonlinearities," International Journal of Control Engineering and Applications, 2020.

[16] Mustafa, Mohammed Obaid, Optimal Parameter Values of PID Controller for DC Motor Based on Modified Particle Swarm Optimization With Adaptive Inertia Weight (February 26, 2021). Eastern-European Journal of Enterprise Technologies, 1 (2 (109)), 35-45, 2021. doi. 10.15587/1729-4061.2021.225383, Available at SSRN: https://ssrn.com/abstract=3801063

[17] W. Xu and L. Zhang, "PID control strategy for PWM-based speed regulation in electric motors," International Journal of Electrical Engineering, vol. 40, no. 5, pp. 612-623, 2017.

[18] J. Kennedy and R. Eberhart, "Particle swarm optimization," Proceedings of the IEEE International Conference on Neural Networks, 1995.

[19] M. A. T. F. Sousa, S. Caux, and M. Fadel, "Design of robust PID controllers for PMSM drive with uncertain load inertia," Control Engineering Practice, vol. 23, pp. 1–12, 2022.

[20] Y. Shi and R. C. Eberhart, "A modified particle swarm optimizer," in Proceedings of the IEEE International Conference on Evolutionary Computation, 1998, pp. 69-73.